Assessment of the CORONA series of satellite imagery for landscape archaeology: a case study from the Orontes valley, Syria

Galiatsatos, Nikolaos

Assessment of the CORONA series of satellite imagery for landscape archaeology

A case study from the Orontes valley, Syria

by

Nikolaos Galiatsatos

A thesis presented for the degree of

Doctor of Philosophy

University of Durham

Department of Geography

July 2004

Table of Contents

Index of figures

Index of tables

1. List of abbreviations

ASTER – Advanced Spaceborne Thermal Emission and Reflection radiometer

B/H ratio – Base-to-Height ratio

BTL – Black TeLemetry

CCD – Charged Coupled Device

CIA – Central Intelligence Agency

CMOS – Complementary Metal Oxide Semiconductor

CR – Constant Rotator

DAAC – Distributed Active Archive Centre

DEM – Digital Elevation Model

DGAM – Directorate General of Antiquities and Museums

DGM – Digital Ground Model

DGPS – Differential Global Positioning System

DLR – Deutches Zentrum für Luft- und Raumfahrt (German aerospace centre)

DSM – Digital Surface Model

DTM – Digital Terrain Model

EMR – ElectroMagnetic Radiation

EROS – Earth Resources Observation Systems

ERSC – Environmental Remote Sensing Center

ERTS – Earth Resources Technology Satellite

ETM+ – Enhanced Thematic Mapper plus

FMC – Forward Motion Compensation

FOIA – Freedom Of Information Act

FOV – Field Of View

FWHM – Full Width at Half Maximum

GBP – Great Britain Pounds

GCPs – Ground Control Points

GDS – Ground Data System

GIS – Geographical Information Systems

GLIS – Global Land Information Systems

GORS – General Organisation of Remote Sensing

GPS – Global Positioning System

GRS – Ground Receiving Station

GRS'80 – Geodetic Reference System 1980

GSD – Ground Sample Distance

HRV – High Resolution Visible

HSSF – Hellenic State Scholarship Foundation

HYAC – High Acuity

ICPs – Independent Check Points

IEFP – Instantaneous Equivalent Frame Photograph

IFOV – Instantaneous Field Of View

IMC – Image Motion Compensation

IR – InfraRed

IRS – Indian Remote Sensing satellite

JERS-1 OPS – Japanese Earth Resources Satellite Optical Sensor

JPL – Jet Propulsion Laboratory

KH – KeyHole

LE90 – Absolute Linear Error 90%

LOI – Loss On Ignition

MVA – Multiple-View-Angle

MOMS – Modular Opto-electronic Multispectral Stereo scanner

MSS – MultiSpectral Scanner

NARA – National Archives Record Administration

NASA – National Aeronautics Space Administration

NIIRS – National Imagery Interpretability Rating Scale

NIMA – National Imagery and Mapping Agency

NIR – Near InfraRed

NMAS – National Mapping Accuracy Standards

NPIC – National Photogrammetric Interpretation Centre

NRO – National Reconnaissance Office

NSLRSDA - National Satellite Land Remote Sensing Data Archive

RBV – Return Beam Vidicon

RCPs – Registration Control Points

RFM – Rational Function Model

RMS – Root Mean Square

RPCs – Rational Polynomial Coefficients

RV – Recovery Vehicle

SA – Selective Availability

S/N ratio – Signal-to-Noise ratio

SPOT – Système Pour l'Observation de la Terre

SRTM – Shuttle Radar Topographic Mission

SWIR – ShortWave InfraRed

TIN – Triangulated Irregular Network

TIR – Thermal InfraRed

TM – Thematic Mapper

UTM – Universal Transverse Mercator

USA – United States of America

USD – United States Dollars

USGS – United States Geological Survey

USM – Universal Sensor Model

USSR – Union of Soviet Socialist Republics

UV – UltraViolet

VNIR – Visible to Near InfraRed

The work contained in this thesis has not been submitted elsewhere for any other degree or qualification and that unless otherwise referenced it is the author's own work.

Dedicated to the passing moment…

5. Acknowledgements

A PhD thesis is a lonely work. But it cannot be done without interaction and communication with other people. It also needs money, time, patience, persistence, understanding, and a very strong stomach.

First and foremost than anybody I would like to thank the HSSF (Hellenic State Scholarship Foundation), and in particular Mrs Metaxa. Their offer was more than just financial support. Without the HSSF, this PhD would have never started, and would have never been completed. I am most grateful to these people. I cannot thank them enough.

Fortunately, there is supervision in a PhD, and my research never lacked of it. It was much needed and there was response. Again, no beginning or end would ever be without these people. I would like to thank my supervisors Dr Elli Petsa, Dr Danny Donoghue and Dr Graham Philip for their guidance and patience. Their offer was more than valuable. Many thanks go to Dr Jon Mills and Dr Nick Drake for their thoroughness and detail of scrutiny through examining this thesis. Their comments improved the thesis and resulting papers substantially.

Unfortunately, there were people who suffered because of this PhD. And I would like to thank them for their patience and understanding. Of course, I am referring to my family, relatives, and friends. In particular, many thanks to my father and mother, my sister and brother for their support. Many thanks to my aunt Irini Koutsioumpi, for she was keeping me up-to-date, concerning my homeland's reality. Even more thanks and more than just thanks to Ourania Kloni and Barbara Froner, for their love, which was unrivalled.

For their contribution to my research, thanks go to many people. For their help in the CORONA information, many thanks go to Bill Happel and Ron Ondrejka. For allowing access to the Geomatics lab facilities of University of Newcastle, his help with the photogrammetry software Socet Set and his advice on Photogrammetry many thanks to Dr Jon Mills. For providing the panoramic camera module of Socet Set many thanks to Bob Taft of Leica-Geosystems. For their help in Archaeology information and knowledge exchange, many thanks to Dr Darja Grosman, Dr Graham Philip and Anthony Beck. For providing CORONA documents free of charge, many thanks to FOIA (Freedom Of Information Act) coordinator of the NRO (National Reconnaissance Office). For their help in side-work, many thanks to Derek Coates, Derek Hudspeth,

Terry Harrison, Stella Henderson, the technicians of the department Brian Priestly and Neil Tunstall, and the secretaries Christine Bones and Freda Denby.

I would also like to thank all of my friends who had the patience to stand my emotional fluctuations and stand by me whenever I needed them. Names should not be mentioned because I am afraid of missing someone after all these years in Durham. Thank you very much my friends. I will remember you all!

Also many thanks to people that I forgot to mention at this stage (and I apologise for this), but helped or supported me in any way. I shall be indebted to all of you forever.

1. Introduction

According to Clark *et al.* (1998):

> *"Landscape archaeology is a geographical approach whereby a region is investigated in an integrated manner, studying sites and artefacts not in isolation, but as aspects of living societies that once occupied the landscape"*

In Landscape archaeology, the integration of data such as land cover, land use, vegetation, geology, geomorphology, and the location of major roads and hydrographical features help to provide the context for human activity and evidence of human occupation in the landscape. The spatial context and geographical distribution are important for the interpretation and understanding of the historic landscape. For example, as part of the theoretical framework of landscape archaeology, roadways reflect the interplay among technology, environment, social structure, and the values of a culture (Trombold, 1991). And under certain circumstances, it may be possible to make inferences regarding past environments by interpreting the contemporary landscapes. Gathering such data from the ground might be possible, but often is prohibitively expensive because of the need to collect large amounts of data. Therefore, archaeologists are increasingly interested in effective, objective and cost-effective methods to gather information from the sources such as aerial photography and satellite remote sensing. Aerial photography often provides a mechanism to detect traces of the past like soil and crop marks (Scollar *et al.*, 1990). On the other hand, satellite remote sensing provides environmental and archaeological information over large areas such as patterns in the landscape and field systems. By allowing archaeologists to recognise patterns at different spatial and temporal scales, satellite imagery provides the means for moving from local to regional and from static to dynamic descriptions of the landscape (Kouchoukos, 2001).

In many countries the aerial photography coverage is poor or not available to the public. However, in 1995, the USA announced the declassification of satellite photography from reconnaissance military satellites. This satellite photography was collected in 1960-1972 during the CORONA project missions. It evolved in six different designs, from which the sixth (1967-1972) reached a level of detail of two meters. This is equal to the detail provided by a conventional 1:50,000 aerial

photography (Slama *et al.*, 1980)[1], and not 1:10,000 like Goossens *et al.* (2000) report. This satellite photography is easily accessible through the World Wide Web, it has a low cost and each scene covers an area of 200x15 km^2 approximately. Importantly, it has worldwide coverage, which means that it can be used instead of aerial photography in countries where aerial photography is not adequate or simply absent.

Digital satellite imagery goes back to 1972 (Landsat MSS), but the level of detail it provides is not appropriate for archaeology or landscape assessment. In 1984, the TM sensor enhanced the capability of the Landsat satellite series but its principal benefit is to give environmental data. September 1999 saw the launch of the first civilian earth resources satellite to provide high spatial resolution, named IKONOS. This satellite can provide detail up to one-meter ground resolution in panchromatic mode and four meters in multispectral mode. This satellite imagery is comparable to aerial photography, and will prove useful for mapping in countries where aerial photography is not readily available. According to Gerlach (2000), it satisfies the National Mapping Accuracy Standards (NMAS) to the scale of 1:2,400. Also, its spatial resolution is similar to CORONA; that is of the same spatial scale. Therefore, it should be possible to detect landscape change to a good level of detail from the analysis of CORONA in conjunction with IKONOS, and later high-resolution sensors such as EROS, Quickbird and Orbview.

The combination of CORONA and IKONOS has never been evaluated for archaeological landscape assessment in the Middle East and so there are very few publications about their use. There are a few publications that illustrate declassified photography, such as Kennedy (1998) and Fowler (1996), but they just illustrated rather than analysed the data. Many archaeologists are interested in using CORONA to help with fieldwork. However, most archaeologists have no experience with satellite data. In Oriental Institute of the University of Chicago, they use declassified photography for their research in western Syria and Iraq (Wilkinson *et al.*, 2001) but they have problems in understanding the photography (Wilkinson, 2000a). Moreover, they use a less elaborate method without control of the accuracy (Ur, 2003), and with more focus on the archaeological imagery interpretation (Ur, 2002). Wilkinson (2003) recognises the value of satellite remote sensing for landscape archaeology studies, and he highlights the need for the application of archaeological remote sensing in the Middle East because very few studies are currently published.

[1] A new edition (fifth) of the manual of photogrammetry is published on 20th July 2004 (McGlone *et al.*, 2004).

Non-archaeology applications of CORONA data include monitoring of land use, land cover and natural resource changes in desertification-prone Sahelian countries over a period that spans 4 decades (USGS, 2004b; Tappan ***et al.***, 2000). Also, the department of Anthropology of the University of California, Santa Barbara, is using CORONA imagery to investigate the distribution of Yanomamö settlements in the Amazon region (Craig, 2004).

The main benefits that this research has to offer are: First, to study the characteristics of the satellite imagery in detail, in particular the spatial resolution and geometric distortions. Secondly, to address questions such as how and in what context can such data be used effectively to assist in the study of landscape archaeology? For example, what kind of digital enhancements may be applied for best interpretability and why? Last but not least, by use of a case study to demonstrate how can these data be used in a practical application? This includes overlay and comparison with other survey data using GIS. IKONOS is the first of a series of new high-resolution satellites to come, and so it is vital to appreciate the characteristics of data such as CORONA imagery in order to take full advantage of the possibilities of using the new imagery, i.e. in change detection applications.

1.1. Aims and Objectives of the research

This research project aims to assess the CORONA series of satellite imagery in landscape archaeology applications and to help elucidate the structure and processes of the Middle East landscape through the use of historical and new high resolution satellite imagery. This will be achieved by studying the Homs region in Syria where a landscape archaeological project is ongoing and where the author will be able to draw on other data such as archaeological evidence to support this research. To fulfil these aims, the project has to proceed through a number of steps linked to the objectives of this research.

The principal objectives of this research project are:

- To investigate the characteristics of the CORONA series of satellite imagery, in order to assess its potential for application in landscape archaeology.
- To use a specific case study to demonstrate how CORONA and IKONOS satellite imagery could assist with archaeological landscape research.

Further objectives are:

- To review the literature and select the satellite sensors appropriate to assist in the assessment of CORONA in landscape archaeology applications. Particular attention is given to the problems of mapping landscapes in the Middle East. For technical details on the satellites, see Appendix I.
- To develop a full understanding of the technical characteristics of the CORONA series of satellite imagery, so as to understand the errors and the distortions (hence understand the limitations).
- To develop a methodology for processing and integrating different data sets together to assist with their interpretation. The methodology includes gathering and processing of reference data such as maps and the ground truth data such as field measurements. Literature searches helped to identify the most appropriate techniques in landscape archaeology applications.
- To evaluate the radiometric and spectral characteristics of the satellite data. This was achieved by combining field survey results with interpretation from satellite data. Fieldwork was undertaken in September-October 2000 and 2002.
- To assess the potential of off-nadir view angle characteristics of the satellite data. In particular, to investigate the effect of different view angle data on image interpretation and most importantly to evaluate the height information that can be extracted from stereopairs. The resulting digital elevation models are qualitatively and quantitatively assessed.

1.2. The study area

The study area (figures 1-1 and 1-2) is the section of Orontes valley between the cities of Homs and Hama. It extends south of Homs covering a total area of approximately 700 km^2. This area was chosen for several reasons. First, it is an area with great potential for archaeological sites but it is not fully explored. Then, it is an area of intense human activities and development such as agriculture, irrigation and urban expansion. The geomorphology of the area varies significantly with basalt in the west, marls in the south and alluvial material along the river. This will allow the assessment of remotely sensed data in three different geomorphological contexts. Also, in western Syria there has been little acknowledgement of the complexity and sheer diversity of ancient Syrian landscapes, within which the archaeological sites are simply one element. Last but not least, it is a test area where a methodology can be developed

that has the potential to be applied through many parts of the developing world where archaeological resource is currently very poorly documented.

There are more things to be identified in the specific study area. Studying images through a time series from the 1960s to the present day will help to understand the dynamics of the area such as the land cover change, and provide more information about the human intervention in the environment. A lot has been written about Syria and the Orontes valley, covering topics such as geology, geomorphology and archaeology. Unfortunately, most books are not in the English language.

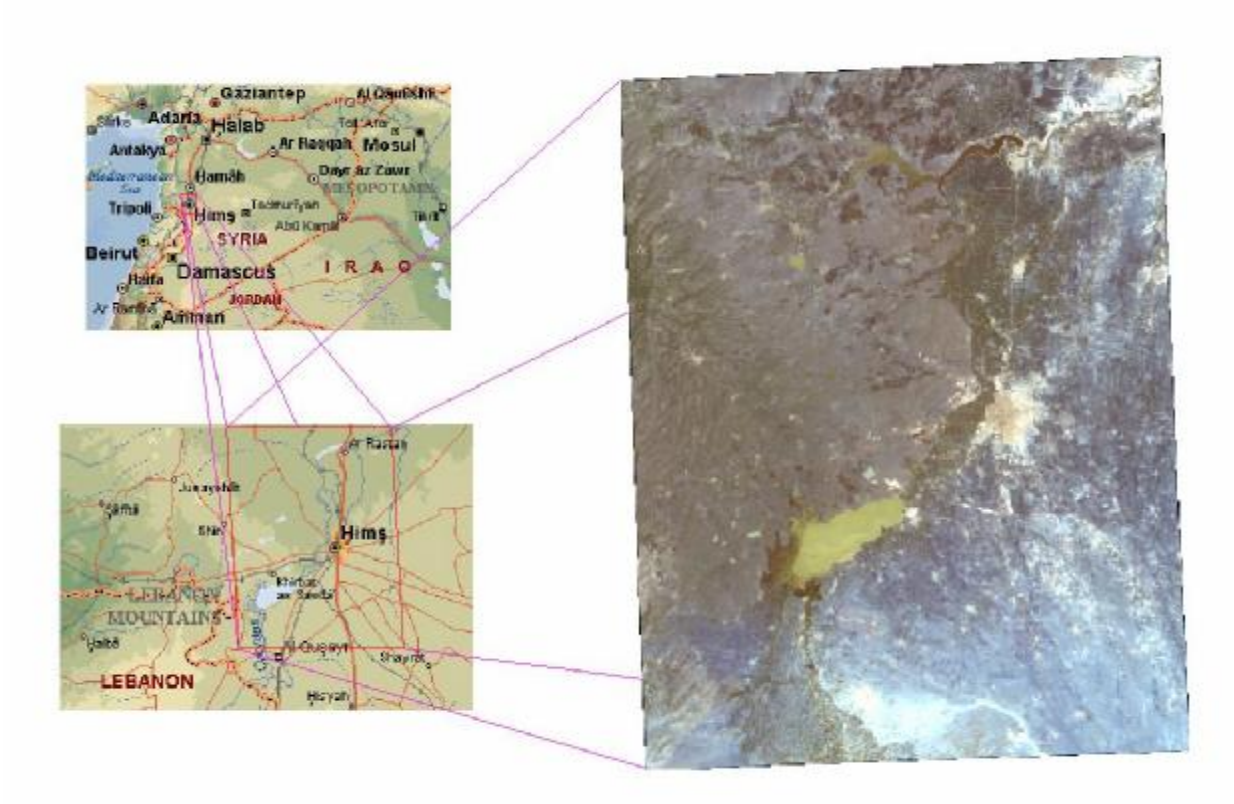

Figure 1-1 – The study area.

1.3. Types of archaeological sites in the area of interest

The types of archaeological sites in the area of interest vary according to the existing landscape. The three main landscapes along with examples from sites of archaeological interest are presented in chapter 5.

Figure 1-2 shows the boundary of the area of interest, clearly separating the study area into north and south parts. In the west of the north part, the main landscape is comprised of a large network of fields and cairns made of basalt stone. The top picture in figure 1-2 shows the way changes are being done to this landscape and highlights the

historical value of CORONA data for the archaeological records. The east part of the north area is comprised of cultivations and alluvium landscape. As seen in the second picture, vegetation covers all the area, and sites of archaeological interest may be identified from height or shape characteristics.

Most of the southern area is comprised of marls and is generally not covered by vegetation. However, the areas near the river Orontes (west part of south area), near lake Qatina (north west part of south area), and near Homs city (north part of south area, irrigated land) are dominated by cultivation and look like the second picture. The main archaeological sites in the south area are of two types. The *tell* looks like a small hill and stands out nicely on the flat landscape (third picture). The *khirbet* is like a flat tell (fourth picture). It has similar colour hue and soil consistency. It can be easily detected in the imagery because it has a brighter response than the surrounding soil.

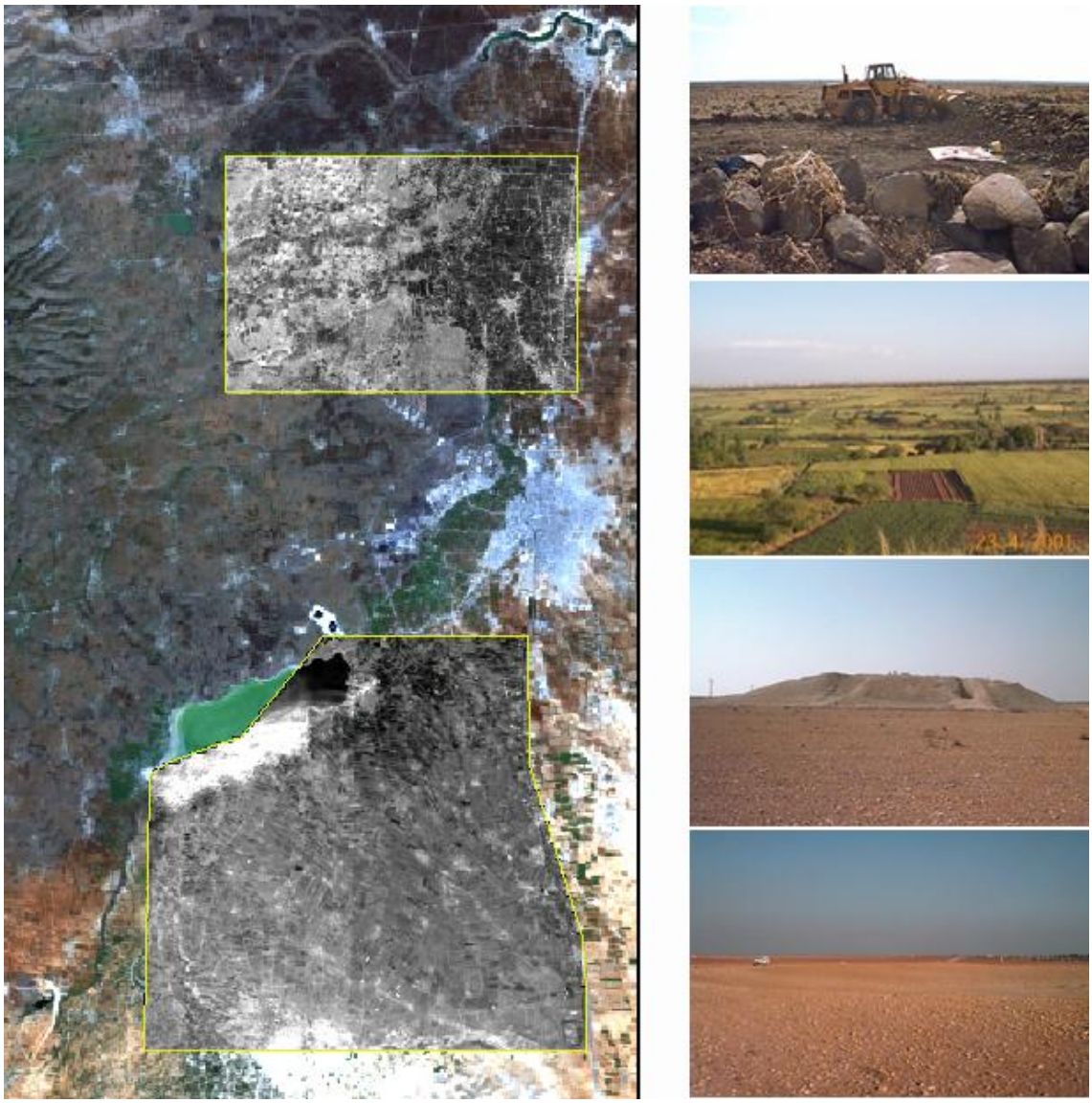

Figure 1-2 – The area of interest and the different landscapes within it.

1.4. The Homs project

While the value of satellite imagery to archaeology is increasingly apparent, most current applications are centred around its use for environmental reconstruction (e.g. Oštir *et al.*, 1999; Marcolongo & Barisano, 2000). Because of the relatively low resolution of the most satellite imagery (e.g. 30 m for Landsat multispectral data), these are of limited applicability for the identification of individual archaeological features (Kennedy, 1998). The resolution issue may explain why there are so few publications which document the systematic use of satellite imagery in the context of archaeological survey in the Mediterranean and Middle East (Sarris & Jones, 2000; Wilkinson, 2000b).

Landsat imagery has been used to help identify settlements and 'linear hollows' around sites in the Jazira of north Iraq (Wilkinson & Tucker, 1995), and alongside SPOT panchromatic data (10m resolution) to identify south Mesopotamian tell-sites and ancient irrigation canals previously known from air-photographs (Verhoeven & Dales, 1994). However, the effectiveness of satellite imagery alone for the identification of archaeological features remains uncertain because latter report while referring to sites as small as 1 Ha in area (Verhoeven & Dales, 1994), does not make it clear by which of these means the smaller sites were, in fact, identified.

The declassification of military satellite photography in recent years offers researchers access to products of far higher resolution. Fowler (1996) claims that KVR data produced a panchromatic image that was 'comparable in detail with medium-scale air-photography'. The value of such data for archaeologists working in parts of the world where detailed map data and good air-photographic data are unavailable is obvious (Kennedy, 1998; Philip *et al.*, 2002a).

Settlement and Landscape Development in the Homs Region, Syria is a joint Syrian-British co-operative project organized by the University of Durham and the Directorate General of Antiquities and Museums (DGAM), Syria. It is a multidisciplinary regional project designed to take a long-term perspective on the relationship between human activity and landscape development in the upper Orontes Valley (Philip *et al.*, 2002b). As such, the effective identification of hitherto undocumented loci of past human activity is of prime importance.

The study area consists of a northern and a southern unit, with a combined area of around 700 km^2. Preliminary assessment in 1998 indicated the presence alongside classic tell sites, most of which appeared on the current Syrian 1:50,000 maps, of numerous low mounds and flat sites indicated by surface artefact scatters. A significant proportion of those observed in 1998 did not appear on the maps, suggesting that they were significantly underrepresented within the extant information base. As there had been little previous archaeological survey work in the area west of Homs, and neither aerial-photography nor topographic mapping at scales greater than 1:50,000 were available, the Homs project required a means of targeting ground survey, and so increasing the rate at which an overall impression of the quantity, nature and distribution of archaeological remains could be obtained. A potential solution appeared to lie in the recently declassified CORONA imagery.

The project will contribute to the broader research objectives by providing the necessary information needed for ground truth support of the satellite imagery. On the other hand, this research will provide an appraisal of the potential of remote sensing for landscape and site assessment. It will also provide information obtained from the satellite photography and imagery.

The Homs project includes other researches that cover different parts of the whole project. Through the Homs project, there is an opportunity to share data among researchers in the same area and such use is acknowledged in the thesis.

1.5. Data

The data can be separated into two broad headings: the satellite data (Table 1-1) and the reference data (maps, survey, etc). The satellite data of interest are CORONA, IKONOS and Landsat data. They are assessed for their strengths and weaknesses in Landscape archaeology applications through the case study of the Orontes valley area in Syria.

Table 1-1 – Summary of satellite data used in study

Sensor	ID-scene	Date
CORONA	DS1108-2203DA042, –043, –044, -045	17 December 1969
	DS1110-1106DF007, -008, -009	28 May 1970
	DS1110-1106DA013, -014, -015	28 May 1970
	DS1111-2135DA001, -002	31 July 1970
HEXAGON	DZB1210-500148L010001, frame 10	15 July 1975
	DZB1210-500148L010001, frame 11	15 July 1975
Landsat 5 TM	LT5174036008714610	26 May 1987
	LT5174036008727410	1 October 1987
Landsat 7 ETM+	LE7174036000001450	14 January 2000
	LE7174036000030250	28 October 2000
ASTER DEM	SC:AST14DEM.003:2005910150	28 October 2000
	SC:AST14DEM.003:2006359665	12 January 2002
IKONOS	2000090508090020000010501090	05 September 2000
	2002020308234080000011610756, -7	03 February 2002

In every project, the existing data define the processing that can be applied. This research project was not an exception to the rule. The starting data were the maps, the CORONA 1110, frames 007, 008, 009 of forward camera, and the Landsat 5 TM imagery. The first year of the project was concerned with the data integration problem. This means translation of the data to digital format (scanning of film, digitizing of maps), and geocorrection to the Syrian coordinate system.

During the second year, more CORONA films were purchased from different seasons, thus increasing the existing information that can be extracted by photointerpretation. Also, the purchasing of the CORONA 1110, 013, 014, 015 frames of the aft camera provided the opportunity for the creation of stereomodel for the extraction of height information.

After the purchase of IKONOS imagery at the end of the third year of this research project, the integration of data took place. This gave a boost to the project. It helped to the creation of the stereomodel, and the bringing together of all other satellite data by registration to the IKONOS imagery. Hexagon and ASTER data were purchased much later and they helped in the definition of future directions, and the establishment of particular points within the text.

The most basic step of the assessment is considered to be the full exploration of CORONA and IKONOS images from their "original" form to the point at which they will be interpreted by the end user. This is a very difficult task because on one hand the CORONA imagery has not been explored in such depth by anyone before, and it is still surrounded in secrecy because of its role in U.S. (United States) intelligence. On the other hand, SpaceImaging Inc. (the IKONOS owner) does not provide to the public the full technical details of the satellite. Landsat TM is a well-documented high quality medium resolution sensor (Markham and Barker, 1985, Salomonson, 1984, Townsend *et al.*, 1987) that has been used extensively for land cover and other mapping applications. For detailed technical information on satellite and reference data, see Appendix 1.

1.6. Methodology

1.6.1. Preprocessing

Despite the fact that some satellite data corrections are carried out at the GRS (Ground Receiving Station) there is often still a need on the part of the user for some further processing. The preprocessing techniques are applied on "raw" data so as to create a consistent and reliable image database. The main steps in preprocessing include radiometric calibration, geometric correction, noise removal and output to a final format to a standard prescription (Schowengerdt, 1997; Jensen, 1996).

For this study the CORONA photography was converted to digital format. Digitising is the technique to transfer data from an analogue form to a digital format in order that

the data can be electronically processed and analysed. The original analogue data can then be preserved in a safe place for future reference. The digitising of CORONA photography will be explored in order to identify the best optical digitising resolution with the least loss of interpretability and the minimum expense for the user. Various types of scanners were tested and assessed. For information on scanning techniques see Georgopoulos (1998), Baltsavias and Waegli (1996).

For the geometric correction there is need to define a projection system and a common map reference. The available maps of the area had a scale of 1:25,000. The information on the maps was digitised into a vector format and geometrically corrected for use in GIS software. The poor quality of the maps only allowed for their use as a reference point. This was an effort to combine them with the rest of the data for better feature identification. Initially, the Landsat and CORONA data were registered to the coordinate system of the maps.

After the purchase of IKONOS, all data were registered to its coordinate system, and thus the project moved from the Syrian coordinate system of the unknown parameters and integrity, to the World Geodetic System (WGS'84).

1.6.2. Image Processing

When an image is available in digital form, several approaches are possible in order to extract information from it. Richards and Jia (1999) distinguish two main complementary approaches; photointerpretation (or image interpretation) where the analyst extracts information according to his experience and ability to interpret; and quantitative analysis where the computer is used to examine each pixel individually and make judgements according to its attributes. Of course, each approach has its own role in image processing and so the user chooses the best approach to attain the objective of the application.

The image interpretation approach uses geometric and radiometric enhancement techniques. Radiometric enhancement techniques include contrast enhancement, histogram equalisation, histogram matching, and density scaling. Geometric enhancement techniques include filtering, edge detection, spatial derivative, and line and shape detection.

An image can be transformed to generate new sets of image components or bands, which may represent an alternative description of the data in linear connection with the original data. Image transformations are a useful method of image enhancement. They

may also be applied for the preconditioning of the image data prior to quantitative analysis. Some image transformations include principal components, spectral and spatial filtering, image arithmetic, band ratios, vegetation indices, and the specialised Kauth-Thomas tasselled cap transformation.

The quantitative analysis approach uses classification techniques for the analysis of the image. These include supervised classification techniques like maximum likelihood, Mahalanobis, minimum distance, parallelepiped, and unsupervised classification techniques based on various algorithms. For more information on image processing see Richards and Jia (1999), Schowengerdt (1997) or Jensen (1996).

The outcome of the image processing will be images that can provide an alternative representation and generalisation of the landscape to that given by maps. Maps always include the mapmaker's selection of what is important to represent. Remotely sensed data can offer a check on what is depicted on maps, show additional information, and sometimes provide a useful alternative thematic perspective (Liverman *et al.*, 1998).

1.6.3. Fieldwork

Fieldwork took place from August to October 2000. The main purpose of the fieldwork was to enhance understanding of the area, gather the necessary data for the image processing, evaluate the photointerpretation-identified sites, and enable discussions with local people. It also included handheld Global Positioning System (GPS) measurements, ground survey and ground spectral measurements.

This was the first ever contact with the area of interest and it proved helpful for understanding what the images show, and comprehend their limits. It also proved the need for a basemap that will be compatible to the GPS receivers for reliable navigation within the area of interest. The lack of compatibility between the maps coordinate system and the GPS receivers led to ambiguities and inaccuracies during the identification of photointerpreted sites of archaeological interest. The ambiguity was lessened by the use of simple coordinate transformations between the two coordinate systems (the maps and the GPS receiver).

The local population was very friendly and helped into the better understanding of the landscape through simple discussions concerning their farming practices and their problems with the land. They also helped to speed up the identification of the sites by providing directions, thus there was less disturbance with the navigation problem.

Furthermore, an effort took place for the establishment of a GPS network through a "pseudo-kinematic"[2] approach. The high state security measures within Syria did not allow for an extended time of measurements, thus all measurements were not longer than one or two minutes. It also did not allow for the establishment of a Differential GPS (DGPS) network.

Last but not least, field spectroradiometry measurements were taken across the sites of interest. The intention is the identification of differences in reflectance between on-site and off-site soil. For practical reasons, almost all field spectroradiometry took place to the south area of interest.

During October 2002, the Homs project group gathered soil samples across the sites and DGPS points from soft detail points. The soil samples were not intended for this research, but it was a chance to proceed with more analysis. Thus, after borrowing a small part of the sample, the research proceeded to laboratory spectroradiometry, particle size and organic content measurements for further understanding of the difference between off-site and on-site soil.

The DGPS points were not from hard-points, thus they could not be used for image geocorrection or as independent checkpoints. However, they were helpful for height comparisons and the digital elevation model (DEM) assessment in chapter 8.

[2] Explained further in section 4.3.2

1.7. Methodology diagram

The table 1-2 shows the structure of the PhD thesis and the methodology followed to achieve the initial objectives.

Table 1-2 – Structure of the PhD thesis

Stage	General approach	Detailed approach
Introduction	Rationale Outline objectives Study area	
CORONA data	Spatial resolution Spectral range Data quality CORONA mechanism	The panoramic principle The designs Guidance and control Ascent and recovery Acquiring CORONA CORONA reports Technical characteristics
Placement of CORONA among other satellite data of the project	Merits and problems Collaboration	Landsat TM & ETM+ IKONOS II TERRA (ASTER sensor) Hexagon
Preprocessing stage	Image rectification Image resampling	Scanning CORONA geometry The basemap problem The in-field navigation problem Data integration in GIS
Qualitative assessment	Photointerpretation	Photointerpretation principles Photointerpretation basics Archaeological approach Landscape influence Analysis
Spectral assessment	CORONA properties Properties of onsite soil	Field spectroradiometry View-angle factor Laboratory spectroradiometry Particle size, Organic content Identification of correlation
Quantitative assessment	Creation of stereopairs	Rigorous panoramic camera approach Empirical non-metric camera approach
	DEM extraction	Qualitative assessment of DEM Quantitative assessment of DEM
Conclusions/Discussion	CORONA Landscape archaeology Summary Future directions	

1.8. Summary of the PhD thesis

The main purpose of the PhD is to assess the CORONA series of satellite imagery in landscape archaeology applications. Thus, chapter 2 discusses the quality of the CORONA data by looking into the mechanics of the camera system and its parts, and by studying the spatial and spectral properties of the CORONA imagery. Chapter 2 also discusses the CORONA imagery acquisition, which is very different from any known satellite to date.

After the assessment of the CORONA program itself from a photogrammetrist point of interest, the CORONA data must be placed among the other satellite data used in the project. Thus, chapter 3 discusses the merits and problems associated with each source of data, and use of multi-sensor data. Chapter 3 also gives details about the other satellite data used in the project.

A very important stage for every project is the preprocessing stage, where the data must be either geocorrected or co-registered. Chapter 4 describes the processes of image rectification and resampling. In chapter 4, all data must be translated to a common format for later integration into a geographical information system. The optimum method of image scanning is presented and the difficulties of CORONA geometry are discussed. The advantages of data integration under a common basemap are also presented. Last but not least, chapter 4 discusses an approach for navigation within the area of interest when the parameters of the coordinate system of the existing data are unknown.

In chapter 5 CORONA data are assessed qualitatively using a photointerpretation approach. The photointerpretation principles and basics are presented to help the reader understand the mentality of the original image analysts, and to see the advantages and disadvantages of the digital approach. All examples are presented with focus on archaeological applications, and the role of the landscape geomorphology and background is discussed. The importance of all the work presented in previous chapters for the processing is highlighted.

During the photointerpretation, the majority of sites of archaeological interest in the marls area presented brighter colour hue than the surrounding soil. In order to understand why this appears to happen, the on-field reflected radiance of the on-site soil in contrast to the off-site soil is researched, along with a further analysis of the radiometric properties of CORONA. The bidirectional reflectance may play a role, and

for this reason view angle effects are studied in CORONA and IKONOS data. After sampling of on-site and off-site soil, the samples are checked for their reflected radiance, the particle size and the organic content, for the detection of correlations that may help to understand the question of site identification.

Chapters 7 and 8 represent a quantitative assessment for the CORONA data. In chapter 7, the creation of stereomodels from CORONA data is discussed using two main approaches, the rigorous panoramic camera approach with a ready software model, and the empirical non-metric camera approach. Chapter 7 also discusses the possibility of creating a stereopair between two IKONOS images or CORONA-IKONOS images, along with the advantages and the difficulties of such an approach.

Chapter 8 presents the automatic and the manual extraction of a digital elevation model from the CORONA triangulation that is achieved in chapter 7. The extracted DEM is assessed qualitatively by contrast to ASTER relative DEM and SRTM-3 DEM. Quantitatively it is assessed in relation to DGPS points taken from soft detail points of the area of interest. Problems with the extracted DEM are presented and researched by going backwards in the process to identify the source.

Chapter 9 summarises the objectives of this PhD and proceeds to discuss on progress on technical understanding of CORONA, and the application of CORONA for landscape assessment. The final conclusions are summarised and future directions are outlined.

Further to the main chapters of the thesis, five appendices are included for the reader. Appendix I presents all data of the project along with their metadata and thumbnails of the satellite imagery. Appendix II describes how to get a duplicate of the original CORONA films that are in NARA (National Archives Record Administration). It also describes how to get access to part of the CORONA reports from NRO library. Appendix III presents rigorous panoramic models from 1980 and 1967 that give solutions to the problem of the CORONA geometry. Appendix IV includes the technical specifications of the instruments used in the project, and in particular the handheld GPS receiver, the spectroradiometer and the photogrammetric scanner. Appendix V includes all the registration tables for CORONA and the triangulation reports from the creation of the DEM.

2. Understanding CORONA data

The first proposal for using a rocket as a photographic platform was made by Rahrmann in 1891. The idea became reality when in 1912 Maul developed a gyro-stabilised camera mounted on a rocket. In 1946, V-2 rockets obtained the first pictures from space. In 1957, the USSR put the first satellite, Sputnik 1 into orbit and the era of satellite remote sensing began with the first systematic satellite observation of the Earth by the meteorological satellite TIROS-1 in 1960. This was a meteorological satellite, designed for weather forecasting.

In the same year, the first photo-reconnaissance satellite emerged from the U.S. military under the secret CORONA project (1958–1972). While civilian satellites evolved along the lines of the multispectral concept with the advent of ERTS-1 or Landsat-1 in 1972, the military reconnaissance satellites proceeded to use higher resolution imagery and follow a very different path (Richelson, 1999).

After 1972, several satellite sensor systems similar to Landsat were launched such as SPOT HRV and the Indian Liss. Other highlights in the history of satellite remote sensing include the insertion of radar systems into space, the proliferation of weather satellites, a series of specialised devices dealing with environmental monitoring or with thermal and passive microwave sensors, and the more recent hyperspectral sensors.

In 1994, the US government approved the development and deployment of 'down to one metre' ground resolution sensors for commercial satellites and in 1995 data from the CORONA military project with 2 metres resolution was declassified. The first commercial high-resolution satellite to be launched successfully was IKONOS in 1999. In 2001, the approved ground resolution for commercial satellites decreased to 0.5 metres, thus preparing the ground for more declassification and more high-resolution satellites in the forthcoming years. This indeed started with the Quickbird commercial satellite (0.61 m) and the declassification of the KH-7 GAMBIT space photography (0.6-1.2 m).

2.1. CORONA space photography

CORONA was a program designed to support U.S. Intelligence between 1958 and 1972. It officially started with a formal endorsement by President Dwight E. Eisenhower on 8th February 1958. The "CORONA" name came after a meeting on 15th March of the same year. There are no minutes for this meeting (Hall, 1997).

The launch operations began on 25th June 1959. On 10th August 1960, the diagnostic mission was successful, and 2 days later, on 12th August, the capsule for the film was "recovered undamaged". After eight failures in photoreconnaissance, the first successful mission occurred on 18th August 1960 when the first CORONA image of an intelligence target was acquired during Mission 9009 (McDonald, 1995).

The camera carried on that Mission would be retrospectively designated the KH-1 (KH for KeyHole). The next successful CORONA Mission would be conducted on 7th December 1960. This time a more advanced camera system, the KH-2, was on board. From that time, through to the end of the CORONA program in 1972, there was a succession of new camera systems – the KH-3, KH-4, KH-4A and KH-4B (Richelson, 1999). In the end, CORONA acquired over 800,000 frames of photographs with a total coverage of at least 600 to 750 million nmi^2 (square nautical miles) of the Earth's surface. On 22nd February 1995, President Clinton signed the Executive Order 12951 that declassified those images (Clinton, 1995a). Furthermore, the President delegated any future declassification approval to the Director of Defence and State. However, the Executive Order 12951 addresses only the imagery declassification. Other declassification (e.g. CORONA reports) falls under Executive Order 12958 (17th April 1995)[3] (Clinton, 1995b).

2.1.1. Two principles used in the CORONA cameras.

The first principle was the panoramic principle, which was first demonstrated in the 1840's. If a lens is rotated about an axis through its second nodal point, the image of a distant object does not move. This principle was first applied to the predecessor of CORONA, the HYAC (for "high aquity") camera (see paragraph 2.1.2).

[3] Amended by Executive Order 13292 (25th March 2003) (Bush, 2003).

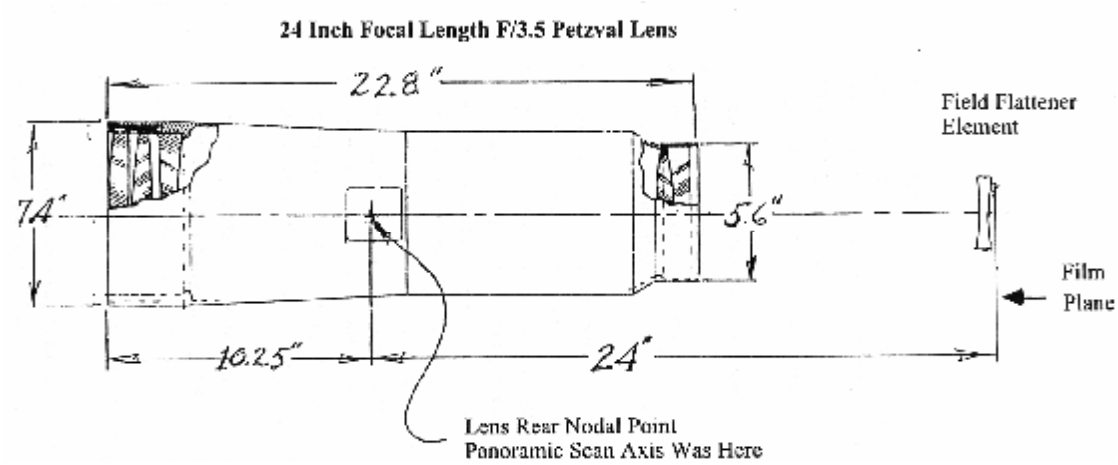

Figure 2-1 – The CORONA Petzval lens design (Madden, 1996)

The second principle was the lens form named Petzval after Josef Petzval who invented it in 1839. The classic lens consists of two widely separated doublet lenses each with positive power and each separately achromatised (Sinclair Optics Inc., 1997). The original Petzval Portrait lens used a cemented doublet and air-spaced doublet, but the term Petzval lens is now generally applied to lenses containing two separate groups (usually doublets) in which both groups contribute positive power. The version used in CORONA consisted of five elements in a three-two configuration plus a field flattening narrow lens at the slit. For more details on the Petzval form of lens used on CORONA, see paragraphs 2.1.3 and 2.1.7.

2.1.2. The HYAC panoramic camera

The panoramic design is an effort to combine high resolution and a wide swath width in one camera. To achieve this, it incorporates a narrow-angle fast lens system where only the portion of lens system, which is on or near the optical axis, is employed in photo imaging. This lens system scans through an angle across the direction of flight, and the film is advanced parallel to the direction of scanning at rates compatible with the vehicle ground speed in order to obtain continuity of coverage along the flight path. The fact that coverage along the flight path is related to the camera's cycling rate suggests that panoramic cameras are best suited for high-altitude missions (Slama *et al.*, 1980).

In 1957, a direct-scanning panoramic camera was incorporated, HYAC. It was the first camera to achieve the goal of 100 lp/mm from high altitude (up to 30,000 m on SO

1213 film). It scanned 120° with 12'' (30.48 cm) focal length on f/5 triplet. The film was stationary on a cylindrical focal surface (figures 2-2 & 2-3).

The lens rotates around its rear nodal point and the film is positioned in the proper focal plane location by means of the two small rollers mounted on the end of a scan arm, which rotates with the lens and carries the scanning slit. The width of this slit determines the amount of exposure, since the lens sweep at a different rate. It should be noted that in the direction scan, only the lens and scan arm move, while the film remains stationary. Also, since the centre of the lens rotates as a unit with the slit, the sharpest possible image is always projected onto the film.

Two main reasons determined the choice of panoramic camera system in CORONA. It could provide high resolution and large swath width, two ideal properties for photo-reconnaissance from space. In the following paragraphs, the evolution of CORONA program is presented through the different satellite system designs.

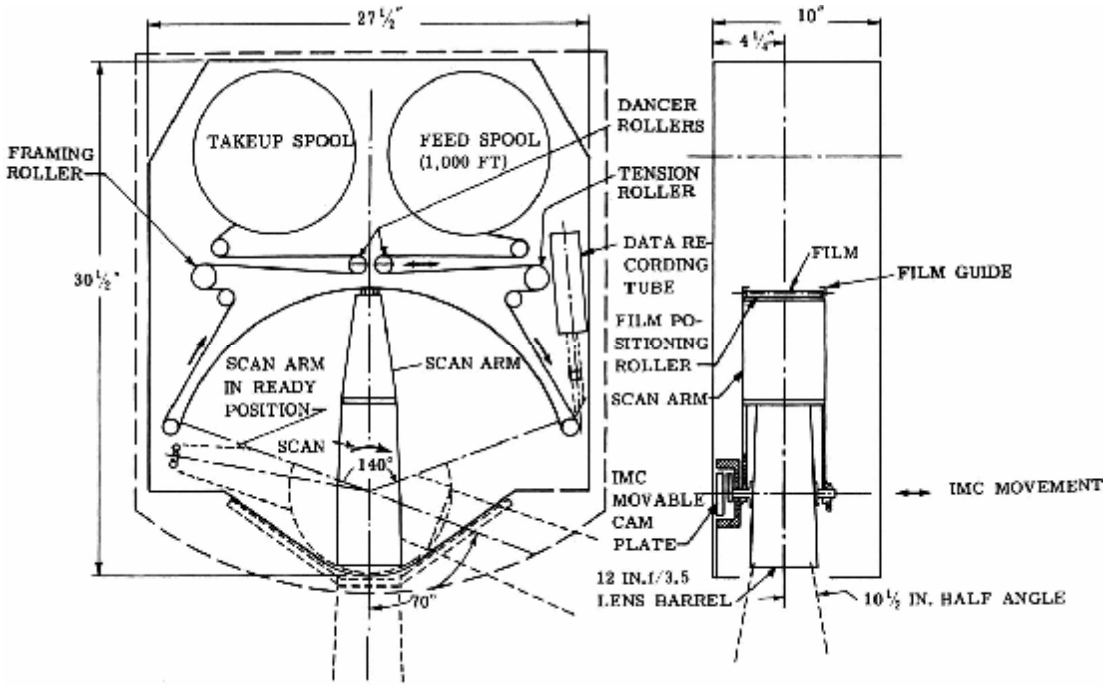

Figure 2-2 – HYAC panoramic camera (Source: Slama et al., 1980).

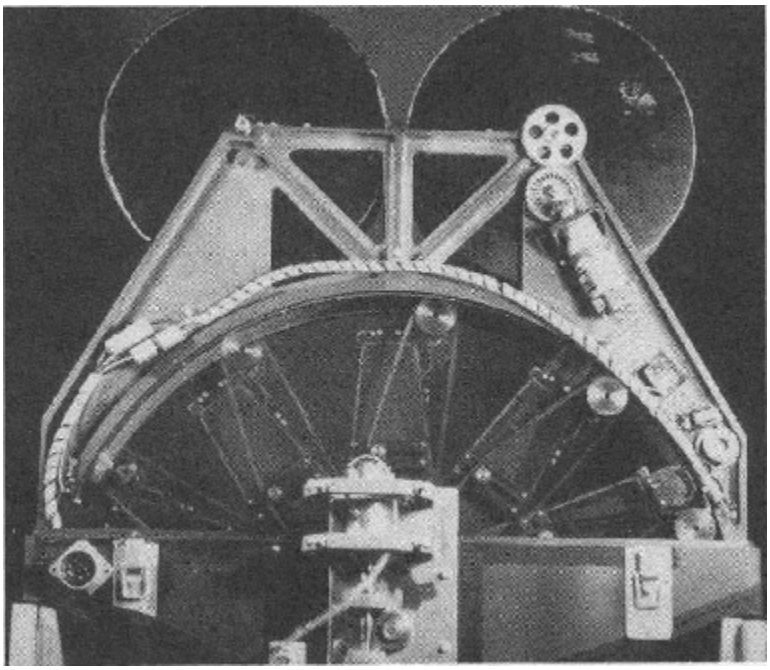

Figure 2-3 – A time-lapse exposure of the HYAC camera as the swing arm travels along the curved film platen, exposing the film.

2.1.3. KH-1, KH-2, KH-3

These are the first three CORONA program satellite system designs.

KH-1 camera system (C camera) operated between 25th June 1959 and 13th September 1960. It had only one successful mission, but during this mission it covered a larger area than the whole series of U-2 aircraft missions together. The amount of film collected during this single mission was 3,548 ft that equates to 1,432 primary camera frames (USGS, 2004a). The C camera was actually a HYAC camera with Tessar f/5 lens[4] and 24'' (61 cm) focal length. The film was located alongside the camera instead of above it. It swung through an arc of 70° at right angles to the direction of the flight (the vehicle faced backwards[5]) and exposed a swath of film 2.10'' (5.33 cm) wide. As the camera oscillated back and forth during operation, it transferred undesirable motions to the spacecraft. To counteract this, the designers installed a momentum balance wheel that oscillated in opposition to the lens/scan arm assembly. Fairchild engineers chose to use a set of gears and a ball pushing on a spiral screw shaft to produce the necessary motion, but this resulted in significant vibration (Day *et al.*, 1998). The first film used was an acetate film, which was 3 mm thick. One serious problem was breakage of the

[4] Notice that the Petzval lens system was not used from the beginning of the CORONA program.
[5] The space was still unexplored in the 1960s. People were afraid of particles being in orbit around Earth that could damage the satellite's cameras and film. To protect them, the vehicle was flying rearward. See footnote of paragraph 2.1.13.

acetate film. It degassed solvents in the vacuum of space and became brittle because it rapidly lost moisture and pliability, making it very susceptible to cracking and breaking. It did not actually tear; it crumbled. A different film had to be found. Kodak created a polyester-based film that was more stable and thinner, so more film could be carried. The first successful flight of CORONA used the 2.75 mil Estar (Eastman Kodak designation for polyester) film. The KH-1 photography had estimated ground resolution of 40 ft (12.20 m). The cycle rate was constant and the Image Motion Compensation (IMC) was set to the anticipated ratio of velocity to height. Because the IMC was constant, the satellite could only fly at one altitude or the images would appear blurred.

KH-2 camera system (C' or 'C prime') managed to successfully complete 3 missions from 26th October 1960 to 23rd October 1961. The amount of film collected was 17,949 ft, which equals 7,246 primary camera frames (USGS, 2004a). While in KH-1 the IMC had a constant velocity, in KH-2 it changed continuously throughout each pass. So, different orbits could be flown because the camera could be adjusted to match the actual orbit. Unfortunately, the mechanics of the IMC were not published in the CORONA documents. The ground resolution was improved to 25 ft (7.62 m).

The second problem that existed was the residual chromatic blur. Doubling the focal length of the lens from HYAC to CORONA had not, in principle, doubled the blur of the diffraction image, since that depends only on the f-number, and that had remained unchanged at 5.0. But the residual chromatic blur, the so-called secondary spectrum, is a geometric aberration and so it inherently increased directly with the focal length (Smith, 1997). The solution to this aberration was applied in KH-3 missions. It was the Petzval form of lens, which offered significant advantages. A problem of the Petzval lens was an introduction of curvature in the image. It was realised that the field curvature of the Petzval lens was not as important when it was being used in a panoramic camera. However, a field flattener was also inserted in the focal plane. Piazzi-Smyth introduced the concept of inserting a field-flattening lens in 1866. A negative plano-concave element placed with its flat side at, or just before, the image plane can be used to reduce the Petzval sum and thereby to flatten the field, as long as astigmatism is also controlled. The Petzval form of lens operated at f/3.5 with a field flattener at the slit and it was improved on later missions.

The KH-3 (C'''- there was no C'', which apparently was another configuration proposed that was not implemented) camera system operated from 30th August 1961 to 13th January 1962 with 5 successful missions. They produced 24,676 ft of film that

equals to 9,918 primary camera frames (USGS, 2004a). In the KH-3 camera, there were five major changes (McDonald, 1995):

1. The structural design was modified to avoid the negative impact of thermal differentials to its components.
2. The camera controls were made more reliable.
3. The method of metering film and achieving and maintaining camera focus was improved. Adjusting the IMC depending upon the orbit, allowed for lower orbits and higher resolution. Also, timing pulses, which determined the scan velocities and IMC for each frame, were marked in the image area rather than the border area of the film.
4. The scan arm design was improved. The C''' camera had the lower section containing the heavy lenses rotate a full 360° while the scan arm at the top oscillated back and forth through a 70° arc. This necessitated aligning and locking in place the scan arm and lens prior to the photograph being taken. This was done using a spring-loaded pin with a V point that engaged a V slot on the rear end of the lens cell. The scan arm itself was driven by a cam that accelerated it up to the lens speed until the V pin engaged the V slot. At the end of the scan, the V pin was retracted, and the cam returned the scan arm to its original position while the lens continued to rotate. These modifications significantly decreased the vibrations because of the back and forth motion of the camera.
5. A faster lens system was installed. The f/3.5 aperture permitted the use of slower film so that the higher resolution in the image could be fully exploited. This immediately doubled the potential resolution of the camera to 12 ft (3.66 m).

All these early missions incorporated small cameras to add a horizon image at the end of each frame to determine vehicle orientation and the attitude of the panoramic camera. Also, these early missions were mainly used for intelligence purposes and not mapping purposes. While photogrammetrists were concerned with the character *of* the terrain, intelligence staff was concerned with the characters *on* the terrain.

2.1.4. KH-4 / The "M" or "Mural" camera.

KH-4 was the first camera from space to provide stereoscopic coverage. It consisted of two KH-3 cameras on a common mount of "M" shape, one looking 15 degrees aft from the vertical and the other 15 degrees forward. The system used counter-rotating

lenses, which further improved stability though the slit assembly still oscillated. The forward-looking camera was actually in the "front" of the spacecraft, and it faced backward along the flight path. The back-first flight continued until spacecraft No 1615 of May 18, 1965. It was the first vehicle to fly nose-first. It would pitch down 120° to attain 60° down and backwards from the direction of flight for recovery (McDonald, 1997).

Stellar and index cameras were added. Stellar cameras were looking out and upward a few degrees above the horizon. They were used for the determination of pitch, roll and yaw during operational cycles. A reseau plate[6] was provided to correct for image distortion and to recover geometric orientation. The index camera was looking downwards to supply wide coverage photography to assist in verifying the location (figure 2-4). It included a reseau grid that was used as an aid for correcting the effects of film shrinkage, lens distortion, and atmospheric refraction.

The KH-4 camera operated from 27th February 1962 to 24th March 1964 and it acquired 239,299 ft of film, which equals to 101,743 primary camera frames (USGS, 2004a). While on earlier missions there was emphasis on USSR areas, in this mission, there was worldwide coverage but the majority of images cover the so-called "denied areas". The ground resolution varied from 10 to 25 ft (3.05-7.62 m). The mission's life was expanded because of a heavier load of film from 3-4 days to 6-7 days.

[6] A glass plate on which is etched an accurately ruled grid. Sometimes used as a *focal-plane plate* to provide a means of calibrating film distortion; used also for calibration of plotting instruments. (Slama *et al.*, 1980)

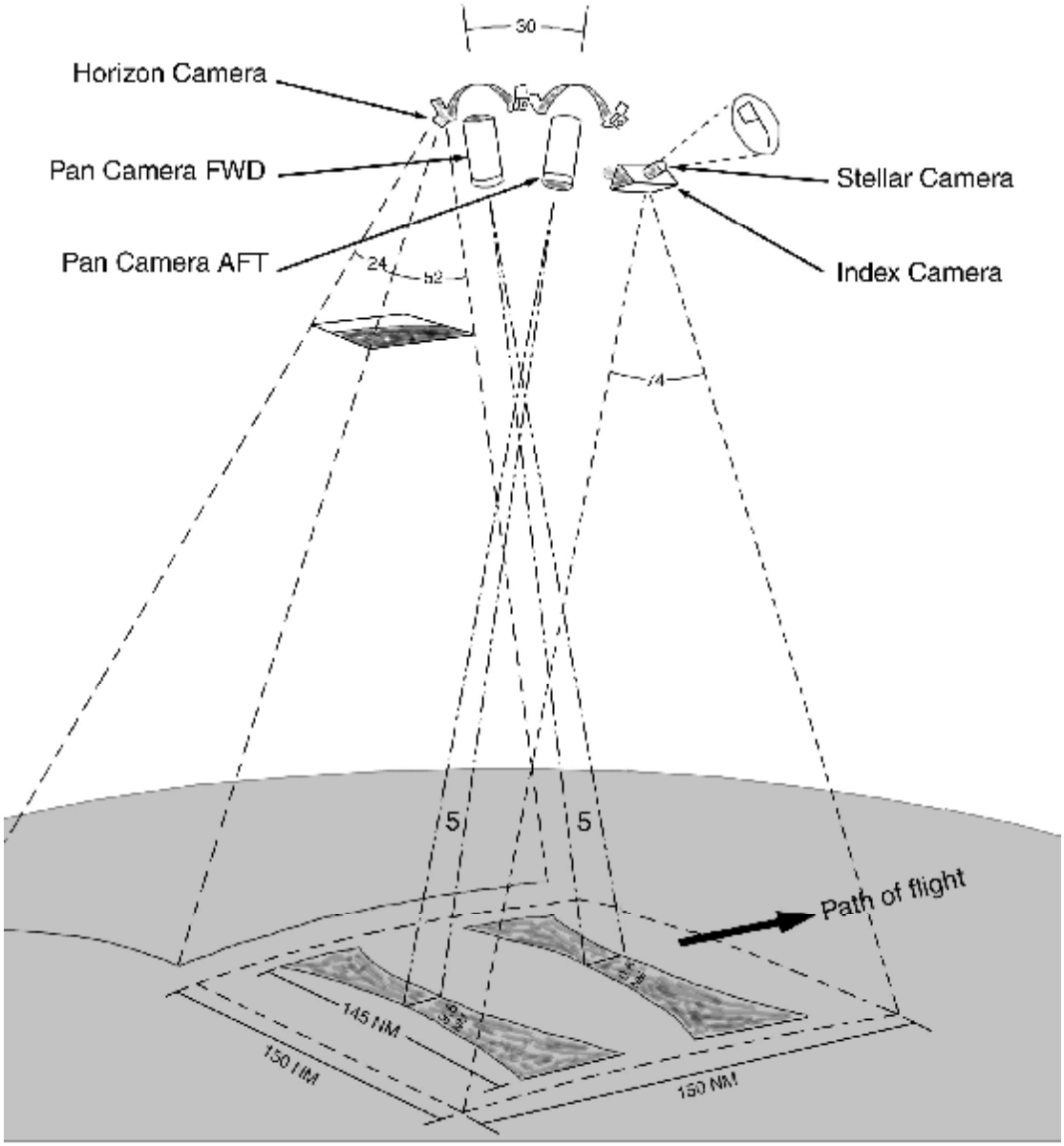

Figure 2-4 – CORONA cameras and coverage.

2.1.5. KH-4A / The "J-1" camera.

In KH-4A, the "J-1" camera was identical to the "Mural" or "M" camera. The only change required was to double the capacity of the film-supply cassette and to strengthen the main support plates to accommodate the increased weight. The boost capacity was increased and so the satellite could become bigger and heavier. Thus, there was added a second "bucket" of film in the satellite and the film load was increased. The introduction of a second RV (Recovery Vehicle) required a different film path in the small diameter of the spacecraft.

Engineers designed a transfer roller into the hub of the take-up spool in the RV-2 (2nd Recovery Vehicle), which was closest to the cameras. This allowed the film to wind around the transfer roller and exit the RV. They also installed an intermediate roller assembly, which was mounted to a vehicle bulkhead just in front of the forward panoramic camera. As the filmstrip left the camera, it went into the intermediate roller assembly and then into and out of RV-2, through a film cutter and into RV-1, where it was connected to the take-up reel. When the two take up reels in RV-1 were full, or when ground controllers felt that the RV contained critical information, the controllers sent a command to the spacecraft to cut the film. The forward cut ends of the two film-strips (one per camera) would be wrapped onto the RV-2 spools. RV-1 would then detach from the spacecraft, leaving RV-2 ready to accept film from the cameras (figure 2-5).

This increased the mission's life to 15 days and now the coverage of each mission was almost doubled. Also, there were no more oscillating parts in the system. Auxiliary rockets were used to control orbit decay and so lower altitudes could be used. Because of this, even 9 ft (2.74 m) ground resolution was reported. KH-4A operated from 24th August 1963 to 22nd September 1969 and acquired 1,293,025 ft of film, which equals to 517,688 primary camera frames (USGS, 2004a).

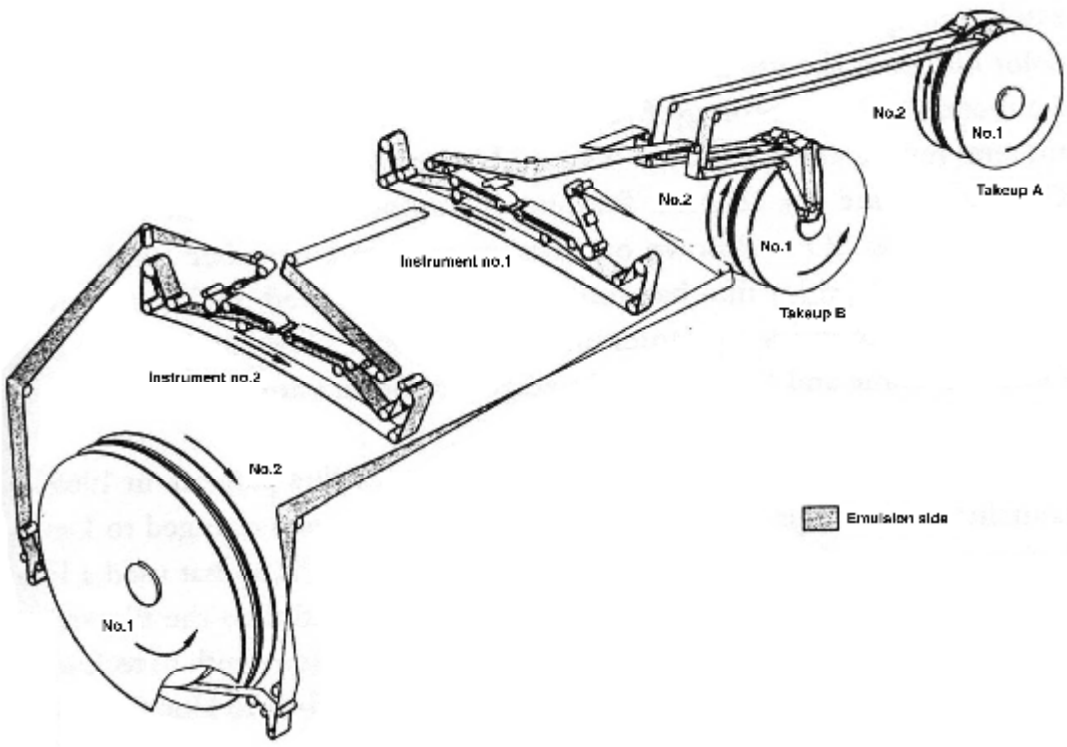

Figure 2-5 – The film path of the KH-4B spacecraft. It has all these twists and turns because of the need to accommodate the small diameter of the satellite. The counter-rotating motion of the film and the cameras improved stability of the satellite (NRO, 1970b).

2.1.6. KH-4B / The "J-3" camera.

In the KH-4B (J-3 – there was no J-2) camera system, a lot of important changes were made. The design of C''' camera still suffered from vibration when the scan arm moved back and forth and came to a full stop at the end of each scan. The Mural and J-1 cameras doubled the vibration because they were two cameras connected together. Vibration smeared the image and lowered resolution. In the J-3 camera the lens cell and the scan arm were connected and placed in a drum that rotated 360°. It was known as the Constant Rotator (CR), and it was possible only because of the increased diameter of the payload. The film scan was still 70° and the vibration was eliminated.

The J-1 camera system had only a single exposure for the entire mission. In J-3, each camera had two changeable filters and four changeable exposure slits and so it had greater performance in low sun angles.

Some refinements in the control of the system were introduced which allowed it to operate in orbits of 150 km. The IMC was improved. This made possible the production of higher ground resolution of 6 ft (1.83 m). Also, the mission life increased to 19 days. The KH-4B system operated from 15th September 1967 to 25th May 1972 and it produced 505,970 ft of film, which equals to 188,526 primary camera frames (USGS, 2004a).

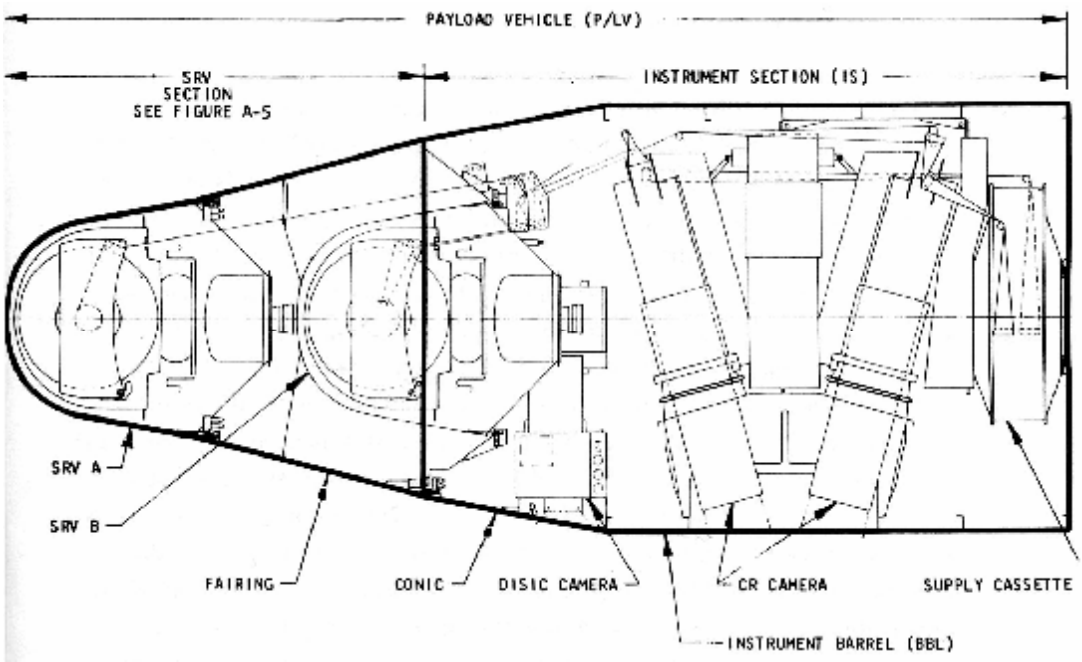

Figure 2-6 – The KH-4B satellite (Source: Day *et al.*, 1998)

A very detailed report on the characteristics of KH-4B covering cameras, films, and general ephemeris information is given by NRO (1967a).

2.1.7. The Petzval lens systems

The Petzval design was large. It used three 7'' (17.78 cm) diameter elements at the front and two 5.5'' (~14 cm) at the rear. These were all in a 22'' (55.88 cm) long cylindrical cell. The lens rotated around an axis about 10'' (25.40 cm) from the front of the cell. The field flattener was located 0.25'' (0.635 cm) in front of the film. The whole weight was 20 pounds (~9 kg). On an optical test bench under controlled laboratory conditions, the Petzval lenses were able to resolve, on film, targets equivalent to about 280 lp/mm for high contrast targets and 190 lp/mm for low contrast targets. Operational resolving power when looking through clear, dry air appears to have been about 200 lp/mm allowing detection of 6-8 ft (1.83-2.44 m) objects from 100 nautical miles (~185 km) altitude (Madden, 1996).

The physical characteristics of the Petzval lenses remained unchanged through the CORONA mission. However, the performance of the lenses had been continually upgraded from 1964 onwards, while necessitating no changes in either camera or vehicle. This was accomplished by taking advantage of improvements in materials, software, and improved fabrication and test techniques, coupled with an overall tightening of lens tolerances. The result of these upgrades from the first Petzval to the last was a 15 % and 30 % improvement in low contrast resolution with a Wratten-21 and a Wratten-25 filters respectively (NRO, 1970a).

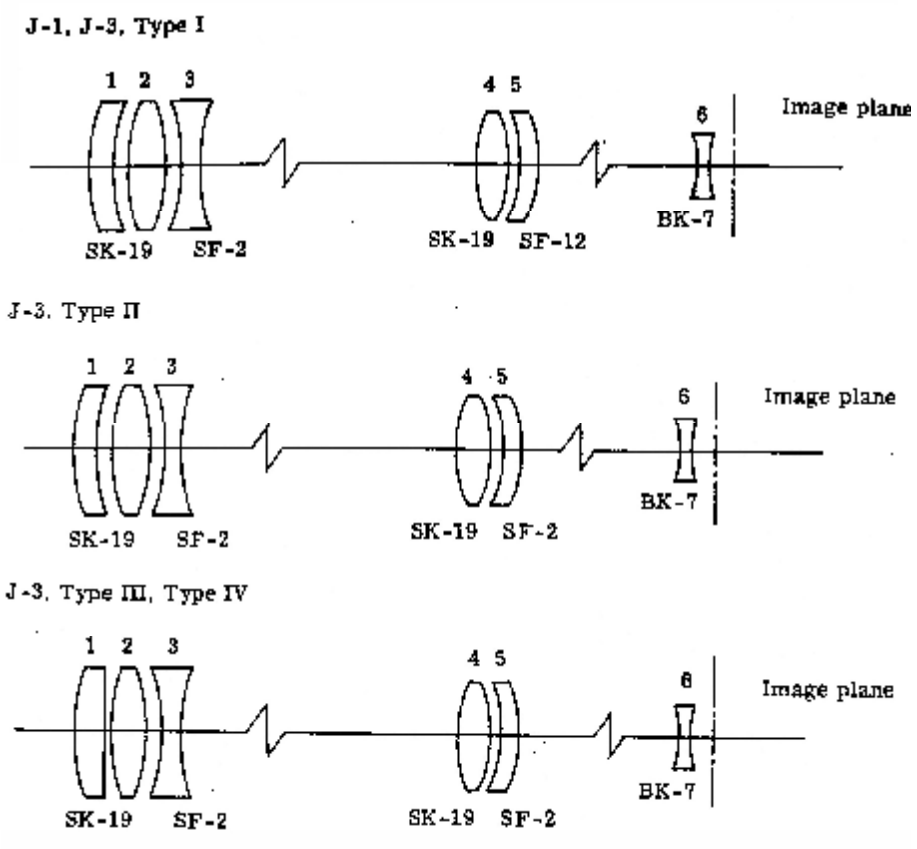

Figure 2-7 – Petzval lens diagrams (NRO, 1970a)

Table 2-1 – Petzval lens characteristics (NRO, 1970a)

Petzval lens	Glass quality	Design wavelengths, microns (lower, central, upper)	Comments
J-1 & J-3 type I	Normal (Schott RQ)	0.5461, 0.6200, 0.6900	Elements 1 & 3 relatively thin; fabrication problem. Element 3 undersize in diameter. Loss of resolution with W-25 filter.
J-3 type II	Precision (Schott AO)	0.5461, 0.6200, 0.6900	First three elements same diameter; alignment improved. Astronomical objective glass used, more homogeneous. Elements 1,3 & 4 thickened for structural integrity. SF-2 (more readily available) replaced SF-12 in element 5.
J-3 type III	Precision (Schott AO)	0.6000, 0.6500, 0.7100	Design central wavelength raised to improve performance with W-21 and W-25 filters. Slightly different radii, airspaces.
J-3 type IV	Precision (Schott PH-3)	0.6000, 0.6500, 0.7100	PH-3, selected precision quality for improved homogeneity reduced optical path difference at image plane. Tighter tolerances and improved material for hardware used to mount optics. Surface quality of optical elements improved.

2.1.8. KH5 – The "Argon" system

Argon was a mapping system developed in parallel with CORONA. It flew 12 missions between 17th February 1961 and 21st August 1964 and it produced 22,503 ft of film, which equals to 38,578 primary camera frames (USGS, 2004a). The purpose of this system was to be a reconnaissance satellite that could obtain precise geodetic data of the Soviet Union for pinpointing strategic targets. The earlier Argon missions were flown independently, but the later missions were flown piggyback with CORONA camera.

Argon had one Recovery Vehicle and targeted worldwide. The camera had a 3'' (about 7.62 cm) focal length and the film had a resolution of 30 lp/mm. Every frame photograph had dimensions 4.5''x4.5'' (~11.43x11.43 cm) and swath width of 300x300 nautical miles (~555x555 km). The estimated ground resolution was 460 ft (~140 m).

Argon imagery has been used in change detection applications (Tappan *et al.*, 2000; Sohn *et al.*, 1998; Kim *et al.*, 2001), orthorectification (Zhou & Jezek, 2002; Zhou & Jezek, 2004), and assessed for their horizontal accuracy in Sohn & Kim (2000).

2.1.9. KH6 – The "Lanyard" system

Lanyard was a system designed to acquire high-resolution photographs of specific targets in the Soviet Union. It was expected to provide 2 ft (~61 cm) ground resolution, but the result was only 6 ft (~1.83 m). It achieved only one mission, on 31st July 1963, and it produced 2,251 ft of film, which equals to 910 primary camera frames (USGS, 2004a). Its focal length was 66'' (~167.64 cm) and the film resolution was 160 lp/mm. The camera was a single-lens cell that obtained stereoscopic coverage by swinging a mirror through a 30° angle. The frame's dimensions were 4.5''x25'' (11.43x63.50 cm) with a swath width of 7.5x40 nautical miles (~14x75 km).

2.1.10. CORONA coverage

The main interest for reconnaissance flight was initially focused on the USSR and later on areas where aircraft overflight was denied to the USA or conflict areas (for example Arab-Israel war). Figure 2-8 shows an example of four-day coverage during a single KH-4A mission 1017. The image capture was controlled through telemetry from the ground station. Thus, the controllers could switch on and off the capture according to the needs and the weather. The orbit inclination and the equator crossing time were changing from mission to mission (Peebles, 1997). Thus, one cannot talk about "systematic" coverage.

Concerning Syria, there is no coverage from KH-1 or KH-2 satellites missions. KH-3 mission 9022 covers the east Syria and the mission 9029 covers the part of Syria west of Aleppo. KH-4 mission 9032 covers east Syria and mission 9050 crosses middle Syria. Later missions (KH-4A and KH-4B) cover all of Syria.

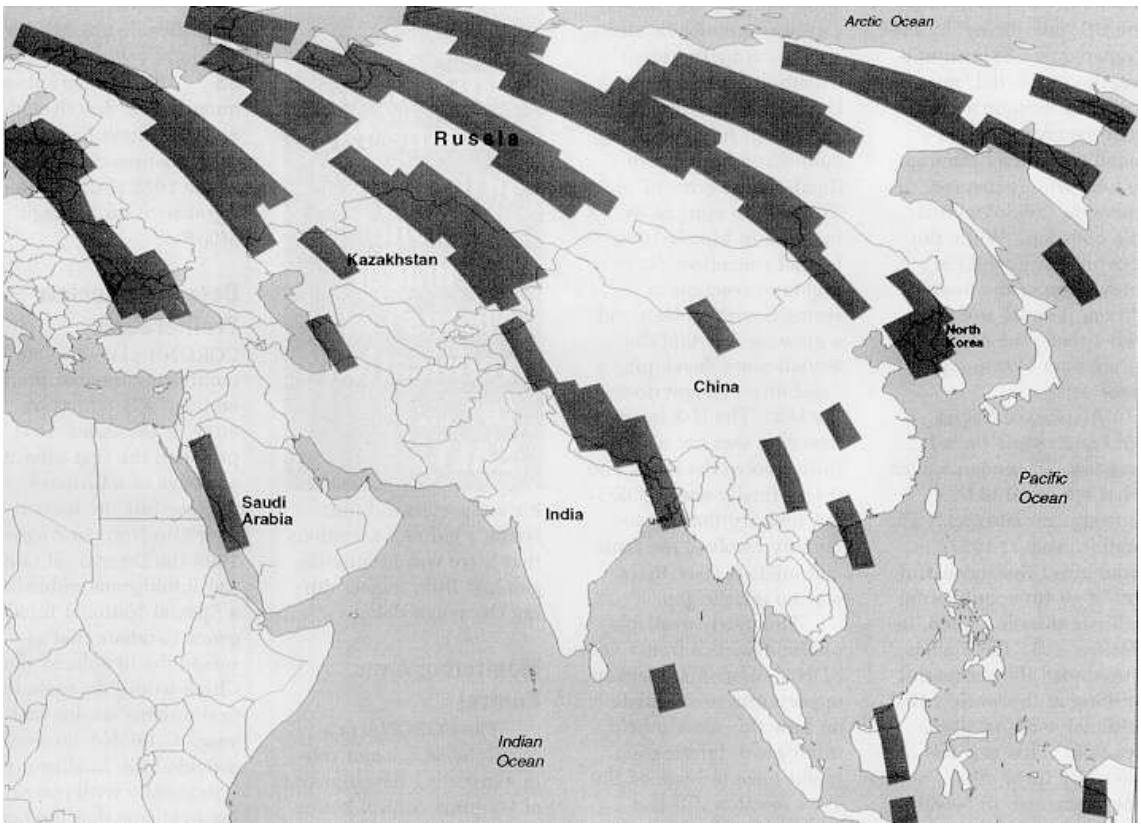

Figure 2-8 – Example of four-day coverage of Eurasia during KH-4A mission 1017 (From: www.nro.gov, accessed July 2004).

2.1.11. Summary

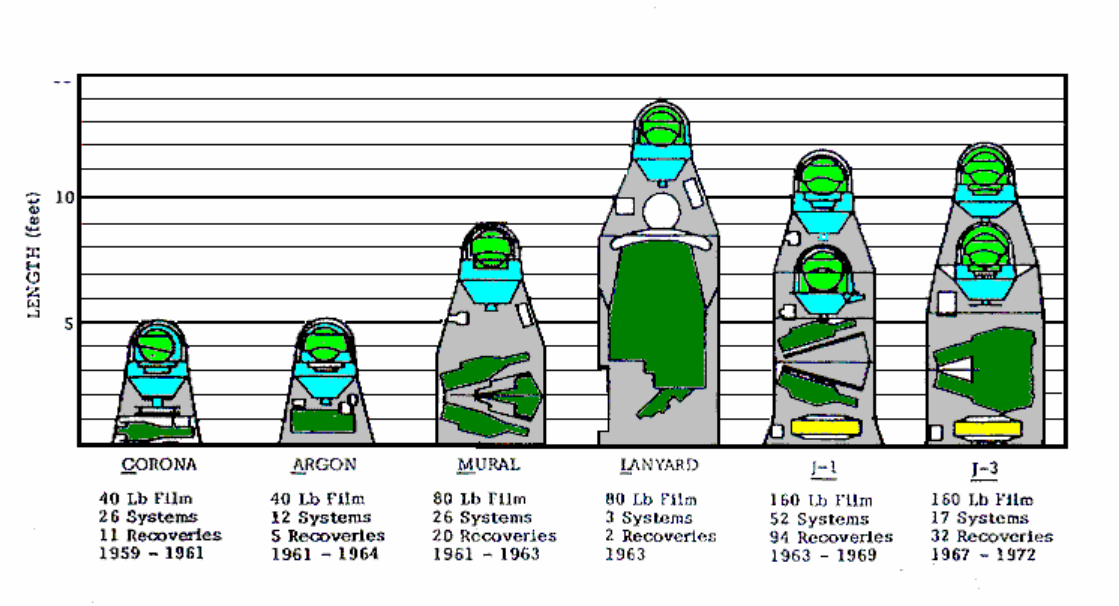

Figure 2-9 – The development of the CORONA's cameras and shape. The incorporation of the second capsule is clear in "J" cameras. Also, the two cameras are clear in "Mural" and "J" camera. In Lanyard, there was a slit moving the camera fore and aft. (Source: Clarke, 2000)

Table 2-2 summarises the major developments in the CORONA satellite programme. The main differences lay in the improvement of the lens, the creation of tougher and finer film, the boost capacity of the rocket, the better control of vehicle stability, and last but not least, the freedom to innovate and to redesign the satellite from scratch. It must be noted that improvements were incorporated into every mission.

At the end of the CORONA programme, the total amount of data produced was 2,109,221 ft of film, which equals 866,041 primary camera frames (USGS, 2004a).

All the values in table 2-2 are nominal. For precise values in every mission, the reader should consult the original NRO and NARA reports (see paragraph 2.1.15). Table 2-2 was made based on information from McDonald (1997), Madden (1996), Day *et al.* (1998), and Peebles (1997).

Table 2-2 - Major operational and construction difference among CORONA designs

	KH-1	KH-2	KH-3	KH-4	KH-4A	KH-4B
Period of operation	27/6/59-13/9/60	26/10/60-23/10/61	30/8/61-13/1/62	27/2/62-24/3/64	24/8/63-22/9/69	15/9/67-25/5/72
Amount of frames	1432	7246	9918	101743	517688	188526
Mission life (days)	1	2-3	1-4	6-7	4-15	19
Altitude (km)						
Lower (estimated)	192	252	217	211	180	150
Higher (estimated)	817	704	232	415	n/a	n/a
Successful missions	1	3	5	20	49	16
Targets	USSR	Emphasis on USSR		Worldwide/emphasis on denied areas		
Aperture width	5.265°	5.265°	5.265°	5.265°	5.265°	5.265°
Pan angle	71.16°	71.16°	71.16°	71.16°	71.16°	71.16°
Stereo angle				30°	30°	30°
Lens	F/5.0 Tessar	F/5.0 Tessar	F/3.5 Petzval	F/3.5 Petzval	F/3.5 Petzval	F/3.5 Petzval
Focal length (cm)	61	61	61	61	61	61
Resolution						
Ground (m)	12.20	7.60	3.70-7.60	3.00-7.60	2.70-7.60	1.80-7.60
Film (lp/mm)	50-100	50-100	50-100	50-100	120	160
Nominal ground coverage image frame	15.3x209 to 42x579 (km)	15.3x209 to 42x579 (km)	15.3x209 to 42x579 (km)	15.3x209 to 42x579 (km)	17x232 (km)	13.8x188 (km)
Nominal photoscale in film	1:275,000 to 1:760,000	1:275,000 to 1:760,000	1:275,000 to 1:760,000	1:300,000	1:305,000	1:247,500

2.1.12. Ascent sequence

The major sequence of ascent events is illustrated in figure 2-9. BTL (Black TeLemetry) was a tracking and command station located at the launch base to command and steer the Thor and the Agena rockets during ascent until the Agena went over the radio horizon. Agena had also a mechanical timer for ascent events as well as one for orbital events.

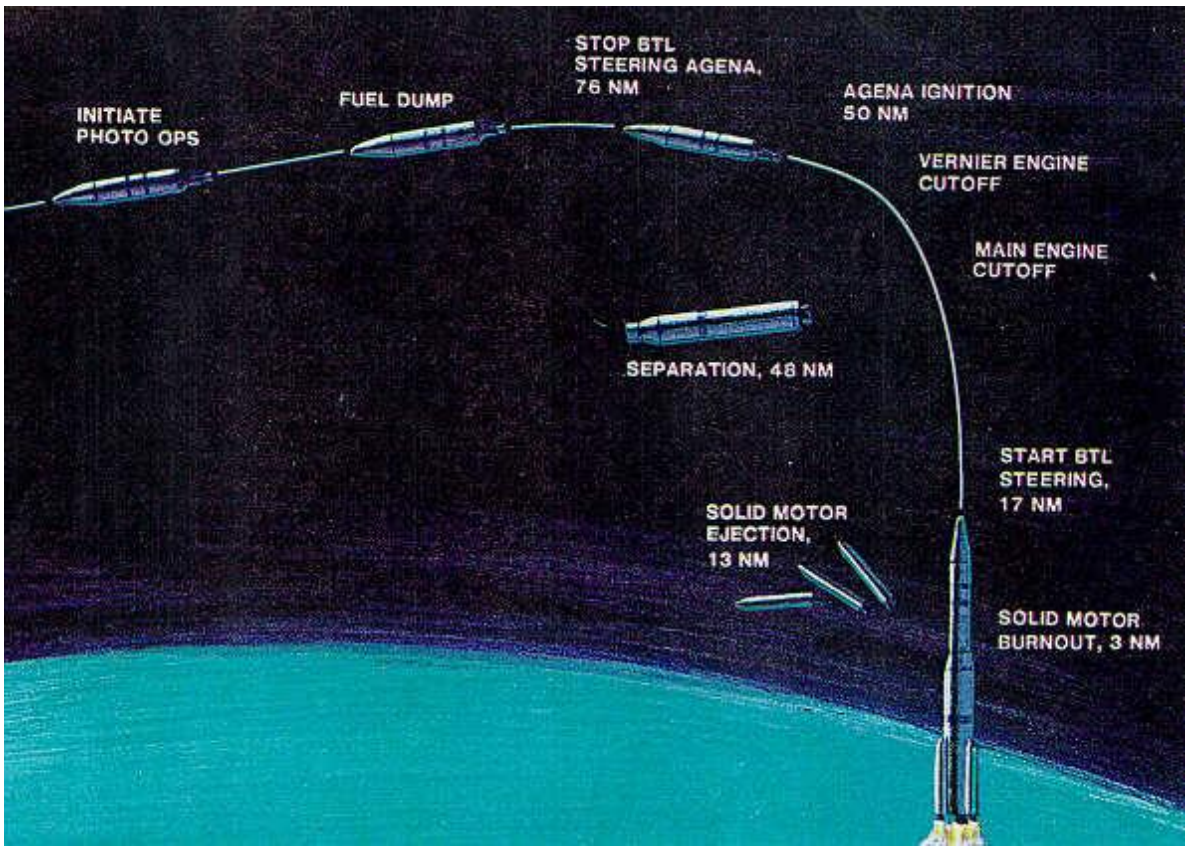

Figure 2-10 – The ascent sequence (Source: Powell, 1997)

2.1.13. Guidance and control

All information in the guidance and control of the CORONA program satellite designs are taken from Powell (1997).

2.1.13.1. Guidance system module (figure 2-10)

The guidance system module was installed in the forward equipment racks to facilitate handling, check out and alignment. The control components (gas jets, hydraulic activators and their associated components) were electrically connected to the guidance module.

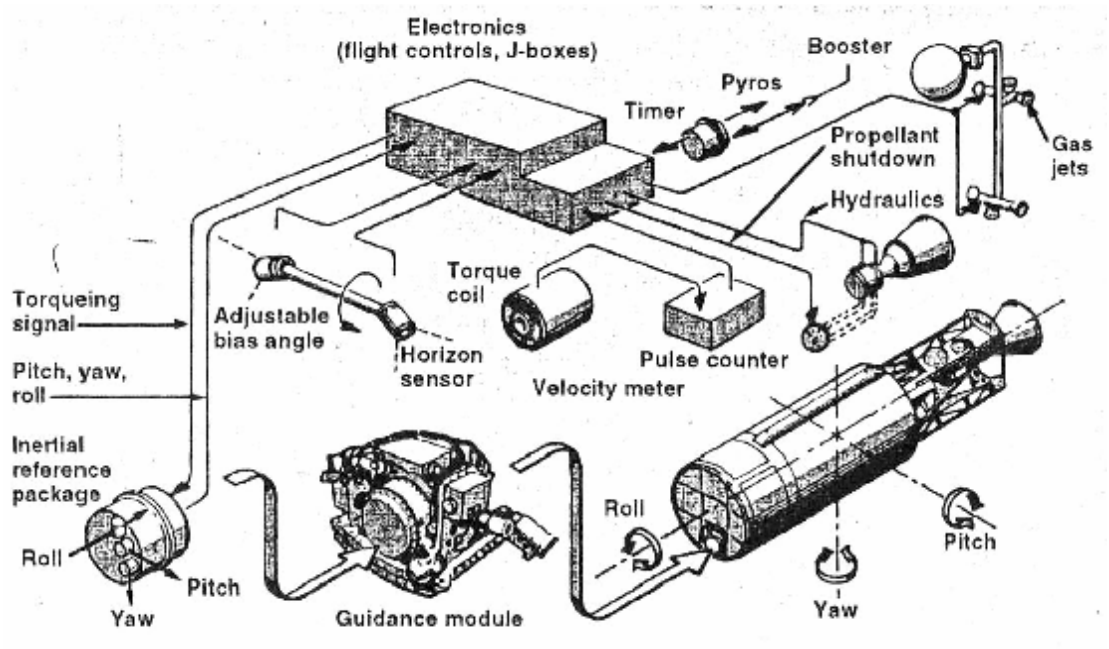

Figure 2-11 – The guidance and control system (Source: Powell, 1997)

2.1.13.2. Timing and sequencing function

The timer was a resetable electromagnetic device that had a running time of 6000 seconds and was capable of programming 24 events. It was used during ascent to provide separation signals, engine start commands, change in pitch rates, and so on.

2.1.13.3. Attitude sensing function

The basic attitude sensor was the three-gyro inertial reference package. It contained two air-tight integrating gyro units to sense pitch and yaw, and one miniature integrating gyro unit to sense roll. The pitch and roll gyros were torqued by signals obtained by two Barnes mod IIA infrared horizon sensors. Gyrocompassing oriented the vehicle to an orbit plane yaw reference by detecting a component of the programmed pitch rate through the roll horizon sensor. The geocentric pitch rate (typically 4 deg/min,

for a low-altitude orbit) was programmed as a constant torque to the pitch gyro. This pitch component, if a yaw error were present, would be sensed differentially when compared with the roll components of the two horizon-sensor heads. The differential would be seen as a function of yaw error. The roll output was separated into a constant yaw-induced error and a normal roll oscillation by integrating over a time period. The roll-error component caused by yaw was fed as a torquing signal to the yaw gyro, the output of which then corrected the vehicle's yaw orientation.

2.1.13.4. Velocity-sensing function

The single-axis velocity meter consisted of a pendulous torque coil that detected acceleration in the longitudinal axis, causing the coil to move off centre. The coil was returned to centre by a series of electrical pulses proportional to the acceleration. These digital pulses were summed to in a binary counter to determine the integral of acceleration, or velocity. The digital pulses from the accelerometer were used to count down from the preset binary number representing the desired velocity increment. Two such binary numbers were preset in the velocity meter. These numbers would represent the predetermined velocity increments required for first and second burns, if required. When the prescribed velocity was attained, zero coincidence in the counter was reached and a signal was given to close the propellant shutdown valves.

2.1.13.5. Gravity-Gradient stabilisation

When placed in a nose-down position on orbit, the Agena was essentially gravity-gradient stabilised by virtue of its moment-of-inertia distribution. However, some form of damping was required to nullify oscillations that could build up to appreciable amplitudes as a result of the local gravity-field restoring torques. An active damping system employed control moment gyros that damped out vehicle oscillations before they reached sizable amplitudes.

2.1.13.6. Backup stabilisation system

This was developed to provide redundant capability if the primary Agena attitude-control system failed. The redundant control was used to successfully provide attitude control on Agena flights. This backup system was a self-contained command, sensing,

and gas jet control system. The Earth's magnetic field was used to establish the correct orientation of the Agena at a given point in orbit. Magnetometers were set according to the orientation of the magnetic field at a given point, and upon command, the magnetometers activated gas jets to align the Agena to the local magnetic-flux field. This would ensure the correct vehicle attitude.

2.1.13.7. Agena communications and control

The Agena employed the Type5 FM/FM telemeter system to provide required data on vehicle subsystem flight performance, and an S-band beacon/transponder.

2.1.13.8. Telemetry

The Type5 FM/FM telemetry system was used, which was initially VHF, but on the final series of vehicles S band was used. Approximately 85 points in the Agena subsystems were monitored during ascent and orbit to determine subsystem performance. The telemetry provided seven continuous channels and two communication channels. Two channels were available to telemeter payload functions.

2.1.13.9. Tracking and command

A Philco S-band transponder was used to track the Agena during ascent and while in orbit. It also was used to command the spacecraft and employed three pulses to send commands to the Agena. The first and third pulse triggered the transponder. The position of the second pulse, relative to the first and third, was tone-modulated by a prelort ground radar and used a combination of two audio frequencies to represent one distinct command.

The decoder could provide fifteen commands by using 6 frequencies in all possible combinations of two. One frequency was dedicated to the Fairchild Type7 programmer for commands to be executed out of sight of the ground station. This programmer consisted of two magazines that stored punched Mylar tape. The programmer also had a drive motor, a reset motor, latching relays, and associated transistorised circuitry. This Type7 programmer was capable of 256-programmed sub-cycles. 26 commands could be executed repeatedly for 256 orbits. In addition, the length of each sub-cycle could be adjusted by command to allow for variations from 87 to 108 minutes in the orbit period.

Other command components included a four-magazine programmer (52 pre-programmed commands), a 32-command flight loadable storage register, and a redundant real-time (UHF and S band) 32-command system.

2.1.14. Recovery sequence

The centre space of the recovery vehicle (RV) held a large take-up reel for the 70 mm film. A small rocket motor was fitted to the rear of the RV. The spacecraft would re-orient itself at the end of the mission and separate the RV that now contained the exposed film[7]. The RV would "spin-up" for attitude stability, and then fire its rocket motor to reduce its speed by 1300 ft per second. The rocket was fired after tilting down 60 degrees from the forward direction to minimise the influence of alignment errors on the impact zone. This was enough to send it back to Earth after travelling a quarter turn in orbit.

The maximum heating rate during re-entry would occur at 350,000 ft (~106 km) altitude, where the ablation heat shield would reach temperatures of 4,000 degrees Fahrenheit. A parachute would deploy when the RV reached 50,000 ft (~15 km), and would slow the descent rate to about 30 ft/sec (~9 m/sec). A fleet of C-119 aircraft were deployed from Hawaii to snatch the descending capsule. These planes each towed a long loop with which the air crew attempted to snare the parachute and then reel it into the aircraft. Ships and helicopters were also deployed to recover the RV if it was missed and fell into the sea.

If a RV was missed and landed in the water, it would float while its strobe light flashed and its radio beacon emitted a signal. The signal was a very distinctive, high-frequency repetitive sweeping sound that could be picked out of the background noise After one to three days, a plug made out of salt would dissolve and the capsule would fill with water and sink, thus preventing its recovery by an adversary.

Aboard the C-119 or C-130 aircraft the bucket was loaded into a light-tight bag inside a steel drum and transported to Hawaii. Light-sensitive film was placed inside the bag to help determine if any accidental exposure occurred during the trip. There, the drum was transferred to whichever Air Force plane was available at the time and flown

[7] In the early years of CORONA, there was great concern about the reserve of control gas available in the Agena, and also concern about potential damage to the RV from impact with particles in space. To minimise these risks the Agena performed a 180-degree yaw manoeuvre required to de-orbit. As more was learned about space and the reliability of the Agena improved, the yaw manoeuvre was eliminated and the recovery tilt down became 120 degrees. This allowed the main Agena engine to be restarted, if desired, to accomplish a change of orbit during the flight (Day *et al.*, 1998, p.250).

to Moffett Field or Travis Air Force Base in California. The drum was then taken to the Advanced Projects facility, where the bucket was removed. The film cassettes were flown to a processing centre in the Northeast for development. The original negative was developed and copied and two duplicate positives were produced for use by the photointerpeters. The duplicate positives were flown to Andrews Air Force Base near Washington, D.C. and were delivered to the Photographic Interpretation Centre (later NPIC) for analysis (Day *et al.*, 1998). The average shipment, transfer and processing time of CORONA material were 96-99 hours from the recovery until receipt by NPIC (NRO, 1970a).

2.1.15. Acquiring CORONA imagery

After the declassification of the imagery, it was deemed appropriate that a non-intelligence agency would archive and distribute the imagery to the public. The US Geological Survey (USGS) as the National Satellite Land Remote Sensing Data Archive (NSLRSDA) was given this role because of the value of the data for environmental monitoring and because the USGS had the infrastructure in place for ordering and distributing these newly declassified photographs (Scholz, 1997). Vick (1999) reported that:

"*The USGS product has been found to be noticeably out of focus, and to have automatic exposure processing features that rendered many scenes unusable*".

According to USGS, the methodology used for the reproduction of the duplicates supplied by Eastman Kodak is:

- Duplicate negatives are printed emulsion-to-emulsion on a direct duplicating film and processed to a gamma of approximately 1.00. Exposure is adjusted to retain highlight detail and generally matches the working master from which it was made.
- Duplicate positives are printed emulsion-to-emulsion on a negative working film and processed to a gamma of approximately 1.30. Exposure is adjusted to retain highlight detail.
- Contact paper prints are printed right-reading on a select contrast paper. Contrast adjustments are made on a scene-by-scene basis.
- Paper enlargements are printed right-reading on a select contrast paper. A choice of two standard size templates is required to identify area of interest. Contrast is adjusted during printing on a condenser enlarger.

All of the contact images are produced on a Kodak Colorado Continuous Contact Printer. This roll drum printer introduces a slight stretch in the Y-axis when printed. However, this has not been a problem for the people who have been using this product. Paper enlargements are produced on Durst or DeVere enlargers depending on enlargement factors and printer availability. The USGS duplicate negatives are made on Kodak Aerographic Direct Duplicating Film 2422 which has a resolution capability of 200 lines/mm with a T.O.C. 1.6:1. The positives are produced on AGFA's Avitone P1p, which has a resolution of 163 lines/mm (Happel, 2000).

However, USGS do not duplicate the originals. The CIA (Central Intelligence Agency) gave the originals to Eastman Kodak for duplication. The source of the "bad" quality of the USGS product reported by Vick (1999) could be because of the duplication by Eastman Kodak. During the writing of this thesis, no reply has yet been received from Eastman Kodak on how they duplicated these frames. After their duplication in Eastman Kodak, the original films were sent to NARA (National Archives Record Administration) for long-term preservation, along with a positive copy. A second copy was sent to USGS. It must be noticed that the term "original" refers to the closest to the original generation of film that the intelligence community was able to locate for inclusion in the USGS collection (McDonald, 1997). This is because during the processing of the film in the 1960s, more than 10 duplicates were made (Ruffner, 1995, p.79-80). The public access to the imagery began on 1st March 1996.

From 23rd April 1996, the inventory of the images became accessible over the Worldwide Web through the GLIS (Global Land Information Systems) graphical x-windows interface of USGS. Metadata describing each image were spatially linked to a jpeg format browse image. Kodak produced these images. Their quality is 50 dpi (dots per inch), 8-bit black and white images, in jpeg compression with 70% quality. They have a 122-byte header that contains mission, revolution, camera, frame, date, number of lines, and geographic coordinates. In 2003 the inventory of the images was integrated into the EarthExplorer graphical interface of USGS, along with most of the USGS satellite data.

In Donoghue et al. (2002), the issues of cloud cover and seasonal photography are illustrated. One must be careful of cloud cover when purchasing a filmstrip of interest. Fortunately, there may be several frames covering the same area, thus an archaeological feature that is not visible in one photograph may be visible in another. Concerning

seasonal photography, one must be aware of the atmospheric conditions. For example, a summer photograph of an area in Middle East can provide poor quality data due to dust particles in the atmosphere, but a winter photo of the same area may provides excellent quality data especially when recent rainfall has cleared the atmosphere from dust. This subject is covered in detail in chapter 5 of the thesis.

One must also be aware of the difference in the various CORONA launches. For example, the mission 1111 was very different from the other missions. Most CORONA launches were made between 10:00-14:00, to optimise lighting conditions. Mission 1111 lifted off at 18:25. Also, while most missions had an inclination orbit 81-88 degrees, mission 1111 had an inclination orbit of 60 degrees. It passed above Middle East areas at about 18:00 in the afternoon when ground objects could cast long shadows, thereby helping to identify features on the ground. Also, the dry summer afternoon air improved the clarity of the photos, thus providing 3-4 ft (~0.90-1.20 m) resolution.

One of the problems that a prospective user of CORONA data may face derives from the model used for the definition of the corner coordinate data of the photographs on the index. The imagery may not be located exactly as stated and so the user may be provided with an image of the area adjacent to his/her area of interest. Technical information of the model is given by Selander (1997) and USGS (2004a).

The prices of the USGS CORONA products are (USGS, 2004a):

KH1-KH4B		
	Film	
	2.25 by 29.8 inch (5.72x75.69cm) b&w negative	18.00 USD
	2.25 by 29.8 inch (5.72x75.69cm) b&w positive	18.00 USD
	Paper	
	2.25 by 29.8 inch (5.72x75.69cm) b&w print	14.00 USD
KH5		
	Film	
	4.5 inch (11.43 cm) b&w negative	18.00 USD
	4.5 inch (11.43 cm) b&w positive	18.00 USD
	Paper	
	4.5 inch (11.43 cm) b&w print	8.00 USD
	10.0 inch (25.40 cm) b&w print	12.00 USD
	20.0 inch (50.80 cm) b&w print	18.00 USD
KH6		
	Film	
	4.5 by 25.0 inch (11.43x63.50 cm) b&w negative	18.00 USD
	4.5 by 25.0 inch (11.43x63.50 cm) b&w positive	18.00 USD
	Paper	
	4.5 by 25.0 inch (11.43x63.50 cm) b&w print	14.00 USD

Custom made enlargements may be ordered for any selected portion of a photograph. This type of enlargement allows for a potential enlargement factor of up to 16x for the selected area. The cost of the enlargement is 25 USD (USGS, 2004a).

Another way of acquiring these images is proposed by Vick (1999). He proposes a visit to NARA, where they hold the originals and one positive duplicate. He gives detailed instructions on how to create better products than the USGS provide. He insists that if his instructions are meticulously followed then the result will be better. See Appendix II for a copy of the original article.

2.1.16. The CORONA reports

For every CORONA mission, the CIA recorded an evaluation report on that mission's photographs. The reports of the early KH-4 missions contain detailed analyses of the operation and products of the master, slave, stellar, index (also known as "terrain" or "framing"), and horizon cameras, analyses of vehicle attitudes and film density charts.

The reports of the later KH-4, KH-4A, KH-4B and KH-6 missions contain information on camera operation, film processing, degradations and densities; image quality and image suitability for interpretation, including numerous samples of enlarged photographs; system specifications, including diagrams of the vehicle layout and panoramic camera film format; operation of each camera; density readings, including tables and graphs; and mission coverage statistics, including cloud cover percentages.

Several reports contain information on radiation studies and temperature samplings conducted during particular missions, mensuration quality and microdensitometry. For certain missions, two copies of each report exist, one containing the textual information, and one containing both the textual information and photographic samples. Contained in several of the reports are special studies on such topics as: short range computation relative to universal grid coordinates, scan speed deviation analyses, dual gamma/vicose versus conventional/SPRAY processing analysis, film type comparisons, and image quality comparisons between original negative and duplicate positive film. A glossary of terms pertinent to the use of the data in these reports is included in most of the reports. All these reports are in NARA, in Cartographic and Architectural Branch, record group 263, series COR8, stack 331:113/8/4 through 113/8/5, containers #1-8.

In addition, the National Reconnaissance Office (NRO) declassified a lot of CORONA records on 26th November 1997. These records consist of documents related to the development, acquisition and operation of the CORONA, Argon and Lanyard systems. These include information on overall program management, policy and analysis, operational support and user applications, public affairs records, budget and finance records, contracting, procurement and logistics records, security, technology studies and research and development records. They also include specifications that discuss the performance of the CORONA system, test reports, engineering data, and recordings of the pre-launch assembly of flight vehicles and payloads, and periodic reports summarising the capabilities, performance, and product of the systems for NRO management and customer reviews. Some of these documents are provided from Presidential Libraries. The NRO document list exists online from the NRO webpage. With the list as a guide, a person may request the documents by FAX. A sample of the FAX and directions about access on the list are provided in Appendix II.

In June 2000 NRO declassified the Itek records collection, plus four volumes of the history of satellite reconnaissance through NRO history.

For each mission, a calibration report was prepared. This calibration report would contain: a sketch of the format (including the point identification system and coordinate system), calibration statistics (including average variance for the rail holes and for each of the traces), focal length and cam constant (+ or -) in microns, a point-by-point plot of individual readings on each trace, and a list of coordinates for all 73 holes on each rail and 73 points on each trace (see figure 2-15). Points on the traces are defined by the intersection of the traces and the lines connecting each pair of opposite holes.

The following two figures (reproduced from NRO, 1967b) describe the coordinate system and point identification key as they are referenced in the calibration reports and as they would appear on a positive side emulsion up. The numbering system takes the form of a matrix of 5 rows and 73 columns with an irregular row numbering system. The first two digits are the row indicators and the last two digits the column indicators. Note that the +X is in the direction of flight (NRO, 1967b).

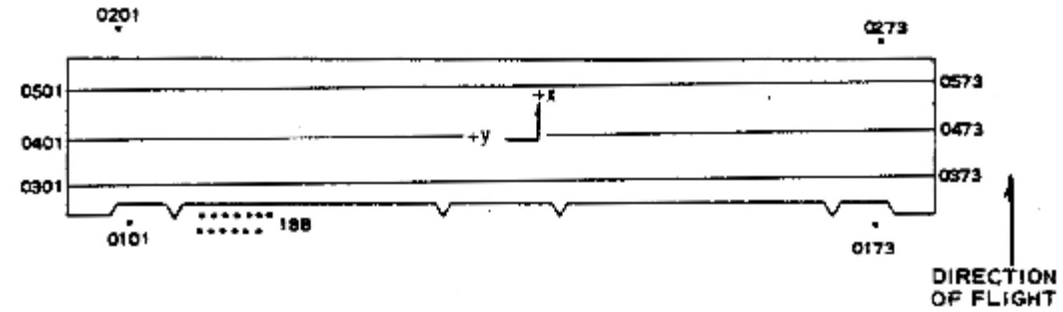

Figure 2-12 – Fwd looking camera panoramic geometry feature.

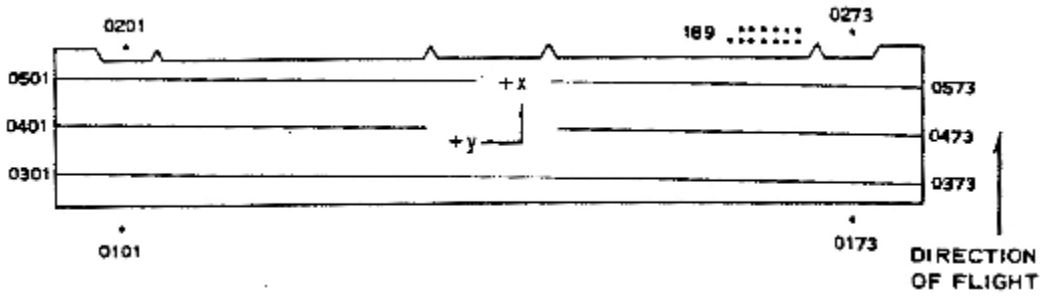

Figure 2-13 – Aft looking camera panoramic geometry feature.

2.1.17. Technical characteristics

2.1.17.1. Filters

Filters are required for most aerial reconnaissance systems in order to counteract the contrast reduction effects from the bluish haze light. The filters commonly employed in CORONA project are Wratten gelatine filters and are yellow to red in colour. Generally, the deeper red the filter, the greater the haze cutting ability, and the higher the contrast. However, the redder the filter, the higher the filter factor which in turn makes longer exposure times necessary. Apart from Wratten filters, there were experiments with colour correction and polarising filters in various missions.

At the outset, a gelatine filter by Kodak was tested for CORONA use but it appeared to dry out when in a vacuum and took a cylindrical shape with its axis across the film. The curvature of the cylinder was enough to cause poorer image quality along rather than across the film width. To overcome this, Itek developed the capability to produce glass filters the same thickness as gelatine filters (0.0048 inches, about 12.2 mm) and with the proper spectral transmission provided by an evaporated thin film on clear glass.

Twenty years later the same 'thin glass' technique was used by Itek to fabricate 12-inch by 18-inch (~30.5x45.7 cm) sapphire windows only 0.010 of an inch (~25.4 mm) thick to support another government program (Madden, 1996).

The main filters for the KH-4B were a Wratten 21, 2B, 23A, or 25. The choice of filter for every mission depended on operational conditions and the specific lens type. For example, the third generation of Petzval lens was designed for a Wratten 25 filter. Alternatively, for a winter mission, the Wratten 23A filter could enhance the system performance with an appropriate reduction in exposure time.

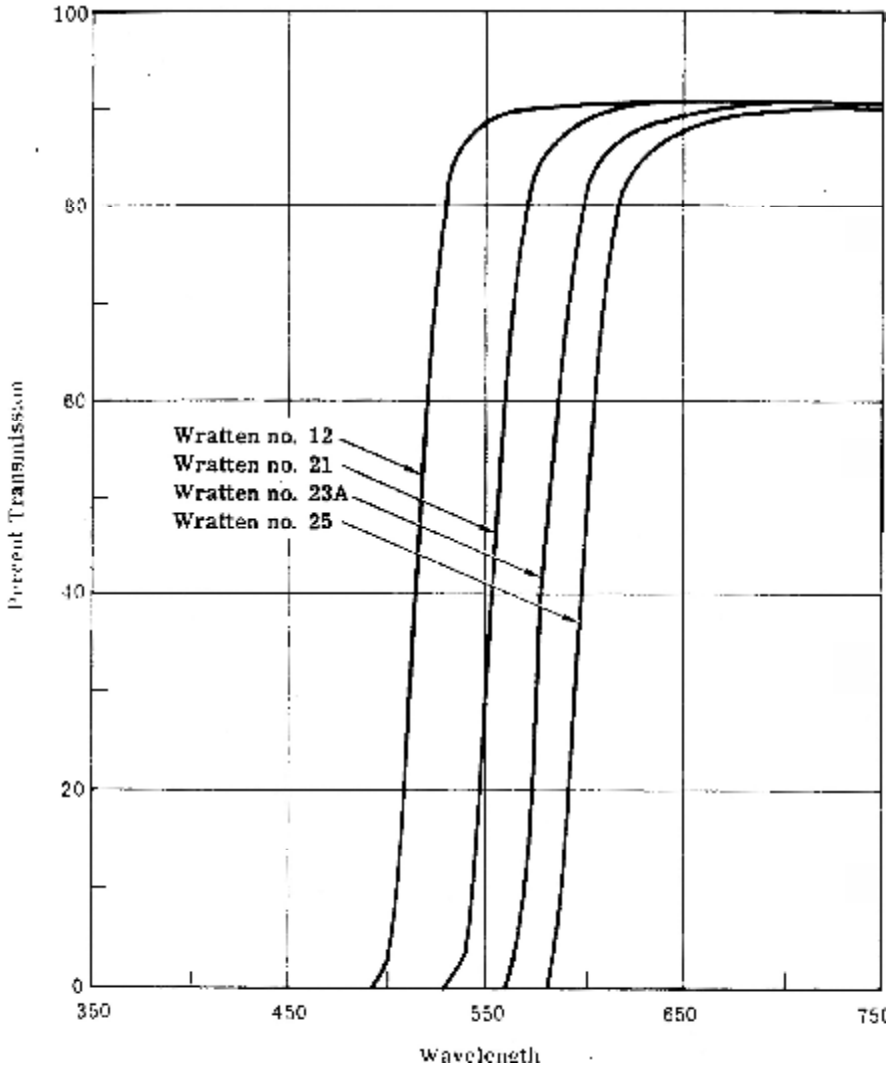

Figure 2-14 – Characteristic curves of CORONA filters (NRO, 1970b).

KH-4B had a filter switching mechanism that allowed the mission to be flown with two filters per camera. The primary filter was used for most missions, and the alternate

filter could be ordered into position. The change in filter factor could be accommodated by changing the exposure slits (NRO, 1970b).

2.1.17.2. Film

The film type used in CORONA missions has always been under question since Kodak preserves a high degree of secrecy regarding its projects with the government even if they are declassified. There is no doubt that Kodak experimented with films with every CORONA mission (Happel, 2000). The secrecy remained during the construction of the satellites, when only Kodak staff knew the film type to be used, without telling anything to other colleagues.

Apart from the film type, there have been questions about film resolution. It was 1969 when the American National Standards defined that the l/mm (lines per mm) and lp/mm (line pairs per mm) are the same film resolving power. Thus, a film with 160 lp/mm resolving power has 160 l/mm resolving power as well. The l/mm and lp/mm are separated only in television terminology, where 160 lp/mm are actually 320 l/mm. From these, we may assume that the lp/mm in CORONA documentation up to 1969 could have followed the television terminology.

According to Day *et al.* (1998), the film types used in CORONA are:

Table 2-3 - CORONA film types

	KH-1	KH-2	KH-3	KH-4	KH-4A	KH-4B
Main film type	1213/acetate	1221	4404	4404	3404	3404, 3414[8]
Nominal film resolution	50-100	50-100	50-100	50-100	120	160
Exposure time (sec)	Fixed (1/1000)	Fixed (1/500)	Fixed (1/500)	Fixed (1/270)	Fixed (1/339)	(4) selectable
Filter control	Fixed (W-21)	Fixed (W-21)	Fixed (W-21)	Fixed (W-21)	Fixed (W-21)	(2) selectable

The NRO data book (NRO, 1967a), Ondrejka (2000), and Ruffner (1995) state that the KH-4B used the Estar based 3404 film. But according to the Kodak technical specifications of the 3404 film (1992), the film resolution is 130 lp/mm (TOC 1:1000), something that contradicts the 160 l/mm reports. According to a 1970 Kodak publication of the 3400 film type, that film's resolving power is 160 l/mm.

Various factors affect the resolution of the cameras. Thus, the above discussion about film resolution within CORONA should not be overemphasised. The resolution capacity of the optics (Petzval lens), the resolution capacity of the film, the focus condition of the

[8] Also available SO-380, SO-242, SO-230, SO-205, SO-121, and SO-180 (colour and infrared films)

lens, the exposure and development of the film, and the blur are all factors affecting the resolution of the CORONA cameras (NRO, 1967c).

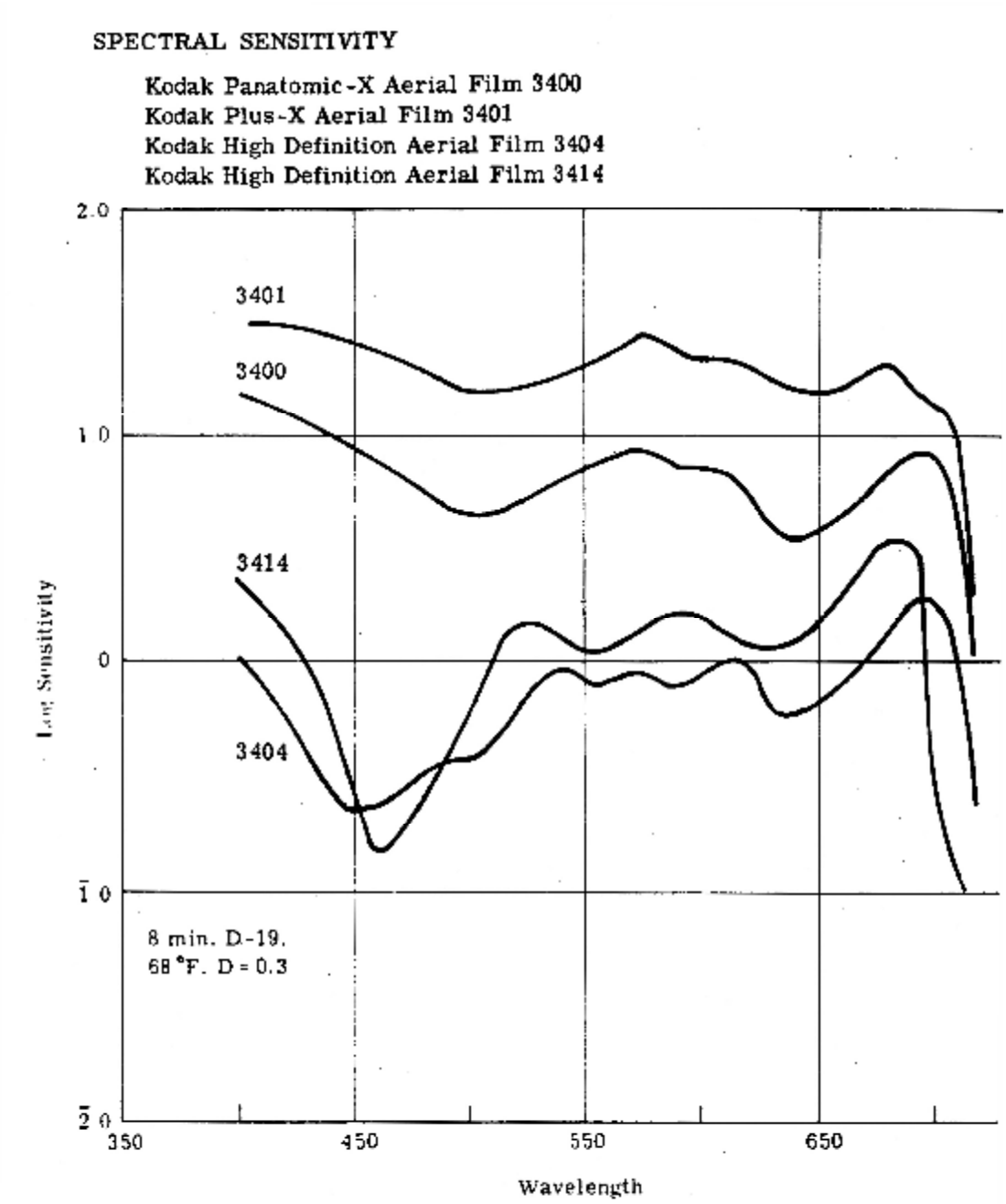

Figure 2-15 – CORONA films. Spectral sensitivity curves (NRO, 1970b).

According to NRO (1970b), during the earliest missions, the CORONA project used variable spray processing conditions for 3404 film. This included a three-level processing – primary, intermediate and full (which provided different sensitometric responses). Beginning with mission 1104 (7 August 1968), a single level yardleigh viscous process was used. On July 1970 Eastman Kodak replaced film 3404 with film

3414. According to NRO (1970b), the 3414 emulsion characteristics are similar to 3404 emulsion with the exception of spectral response and film speed.

Figure 2-14 displays the spectral sensitivity of the films 3404 and 3414, along with the films used in index, horizon and stellar cameras.

2.1.17.3. Geometry

In figure 2-16, the panoramic geometry of KH-4A film is presented. One of the pioneering CORONA camera efforts, and eventual incorporation into a number of KH-4A camera systems, was a geometrically calibrated angular reference system, which was "imaged" alongside the terrain image at the time of photographic exposure. The purpose of the reference was to better describe the "true" geometry of the acquired terrain image by incrementally correcting the effects of lens distortion, the location of the lens during scanning, film movements in the camera, and film deformations after exposure and after film processing and duplication. These corrections would provide more precise photogrammetric measurements and mathematical models of the panoramic stereophotos for computer-based mapping and target image locations. For more information on the distortions of CORONA imagery, see paragraph 4.1.2, and for the mathematical models see paragraph 4.1.3.2 and Appendix III.

The cameras initially incorporated a "dot" reseau at 1-degree scan intervals along both edges of the film. The photo image of the dot was designed to be 0.010 mm in diameter and the dots had an interval of approximately 10 mm. These dots were exposed sequentially during lens scan, adjacent to the imaged terrain photo element, not unlike a fixed angular "scale" in a surveyor's theodolite. The dots were created by holes drilled in the metal rails holding the film and the terrain illumination beyond the ends of the photo imaging slit passed upward through the holes and imaged as a dot on the film.

The rails remained a standard feature on all further CORONA cameras and variations of this scan-angle reference are incorporated in present day panoramic cameras.

Itek took the panoramic geometry concept even further at the request of the mapping community because the use of the ultra thin base films was causing excessive deformations in the image during film take-up, processing, drying and duplication. The Itek solution was to incorporate three tiny light projecting collimators that were "parasites" to the lens cell with their projection axis angularly referenced to the optical axis of the camera lens. The result was three very thin lines along the panoramic photo,

one representing the optical axis, and the other two at the upper and lower edges of the image. Measurements of these lines gave "true" image angles in the field of the lens (along the camera focal plane silt) while the rail dots gave "true" angles along the scan.

Because these collimator "traces" (on the terrain image) caused some confusion for intelligence photointerpreters, they had a "short-run" in the cameras, but they had served their purpose in describing the location and magnitude of the ultra thin base effected geometry for the duration of the CORONA program (Ondrejka, 2000).

Other important features on film are the time pulses, and figure 2-15 illustrates the "image" of a missing time pulse and a smeared time pulse. Also, the figure illustrates the "image" of shrinkage marks. The above are of importance to the photogrammetrist and the mapping community.

The different items showed in figure 2-15 on the film are:

Film shrinkage marks: Images of arrowhead-shaped cut-outs on the film guide rails. The actual distance between these marks is available from the calibration report. The measured on film distances may be used for determination of the shrinkage.

Camera serial number: Even number indicates the master camera, and odd number the slave camera.

Binary time word: A recording of vehicle clock time to the nearest millisecond. The time word contains 29 bits and 2 index marks. For a list, see NRO, 1967a.

Titling data: Pass number, frame number, an arrow (indicates frame), mode (S for stereo, M for mono, MS for mixed), date, mission number, camera (fwd or aft), and classification. The letters D, A, M, and E of the pass number indicate descending, ascending, mixed, and engineering respectively.

IMC collimator traces: Imaged records of fixed angular separations on the camera scan head.

Panoramic geometry fiducial marks: An image of the 73 holes through the film guide rails. Each hole is 40 microns in diameter spaced at one cm intervals.

Time track: An image of a 200 cycle per second light pulse that records the camera lens scan rate.

Missing time pulse indicates scan arm position when clock was interrogated.

Smeared time pulse is a stretched pulse that normally is imaged every seventh frame on the fwd camera. It indicates a stellar index firing so that panoramic frames may be correlated to stellar index frames.

End-of-operation indicator is a cross imaged on the last frame of camera operation.

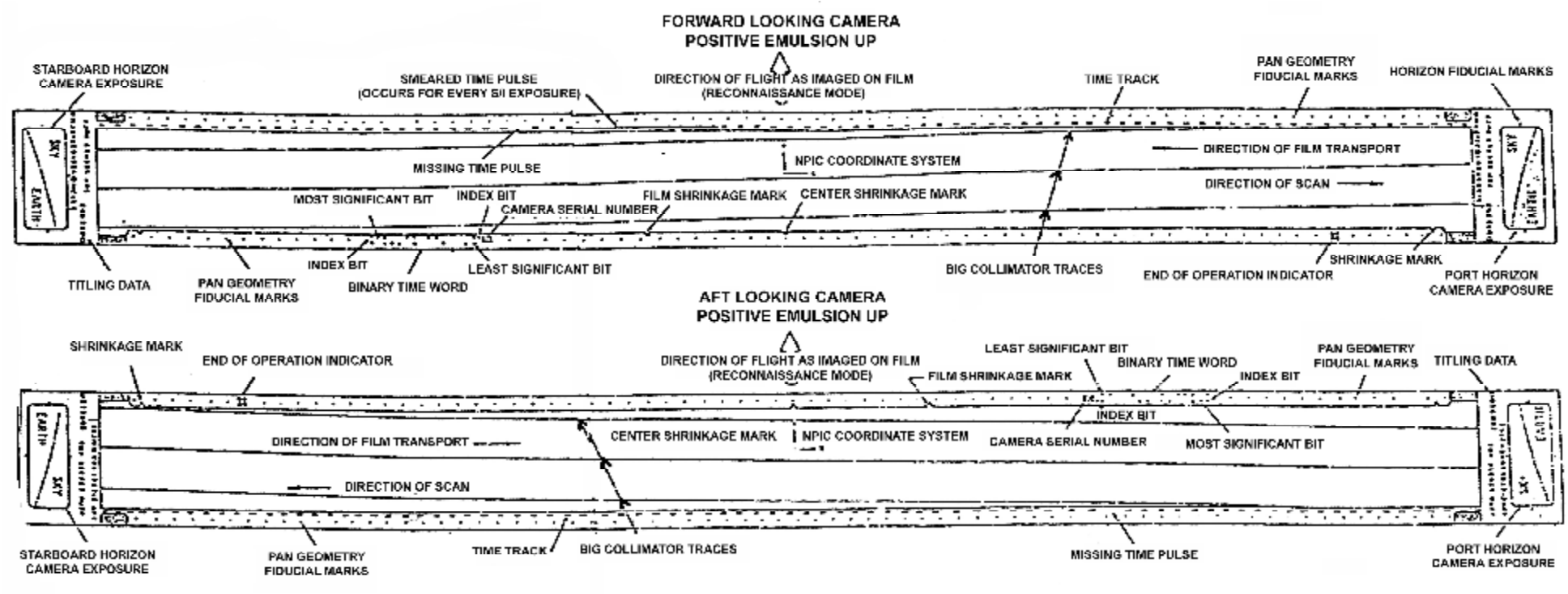

Figure 2-16 – Illustration of the CORONA panoramic geometry system with other format assists on the forward and aft CORONA cameras (reproduced from NRO, 1967b).

2.1.17.4. Image Motion Compensation (IMC)

In KH-1, the IMC was constant, thus the satellite could only fly at a particular altitude. Later on, the IMC was improved and after KH-2 it could change, and so the satellite could vary its altitude. Later on, the Motion Compensation system became more complex due to the inclusion of two cameras.

In J-3, each camera was nodded independently about an axis parallel to the pitch axis of the vehicle to accomplish forward motion compensation (FMC). The compensation for any given combination of altitude and ground speed (V/H) required a constant angular rotation during the photographic scan. Since the cycle rate required maintaining a constant overlap and was also a function of V/H, the nod rate had a fixed relation to the scan rate. The overlap of this system is 7.6 % at centre of format. The required nod was accomplished by a cam-driven linkage, with the pivot point of the camera being located as close to the centre of gravity as practical to keep the inertia forces to a minimum.

The FMC cam and linkage form the equivalent of a planar 4-bar linkage, with the extensive link (cam pushrod) restrained at a constant angle with the driven link (scan shaft), one link fixed (delta), and one member (upper rod) rotatable at each end. The nod axis bearings were offset from each side of the central plane, while all other links were restrained in the centre plane by clevis attachments and grooved rollers. The FMC cam and linkage were designed to give a specified ratio of nod angle rate to scan angle rate, and a specified stereo half angle at mid-scan (15.23 degrees).

Photographic mission requirements determined the angular rate ratio between nod (FMC) rate and scan rate during the active scan section of the cycle. This ratio was constant and positive for the aft-looking camera and constant and negative for the fwd-looking camera.

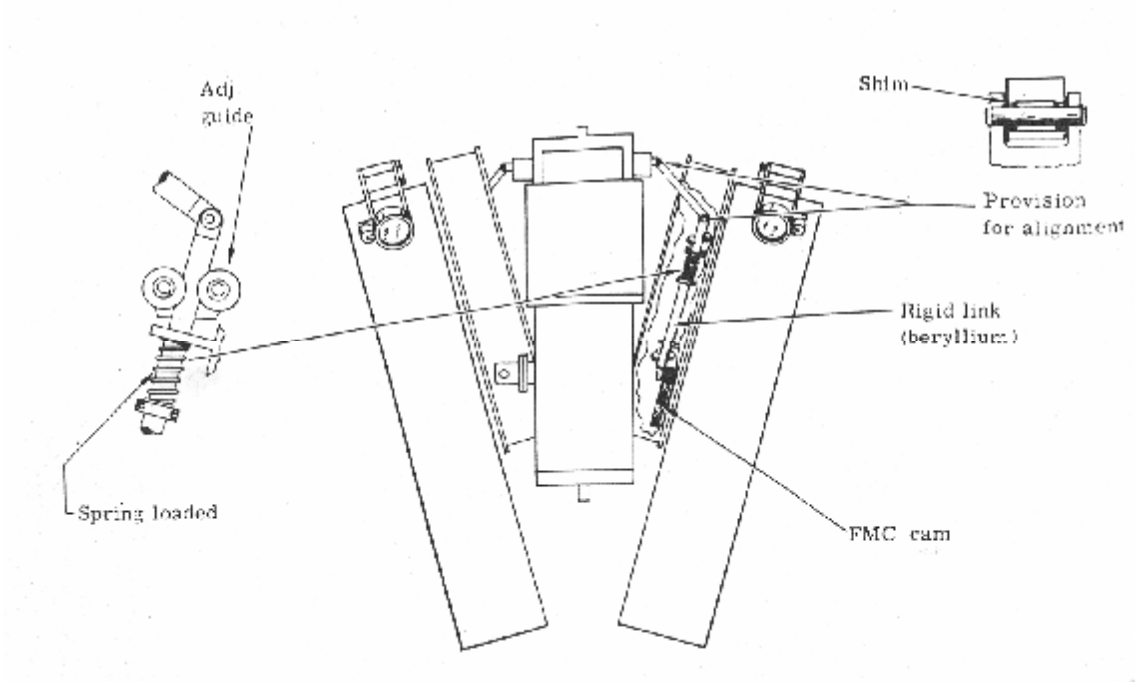

Figure 2-17 – Forward motion compensation mechanism (NRO, 1970b)

Even though the FMC cam was nearly symmetrical, there was a 180-degree phase difference of nod angle to scan position for the two cameras making it impossible to interchange the cameras within a system. Once the cameras were assembled they had to remain as such in order to get proper FMC. The cam pushrod assembly was preset and pinned at assembly for proper spring pre-loading. This assembly was shimmed, aligned and pinned to a given camera structure and had to remain with that structure. The upper rocking link was carefully shimmed to ensure that it (the pushrod) and the scan shaft were coplanar.

2.1.18. The imagery of the project

From the above analysis, it is apparent that no mission was the same as another and no camera was the same as another. The experiments with cameras, films, filters, slits, lens and other satellite systems were continuous. Information taken from declassified CORONA documents such as NRO (1970a) and NRO (1970b) allowed acquisition of the specific satellite system design for the imagery used in this thesis (Table 2-4). There are still some unanswered details, such as whether the alternate or the prime filter was used for the particular frames, or whether the film is the main one or was spliced-in for the particular frames. Such details may be included in the mission reports in NRO library, but are probably not of vital importance for archaeological purposes.

Table 2-4 – The particular design of the satellite system for the imagery of the project.

Mission	Cameras	Frame No.	Date	Petzval	Film	Filters[$]
1108	Aft	42,43,44,45	17/12/1969	Type III	3404	25/25
1110	Fwd	07,08,09	28/05/1970	Type II	3404/14[*]	21/23A
1110	Aft	13,14,15	28/05/1970	Type III	3404/14[*]	23A/25
1111	Aft	01,02	31/07/1970	Type III	3414	25/25[¥]

[$]Prime/Alternate. The most likely filter for the images in the project is the prime. Without the mission reports, there is uncertainty.

[*]3414 film was spliced-in. Without the reports there is uncertainty if the film of the project was 3404 or 3414. Most probably it was 3404.

[¥]The alternate filter was glass filter 0.007 inch for increase of 0.001 inch in focus.

From Table 2-4, it is apparent that the two cameras of mission 1110 have a different generation lens, the forward camera has a second generation and the aft camera a third generation petzval lens. This has an impact in the film resolution. According to NRO (1970a), the performance nadir prediction of the second generation lens is 130 lp/mm and the third generation lens is 155 lp/mm (for a 2.44 msec exposure time, 3404 film type, 2:1 contrast, field angle 0°, and 152 km altitude).

2.1.19. Concluding summary

Although CORONA was a military reconnaissance satellite system, it produced the first systematic image maps of the Earth's surface at high spatial resolution. It was also the first remote sensing mission to produce stereoscopic image pairs for photogrammetric use.

When the current research started, the precise details of CORONA satellite imagery were largely unknown among the user community. After intense research and establishment of contacts, a lot of information was acquired about the CORONA project, the missions, and the cameras. All this information is now summarised in this chapter. Although more work could be done (for example, a visit to NRO library) this would be very time consuming, and this is not the prime objective of this PhD thesis. Hopefully the work to date will prove useful and will provide a sound basis for future research on the CORONA program.

The value of the CORONA series of satellite imagery mainly lies in its high spatial resolution and low cost as much as the area each frame covers. It is also of historical value, since it provides data from time periods and areas where alternative information (e.g. aerial photos) can be very hard to obtain.

There are various tradeoffs that must be considered when selecting the appropriate frames for any given area of interest. The cloud cover, image quality, the possible photographic system usage problems are all important considerations. From the six different satellite designs of CORONA program, the first three (KH-1, KH-2, and KH-3) mainly have qualitative value, and the latter three (KH-4, KH-4A, and KH-4B) offer qualitative and quantitative information (Galiatsatos et al., 2000).

The knowledge of the CORONA camera system (including film, filters and lens system) is vital for spectral analysis of the imagery. It is a fact that throughout the whole CORONA program there were a lot of experiments and analysis with different combinations of the camera system elements, and a continuous improvement in every mission. These made each mission unique. Thus, the image analyst should check the details of a particular mission before applying any analysis to the relevant data. The interested analyst may also wish to look into the CORONA reports either in NARA or in NRO. The panoramic geometry may also be a problem for many users. This is further discussed in chapter 4.

For this research, the work presented in chapter 2 proved helpful for all the other chapters of this thesis. The knowledge of film resolution proved helpful for image scanning. The knowledge of the camera system geometry proved helpful for the geoprocessing and establishing the best approach for geometric corrections. The knowledge of the films, lenses and filters proved helpful for the spectral analysis of the archaeological sites. The knowledge of focal length and satellite geometry proved helpful for the DEM production.

3. Understanding satellite data

A good understanding of the characteristics of satellite data should be developed in order to make best use of the information they contain. It is important to know their spectral characteristics to assess image quality for photointerpretation and for spectroradiometry studies. It is also important to appreciate their spatial characteristics particularly if these data are to be used in image analysis. The technical characteristics of image data must be well understood before image analysis begins.

The previous chapter described the CORONA program because it is the least well understood of the images used in this thesis. In this chapter, the satellite data of Landsat 5 TM, Landsat 7 ETM+, IKONOS, Terra-ASTER and HEXAGON will be presented. The technical characteristics of each sensor are discussed in the context of archaeological applications. Future satellite missions are presented to illustrate the potential for further use of remote sensing data in the field of study.

3.1. Landsat 5 TM and Landsat 7 ETM+ imagery

The Landsat program began in July 1972 with Landsat-1 and has operated continuously until the present day with Landsats 5 and 7. The Landsat Earth resources satellite system was the first designed to provide near global coverage of the Earth's surface on a regular and predictable basis. A description of how the multispectral data analysis technology, which has come to be synonymous with Landsat, was begun and how it developed and spread through to a broader research and user community is presented by Landgrebe (1997).

Four imaging systems have been flown on the Landsat satellites. These are the Return Beam Vidicon (RBV), the Multispectral Scanner (MSS), the Thematic Mapper (TM), and the Enhanced Thematic Mapper Plus (ETM+).

The RBVs were television camera-like instruments that captured image frames of 185km x 185km. Three RBV cameras were used in each Landsat 1(23/7/72-6/1/78) and Landsat 2 (22/1/75-27/7/83) satellites with different transmission filters (blue, red, near IR) and a spatial resolution of 79m. On Landsat 3 (5/3/78-7/9/83) two panchromatic RBVs were used, each with a data swath of 98km, overlapped to give 185km total. Thus, the spatial resolution was 40m.

The MSS was the principal sensor on Landsat 1, 2 and 3. It has four wavelength bands (green, red, 2x near IR) with an additional thermal band in Landsat 3. The MSS is

a mechanical scanning device, where six lines are simultaneously swept through an oscillating mirror, acquiring data by scanning the Earth's surface in strips normal to satellite's motion through 24 signal detectors (4 bands times 6 scan lines). The IFOV of each detector was 79km x 79km. However, it is sampled in time to produce discrete measurements across a scan line. The sampling rate corresponds to pixel centres of 56m giving a 23m overlap of the pixels. The IFOV of the MSS on Landsat 4 and 5 have been modified to 81.5m and 82.5m respectively. The pixel centre spacing of 56m has been retained.

The TM is a mechanical device like MSS, but with improved spatial, spectral and radiometric characteristics. Seven bands are used (blue, green, red, near IR, 2x mid IR, thermal) with 16 scan lines. The IFOV is 30m x 30m (120 m for the thermal band). It is included in Landsat 4 and 5. Landsat 4 (operated since 16/7/82) completed deorbiting manoeuvres in June 2001. Landsat 5 (operated since 1/3/84) will continue operations even in 2005 if there is enough funding. Landsat 6 failed to achieve orbit.

In 1992, the US Congress authorised the procurement, launch and operation of a new Landsat satellite. On 15th April 1999, the Landsat 7 satellite was successfully launched. Landsat 7 was expected to have a unique and essential role in the realm of Earth observing satellites in orbit by the end of the 1990s.

The Earth observing instrument on Landsat 7, the Enhanced Thematic Mapper Plus (ETM+), replicates the capabilities of the highly successful Thematic Mapper instruments on Landsat 4 and 5. The ETM+ also includes new features that make it a more versatile and efficient instrument than its predecessor for global change studies, land cover monitoring and assessment, and large area mapping. The primary new features on Landsat 7 are a panchromatic band with 15m spatial resolution, 5% absolute radiometric calibration, and a thermal IR channel with 60m spatial resolution. The cost of a LANDSAT 7 level 1R scene covering an 185km^2 area is 600 USD[9].

For more technical information on Landsat TM, please check Markham and Barker, 1985, Salomonson, 1984, Townsend *et al.*, 1987.

The main mission of Landsat has always been the provision of environmental information. With a spatial resolution of 15 m in the panchromatic channel, Landsat could never be used as a substitute for aerial photography. However, the multispectral capability of Landsat can derive important environmental information that is of considerable value in archaeological landscape assessment (Drake *et al.*, 1999). Landsat

[9] http://edc.usgs.gov/products/satellite/landsat7.html#prices (July 2004)

TM imagery has been used for detecting Anasazi roads in New Mexico (Sever, 1990), prehistoric footpaths in Costa Rica (Sheets and Sever, 1988), and roadway segments in Peten of Guatemala (Sever, 1998). It has been used to identify forest cover and change in Southern Madagascar (Clark *et al.*, 1998). It has been used in palaeoenvironmental studies in southern Tunisia combined with geomorphological and archaeological evidence (Drake, 1997) and in the monitoring of the changing position of Nile Delta coastlines (White & El Asmar, 1999). Also, the classification of Landsat data for defining soils and land use categories is invaluable for interpreting agricultural potential, a variable that is frequently used in archaeological landscape studies.

On 31st May 2003, the Scan Line Collector (SLC) instrument on Landsat-7 failed to operate. This instrument compensates for the forward motion of the satellite. At the present time the problem appears to be permanent. The sensor is still capable of acquiring data during SLC-off mode, and the USGS EDC is implementing a series of improvements to these products.

The SLC-off mode resulted in scenes with gaps. These scenes are now sold at the price of 250 USD. One of the efforts of USGS EDC included the filling of the gaps with imagery taken prior the malfunction. The price of these filled gaps scenes is 275 USD. These were the prices in July 2004.

3.2. IKONOS imagery

The IKONOS satellite was launched on 24th September 1999 with all detectors operable. It is the first of the new generation of high-resolution satellites, which was prepared by studies such as Fritz (1996) and Ridley *et al.* (1997). IKONOS was launched into sun-synchronous orbit with an inclination of 98.1° to the equator at the altitude of 681 km, and an orbital period of 98.3 minutes. Local crossing time at descending node is 10:30 a.m.

IKONOS is capable of pointing off-nadir, thus it is possible to increase the frequency of revisit time with the trade-off of a small decrease to the spatial resolution of the image, always depending on the latitude and the elevation of the target (see Table 3.1, Gerlach, 2000).

Table 3-1 - IKONOS revisit frequency

	Target	Point Target Location	
GSD (meters)	Sensor elevation	Equator (days)	40 degrees (days)
0.84	79°	11	8.5
1.00	60°	3.9	2.9
1.18	50°	2.8	2

Unlike other sensors, IKONOS has the capability to collect data in either whiskbroom or pushbroom mode. The IFOV equates to 11 km when at nadir, and 13 km off-nadir with 1 m spatial resolution. A contiguous area of 4700 sq. km. can be acquired on a single pass in 128 sec with a GSD (Ground Sample Distance) of 1 m. In addition, IKONOS can image long stripes of 13 km x 1000 km for 1m GSD. Same pass stereo images can be acquired by pointing the sensor forward of nadir and then aft of nadir to create a stereo-pair. The satellite is designed to operate 120 minutes per day, but there were days of 200 minutes operation (Gerlach, 2000).

Table 3-2 - Main IKONOS characteristics

Bands (μm)	Spatial Res.	Radiometric Res.	IFOV	Metric accuracy
Panchromatic	(nominal)			10 m horizontal, 12 m vertical without GCPs.[1] 2 m horizontal, 3 m vertical with GCPs.
0.45-0.90	1m	11-bit	1.2 μ-radians	
Multispectral				
1: 0.45-0.52 2: 0.52-0.60 3: 0.63-0.69 4: 0.76-0.90	4m	11-bit	4.8 μ-radians	

[1]Ground Control Points

In Table 3-2, some of the main characteristics of IKONOS are shown. The multispectral bands are similar to bands 1-4 of Landsat TM and ETM+. Also, the 11-bit radiometric resolution adds one more advantage to IKONOS. With 8-bit data, bright areas and structures are often overexposed, and dark and shadowed objects are often indistinguishable. By quantizing the optical signal to 11-bits, it is possible to improve the contrast in bright and dark image areas significantly. Although 11-bit quantization equates to 2048 counts, only 1800 are used by IKONOS (Gerlach, 2000). The camera IFOV shows that at 681km altitude, the spatial resolution equals to 0.82m and 3.26m, but due to legal restrictions it is resampled to 1m and 4m respectively. In figure 3-1, the IKONOS relative spectral response is presented. The Panchromatic band does not incorporate spectral filtering. The response is that of optics/detector only.

Accuracy without ground control requires excellent knowledge of orbital ephemeris

data, satellite attitude (pointing direction), and interlock angles between the telescope bore-sight and star trackers. On-board GPS receivers and ground processing determine orbital ephemeris. Star trackers determine satellite attitude. Combining ephemeris, attitude, and interlock information enables ground processing to triangulate on ground features and determine their position. By using GCPs, accuracy is significantly improved.

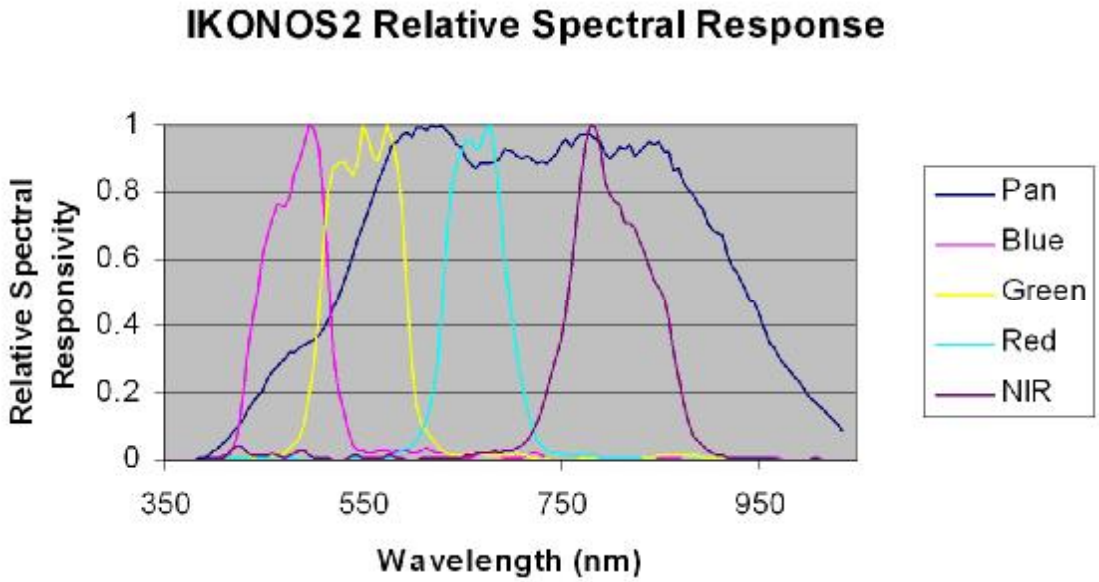

Figure 3-1 – IKONOS relative spectral response (Source: Spaceimaging web page, 2004)

Spaceimaging offers a variety of products that are separated according to accuracy and level of preprocessing. These products are presented in table 3-3. For information on prices, please check the price-book in the following web page http://www.spaceimaging.com/products/SI_pricebook.pdf (last accessed: July 2003).

Table 3-3 – IKONOS product levels at a glance (Spaceimaging product guide, 2004)

	Positional accuracy (m)			Ortho corrected	Target elevation angle	Mosaicked	Stereo option	Applications
	CE90	RMS	NMAS					
Geo	15.0*	N/A	N/A	No	60° to 90°	No	No	Interpretation
Standard Ortho	50.0**	25.0	1:100,000	Yes	60° to 90°	No	No	Basic mapping
Reference	25.4	11.8	1:50,000	Yes	60° to 90°	Yes	Yes	Regional, large area mapping
Pro	10.2	4.8	1:12,000	Yes	66° to 90°	Yes	No	Transportation, infrastructure, utilities planning
Precision	4.1	1.9	1:4,800	Yes	72° to 90°	Yes	Yes	High positional accuracy
PrecisionPlus	2.0	0.9	1:2,400	Yes	75° to 90°	Yes	Yes	Infrastructure mapping

*Exclusive of terrain effects

**May be up to 75 metres CE90 (Circular Error with 90% trust) in undeveloped areas with high terrain relief (e.g. Andes or Himalayan mountain ranges).

There are other high-resolution satellite systems operating and more planned for the future. The Russian ex-military satellite, KVR-1000 now provides 1 m resolution panchromatic images. EROS A1 successfully reached orbit in December 2000. It offers a spatial resolution of 1.8 m in Standard mode and sub-metre in Hypersampling mode, with a swath width of 13.5 and 9.5 km respectively. Orbview 3 succesfully reached orbit in June 2003. It has similar resolution characteristics to IKONOS, but with 8 km swath width instead of the 11 km of IKONOS. The U.S. government allowed the operation of private satellites with spatial resolution of 50 cm. Thus, in October 2001, the Quickbird satellite became the first to proved sub-metre resolution imagery with 16.5 km swath width. Also, in September 2002, more declassification took place with the Hexagon (KH-9, resolution 6-9 m) and Gambit (KH-7, resolution 0.60-1.20 m) space photography.

High resolution satellite data can provide: i) an alternative source of high resolution imagery to conventional aerial photography, ii) an alternative to topographic maps for field survey work in many developing countries, and iii) a source of modern imagery to compare with historical CORONA data from the 1960s.

3.3. ASTER (Advanced Spaceborne Thermal Emission and Reflection Radiometer)

ASTER (Advanced Spaceborne Thermal Emission and Reflection Radiometer) is an imaging instrument that is flying on Terra, a satellite launched in December 1999 as part of NASA's Earth Observing System (EOS). ASTER is used to obtain detailed maps of land surface temperature, emissivity, reflectance and elevation. The EOS platforms are part of NASA's Earth Science Enterprise, whose goal is to obtain a better understanding of the interactions between the biosphere, hydrosphere, lithosphere and atmosphere (Abrams, 2000; Abrams & Hook, 1999).

Table 3-4 – Instrument specifications

Platform	Terra (AM-1)
Number of channels	14
Instrument type	Multispectral imager for reflected and emitted radiation measurements of the Earth's surface
Spectral bands (channels)	0.52 to 12 microns
Swath	60 km at nadir, swath centre is pointable cross-track +/-106 km for SWIR and TIR, and +/-314 km for VNIR
Spatial resolution	VNIR-15 m, SWIR-30 m, TIR-90 m

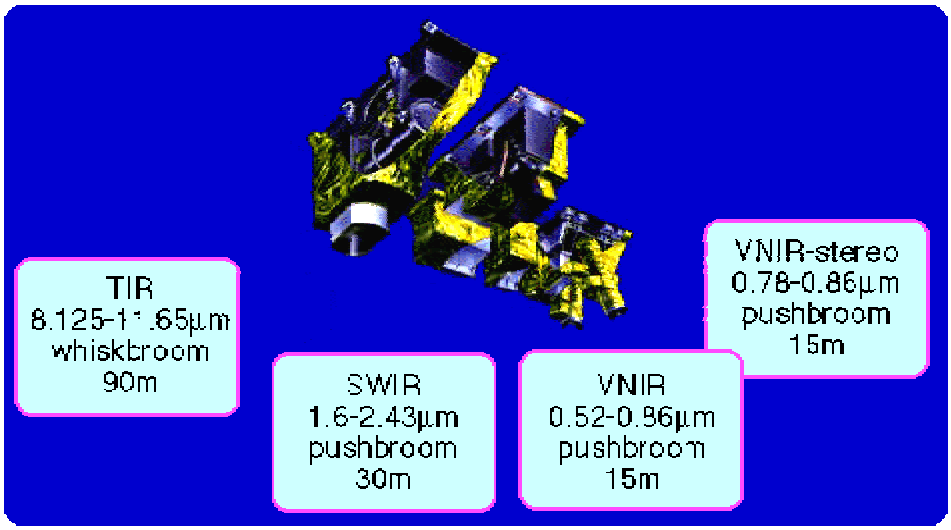

Figure 3-2 – ASTER instrument parts

Table 3-5 – Channel information for the ASTER instrument

Subsystem	Band number	Spectral range (microns)	Spatial Resolution (m)	Radiometric Uncertainty
VNIR (visible to near IR)	1	.52 to .60	15	<0.5%
	2	.63 to .69	15	<0.5%
	3 Nadir looking 3 Backward looking	.76 to .86	15 (stereoscopic imaging, base/height = 0.6)	<0.5%
SWIR (shortwave IR)	4	1.6 to 1.7	30	<0.5%
	5	2.145 to 2.185	30	<1.3%
	6	2.185 to 2.225	30	<1.3%
	7	2.235 to 2.285	30	<1.3%
	8	2.295 to 2.365	30	<1.0%
	9	2.36 to 2.43	30	<1.3%
TIR (thermal IR)	10	8.125 to 8.475	90	<0.3K
	11	8.475 to 8.825	90	<0.3K
	12	8.925 to 9.275	90	<0.3K
	13	10.25 to 10.95	90	<0.3K
	14	10.95 to 11.65	90	<0.3K

From an early evaluation of the ASTER imagery (Yamaguchi *et al.*, 2001), the quality of the images seems to exceed current Earth observation systems even at a preliminary processing level.

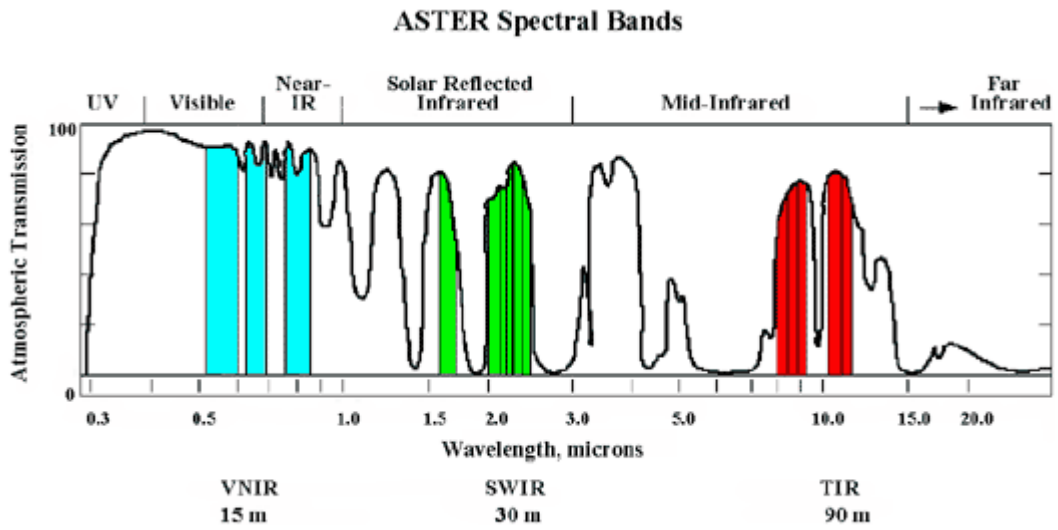

Figure 3-3 – ASTER bands superimposed on model atmosphere

3.3.1. ASTER data for Homs

After a search in http://edcimswww.cr.usgs.gov/pub/imswelcome/ (last accessed: July 2004) with the following criteria:

Sensor: ASTER

- Area of interest: North latitude = 34.8750, South latitude = 34.5000, West longitude = 36.5000, East longitude = 36.7514

Date of interest: 24-Feb-2000 until today.

The results of the above search criteria are shown in table 3-5. On-demand ASTER data can be also ordered from NASA (http://e0ins01u.ecs.nasa.gov:10800/).

Table 3-6 – ASTER data for Homs

Data Set	Number of granules
ASTER Digital Elevation Model V003	3 (of 3)
ASTER L1A Reconstructed Unprocessed Instrument Data V002	6 (of 6)
ASTER L1A Reconstructed Unprocessed Instrument Data V003	16 (of 16)
ASTER L1B Registered Radiance At The Sensor V003	2 (of 2)
ASTER L2 Decorrelation Stretch SWIR V003	3 (of 3)
ASTER L2 Decorrelation Stretch TIR V003	3 (of 3)
ASTER L2 Decorrelation Stretch VNIR V003	2 (of 2)

None of the imagery of Table 3-5 covered the area of Homs. The overlapping parts may be seen in figure 8-10. More on the ASTER data for the Homs area are included in Appendix I. The following paragraphs discuss only the ASTER data that are presented in Table 3-5.

3.3.2. AST14 - Digital Elevation Model (DEM)

This data set contains topographic information derived from the along-track, 15 m ASTER optical stereo data acquired in near infrared bands 3N (Nadir looking) and 3B (Backward looking). It can be created as a Relative DEM (no ground control) or an Absolute DEM (with ground control which must be supplied by the user). These high spatial resolution DEMs (up to 7 m absolute horizontal and vertical accuracy with appropriate ground control, and up to 10 m relative accuracy without ground control) can be used to derive absolute slope and slope aspect good to 5 degrees over horizontal distances of more than 100 m. ASTER DEMs should meet 1:50,000 to 1:250,000 map accuracy standards.

This is an on-request product, which is generated by the Land Processes DAAC (Distributed Active Archive Centre) at EROS Data Centre at a rate of one 60 km X 60 km stereo pair/day. ASTER digital stereo data set with a base/height ratio of 0.6 cover the Earth's entire land surface below 82 degrees latitude. ASTER stereo pairs also can be processed to DEMs by users operating their own software.

Generation of elevation models from stereo photographic data, now a routine adjunct to standard surveying methods, has been developed over the past 60 years based on the principles of photogrammetry. Extensions of these principles to the generation of DEMs from optical, digital stereo satellite data has been implemented over the past two decades. Examples of these satellite stereo systems include SPOT, JERS-1 OPS, and MOMS (see chapter 7). Currently, there are large areas of the globe for which no consistent, high-resolution, widely available elevation models exist. ASTER DEMs will help provide much needed coverage over many of these areas.

An autocorrelation approach using commercial software at the Land DAAC is producing DEMs from Level 1A or 1B digital stereo pairs. This product is produced using off the shelf commercial software. Absolute accuracy depends on availability of investigator-provided ground control points.

3.3.3. L1A Reconstructed Unprocessed Instrument Data V002, V003

The level 1A data are reconstructed unprocessed instrument data at full resolution, time-referenced, and annotated with ancillary information, including radiometric and geometric calibration coefficients and georeferencing parameters (i.e., platform ephemeris) computed and appended (but not applied) to the Level 0 data.

The level 1A data product consists of the image data, the radiometric coefficients, and the auxiliary data. The image data are raw Level 0 data. Data are separated by telescope (VNIR, SWIR) into band sequential format. The radiometric coefficients are determined from pre-launch engineering measurements and post-launch engineering vicarious calibration determinations. The coefficients can be used in the Level 0 data to calibrate radiance at the sensor. In-flight blackbody observations are used to calibrate the TIR signals. Geometric correction parameters are also determined and stored. These include spacecraft attitude vectors, inter-telescope registration, band-to-band registration, etc. The data are reported in counts or digital numbers scaled to 8 bits. This form of data is requested by users who do not want their data resampled in any way and ASTER data in as close to raw condition as possible.

3.3.4. The difference between V002, V003

The Japanese Ground Data System (GDS) started processing ASTER Level-1 data (and re-processing earlier data) using a newer, improved algorithm (Version 04.00R00) and also an improved set of radiometric calibration and geometric correction coefficients databases on May 1, 2001. To avoid user confusion in identifying different versions of the same granule in search results, it was decided to migrate Level-1 data produced in Japan on and after May 1, 2001 (and the routinely-produced higher-level products derived from them) to a separate collection, which is version 003.

The key determinants of the collection split are:

Production Date & Time: May 1, 2001 at GDS, Japan

PGE Version: Version 04.00R00 (and higher versions) at GDS, Japan

Geometric Database Version: 02.00 (and higher versions)

Radiometric Database Version: 02.05 (and higher versions)

Therefore, there are 2 separate collections (Versions 002 and 003) of ASTER Level-1, Level-2, and Level-3 data sets available from the LP DAAC archives.

3.3.5. L1B Registered Radiance At The Sensor

Level 1B data are generated from the Level 1A data by applying the radiometric coefficients to calibrate the data to radiance-at-the-sensor; and by applying geometric coefficients to produce the map projection requested by the user. These data are reported in units of radiance (W m^{-2} sr^{-1} μm^{-1}). The user can also select the resampling method used for both of these transformations. This format is the one most users will probably order who want ready-to-use ASTER data, rather than raw data.

3.3.6. AST06 - L2 Decorrelation Stretch SWIR, TIR, VNIR

This product, which is available for each of ASTER's three telescopes, is a decorrelation stretched image of ASTER radiance data. The decorrelation stretch is a process to enhance the colour differences found in a colour image by a method that includes the removal of the inter-channel correlation found in the input pixels; hence, the term "decorrelation stretch". The image is produced at pixel resolutions of 15 m for VNIR, 30 m for SWIR, and 90 m for TIR. Decorrelation-stretched images provide an overview that enhances spectral reflectance variations.

If one views the pixels in an ASTER scene as a set of 3-vectors, a linear transformation can be found which results in removing the correlation among the vectors in the transformed space. This is an eigenvector problem, and can be thought of as a rotation of the coordinate system of the original vector space. Within this rotated space, each component is rescaled (contrast stretched) by normalizing the variances of the eigenvectors. If processing were to stop here, the result would be a principal component image. To produce the decorrelation stretched image, the principal component image is modified by the linear transformation that rotates the vectors back into the original coordinate system. In practice, the original transformation, the variance normalization step, and the reverse transformation are combined into a single algebraic step.

These images are used as a visual aid in reviewing the ASTER scene data and making the selection of suitable scenes for further analysis and research. In particular, a decorrelation stretched image would show the potential user which scenes have spectral variations large enough to be useful for subsequent spectral analysis

The decorrelation stretch algorithm is best suited to the case where the input data of

all three channels have a joint frequency distribution that is Gaussian (or near Gaussian) in form. Fortunately the algorithm is fairly insensitive to substantial deviations from the ideal. One should be aware, though, that if the distribution of the input pixels is strongly bimodal (or multimodal), the effectiveness of the decorrelation stretch is weakened, and there will be less diversity of colour in this image than in other images.

Additionally, the decorrelation stretch algorithm is a method of colour enhancement that exploits whatever inter-channel differences may exist. Implicit in this technique is the assumption that the differences are real, and not noise or processing artefacts. The algorithm single-mindedly produces a colour-enhanced output; if noise is a major component of the scene variation, the algorithm will enhance those noise differences to produce an output that, while colourful, will be noisy.

3.4. HEXAGON KH-9

On 14 August 2002, the NIMA delivered to NARA the original images from two more military satellites programs, the GAMBIT (with the KH-7 design satellite system), which is not examined in this thesis, and the HEXAGON (with the KH-9 design satellite system). NIMA gave a set of duplicate positives to NARA and a set of duplicate negatives to Earth Resources Observation System (EROS) Data Centre, where the public has access and may purchase them according to the prices below. The imagery that contains Israel is not declassified.

The KH-9 system operated from March 1973 to October 1980. It flew 12 successful missions with durations from 42 to 119 days. It was a frame camera system, devoted solely to mapping, charting and geodesy. For each mission, it returned a single bucket of film to Earth. In total, it gave 29,000 frames, or 48,000 ft of film. The footprint on the ground was approximately 70x140 nautical miles (130x260km)[10]. This image format increased the ground coverage and allowed for the creation of trilaps (three images of the same area), thus providing better control for height extraction.

The ground resolution of KH-9 (6.00-9.00 m) may not be as good as KH-4B (1.80-7.60 m), but the image is vertical and it is a frame camera. Also, most coverage of key control point areas was imaged in stereo and sometimes three times (called trilaps) on a single operation to give the geospatial analysts enough information to create precise maps and charts. On top of this, the KH-9 imagery contains reseau points, a help for the

[10] http://www.globalsecurity.org/intell/library/news/2002/kh-7_kh-9_factoids.htm (Accessed: July 2004).

photogrammetrist to correct and remove distortions in the image. It provided key cartographic information for Level 1 digital terrain elevation data and 1:200,000 scale maps.

The prices of the USGS HEXAGON products are (USGS, 2004a):

KH-9 (image size: 9 by 18 inch = 230x460 mm)

Film		
	b&w negative	16.00 USD
	b&w positive	16.00 USD
	colour positive	50.00 USD
Paper		
	b&w print	12.00 USD
	colour print	35.00 USD

Standard Enlargements are available for any selected 9"x9" (230x230 mm) portion of a photo, which allows 2x or 4x enlargement up to 18"x18" (460x460 mm) or 36"x36" (920x920 mm) prints. *Custom Enlargements* may be ordered for any selected portion of a photo. This type of enlargement allows for a potential enlargement factor of up to 16x for the selected area. In addition to the price of the enlarged paper prints, a setup fee of 25 USD per frame will be charged for each standard and custom enlargement.

Two KH-9 satellite images were chosen for the area of interest. From these, a DEM may be extracted, and because of the reseau points it may be possible to correct the CORONA imagery geometry from them. These are black and white negative films:

Acquisition date: 15 July 1975, Mission No. 1210-5.

Entity ID: DZB1210-500148L010001, Frames No.10 and 11.

Undoubtedly, the camera system information may vary from mission to mission, because of possible experiments with film, filters and lens, exactly as was the case with CORONA program. This information most probably exists in the HEXAGON reports, which were not declassified at the time of writing this thesis.

3.5. Comparison of the satellite data

The satellite data used in this research project are all presented in chapters 2 and 3 of this thesis. A brief comparison among them in terms of spatial, spectral, and radiometric resolution, and in terms of swath width, price and availability is presented in table 3-7.

Each of these satellite data has its own strengths and weaknesses for the potential user, in this case, archaeologists. First is the price. IKONOS may be the most expensive, but the price reflects a wholly useful image covering all the area of interest without redundant data. Table 3-6 compares the prices in USD (United States Dollars) per square kilometre for the minimum contiguous area of IKONOS (49 km^2) for all satellite data used. The scanning expenses should be included for the declassified imagery for an accurate comparison of the total cost per square kilometre. In this project, the cost of scanning was about 0.73 USD per km^2. It must be noted that the handling and shipping fees are not included in these calculations.

Table 3-7 – Cost comparison in USD per km^2

CORONA	HEXAGON	IKONOS	ASTER	Landsat TM	Landsat ETM+
1.10	1.06	16 - 39	1.13	8.67	12.25

Thus, IKONOS is by far the most expensive among the project data, and the declassified imagery is the cheapest along with the ASTER data. The ASTER DEM may add more value to the ASTER data for an archaeologist. The ASTER DEM is assessed in chapter 8.

Table 3-8 – Satellite data comparison

Data	*Spatial (m)*	*Spectral (µm)*	*Radiometric*	*Price*[§]	*Area coverage*	*Swath width*	*Time coverage*
CORONA KH-4B	1.8 – 7.60 [*]	Filter dependent	Scanner dependent (8-bit)	18 USD	Worldwide limited[€]	15x200 km^2 (nominal)	September 1967 – May 1972
HEXAGON	6 – 9 [*]	N/A	Scanner dependent (8-bit)	16 USD	Not Available	130x260 km^2 (nominal)	March 1973 – October 1980
IKONOS Pan	1 (nominal)	525.8-928.5[#]	11-bit	16-39[¥] USD/km^2	Worldwide According to orbit inclination	11x11 km^2 (nominal)[¤]	September 1999 – present
IKONOS Ms	4 (nominal)	444.7-516.0					
		506.4-595.0					
		631.9-697.7					
		757.3-852.7					
Landsat TM or Landsat ETM+ Ms	30	450-520	8-bit	425 USD or 600 USD[&]	Worldwide According to orbit inclination	185x185 km^2 (nominal)	March 1984 – present (TM) or April 1999 – present (ETM+)
		520-600					
		630-690					
		760-900					
		1550-1750					
	120 or 60	10400-12500					
	30	2090-2350					
Landsat ETM+ Pan	15	520-900					
ASTER	15	520-600	8-bit	Levels 1A, 1B and 2 (standard products) 55 USD Level 2 (On-demand products) and DEM (30m cell size) free	Worldwide According to orbit inclination No oceans	60x60 km at nadir	December 1999 – present
		630-690					
		760-860					
	30	1600-1700					
		2145-2185					
		2185-2225					
		2235-2285					
		2295-2365					
		2360-2430					
	90	8125-8475	12-bit				
		8475-8825					
		8925-9275					
		10250-10950					
		10950-11650					

[§]For all USGS orders (all data apart from IKONOS), add 5 USD handling fee and 20 USD international shipping (unless FTP download used, then shipping is free) per order. Prices correct in July 2004.
[*] Nominal values, scanner and mission depended/
[#] Panchromatic Band does not incorporate spectral filtering - response is that of optics/detector only.
[¥] The price varies according to location, data owner, and imaging date. The area must be contiguous and at least 49 km^2.
[¤] Nadir looking. When off-nadir, then the swath width can be 13x13 km^2.
[&] It is 425 USD for the Landsat TM and 600 USD for the corrected Landsat ETM+. For the raw Landsat ETM+, the price is 475 USD. The Scan Line Corrector stopped functioning properly in May 2003. This resulted in gaps within the satellite data. All scenes with these gaps are now sold at a price of 250 USD. Scenes with gaps filled by prior Landsat imagery will be sold at the price of 275 USD.
[€]CORONA did not have a systematic coverage (the equator crossing times varied from mission to mission). See sections 2.1.10 and 2.1.11 for more details. It was mainly targeting sensitive areas.

The next important part is the availability of data for the area of interest. While modern day satellite data have global coverage availability (limited to the orbit inclination), the declassified data have a limited availability (there is no information about the coverage of Hexagon). This means that some areas may not be covered. Concerning time-availability, the modern satellite data have a revisit time of a few days, thus allowing for more than one image to be obtained for the area of interest, thus covering different times of the year, and different years. The CORONA KH-4B data offer specific imagery from a period (1967-1972) and there are no particular revisit times. The revisit was based on political issues and military targets. Hence, the CORONA data may not be available for particular narrow time window for an area of interest. As for HEXAGON data, they cover a period of 7.5 years, and they follow the same pattern as the CORONA data.

The last but not least important part is the satellite data characteristics, namely spatial, spectral and radiometric resolutions. Each of these characteristics enhances different parts of a project. The spatial resolution depends mainly on the scale of the project. The spectral resolution is helpful to derive information concerning the character of the area of interest (such as moisture, geology, vegetation). The radiometric resolution determines the quality of the information derived from every band.

In an archaeological project in particular, there is need for as much spatial detail as possible. This increases the usefulness and value of the declassified imagery and IKONOS for archaeology. Between Landsat and ASTER, the latter looks more attractive because of the better spectral and spatial characteristics.

3.6. New Satellites

The future for remote sensing looks very encouraging. Numerous Earth observation satellites are to be launched in near future. These satellites can help in almost every application, and further research is needed, to support their use in landscape archaeology applications. Table 3-8 shows the satellites that may be launched in the period 2004-2010.

Most of these satellites offer high resolution and have similar attributes and characteristics to the satellites being studied in this research. Thus, they may be useful for landscape archaeology and it is expected that this research project will offer important information to those who will want to work with these newer satellites.

Table 3-9 – Future satellites (Source: National Aerospace Laboratory, 2004)

Satellite Name	Country	Expected Launch	Revisit/pointing	Swath width (km)	Panchromatic (m)	Multispectral (m) (no. of bands)
ALOS	Japan	2004	46 days/yes	35/70 | 70/250	2.5	10(4) 10/20/100(L-band)
Cartosat 2	India	2004-2005	4 days	10	1	
CBERS 3+4	China+Brasil	2008+2010	Yes	60/120, 866	5.0/10	20(5), 40(4), 73(4) TIR: 80(1)
Cosmo/Skymed	Italy	2003-2007			0.7	2 (4) 1-2 (X-band)
DMC-2 Surrey	UK	2004-2006			2.5	5
EROS B1-5	USA+Israel	2005-	Yes	12.5	1.8	
Ikonos 3	USA	2006	Yes		0.5	1
IRS P5	India	2003-2004	5 days	30	2.5	
KOMPSAT 2	Korea/Israel	2004		15	1	4(4)
Pleiades (2x)	France	2008/2009	26 days	20-120	0.7	2,8 (4)
Rocsat 2	Taiwan	2004	Yes	24	2	8(4)
DMC Surrey	UK	2002-2005		600		32(3)
RapidEye (4x)	Germany	2004		80		6.5(6)
Radarsat 2	Canada	2005	3 days	20/100/500		3-28-100 (C Band)
TerraSAR (2x)	Germany	2005		10-200		1.5-30 (X/L-band)
Helios 2	France	2004			0.5	TIR: 2.5
Ofeq 5	Israel	2002-2006	Yes		~0.5	
SARLupe	Germany	2005-2008				Radar: 1-
Topsat	UK	2004	6 days/yes	17	2.85	5.7(3)
Techsat21	USAF	2005	Yes		yes	

3.7. Discussion

With this chapter, the analysis and understanding of the project's satellite data is completed. Other data used in the project such as maps, GPS measurements, and field samples are discussed in the following chapters.

The project's satellite data were chosen because they were readily available, they were new in the market (all but Landsat TM), and their potential for archaeology in the Middle East was not well understood (Galiatsatos et al., 2001). Chapters 2 and 3 show the potential of these satellite data for their use in different applications. In chapter 4, there is discussion on the identification of a proper basemap for data integration. In chapter 5, there is discussion on the qualitative extraction of information from the data. In chapter 6, the spectral characteristics play a vital role. And in chapters 7 and 8, height information extraction is discussed. Further applications for these data include change detection and image fusion that can be included in future research projects.

The comparison of the satellite data provides a brief overview of all of them, and discusses their strengths and weaknesses with a focus on the needs of archaeology. One

thing that was not discussed is the data handling[11]. A preliminary assessment shows that the declassified imagery needs an extra stage of processing, by transforming the data into digital format. This extra stage demands money and time. Preprocessing is discussed in chapter 4. During the preprocessing stage all data were integrated on a uniform base layer, and were spatially georeferenced.

When georeferenced, the satellite data may be combined to deliver information. For example, change detection between CORONA and IKONOS can provide information on changes in the area of interest within the last 30 or more years, and so detect sensitive areas where the human intervention has changed the landscape. Another example is the creation of a DEM from the CORONA stereoscopic cameras that is discussed and assessed in Chapters 7 and 8 of this thesis. The low/medium spatial resolution sensors provide environmental data that are of value to landscape archaeology. In particular, Landsat data has been widely used by archaeologists to provide environmental context information, for example, to assist with landscape projects (see examples in paragraphs 3.1 and 4.1.6).

[11] Data handling is working with, and drawing conclusions from, collections of related information.

4. Preprocessing of satellite data

The preparation of the data before the processing stages has become a key issue for applications using multi-source digital data. The main steps include the translation of all data into digital format, and geometric and radiometric correction. The kind of application and the level of accuracy required define the methods utilised for preprocessing. It mainly depends on the data characteristics and the nature of the application. The data preprocessing stage demands high accuracy and so the best approach must always be sought according to the available means.

This chapter discusses the best approach for the data integration. First, it discusses the translation of all data into the same digital format. Then, the lack of ground control in the area of interest leads to a search for the optimal base layer upon which to integrate the data. Existing rectification and resampling techniques are discussed with emphasis on the CORONA image geometry. Last, but not least, the primary advantages of data integration within a GIS are presented.

4.1. CORONA space photography

CORONA space photography is supplied in the form of a 7x80 cm filmstrip (including the horizon camera images at the edges) when purchased from USGS (see figure 4-1). It is supplied as negative or positive film. In this application, only negatives were used.

Figure 4-1 – Sample image of a CORONA filmstrip.

This strip needs to be in a digital form to allow the application of computer based image analysis and digital photogrammetry. To achieve this, one has to select the most appropriate pre-processing methods. The following paragraphs discuss the digitising options, the removal of distortions and the techniques of image rectification and resampling.

4.1.1. Digitising CORONA

In McDonald (1997), Leachtenauer *et al.* describe an experiment that tested a sample of CORONA data with both commercial and prototype scanners, and they found that the images could be digitised with no loss of information content, but to do so required using a very small digitising spot, which took substantial time and produced large digital files. According to first principles, the 160 lp/mm (line pairs per millimetre) of KH-4B would have no loss of interpretability at a scanning resolution of 3 μm (~8000 dpi) and the 100 lp/mm of KH-4 would need 5 μm scanning resolution (~5000 dpi).

According to the Leachtenauer *et al.* (1997) test on KH-4B photography, there was no loss of interpretability at a scanning resolution of 4 μm, that is 250 dots/mm or 6350 dpi (dots per inch). This indirectly confirms the use of 3404 film with 130 lp/mm resolution in KH-4B missions. In their analysis, they used NIIRS (National Imagery Interpretability Rating Scale) criteria, a perceptual measure of quality or interpretability (Leachtenauer, 1996). It consists of sets of interpretation tasks or criteria of successively increasing difficulty. Experienced image analysts view an image and define the most difficult task that can be performed with this image. This defines the NIIRS of the image. They concluded that there was a 0.2 NIIRS loss at 8 μm (3175 dpi), and a 0.5 NIIRS loss at 15 μm (1700 dpi). They estimated that there would be a 1 NIIRS loss if an image was scanned at 30 μm (850 dpi).

According to NIIRS criteria, we can distinguish some features:

At best CORONA's ground resolution of 1.82 m provided by KH-4B falls into the NIIRS category 4. This means that it should be possible to detect farm buildings, greenhouses, basketball or tennis or volleyball fields in urban areas, the deep traces of a jeep on grass, tractors and marihuana agriculture (Pike, 1998). At worst CORONA's ground resolution of 12.20 m provided by the KH-1 camera system falls into NIIRS category 1. This means that it is only possible to distinguish among different land uses (agriculture, forest, water, urban, bare land, etc.) (Pike, 1998). For the NIIRS criteria sets for civil application, see Hothem et al. (1996). A similar interpretation scale was also developed for use with multispectral imagery by Mohr et al. (1996).

Today's commercial scanners cannot reach the required resolution of 6000 dpi. For this reason, Tappan *et al.* (2000) chose to apply photointerpretation straight on the film, thus avoiding any loss of information due to scanning. Drum scanners may be able to reach high optical resolutions but they present problems of geometric reliability mainly

because of the way they operate (Georgopoulos, 1998; Scollar *et al.*, 1990). Closer to the high demands of CORONA imagery are good quality flatbed A3 scanners. Their main problems lie in their geometric accuracy and resolution. However, they appear to have been used with satisfactory results by Ur (2003), although the description of the scanning technique is not clear.

For the use of flatbed scanners in photogrammetric applications, there is need for radiometric and geometric calibration before scanning the film. The geometric calibration of a flatbed scanner can be done by *a-priori* scanning of an accurate grid. Any offset measurements are then used to correct the resulting digital image. Radiometric calibration demands the use of a radiometric prototype, such as a known scale of grey tones. The correction procedure is given in Baltsavias and Waegli (1996).

However, there are also specialist photogrammetric scanners, which have the following characteristics that distinguish them from other scanners:

- They have the capability to scan at high resolution without interpolation.
- The resulting digital files are geometrically corrected. This is achieved by the use of specific algorithms that reproduce the correction model of the scanner's errors.
- They have the capability of frame scanning, usually with simultaneous creation of the interior orientation of the frames.

This research project used the photogrammetric scanner Vexcel VX4000 (figure 4-2). It is capable of scanning an entire roll of aerial film at one time, significantly automating the digital imaging process. It accepts rolls of film up to 305 m in length. For information on the technical characteristics of this scanner, please see Appendix IV.

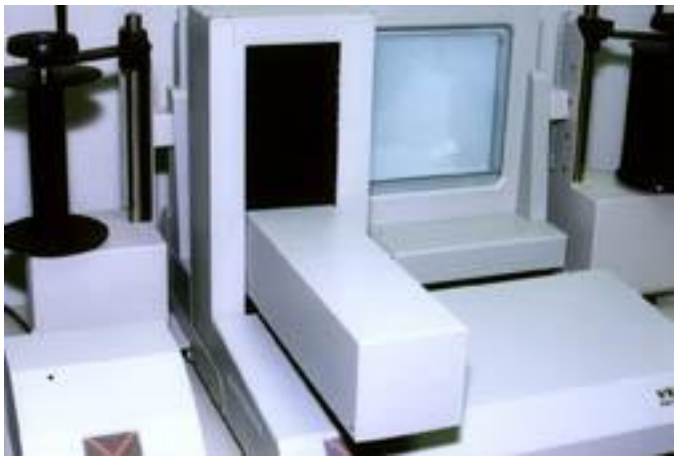

Figure 4-2 – Vexcel VX4000 photogrammetric scanner

Initially, the CORONA film was scanned in four different resolutions to see the differences and assess their importance. The optical scanning resolutions were 7.5 μm (~3400 dpi), 15 μm (~1700 dpi), 20 μm (~1300 dpi), and 22.5 μm (~1100 dpi) (figure 4-3). The scanning results identified significant improvement as scanning resolution increased from 15 μm to 7.5 μm. The difference in price was 18 GBP for one 7.5 μm B&W scan, and 5 GBP for one 15 μm B&W scan[12]. However, it was decided to scan all images at the optimal 7.5 μm resolution, which was still very cheap in project budget terms.

There are other ways in which CORONA data can be used. For example, the film can be projected and magnified on paper to create a photograph. This can be interpreted directly or scanned on a flatbed scanner with a low optical resolution (Palmer, 2002; Tappan *et al.*, 2000). However, this procedure is not well controlled. The production of the photograph can vary significantly in terms of brightness/contrast and radiometry.

It is necessary to mention here that the method followed and the scanning resolution depends heavily on the demands of the application. For example, Bindschadler & Vornberger (1998) scanned the CORONA negative film in a resolution of 600 dpi. This resolution was adequate for the scale of their application. On the other hand, Schmidt (2003) used as high resolution as possible (7 μm) for his DEM creation.

To create figure 4-3, the same CORONA frame was scanned at four different optical resolutions with a photogrammetric scanner, and a small part of the image was extracted for the illustration. At the top left image, one can see large buildings that resemble a factory. The coastline of the lake appears from the north towards the east part of the image. At the lower right part, small domestic buildings appear. The rest of the image shows dry land.

In both the upper two images of figure 4-3, the pixelisation of the coastline is apparent, an indicator that the scale of the particular image part is larger than the scale allowed by the resolution. In the two upper images it is difficult to distinguish the houses and the roads of the small village in the lower right corner.

In the two bottom images, the houses become clearer and one may distinguish the main roads. Still, the information content of the low right part is greater than the low left part. The houses and roads have a clearer line and the barren area on the left of the village includes some distinct soil marks, not well visible in the lower left image part.

[12] Prices correct in May 2001.

For the identification of large features such as the square feature of the top left corner (possible factory building), all resolutions are considered adequate.

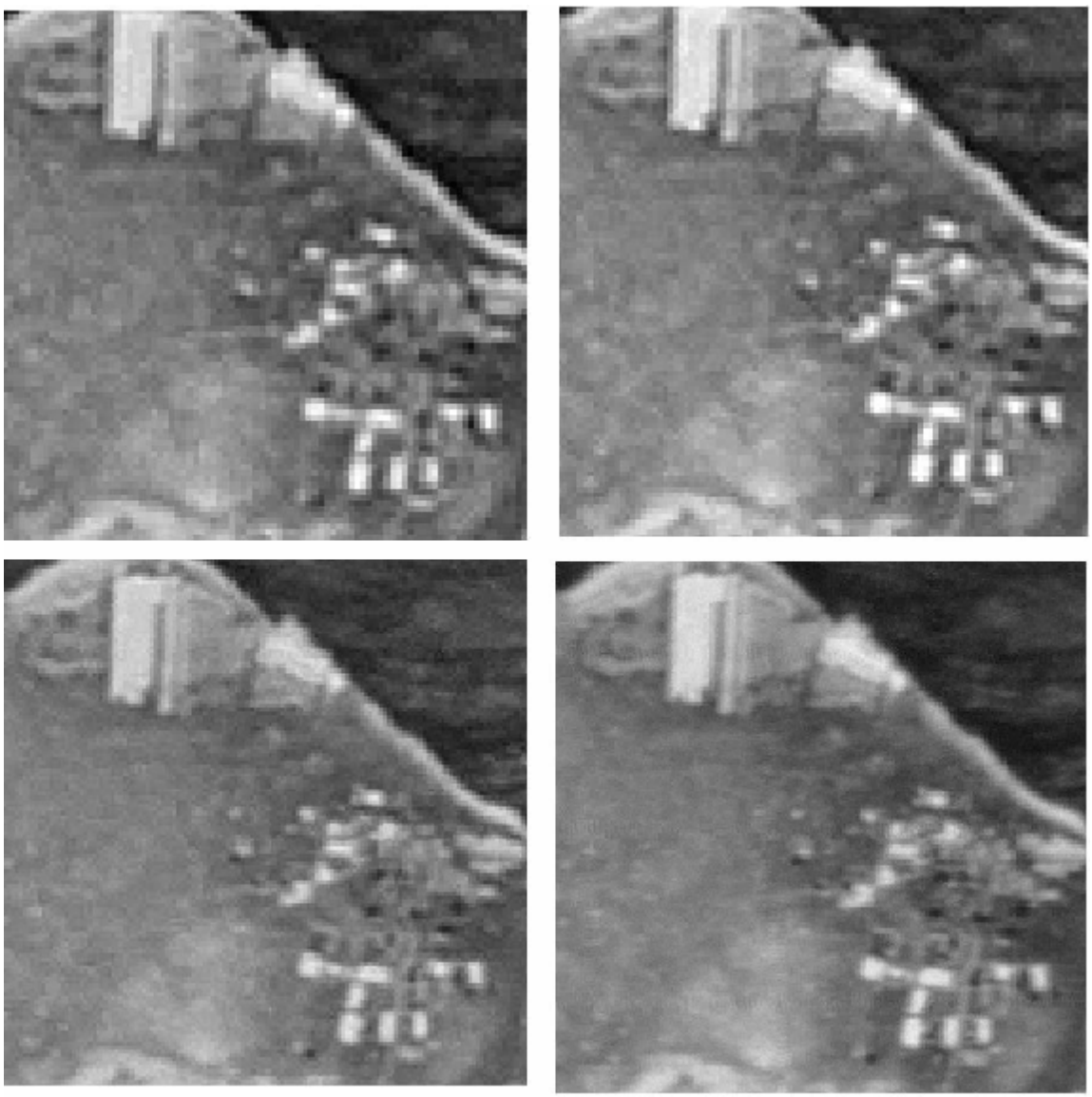

Figure 4-3 – Different scanning resolutions of the same area. Upper left 22.5 µm (~1100 dpi), upper right 20 µm (~1300 dpi), low left 15 µm (~1700 dpi), and low right 7.5 µm (~3400 dpi).

4.1.2. Distortions

Direct-scanning panoramic photography in its raw form poses a major inconvenience to the user (Slater, 1980). There are significant distortions in panoramic cameras, and for this reason a lot of users have avoided using the CORONA imagery for quantitative analysis (Cerasetti & Mauri, 2002; Palmer, 2002; Trelogan et al., 2002; Tappan et al., 2000). A schematic diagram of the CORONA distortions can be seen in figure 4-4.

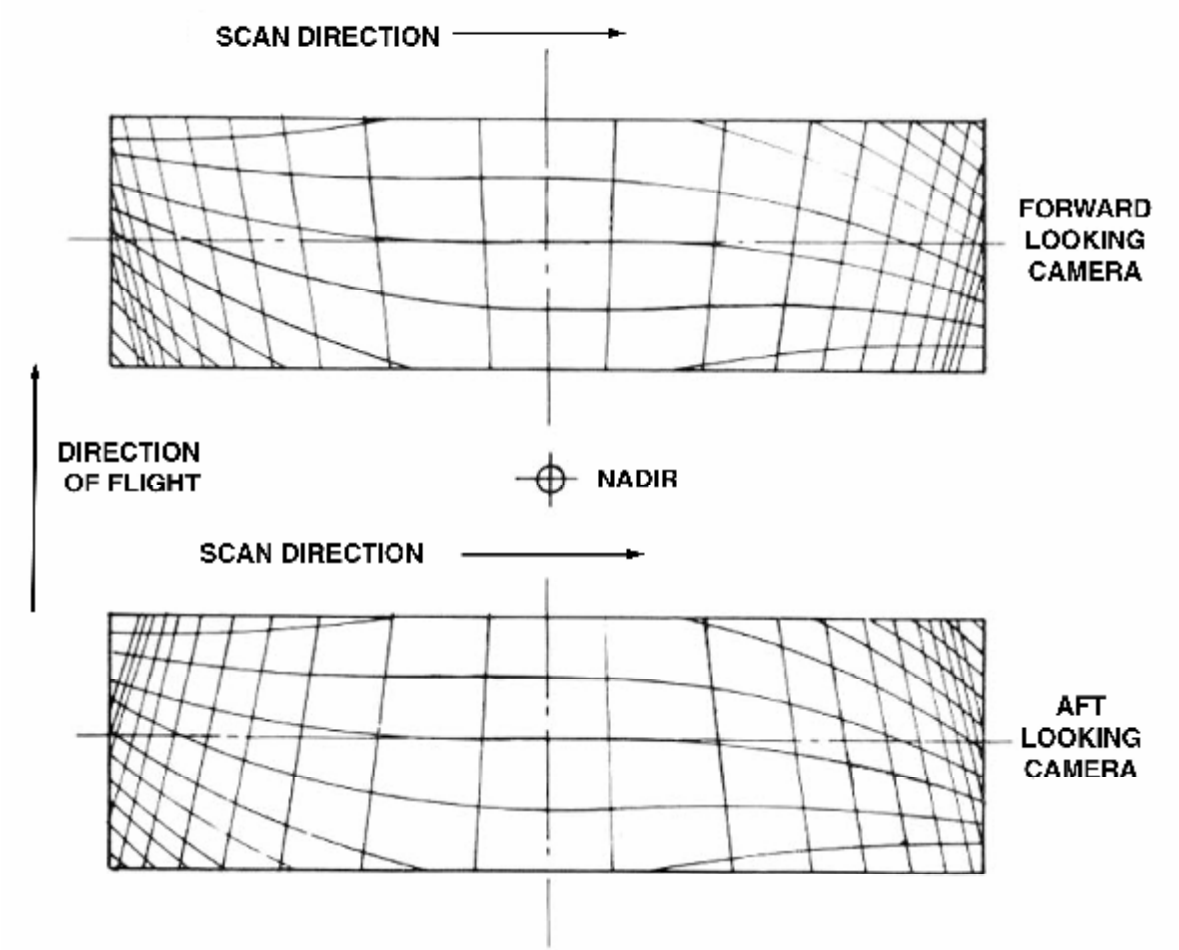

Figure 4-4 – Images of a unit grid on the ground obtained with a pair of convergent panoramic cameras in flight.

In Slama et al. (1980), there is a list of quantities that may be affected by error in panoramic geometry[13]:

- Location of spacecraft (time, orbit)
- Location of scene (atmosphere refraction, Earth curvature, Earth rotation)
- Position of camera (scale of geometry – velocity/time, attitude of support – pitch/roll/yaw)
- Attitude of nominal camera axis vs. support (relative pitch, relative roll, relative yaw)
- Attitude of optical axis vs. nominal axis (convergence in pitch, FMC in pitch, bearing runout in pitch, bearing runout in yaw, scan angle)
- Interior orientation (scale – focal length, optical axis location – principal point location/ lens distortion/ pointing errors/ point location in time).

[13] Note: lens distortion, film distortion, pointing errors and parallax clearance errors contribute to all of these items

- Image-point location (point location along slit relative to principal point, point location along scan relative to scan indicators, point location in time).

Thus, one of the first requirements for the use of panoramic photography is to remove the distortions.

Slama *et al.* (1980, p.206) describe four approaches which have been used in the past for the rectification or transformation of the panoramic image. These are purely electronic, computer-electronic, computer operated optical-electronic, and purely optical. The optical methods for rectifying or transforming the panoramic image offer a lot of advantages, such as high resolution, rigid image geometry, and equipment reliability. Disadvantages include the time factor and the difficulty to integrate with other datasets. On the other hand, technology has improved and the photogrammetric scanners offer enough resolution for most applications. Although there is loss of interpretability with the use of a scanner, there are many advantages when it gets to the processing point. This is further discussed in chapter 5.

For the correction of CORONA geometry, many methods can be applied once data is in digital format. These methods are discussed below.

4.2. Rectification

When the USGS received the CORONA frames from Kodak, they had to index them according to corner coordinates. The accuracy in locating corner coordinates varied according to how the coordinates were derived and according to the accuracy of information that was available for the derivation. About 76% of the image coordinates were derived from legacy databases. For 2% of the imagery, no position could be calculated. For 22% of the imagery, corner coordinates were calculated by camera model algorithms in 1995 using ephemeris documents that estimated the orbital position of the vehicle and camera orientation at the time each photograph was acquired (Selander, 1997).

With the use of orbital ephemeris, one could rectify the CORONA space photography with satisfactory results. However, the ephemeris data were not declassified, and since USGS could only find 20% of the original ephemeris, then it is easily understood that the orbital rectification cannot apply to most imagery. According to Ondrejka (2000) and Slama *et al.* (1980, p.920):

"In fact, when sufficient ground-control is available, the attitude and ephemeris are not required".

But, in areas like the Middle East it is either forbidden or difficult to take measurements to create GCPs (Ground Control Points) and military survey organisations will not provide coordinates, or accurate and comprehensive maps to use as a basemap.

For this reason, other rectification methods were sought for this project. One solution could be the preparation of special computer programs and the application of specific transformations for the data according to Slama *et al*. (1980) §4.2.2.3. However, this would require a lot of effort and it may result in a dead-end, since the algorithms need some ephemeris data that may not be available and ground point coordinates that may be inaccurate.

Another approach was pioneered by Case (1967). He assumed that if the internal geometry of panoramic photography can be determined, then, by employing analytical techniques, such operations as control extensions and topographic mapping may also be performed since such photography obeys the projective equations of photogrammetry. The basic concept utilised is that of reducing the panoramic photograph to an equivalent frame photograph having the same focal length and tilt. In Appendix III of this paper, one may find the formulation of Slama et al. (1980), and the Instantaneous Equivalent Frame Photograph (IEFP) method by Case (1967).

Deveraux (1973) investigated the feasibility of using a co-mounted frame camera to generate the necessary density of control required to perform the in-flight calibration of the panoramic camera. His hypothesis could not be confirmed as modelled in his study, but two of his observations are of interest. The first observation is that ground controlled panoramic data performed reasonably well. The second observation is that the use of the Case (1967) approach should be explored, because it is the most promising from a practical point of view.

Sohn *et al*. (2004) describe the mathematical approaches that are presented in Appendix III, and they also include the terrain-dependent RFM (Rational Function Model) approach by Tao & Hu (2001). Whatever approach is adopted adequate ground control is needed. Shin (2003) and Schenk *et al*. (2003) developed a rigorous model with less (but still enough) need for ground control. However, Case (1967) suggests a procedure involving iteration, thus improving the parameters and the image control. Of interest to any of the above procedures is the description of panoramic geometry in

paragraph 2.1.17.3 of this thesis. Given these difficulties, the solution appears to be the registration of CORONA data to some kind of basemap.

4.3. The basemap problem

An important concept in spatial integration is the spatial standard. Geographical information systems (GIS) provide tools to make two or more different spatial data sources match each other, but without reference to a common basemap standard it is difficult to go any further. A spatial basemap provides a common framework that any data source can be registered to, and once registered, all other data meeting that same standard are immediately available for comparison with the new data. A basemap also commonly includes control points, precisely located benchmark coordinates that allow the error and accuracy of positional data to be readily determined.

Thus, it is important to establish a good basemap standard where all data can be registered. The basemap should offer good and reliable control for the rest of the data. For this, one should have a look at the quality of the data, and their suitability as a basemap. The available project data are separated into two broad categories, the satellite data, and the reference data.

4.3.1. Maps as a basemap

The only maps available that cover the study area are copies of Syrian maps of 1:25,000 scale. They are black and white photocopies. The paper is plain paper, wrinkled, and torn in places. The language of the maps is Arabic. There is a legend, explaining the cartographic symbols and the scale. But there is no indication of the coordinate system of the maps. A cryptic reference to the "4^{th} spheroid UTM" is at the top-right corner. However, initially there were no more data to use as a georeference and from which to derive control points. Differential Global Positioning System (DGPS) could not then be applied because of security restrictions in Syria.

Despite the poor quality of the maps, they were scanned on a roll scanner. Although scanning errors will have been introduced, the existing map grid was used to compensate for the geometrical distortions of photocopying and scanning. The result gave an RMS error < 1.00 pixel.

It was impossible to define the coordinate system from the maps. Thus, there were efforts to meet with people from the Syrian authorities and thus obtain the necessary

details. A report was promised with an application that could help, but it was never received. Other people were simply reluctant to cooperate, and the Syrian authorities could not provide the details, nor could the General Organization of Remote Sensing (GORS) in Damascus. There were also efforts towards the private sector, but they did not know the details of the maps.

During the first year of the PhD, the maps were the best option to use as a basemap in the project. As explained in chapter 1, this was because the data were not all together from the beginning of this research, but they arrived at different times. Thus, the research direction was following the existing data at the time. For this reason, the satellite data were registered to the maps with satisfactory RMSe. However, the registration was accepted with caution, mainly because there was no way to adequately quantify the distortions of the maps due to photocopying, scanning and paper condition. Also, the lack of information on the coordinate system led to navigation and allocation problems.

Apart from the creation of a basemap, the maps were the only way to allocate and navigate during fieldwork in the study area. They were used in conjunction with a handheld GPS. For the best allocation and navigation there was need to set up the map co-ordinate system in the GPS instrument, that is to input the required parameters of the grid and the datum. These parameters are scale, longitude beginning, false Easting and false Northing. The datum parameters are dX, dY, dZ, dA and dF. These parameters were unknown and the Syrian authorities could not provide them. For this reason, other navigation methods were used, which are described in paragraph 4.4.

In the third year of the PhD, Meredith Williams of Newcastle University viewed the maps. He immediately recognised them as Russian military maps. The UTM-like projection that we could identify on the maps was the Gauss-Kruger projection. Almost all-Russian military maps use the latter; it is very similar to UTM, using 6-degree wide zones. All the maps use the Krasovsky ellipsoid. The Serapinas 1998 is the closest fit datum, though Pulkova 1942 is very commonly used in maps of the Middle East (Williams, 2002). However, by this point, the project had moved beyond reliance on the map data, having explored alternative solutions.

4.3.2. GPS measurements as a basemap

The GPS-based geocorrection is more accurate than the map-based geocorrection at the scale of Landsat pixel size (autonomous GPS) or SPOT pixel size (differential GPS, or repetitive loggings GPS, or post-processing GPS) (Cook & Pinder, 1996; Kardoulas *et al.*, 1996; Gao, 2001). This was strengthened by the deactivation of the Selective Availability (SA) decoding by the U.S. government in 2000. After-SA studies (Smith and Atkinson, 2001; Turker and Gacemer, 2004) showed that GCPs acquired by autonomous GPS are much superior to the map-based GCPs, even at scales of SPOT pixel size (5 m). After-SA differential GPS shows an accuracy equivalent to the pixel sizes of CORONA and IKONOS.

Since it was not possible to use differential GPS, and with only a single handheld GPS available, there was an effort to establish a grid with handheld GPS using a "pseudo-kinematic" positioning autonomous method. The GPS GCPs were chosen on crossroads, bridges and places where the GPS could be identified in satellite images. Unfortunately, those points are considered as "sensitive" by the national security (in other words, 'possible targets'). Thus, it was not possible to stay longer than a minute or two above these points to take the measurement. The autonomous GPS-measurements took place during the fieldwork of September 2000, which occurred after the deactivation of SA (May 2000).

The application of those GPS points as a basemap showed unacceptable RMS errors. When these points were subsequently overlaid on the IKONOS imagery the error reached in places more than 20m in various directions (no standard error or offset). This error could be acceptable for Landsat imagery, but the high spatial resolution of IKONOS needs more than this. Because of the uncertain quality method and the results of it, it was decided not to use the GPS points as a basemap.

4.3.3. Satellite data as a basemap

A satellite system is composed of a scanner with sensors and a satellite platform. The sensors are made up of detectors.

- The *scanner* is the entire data acquisition system. It includes the sensor and the detectors. (Lillesand and Kiefer, 1992)

- A *sensor* is a device that gathers energy, converts it to a signal and presents it in a form suitable for obtaining information about the environment. (Colwell, 1983)
- A *detector* is the device in a sensor system that records EMR.

Satellite sensor data are normally distributed with different levels of processing, from the lowest level of unprocessed raw imagery to the highest of precisely geocorrected or orthorectified imagery. In this research project all satellite digital imagery is geometrically and radiometrically corrected. IKONOS is "Standard geometrically corrected". Landsat 5 TM is under processing level 08, "systematically corrected"[14]. Landsat 7 ETM+ is under processing level 1-G[15].

According to Gerlach (2000), IKONOS imagery accuracy of the "standard geometrically corrected" level product is 23.3m RMS, not including the effects of terrain displacement. According to the latest IKONOS product guide (2004[16]), the positional accuracy of the Geo product is 15.0 m, exclusive of terrain effects. Pixel size is 1m. From GPS measurements in the area of interest during summer 2002, it came out that the IKONOS accuracy was as good as 10 m (Beck *et al.,* in press).

IKONOS seems to be the best choice for a base layer in this research project. The accuracy of the 23.3 m is slightly worse than the GPS points, but considerably more reliable because of the respective data capture methodologies. The fieldwork of summer 2002 showed a very good match between GPS navigation lines and IKONOS imagery (Beck, in prep). It is worth noting that in a relatively flat area, a strictly vertical IKONOS Geo product can provide better accuracy than 23.3 m (Beck, in prep). However, this is not the case with the data of this thesis. The area may be relatively flat, but the IKONOS imagery is not vertical. The implications of the non-verticality are detailed in section 7.4.

Nevertheless, the information content of IKONOS can provide an ideal base layer for the rest of the data. With enough data to create IKONOS orthoimage, then the planimetric accuracy would be suitable for its use as a base layer. This is proven by Davis & Wang (2003).

Landsat 7 ETM+ sensor was expected to have a geometric accuracy of 250 m in flat areas at sea level, excluding terrain displacement effects without ground control. But

[14] http://edc.usgs.gov/guides/images/landsat_tm/nlapsgeo2.html#Table%20B-3 (July 2004)
[15] http://ltpwww.gsfc.nasa.gov/IAS/handbook/handbook_htmls/chapter11/chapter11.html#section11.3 (July 2004)
[16] http://www.spaceimaging.com/whitepapers_pdfs/IKONOS_Product_Guide.pdf (July 2004)

after alignment calibration, the geodetic accuracy of the processing level 1-G products reached a maximum of 50m, with occasional better accuracy (20 m)[17].

Landsat 5 TM sensor shares similar geodetic accuracy to ETM+. With precision processing model 09, the satellite imagery has a 25m RMS error[18]. Referring to the registration error of 7m between two Landsat-7 images, one can assume of a similar registration error between a Landsat-5 and a Landsat-7 image.

The spatial resolution of Landsat satellite data (30 m) does not allow it to be used as a base layer. It is very difficult to find common points between Landsat and CORONA, since the information content in each of them is very different. In one Landsat pixel, there are 225 CORONA pixels. Thus, the registration error will be at least 100 CORONA pixels. This is much higher than the acceptable 'less than one' pixel RMS error. Also, the accuracy of the processing level of Landsat is 50 m. This is considerably worse than the GPS points accuracy.

4.4. The in-field navigation problem

During early years of fieldwork, the location of sites and navigation in the study area were a major problem. Quite often, the present landscape situation was found to be completely different from that shown on the maps or in the CORONA data, and navigation in the area was very difficult. Handheld GPS was considered to be the solution.

Initially, the registration of all data was done according to the Syrian maps' coordinate system. Although the GPS should be calibrated to provide co-ordinates according to this system, the necessary parameters could not be obtained. To provide a temporary solution to the problem, two "coarse" methods were suggested. The first method is based on the "trial and error" practice. The second method is based on the creation of a conversion algorithm from UTM to Syrian grid, with the aid of some known co-ordinate points. The GPS used was a "Garmin GPS12XL Personal Navigator" and its specifications are shown in Appendix IV.

The "trial and error" method can be adopted for the navigation and site allocation in small areas (approximately 2x2 km). All the user needs is the co-ordinates of a known point within his area of interest. Then, by adjusting the parameters of the "user grid" in the GPS, the user can calibrate the GPS to show the correct co-ordinates at that

[17] http://ltpwww.gsfc.nasa.gov/IAS/handbook/handbook_htmls/chapter13/chapter13.html (July 2004)
[18] http://edc.usgs.gov/glis/hyper/guide/nlapssys3.html (last accessed: September 2002).

particular point. These parameters are the longitude beginning, the scale, the false Easting and the false Northing. From the map co-ordinates, the user can easily identify the longitude beginning. Then, with the use of a number of points (whose co-ordinates are known in WGS '84 and the local grid), the user can approximate the scale. The false Easting and false Northing are the numbers that the user may change so as to define the best approximation of the known co-ordinate point of his area of interest. Then, the error of the navigation or the site allocation will not be significant (less than 30 m).

The creation of a conversion algorithm is based on good measurements of known co-ordinate points in two systems. There is also the need to have a good mathematical background and preparation (i.e. geodesy books of conversion algorithms). The algorithm used in the Homs area is based on plane conversions and it does not take into account the curvature of the Earth, the map projection used in the two systems, the datum, and the measurement errors. No preparation was done for the creation of the algorithm, and so it is considered very crude. It may be used in areas of approximately 5x5 km, even though acceptable errors of 40m were recorded from a distance of 20 km.

First, GPS measurements are taken in the WGS'84 system of some points of the area, which can be identified in the map. Then the coordinates of the same points are obtained from the map system. The distance between the points is calculated from the following equation:

$$S_{AB} = \sqrt{(E_B - E_A)^2 + (N_B - N_A)^2} \qquad (1)$$

where S_{AB} is the distance between two points A and B, and E_A, N_A, E_B, N_B, are the Easting, Northing co-ordinates of A and B respectively.

Then, by comparing the distances of the two systems and by averaging, the scale for the conversion from one system to the other is calculated.

The calculation of the rotation is a bit more complicated. First the azimuth angle is calculated with the aid of the following equation:

$$A_{AB} = \operatorname{atan}\left(\left|\frac{E_B - E_A}{N_B - N_A}\right|\right) \qquad (2)$$

where A_{AB} is the azimuth of the points A and B.

If $E_B - E_A > 0$ and $N_B - N_A > 0$ then the azimuth angle is A_{AB}.

If $E_B - E_A > 0$ and $N_B - N_A < 0$ then the azimuth angle is $\pi - A_{AB}$.

If $E_B - E_A < 0$ and $N_B - N_A > 0$ then the azimuth angle is $2\pi - A_{AB}$.

If $E_B - E_A < 0$ and $N_B - N_A < 0$ then the azimuth angle is $\pi + A_{AB}$.

Then, the azimuth angles of the two systems are compared. The differences of the azimuths (where the A-point is the same) are then averaged. And the resulting number is the rotation of the conversion around the A-point. One should make sure that the A-point used in the conversion is near the centre of the area of interest.

In averaging, either for scale or for rotation, it will be wise to use levels of confidence for each of the points used. For example, if 8 points show that they have a difference between the two systems of DN=500±100 and DE=10000±800, and 1 point shows difference DN=100 and DE=12000, then this point will not be included in the averaging. In general, the measurements of the points should follow a normal distribution with most measurements clustered and a few extremes in both positive and negative directions. Measurements outside this normal distribution may be considered as false.

After the definition of scale and rotation, we can proceed to the conversion. First, we calculate the distance S_{AX} of the point A with the point X (the point we want to convert) with the use of equation 1. Then, we calculate the azimuth A_{AX} with the use of equation 2. These calculations are done in the system we want to convert X point **from**. The algorithm then is:

$$E_X = E_A + l\,S_{AX}\sin(A_{AX} \pm r) \qquad (3)$$
$$N_X = N_A + l\,S_{AX}\cos(A_{AX} \pm r)$$

where E_A, N_A, the co-ordinates of A in the system we want to convert X point **to**, λ is the scale, and ρ is the rotation.

Because of the simplicity of the algorithm, it can be programmed in a portable calculator and used for navigation in the area. Any GPS shows co-ordinates in UTM. Any calibration to another system without correct parameters (i.e. the “trial and error” method) may result in loss of time for the definition of the calibration point and eventually this will cover a small area (2x2 km). So, a programmable calculator was used to convert map grid co-ordinates to UTM. Printed maps of the area were used with the map grid on them. Then, with the use of the calculator the co-ordinates of one grid point were converted into UTM. By comparing them with what the GPS was showing (for a point X), one could approximate the location of point X in the maps. That is, one could approximate the location (navigate) without the need for calibration every 2 km.

It must be noted that these methods may only be applied in areas where the Northing, Easting TM (Transverse Mercator) projection system is used. In areas of other projection systems (i.e. Lambertian Conical), the results may be significantly different.

These methods were used as a solution to the lack of adequate coordinate system information. In the case where there is a known coordinate system basemap, then it is advised to avoid using such methods.

Much later, when IKONOS imagery was purchased for the project, navigation in the area became much easier with the use of Pocket PC with ArcPad software connected to a handheld GPS. This is an attractive alternative method of navigation because of the ease of use and the gain of time from digitising since all data are held in digital format. However, as the author personally never used it, he cannot comment on its application.

4.5. Image rectification and resampling

At this point, there is understanding about the satellite data, all the data are in digital format, and the basemap layer is assessed. The next step is the rectification and resampling of the data for integration under a common basemap.

Ehlers (1997) defines remote sensing image rectification (or 'geocoding') as the process of an actual pixelwise geometric transformation of an image to an absolute coordinate system. In this project, there is no absolute coordinate system. Instead, there are datasets of satellite and reference data, with an estimated error from an absolute coordinate system. For this reason, a better definition needs to be adopted for the action of the integration of the project data. According to Ehlers (1997), this is defined as ***registration***, which is the process of an actual geometric transformation of a 'slave' image to the geometry of a 'master' image or dataset.

The possible error sources that need to be corrected in an image are separated into two broad categories, the errors because of the acquisition system, and the errors because of the observed area of interest. Some of these distortions, especially those related to instrumentation, are corrected at the ground receiving stations. Toutin's (2004) categorisation of all such errors is shown in Table 4-1.

There are two main ways to rectify these distortions. Both require models and mathematical functions to be applied. One way is the use of rigorous physical models. These models are applied in a distortion-by-distortion correction at the ground receiving station to offer different products (for example the IKONOS group of image products). The physical model is applied in chapter 7 with the CORONA data. In the same chapter, there is a discussion of the IKONOS sensor model.

Table 4-1 – Description of error sources (Toutin, 2004).

Source	Relation	Description of error
Acquisition system	Platform-related	Platform movement (altitude, velocity)
		Platform attitude (roll, pitch, yaw)
	Sensor-related	Viewing angles
		Panoramic effect with field of view
		Sensor mechanics (scan rate, scanning velocity, etc.)
	Instrument-related	Time-variations or drift
		Clock synchronicity
Area of interest	Atmosphere-related	Refraction and turbulence
	Earth-related	Rotation, curvature, topographic relief
	Map-related	Choice of coordinate system, approximation of reality

The other way is the use of empirical models either with polynomial or rational functions. The rational functions are discussed in chapter 7 of the thesis. The empirical method was tried with success and is mostly used in this research project. The polynomial functions are still in use today by many users mainly because of their simplicity. Their usage was prevalent until the 1980s. But with the increased need for accuracy, other more detailed functions replaced them. Today, polynomial models are limited to nadir-viewing images, systematically corrected images or small images on relatively flat terrain (Bannari *et al.*, 1995), and according to De Leeuw *et al.* (1988), the GCPs[19] have to be numerous and distributed as evenly as possibly in the area of interest.

For this research project, the polynomial functions were chosen for the registration of all data to the base layer. This was due to their simplicity, and due to the fact that the Homs area of interest is relatively flat and small (thus, the images are small). Also, during the image registration process there was effort to identify as many GCPs as possible, evenly distributed across the imagery.

By looking at the existing data, the best solution is to use IKONOS as a base layer. It is the most reliable solution compared to the existing maps and GPS points, it is free of non-linearities (Fraser *et al.*, 2002a), it has less distortion (always depending on the viewing geometry and the ground relief), and it has enough information content to register all the other data on it. All tables with RMS errors are included in Appendix V. However, one must always keep in mind that the RMSe can be a useful indicator of accurate image rectification, only if another means of calibration is available to evaluate standards (Morad *et al.*, 1996). Otherwise, it is just a diagnostic of weak accuracy value (McGwire, 1996). The use of independent well-distributed test points that are not used

[19] Chen and Lee (1992) use the term RPCs (Registration Control Points) that is more precise. However, to avoid confusion, this term will not be used.

in the image geometric transformation would give a more precise estimate of the residual error (Ehlers, 1997).

The truth is that there were hardly enough GCPs to register the different image sets because of landscape changes between the 1969-1970 and 2002. Thus, independent check points (ICPs) were a luxury that could not be afforded. Buiten and van Putten (1997) suggest a way to assess qualitatively the satellite data registration through applying tests. Thus, the user could gain a better insight into the quality of the image registration. For a detailed review on image registration see Zitová & Flusser (2003).

The image registration process has one more step after the application of the model, the *resampling,* which is part of the registration process. When transforming the 'slave' image to the new geometry/location, then the pixel position will not be the same. Thus, new pixel values need to be interpolated. This is called resampling (Ehlers, 1997).

The three main resampling methods are *nearest neighbour*, *bilinear interpolation*, and *cubic convolution interpolation*. Nearest-neighbour resampling is simply the assignment of the brightness value of the raw pixel that is nearest to the centre of the registered pixel. Thus, the raw brightness values are retained. This resampling method is mainly preferred if the registered image is to be classified. The bilinear interpolation uses three linear interpolations over the four pixels that surround the registered pixel. The cubic convolution interpolation uses the surrounding sixteen pixels. Both bilinear and cubic interpolations smooth the image, and they are mainly used for photointerpretation purposes. However, they are not suggested if the spectral detail is of any importance to the application (Richards and Jia, 1999).

In this application, the nearest-neighbour resampling was chosen in order to preserve the spectral detail in the image, and any geometric detail that the interpolations could smooth and thus hide from the eyes of the photointerpreter. According to Richards & Jia (1999), the cubic convolution would be the resampling method used for photointerpretation purposes. But Philipson (1997) argues that the contrast must be preserved and not smoothed. The resampling method is merely personal choice of the photointerpreter. Nevertheless, the spectral detail is of particular importance for the spectroradiometry process described in chapter 6, and thus the nearest-neighbour resampling was adopted for the image registration.

Summarising from Appendix V, the results of the image registration are presented in table 4-2. This table shows how well using the polynomial method adopted models the distortions inherent in the scanned portion of CORONA imagery.

Table 4-2 – Summary of the CORONA registration control point errors

Mission No.	Frame No.	X (pixel)	Y (pixel)	Total (pixel)
1108	043	0.9569	1.8136	2.0506
	044	1.3138	1.1598	1.7525
	045	1.5002	1.3465	2.0158
1111	001	2.8527	1.1200	3.0647
	002	1.1069	1.4473	1.8220
1110	007	0.6115	0.9516	1.1311
	008	1.5145	1.8880	2.4208
	009	0.7488	1.5748	1.7438

4.6. Geographical Information Science

The idea of portraying different layers of data on a series of base maps, and relating things geographically, has been around much longer than computers. The best-known example is the case of Dr. John Snow. He used a map showing the locations of death by cholera in central London in September 1854, trying to track the source of the outbreak to a contaminated well.

For such applications, a software system was developed that later expanded into a science, the Geographical Information Systems/Science (GIS). The users of GIS span many fields, including city and regional planning, architecture, geology and geomorphology, hydrology, geography, computer science, remote sensing and surveying. Given such wide application and divergent constituencies, there is no single universally accepted definition of GIS. An early functional definition states (Calkins and Tomlinson, 1977):

> *"A geographical information system is an integrated software package specifically designed for use with geographic data that performs a comprehensive range of data handling tasks. These tasks include data input, storage, retrieval and output, in addition to a wide variety of descriptive and analytical programs."*

A more recent definition (Goodchild *et al.*, 1999) states the meaning of geographical information and geographical information science:

> *"Geographical information (GI) can be defined as information about the features and phenomena located in the vicinity of the surface of the Earth. […] The fundamental primitive element of GI is the record <x,y,z,t,U> where U represents some 'thing' (a class, a feature, a concept, a measurement or some variable, an activity, an organism, or any of a myriad possibilities) present at some location (x,y,z,t) in space-time."*

Information science generally can be defined as the systematic study according to scientific principles of the nature and properties of information. From this position it is easy to define GIScience as the subset of information science that is about GI.

In every application, the inclusion of GIS as a processing tool is an approach that leads to a different perspective on the underlying problem. By using the simple topological figures of polygon, line and point, one can express everything that exists in the (x,y,z,t) space. Under one coordinate system, all real world data can be overlaid and analysed. The choice of coordinate system in our application was the coordinate system that IKONOS could offer, that is World Geographical System 1984 (WGS'84). It uses the Universal Transverse Mercator projection of 6 degrees, the Geodetic Reference System 1980 (GRS80) ellipsoid parameters[20], and WGS84 datum.

The pixel size of panchromatic IKONOS imagery is one meter. GIS can offer adequate display and analysis at this scale. It would take many pages to analytically detail the capabilities of GIS in data analysis. In few words, the conceptual components of a GIS are (Jakeman *et al.*, 1996):

The *database* is all data files that can be assessed by the user. Data are organised via some common and controlled approach. The *database manager* performs all database retrieval, handling and storage functions. The *manipulation* consists of tasks needed to respond to simple user data summary requests and preliminary to analytical processes. The *data entry and cleaning* are procedures for entering and editing data. The *user interface* is the main working environment that has moved from one-dimensional command line to the object-oriented one. It is the interaction space between the user and the computer. The *analysis* includes procedures that derive information from the data. It is the most important part of a GIS. It incorporates a variety of analytical techniques, which when combined answer the specific needs of the user of the system.

In the previous sections, the IKONOS imagery was used as base layer and all data were registered onto IKONOS in an effort to get as close to reality as possible. Thus, all data were integrated into a GIS, where inferences could be made with the combination of two or more different data sources to provide valuable information. Before the processing of imagery, simple GIS analysis tools can be used to create thematic maps. For example, it is now possible to:

- Interpret the imagery with the aid of reference data such as the maps. For example, the previously identified and mapped archaeological sites have a common interpretation signature. With the use of this 'key', one can identify signatures and confirm their archaeological identity.

[20] http://dgfi2.dgfi.badw-muenchen.de/geodis/REFS/grs80.html (last accessed: July 2004).

- Identify the extent of intensive human development over the years, thus highlighting the importance of CORONA data to provide archaeological information that today simply do not exist.
- Make decisions. For example, the distribution of GPS points could not be assessed without visualisation, by overlaying them on the imagery or maps.
- Create archaeological site topology and link to a database of archaeological record.
- Analyse the data. For example, classification of sites according to size, or classification of sites according to distance from a water source.
- Create thematic maps of the area.

4.7. Discussion

This chapter discussed the translation of CORONA film to a digital format, the reasons for it and the possible ways to correct the panoramic imagery distortions. It then presented the problem of defining a base layer for the research project, outlining its importance and all possible solutions to it. To conclude, the importance of GIS in geographical analysis of an area is illustrated, and ways are shown about how one can use the data until this stage without further image processing.

From the above, one may conclude that the creation of a base layer and the transformation of all data into a common reference system is a very important issue. The quality of the data is an important issue, particularly when one does not know how far one can rely on any given data set.

The best method for the CORONA image rectification is the use of differential GPS, on a fixed point of known coordinates and a "rover" GPS instrument taking measurements around the area, making sure that they both use the same constellation of satellites. The use of GPS orbital ephemeris would be useful here. At the end of each day of measurements, a post-processing of the points with the use of survey techniques (like traverses and triangles) will offer results good enough for the CORONA spatial resolution.

One may wonder whether the relief of the ground plays an important role in the image rectification or not. According to Palà and Pons (1995), the amount of displacement can be important when there are large height differences (maximum-minimum) within the area of interest. In the Homs project, the height differences are small, and this results in a negligible displacement due to relief of the ground. However,

where CORONA project offers stereo imagery, it is better to proceed to orthorectification through triangulation (see chapter 7), which is a better-controlled approach than the simple image rectification (Novak, 1992; Rocchini, 2004). Generally, the rigorous models should be the primary choice whenever available, because their mathematical function corresponds to physical reality of the viewing geometry, while empirical model parameters do not have any physical meaning (Dowman and Dolloff, 2000; Toutin, 2004).

However, it all depends on the specific application needs. There is a need to have knowledge of the existing methods, the results one should expect, and acceptance of the limitations, always keeping in mind the "proper" (what should be done) and the "viable" (what can realistically be done).

5. Site detection

After the data is integrated under a common coordinate system, it is time for the processing to begin. The most common image processing approach for archaeological applications is photointerpretation. In this chapter, CORONA KH-4B satellite data will be assessed for its potential to detect features, especially those of archaeological interest. The assessment approach first reviews photointerpretation issues. In particular, it discusses the source of data, the human and computer factors, and the elements and levels of photointerpretation. Then, it discusses the Homs project and in particular discusses the landscape and archaeological variety in the area. Last but not least, examples of the synergy between image analysis and photointerpretation are presented.

5.1. Photointerpretation

5.1.1. History and terminology

Photography existed long before satellite observation. L.J.M. Daguerre and J.N. Niepce developed the first commonly used form of photograph between 1835 and 1839. In 1845, the first panoramic photograph was taken, and in 1849 an exhaustive program started to prove that photography could be used for the creation of topographic maps. The same year, the first stereo-photography is produced. In 1858, Gaspard Felix Tournachon took the first known photographs from an overhead platform, a balloon (Philipson, 1997). For the next 101 years, aerial photography was developed and widely used in military and civilian applications. The platforms changed to include kites, pigeons, balloons and airplanes (chapter 2 in Reeves, 1975). The era of satellite photogrammetry[21] starts in 1960 with the CORONA military reconnaissance program. The era of using satellite images for mapping and making measurements starts in 1962 with the CORONA KH-4 satellite design.

Colwell (1960) defined *photographic interpretation* (also termed *photointerpretation*) as

[21] A definition of *satellite photogrammetry* may be found in Slama *et al.* (1980): "Satellite photogrammetry, as distinguished from conventional aerial photogrammetry, consists of the theory and techniques of photogrammetry where the sensor is carried on a spacecraft and the sensor's output (usually in the form of images) is utilised for the determination of coordinates on the moon or planet being investigated." From this definition, it is obvious that people were not openly aware of the military use of same techniques towards our planet, Earth.

"the process by which humans examine photographic images for the purpose of identifying objects and judging their significance"

With the advent of computer technology, the methods for photographic interpretation changed and the new term *image analysis* (also termed *quantitative analysis*) came to complement (underlined) the old term:

"Image analysis is the process by which humans and/or machines examine photographic images and/or digital data for the purpose of identifying objects and judging their significance" (Philipson, 1997)

Photointerpretation involves direct human interaction, and thus it is good for spatial assessment but not for quantitative accuracy. By contrast, image analysis requires little human interaction and it is mainly based on machine computational capability, and thus it has high quantitative accuracy but low spatial assessment capability.

Today, both techniques are used in very specific and complementary ways, and the approaches have their own roles. On one hand, if digital image processing is applied beforehand to enhance the imagery, then this helps the photointerpreter in his work. On the other hand, image analysis depends on information provided at key stages by an analyst, who is often using photointerpretation (Richards & Jia, 1999).

Konecny (2003) defines *remote sensing* and *photogrammetry* according to their object of study:

"Photogrammetry concerns itself with the geometric measurement of objects in analogue or digital images"

"Remote sensing can be considered as the identification of objects by indirect means using naturally existing or artificially created force fields".

Thus, photogrammetric techniques were adopted by remote sensing mainly for quantitative analysis. In its turn, remote sensing expanded the data that could aid an image analyst with the extraction of quantitative information.

All of the above terms give a specific meaning to the approaches, but the approaches complement each other when it comes into implementation. In other words, the sciences of photogrammetry and remote sensing moved from the previous independent way of working, towards a more interdisciplinary network, where in comparison with other sciences like Geographical Information Systems, Geodesy, and Cartography, they

produce better results and increase the processing capability for modern day applications (figure 5-1).

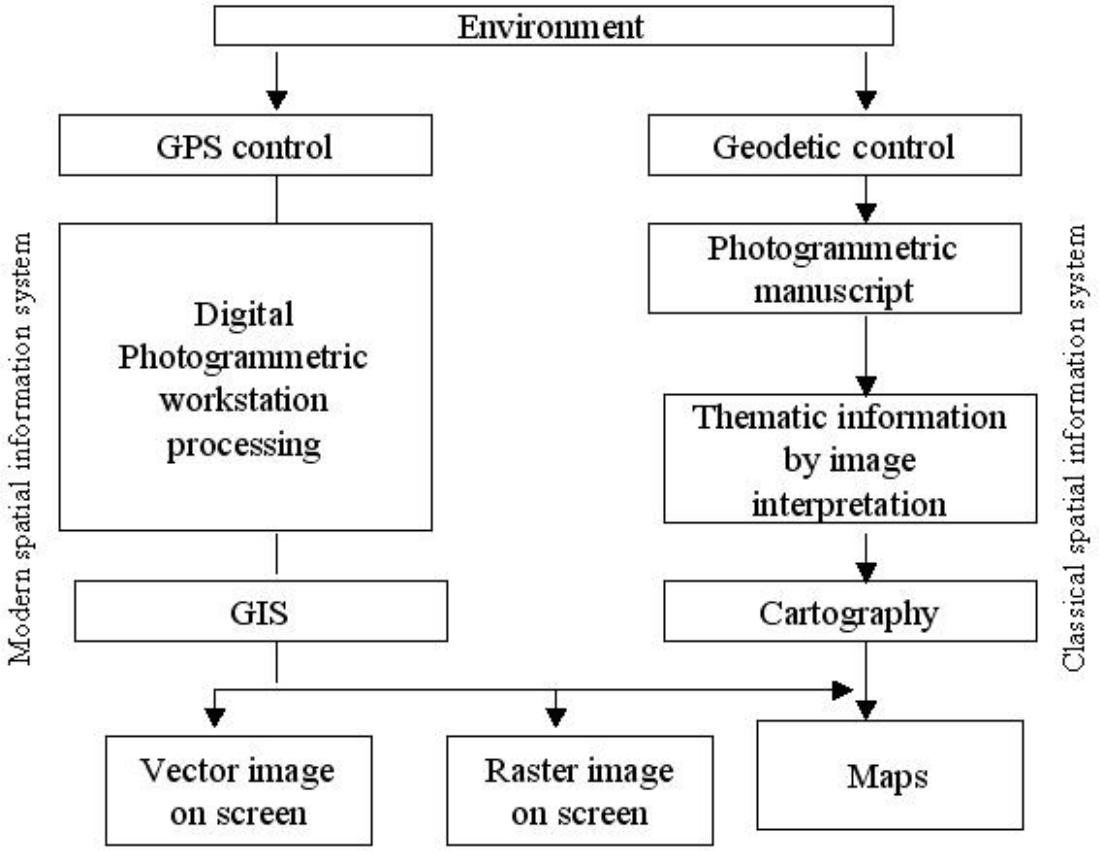

Figure 5-1 – Classical and modern geospatial information system (reproduced from Konecny, 2003)

5.1.2. Photographic film versus digital product

The interdisciplinary approach has been encouraged by developments in computer technology, especially Geographical Information Systems. In the past, the main product was film or photographic print recorded at visible wavelengths[22]. The distance of cameras from the Earth's surface and the need for high ground resolution (especially for military reconnaissance programs) demanded a sufficiently high resolution film. This led to the production of films with 160 lp/mm resolution (CORONA program), 320 lp/mm (GAMBIT program), and higher. Even with today's technology, such resolutions cannot be transferred to digital format for computer processing without loss of data and interpretability. During that era, the best approach was photointerpretation alone, since the computers were not powerful enough to read and analyse such huge amount of data.

[22] Some special colour films were sensitive in IR light too.

Thus, with the use of large light-tables and magnifiers, the film was analysed by the most advanced computer in existence, the human brain.

In 1970, W. Boyle and G. Smith of Bell Labs discovered the CCD (Charged Coupled Device)[23] (Boyle & Smith, 1970). Later, the CCD was improved and it became the dominant process for image capture. Although other devices became available (e.g. CMOS, Complementary Metal Oxide Semiconductor), the CCD gives the best performance in terms of resolution, sensitivity, and other parameters, with the exception of cost. Felber (2002) provides a very good summary of the development, structure and operation of CCDs.

The product of CCD image capture is a matrix of digital picture elements (pixels). It can be attached to detectors that are sensible to a wide range of wavelengths. It is sensitive to the visible, near-infrared, near-ultraviolet, thermal and microwave parts of the electromagnetic spectrum. On the contrary, film is limited to available film emulsions and spectral characteristics.

When comparing film with the CCD in photogrammetry and remote sensing applications, the former has the advantages of finer resolution, rigorous geometry and being a mature technology (established reliability of performance, with support and systems existing worldwide). But the processing of the film itself introduces distortions that are nearly impossible to model (treatment during film development, film must be scanned).

The product of CCD image capture may be derived from CCD matrices or CCD linear arrays. Depending on the product, the user has to apply different techniques for the optimum gain of qualitative and/or quantitative information. Always, the user must know as much as possible about the product's background. Further processing mainly depends on the aims and objectives and the tools used to aid the process.

The CCD matrices share the same conical geometry with film cameras. The resolution is coarser, but there is rigorous geometry with better precision and fewer distortions when compared to film (Kasser, 2002a).

On the other hand, the CCD linear arrays have cylindro-conical geometry. This type of geometry is found on most of today's satellite sensors (Landsat, IKONOS, SPOT, etc.), even though not all of them use CCDs (Landsat) (Kasser, 2002b). This geometry implies new digital data process approaches, which forbid the use of standard software of classic photogrammetric stations (Kasser, 2002a).

[23] CCD is an imaging electro-optical sensor. It can record radiation from a ground resolution element for representation within a pixel in an image. The simplest CCD array is linear (Rees, 1999).

Torlegard (1992) wrote that the aerial film camera would be the main sensing system for map production and revision in large- and medium-scale cartography for the next several years. Light (1996) presents a list of tradeoffs between CCD and film sensors. Today, one would agree that the high resolution space systems and the CCD sensors have improved significantly and are already replacing film cameras in most applications.

5.1.3. Elements and levels of photointerpretation

5.1.3.1. Elements

The basic elements of photointerpretation are: size, shape, shadow, tone/colour, texture, and pattern (Colwell, 1960). Later, Colwell (1983) added three more: height, site, and association. The latter two (site and association) are sometimes perceived as one single element (Schott, 1997). Philipson (1997) completed the list with the element of time.

The most fundamentally important of all elements is *tone/colour*. The imagery may be either B/W (black and white), thus the brightness values of the pixels will be hues of grey, or colour composite, in which selected features are chosen to be associated with the three additive colour primaries in the display device which produces the colour product (Richards and Jia, 1999). NB. colour prints use subtractive colour models. When it comes into digital processing, the number of distinctive colours is defined by the radiometric resolution of the satellite/scanner sensor. In the case of CORONA film product, the scanner sensor gave an 8-bit B/W product, which translates to 2^8=256 possible brightness values. In the case of IKONOS image product, the satellite sensor gives an 11-bit product, which translates to 2^{11}=2048 possible brightness values.

Four of the elements (*size, shape, height* and *shadow*) describe the geometry of the objects displayed in the image. *Size* describes the scale of an object in an image. It also describes objects in one (length), two (area) or three (volume) dimensions. *Shape* describes the outline of an object. Usually, geometrically perfect features are man-made while non-canonical features are naturally made. *Height* information offers the third dimension in the size element. For the best perception of *height*, there is need to create stereoscopic pairs. In chapter 7 of this thesis, stereoscopy and parallax are discussed. The *shadow* element can be a problem when covering a dark-toned area, and it can be

less of a problem when covering a light-blooming area. But it can also give information like the sun azimuth and elevation, the light conditions, and height inferences.

Texture and *pattern* are actually higher-level abstractions of the tone/colour element. *Texture* describes the structure of the variation in brightness within a product. *Pattern* is usually a formation of objects in the picture. The formation takes a meaning when the interpreter recognises it as something perceivable by his mind. Random natural patterns are usually ignored, while geometrical man-made patterns are noticed in an instant.

Site and *association* are mainly based on the cultural and geographic knowledge of construction patterns in the area of interest. *Site* refers to the geographic location of the object, while *association* refers to the object's spatial relativity with the surrounding objects and environment. Feranec (1999) extends association to also refer to the capabilities of an interpreter to understand and identify this relativity.

Time describes phenomena and changes, which combined with proper knowledge and understanding can assist with the description and characterisation of objects.

Naturally, all the above elements are always combined during the interpretation process. For example, the *size* of different herds of animals may be *associated* with the *size* of other features to identify an animal species.

Also of use are the references from other studies, like the study by Hoffer (1978) on the spectral reflectance characteristics of common Earth surface cover types.

5.1.3.2. Levels

During *observation*, there are three things that differentiate the photo interpreter from an untrained observer. First, the perspective is overhead. Second, the scale and resolution perspective is very different. Third, the imagery may well depict data from outside the visible part of the spectrum (Campbell, 2002). All the photointerpretation is done similarly to every day visual perception. The interpreter cannot observe the whole situation in the image at once, but it is the "something specific" he/she is expecting to find. For this, *detection* is the first stage. According to Marr's theory (1982), the detection of objects is primal and vital in order to proceed to object recognition and understanding of reality.

Once an object is detected, it must be identified. To identify an object, the human brain calculates *measurements*, mainly based on the elements of photointerpretation. The *identification* of the object is complete once the photointerpreter labels the object.

After the basic steps of observation, detection, measurements, and identification, the remaining part is the thinking area. The identified objects must be associated and assessed for the final analysis and interpretation. This is a task that can be better accomplished when the interpreter has more experience. Thus, the interpreter can give meaning to the picture and the identified object. The more experienced is the interpreter, the more selective and precise will be the identification, thus the better the final interpretation and meaning of the imagery.

5.1.4. The human factor

The whole process of photointerpretation depends on individual knowledge, experience, limitations and expertise.

But apart from the above, there are also the physiological and psychological factors that affect the photointerpretation. The subject of the human factor in photointerpretation is vast and there are many questions still unanswered among researchers (Colwell, 1960; Philipson, 1997; Hoffman & Markman, 2001). This paragraph does not address these questions, rather it seeks to emphasize that such factors need to be considered in every photointerpretation project.

5.1.4.1. Physiological aspects of vision

Physiologically, the central point is the eye and the neural system that transfers the light signal to the brain. The eye collects the light from the environment. The spatial and temporal pattern of light converging on a point in a land or water environment provides information about the structure of the environment and events occurring in it. Most animals that are sensitive to light have photoreceptor cells to transform light into a receptor potential. The purpose of the photoreceptor cells is to increase the animal's directional sensitivity. Thus, they may be scattered over the skin (i.e. earthworm), or may be concentrated into eyespots (i.e. bivalve molluscs), or may be under the skin to form eyecups (i.e. snails). Further directional sensitivity requires the possession of a true eye. The true eye can be either compound (i.e. bee) or single-chambered. The single-chambered eye can be like a pinhole camera (i.e. nautilus), a concave mirror (i.e. scallop), or a convex lens (i.e. human) (Bruce *et al.*, 1996).

To understand the optics of the human eye[24], a camera provides a useful analogy[25]. However, there are features of the eye that differentiate it from the camera. The quality of the image decreases in the eye by a yellowish cast and by a shadow of the dense network of blood vessels. Also, the eye moves smoothly and includes tremor, thus the image moves continually. A camera would produce blurred photographs this way. One understands that the image the eye produces is imperfect. This is because the eye does not transmit pictures to the brain, but information about the pattern of light reaching the eyes, and so information extraction begins in the retina of the eye itself.

The photoreceptor cells are separated into rods and cones. The rod cells respond to light at low-illumination levels, they do not provide any colour information, and this type of vision is called scotopic. The cone cells require a higher illumination level, they allow the distinction of colours or hues, and this type of vision is called photopic (Mather, 1999). Colour is thought to be associated with the cone cells because there are three kinds of cones, each of them being responsive to one of the three primary colours of light (red, green, blue). In figure 5-2, there are the absorption spectra of human photoreceptor.

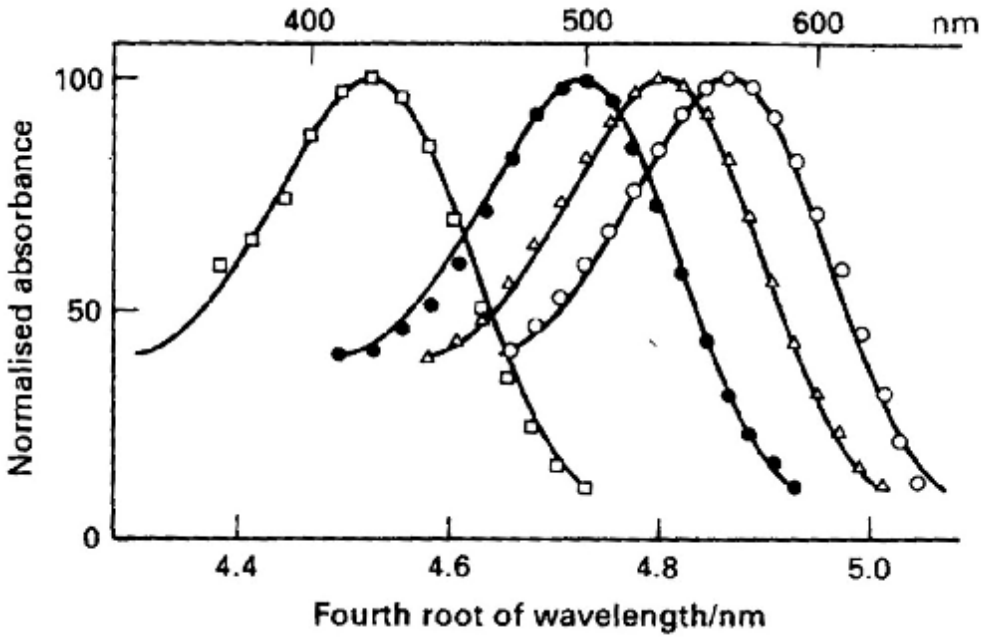

Figure 5-2 – Absorption spectra of the human photoreceptors. From left to right: blue-sensitive cones, rods, green-sensitive cones, and red-sensitive cones (after Dartnall *et al.*, 1983).

[24] From now on, "eye" will mean "human eye".
[25] The author assumes that the reader knows how a camera is operating.

5.1.4.2. Psychological aspects of vision

Each of us has his own perspective of the environment, or of a particular scene. This perspective is always enriched with previous experience and knowledge. Thus, a cartographer will be better interpreter of a map than a lawyer. This perspective is further enriched when the person has developed the visual perception and understanding more than other senses. For example, a hard-of-hearing person will develop other senses to survive in the environment, perhaps vision.

Generally, visual perception can be either structured through basic elements of the image, or be formed through the geometric and radiometric characteristics of the various objects in the image. However, there may be illusions in an image that can trick the interpreter. The most common illusions are shading, form, parallel lines, continuity, size, and colour (Philipson, 1997). For this, the interpreter must be properly trained, and the image photointerpretation must be done using as many elements of photointerpretation as possible.

5.1.5. The computer factor

The computer is a tool for many tasks. It is a tool for photointerpretation too. The human may be the actual photointerpreter, but since the image is in digital format, it is displayed on a computer screen. Furthermore, the image may be processed, enhanced, and made to highlight certain features, according to the application. This processing is of two main types: radiometric and spatial (or geometric) enhancements. Radiometric enhancement deals with the brightness values of the image. Spatial enhancement has to do with the perceived spatial or geometric character of the image.

Radiometric enhancement differs from spatial enhancement in that the first deals with individual values of pixels in the image, while the latter takes into account the values of neighbouring pixels. Both of them highlight spatial information. However, generally, only the radiometric enhancement amplifies the spectral character of an image (Richards & Jia, 1999).

Other enhancement techniques may be used by the photointerpreter if this is judged important. For example spectral enhancement techniques may be used to compress similar data, extract new bands of data that are more interpretable to the eye, apply transformations, or display a wider variety of information. The image analyst may also

wish to reduce noise or remove periodic features from the image using Fourier domain filtering.

Generally, the techniques to be used depend upon the data, the objective, the expectations of the user, and his/her background. The images may be separated into two broad categories, the single-band and the multi-band [Richards and Jia (1999) call them *scalar* and *vector* images respectively]. Most enhancement techniques relate to single-band images.

The analysis of these enhancements is not within the scope of this chapter. The interested reader should look at Gonzalez & Woods (2002), Schowengerdt (1997), and Mather (1999). This chapter includes a brief explanation of the main enhancement methods explaining *why* a person would use these enhancements and *what* to expect from them. In the following paragraphs, only the simple techniques are explained. More complex techniques such as spatial derivatives for edge detection, or other data techniques such image radar enhancement are not discussed here.

5.1.5.1. Radiometric enhancement techniques

The main radiometric enhancements are contrast stretching (linear, non-linear, other variants), histogram[26] equalisation, histogram matching, brightness inversion, and density slicing.

Contrast stretching is mainly used to improve the contrast of the image. The simplest way to do this is using a *linear* contrast stretch. In the raw image, the area of interest may occupy a restricted brightness value range. Contrast stretching expands this range to the lowest and highest brightness levels supported by the display device. Most image analysis software applies an automatic linear contrast stretch by choosing the limits to be equal to the mean brightness value plus/minus a number of standard deviations for the maximum/minimum value respectively.

While the linear contrast stretch applies the same amount of contrast to the entire image, the *non-linear* contrast stretch is used to bring out the contrast in one range while decreasing it in other ranges. To enhance areas in shadow or where there is low contrast, a very useful technique is the *piecewise linear* contrast stretch. It is more

[26] A more appropriate description for images is the *histogram*. It describes the statistical distribution of image pixels in terms of number of pixels assigned to a particular integer value of brightness. It is important to remember that the histogram does not provide information about the spatial distribution of the pixels. It only contains radiometric information and it is a good assessment display of the radiometric quality of the image (Schowengerdt, 1997).

controlled and it can be applied manually. By manipulating the histogram or using any combination of the above techniques, the user may create any *variant* of contrast stretch he/she wishes.

A type of non-linear stretch of interest is *histogram equalisation*. This redistributes the pixel values so that there is approximately the same number of pixels with each value within a range. Thus, the contrast is increased for the brightness values where the majority of the pixels lie and decreased for the minority. However, the user should be aware of histograms with an abnormally large number of pixels assigned in a particular value (for example an infrared band image where there is a large area of water). Then, the histogram equalisation technique would give low contrast and little detail. To avoid this, the user should reduce the significance of the dominating values.

Sometimes it is desirable to match the histogram of an image with another image or a mathematical expression (i.e. Gaussian function of brightness). To do this, the *histogram matching* technique is used, which is the process that converts the histogram of an image to resemble the histogram of another, or a pre-defined shape. Image-to-image matching is useful for mosaicking or for change detection. For best results, the spatial and radiometric resolution should be the same, and the spatial and radiometric distributions should be similar. Image-to-shape matching requires another histogram of the shape the user needs or to a normal distribution, where most pixels are assigned grey values with fewer extremes toward the black and white edges.

Density slicing is mostly used for highlighting specific brightness ranges of interest within the image. It actually segments the image into regions, acting like a one-dimensional parallelepiped classifier. *Brightness inversion* can be used for the inversion of a positive film to negative and *vice versa*. *Brightness reversion* can be used for the emphasizing detail in the dark (low brightness) areas of an image.

5.1.5.2. Spatial enhancement techniques

Instead of enhancing the radiometric character of a pixel, using spatial enhancement techniques the emphasis is placed on the *spatial frequency*[27], which characterises the spatial character of the brightness values. The main spatial enhancement techniques are

[27] Spatial frequency is the number of changes in brightness value per unit distance for any particular part of an image (Jensen, 1996). Spatial frequency is the image analog of a signal in time (Richards & Jia, 1999).

convolution filtering (zero-sum, low frequency, high-frequency), edge detection, line detection, shape detection, and filtering (adaptive, statistical).

Convolution filtering is used to change the spatial frequency of an image. During convolution, a table called ***kernel*** is defined and moves over the image row-by-row and column-by-column. The pixels brightness values are multiplied by the corresponding kernel values, and then summed together, and the total is divided by the sum of the values in the kernel to give the final response. The size of the kernel and the kernel values differ according to the application.

For image smoothing and noise removal purposes, ***low-pass*** filtering is used. With this method, the pixel at the centre of the kernel takes the average brightness value of the neighbourhood defined by the kernel's size. Unfortunately, this can lead to a loss of high frequency detail. For this reason, a threshold can be specified. This threshold is determined by an estimate of scene signal to noise ratio, or it can be chosen as a multiple of the standard deviation of brightness within the kernel. Thus, the noise is removed and there is better preservation of the high frequency detail. Alternatively, ***median*** filtering may be used, which is the same procedure without a threshold, and the only difference being that instead of the average, the median of the neighbourhood is used. For this reason, median filtering is not a linear operation. Another simple alternative can be the subtraction of the smoothed image from the original (the result being the high frequency that was lost during low-pass filtering) and the addition of the result (in varying proportions) to the smoothed image.

The opposite of low-pass filtering is ***high-pass*** filtering, which increases spatial frequency. It serves to enhance high frequency information including highlighting edges without attenuating other features. Another kind of kernel is ***zero-sum*** filtering, where the sum of the values of the kernel equals zero. Of course, in this case no division is performed. This kernel attenuates the low spatial frequency areas and highlights the high spatial frequency areas. Thus, this kernel also acts as an edge detector. Zero-sum kernel can be biased to detect edges in a particular direction.

Generally, kernels can be used to perform linear or non-linear operations such as ***statistical*** filtering. The kernel mainly focuses on the central pixel. Thus, it is highly dependent on its neighbours, which in some cases can result in a situation, where a single filtering operation cannot apply. For this reason, ***adaptive*** filtering was developed. It varies the contrast stretch depending upon the values of the neighbour pixels (Peli & Lim, 1982).

Many researchers have applied different kernel coefficients with different algorithms and different sizes for edge, line or automatic shape detection. Such techniques were mainly developed for computer vision. With the advent of high (sub-metre) spatial resolution satellite images, the techniques of image enhancement and pattern recognition are very relevant to remote sensing (e.g. Radeva *et al.* (1999) for line detection, Pujol *et al.* (1999) for shape detection, or Gracia & Petrou (1999) for line detection of archaeological interest).

5.1.5.3. Spectral enhancement and Fourier analysis techniques

When it comes to multi-band imagery, spectral enhancement techniques are utilised. Not all spectral enhancement techniques are used to aid or improve photointerpretation. They may also be used for data pre-conditioning before classification methods. The main techniques for image enhancement include principal components transformation (Taylor method), ratio images, and the Kauth-Thomas tasselled cap transform.

A very important tool for the analysis of multispectral data is the *covariance matrix*. It describes the scatter or spread of the pixels in multispectral space. From the covariance matrix, it is easy to get the *correlation matrix*, which describes the correlation between different bands. The principal components concept is based on the idea that the image may be represented according to inter-band correlations and covariance. This is achieved by projecting each band's brightness values to an axis and by rotation of the image brightness values axis to match the inter-band correlation. The new covariance matrix will be diagonal and the non-zero values will display the variance for every principal component. Naturally, the non-diagonal values are zero because the principal components are by definition uncorrelated.

The more correlated are the original image bands, the more variance will be contained in the first principal component. For every image, it is expected that about 95% of the total variance will be included in the first three principal components. Thus, the latter may be displayed with the primary colours, and actually display the 95% of the original multi-band image. However, for some applications, useful information can be gathered from the principal components with the least variance. For example, they may show details in the image that were obscured by higher contrast in the original image, or they may simply show regular noise in the data.

The principal component bands do not represent spectral vectors, but a linear combination of spectral components. Thus, it is difficult for the photointerpreter to

intercept the colours of the displayed image. One exception is in exploration geology, where the actual colours are of little interest, and the structural differences (which are of more interest) may be well enhanced by the principal components transformation (Richards & Jia, 1999).

Taylor (1973) presented an utilisation of principal components that greatly improved the image display for photointerpretation. Simply, he applied radiometric enhancement techniques to the principal components and then inverted them back to the original image. This way, the covariance matrix was preserved and no correlation was introduced, while the data showed good utilisation of the colour space using the original image data components. This method is also called *decorrelation stretch*. Some noise is induced while the colour space is 8-bit because of the rounding of brightness values to the closer integer. But this noise is reduced in the 11-bit colour space of IKONOS and other future satellites. Decorrelation stretch imagery is also discussed in paragraph 3.3.6.

The most common implementation of radiometric enhancement techniques in the decorrelation stretch is the histogram equalisation applied separately to each of the three first principal components. The final images are still a linear transformation of the original image data. They cannot be sensibly interpreted unless the spectral contrasts are given (Campbell, 1996). ERDAS LLC (2002) suggest the radiometric enhancement of only the first principal component assuming it contains the overall scene luminance, and the other principal components represent the intra-scene variance. This is an enhancement used when the image is blurred (atmospheric haze, rapid sensor motion, or other reasons), thus sharpening the luminance of the image.

As principal components are aligned according to the variance in the multiband image space, there may be other types of axis alignment according to the absorption features in which a scientist is interested. One of these alignments, the Kauth-Thomas Tasselled-Cap transformation, is used in vegetation studies. It is sensor dependent and the first component expresses brightness, the second expresses greenness (mostly biomass index), the third expresses wetness (relates to canopy and soil moisture), and the fourth expresses “non-such” or haze. It offers a way to optimise data viewing for vegetation studies (Kauth & Thomas, 1976).

Other spectral enhancements of interest to photointerpretation are indices, otherwise called *image arithmetic*. Addition, subtraction, division, multiplication, all are simple transformations and may be implemented to form new images. Band differences and

ratios are the most commonly used. The first is mostly used to highlight changes between two images. The latter are extensively used in mineral exploration and vegetation analysis to highlight and enhance rock types and vegetation class differences that cannot be readily seen in original image data. Image ratios may also be used to minimise shadow effects. Variations of band arithmetic are also sometimes used as indices. Band ratioing is not a linear transformation.

Last but not least of the computer tools for a photointerpreter is the *Fourier transformation*. During the geometric enhancement techniques, there was talk about the kernels that run all over the image. More flexibility is offered if procedures are implemented in the spatial frequency domain by means of Fourier transformation. Because of the complexity of the background calculations, Fourier transformation was too demanding for the personal computers of the past. But modern systems are much more powerful and they allow the implementation of complex calculation thus offering more flexibility and precision in the results. The background mathematics is presented as an introduction to Fourier transformation in Richards & Jia (1999). The interested user may look into Brigham (1988). Applications of Fourier transformation include the removal of noise (striping, spots, or vibration) in imagery by identifying periodicities, and the technique may also be used across bands as another form of pattern/feature recognition.

5.1.6. Archaeological photointerpetation

For aerial photogrammetry the optimum photography is nadir looking vertical with good light and stable line of flight. This allows the user to create maps and make measurements of the area of interest. Vertical photographs are also capable of being used as stereopairs. From these, height information may be extracted. The image is thus enhanced for photographic interpretation.

However, this does not always suit the archaeologist. The main reasons for this are cost, purpose and object. The purpose of the archaeologist is to discover and record. Apart from commercial vertical survey companies, who use calibrated vertically mounted cameras, the majority of archaeological aerial photographers use either 35mm hand-held cameras or medium format cameras which take 220, 120, or 70mm film (Bewley *et al.*, 1999).

Normally it is difficult to see an archaeological site from the air since most of it is underground. The archaeologist is looking for surface traces as crop or soil marks that

correspond to past human activity. These traces are usually of geometrical shape, or form a particular picture. Also, they usually occupy a small area. What one often sees are the traces left on the surface by the actions of the past, or the effect that the underground man-made object has on the surface. There are many occasions where the sites become visible only through a very tiny time window, and this happens because of optimum moisture, soil, environment and crop conditions. A list of the possible sites along with the conditions dependency is provided by Scollar *et al.* (1990).

In this research project, the platform is not an aircraft but a satellite. This means that the imagery is looking in a particular angle, the radiometric resolution is limited, the re-visit time is specific, and the image capture can only be scheduled through cloud-free day windows without the freedom of time choice. Also, until recently archaeologists found commercial satellite data to be of limited practical use because of its poor spatial resolution. On top of that, the cost of the satellite imagery is usually forbidding.

Multispectral sensors such as Landsat have low spatial resolution and even the 15m panchromatic band on Landsat 7 would not be a sensible alternative to aerial photography for site detection and mapping. On the other hand, there have been several studies that have demonstrated the capability of satellite imagery to derive important environmental information that is of considerable value in archaeological landscape assessment. For example, the North-west Wetlands Project in the UK used Landsat TM image data to help define the extent of peat deposits and former wetland environments. The satellite data identified a considerably larger area of wetland than could be confidently identified from aerial photography or Soil Survey data (Cox, 1992). A similar application saw satellite data used to predict possible wetland sites for archaeological investigation along the Delaware coast (Custer *et al.*, 1996). In Mediterranean landscapes, Landsat and SPOT satellite data has helped to identify both modern and relict agricultural systems and land use patterns (Urwin & Ireland, 1992, Stein & Cullen, 1994, Sussman *et al.*, 1994, Wiseman, 1992). In tropical forests where ground survey is extremely difficult, satellite data has proved valuable for both characterising the environment and for visualising the rate and patterns of change (Behrens & Sever, 1991).

The declassification of Russian and American reconnaissance space photography has made available a substantial archive of images with ground resolutions down to two metres. The importance of the archive lies in its historical value, and its low cost. The

archaeologist should also not ignore the existing archives of aerial imagery for an area (Going, 2002), i.e. aerial photography of the Second World War period.

In 1999 the era of commercially operated metre and sub-metre resolution satellites began. Although expensive for an archaeologist, this imagery adds great value to the data because of improved radiometric resolution, spatial resolution, and very good image geometry.

5.2. Different landscapes

From the geological map of Syria of 1964, the Homs project study area is separated into three main geological formations. The north-northwest reddish part is basalt, the south-southeast yellowish part is limestones, marls, sandstones and cemented gravels, and there are pebbles, sands and loams along the Orontes River (fig. 5-3). A more elaborate work on the geology of the Homs area is presented in Bridgland *et al.* (2003).

The patches (pale colour with small triangles inside) within the main areas are rock debris, slope mantle, and talus. Similar geological formations are common in the Middle East, thus extending the value of this research project beyond just the Homs region of Syria.

The quality of the image in figure 5-3 is poor due to the poor quality of the geology map that was provided to the project. It is here presented to provide a picture of the main geological formations in the area of interest.

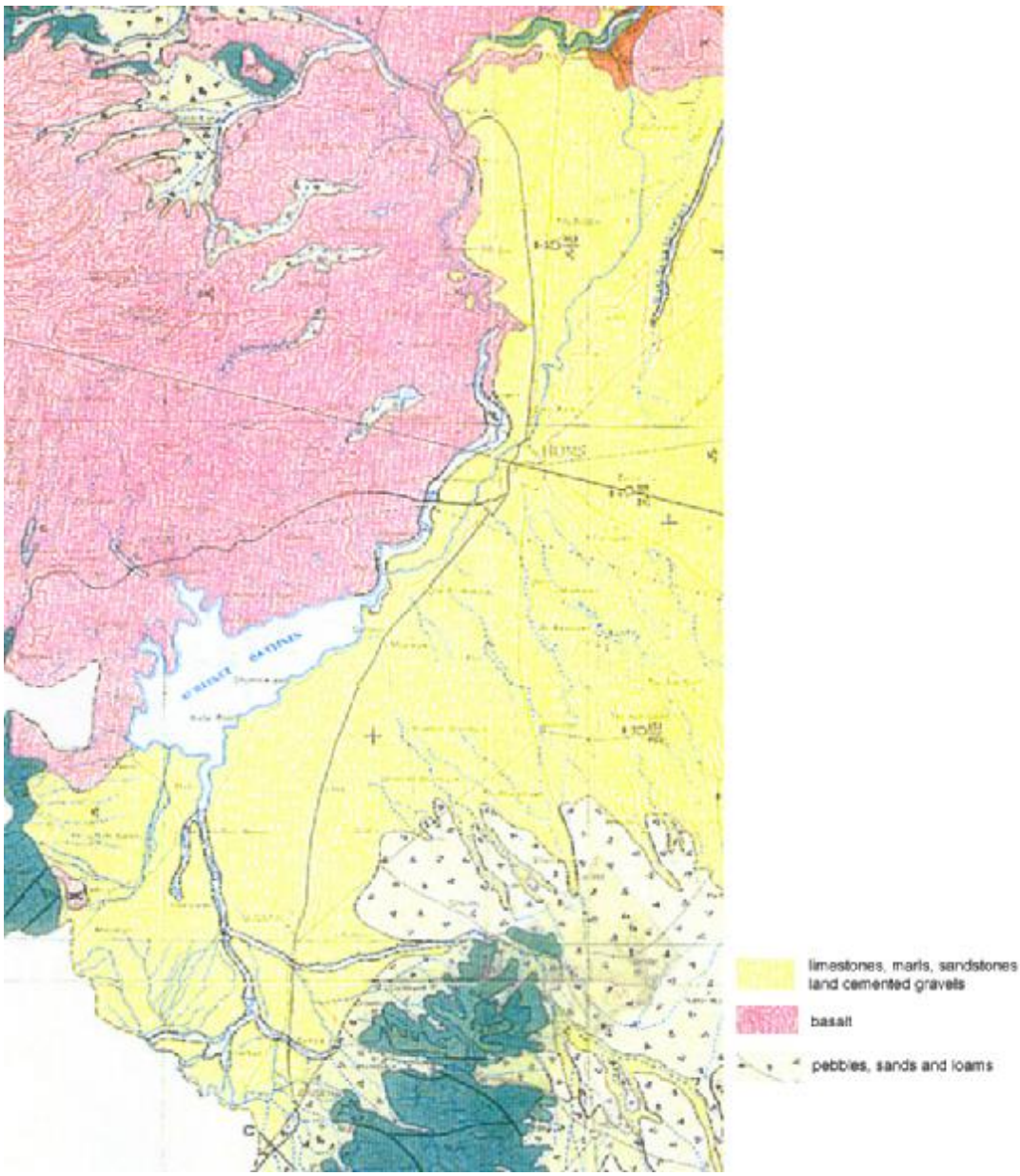

Figure 5-3 – Part of geological map covering the area of interest. The map is dated 1964, and the scale is 1:200,000 (Ponikarov *et al.*, 1963).

The Homs study area is separated into three main geological units. The *Basalt* unit meaning the basalt area, the *Marls* unit meaning the limestones, marls, sandstones and cemented gravels area, and the *Alluvium* unit meaning the pebbles, sand and loams area.

5.2.1. Basalt

Basalt is an extrusive volcanic rock, and it is usually black in colour. Generally, it is made of about 60% pyroxene, 20-40% plagioclase feldspar and 0-20% olivine. Basalt and andesite are the most common types of lavas (Strahler & Strahler, 1997).

Most of the basalt area is covered by a multi-layered net of field-walls and cairns. The landscape is characterised by extensive areas of rectilinear walls, which probably demarcate ancient field systems. The CORONA imagery shows considerable variability between the size and the shape of fields in different areas.

In figure 5-4, the imagery permits detailed assessment of the size and layout of individual fields, and suggests the existence of major wall alignments, which organise the fields into blocks. It is also possible to differentiate between stone cairns (dark, circular features within the field systems) and hollow ovoid features (clusters of circular enclosures). CORONA imagery appears to be sensitive to the differential reflectivity characteristics of the concentrations of basalt represented by walls and cairns, and the soil and vegetation matrix occurring within fields and enclosures.

Ground survey showed that the field systems include a variety of walls of different breadths, heights and methods of construction. The 'cairns' fall into a number of distinct types (Philip *et al.*, 2002b). These distinctions are not always apparent from satellite imagery, and they can only be assessed by fieldwork.

The value of CORONA imagery as an historical map shows up very well in figure 5-5. The years between 1969 and 2002 witnessed the construction of a railway, a new road, new fields on top of the old, few enclosures re-used, and the destruction of many fields. These changes are very clear in the figures 5-4 and 5-5, where the same basalt area is shown. The figure 5-4 shows the landscape in December 1969, and the figure 5-5 shows the landscape in February 2002.

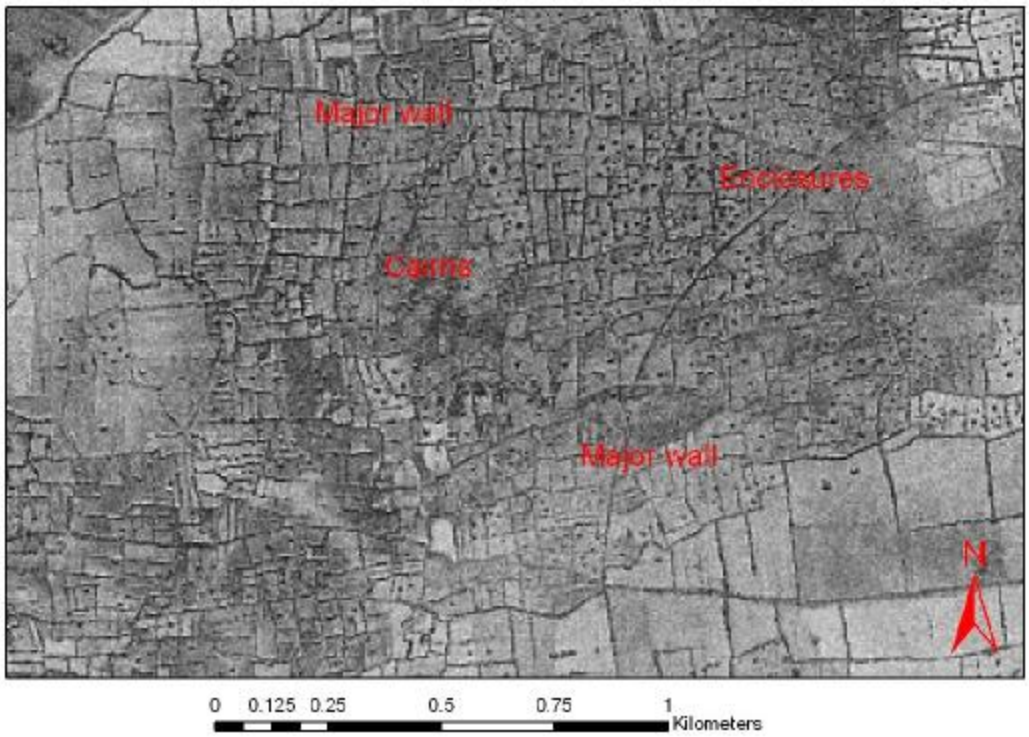

Figure 5-4 – The basalt landscape. Cairns, enclosures and major walls. CORONA 1108, negative film, 17 December 1969 (after Philip *et al.*, 2002a).

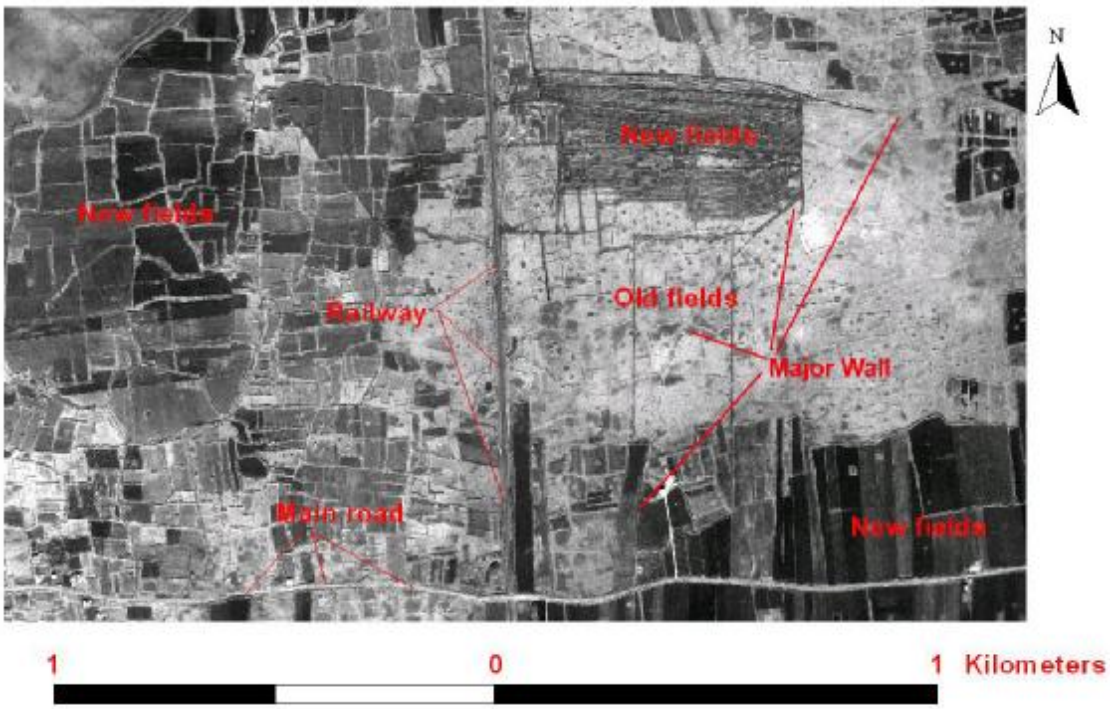

Figure 5-5 – Photointerpretation of the basalt area. IKONOS, 03 February 2002.

5.2.2. Marls

The landscape is derived from ancient lake deposits (lacustrine marls) with a red-brown calcareous soil. The area is characterised by extensive farming, dry thin calcareous soil, and a general lack of stones like basalt. It is crossed by a series of Pleistocene river channels, now preserved as fragmented outcrops of cemented gravels also termed conglomerates (Bridgland *et al.*, 2003).

Figure 5-6 shows some of the different types of archaeological sites found in the area. The image is displayed as a negative, thus the dark areas are bright in reality and *vice versa*. Some archaeological sites are depicted on the maps (see chapter 3), other potential sites can be seen on the CORONA imagery and the remainder are only identified through ground survey. Tells 255 and 256 come out clearly in the imagery and they also appear in the maps. Tells present a distinctive brightness which can be seen in other places on the imagery, here presented as sites 308 and 454. And indeed, through field walking, these proved to be sites of archaeological interest. However, they are flat areas and not as easily detected on the ground as tells. Further photointerpretation suggested there is a soil colour anomaly that extends beyond the tell 256 itself southwards. Field-walking revealed the existence of a flat site, here marked as 458. Further field-walking in the area revealed the existence of smaller or sparse artefact scatters, here marked as 447, 446 and 472. They are not detectable in the CORONA imagery.

Archaeological investigation confirmed sites 447 and 472 to be prehistoric, while site 446 to be from the Roman/Islamic period. The detectable sites 308 (Islamic), 454 (Roman/Byzantine) and 458 (Roman/Islamic) presented a significantly greater abundance of artefacts and a distinctive light soil colour and thinner soil texture than the surrounding geological soils.

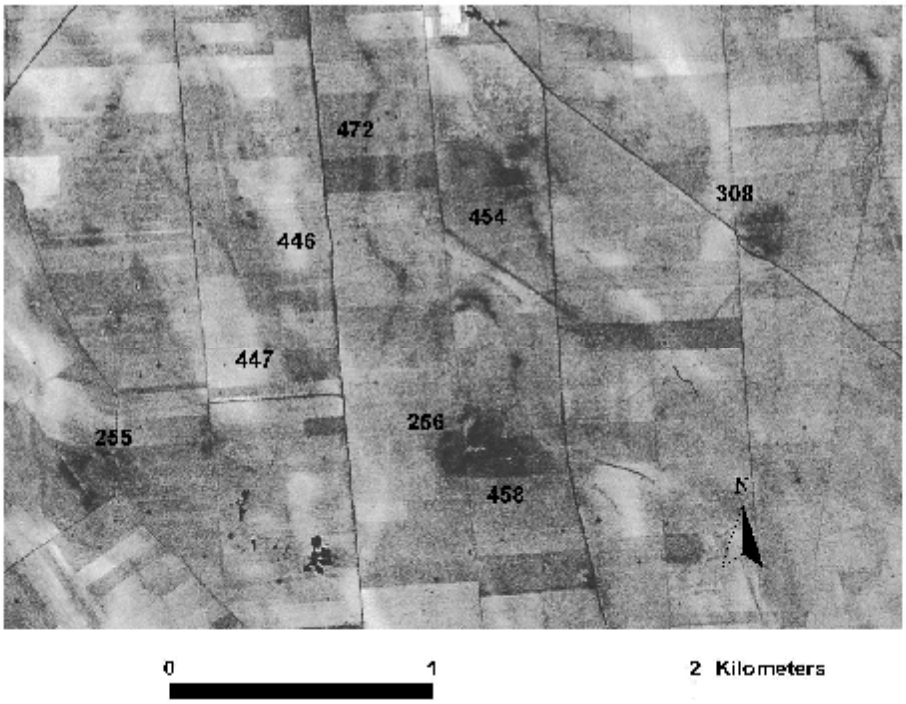

Figure 5-6 – Visibility of archaeological sites in the limestone soils of the southern unit, post-harvest landscape. CORONA 1111, negative film, 31 July 1970 (after Philip *et al.*, 2002a).

5.2.3. Alluvium

The alluvium area is of high interest to archaeology, because of the presence of water, which made the river a hospitable environment for human occupation.

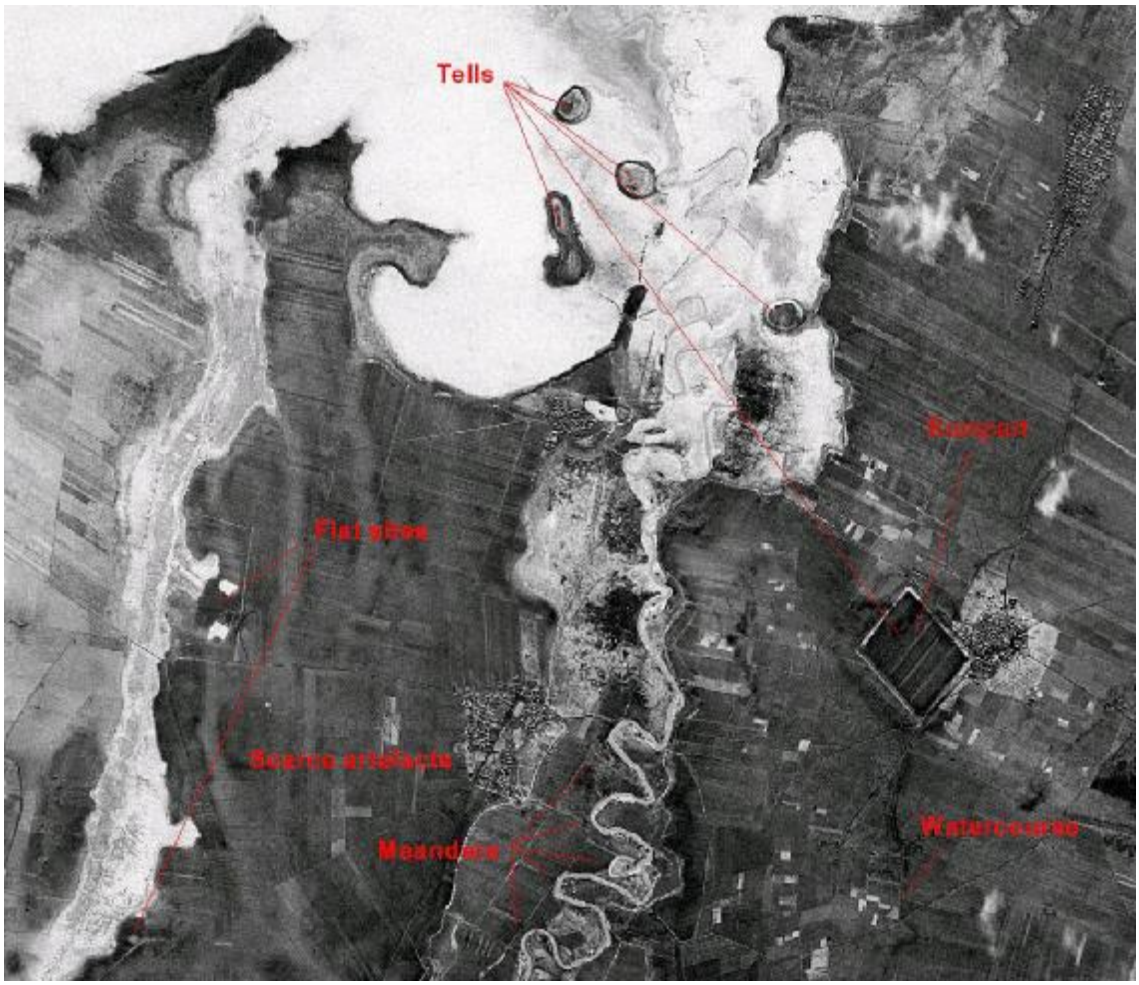

Figure 5-7 – Photointerpretation in the alluvium area. CORONA 1108, negative film, 17 December 1969.

Preliminary archaeological visits to the alluvium area indicated that alluvial deposition was potentially deep but uneven, and certainly enough to bury small sites. There is need for further geomorphological work to better understand this environment.

However, archaeological traces were detected within almost every meander of the river Orontes. Small tells emerge left and right of the river, and there is archaeological evidence throughout the area near the lake.

In figure 5-7, the river “meets” a number of tells when entering the lake. Along the river, and where the meanders are, some smaller tells appear. Survey showed evidence of archaeology either on the surface of tell sites or at the banks of the river inside layers of soil. A couple of flat sites may be interpreted where another river channel appears, mostly man-made, without meanders. At the lower right part of the image a large rampart appears and a watercourse appears to lead to it. It appears to be manmade, and the watercourse seems to be manmade too, since it appears in a different hue than the natural courses (where the scarce artefacts are), and after overlaying it with contour

lines, it was seen to follow one of the contours. This watercourse is no longer visible in the IKONOS imagery of 2002, as a result of recent agricultural works.

5.3. Satellite image analysis

The characteristics of the imagery (radiometric and ground resolution, image geometry), the quality of the imagery (cloud-free, satellite attitude, film acquisition, film duplication and originality), and pre-processing stage can all impact in photointerpretation. The psychology and background knowledge of the photointerpreter also play a vital role in the quality of the information obtained.

5.3.1. Importance of the imagery characteristics

Landscapes are composed of unique features, which should be thought of as useful information rather than as physical objects on the Earth's surface. These features are arranged either as a mosaic that completely covers the area or as discrete elements distributed on a continuous background. Landscapes can be simple, composed of one element and the background, or complex, composed of many elements (Woodcock & Strahler, 1987). The ground (or spatial) resolution of the satellite imagery reflects the information content.

Higher spatial resolution does not always produce more useful information. The reason is related to the maxim "not seeing the wood for the trees". For example, we may be able to detect a landscape of mixed wooden savanna using 30 m resolution Landsat ETM+ imagery and thus contrast it to pure forest and pure grassland. Yet, if we increased the resolution by using 1 m IKONOS panchromatic imagery, individual pixels within wooden savanna areas might now be classified as either trees or grasses. Although objectively accurate, the higher resolution of the data actually reduces the useful information content of the image making it harder to distinguish mixed wooden savanna from forest or grassland (Wilkie & Finn, 1996).

But how do we know which is the best spatial resolution for the field of landscape archaeology? Initially, we do not know. There are many methods that can be used to detect resolution effects. However, there is no established systematic and comprehensive procedure for this in geographic research (Cao & Lam, 1997).

Table 5-1 - Comparison of image resolutions

	Spatial	Radiometric	Spectral	Band details (nm)
CORONA KH-4B	1.83 m[Ↄ]	8-bit	1 band	400-700
IKONOS Pan	1 m	11-bit	1 band	525-928
IKONOS Ms	4 m	11-bit	4 bands	445-516 506-595 632-698 757-853
Landsat ETM+ Pan	15 m	8-bit	1 band	520-900
Landsat ETM+ Ms Landsat TM	30 m[‡]	8-bit	7 bands	450-520 530-610 630-690 780-900 1550-1750 10400-12500 2090-2350

[‡]Band 6 (thermal) has 60 m spatial resolution in Landsat ETM+ and 120 m in Landsat TM.
[Ↄ]The spatial resolution varies according to the mission success.

Table 5-1 provides a summary comparison of the CORONA, IKONOS and Landsat resolutions. CORONA offers 1.83 m spatial resolution. IKONOS Pan offers the highest spatial and radiometric resolution. Landsat offers the highest spectral resolution. The smallest item one may detect and interpret is the 3/2 of the spatial resolution (Slama ***et al.***, 1980). Thus, IKONOS Pan detects the smallest item. The 11-bit radiometric resolution of IKONOS offers more information than the 8-bit data from areas with high light intensity or deep shadow. The seven bands of Landsat gather data from a larger part of the electromagnetic spectrum, thus offering information that the other two satellites cannot provide.

Figure 5-8 uses a tell site to provide a visual comparison between the three main satellite data used in this research project. The difference in spatial detail becomes obvious when comparing (a), (b) and (c). It is the 1 m spatial resolution of IKONOS Panchromatic compared with the 2 m ground resolution of CORONA and the 15 m spatial resolution of Landsat ETM+ Panchromatic respectively. Spatial difference may be viewed between (e) and (f), the IKONOS Multispectral (4 m) and the Landsat Multispectral (30 m) respectively. In images (a) and (e), one may see the better radiometric resolution of IKONOS which gives a clearer picture than the 8-bit images of Landsat and CORONA. Last but not least, the intense study of Landsat and its use have provided a lot of spectral processing tools. In example (d), there is a Tasseled Cap band 1, which represents brightness.

Concerning image geometry, the CORONA satellite contains the most serious distortions. Landsat and IKONOS imagery geometry depends on the product one

purchases. In this project, the IKONOS Geo product was used, for which (always depending on the viewing angle and the relief of the ground) the imaging system is free of significant non-linearities (Fraser ***et al.***, 2002a). Also in this project, the Landsat ETM+ Level 1G (systematic correction) product was used, which includes both radiometric and geometric correction. Image data is provided in rescaled 8-bit (DN) values. The scene is rotated, aligned, and georeferenced to a user-defined map projection. Geometric accuracy of the systematically corrected product should be within 250 meters for low-relief areas at sea level.

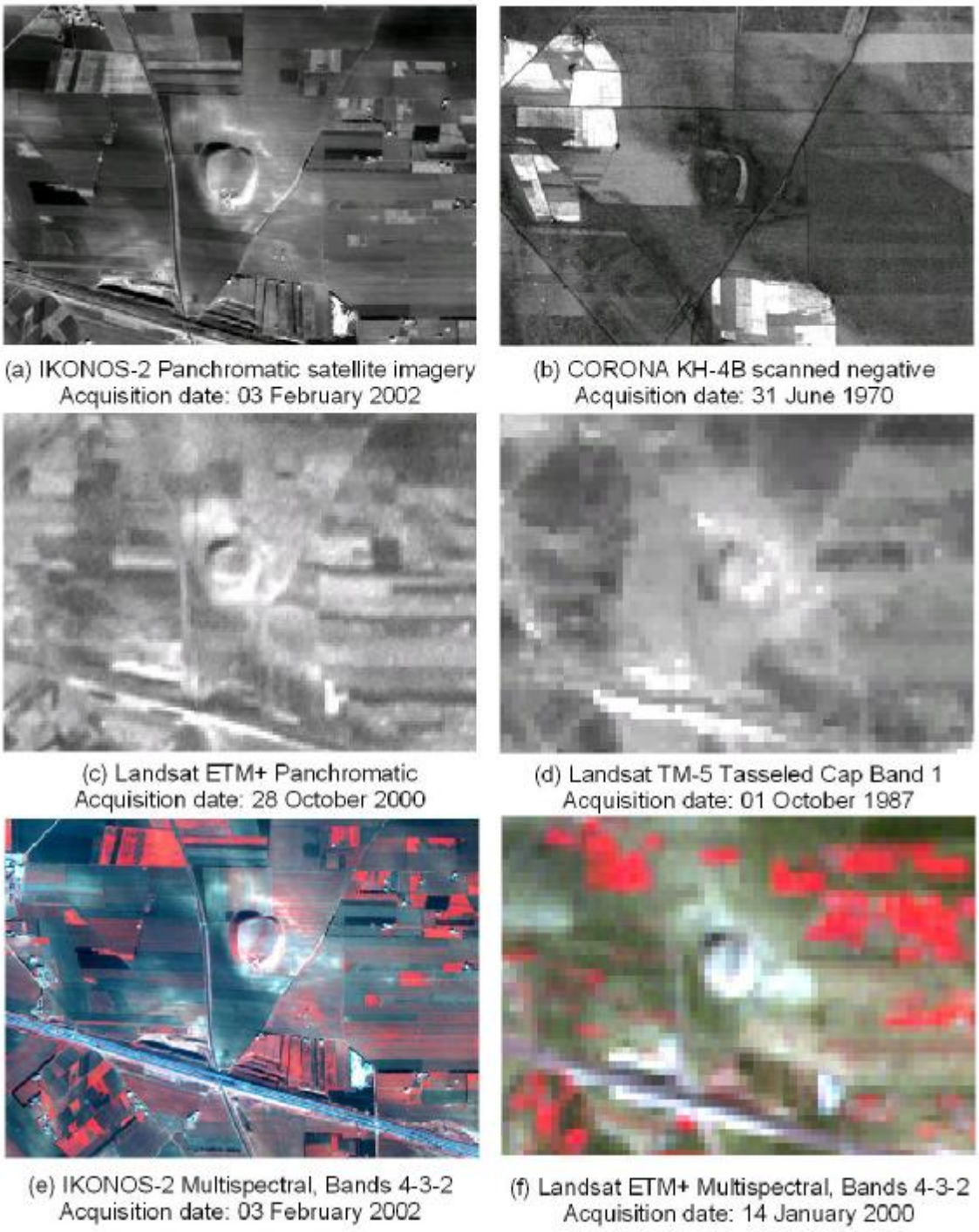

Figure 5-8 – Spatial, radiometric and spectral comparison of the CORONA, IKONOS and Landsat images. The central point of this comparison is a tell site.

5.3.2. Importance of the imagery quality

The quality of the data is very important for the quality of the results. Landsat and IKONOS data offer digital products. Markham & Barker (1985), Salomonson (1984), and Townsend et al. (1987) did research work on Landsat TM product quality. Dial & Grodecki (2003a), Toutin & Cheng (2000), and Cook *et al.* (2001) researched IKONOS

product quality. In the case of CORONA the film acquisition, film duplication and originality of the film, and satellite attitude were discussed in chapter 2 of this thesis.

Clouds form an obstacle for the photointerpreter of passive satellite imagery. The data from the IKONOS satellite is very expensive; hence the imagery must be more than 90% cloud free for the user to take full advantage of it. For this, Spaceimaging are searching for clear skies above the area of interest before capturing the image. However, the high radiometric resolution of IKONOS can give information from an area under cloud shadow. Concerning Landsat, preview images exist in the online catalogues and the user may choose the most appropriate images from the archive. The same preview system applies for CORONA. Also, for many areas CORONA offers more than one image, especially in the Middle East area. Because of the low cost of the film and its scanning, a good strategy would be to buy all of the available cloud-free films in the area.

Figure 5-9 shows an extract from the CORONA mission 1110 where cloud and cloud shadow obscure a major archaeological site. Fortunately, there are more CORONA photos from this area and they are not expensive. Thus, in CORONA mission 1111 the archaeological site is cloud-free and easier to detect and interpret. In figure 5-10, the IKONOS radiometric resolution allows the photointerpreter to depict details of the ground from a cloud-shadowed area. Naturally, optical sensors such as IKONOS cannot see through clouds.

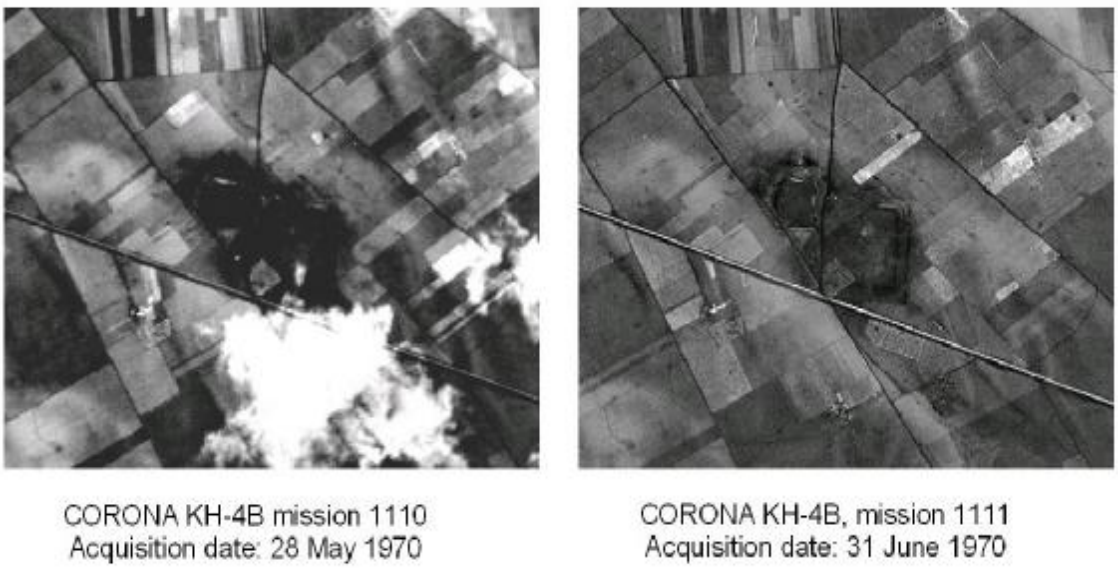

CORONA KH-4B mission 1110
Acquisition date: 28 May 1970

CORONA KH-4B, mission 1111
Acquisition date: 31 June 1970

Figure 5-9 – The clouds or their shadows can sometimes hide an archaeological site from the photointerpreter's eyes.

Figure 5-10 – The clouds throw their shadow on the ground. Naturally, IKONOS cannot see through the clouds. But, the photointerpreter can still depict details of the ground that is in shadow. No enhancement is applied on the image.

5.3.3. Importance of the preprocessing

In chapter 4, the preprocessing stage was discussed. As described in chapter 4, the preprocessing stage removes systematic errors from the data and prepares them for further processing. The film scanning (thus bringing it into digital format), the geometric and radiometric correction, the need for a basemap for integration of data into G.I.S. are all discussed in chapter 4. When it comes to photointerpretation, the preprocessing is a stage that can influence the photointerpretation. The photointerpreter must be confident about the preprocessing stage, which must be as controlled as possible for more objectivity and less doubt. Also, the photointerpreter should have access to reference data including G.I.S. data if available.

Figure 5-11 shows the results from two different film-scanning processes. The left image shows part of a film scanned by a drum scanner at an optical resolution of 1200 dpi. The right image shows the same part scanned by a photogrammetric scanner at an optical resolution of 3500 dpi. There is loss of interpretability from the 3500 dpi to the

1200 dpi. In the same example, the photogrammetric scanner has more radiometric fidelity and the scanning is fully controlled.

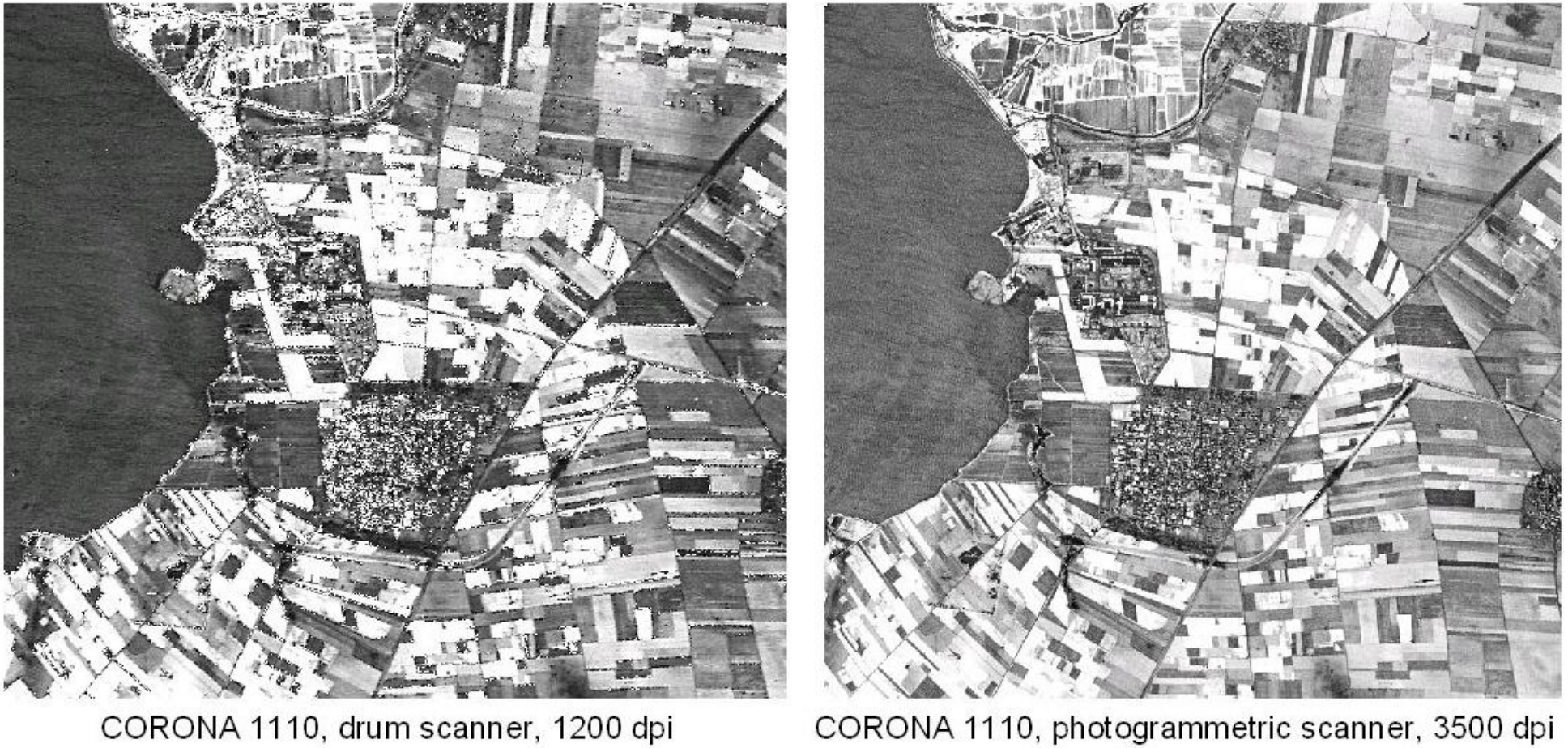

Figure 5-11 – Comparison between drum scanner and photogrammetric scanner.

5.3.4. Computer-aided photointerpretation

In this paragraph, some examples of enhancements are presented from the area of interest. The main purpose is to show the ways the computer helps the interpreter to detect features through highlighting/enhancing of the image.

Figure 5-12 shows a number of 'classic' radiometric enhancements. Their result is displayed on the left part of the figure and the respective histogram is on the right. The line in the histogram represents the function applied to the input histogram (grey) to produce the output histogram (yellow). The general function is output=function(input). For example, the raw image function is output=input (y=x).

The enhancements presented are all customisable and the interpreter can provide different parameters for each enhancement. Furthermore, the interpreter can create a customised enhancement. The experienced interpreter knows which parts of the image to highlight, and so applies the most appropriate enhancement. It is also possible to select the part of the image on which to apply the enhancements.

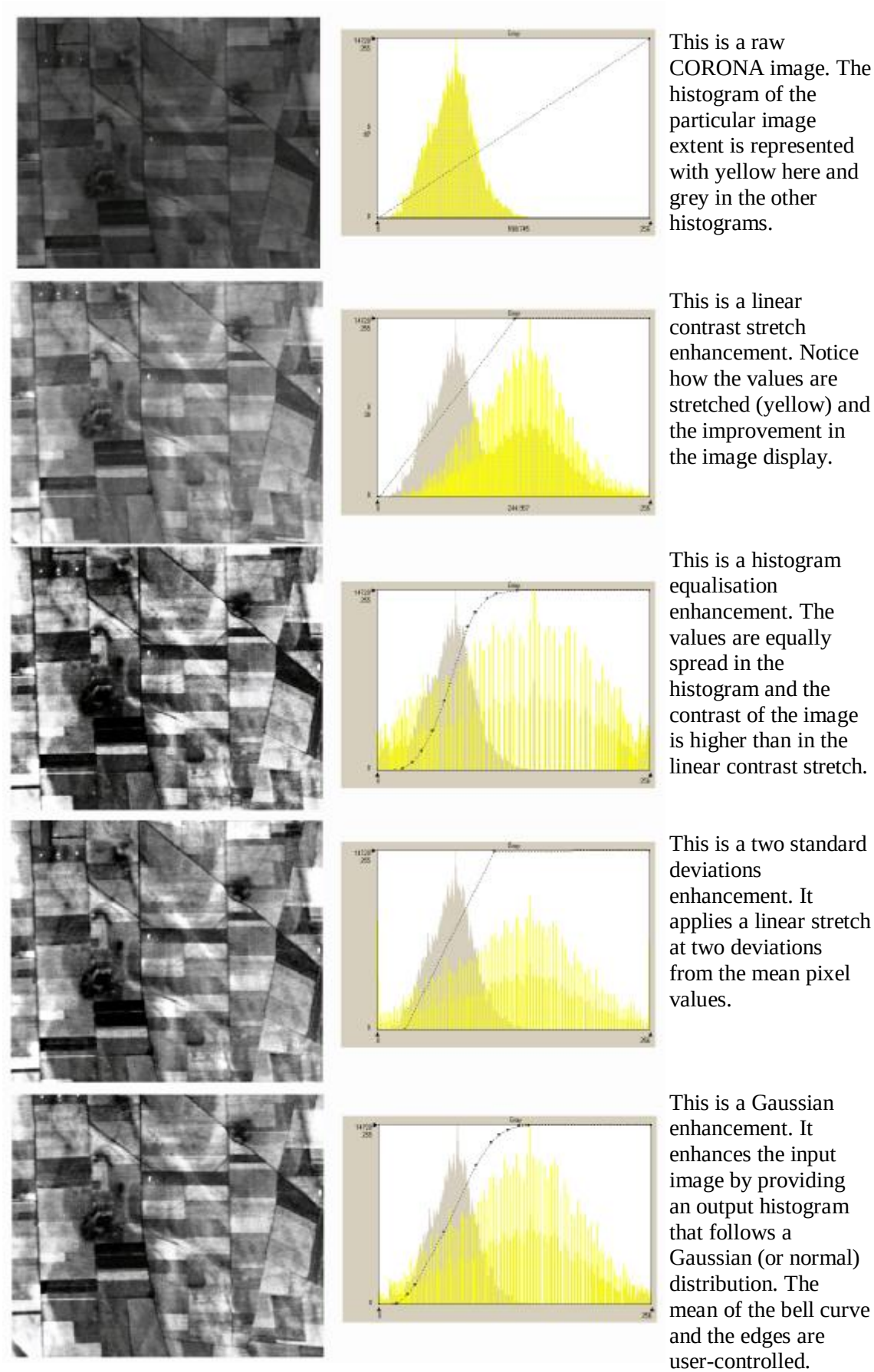

This is a raw CORONA image. The histogram of the particular image extent is represented with yellow here and grey in the other histograms.

This is a linear contrast stretch enhancement. Notice how the values are stretched (yellow) and the improvement in the image display.

This is a histogram equalisation enhancement. The values are equally spread in the histogram and the contrast of the image is higher than in the linear contrast stretch.

This is a two standard deviations enhancement. It applies a linear stretch at two deviations from the mean pixel values.

This is a Gaussian enhancement. It enhances the input image by providing an output histogram that follows a Gaussian (or normal) distribution. The mean of the bell curve and the edges are user-controlled.

Figure 5-12 – Radiometric enhancements of part of a CORONA image

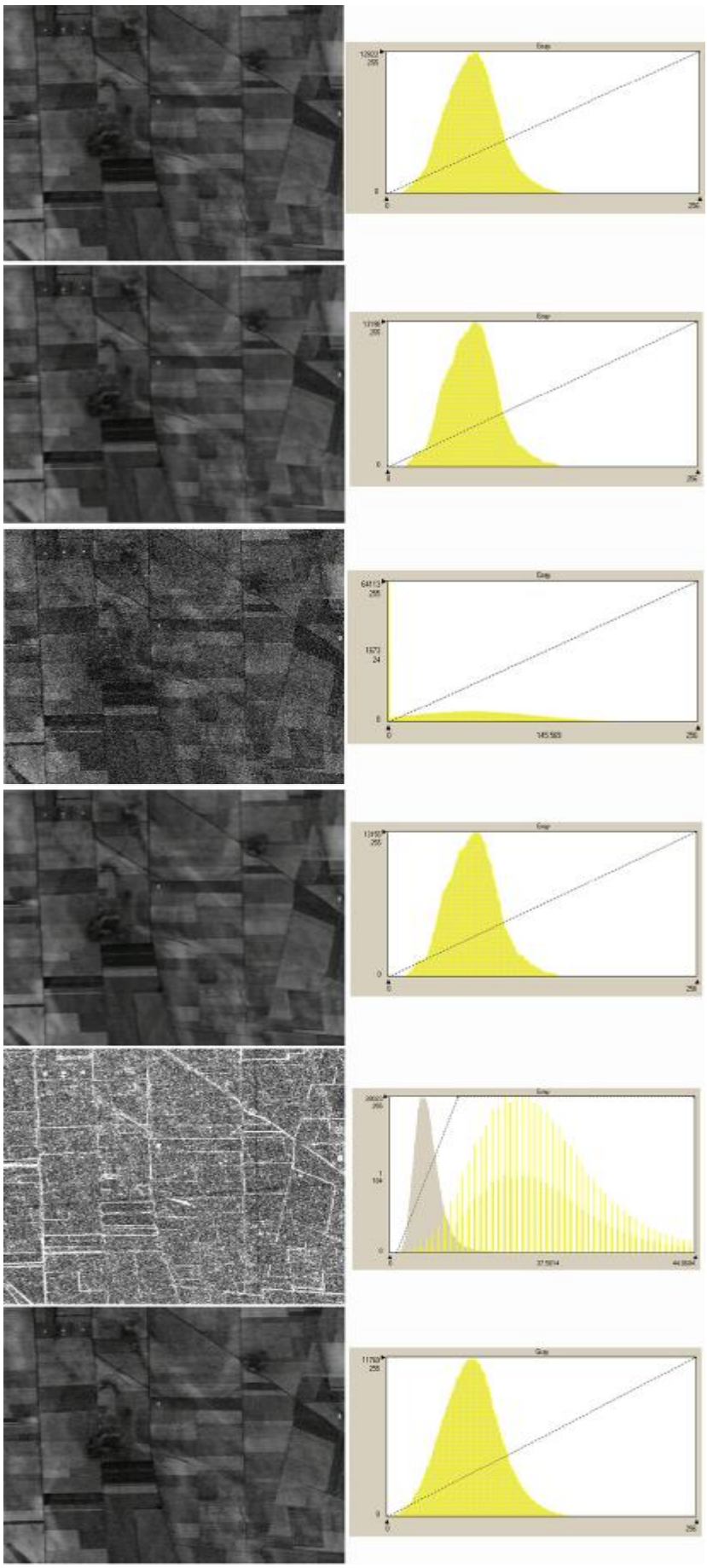

This is the raw image chip and its histogram.

This is the image after the application of a 3x3 low pass filter. The filter smoothed the image, with very little change in the histogram.

This is the image after the application of a 3x3 high pass filter. The filter sharpened the image. Notice the substantial change in the histogram.

This is the image after the application of a median 3x3 filter. There is small difference from the histogram of the low pass filter, but the image looks much clearer.

This is the image after the application of a standard deviation 3x3 filter. The image was then stretched for better display here. In the histogram, the pre-stretch values are in grey colour, while the stretched values in yellow.

This is the image after the application of an adaptive 3x3 filter. Notice the nice bell-curved histogram.

Figure 5-13 – Spatial enhancements of part of a CORONA image

Figure 5-13 shows examples of different spatial enhancements applied to a small part of the CORONA image, along with the resulting histograms. The first image displays the raw image chip, without any stretch applied to it.

The kernel of the low-pass filter is a 3x3 matrix whose values are all equal to one. This filter returns the average brightness value of the surrounding pixels, thus smoothing the image. The median filtering is again sampling through a 3x3 matrix, but instead of returning the average, it returns the median. The histograms of these two filters are similar, but the resulting image from the median filter shows better results than the resulting image from the low-pass filter.

The kernel of the high-pass filter is a 3x3 matrix whose values are equal to one, apart from the central value that is equal to nine. Contrary to the low pass, it doesn't smooth the image but it sharpens the image to enhance edges. And indeed, with careful notice one may see that the borders between different fields are highlighted after the application of the high-pass filter.

The adaptive filter varies the contrast stretch depending upon the values of the neighbouring pixels, in this case the immediate neighbouring pixels since the kernel is a 3x3 matrix. The resulting image has small differences from the median filter. The histogram has taken by coincidence a nice bell-curved shape, very near to a Gaussian distribution.

The image before the adaptive is created after the application of a 3x3 matrix that returns the standard deviation of the neighbouring pixels. The image was afterwards linearly stretched for better display. This particular filtering showed a surprise, which were two grids of different brightness and density appearing on the image. One grid is bright with small size of sides and can be seen here crossing diagonally the image. The other grid is dark with too large sides to be viewed at a whole here. However, the lines of the grid are still appearing straight, crossing the image from one edge to the other.

These grids will again be discussed in chapter 8, because they coincide with another artefact that emerged after the automatic extraction of the digital elevation model. Nevertheless, it should be noted here that an image hides more than the eye can see. For this reason, the enhancements are extremely useful. They are applied to help the human interpreter to see beyond the simple photograph. They help the interpreter to better comprehend the relationships between different features and artefacts within the area of interest.

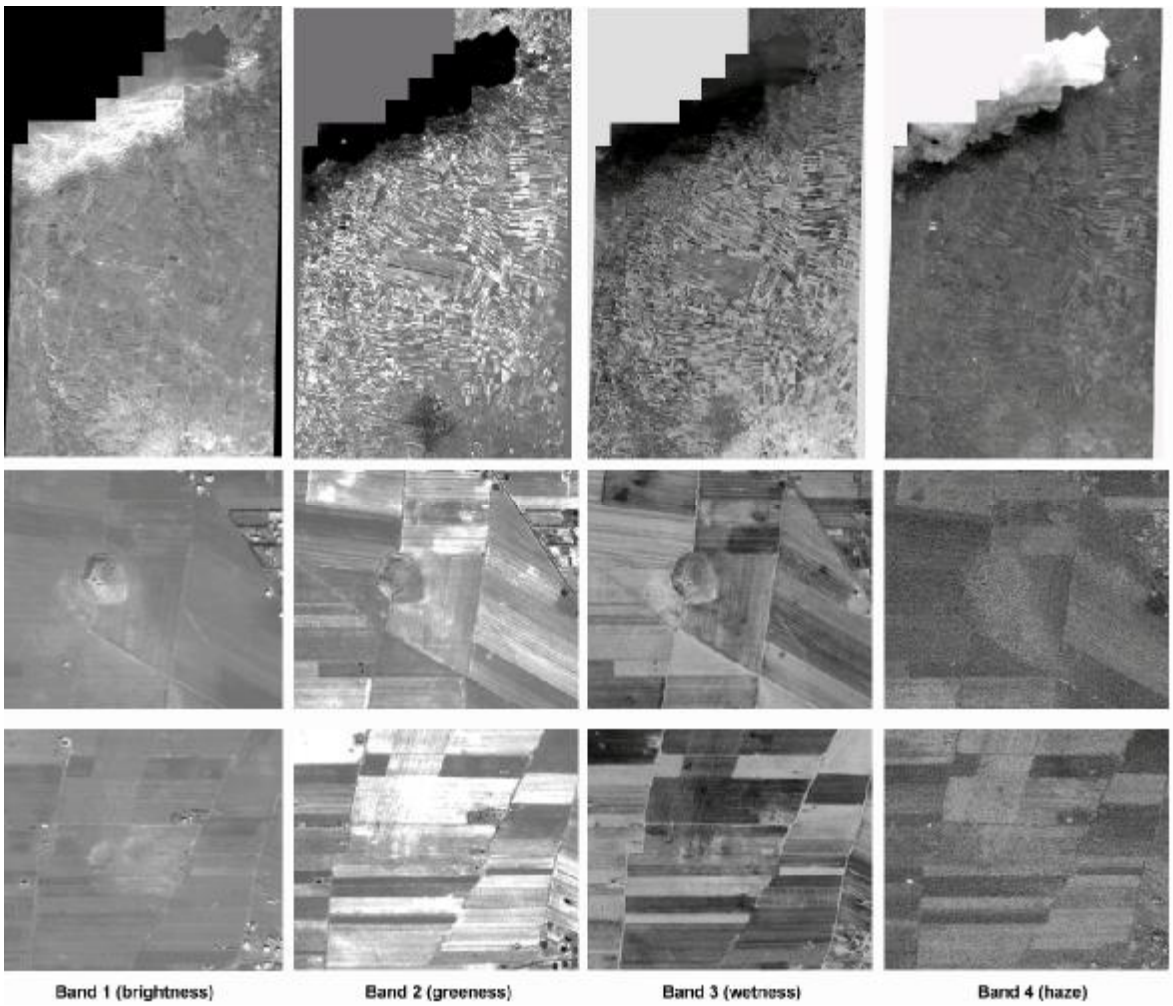

Figure 5-14 – Tasselled-cap transformation applied to IKONOS multispectral image.

Figure 5-14 illustrates the result of a tasselled-cap transformation for IKONOS imagery (Horne, 2003). Each band is displayed separately. The figure displays the whole southwest area (top row of images), a tell example (middle row of images) and a khirbet example (bottom row of images).

In the brightness band, the sites have higher pixel values than the surrounding area. In the greenness band the sites present pixel values that are similar to the surrounding area, while in haze band, they disappear. In the wetness band, the sites show differences from the surrounding environment, but not as obvious as in the brightness band.

The photointerpreter can apply more transformations, or enhancements, or combinations and proceed to comprehend the results of each applied task. By knowing what each transformation is doing and how it operates, it is easier to understand what the result shows. Hence, it is easier to detect and interpret features on the ground.

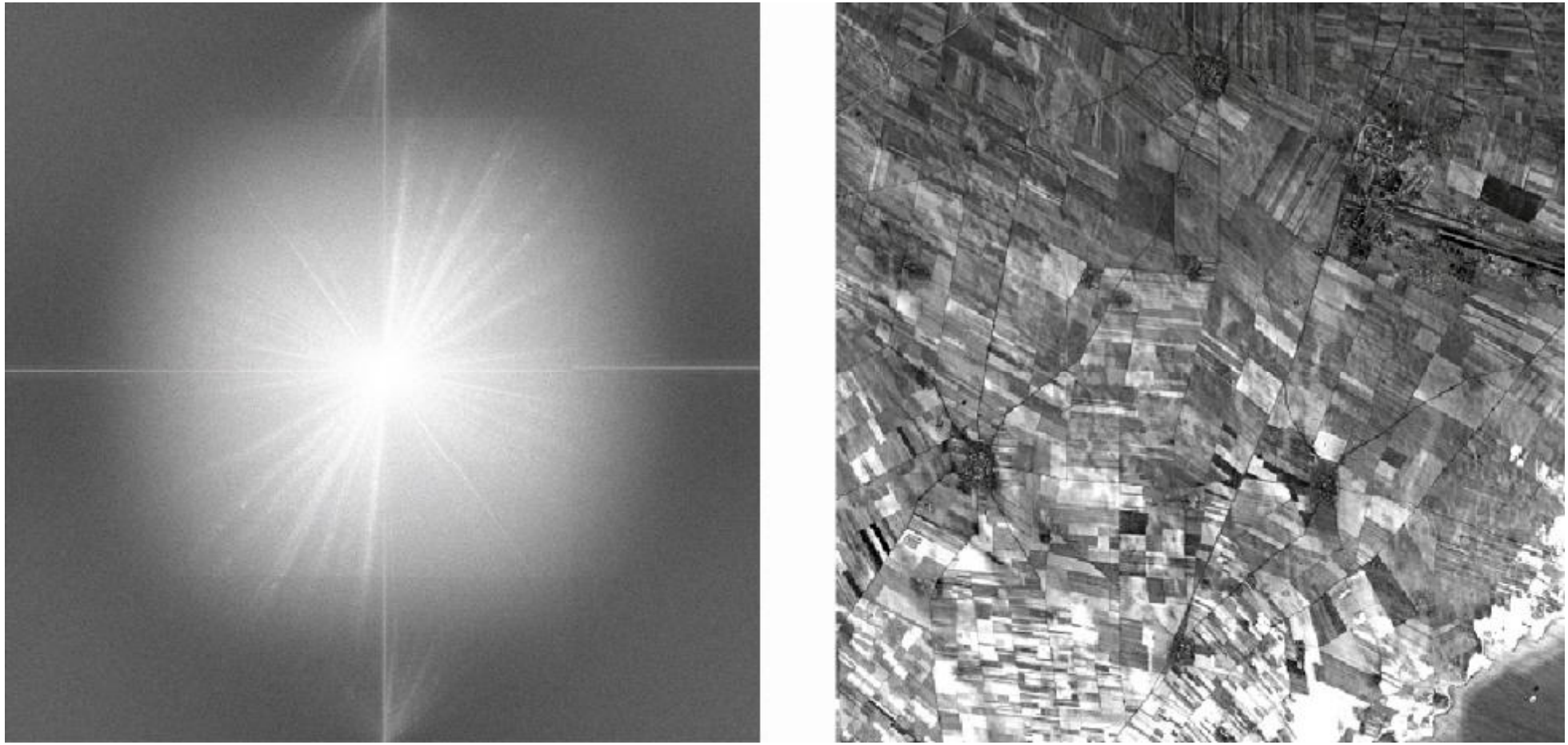

Figure 5-15 – Fourier transform of a part of CORONA image.

Figure 5-15 shows part of a CORONA image and its Fourier transform. It should be noted that to perform Fourier transform on an image, the rows and columns of the image must be equal to one of the powers of two (e.g. 128, 256, 512, 1024, 2048…). The Fourier image is a mosaic of images, because it was not possible to capture the whole image at once. The reader may notice the smaller images that form the mosaic. Generally, it is not easy to "read" a Fourier transform and only through experience can one distinguish the different features. However, suspicious lines can be detected and may indicate unwanted artefacts such as noise and these can be filtered out. Thus, it is possible to eliminate systematic image noise, for example the grid that was detected earlier during the spatial enhancement with the standard deviation kernel.

5.4. Conclusions

The photointerpretation approach has long been used for qualitative information extraction. With the advent of computers and the discovery of new light recording techniques, photointerpretation (instead of becoming obsolete) has evolved and became more important than ever.

It is an approach highly dependent on human physiology and psychology, and it is analysed into elements and levels. The computer as a tool increases the interpreter's perception and photointerpretation ability through image enhancements in the radiometric, spectral and spatial space, and in the spatial frequency domain.

The development of computers allows users to apply calculation-demanding processes with the use of affordable machines and within a reasonable time scale. The size of the images and the enhancement-produced files is no longer an issue for the photointerpreter. The navigation on the imagery is quick and easy, and the results can be easily exchanged with other users for a more interdisciplinary approach, or for a second opinion.

In archaeology, photointerpretation is mainly used for site detection and qualitative assessment of the landscape. Examples of simple archaeological photointerpretation were presented in the three main landscapes of the case study. Also, the importance of image quality, image characteristics and preprocessing were highlighted and presented. The value of the data is increased with adequate preprocessing and when the photointerpreter is aware of the data quality and characteristics.

In particular, in the Homs area, the satellite data come from different satellites (see comparison in chapter 3) and so they have different strengths and weaknesses. For an optimum elucidation of the structure and processes of the Middle East landscape, the user can combine the different strengths of all available satellite sensors. Thus, in Homs project, the spectral resolution of Landsat and ASTER is combined with the spatial resolution of CORONA and IKONOS. The main problem is the difficulty in co-registration and integration of all imagery with acceptable levels of accuracy.

However, after careful photointerpretation many sites of archaeological interest were detected. The basalt area presents a whole network of field-walls and cairns. The size and large number of the fields/cairns in the area demands careful approach with a highly detailed image. For this area, the best image seems to be IKONOS because of the spatial and radiometric resolution. The pan-sharpened image of IKONOS (thus adding its spectral resolution) can add spectral information to assist archaeologist to map this complex landscape.

The alluvium area contains reclaimed land due to human intervention (cultivations, irrigation, roads, houses), and thus it is difficult to detect sites of archaeological interest in this particular area. However, with combination of height information derived from the construction of digital elevation model (see chapter 8), it is possible to detect sites of interest because of their height differences from the surrounding environment. The use of heights does not need to be restricted to the alluvium area, but here is where it is needed most, because of lack of surface traces and shapes.

The easiest area for the detection of sites of archaeological interest was the marls area. For some reason (this is further discussed in chapter 6), many of the detected sites present a brighter hue than the surrounding environment. This is most important for the flat sites (khirbet), rather than the tells. The latter can be easily detected because they are upstanding on a generally flat landscape. However, prehistoric sites and some Roman/Islamic sites did not display any difference in brightness with the surrounding environment and thus they were not detectable from the satellite imagery.

6. Spectroradiometry

Spectroradiometry may be defined as the technique used to characterise spectrally any type of surface by the spectral distribution of radiant flux. The instrument that makes these measurements of radiant power is called spectroradiometer or spectrometer. In this chapter, the term 'spectroradiometer' will be used to define the instrument that makes the measurements of radiant power. The term 'spectroradiometry' will be used to define the technique. And the terms 'field spectroradiometry' and 'laboratory spectroradiometry' will be used to define the methods. To be certain of the reliability of the spectroradiometry results, the conditions of the measurements, the specifications of the spectroradiometer, and the techniques will be described with as much detail as possible.

In this chapter, spectroradiometry is used as a means to try to address the question of why most of the archaeological sites in the marl landscape south of Homs have a distinctive light soil colour that makes them identifiable on CORONA photography. Furthermore, the relationships between reflectance and key soil characteristics such as grain size and organic content are investigated. Last but not least, this is an effort to understand the effect that sensor characteristics (spectral and spatial resolution) might have on site detection-identification. Because of the different viewing angles of the CORONA and IKONOS sensors, it is possible to investigate whether the view angle impacts upon the reflectivity of archaeological sites.

6.1. Tools

There are four general attributes that describe a spectroradiometer. First is the sensor type and its spectral range. Second, is the spectral bandwidth, which describes the width of an individual spectral channel in the spectroradiometer. Both of the above two attributes describe the spectral resolution of the spectroradiometer, that is the number and widths of bands and their range. The two other attributes are the spectral sampling and the signal-to-noise (S/N) ratio.

Spectral sampling is the distance in wavelength between the spectral bandpass profiles for each channel in the spectrometer as a function of wavelength.[28] Bandpass is the narrow wavelength range through which the light passes to be recorded by the

[28] http://speclab.cr.usgs.gov/PAPERS.refl-mrs/ref4.html (page 6) (accessed April 2001)

specific sensor. The most common bandpass in spectrometers is the Gaussian profile. The width of the bandpass is defined as the width in wavelength at the 50% response, and it is called Full Width at Half Maximum (FWHM).

The S/N ratio expresses the ratio between the recorded surface's spectrum and the background noise. It mainly depends on the detector's sensitivity, the spectral bandwidth, and the light intensity from the surface being measured. S/N ratio improves with the square root of the sampling time.

Taking into consideration the above attributes of a spectroradiometer makes it easier to obtain a picture of the capabilities of the GER 1500 spectroradiometer[29] used in this research. The GER 1500 is a field portable spectroradiometer covering the UV (UltraViolet), Visible and NIR (Near InfraRed) wavelengths from 350 nm to 1050 nm. It uses a diffraction grating with a silicon diode array. The silicon array has 512 discrete detectors that provide the capability to read 512 spectral bands. The bandpass is 3 nm FWHM. The spectrum acquisition time is 6-150 milliseconds. The Field of View is 15°, and it is a cosine receptor[30]. Its environmental limits are -10° to 50°C.

6.2. Field spectroradiometry

Field spectroradiometry has three main applications in remote sensing (Milton, 1987):

a) Calibration. It forms a bridge between laboratory measurements of spectral reflectance and the real field spectral situation. Thus, airborne and satellite sensors may be calibrated. These measurements require high accuracy and precision. Gu *et al.* (1992) give a detailed analysis for the different causes of error in satellite calibration based on field spectroradiometry measurements. An example of satellite calibration may be seen in Slater *et al.* (1987).

b) Prediction. The field spectroradiometry measurements may be used to help identify the optimum spectral bands, viewing configuration and time to accomplish a remote sensing task. It helps to address questions such as: "What are the optimal spectral bands?", "What is the optimum geometric configuration of source and sensor?", "What is the optimum time of the year?". It needs moderate accuracy, but high precision and good collateral data. One good example of predictive modelling is the paper on

[29] Further information and calibration tools may be found in http://www.soton.ac.uk/~epfs/resources/1500_resource.shtml (Accessed December 2003).
[30] There are different kinds of detectors. In this case, the cosine detector samples radiant flux according to the cosine of the incident angle.

radiometric processing of aerial and satellite remote-sensing imagery by Franklin & Giles (1995).

c) Modelling. For the relation of biophysical attributes to remotely-sensed data, field spectroradiometry may help in the development, refinement and testing of the relevant models. One example of such an application is Shafique *et al.* (2002).

Before usage, the spectroradiometer should be calibrated (Schaepman, 1998; Schaepman & Dangel, 2000) or otherwise checked and tested for a quality assessment. The main tests include S/N test, wavelength accuracy and precision test, and radiometric accuracy test (Milton *et al.*, 1997). The experimental design of field spectroradiometry should take into consideration issues such as the timing of data collection, spatial scale of field measurement, target viewing, illumination geometry, and collection of reference data (i.e. positioning of samples and recording of environmental conditions)[31].

For field spectroradiometry data to have long-term value they must be collected with care and the conditions of observation must be documented in a consistent fashion. Before fieldwork, potential archaeological sites were chosen through simple photointerpretation of the existing CORONA imagery[32]. During the fieldwork, all measurements were timed. For every sample, its description was kept in a notebook, along with a description of the relevant environmental conditions. The target was mainly bare soil, with a smooth surface. Other targets were collected too, like grass, stones, or mixed surfaces. The angle of spectroradiometer-sample-sun and the sampling interval were kept as constant as possible.

In September 2000, the portable spectroradiometer GER1500 was used for the identification of the surface reflectance across a sample of sites in two directions, North→South or South→North, and West→East or East→West. The measurements were started and finished about 30 m beyond what was believed to be the boundary of the site. Soil colour and the density of surface pottery scatter were used to define the boundary of the site. The sampling interval was approximately 10m, running on an approximate straight line across the site. The target was the site's soil, but within the FOV (Field Of View) other features were observed such as stone, basalt, conglomerate, dry grass, and vegetation, wherever they appeared to be important in characterising the total spectral reflectance of the site. The time of the measurements was mainly at 9:30 a.m., although some were taken at later times. At two sites, measurements were taken at

[31] http://www.asdi.com/asdi_ap_en_apnts_f.html (accessed December 2003)

[32] In September 2000, photointerpretation was mainly based on imagery from mission 1110 forward camera, and partially from missions 1108 and 1111.

6:30 a.m. and 12:30 p.m. The time length of the measurements varies according to the transect length. Generally, every individual measurement (10 steps walking and sampling time) took around 10 seconds. The measurements were taken under sunny and dry environmental conditions of similar light intensity, and usually under windy conditions. The exact location of the measurements is unknown, because the project was not permitted to use GPS in Syria at that point. Therefore, sample transects can only be positioned relative to the positions of the sites as seen in the image data.

A reflectance measurement takes the scan of a Spectralon™ reference panel and ratios the target scan to that reference panel. In other words, the incident light is calibrated by measuring the intensity from a reference material of known scattering properties. Then, the reflectance is given by $r(sample) = \frac{I(sample)}{I(reference)} r(reference)$. The reference material must be very highly reflective and stable with time (Hapke, 1993). The reference target was a Spectralon™ panel 4''x4'' (10.16 cm x 10.16 cm).

A reference measurement should be taken before a series of target measurements, if a new set of scans begins, or if a change in the collection optics occurs, or if the instrument has been idle or turned off for an extended period, or if the lighting conditions change (clouds, etc.). In this way, there was an effort to minimise the error introduced by short-term variations in spectral irradiance, mainly caused by invisible patches of water vapour passing through the direct solar beam (Milton & Goetz, 1997).

The fieldwork was part of a larger archaeological mission. For logistical reasons there was limited freedom to select the sites where ideally one would sample as different people with different aims shared the car. While the other people were examining the sites, the author was taking spectroradiometry measurements.

During measurements, there was complete recording of the sample and the conditions around it (cloudy, windy, vegetation, soil texture, soil moisture, soil colour, temperature) based on personal observations rather than instrumental measurements. The route of the measurements was recorded on a sketch map with details to help the definition of the lines. Also, the break points (beginning of soil colour change, beginning of tell – bottom of tell-side, top of tell – top of tell-side, road, meeting of the transects) were noted onto the sketch for future reference to the results.

Eighteen sites were sampled in total. Seventeen of them are in the South area, where the sites were more obvious, and one in the North area. Two of the sites (site 97 and 197) had very low S/N ratios, thus they became unusable. Thus, sixteen sites remained,

all of them from the South area of interest. The distribution of field spectroradiometry sampling of archaeological sites is shown in Figure 6-1.

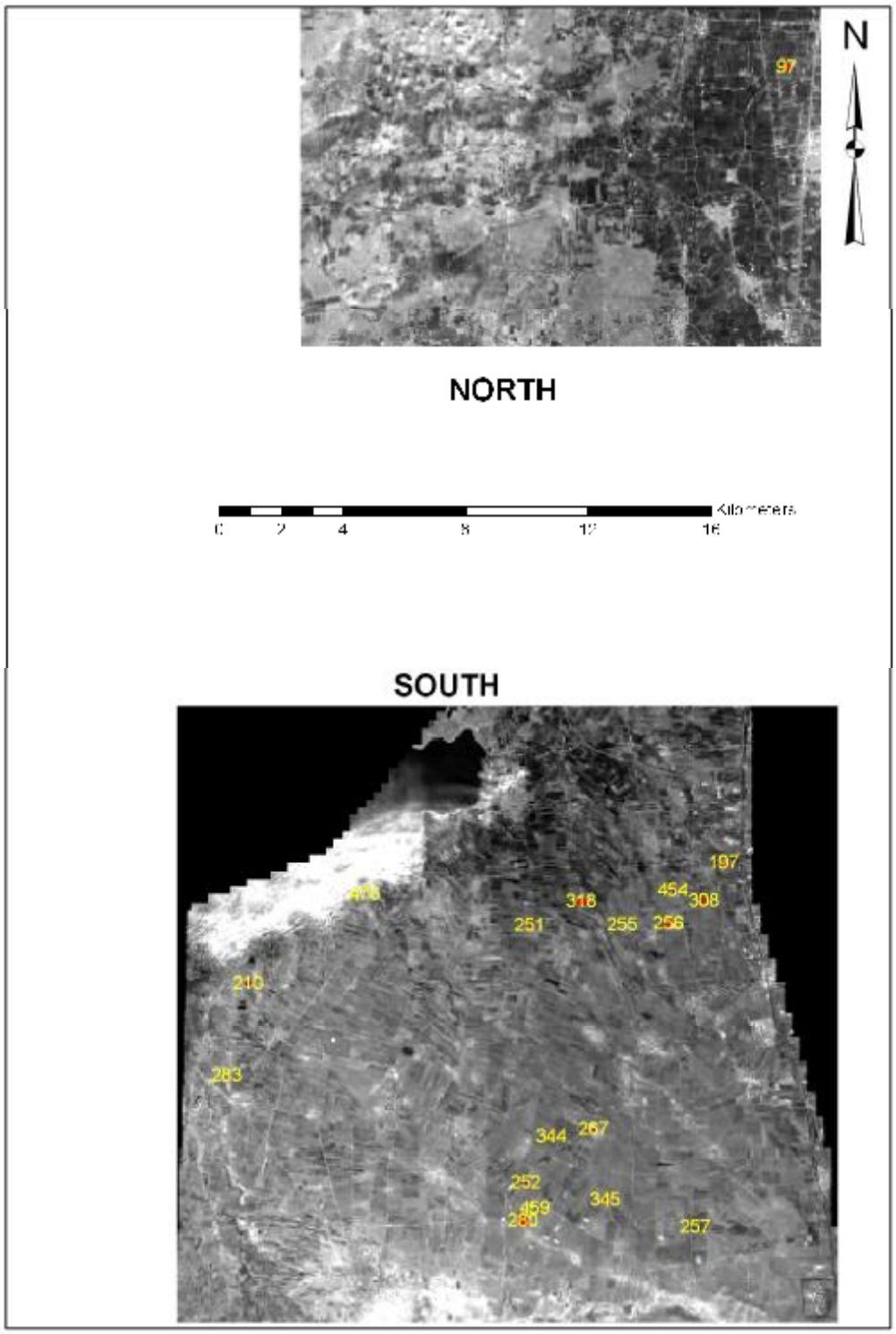

Figure 6-1 – Location of sites where spectroradiometry was recorded.

The figures 6-2 until 6-17 display the average reflectance in the visible part (400-700 nm) of the electromagnetic spectrum signal across the archaeological sites. The spectroradiometry values were convolved to image bandpasses according to the filters of the particular CORONA mission (see table 2-4). As shown in figures 6-26 and 6-27, there is not much difference between different missions. Hence, the display in figures 6-2 until 6-17 is showing the convolved mission 1110. As for the IKONOS imagery the spectroradiometry values were convolved to image bandpasses according to the numbers of relative spectral response provided by Spaceimaging web page (2004).

The left part of the figures 6-2 until 6-27 displays an IKONOS panchromatic image chip of the relevant site. The graphs represent on the Y-axis the relative reflectance in the visible part of the electromagnetic spectrum; and on the X-axis is the distance along which the samples were taken. Error-bars are added in the graphs indicating the standard error *e*, which was taken from the equation:

$$e = \sqrt{\frac{\sum_{i=1}^{n} x_i^2}{n(n-1)}}$$

where x is the measurement of the spectroradiometer and n is the number of measurements.

The directions are displayed with the initials NS (North→South), WE (West→East), SN (South→North), NESW (Northeast→Southwest), SWNE (Southwest→Northeast), NWSE (Northwest→Southeast), EW (East→West). They are illustrated with lines crossing the sites. The lines are recreated from field sketches drawn at the time of the measurement. In these figures, with the exception of archaeological site 283, one may notice that the signal increases by 5-10 % while inside the archaeological site, compared to the edges of the sampling line. The line of increase is not smooth, and after careful study of the ground survey notes, it may be concluded that the measurement points of "discontinuity" of the line are affected by conditions such as shadow (especially on slopes), wind (thin dust in the air), and differences in the smoothness (different particles size) or quality (organic material in the sampling area) of the sample, all factors that may influence the reflectance of the surface.

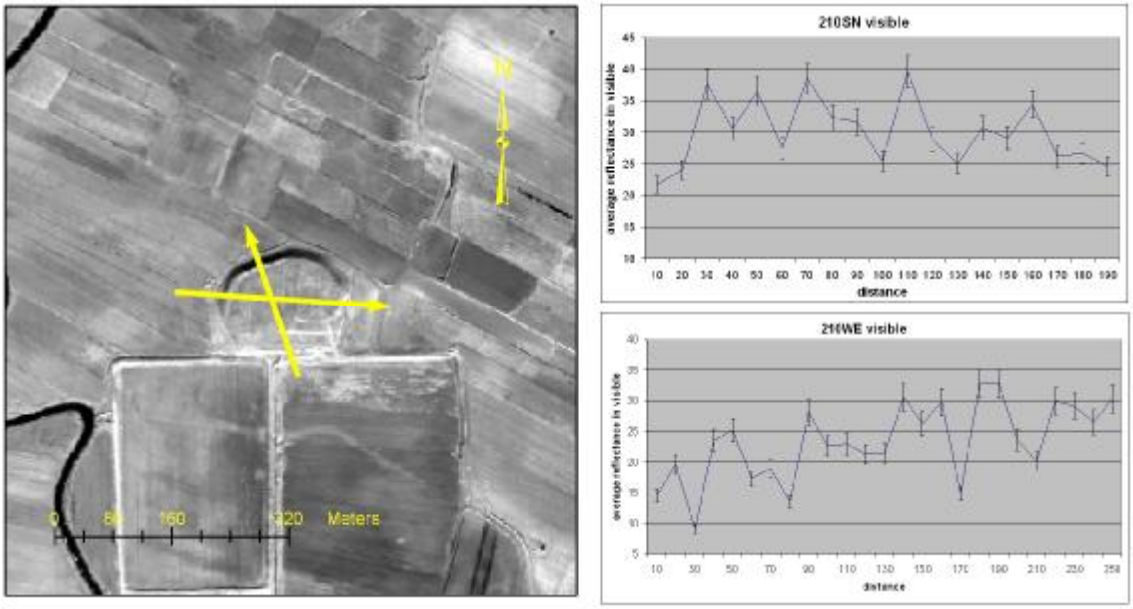

Figure 6-2 – Site 210 (Tell as-Sir).

Site 210 represents a large tell that was once within lake Qatina. The top is flat and the sides are very steep, looking artificially made. The south side is heavily bulldozed and the east side is cut steep. The north and west sides are mainly untouched and characterised by slope washed layers. The on-site soil is mainly silty clay loam, and the off-site soil is lacustrine deposit.

The soil spectroradiometry shows fluctuations, which can be related to the fact that the site is “disturbed”. The flat top could have been used for farming in the past. The top of the site has been bulldozed in places and thus deposits are redistributed. Generally, this site is visible because of its shape and height, rather than its brightness responses.

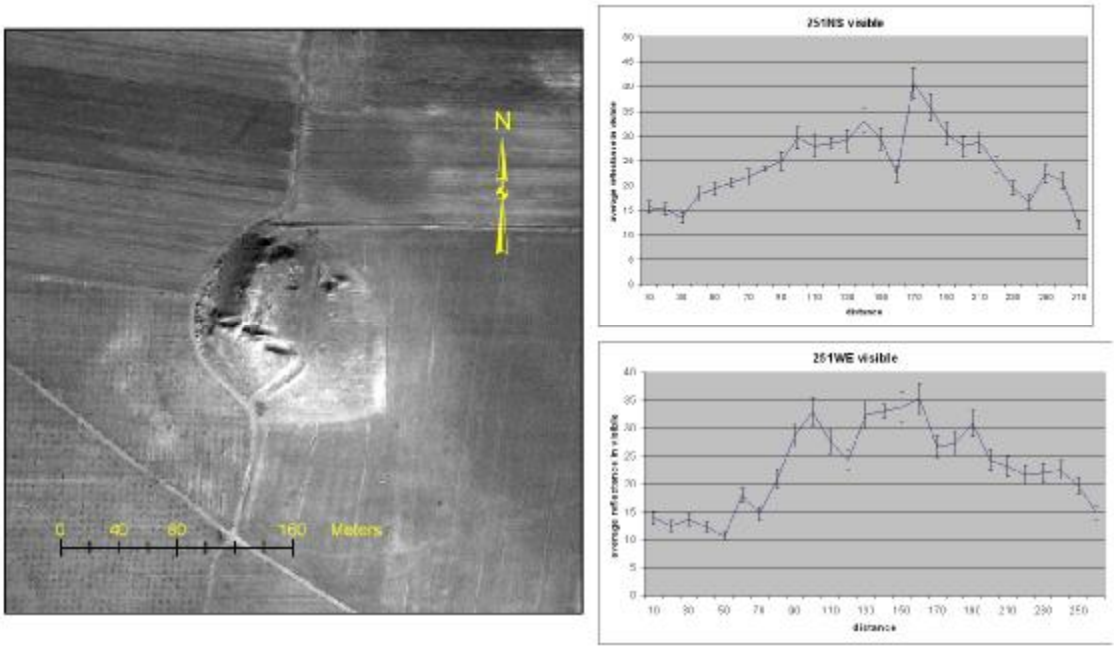

Figure 6-3 – Site 251 (Tell Hisan).

Site 251 is an ashy tell in flat landscape. Possible military trenching and one concrete building were found on top of the tell, along with evidence of modern truncation by bulldozing on the upper occupation plateau. A three-dimensional topographic total station survey took place in September 2000.

The spectroradiometry graphs show increased brightness levels while on-site. The measurements were taken during morning hours. The very low brightness at the north and the west slopes (compared to the east and south slopes) are related to shadow and low sun angles. Sudden fluctuations at the top of the tell are related to vegetation. Unfortunately, the field sketch was not good enough to permit accurate lines to be drawn.

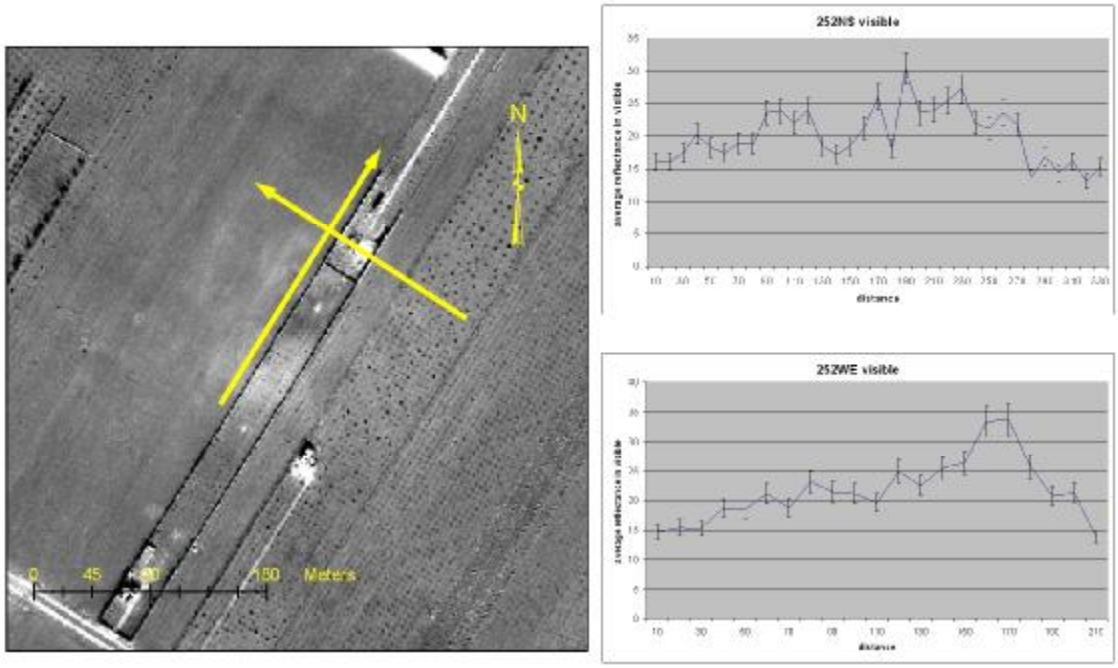

Figure 6-4 – Site 252 (Khirbet Sulayman)

The figure 6-4 shows a very low khirba site, which is bisected by a breezeblock wall running SW (olive grove)-NE (wheat). The site is characterised by an ashy deposit but shows very subtle colour changes from the natural soil.

Here is a site where GPS measurements would be helpful. The transect lines could not be possible to be strictly NS or WE because of the wall bisecting the site. According to the field notes, the "NS" measurements were actually along the left (in the image) wall from SW towards NE. And the "WE" measurements were across the end of the wall. The structure at the NE edge did not exist in September 2000 (the image is from February 2002).

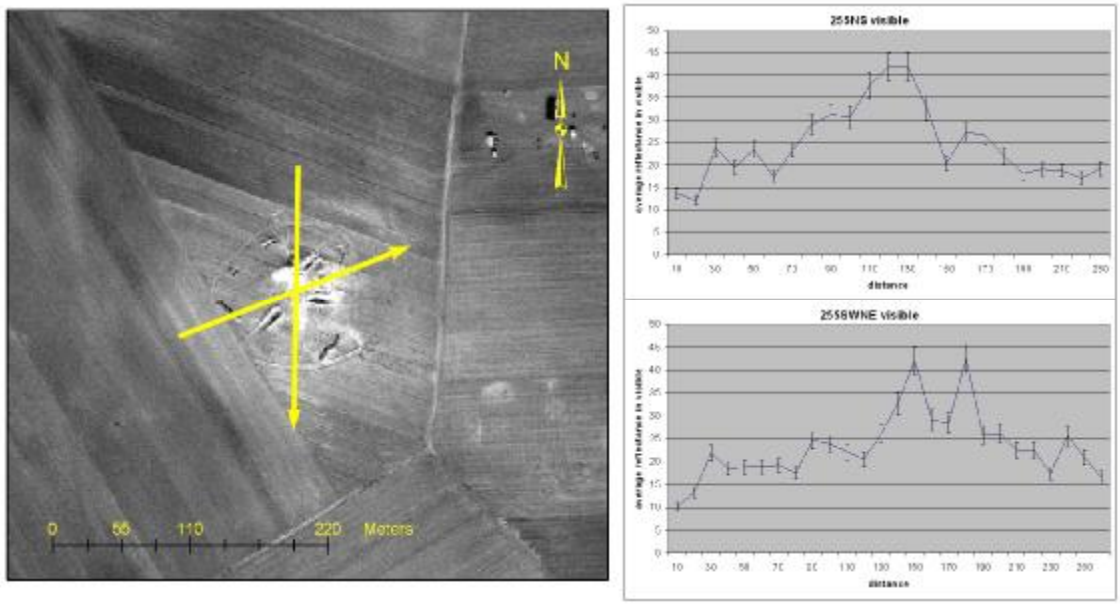

Figure 6-5 – Site 255 (Tell Aqarib)

Figure 6-5 shows a characteristic ashy low tell (higher at north than south) on limestone plateau, surrounded by agriculture fields. High military use appears on the tell. A three-dimensional topographic total station survey took place in September 2000, along with archaeological surface collection.

The difference of brightness between off-site and on-site measurements is very obvious on this site. At the top of the site (where the two transects meet), the higher values are observed. The SW edge shows lower brightness values than the rest of the site. It is also the side with the lower inclination.

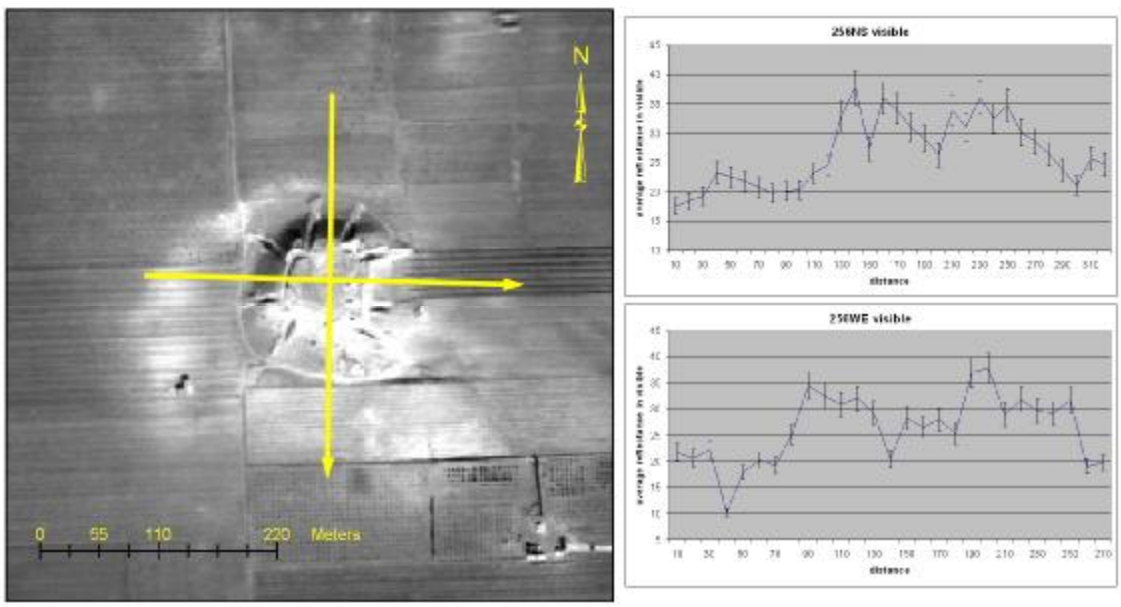

Figure 6-6 – Site 256 (Tell Ahmad)

Tell Ahmad is a high ashy oval tell that had been subjected to extensive truncation by bulldozer. Lighter areas of soil extend to south and west of the tell. The southern profile is shallower than other sides. Ploughing exists all around the tell. A three-dimensional topographic total station survey took place in September 2000.

The data were acquired during a misty morning, clouds coming and going, and a very low sun zenith angle (6:30 am). All these mean measurements displayed many fluctuations (the reference plate was used a lot during these measurements), and a very low profile for the west part and the north part (which were in shadow). But again, the difference between on-site and off-site measurements is apparent.

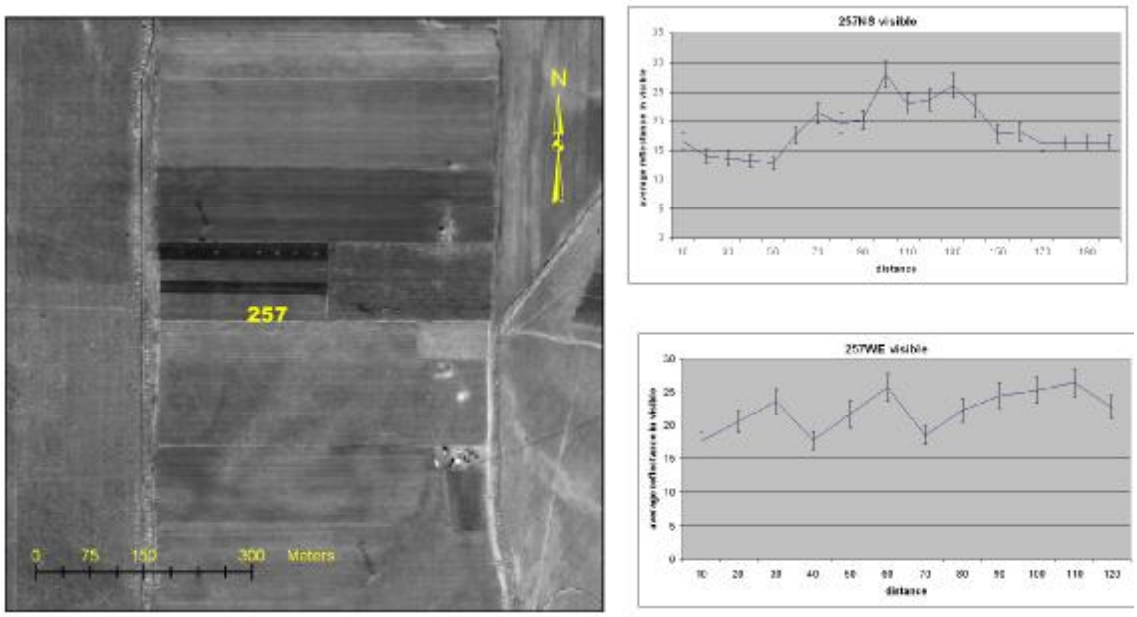

Figure 6-7 – Site 257 (‘Um Al-Qulud)

The site is in a flat limestone plateau, and it is truncated to the east by military training ground. The site is dotted with small depressions and it has characteristic ashy deposits with colour close to natural soil. A modern track bisects the site in a North South direction.

This is another site where GPS measurements or a better field sketch would be helpful. The site covers the area where the “257” is in figure 6-7 and around it. Although the site is not apparent in the IKONOS imagery, the on-site spectroradiometry measurements of NS brightness are higher than off-site. The road bisecting the site mainly affects the WE measurements, where a fluctuation occurs in two points.

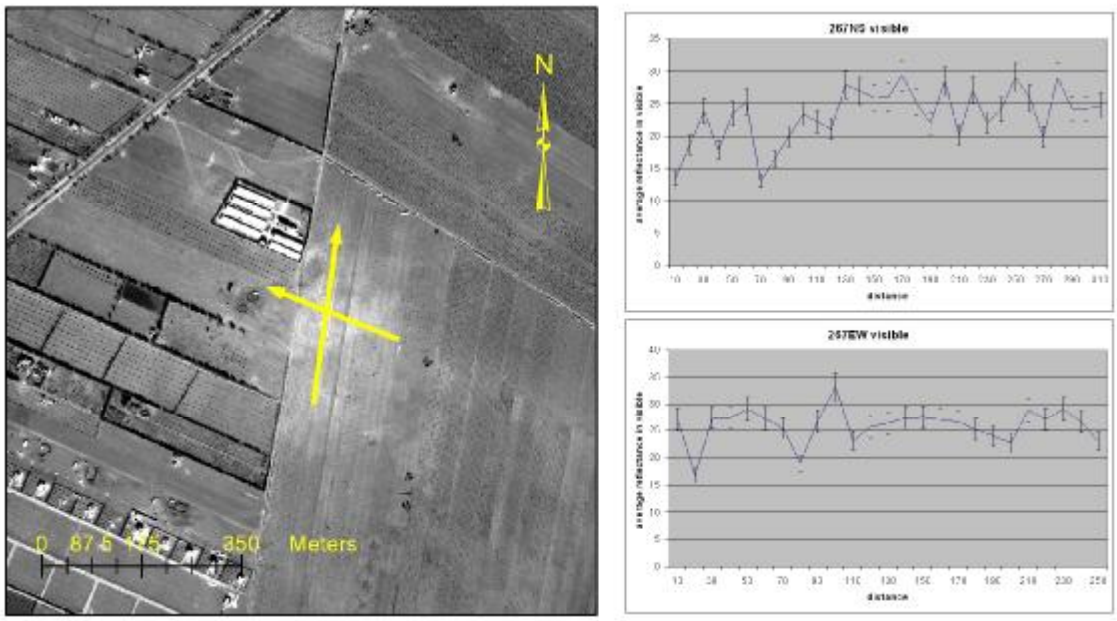

Figure 6-8 – Site 267 (Khirba Al-Bataineyeh)

This site is on limestone plateau in an olive grove. A road running north-south truncates the western part of the site. There are small depressions to south and north of the site at the east of the road part.

Many fluctuations can be observed to the measurements of this site without obvious difference between off-site and on-site measurements. The fluctuations are related to vegetation and soil disturbance (the site is inside an olive grove). The latter may be responsible for the non-apparent difference between off-site and on-site measurements.

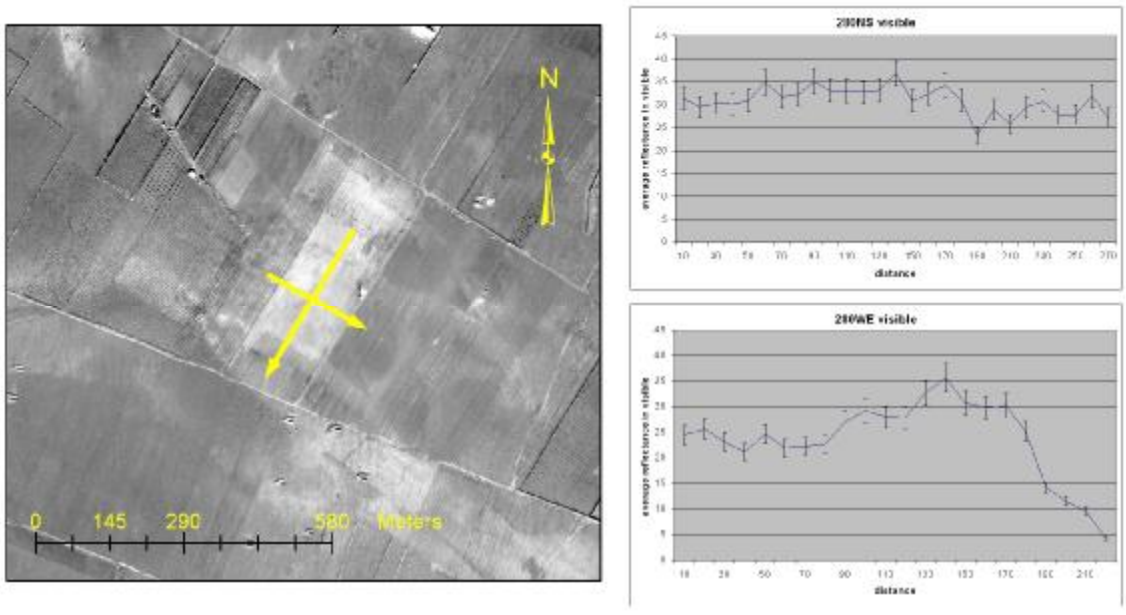

Figure 6-9 – Site 280 (Khirba Al-'Ali)

Figure 6-9 shows an ashy low site with a combination of wheat and olive grove. The on-site soil is sandy clay loam, and there is a depression at the Northeast part. There was an irregular scatter of archaeological evidence such as flints and ceramic artifacts. The borders of the site are not obvious.

The spectroradiometer measurements show fluctuations and the changes occur mainly when the farming field changes.

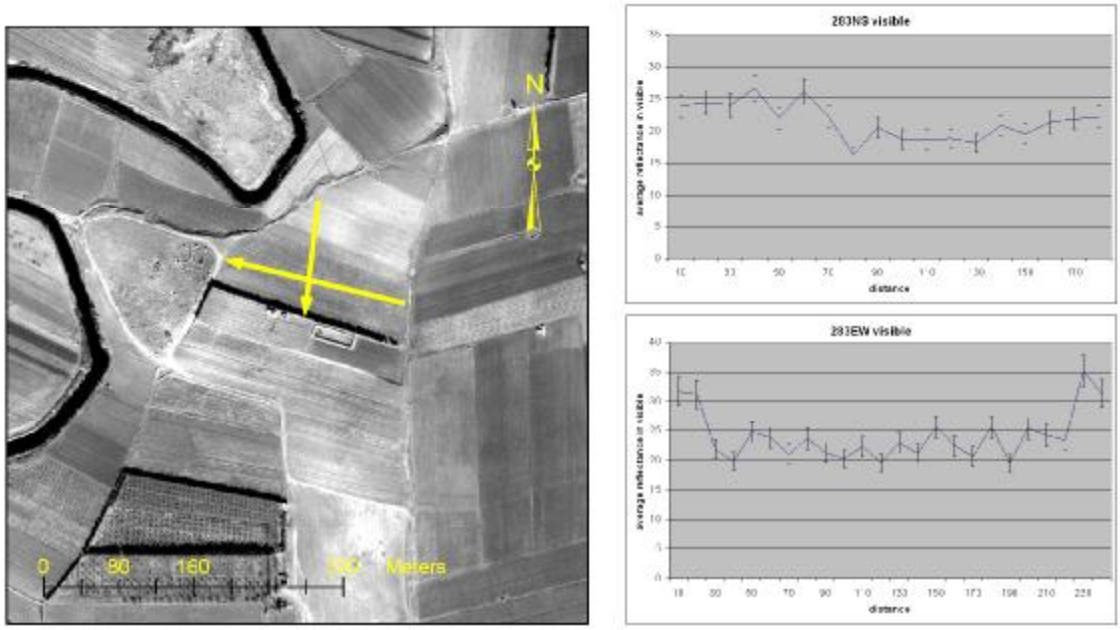

Figure 6-10 – Site 283 (Khirba Al-Zariqat)

This was thought to be discrete site during the September 2000 survey, but later evidence (July 2002) indicates that the site was probably part of site 286 and the subsequent tell has less intensive occupation on the same site. However, the on-site soil is silty clay and it has a more subtle colour change than the surrounding area.

This is the only site where the spectroradiometry measurements show a decrease in reflectance compared with the surrounding soils. The differences are observed at the changes between two farming fields (see NS difference), and at the edges of the site field. The site presents homogeneous brightness response with small fluctuations.

This site is hard to identify in the imagery, but was known because of earlier surveys. Note that it is a Neolithic site, which has been heavily deflated, so it is possible that the soil matrix distinctive of the other sites has been lost.

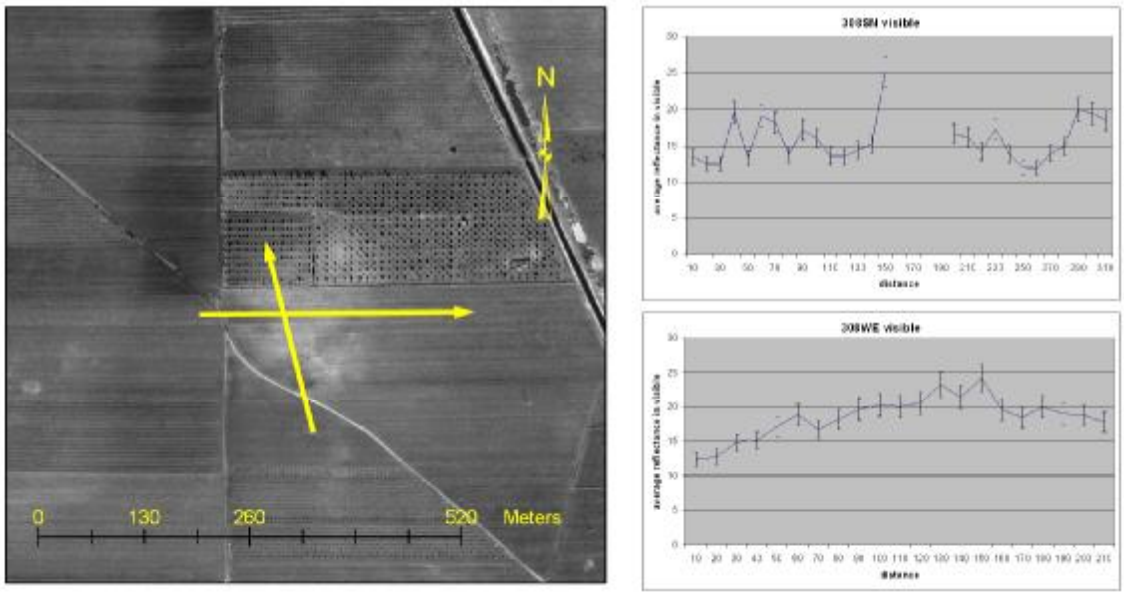

Figure 6-11 – Site 308 (Khirbet el-Matr)

This is a flat site in a predominantly flat landscape. There are olive groves to the north and south of the site, with the north grove entering inside the site. The site has three depressions and the soil is obviously lighter in colour and thinner than the surrounding soil. The modern road plan respects the site extents. A three-dimensional topographic total station survey took place in September 2000.

The conditions during spectroradiometry were constantly changing from sunny to cloudy and vice versa. This caused difficulty in the measurements. However, a slight difference between on-site and off-site measurements is still visible.

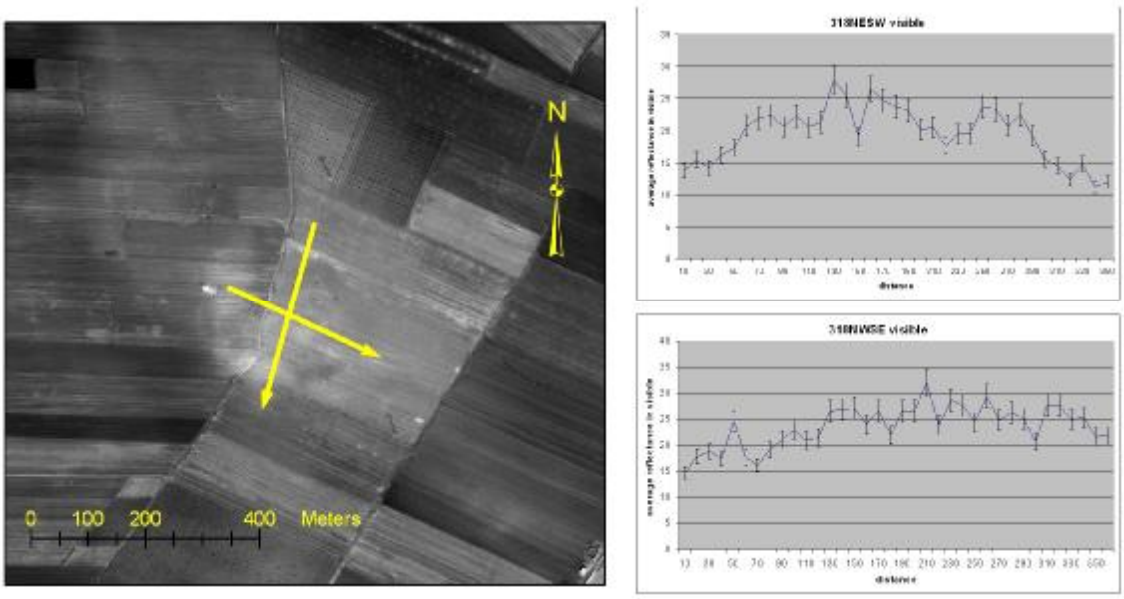

Figure 6-12 – Site 318 (Khirbat Siah)

This site has an ashy scatter, with an extent that is relatively easy to determine due to soil colour change. It is bisected by a road, and surrounded by dry arable land consisting of grove, wheat and fallow. There are depressions at the north, northeast and south of the site. The soil class is silty loam.

The spectroradiometer measurements show increase in the site reflectance (when compared to off-site) with slight fluctuations along the main curve. From the two transects, the NE-SW shows the difference better. Some fall off in the reflectance is noticed in NW-SE transect when crossing the road.

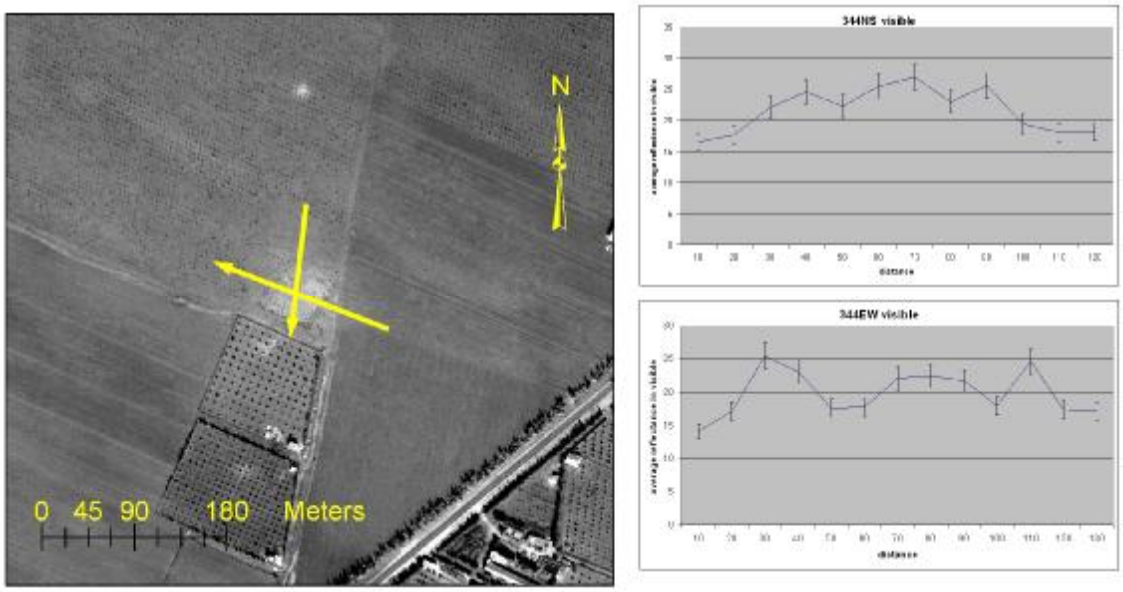

Figure 6-13 – Site 344 (unknown site)

This is a site of ambiguous archaeological interest. While it presents the same ashy soil as other sites, not much archaeological material was found on field walking. It is a small site and the modern road system respects its extent. It is in a slight depression and the soil class is sandy clay.

Both spectroradiometry transects show three increases along the site. The EW first increase is happening on the road, the middle at the middle of the site and the third just a bit outside the site. All the NS increases occur inside the site. The small size of the site reflects to the amount of spectroradiometry measurements taken.

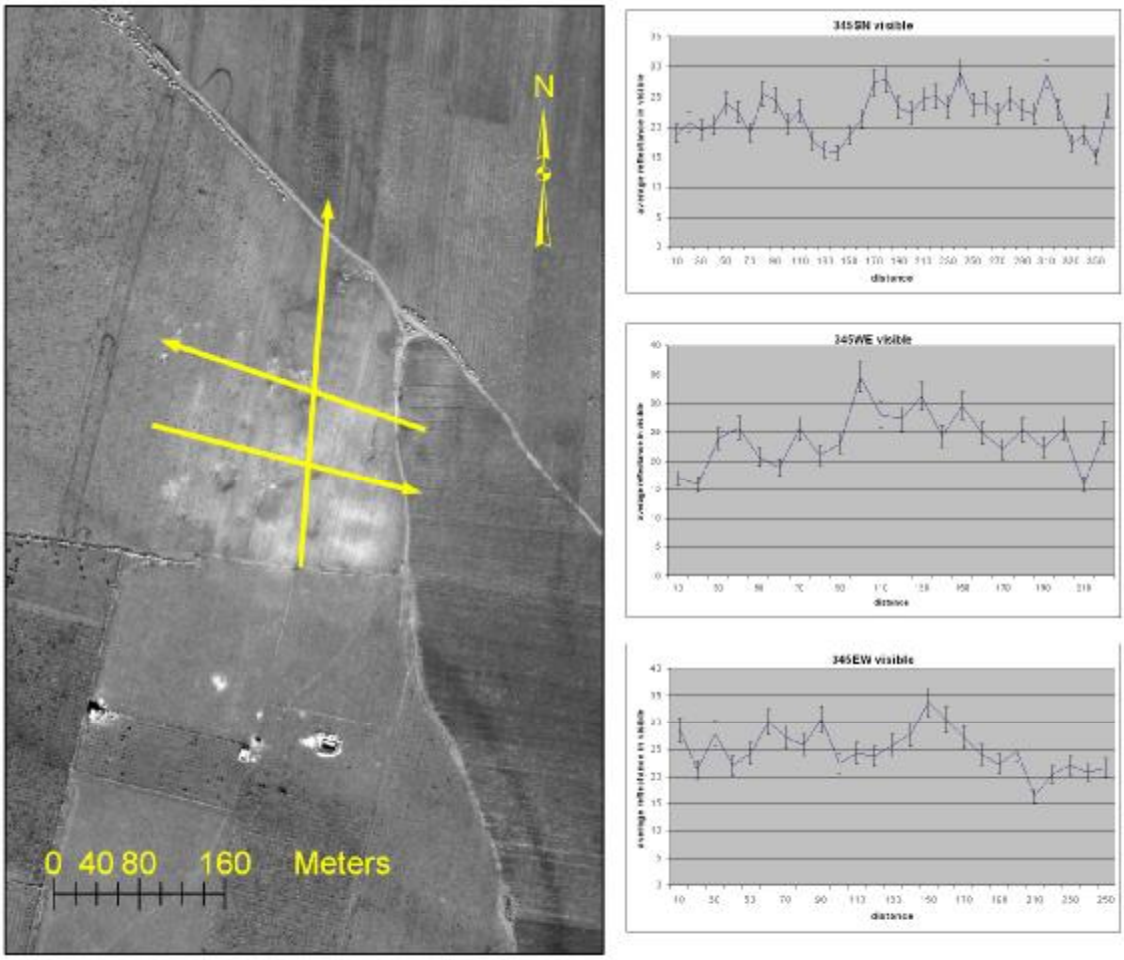

Figure 6-14 – Site 345 (unknown site)

Another site of ambiguous archaeological interest is displayed in figure 6-14. The site extends over a large area and this explains the three transects of spectroradiometry measurements. It is full of holes and depressions with lots of limestone fragments. However, the archaeological evidence was sparse.

The spectroradiometry measurements show fluctuations of such a magnitude that one cannot really tell about reflectance differences. The site presents an on-site/off-site reflectance pattern that is similar to the other sites.

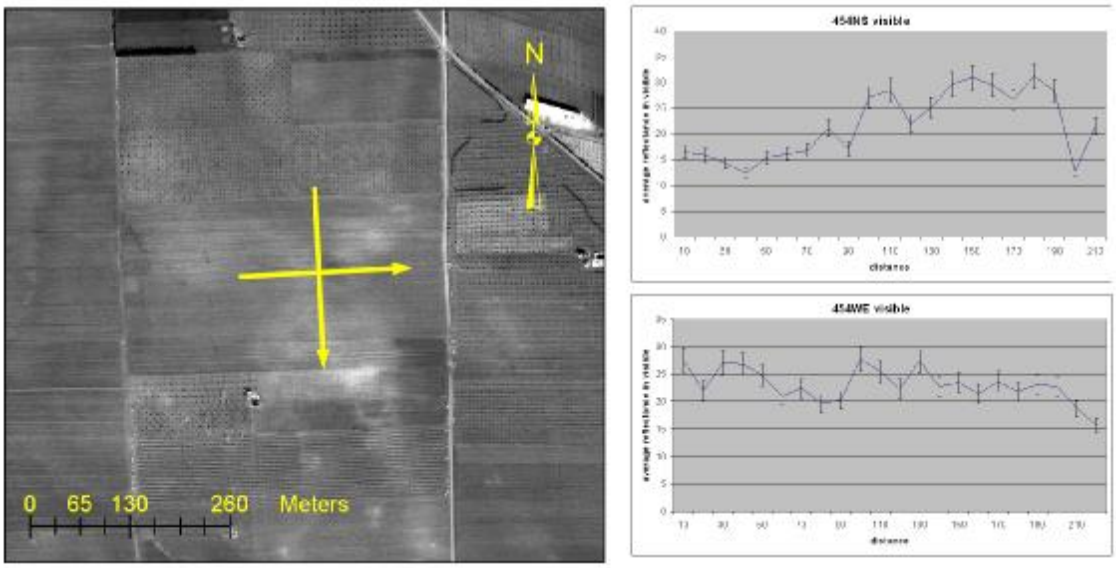

Figure 6-15 – Site 454 (unknown site)

This is a flat site with the characteristic ashy deposit present in all sites in the area, containing good archaeological evidence. A three-dimensional topographic total station survey took place in September 2000. During April, the site was covered with wheat.

The spectroradiometry measurements show higher reflectance at the centre-south and centre-west parts of the site rather than the east and the north. And indeed, the north part of the NS transect is outside the site while the south is at the centre. The same applies to the other transect. A good example in that higher reflectance is a characteristic of most sites in the Marl area.

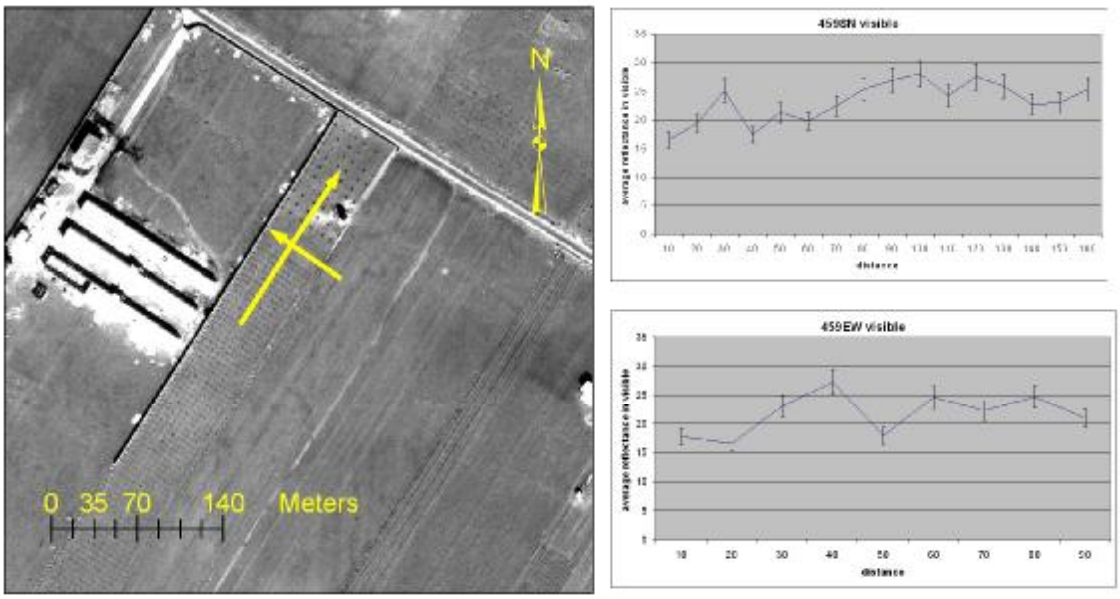

Figure 6-16 – Site 459 (Khirba al-Tab')

This site is a slight rise in a flat plateau with loamy sand on-site. It is difficult to distinguish today due to ploughing and building construction in the area. Limited artefacts were found on the surface. The spectroradiometry measurements do not show any particular results in this site.

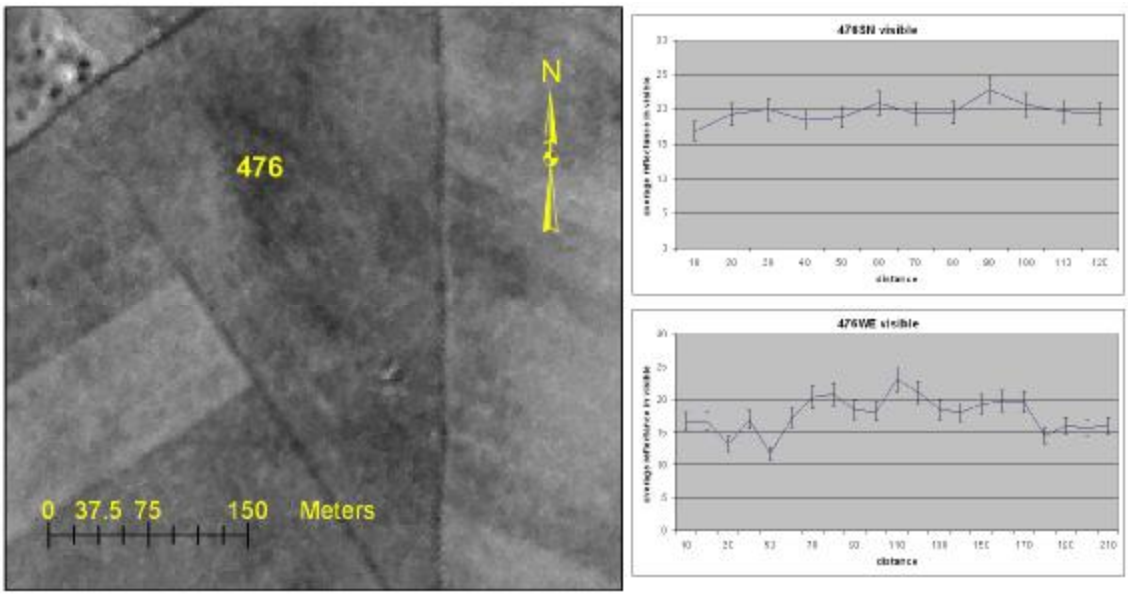

Figure 6-17 – Site 476 (unknown site)

This is a small rise in marl plateau with ambiguous archaeological interest. Other rises at the surrounding area offer evidence that this is part of an undulating landscape. The variation in soil colour is attributed to deep ploughing.

Once again, the field sketch is not helpful enough to identify the spectroradiometry transects across the site. However, the graphs show a small increase in brightness on-site when compared with off-site. Because clouds in this area covered the IKONOS image, the image displayed is from negative film of CORONA 1111 mission.

6.2.1. Summary

The sixteen sites described above can be distinguished in three broad categories: tell sites (sites 210, 251, 255, and 256), khirbet sites (sites 252, 267, 280, 283, 308, 318, and 459) and unknown (not previously recorded) sites (sites 257, 344, 345, 454, and 476).

All the tell sites, with the sole exception of the WE transect of site 210, present an increase in the on-site brightness, when compared with the off-site.

The khirbet sites do not present the same strength in the increase wherever this is met. The morphology of these sites allows for cultivation and development, and most of

the khirbet sites are today ploughed or built on. Hence, the soil is disturbed and the site is not as obvious in IKONOS imagery as in CORONA. And the brightness increase is not obvious in the field spectroradiometer measurements. However, less disturbed khirbet sites like 308 and 318 do present as features with an increase in the on-site brightness.

The unknown sites show mixed results. Among the unknown sites, the sites 257 and 454 are confirmed as archaeological from the artefact evidence. Site 344 is of ambiguous archaeological interest, because of the meagre amount of artefacts found. The sites 345 and 476 are considered to be traces of a quarry and a deeply ploughed field respectively. Field spectroradiometry showed a small increase in the on-site brightness in sites 257, 454 and 344. Across the sites 345 and 476, spectroradiometry measurements showed fluctuations in brightness.

The photo interpretation of the south area of interest detected possible archaeological sites, based on differences in soil colour. These sites were later visited and inspected for artefact evidence to define the character of the site. Simultaneously, field spectroradiometry measurements were taken to assess the difference in reflectance between the possible site and its surrounding environment.

Overall, there is a correlation between the field spectroradiometry measurements and the character of the sites. Within the site, different degrees of reflectance variability are seen. This can be assigned to the mixed character of a site. However, the ratio of on-site measurements towards the background soil is positive with a 10-15% brightness increase at most archaeological sites.

The field spectroradiometry showed the ‘spectral’ character of the sites with measurements of ground reflectivity. The main purpose was to identify the reason why most south area sites were identifiable in the CORONA imagery, and the field spectroradiometry gave a partial (if not complete) answer. Soil brightness is a characteristic of the tell and khirbet sites in the Marls area.

Even though ground texture is included in the measurements, environmental factors like illumination changes, wind, dust, organic material, or particle size can affect the measurements.

6.3. View-angle factor

Is the process of identifying possible archaeological sites from soil colour variations dependent on the view-angle of the imagery? To help answer this question the

brightness values of the CORONA aft and forward images from a single mission (also IKONOS overlapping images) will be compared. The brightness values taken from satellite observations with different view-angles are also compared with ground based spectroradiometry measurements, taking into account the topography of the site. For example, in the case of a tell, brightness values of the slopes, the top and the off-site ground will be sampled and subsequently compared.

Multiple-view-angle (MVA) remotely-sensed imagery offers a number of advantages including revisit frequency, stereoscopy, sun-glint avoidance over oceans, and the potential to infer information on Earth surface materials through an investigation of their angular reflectance properties (Barnsley, 1994). The information content of single-band MVA images (like the CORONA images of this project) and their potential for distinguishing land cover types that differ in terms of spatial or geometric structure are investigated in Barnsley *et al.* (1997). This ability to distinguish different land-cover types is a function of both directional reflectance properties and the absolute reflectance of the ground features. Thus, spectral effects are also important. This was demonstrated by Hyman & Barnsley (1997) for a simple agricultural scene, and by Abuelgasim *et al.* (1996) for a forest and wetland scene.

In this project, the MVA comparison focuses on archaeological features such as tells and khirbets. Its purpose is to define whether the ability to identify possible sites from their soil colour is view-angle dependent. The MVA comparison for the CORONA data is restricted to the imagery from mission 1110 for two reasons. First, the time difference between the two images is only 12 seconds (Madden, 1996). This allows the assumption than the atmospheric conditions changes between the two images are negligible. Second, the two images are taken from different points in space, along the same flight line, with almost the same sun elevation angle.

The same assumptions apply to the IKONOS imagery. The difference in time is a minute or less, thus the difference in atmospheric conditions or sun positions can be considered negligible. However, when comparing the different bands of the IKONOS multispectral imagery, the shorter wavelengths will be more affected by the atmospheric path. Also, the two IKONOS images that overlap are scanned in different mode (see paragraph 7.4), which means that in the 'Forward' scanning mode, the scan is in the opposite direction to the satellite trajectory and the sensor elevation angle is changing at roughly 1 °/sec. (Fraser & Yamakawa, 2004). This means that a mild degradation may be anticipated in the result of the MVA study.

There are two further factors that may affect the result. One factor is the topography of the area, which cannot be considered completely flat. Thus, there may be radiometric and geometric effects (Proy *et al.*, 1989) influencing the results of the MVA comparison. With the exception of buildings and tells, the area of interest is relatively flat. The other factor is data misregistration, since geometric correction can never be perfect. Hence, it is expected to find differences between the two images that derive from buildings or tells because of slope and shadow effects. It is also expected to find differences at linear or point features, because of the misregistration effect. The latter differences will be present in couples, because it is a two-way factor influence.

The approximate sun positions and CORONA mission 1110 satellite angles are displayed in figure 6-18 for the 28th May 1970. The satellite has an orbit inclination of 83°. The cameras scan at an angle of 71.15° (red display), and they are tilted at the centre of the film at an angle of 15.23° (not displayed here). The aperture is 5.625° (blue display). All these values are nominal.

The yellow squares show the part of film that includes the Homs area. The actual parts of the film that are used in the project are different in size, and not equal as is displayed here. This is best visualised by the angles shown in yellow colour that depict the horizontal angles between the centre of the film, the camera and the centre of the Homs area. The relevant calculations are described in chapter 7. The vertical angles between the nadir point, the camera and the centre of Homs area are also calculated (simple trigonometry) and displayed. All calculations are rounded up to the second decimal place and they are based on the known nominal values. Notice that the aft camera is actually looking forward and the forward camera is looking backwards relative to the direction of flight.

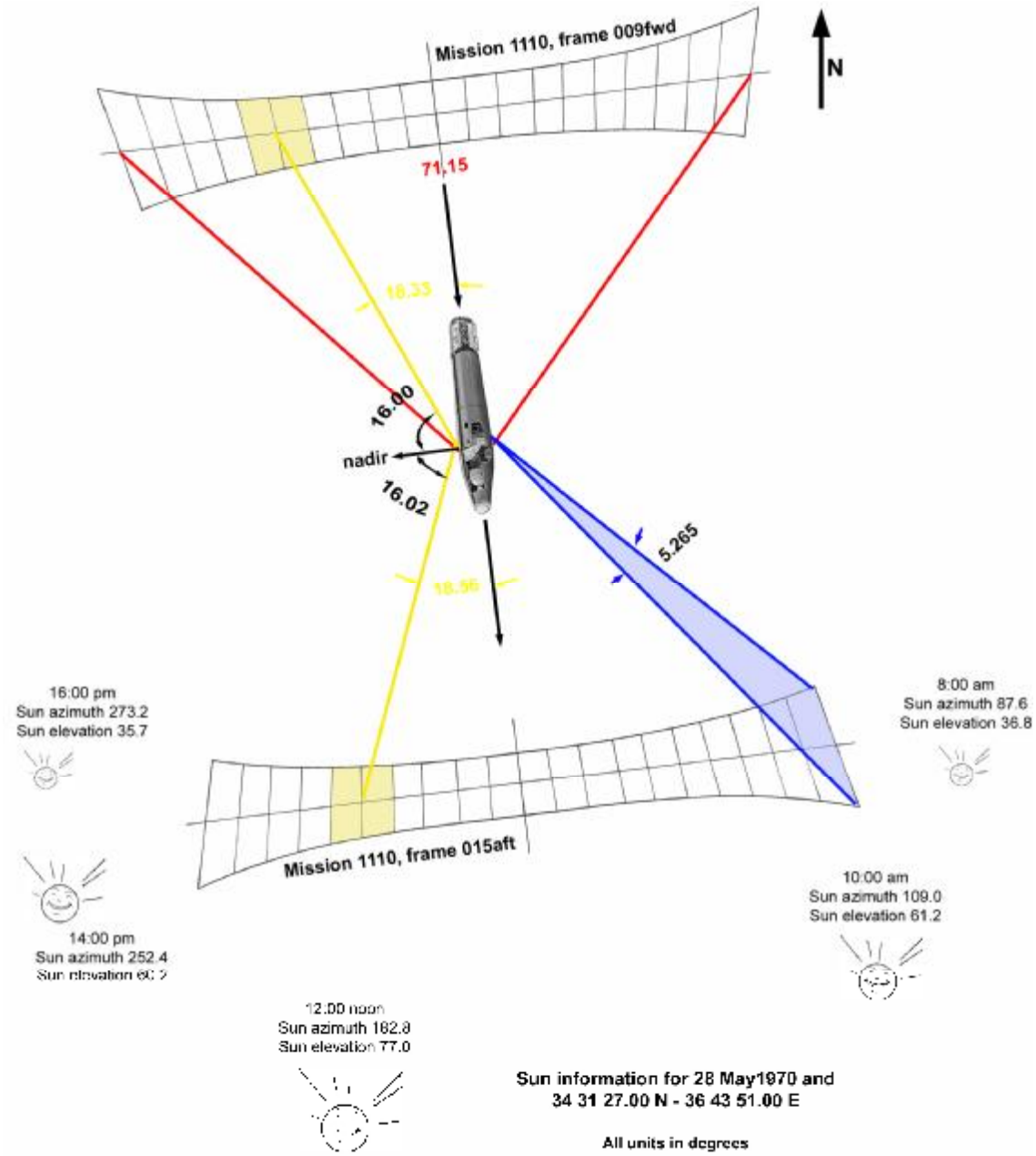

Figure 6-18 – View angle illustration of the sun and the CORONA 1110 mission.

The sun azimuth and sun elevation angles are nominal values taken from astronomical ephemeris, and they refer to different times of the day of image capture by CORONA. The sun azimuth is displayed with centre of axis being the centre of the Homs area. The sun elevation is illustrated with the size of the sun image. All units are in degrees.

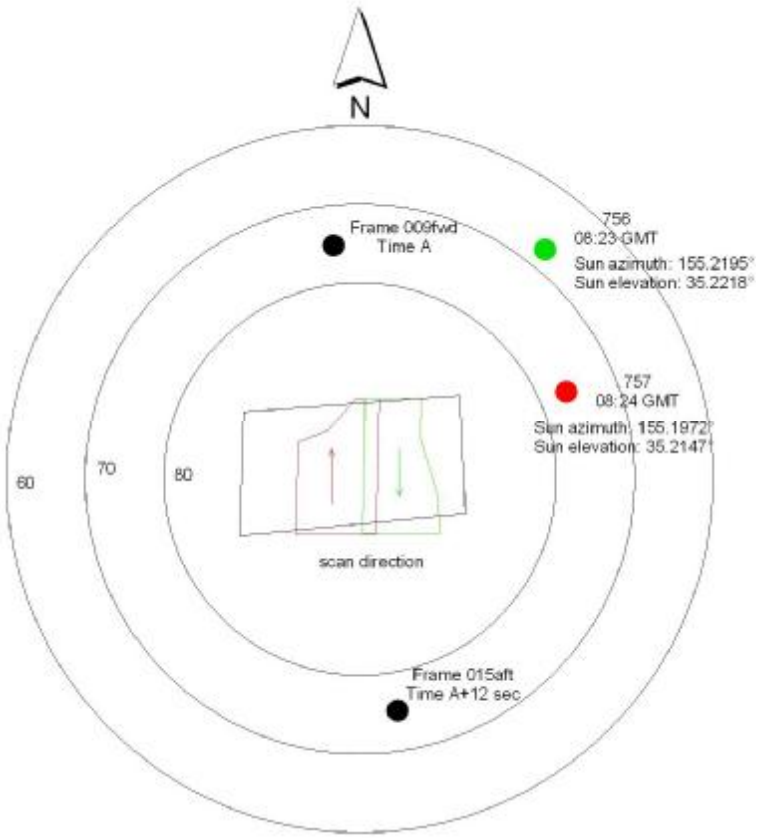

Figure 6-19 – The positions of CORONA and IKONOS in relation with the south area.

Figure 6-19 displays the sensor elevation angle in polar coordinates and the sensor azimuth in relation with the area of interest. The sun angle azimuth and elevation from IKONOS metadata could not be illustrated here. For this reason, they are just mentioned in the figure. The figure 6-19 also illustrates the footprint of the cameras, where the overlap of the two IKONOS images is visible. The CORONA images have an almost 100 % overlap.

Each CORONA mission was carrying a slightly different camera system probably because the engineers and data interpreters were constantly experimenting. As described in chapter 2, the CORONA cameras had different filters, films and lens system. These are displayed in table 2-4. In mission 1110, the two cameras have the same film but they vary in both lens system and optical filters.

The difference in lens system provides different resolving powers. As discussed in section 2.1.17, the third generation Petzval lens had better performance than the second generation Petzval lens. This gives two images of different spatial scale. The effect of the difference in filters is illustrated in figures 6-25 and 6-26 for two archaeological sites. When the different filters were applied to the spectroradiometry measurements, the averaged brightness values of the samples showed the same profile of the

spectroradiometry transects with only a small offset. This would suggest that the effect of the different camera filters is negligible.

One more thing that must be taken into account is the possible difference of scanning parameters among the imagery. Unless the scanning parameters (brightness, contrast, gamma, etc.) were kept constant for all CORONA images, the user should bring the imagery to the same levels of these parameters before checking for MVA effects. To do this, the brightness values of the two images must be radiometrically normalised.

The scatter plot of the two CORONA images is shown in figure 6-20. The X-axis represents the reflectance in CORONA 015 image and the Y-axis represents the reflectance in CORONA 009 image. According to Barnsley *et al.* (1997), this scatter plot represents the MVA feature space, and the position of every pixel within the MVA feature space is conditioned both by its spectral and bidirectional properties. The spectral component lies along a radial vector passing through the origin, while the directional component lies at a tangent to this (Barnsley *et al.*, 1997).

The scatter plot of the two CORONA images shows three main concentrations of points. The small "island" is the water element that is present in the imagery (lake, river, ponds). The larger concentration is the marls area that dominates the south area. The smaller concentration (low-left) is the basalt area that covers a small part at the northwest of the lake. From this scatter plot, it can be seen that the water element is view angle dependent, because of the different tangent of its spectral vector axis. The basalt area has similar bidirectional properties to the marls area, but it differs to the spectral properties. In the MVA feature space, the basalt area has smaller spectral vector than the marls area. The tangent of the two spectral vectors is almost the same.

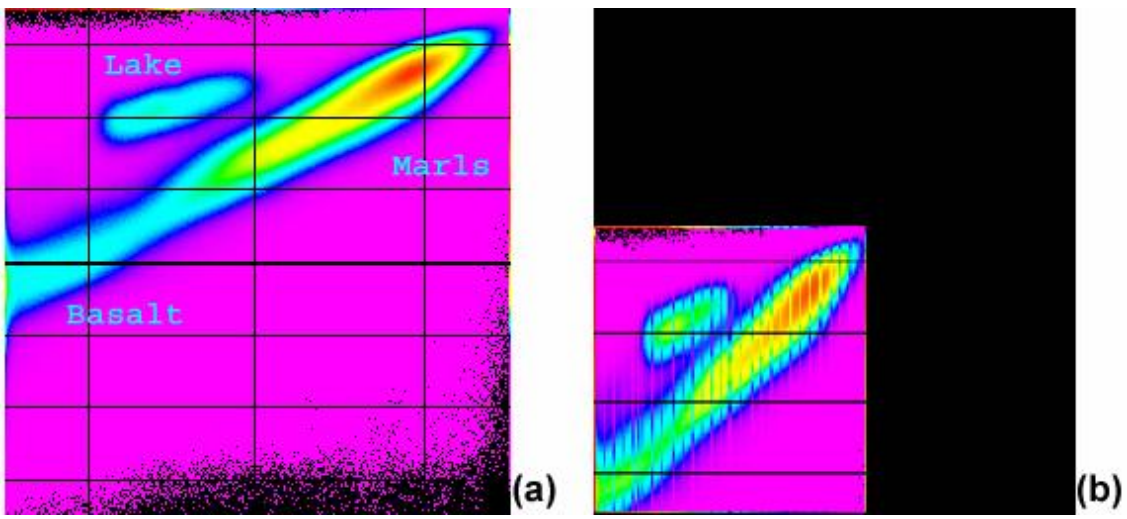

Figure 6-20 – Scatter plot before (a) and after (b) regression. The images are in the same scale.

For the radiometric normalisation of the marls area, a sample of pixels that represents about 10% of the marls area was used for the calculation of the regression line. The regression was then applied to one of the two CORONA images, and the resultant scatter plot is shown in figure 6-20(b).

The black grid of 6-20(a) and the black horizontal lines of 6-20(b) are artefacts of the image reversing from negative to positive. The vertical noise in 6-20(b) is possibly an artefact of the transformation through the regression line.

The figures 6-21 and 6-22 show the MVA feature spaces of panchromatic and multispectral IKONOS images respectively, at the point of overlap. The X-axis represents the reflectance in IKONOS 757 image and the Y-axis represents the reflectance in IKONOS 756 image. The images were registered with sub-pixel accuracy before the creation of the MVA feature space.

The correlation values for the CORONA and IKONOS images are presented in table 6-1. The Panchromatic band covers the spectral range of all the multispectral bands (see figure 3-1), but because of the smaller pixel size, image to image misregistration has more influence in the resulting scatter plot.

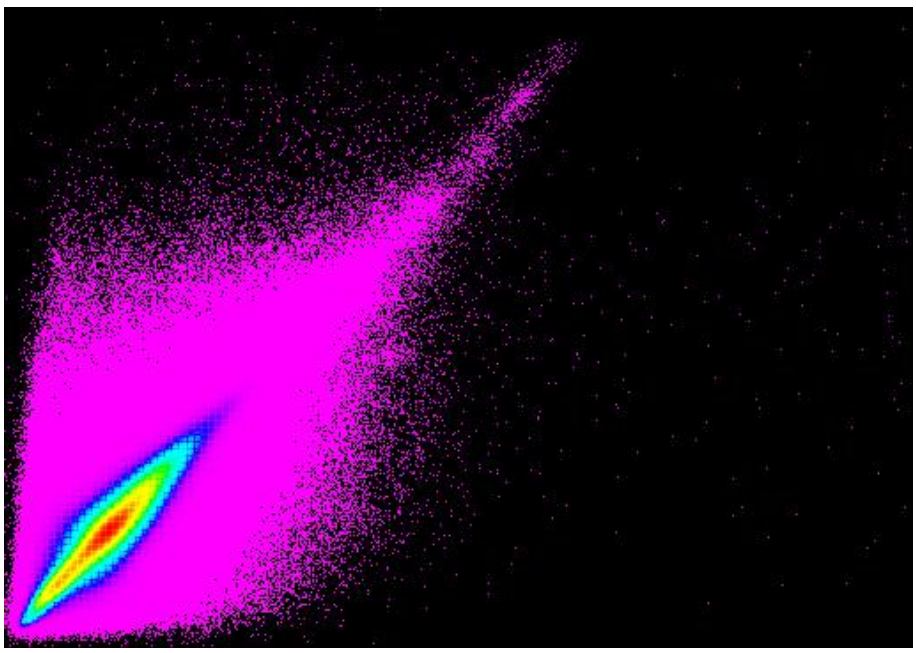

Figure 6-21 – Scatter plot of the IKONOS panchromatic images overlap.

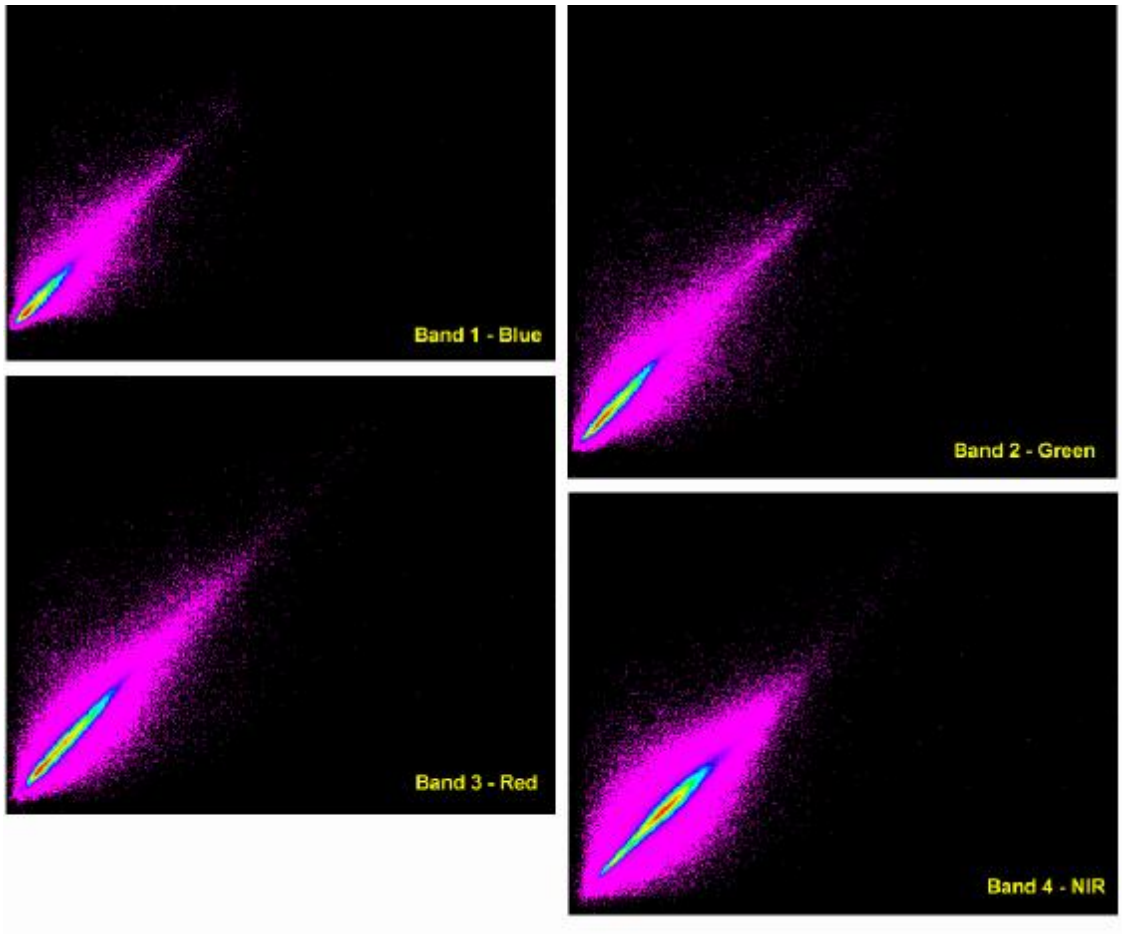

Figure 6-22 – Scatter plots of the IKONOS multispectral images overlap.

Table 6-1 – Pearson's product-moment coefficient of linear correlation between the CORONA and IKONOS images obtained at two separate sensor view angles

	CORONA Pan	Pan	Blue	Green	Red	NIR
Correlation (r)	0.888945	0.891256	0.941064	0.948245	0.957411	0.929426
Determination (r^2)	79 %	79.4 %	88.6 %	89.9 %	91.7 %	86.4 %
Remaining	21 %	20.6 %	11.4 %	10.1 %	8.3 %	13.6 %

In table 6-1, the results are also expressed in terms of determination coefficient r^2, which shows the percentage of variance by the spectral component. The remaining row is attributable to differences in the directional properties, the misregistration effect and the topography effect (wherever it appears).

To identify the view angle dependent features, the two images were put into a ratio. The resulting values that are at or near to one (threshold of 0.20) are considered to belong to features that are unchanged from one image to the other (white in figures 6-23, 6-24). All the other values in figures 6-23 and 6-24 show in colour features for which the view-angle can make a difference. However, it should not be forgotten that

these values could also be products of misregistration. For this reason, the images are displayed one next to other, and linear or point results are checked for misregistration.

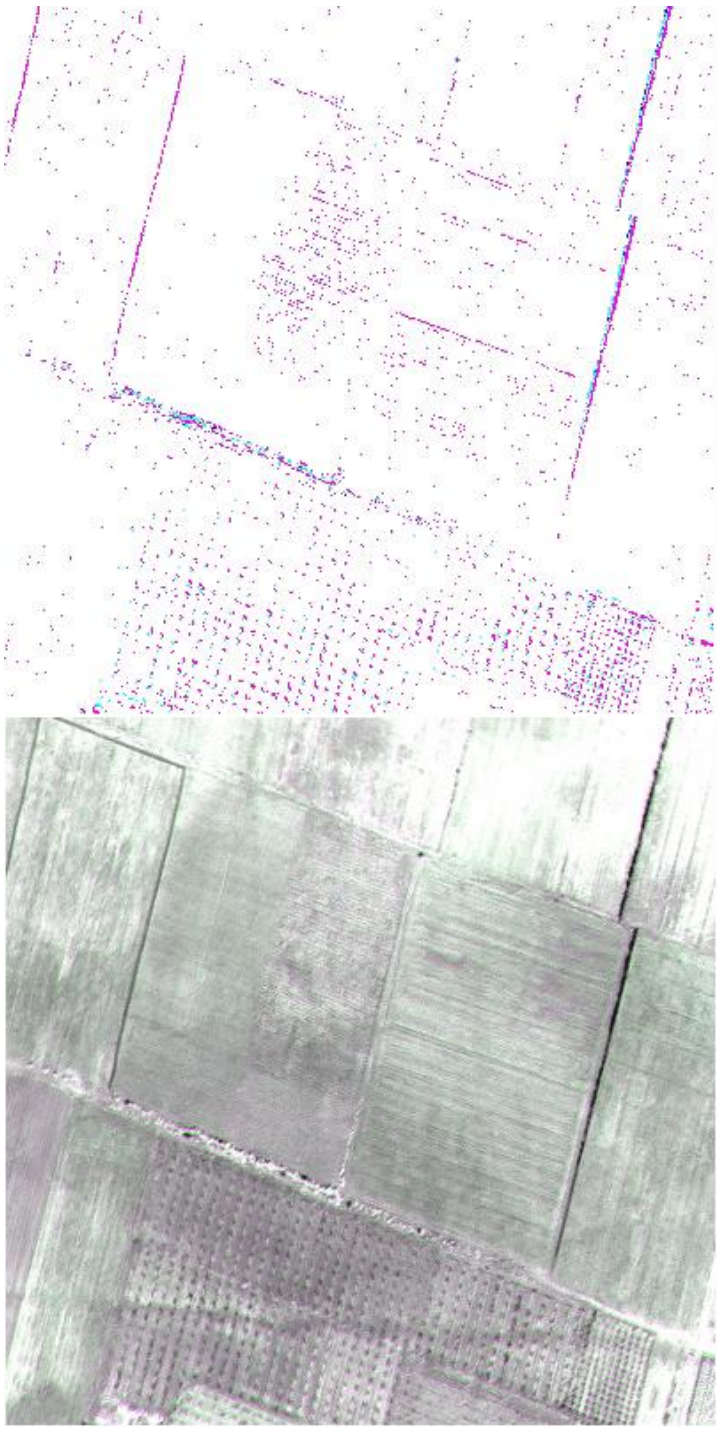

Figure 6-23 – IKONOS panchromatic view-angle dependent features

In figures 6-23 and 6-24, surely misregistered can be considered areas where the image differences are in couples (in this case, where the blue and red hues form similar neighbouring shapes). There are features that are view-angle dependent in both the

CORONA and IKONOS pairs. In IKONOS, the small view angle between the two images does not allow for many such features to be detected. However, some fields (see figure 6-23) show that they are view angle dependent.

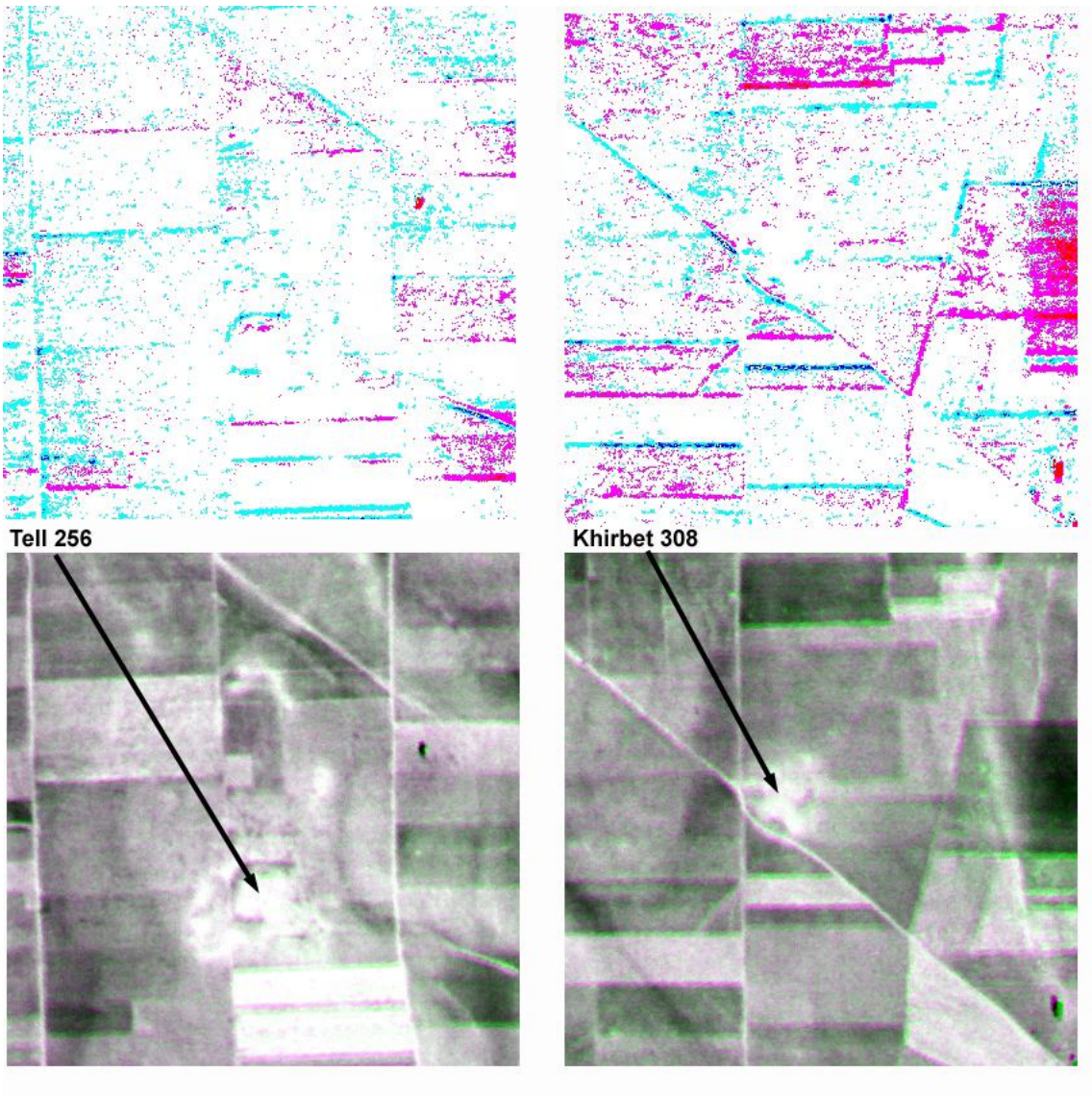

Figure 6-24 – CORONA view-angle dependent features. Examples of tell 256 and khirbet 308.

In CORONA, the example focuses on two archaeological sites that are characteristic of the south area, the tell 256 and the khirbet 308. In this example, the khirbet presents no differences between the two view angles. But in the case of the tell, only the sides present a view angle dependence. The rest of the tell along with the southwest attached khirbet show no difference between the two CORONA images.

It is of interest that almost all the image chip of the khirbet presents differences apart from the khirbet itself.

IKONOS Band 1. There are not many view angle dependent features. Only the houses and part of the tell present some difference.

IKONOS Band 2. In comparison to Band 1, the differences include now some of the field boundaries. The tell presents a few more differences than before, but still not much.

IKONOS Band 3. On top on what one could see in Band 2, some of the roads are now included in the differences, and the field boundaries are more intense. The tell is now almost clearly formed.

IKONOS Band 4. More details from the fields are presented here. Some of the field boundaries and some roads appear but others that were visible before, here they do not present differences. The tell shows small amount of differences.

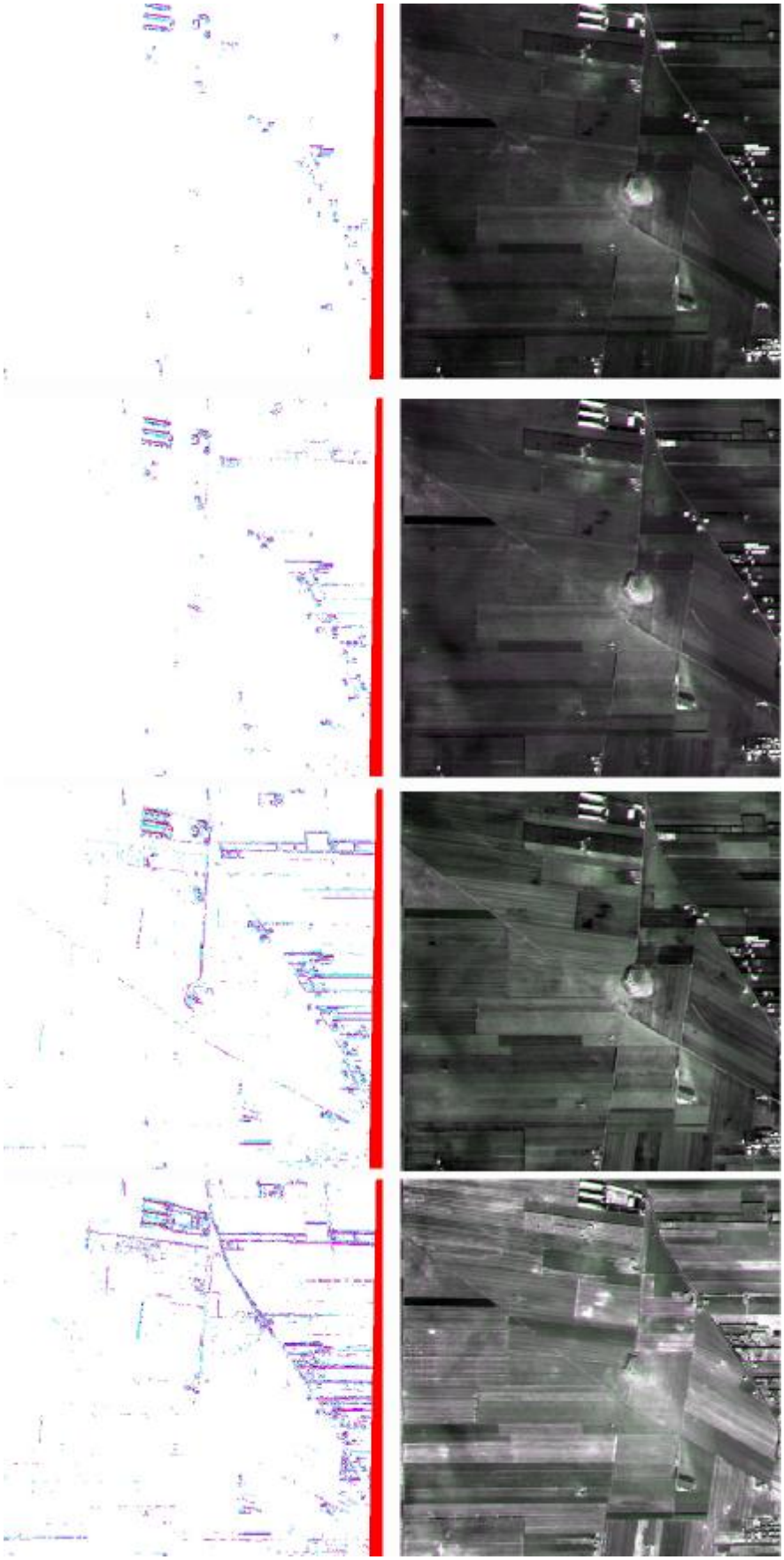

Figure 6-25 – IKONOS multispectral view angle dependent features.

In figure 6-25, the IKONOS multispectral bands are displayed as images on the right and the ratios on the left. The images are composites of the two view layers as {R,G,B}={Layer1, Layer2, Layer1}. While band 3 presents the higher correlation, it also presents a higher number of differences. Another visual observation is that band 4 presents differences in other features than the other bands.

Figures 6-26 and 6-27 display the spatial profile of the field spectroradiometry transects in the different images. This gives a visual comparison between the different satellite images and the ground data. Figure 6-26 shows tell site 256, and figure 6-27 shows khirbet site 308. These sites were chosen because they are typical archaeological sites within the south area of interest.

The spatial profiles of the CORONA MVA data (mission 1110) are very similar. In the profile of the forward camera 009, a noise is visible in the profile. This noise can be assigned to the regression that was applied to the data during the normalisation procedure. These profiles support the fact that the sites of archaeological interest are view-angle independent.

The other CORONA spatial profiles are different but the general pattern is preserved. The existing differences can be assigned to the difference in time and the difference in scanning parameters. The IKONOS panchromatic spatial profile shows the difference in spatial resolution by displaying more points in the same transect. To put all graphs together would be difficult mainly because of the different radiometric and spatial scales.

The IKONOS multispectral spatial profile shows that the near-infrared band highlights better than the other bands the difference in brightness between off-site and on-site pixels. Generally, both IKONOS panchromatic and multispectral graphs show a similar pattern with the CORONA imagery. No matter how difficult it is to locate the field spectroradiometry graph (because of the lack of coordinates of the samples), the spatial profile shows similar patterns with the imagery.

Summarising, the sites of archaeological interest and in particular khirbet and tells are view-angle independent. However, the data clearly shows that vegetation is view angle dependent and so this helps to separate dark soils from vegetation in panchromatic imagery. This could be very important for the photointerpretation of CORONA and IKONOS panchromatic imagery.

Also, the CORONA pairs of imagery present a potential for MVA studies in any area always taking into account topography, scanning and preprocessing procedures. The

IKONOS imagery can provide higher spatial resolution and it also provides multispectral data. The small view angle could not provide much results but it shows that there is potential for MVA studies with larger view angles.

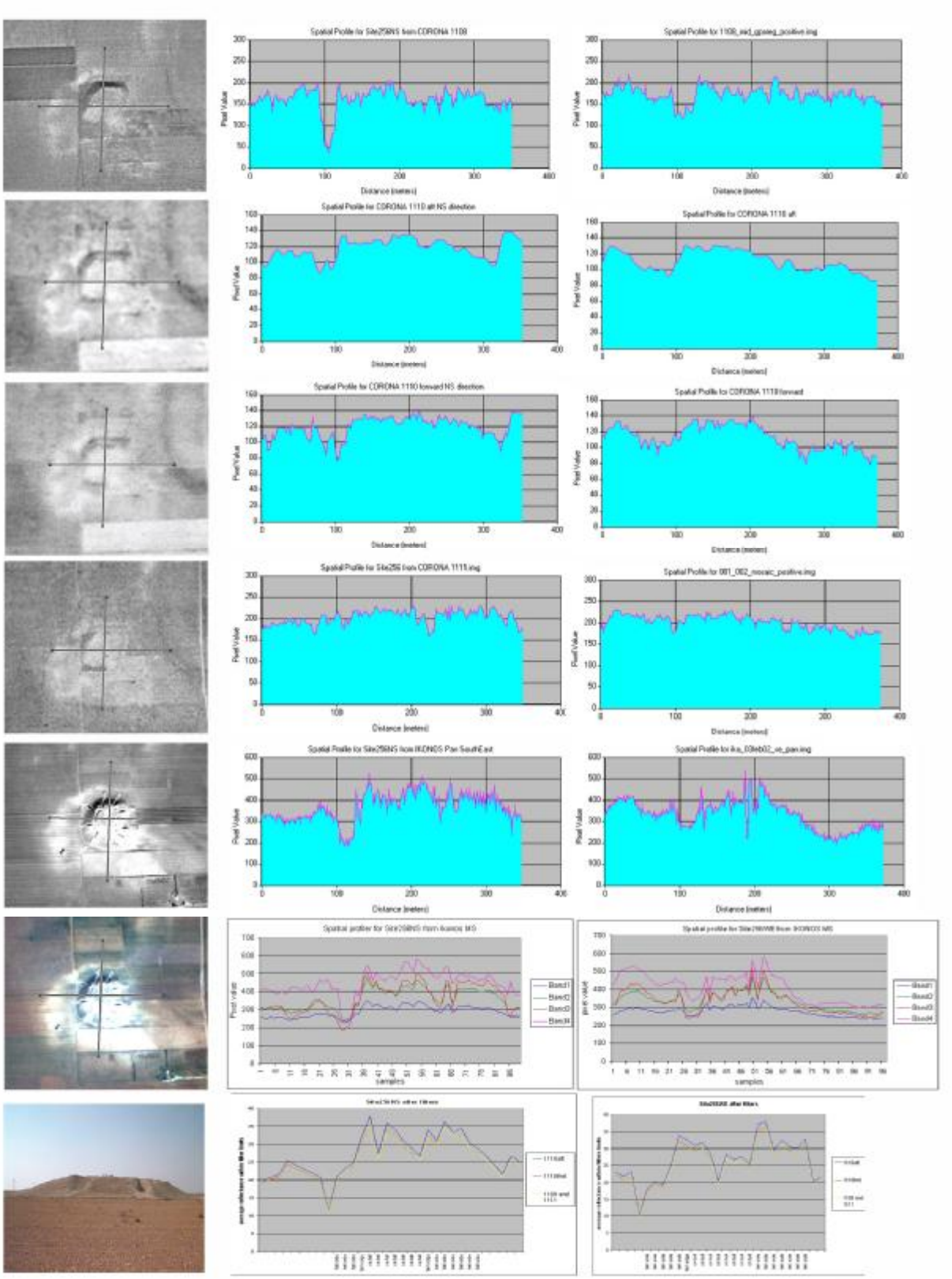

Figure 6-26 – Illustration of the satellite pixels brightness of the spectroradiometry transects of tell site 256.

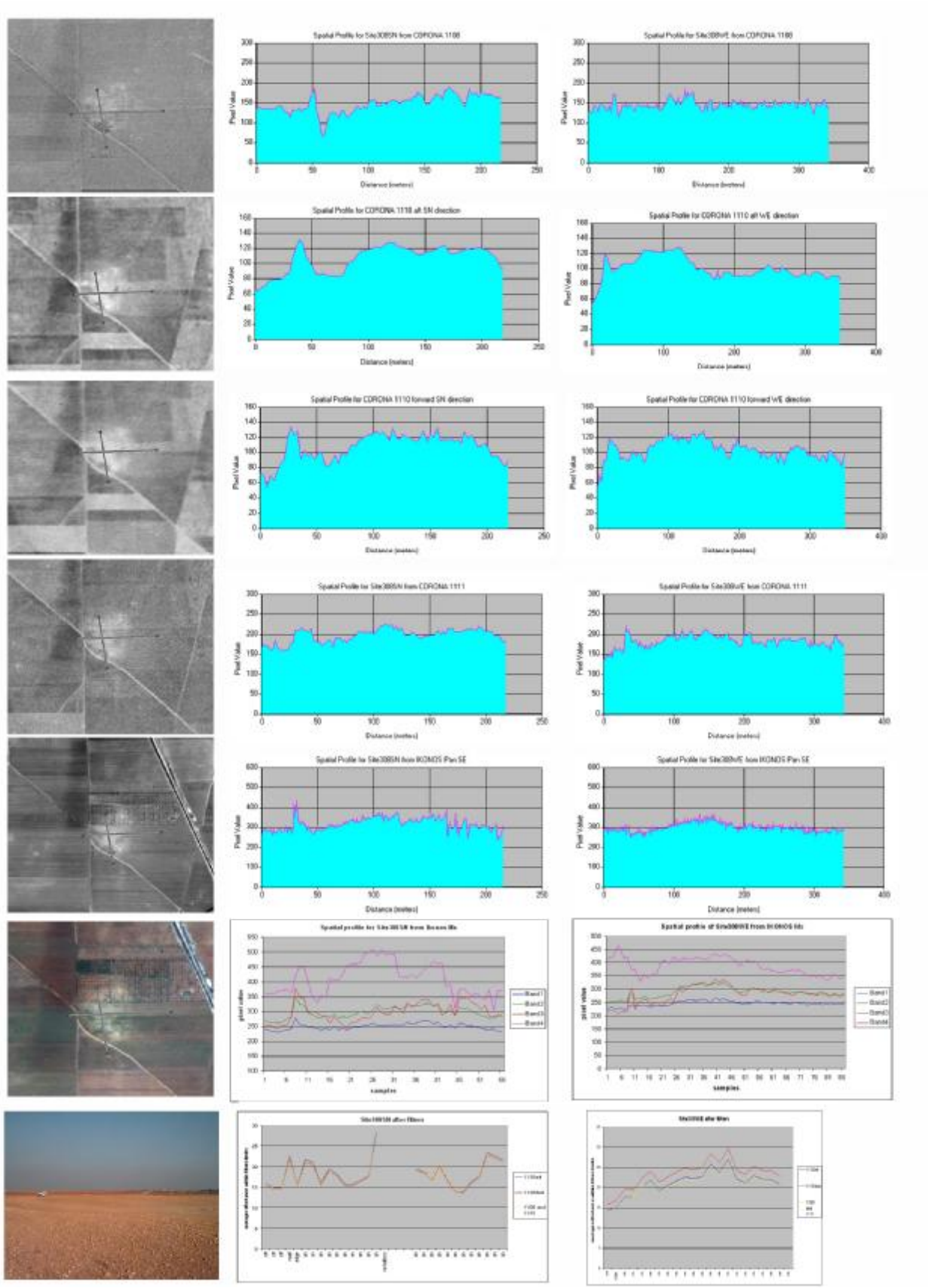

Figure 6-27 – Illustration of the satellite pixels brightness of the spectroradiometry transects of khirbet site 308.

6.4. Laboratory spectroradiometry

The main difference between field and laboratory spectroradiometry is that in the field reflectance comes from natural sunlight and from the existing soil texture, while laboratory spectroradiometry uses an artificial light source and is unlikely to retain "in situ" texture and moisture status.

Laboratory reflectance measurements are often used to determine the spectral absorption coefficients of the material, or, by inversion of the reflectance, some quantity proportional to it. For example, Kooistra *et al.* (2001) use laboratory spectroradiometry with partial least squares regression model to determine soil properties and metal concentration.

The particle size of surface soil is an important factor in determining its reflectance characteristics (Hapke, 1993). The transportation of soil from the field to the laboratory breaks down the particles, alters its moisture status and produces a change in the reflectance properties (Longshaw, 1974). There are also problems of ensuring that the sample is representative of the area where it was collected, and problems of simulating the natural radiation in the laboratory. Thus, the field and laboratory measurements are of a different nature and used for different purposes.

In this research, the purpose is the environmentally undisturbed measurement of off-site and on-site samples for determination of reflectance differences by partially excluding the soil texture factor. The samples are checked in both 'as is' and 'air-dry' conditions and they are equally ground. It must be mentioned here that the distinction between on-site and off-site samples is solely based on photointerpretation. Since the samples were collected for a different purpose, it was not possible to record the boundaries of the site.

During September 2002, 68 soil samples were taken and returned to the UK for analysis. These soil samples were from sites 254, 259, 339, and 611. Each sample's location was measured with a handheld GPS using the UTM coordinate system. During this fieldwork season the Syrian authorities allowed the use of a handheld GPS for non-sensitive points (i.e. not bridges, crossroads, etc.).

Part of the each soil sample was sent to the Department of Archaeology, King Alfred's College Winchester, for soil chemical analysis by Dr Keith Wilkinson. The analysis gave results of the potassium, sodium, iron, copper, manganese, and the moisture content. The remainder of the sample was kept to Durham for reflectance

spectroradiometry, organic content and particle size analysis. Reflectance spectroradiometry under laboratory conditions has better signal to noise ratio.

For the elimination of the background noise such as stray light, a large piece of non-reflective cloth was spread on the table and the surrounding walls. The table was placed at the corner of the room. The cloth is made of non-reflective black stuff. The source of light[33] was placed higher than the spectroradiometer, and it was securely fastened on the wall, illuminating the target from an angle of about 15°. The spectroradiometer was in fixed nadir-looking position, at a distance of 30 cm. Thus, all measurements were taken under the same illumination and viewing geometry. The user was always wearing dark clothes to further eliminate background noise.

According to Hapke (1993) and Kooistra *et al.* (2001), the soil sample preparation should include grinding by a mortar and passing through a 2 mm sieve. The sample preparation was simply a grinding of the material. It was not sieved, mainly because of the size of the samples (reminder: it was a sample out of sample, thus a small quantity). The material's reflectance was measured into four different samples preparations. The preparations vary according to the container and the preparation. Two types of containers were used (presented in figure 6-28), tin-dishes (aluminium sample dish) and petri-dishes (plastic sample dish). The material was sampled 'as is' and dry (after one night under 100°C). The results are illustrated in figures 6-29 until 6-32. These include graphs of the four conditions under which the laboratory spectroradiometry took place, and IKONOS imagery with the position of the soil samples. The samples are located on the site because of the handheld GPS measurements (positional circular error ±4-10 m). The graphs illustrate the average reflectance in the visible spectrum along the sample line that runs the site.

In these graphs, it is more obvious than in the field spectrometry that there is a 5-10 % increase in reflectance in the visible spectrum when inside the archaeological site (when compared with the 'outside the archaeological site' reflectance). When comparing the different conditions, the tin-dishes offered slightly higher reflectance than the petri-dishes. The dry conditions gave more reflectance than before drying the samples. An important point is that the dry conditions increased the reflectance more in the on-site samples than the off-site samples.

[33] Spotlight model SC915 220-240 V, 50 Hz, Maximum 500 W, manufactured to IP44 specification for external use.

These results are confirmed by the literature. Hoffer (1978), Irons *et al.* (1989) and Baumgardner *et al.* (1985) all agree that with increase in moisture there will be decrease in reflectance. Almost everyone has observed this phenomenon many times in life. As rain drops fall on the soil (either beach or garden or sidewalk), the wet areas become darker in colour due to a decreased reflectance (Hoffer, 1978). As reviewed by Planet (1970), Angstrom (1925) attributed the decrease in reflectance to internal reflections within the film of water covering soil surfaces and particles.

However, the pattern of the graph remained the same no matter the conditions or the containers. As reviewed by Atzberger (2002), Obukhov & Orlov (1964) were among the first observing that the spectral curves do not change in appearance upon wetting of soil.

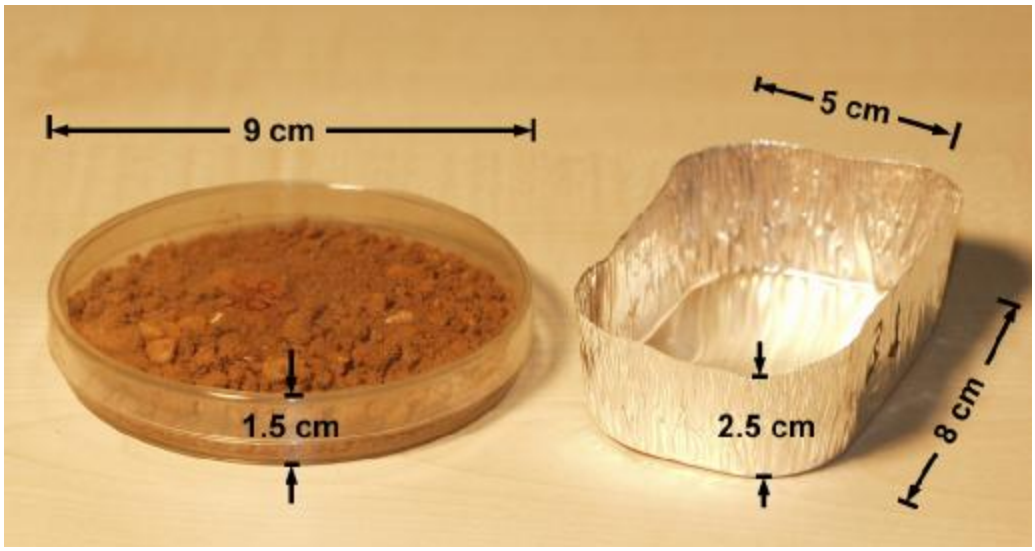

Figure 6-28 – Petri-dish and tin-dish containers for the soil samples

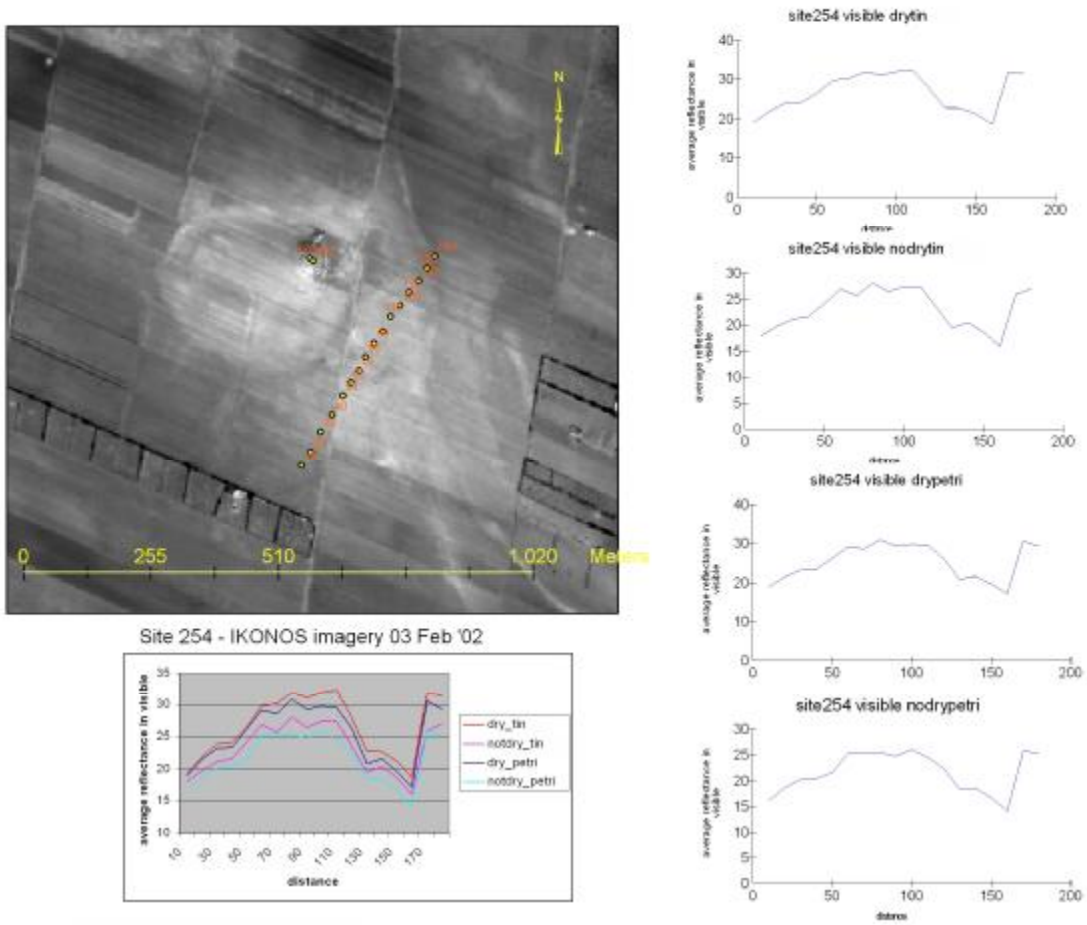

Figure 6-29 – Site 254 (Tell 'Arquni), transect is on site 602.

Site 254 represents a high grey ashy tell next to a wadi (a seasonal water channel east of the tell) with good all round views. The on-site soil class is sandy loam. The general topography of the area is flat plateau. The high area of the tell is small, but there is extension of the light soil colour towards the south and east. To the north of the tell there are some undulations of the landscape. The soil colour spread indicates a possible khirbet existing near the tell. As the reader will notice, the transect runs next to the tell and across the possible khirbet, which is designated as "site 602" in the database of the Homs project. This change in name does not alter the results of this research.

From the 50m point until the 130m point, a clear pattern of brightness increase shows up, which is confirmed by the existence of a khirbet next to the tell. The last two samples come from inside the tell site, and again they have an increase in brightness, when compared to off-site samples.

The comparison of the four different measurements (according to container and conditions) shows that there are no large differences in the pattern of the recordings. However, the tin-dishes containers give a higher reflectance than the petri-dishes. Also,

when the soil is under dry conditions, the reflectance increases. An important point here is that the increase of the reflectance is higher on the on-site than the off-site soil samples.

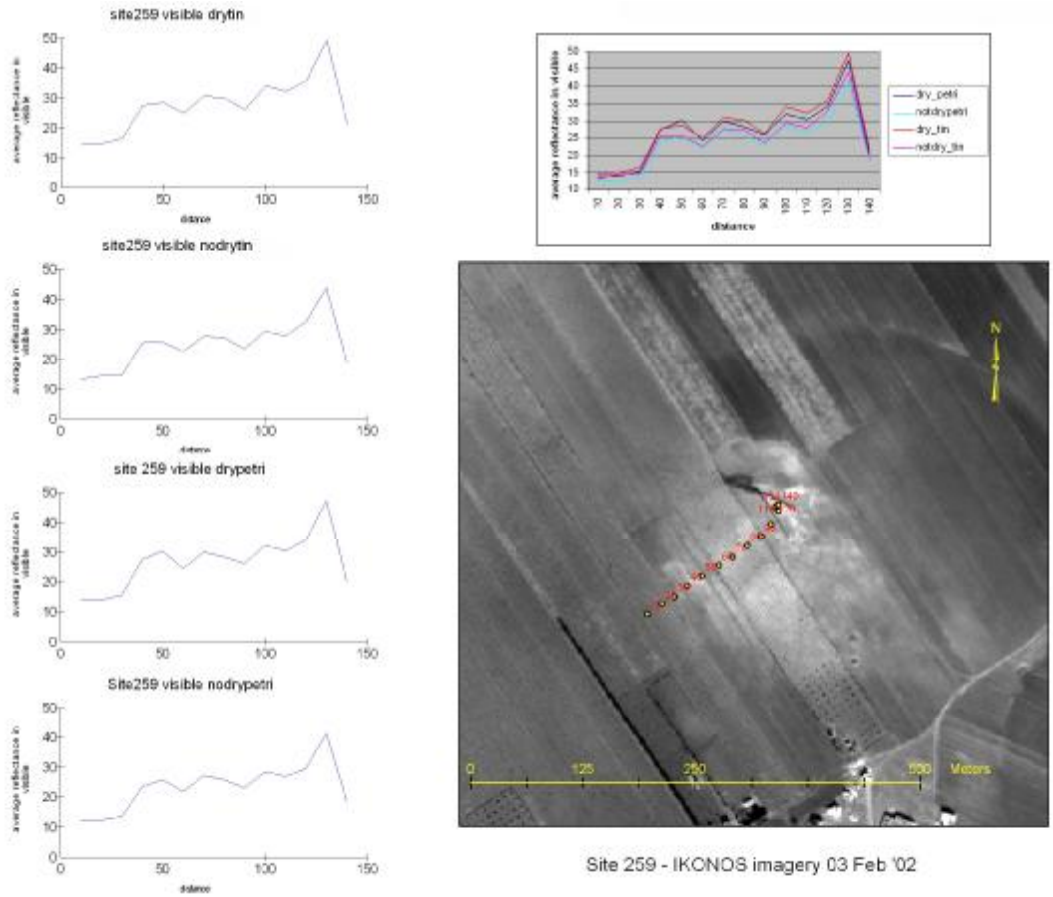

Figure 6-30 – Site 259 ('Um Al-Sakh)

This is a flat, steep-sided site with the eastern part lost due to bulldozing in the area. The on-site soil class is sandy loam and the general topography is flat plateau.

At this site, the soil samples 10m until 30m are taken from off-site and all the others move towards the centre of the site. The measurements show a pattern of increased reflectance when entering the site and then slight increase with slight fluctuations until the end. The last two samples were taken close to the area cut about by bulldozing. The redistribution of the soil due to bulldozing can explain the sudden fluctuation that is noticed in the graph.

Concerning the containers for the samples, data show the same pattern as in site 254.

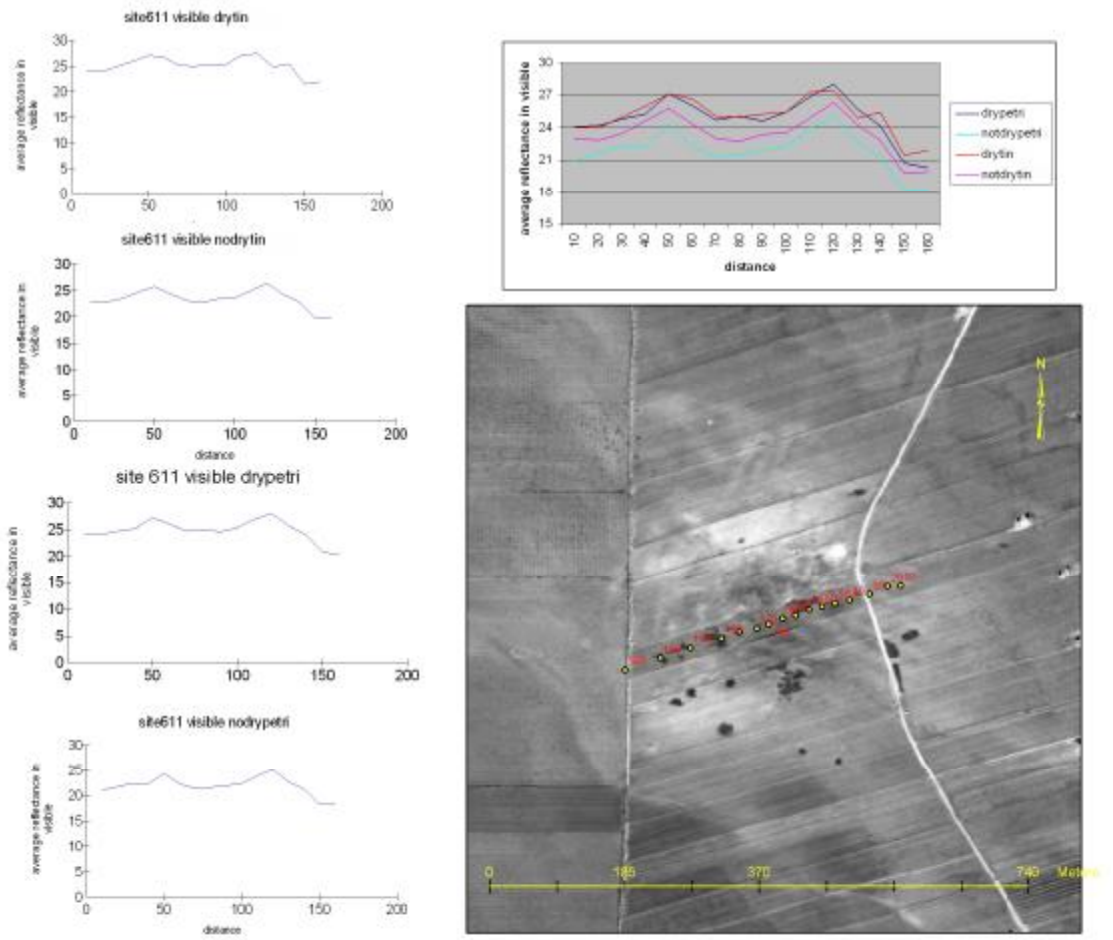

Figure 6-31 – Transect 611 [Site 279 (Khirbet Al-Qatisiyya)]

Near the end of the research, it was discovered that the "611" was a code given to the transect of the samples and not the actual site code, which is "site 279". When this was realised, it was too late to change all the graphs. This small glitch does not affect the work done. It is only a name change.

This is a flat site west of a tarmac road and east of a wadi. The site has terraces on eastern side. It is mostly fallow but with potato crop and surrounded by wheat. One exposed section at the centre of the site indicates bulldozing. Some piles of red and brown soil on-site show import of new soil material.

The pattern of the spectroradiometry measurements in figure 6-31 is not like the obvious patterns of sites 254 and 259 discussed in figures 6-29 and 6-30. It is generally homogenous with the only difference to be in the last two soil samples, immediately after crossing the road on the right side of the site.

The containers show the same pattern like in sites 254 and 259, with two exceptions. First, when under dry conditions, the measurements are almost identical. And second, the difference between dry and non-dry conditions is almost the same along the site.

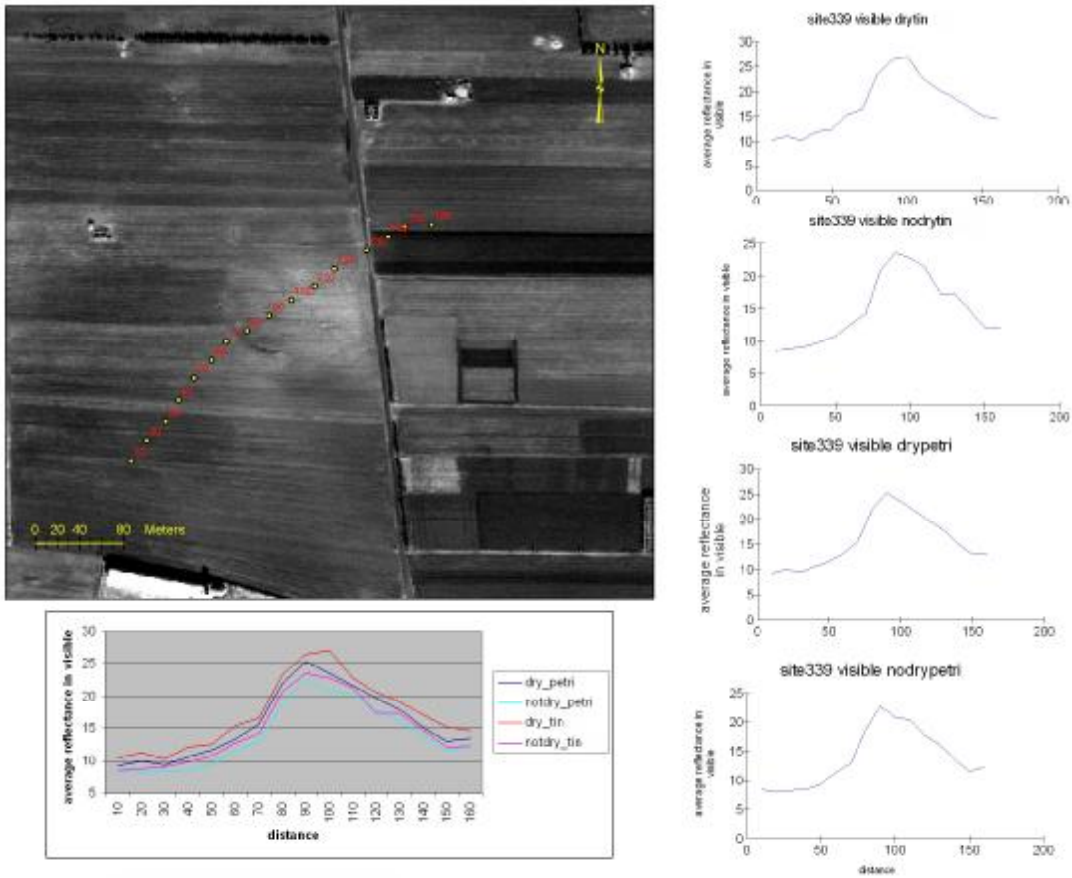

Figure 6-32 – Site 339 (Khirba Al-Tahisah)

This is a flat open area with good view down over the lake. It appears to be orientated around a central hollow. Archaeological evidence include olive press weights which indicate agricultural significance. During April, the site was completely covered by crop and it was impossible to be determined.

From the 70m to the 140m, the spectroradiometry graph shows an increase in the brightness in the visible part of the spectrum. This is a very clear pattern, without fluctuations. It also illustrates that environmental conditions (explained in paragraph 6.2) play an important role in field spectroradiometry data. In lab spectroradiometry the conditions are stable and controlled.

The pattern of the containers is the same as in site 254.

6.5. Granulometry

This is a laboratory-based measurement of particle size distributions from sand to clay, through dry sieving and Coulter Laser granulometer. The granulometry analysis will test for differences in the particle size between off-site and on-site samples. Also, these data can be integrated with the spectroradiometry measurements to identify relations between particle size and the reflectance of the ground within the visible spectrum.

For this task, all samples were sieved through a 2 mm sieve, and about 0.5 g of soil was sampled and put into a 50 ml tube. The soil was mixed well to gain a representative sample of 0.5 g of soil. After that, 20 ml of 20 % hydrogen peroxide were added into the tubes. The tubes were covered in a rack with aluminium foil and they were placed in a boiling water bath overnight. This way, all the organic material should be dissolved. The samples were then centrifuged at 4000 rpm for 4 minutes and the supernatant liquid was decanted off. Then, 20 ml of distilled water and 2 ml of Sodium hexametaphosphate solvent were added to separate the particles one from the other. Thus, the samples were ready for analysis by the Coulter granulometer. During the Coulter granulometer analysis, the directions were meticulously followed and all results were exported to .xls files and printed.

According to Gardiner & Dackombe (1983), the soil categories are:

Clay – less than 2 μm
Fine silt – 2 μm < x < 6 μm
Medium silt – 6 μm < x < 20 μm
Coarse silt – 20 μm < x < 60 μm
Fine sand – 60 μm < x < 200 μm
Medium sand – 200 μm < x < 600 μm
Coarse sand – 600 μm < x < 2000 μm

, where x = particle size.

Figures 6-33 and 6-34 show the graphs, which are categorised according to the above list of soil categories. These graphs display the percentage of particle size categories contained in the samples along the sampling line that runs through the archaeological site. Also in figures 6-35 until 6-38 the graphs are combined to allow spatial comparison.

Transect 611 granulometry shows a high percentage of coarse sand in the middle of the sampling transect, while the other particle size classes distribute evenly with a slight decline at the centre where coarse sand is dominant. Simultaneously transect 611 shows an exception. While in all other sites clay and fine silt dominate most of the samples within the sites, at transect 611 they dominate the edge of the area of interest. At sites 339 and 259, the small particle size classes dominate almost all the samples. At site 254, there is a uniform distribution of the particles in all the size categories, with the exception of a few outliers of the coarse sand in some samples. These outliers can be detected in site 259 too.

Apart from these general comments, there is a similarity in the patterns of clay and fine silt, while the other groups do not show much similarity among them.

In the graphs of figures 6-33 and 6-34, the X-axis shows the samples designated number. For site 254, the numbers 35-52 reflect to distance 10-180m. For site 259, the numbers 17-30 reflect to distance 10-140m. For site 339, the numbers 53-68 reflect to distance 10-160m. For transect 611, the numbers 1-16 reflect to distance 10-160m.

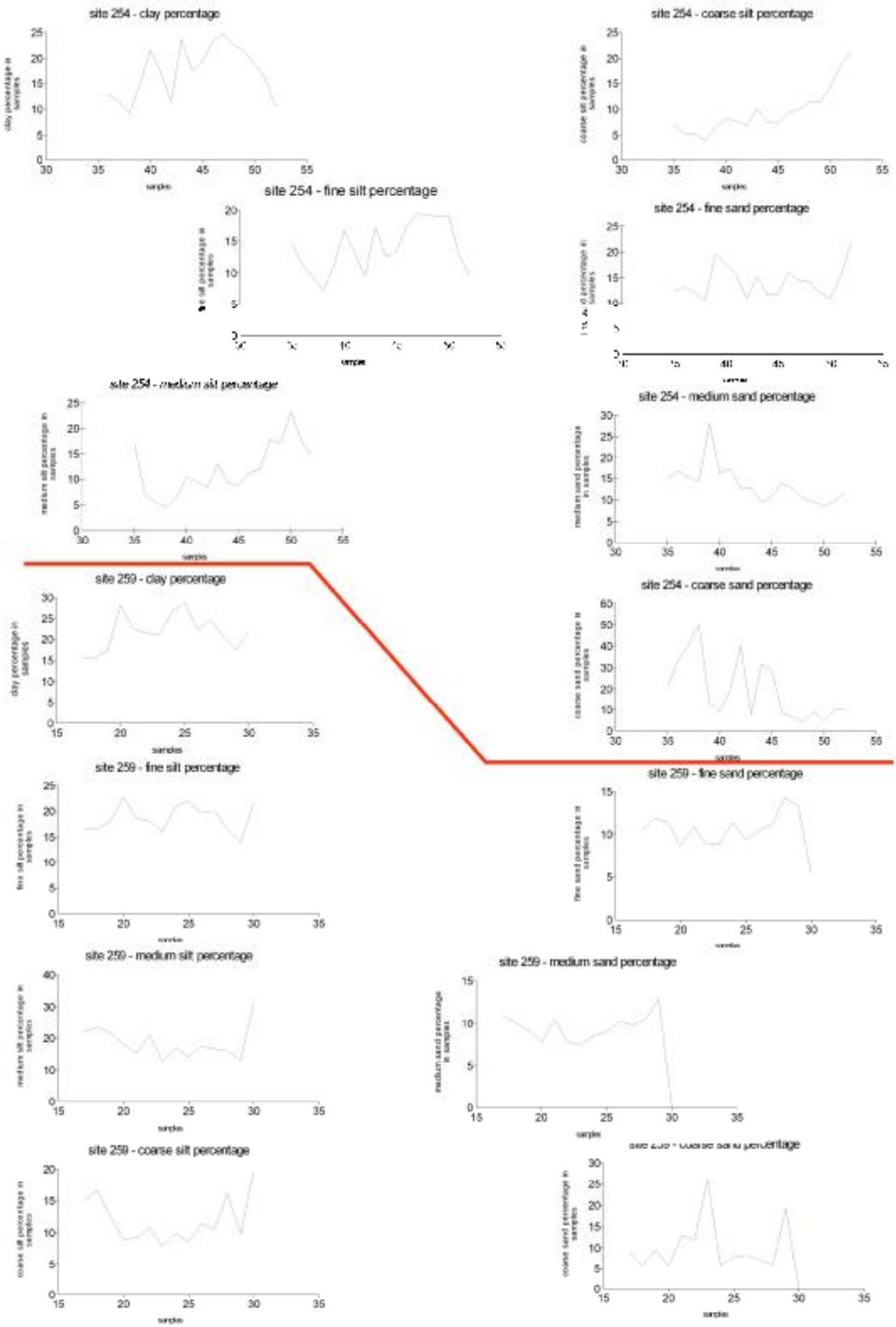

Figure 6-33 – Sites 254 (Tell 'Arquni) (transect is on site 602) and 259 ('Um Al-Sakh) granulometry graphs. Soil samples 35-52 and 17-30 respectively.

In the graphs of figure 6-33, the X-axis shows the samples designated number. For site 254, the numbers 35-52 relate to distance 10-180m. For site 259, the numbers 17-30 relate to distance 10-140m.

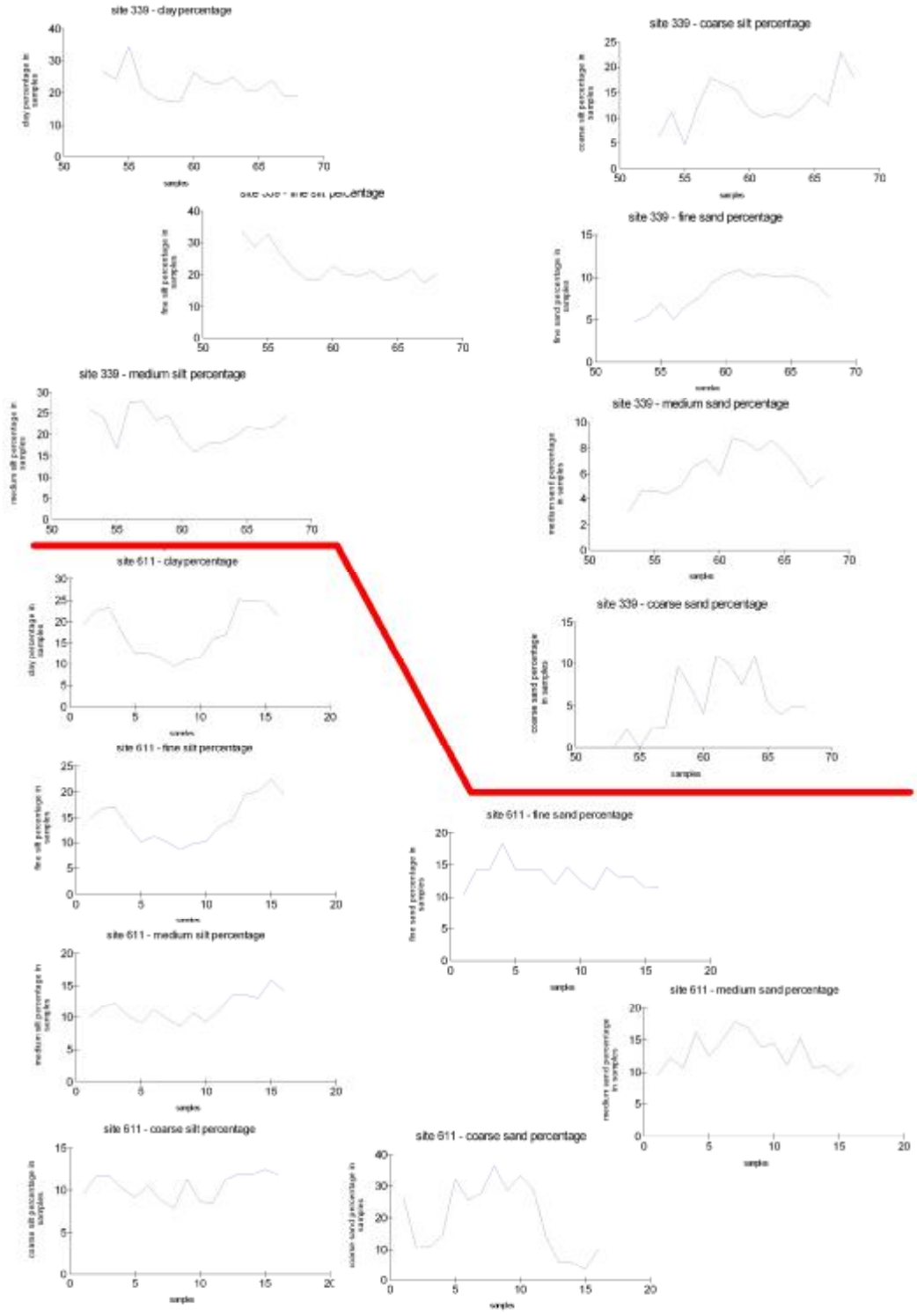

Figure 6-34 – Site 339 (Khirba Al-Tahisah) and transect 611 [Site 279 (Khirbet Al-Qatisiyya)] granulometry graphs. Soil samples 53-68 and 1-16 respectively.

In the graphs of figure 6-34, the X-axis shows the samples designated number. For site 339, the numbers 53-68 relate to distance 10-160m. For transect 611, the numbers 1-16 relate to distance 10-160m.

6.6. Weight loss on ignition

This is the most common and widely accepted routine method for determining the organic content of a sample material. It is based upon measuring the weight loss from a dry soil sample when exposed to high temperatures. The weight loss that occurs is then correlated to oxidizable organic carbon.

As with the granulometry, the purpose is to define differences between on-site and off-site samples, and to identify the relationship between % LOI (Loss On Ignition) and spectroradiometry measurements.

First the containers were weighed and then put in them an appropriate quantity of soil sample. After that, the full containers were put into oven in increments of 40 samples at 100°C to dry overnight. In the morning, they should be left in the air for a while, and then they were weighed (weight = c). Then, they were put in the oven at 550 °C for 4 hours. This was done in increments of 20 samples, mainly because there was not enough space in the oven. This means that the samples 21-40, and 61-68 stayed in the air for more than 4 hours, before entering the oven. After the 4 hours oven, and after the samples were left for 10 min to cool down, they were weighed again (weight = b). The difference in weight c-b shows the LOI, which is correlated to organic material.

In figures 6-35 until 6-38, the % LOI is displayed along the sampling line that runs through the archaeological site. In the graphs of figures 6-35 until 6-38, the X-axis shows the samples designated number. For site 254, the numbers 35-52 reflect to distance 10-180m. For site 259, the numbers 17-30 reflect to distance 10-140m[34]. For site 339, the numbers 53-68 reflect to distance 10-160m. For transect 611, the numbers 1-16 reflect to distance 10-160m. The borders between on-site/off-site samples are presented with red vertical lines in the graphs.

[34] The samples 31-34 are presented in site 259, but they are not from this site. They are samples from Tell Nebi-Noah (site 014), palaeosoil and mud-brick material from this large rampart site.

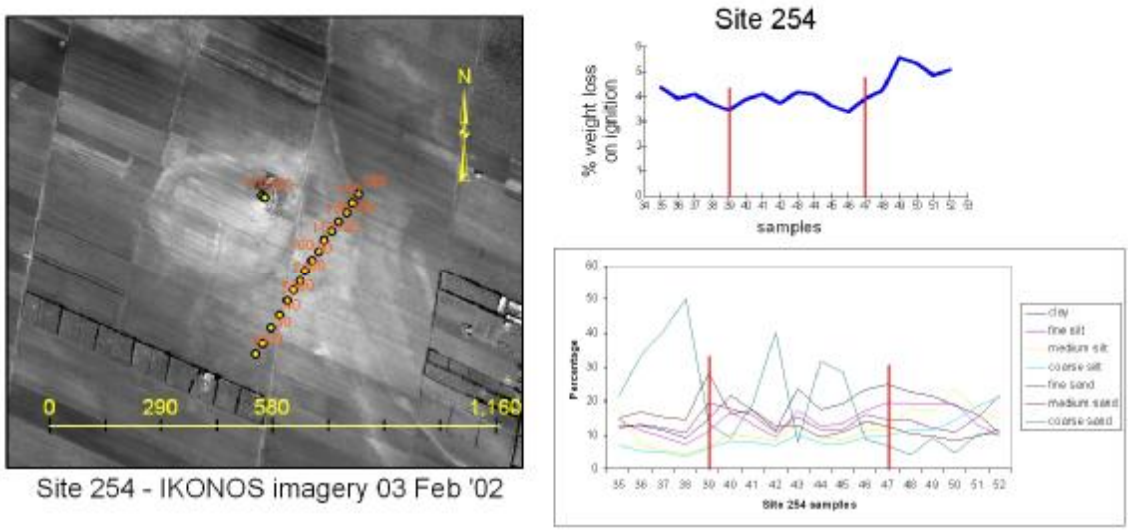

Figure 6-35 – Site 254 (Tell 'Arquni) (transect is on site 602) % LOI and spatial display of granulometry.

The integrated granulometry graph shows the abrupt fluctuations of coarse sand pre-site and on-site. With this exception, the on-site area is characterised by fine sized particles. The % LOI graph shows little difference between the pre-site (samples 35-39) and the on-site samples, while the after-site (samples 47-52) samples show a significant increase. Could the pre-site coarse sand prevalence affect the oxidizable organic content percentage in soil?

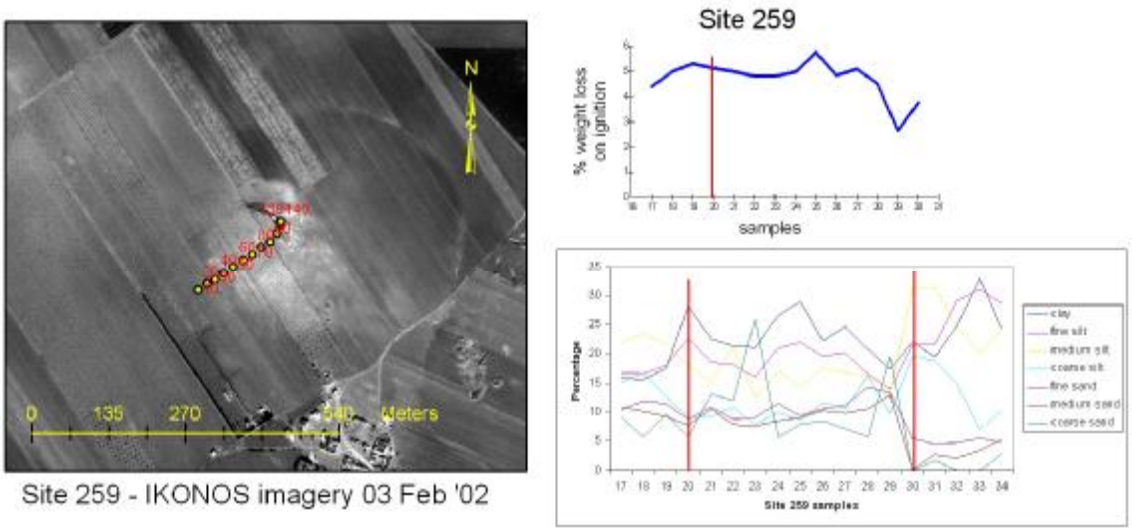

Figure 6-36 – Site 259 ('Um Al-Sakh) % LOI and spatial display of granulometry.

The second vertical line in the granulometry graph separates the soil samples presented in the image chip (17-30) from the samples of archaeological material from Tell Nebi-Noah (31-34).

With the exception of two coarse sand outliers in samples 23 and 29, the finer-sized soil particles dominate the on-site samples. Where the coarse sand is dominant, the % LOI presents depressions, whose lowest values coincide with the samples 23 and 29.

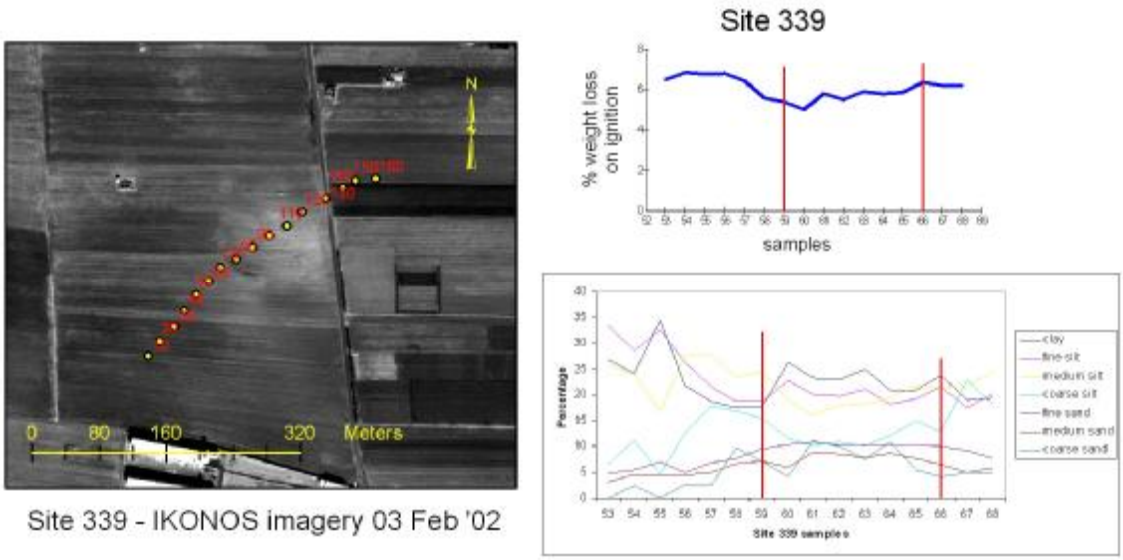

Figure 6-37 – Site 339 (Khriba Al-Tahisah) % LOI and spatial display of granulometry.

In the % LOI graph, a decrease within the site is obvious when compared to the off-site samples. The granulometry graph presents a high prevalence of the finer particles in all samples. The prevalence of the finer particles is decreased inside the site when compared to off-site.

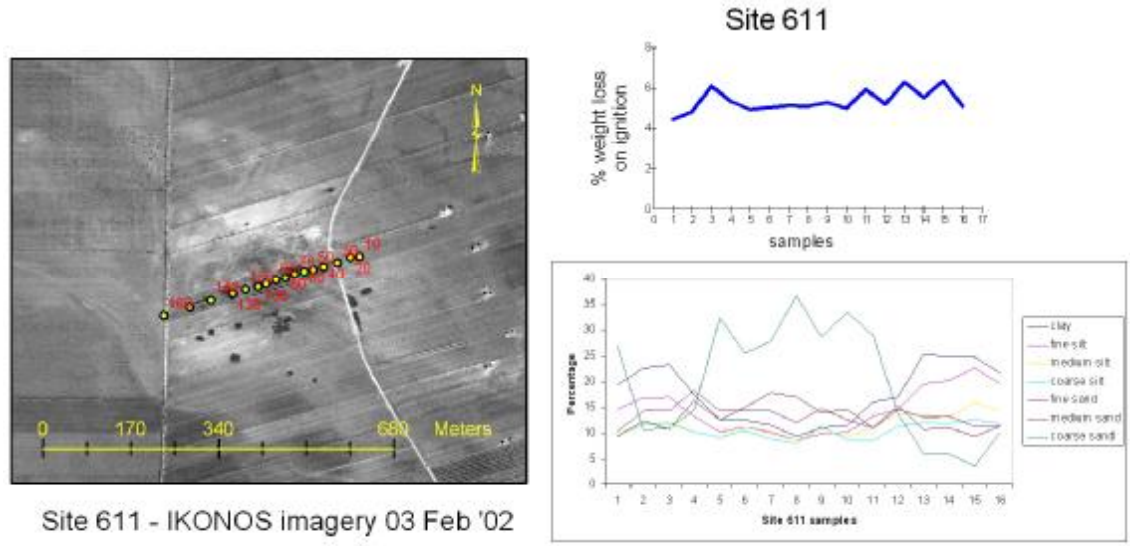

Figure 6-38 – Transect 611 [Site 279 (Khirbet Al-Qatisiyya)] % LOI and spatial display of granulometry.

The most obvious pattern to emerge from the graphs in figure 6-38 is the spatial distribution of coarse sand in the samples. Starting from sample 1, coarse sand dominates this sample. Then, for the next three samples, the finer-sized particles dominate. The next seven samples have 30-35 % coarse sand. And then, again the finer-sized particles dominate the samples, while coarse sand decreases to 5 %.

The % LOI graph shows fluctuations at the edges of the site. The sample 11 is the exception in a pattern between coarse sand and the percentage of oxidizable organic carbon.

6.6.1. Summary

One would expect the archaeological site to have organic material in abundance. This is not observed here, perhaps because the samples were taken from the surface of the sites. There is no protection of the site by the wind. The organic material being light could well be blown away by the wind. Hence, it should not be expected to find organic material in abundance at the surface of the site.

On the other hand, the measurements show more organic material in the off-site samples. The surrounding land is used for farming purposes and the fertilizers may well explain the existence of more organic material outside the site. However, sites like 339 are actually cultivated, and fertilizers should exist there too. It seems that the particles

size contributes to this difference. This is further investigated below in the integration of data, and the computation of correlations.

6.7. Data integration

In this section, the data from laboratory spectroradiometry, granulometry and % LOI are integrated and compared visually. There is an effort to identify their relationships through correlation analysis. The data is not ordinal and for this reason the Pearson's product correlation is chosen. The spectroradiometry samples were not sieved at 2 mm, thus the reflectance measurements are not 100% representative to the granulometry samples[35].

The figures 6-39 until 6-42 display the integration of the three different sets of data. The bottom X-axis is the distance from the beginning of transect, while the top X-axis is the assigned sample number. The total number of samples is displayed in the correlation table. The far left Y-axis is the percentage of the particular particle in the samples. The other Y-axis on the left is the % LOI. The right Y-axis is the averaged reflectance of every sample within the visible part of the spectrum (400-700 nm).

The tables 6-2 until 6-5 present the correlation results to give a picture of the general trend of the data. Admittedly, scatter plots may have been a better choice. But the number of samples is not large enough to give a good picture and the number of scatter plots to be created is too large for inclusion in the thesis. The data integration graphs and the correlation matrices were chosen for compactness of the data presentation. The main focus is the relationships among data, and the on-site and off-site differences in relation with data integration.

[35] The granulometry samples were sieved at 2 mm. The spectroradiometry samples were not sieved. This means that the reflectance measurements include particles of size greater than 2 mm. Thus, they cannot be considered 100 % representative to the granulometry.

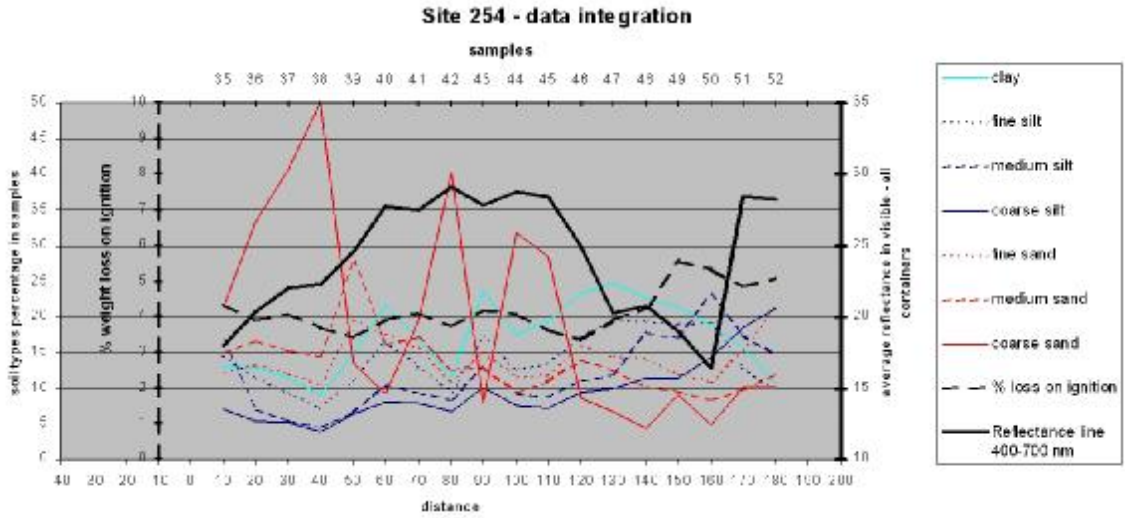

Figure 6-39 – Data integration for the soil samples of site 254 (transect is on site 602).

Some interesting results emerge from visual inspection of the graph of site 254 data integration. With the exception of outliers in the coarse sand fraction, the sand displays similar fluctuations with the reflectance. A negative correlation between % LOI and reflectance is clear in the graph. The % LOI shows the same fluctuations with medium and coarse silt fractions.

Table 6-2 – Correlation matrix of site 254 data integration.

samples=18	clay	fine silt	medium silt	coarse silt	fine sand	medium sand	coarse sand
Reflectance	-0.0533	-0.3840	-0.378	0.1243	0.3679	0.0479	0.124
% L.O.I.	0.0156	0.3067	0.7749	0.6995	-0.0262	-0.5489	-0.4078

Correlation between reflectance and % LOI is –0.3291.

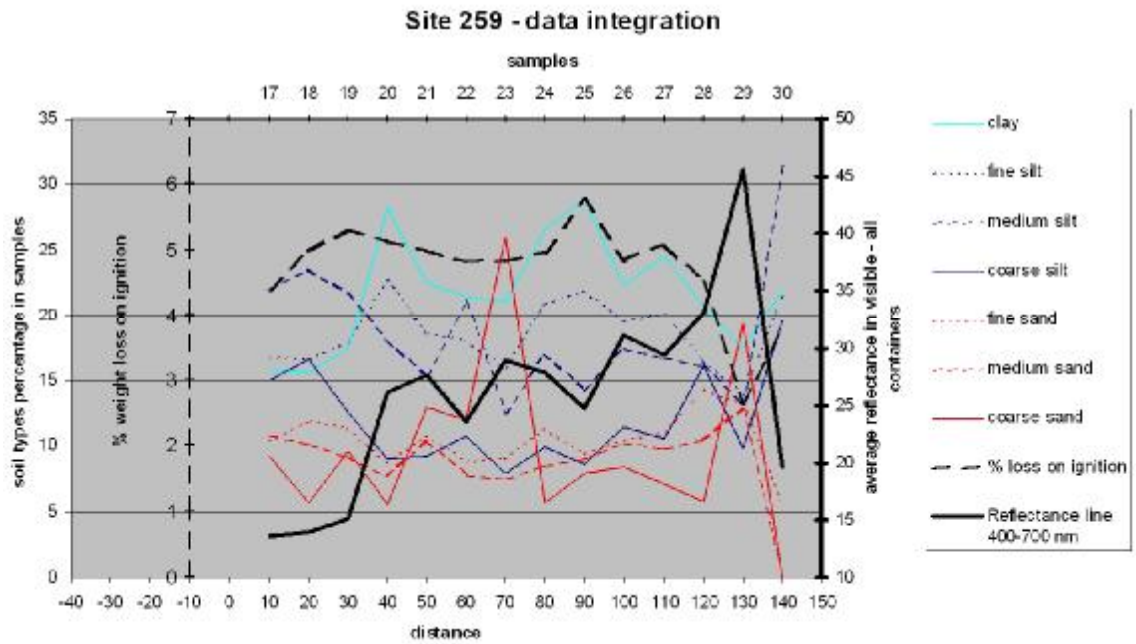

Figure 6-40 – Data integration for the soil samples of site 259.

Visual inspection of the graph of site 259 detects a clear negative correlation between % LOI and reflectance. The graph shows that where the % LOI increases, the reflectance decreases and the opposite. Concerning the other values, the % LOI follows similar fluctuations with the clay and fine silt fractions. The reflectance shows similar fluctuations with the sand fractions.

Table 6-3 – Correlation matrix of site 259 data integration.

samples=14	clay	fine silt	medium silt	Coarse silt	fine sand	medium sand	coarse sand
Reflectance	0.2407	-0.2263	-0.6809	-0.4632	0.3871	0.3458	0.4236
% L.O.I.	0.4635	0.5176	-0.1174	-0.2917	-0.1147	-0.0028	-0.2205

Correlation between reflectance and % LOI is –0.4782.

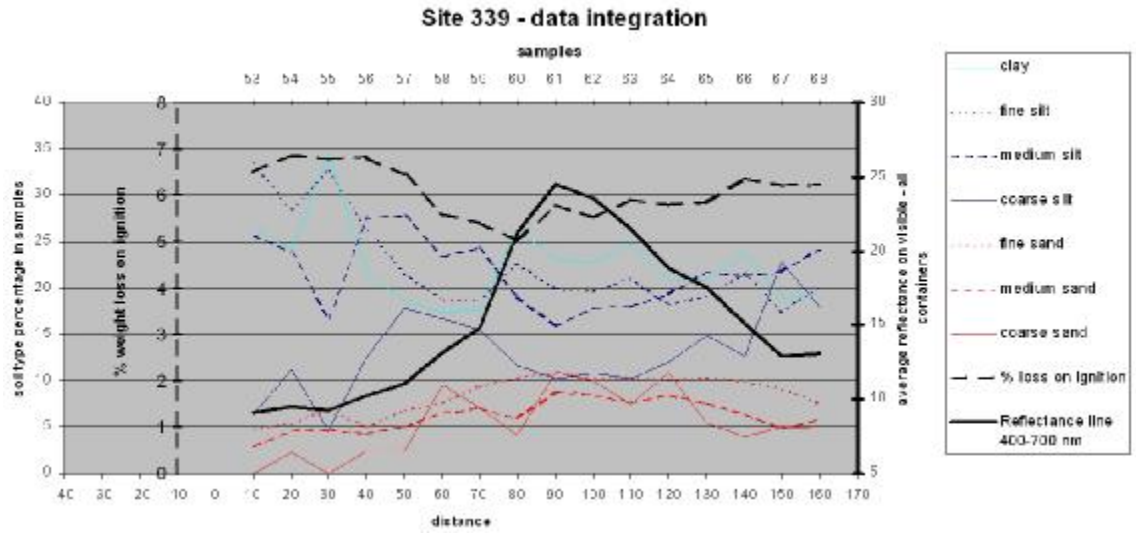

Figure 6-41 – Data integration for the soil samples of site 339.

Like in the previous two graphs, the visual inspection of the graph of site 339 data integration shows opposite fluctuations between % LOI and reflectance. The other relations are not visually clear. However, table 6-4 shows that there is a strong positive correlation between sand fractions and reflectance, and a positive correlation between thin particles (clay, fine silt) and % LOI.

Table 6-4 – Correlation matrix of site 339 data integration.

samples=16	clay	fine silt	medium silt	Coarse silt	fine sand	medium sand	coarse sand
Reflectance	-0.0593	-0.5753	-0.7018	-0.0794	0.8698	0.8632	0.7647
% L.O.I.	0.3039	0.6444	0.3935	-0.1772	-0.7465	-0.662	-0.6825

Correlation between reflectance and % LOI is –0.7477.

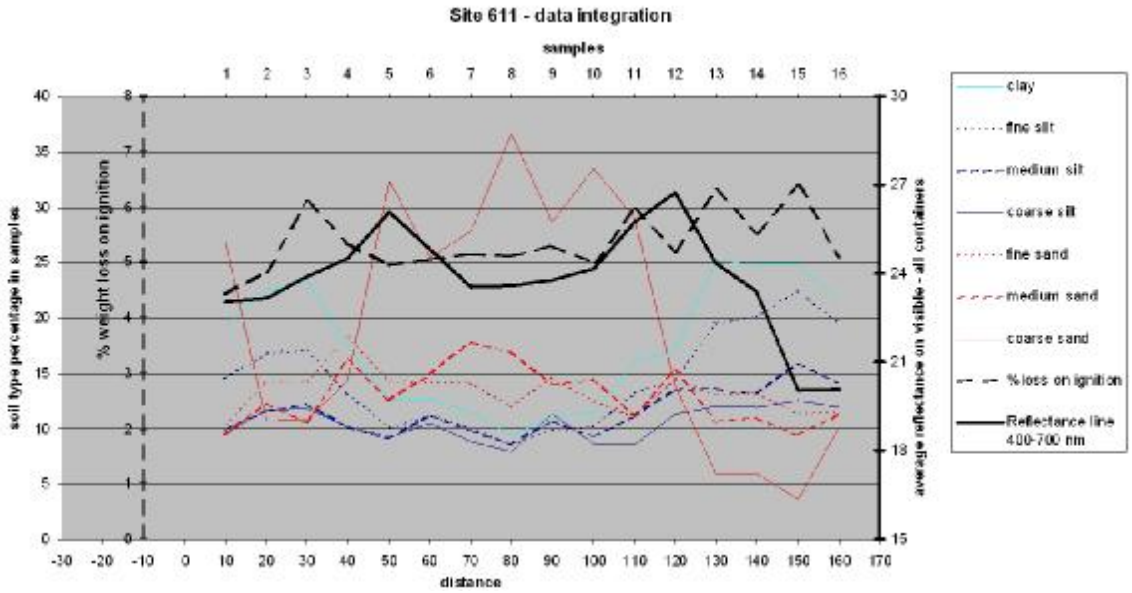

Figure 6-42 – Data integration for the soil samples of transect 611 [Site 279 (Khirbet Al-Qatisiyya)].

This graph of transect 611 clearly shows the sand is the dominant size fraction on-site, while silt fraction dominates at the edges of the site. The opposite fluctuations of % LOI and reflectance that were noticed on the other sites, they are not as clear here. The sand fraction shows a positive correlation with reflectance. Table 6-5 shows that silt fraction and % LOI are positively correlated, while silt fraction and reflectance are negatively correlated.

Table 6-5 – Correlation matrix of transect 611 [Site 279 (Khirbet Al-Qatisiyya)] data integration.

samples=16	clay	fine silt	medium silt	coarse silt	fine sand	medium sand	coarse sand
Reflectance	-0.4215	-0.5541	-0.4662	-0.4079	0.4092	0.3683	0.4085
% L.O.I.	0.5073	0.5425	0.6046	0.4375	-0.0497	-0.3756	-0.5363

Correlation between reflectance and % LOI is –0.1272.

The data presented in tables 6-2 until 6-5 are amalgamated in scatter plots and presented graphically in figures 6-43 and 6-44. The pooled data in the scatter plots are actually supporting the above results and the below conclusions.

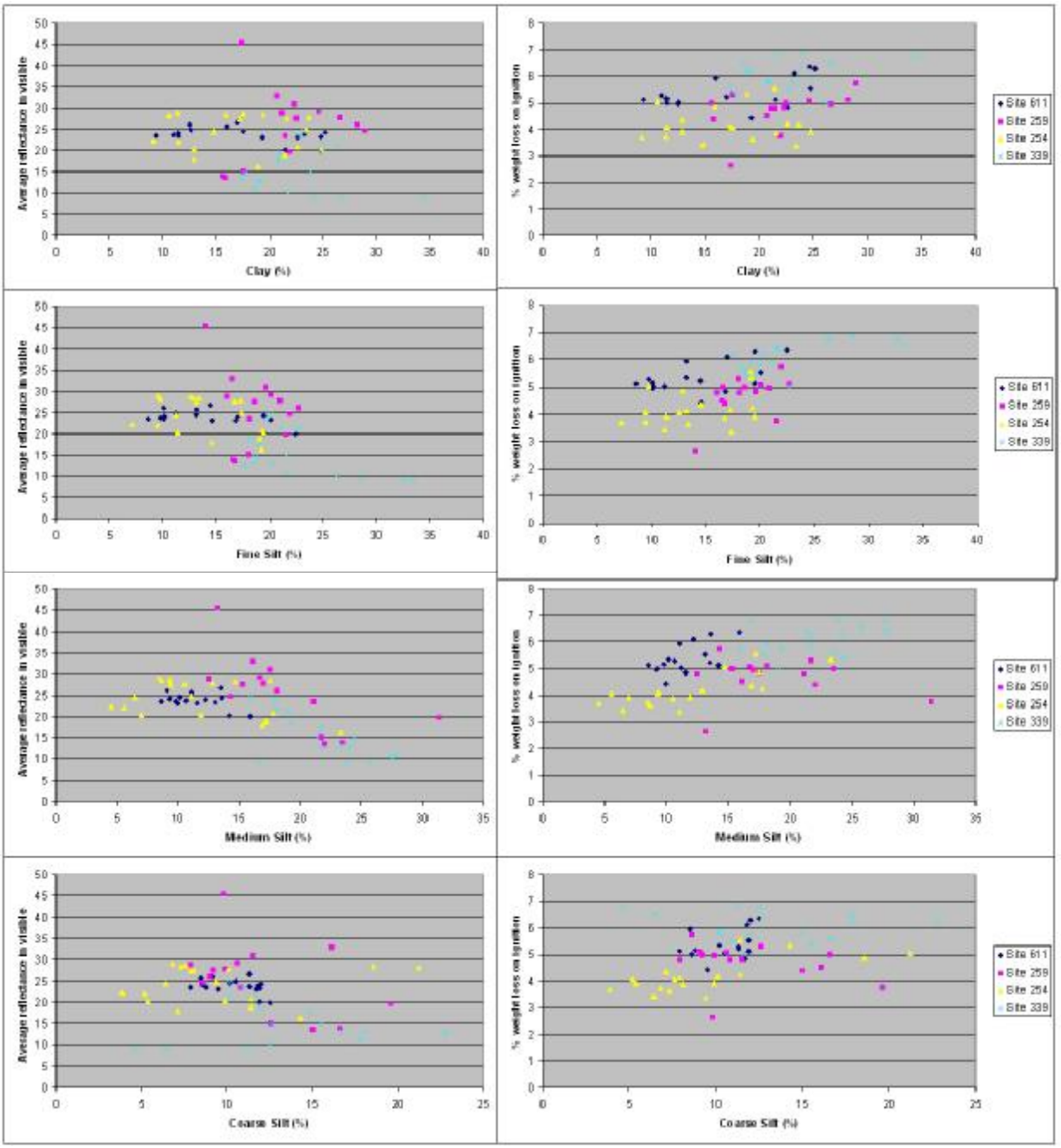

Figure 6-43 – Scatter plots of the relations Reflectance and LOI with Clay and Silt particle size.

Summarising, the reflectance is higher when the sample contains a high percentage of sand. This was expected since most sands are weathered fragments of quartz. In common experience, clayey soils often appear darker to the eye than sandy soils. The difference may be explained in part by the different mineralogies of clay and sand particles, but may be also due to the tendency of clay particles to aggregate. That aggregation into agglomerates and clods larger than sand grains can contribute to the darker appearance of clayey soils (Irons *et al.*, 1989).

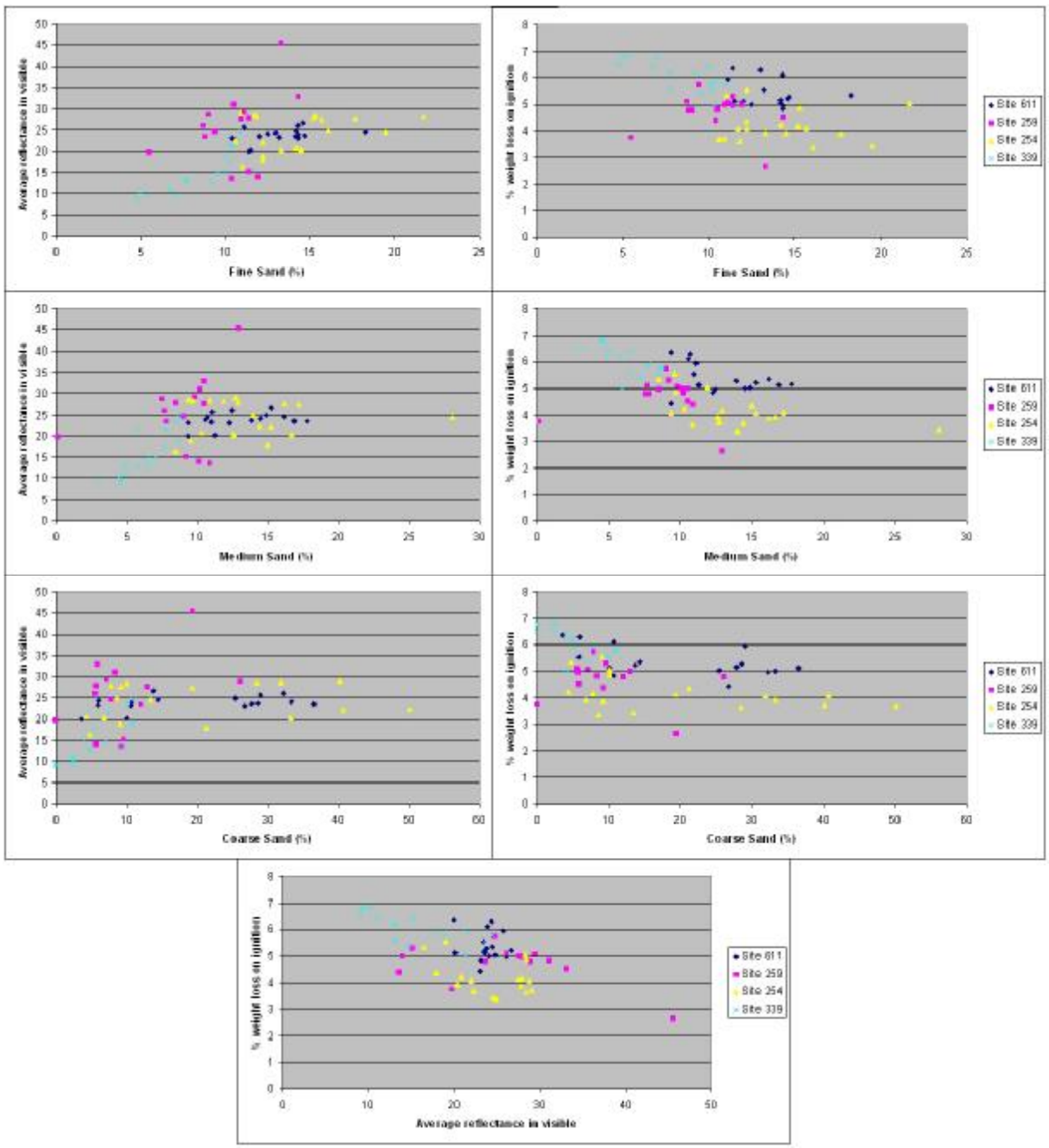

Figure 6-44 – Scatter plots showing the relations of Reflectance and LOI with Sand particle sizes and the relation of Reflectance with LOI.

Table 6-6 – Correlation matrix of all the samples together.

samples=64	clay	fine silt	medium silt	coarse silt	fine sand	medium sand	coarse sand
Reflectance	-0.1571	-0.5209	-0.6030	-0.2589	0.5551	0.4579	0.3771
% L.O.I.	0.3785	0.5768	0.5113	0.3026	-0.4803	-0.5475	-0.4630

Correlation between reflectance and % LOI is –0.6093.

On the other hand, the organic content is higher when the sample contains a high percentage of particles with size less than 6 μm; that is clay or fine silt. Simultaneously,

there is a negative correlation between organic content and reflectance. Spectral reflectance generally decreases over the entire shortwave region as organic matter content increases (Irons *et al.*, 1989; Hoffer, 1978).

However, the factors of organic content, moisture, particle size (and iron oxide which is not discussed here) are closely interrelated. Therefore, the correlations must not be treated as general guidelines but will hold true only for certain conditions (Hoffer, 1978; Montgomery, 1976).

It is difficult to define with certainty the relationship between off-site and on-site samples as applies to the integrated data. Concerning site 259, the off-site samples are too few to establish correlations. As for transect 611 (site 279), it is not possible to detect on the image the limits of the site, and thus it is not possible to identify on-site and off-site samples. This means that the relationship can only be sought in sites 254 and 339, where the archaeological character of the sites is confirmed and the samples are of equal number and not as few as in site 259.

It is apparent in both sites 254 and 339 that the on-site reflectance (average value 25.99 and 19.64 respectively) is more than the off-site (average value 19.85 and 11.04 respectively). Also, in both sites 254 and 339 the organic content is less on-site (average value 3.86 and 5.71 respectively) than off-site (average value 4.46 and 6.43 respectively).

From the above, it appears that the on-site samples have higher proportion of sand than the off-site samples. Sand is positively correlated with the reflectance of the soil. Silt and clay are positively correlated with the organic content. Hence, the on-site reflectance is higher than the off-site reflectance. In contrast, the on-site organic content is lower than the off-site organic content.

6.8. Discussion

The radiometric and soil measurements proved useful to characterise the archaeological sites and their surrounding environment. A difference of brightness of approximately 5-10% was observed between ‘sites’ and their surrounding area. This result may prove useful for interpretation and detection of archaeological sites on other CORONA imagery.

In the laboratory spectroradiometry, the samples are supported with the collateral information of the hand-held GPS. This information is used for the approximate allocation of the samples on the imagery. Obviously, the laboratory spectroradiometry

measurements may not be used for the determination of the ground texture, since the material was disturbed during the transportation. Also, they may not be used for the identification of the material since the samples were not sieved to constrain the particle size. Nevertheless, there is better control of the conditions than the field spectroradiometry measurements, and the laboratory supports the difference of brightness that was detected in the field. But this time, the difference of brightness is more obvious. This is because the laboratory spectroradiometry was looking at pure soil, thus excluding the surface texture, local scattering, effects of absorption by vegetation and other surface artefacts.

When all data were integrated together, it came out (from the three obviously archaeological sites 254, 259 and 339) that the on-site reflectance is positively correlated with the proportion of sand particles in the samples, and negatively correlated with silt and clay particles percentage in the samples. The on-site samples had higher proportion of sand than the off-site samples. Exactly the opposite was happening with the organic content, which was met in less proportion on-site than off-site samples.

In this chapter, the film scanning proved to be of importance. It was detected that the scanning of the film with different parameters or different scanner calibration can provide different scales of data. Thus, when the data are compared, they have differences because the brightness and contrast parameters do not agree. The differences can be minimised through radiometric normalisation, but noise may be introduced and generally the transformation will not be perfect.

The CORONA imagery showed that when imagery from both aft and forward camera exists, then there is potential for MVA studies in the area. Apart from the scanning parameters, other factors that one must take into account are the topography of the area, and the accuracy of the registration of the imagery.

The IKONOS imagery showed that there is potential for MVA studies. The directional component of a MVA study can be combined with the spectral component of IKONOS multispectral imagery for a more elaborate approach to the detection of differences among features in the area of interest. According to Helder *et al.* (2003), the IKONOS panchromatic and multispectral imagery are well co-registered, thus the integration of spectral component with the directional component of the higher resolution panchromatic image shows potential that needs to be further researched.

The archaeological sites of tell and khirbet showed that in the area studied they are view angle independent. The topography of the tell provided response in the MVA

approach, but it was not considered enough for its detection and identification. However, the red band of IKONOS managed to detect the tell after MVA analysis. This should be studied further with a larger IKONOS overlap, where more tells may be included and more results can be compared.

However, the vegetation is angle dependent, and thus it is possible to separate and identify vegetation from dark soils in panchromatic imagery. This is very helpful for the photointerpretation of CORONA imagery, especially when multispectral data is not available.

7. 3-D Analysis

Elevation data are the most important data structure for geo-spatial analysis applications (Toutin, 2001a), and their potential for solving a wide range of theoretical and applied models is long established (Evans, 1972). The advent of computer technology in the early 1980s and the subsequent advancement of technology have made it possible to acquire, process and display elevation data sufficiently and cost-effectively.

Digital elevation data today are usually expressed as DEM (Digital Elevation Model), DTM (Digital Terrain Model), or DSM (Digital Surface Model), while before the 'digital revolution' they were mostly represented as "contour lines". A DEM is defined as:

> *The representation of continuous elevation values over a topographic surface by a regular array of z-values, referenced to a common datum, and typically used to represent terrain relief* (Kennedy, 2001),
>
> and they are the initial data needed to produce all other types of DTM.

DTM (can also be found as 'Digital Ground Model, DGM') can include, apart from DEM, a variety of topographic characteristics. These characteristics can be local (gradient, aspect), non-local (slope length, 'relief'), or combined (topographic factor, topographic power indices) (Florinsky, 1998). On the other hand, DSM includes 3D objects like vegetation and buildings.

Depending on the application, one can choose the most appropriate representation of the elevation data. Typical representations include contour lines, profiles, regular grids, and triangulated irregular networks (TINs).

In landscape archaeology, elevation data may be used for the detection of surface features whose geometry can provide evidence for an anthropogenic modification of the landscape and possible archaeological sites. Moreover, elevation data show the morphology of the ground, thus enabling the identification of channels and hills, and their relation with archaeological sites. Furthermore, tools like viewsheds can be extracted from any given point to analyse the visibility, and information like 'gradient' may be extracted to identify the less appropriate areas for building.

With the above information, one can easily identify areas that might be suitable for the agricultural techniques of the past, drainage areas, water supply areas, and more.

7.1. Introduction

This chapter discusses the derivation of elevation data from satellite imagery, and assesses the accuracy and resolution of the derived DEM.

In fact, any imagery can be used to generate height information from a stereoscopic pair, as long as the terrain is imaged from two different viewpoints. On geometric criteria, satellite imagery can be separated into two different categories: the space cameras and the digital scanners. Due to differences at viewpoint, the stereopairs can be separated into two types: along-track (pictures taken from the same orbit) and across-track (pictures taken from adjacent orbits). Satellite imagery acquired by different platforms may also be used to create stereopairs.

The first space satellite to provide stereoscopic coverage was mission 9031 from the CORONA program; design KH-4, on 27th of February 1962. It could provide along-track stereopairs, with a ground resolution of 3-8 m. The CORONA program continued to provide along-track stereoscopic coverage until 1972, with the designs KH-4A and KH-4B. The latter design is discussed and analysed further in the following paragraphs. Simultaneously, the Russians also produced spy-satellites like CORONA under the name of ZENIT, however their stereoscopic capability is not clear.

The HEXAGON (1973-1980) program, that followed CORONA, provided stereoscopic along track coverage with KH-9 satellite design space cameras with a ground resolution of 6-9 m.

The U.S.A. and ex-Soviet Union both used stereoscopic imagery to map the lunar surface during the 1960s with the Ranger and LUNA missions respectively. The first significant achievement came from Lunar Orbiter I, II and III in 1966. In 1974, cameras on-board Skylab-D used the Earth's Terrain Camera experiment to measure heights (Mott, 1975). He reported an RMS error of 120 m for a strip of four Skylab terrain models and concluded that it was possible to produce contour intervals at 250m spacing. Further attempts followed with different experiment cameras. From these, it is worth mentioning the Zeiss Metric Camera on-board the Space Shuttle STS-9 mission (28/11-7/12/1983), and the Itek Large Format Camera on-board Space Shuttle STS-41-G (5-10/10/1989) with Forward Motion Compensation (FMC) system to improve quality. Petrie *et al.* (1997) generated a DEM with Metric Camera data and they obtained elevation accuracy of 15 m for flat areas to 45 m for complex terrain areas. Murai (1986) generated a DEM with the Large Format Camera and the height accuracy was 15m, mainly because of the FMC. The Shuttle cameras were of experimental status and

so data is limited in its availability. Sibiryakov (2000) generated a DEM from the Russian ex-military satellite TK-350 data with a 10 m height difference between DEM and control points.

The first digital scanner to provide stereoscopic coverage was Landsat. Due to its polar orbit, the across track overlap grows from 10% at the equator to 85% at 80 degrees latitude. However, the more overlap there is, the smaller is the Base-to-Height (*B/H*) ratio. The *B/H* ratio and the intersection angle A are vital contributors toward reducing the error e_h in determining relative heights from stereoscopic pairs. Figure 7-1 shows that e_h will be much larger when using photographs *N* and *N+1* than when using photographs *N+1* and *N+7*, which will greatly reduce e_h as a function of a larger *B/H* ratio. A *B/H* ratio between 0.6 and 1.2 is acceptable for stereoscopic work (Slama *et al.*, 1980).

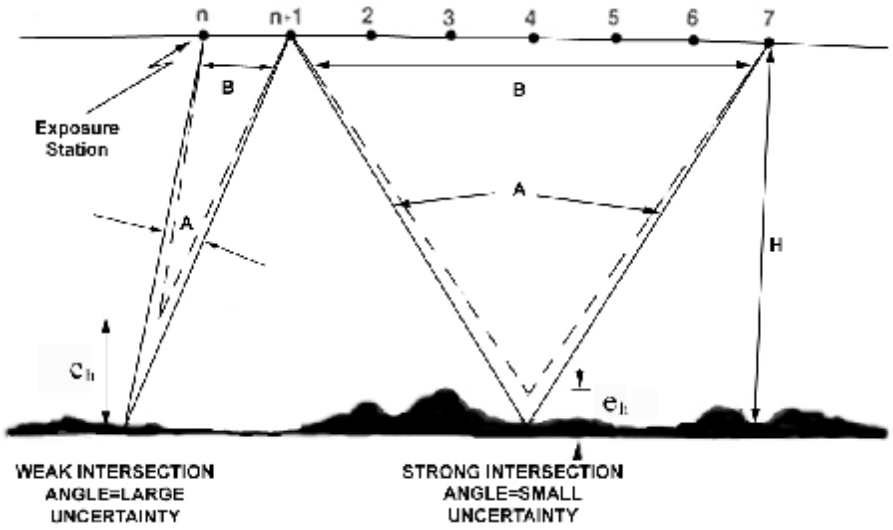

Figure 7-1 – Relative photogrammetric accuracy vs angle of intersection (Source: Slama *et al.*, 1980)

Landsat MSS data has a pixel size of approximately 80m and a *B/H* ratio of about 0.1. Thus, in order to have an x-parallax[36] of at least 5 pixels, Landsat MSS needs a relief of more than 4000 m. The pixel size improved in Landsat TM to 30m, and the

[36] Parallax is called the apparent displacement of the position of a body, with respect to a reference point or system, caused by a shift in the point of observation. The smaller is the distance of the object from the observer, the bigger is the apparent displacement. A simple example of parallax is the apparent movement of the trees when one observes them from the windows of a moving car.
The parallax is analysed into two components, the x-parallax and the y-parallax. Considering a pair of two strictly vertical aerial photographs, the x-parallax of a point is the algebraic difference of the distances of the two images from their respective photograph nadirs, measured in a horizontal plane and parallel to the direction of flight. Similarly, the y-parallax is the difference between the perpendicular distances of the two images of a point from the vertical plane containing the direction of flight. (Slama *et al.*, 1980)

B/H ratio[37] increased to 0.18. This allowed satisfactory height extraction in areas with 500 m relief (Ehlers & Welch, 1987). Qualitative evaluation showed good agreement with the map contour lines. Quantitative evaluation gave an error of about 45m when compared with Independent Check Points (ICPs). However, ICPs, being a limited number of well-defined features, are not a good statistical representation of the terrain. Landsat 7 ETM+ was studied by Toutin (2002) for DEM derivation, in a very challenging area (snow, clouds, glacier and shadowed mountains) with relatively good results.

The SPOT (Système Pour l'Observation de la Terre) satellite was launched in February 1986. It has the capability to provide across-track stereoscopic coverage by pointing the sensor ±26° off nadir. Because of this, SPOT satellites can generate stereopairs with *B/H* ratios between 0.6 and 1.2, thus meeting the requirements for topographical mapping. Under ideal conditions, spatial resolutions extracted from SPOT stereopairs can equal those obtained from a 1:10,000 scale topographical map with submetre vertical accuracies (Al-Roussan *et al.*, 1997). These excellent results from Jordan were due to highly accurate georegistration of a complete set of GCPs, and a relatively flat and homogeneous landscape. In complex mountainous area, DEMs produced from SPOT data resulted in an average error of 58 m, thus providing accuracies equal to or better than the DEM generated from conventional maps (Zomer *et al.*, 2002). From these two studies, it is worth noting that the more intense the relief in an area, the greater the error that is expected for any given determination of height. If the Earth's surface were completely flat, then the image would be exactly the same as a map. However, because of Earth curvature there is a scale difference from nadir to the edges of the image; secondly, there is relief, which produces a scale difference between points of different heights. And the bigger the distance (vertical or horizontal) one has to measure, the larger the resulting error.

In December 1995, the Indian IRS-1C was launched. Its panchromatic sensor, like the SPOT HRV sensor system, is pointable so that oblique views can be obtained for across-track stereoscopic imagery. The IRS-P5 is planned to be launched in 2004-2005, and it will have fore-aft stereo capability with two panchromatic cameras for acquiring along-track stereopairs.

[37] X-parallax has direct relation with the parallactic angle. If A and B are two points of the ground with B being higher than A, then the apparent displacement of B (because of the platform's movement) will be bigger. That is, the x-parallax of point B will be bigger. Thus, the x-parallax is related with the height of a point, and it is bigger for the high points, less for the low points.
Parallactic angle is called the angle subtended by the eye base of the observer at the object viewed. The bigger the parallactic angle, the less the error in determining relative heights from stereoscopic pairs. (Slama *et al.*, 1980)

The digital scanners with along-track stereoscopic coverage include JERS-1's Optical Sensor with a *B/H* ratio of 0.3, the German Modular Opto-Electronic Multi-spectral Stereo Scanner (MOMS) with capability of a *B/H* ratio of 0.8, the Advanced Spaceborne Thermal Emission and Reflection Radiometer (ASTER), the IRS-5P, and most of the high-resolution satellites such as OrbView and Quickbird. IKONOS has sensor-steering capability in both along and across-track directions (Toutin, 2001a).

In the past, there have been applications such as Welch *et al.* (1990) where imagery from different satellites is used for the creation of a DEM. Human interaction is required in these procedures to reject blunders or to fill the mismatch areas, in order to optimise the DEM results. In fact, the human brain can generate the perception of depth by combining the spatial resolution of SPOT and the spectral resolution of Landsat, for example.

In theory, it should be possible to extract DEMs from the CORONA-CORONA, CORONA-IKONOS and IKONOS-IKONOS stereopairs. The purpose is to assess these data for their capability for height extraction and to identify possible limitations. It is hoped to obtain information of sufficient quality to assist archaeology with the assessment of landscapes and landscape features such as wadis, 'river terraces' or even anthropogenic structures such as tells. From a CORONA-IKONOS stereopair, it may be possible to extract height differences, thus identifying landscape relief changes.

7.2. The sensor models

To rectify the relationship between image and object, which is of particular importance in image stereo analysis, sensor models are required. They are separated into two categories: physical sensor models, and generalised sensor models.

Physical sensor models represent the physical imaging process, and they need parameters such as orbital information, sensor, ephemeris data, Earth curvature, atmospheric refraction, and lens distortion to describe the position and orientation of the sensor with respect to an object's position. These parameters are statistically uncorrelated, as each parameter has a physical significance. Physical models are rigorous, such as with collinearity equations, and they normally produce a highly accurate model that can be applied to image stereo pairs.

Because they are sensor-dependent, it is not convenient for users to switch among different software packages or add new sensor models into their systems. And in some

cases, the physical sensor models are not always available. Without knowing the above-mentioned parameters, it is very difficult to develop a rigorous physical sensor model.

For these reasons, generalised sensor models were developed independent of sensor platforms and sensors. These involved modelling the transformation between image and object as some general function without the inclusion of the physical imaging process. The function can be in several different forms such as polynomials, and since they do not require knowledge of the sensor geometry, they are applicable to different sensor types and offer support to real-time calculations, which are used in military surveillance applications. Also, because of their independence from the physical parameters, they provide a mechanism for commercial vendors to keep information about their sensors confidential.

However, when using conventional polynomials, there is a tendency to oscillation, which produces much less accuracy than if using a rigorous sensor model. Thus, there was a need for the civilian and military satellite companies/agencies to develop a generalised sensor model with high accuracy and without a functional relationship to the physical parameters of the satellite. For this reason, the Rational Function Model (RFM) was developed.

The RFM is a generic form of polynomial models. It defines the formulation between a ground point and the corresponding image point as ratios of polynomials:

$$x = \frac{p1(X,Y,Z)}{p2(X,Y,Z)} = \frac{\sum_{i=0}^{m1}\sum_{j=0}^{m2}\sum_{k=0}^{m3} a_{ijk} X^i Y^j Z^k}{\sum_{i=0}^{n1}\sum_{j=0}^{n2}\sum_{k=0}^{n3} b_{ijk} X^i Y^j Z^k}$$

$$y = \frac{p3(X,Y,Z)}{p4(X,Y,Z)} = \frac{\sum_{i=0}^{m1}\sum_{j=0}^{m2}\sum_{k=0}^{m3} c_{ijk} X^i Y^j Z^k}{\sum_{i=0}^{n1}\sum_{j=0}^{n2}\sum_{k=0}^{n3} d_{ijk} X^i Y^j Z^k}$$

where x, y are normalised pixel coordinates on the image; X,Y,Z are normalised 3D coordinates on the ground, and a_{ijk}, b_{ijk}, c_{ijk}, d_{ijk} are polynomial coefficients. If we limit the polynomials to the third order ($0 \le m_1 \le 3$, $0 \le m_2 \le 3$, $0 \le m_3 \le 3$, $m_1+m_2+m_3 \le 3$), then the above equations can be re-written as follows:

$$row = \frac{(1 \quad Z \quad Y \quad X \quad ... \quad Y^3 \quad X^3) \cdot (a_o \quad a_1 \quad ... \quad a_{19})^T}{(1 \quad Z \quad Y \quad X \quad ... \quad Y^3 \quad X^3) \cdot (1 \quad b_1 \quad ... \quad b_{19})^T}$$

$$column = \frac{(1 \quad Z \quad Y \quad X \quad ... \quad Y^3 \quad X^3) \cdot (c_o \quad c_1 \quad ... \quad c_{19})^T}{(1 \quad Z \quad Y \quad X \quad ... \quad Y^3 \quad X^3) \cdot (1 \quad d_1 \quad ... \quad d_{19})^T}$$

The superscript T denotes a vector transpose. Ratios of first order terms represent distortions caused by optical projection; ratios of second order terms approximate the corrections of Earth curvature, atmospheric refraction, lens distortions and more; ratios of third order terms can be used for the correction of other unknown distortions with high order components (Tao *et al*, 2000). Grodecki (2001) offers a detailed explanation of the RFM.

The polynomial coefficients are called Rational Function Coefficients (RFCs) (Tao *et al*, 2000) or Rational Positioning Capability (RPC) data (Open GIS Consortium, 1999), and the imagery provider gives them to the user for the application of the model. They are also termed Rational Polynomial Coefficients (RPCs, a term used by SpaceImaging and Fraser and Hanley, 2003), while the RFM is also termed Universal Sensor Model (Open GIS Consortium, 1999). Dowman and Dolloff (2000) separate RFM and USM, considering USM to be an extension of the RFM. Like everything new, the terminology is not universal, but it varies according to whom is discussing the topic.

In the following paragraphs, the terms RFM (Rational Function Model) and RPCs (Rational Polynomial Coefficients) will be used, to be in accordance with the SpaceImaging terminology.

7.3. The IKONOS sensor model

SpaceImaging does not provide the physical sensor model to the users, thus keeping the ephemeris data confidential. Instead, RPCs are provided for the user to apply the RFM, but only with the relatively expensive Ortho Kit and Stereo products.

The number of the RPCs is stated:

> *"…equations require five offsets, five scale factors, forty coefficients for line, and forty more coefficients for sample. Those ninety numerical values are provided in text format with IKONOS stereo products…"* (Dial *et al.*, 2001).

The application of RFM in the rectification of the image-object relationship has been discussed among researchers, and even though it is useful and accurate with the IKONOS data, it is not possible to attain the accuracy and robustness of the rigorous

photogrammetric techniques, because with the RFM there is lack of complete and rigorous error propagation information (something that is offered by the rigorous photogrammetric techniques). With a bit more complexity in the calculations to improve the geopositioning performance, one can have a better error control (Dowman and Dolloff, 2000). It is widely accepted that the best way would be to include RPCs and then further correct with GCPs (Dial and Grodecki, 2002; Fraser *et al.*, 2002b; Tao *et al.*, 2002), or improve with GCPs (Lee *et al.*, 2002). Generally, and after long updates and discussions during email exchanges among researchers and during conferences such as ASPRS 2002, the RFM can be considered as an effective approximation of the physical model (Dowman and Tao, 2002).

As stated earlier, the RPCs are provided only with the relatively expensive Othro Kit and Stereo products. In our case, the Geo product of IKONOS imagery was acquired and so there are no RPCs included in the metadata file. Hanley and Fraser (2001) managed to achieve very good results (sub-pixel accuracy) in 2D space without the use of the RFM. Fraser *et al.* (2002a) extended their work to 3D space where again sub-pixel accuracy was achieved. This achievement rests mainly on the inclusion of highly accurate GCPs, something that was not available for the Homs area in Syria.

Valadan Zoej and Sadeghian (2003) use an approximated orbital parameter model from metadata, image file and celestial mechanics. The results showed better performance than the generalised sensor models under optimum conditions (large scale maps, abundance of hard points). Toutin (2003) analysed the same method developed in CCRS (Canada Centre of Remote Sensing), called 3D parametric model. Using either of these methods, there is need for GCPs.

In the Homs project, the IKONOS Geo product is not provided with RPCs, and there are no GCPs. Actually, the IKONOS imagery is used as a basemap to which all other spatial data are registered to. The RPCs cannot be calculated since the ephemeris data are not published, and due to local military sensitivity GCPs cannot be established at a sufficient degree of accuracy.

7.4. Preprocessing

Chapter 4 discussed the preprocessing stage of CORONA space photography. The scanning of the images plays a vital role in this stage, since it is important to provide the best possible digital representation of the ground resolution of the imagery in order to reduce the possible errors. It also discussed the geocorrection of the imagery; that is the

correct placement of the imagery in a known coordinate space. In chapter 7, the objective is to construct a stereopair; that is the correct placement of two images in space by restructuring the interior and exterior orientation. The images will be in raw unregistered format before the stereopair construction. According the ERDAS LLC (2002), the suggested resampling method is bilinear interpolation when the DEM pixel size is much greater than the image cell size. There are two methods to achieve the construction of the stereopair.

The first method uses the parameters from the ephemeris data of the satellite to reconstruct the stereopair. However, as noted in chapter 4, the ephemeris data for CORONA are not available or are very difficult to obtain. For this reason, estimations of the physical model data were done, and this method was tried. Concerning IKONOS, there are neither ephemeris data, nor RPCs available. Thus this method will not be applied to IKONOS imagery.

The second method uses 'suitable GCPs' identified in the imagery with the use of the IKONOS imagery as a 'reseau plate'[38]. In other words, there are many distortions in CORONA geometry but in IKONOS Geo product the distortions are much less (always depending on the viewing angle and the relief of the ground), and the imaging system is free of significant non-linearities (Fraser *et al.*, 2002a). Thus, by registering CORONA to IKONOS, the CORONA geometry distortions are much decreased. There is also a need to generate height information for GCPs, something that is not included in the IKONOS imagery. For this, the 1:25,000 maps were registered to IKONOS, and after registration the heights were sampled from the contour lines. This assumes that the contour lines were produced accurately.

Concerning IKONOS, there are no GCPs to use for the application of any of the generalised sensor models discussed in paragraph 7.3. For this reason, the stereopairs where IKONOS imagery is included cannot be created, due to a lack of vital information.

The stereo potential of CORONA can be seen from the high ground resolution and the *B/H* ratio. The ground resolution reaches 1.8 m in KH-4B design and this improves the detectability of GCPs. With simple triangulation, one can easily show that the *B/H* ratio of CORONA is 0.54, very near the suggested lower limit of 0.6 needed to meet the requirements of topographical mapping (Slama *et al.*, 1980). The *B/H* ratio in the

[38] A glass plate on which is etched an accurately ruled grid. Sometimes used as a *focal-plane plate* to provide a means of calibrating film distortion; used also for calibration of plotting instruments. (Slama *et al.*, 1980)

IKONOS-IKONOS stereopair is 0.12, with the images taken from nominal elevation angles of 67.22° and 76.37°. In this pair, there is in the across-track direction a small overlap, forming a long strip about 2 km wide and 20 km long crossing the southern part of the area of interest from North to South.

In the mixed stereopair of CORONA-IKONOS, the geometric set up gets complicated since the images are not along- or across-track, but there is a horizontal angle between them. The *B/H* ratio is difficult to calculate because of the different altitude of the two satellites.

The only CORONA mission to offer a stereopair for the area of interest was mission 1110. For this mission, the overall image quality is less than that provided by other missions before 1110, and 2000 feet of S0-349 (new film) was spliced into the regular film[39]. According to Peebles (1997) the orbit details are: inclined 83.00°, period 88.62°, perigee 162 km, apogee 247 km. Table 7-1 summarizes the mission details. Table 7-2 gives details of the stereopairs, while figure 7-2 shows the part of the filmstrip where the area of interest is located. By comparing to figure 4-4, one can imagine the inclusive distortions of the panoramic space photography for the area of interest.

Table 7-1 – Image data for the stereopair creation

Sensor	ID Scene	Date
CORONA	DS1110-1106DF007, -008, -009	28/05/70
	DS1110-1106DA013, -014, -015	28/05/70
IKONOS	2002020308234080000011610756, -7	03/02/02

Table 7-2 – The stereopairs that can be derived from the image data

Sensors	Forward	Aft	Area	Date
CORONA-CORONA	007	013	North	28/05/70
	008	014	Centre	
	009	015	South	
IKONOS-IKONOS	756	757	South central	03/02/02
CORONA-IKONOS	009	757	South-East	28/05/70-03/02/02
	756	015	South-West	

[39] http://edc.usgs.gov/guides/disp1.html (Accessed: May 2004)

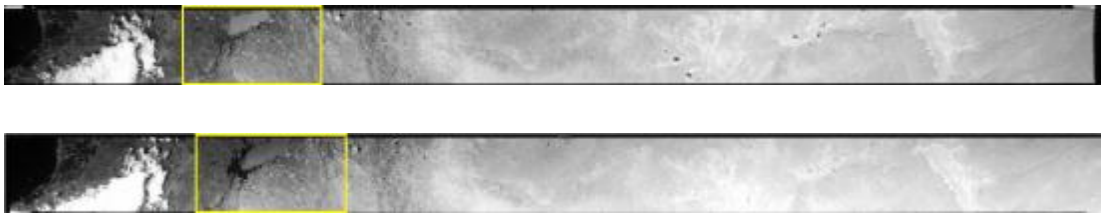

Figure 7-2 – CORONA images / filmstrips

The CORONA-CORONA pairs have almost 100% along-track overlap, and so it is not necessary to show this diagrammatically. In figure 7-3, one can see an illustration of the IKONOS-IKONOS and CORONA-IKONOS pairs, along with the angles of collection elevation (polar coordinates) and collection azimuth, and the scan directions.

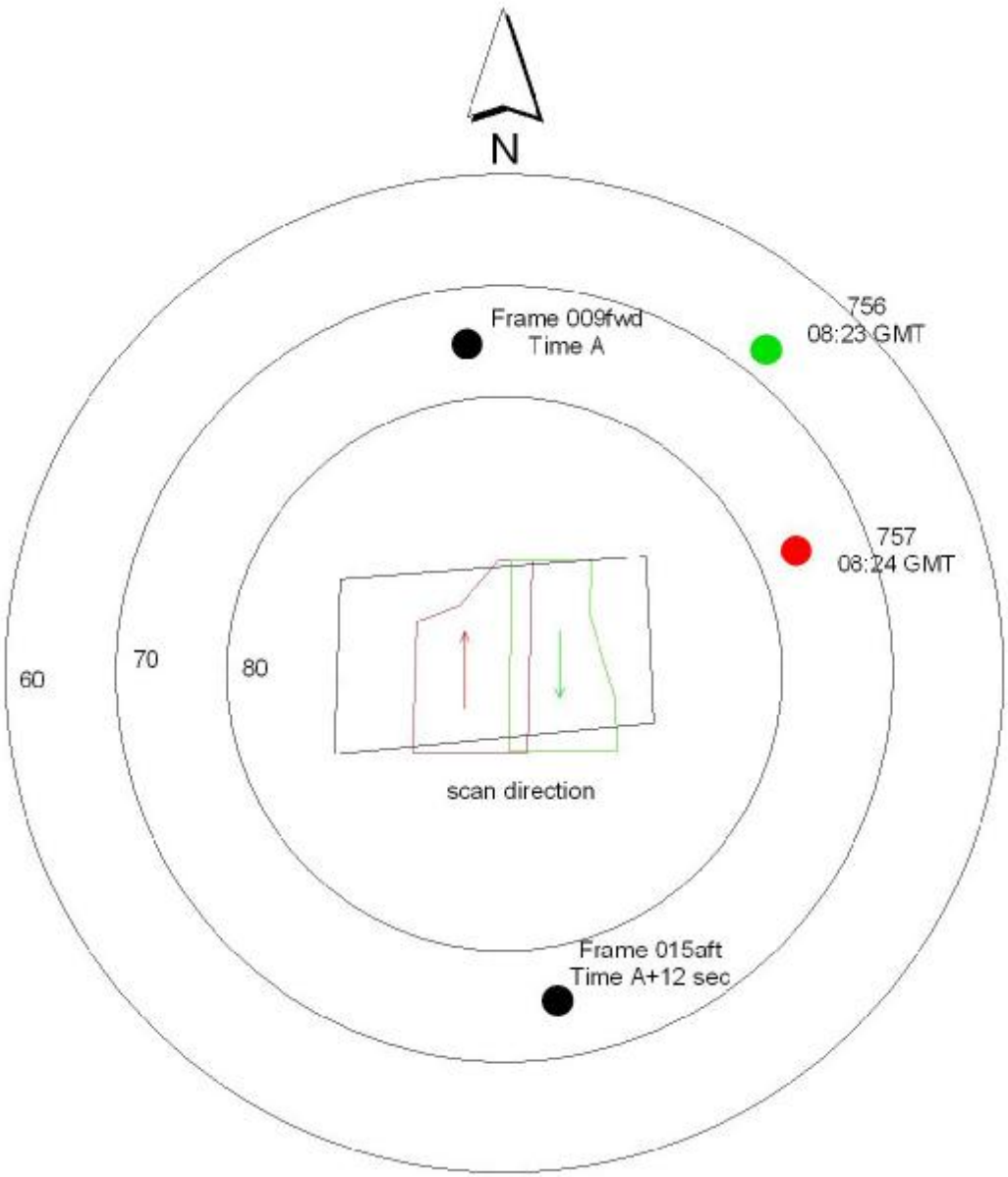

Figure 7-3 – Diagram showing the directions and angles of the south area pairs

The values displayed in figure 7-3 are shown in table 7-3. However, there is need to explain about what each value is. Concerning CORONA, all values are explained in chapter 2 and there is no need for further explanation here. Concerning IKONOS, the *scan azimuth* indicates the direction of scanning. The main values met in metadata are 0° (or near 0°), which indicates that the scene was scanned from south to north, and 180° (or near 180°), which indicates that the scene was scanned from north to south (Lutes, 2004). The *scan direction* could be also called *scan mode*. When the scan mode is 'reverse' then the scan and the orbital velocity vectors are pointing roughly at the same direction. When the scan mode is 'forward' then the scan and the orbital velocity vectors are pointing in the opposite directions (Grodecki *et al.*, 2003). The collection azimuth is defined by the angle between the North and the projection of the line of sight from target to the satellite onto the horizontal plane. It is measured clockwise from the North. The collection elevation is the angle from the horizon up to the satellite (Grodecki and Dial, 2001).

Table 7-3 – Directions and angles of CORONA and IKONOS imagery of the project

IKONOS	Scan azimuth	Scan direction	Collection azimuth	Collection elevation
756	179.97°	Reverse	38.3713°	67.22347°
757	359.96°	Forward	67.8092°	76.36649°
CORONA	Camera looking	Scan direction*	Orbit inclination	Sensor elevation
009fwd	Backward	Anticlockwise	83°	74.77°
015aft	Forward	Clockwise	83°	74.77°

*Looking from behind the satellite.

In the 'reverse' mode, the collection azimuth and the collection elevation angles can be assumed to be constant for the entire image strip. In the 'forward' mode, the result of the opposite directions of scan with velocity is approximately one degree per second rate of change of the collection elevation angle (Grodecki *et al.*, 2003). For this reason, the metadata angles of the 'forward' mode should not be used for orthorectification or other geometric corrections. However, Grodecki & Dial (2001) consider the metadata angles accurate enough for remote sensing analysis purposes such as topographic normalisation.

Jacobsen (2003) produced DEM from IKONOS Geo imagery of different viewing angles and a B/H ratio of 0.13. However, he did not mention the scan mode of his imagery in the paper. Also, to achieve satisfactory results, he had to use 79 GCPs and a couple of point shifts.

The Homs area is relatively flat, without intense relief, with intense agriculture and a lot of human intervention and development. The minimum height is approximately 400 m and the maximum 600 m in an area of about 700 km^2. This helps to improve the accuracy of the DEM, but it demands the detection of small height differences.

7.5. Software and Processing

For the two methods of height data extraction mentioned above, two software packages were used: Socet Set and ERDAS Imagine. Socet Set was chosen for the rigorous approach because in the package there is a panoramic camera model with all necessary algorithms. For the application of the algorithms, there is need for ephemeris data, which will be approximated. ERDAS was chosen for the non-metric camera approach and the user-friendly environment. The non-metric camera approach is empirical. In ERDAS, it needs only the focal length and the scanning resolution of the film (the pixel step). However, the non-metric camera approach was also tried in Socet Set for comparative purposes. Here, the only demand was for the number of image lines and samples.

Other remote sensing or photogrammetry software could be used as well. For example, Case (1967) describes the use of many Instantaneous Equivalent Frame Photographs to substitute the panoramic photograph, Kawachi (1966) describes the distortions of panoramic photography and its image motion compensation, and Slama *et al.* (1980) give algorithms for the correction of distortions in CORONA imagery.

7.5.1. Rigorous panoramic camera model approach

The purpose of the Softcopy Exploitation Tool Set (Socet Set) software is to support image-based softcopy applications such as map-making, mission rehearsal, and photo-interpretation. Socet Set generates databases and products such as Digital Terrain Models (DTM), reports, vector databases, orthophotos, image maps, and image mosaics.

The first thing one must do in Socet Set is create a project, show the software where the imagery is located, and arrange the coordinate system. Then, the user must import the imagery. Socet Set imports *sensor models*. A sensor model is a function that transforms from three-dimensional ground space into image line and sample space. The input to the function is a ground point and the output is an image point. Every sensor

type has a unique sensor formula that reflects the physical characteristics of the sensor. Every image has unique sensor model parameters that reflect the location and orientation of the sensor at the time the image was collected. The sensor models used by Socet Set are *rigorous*, meaning that the functions are exact projective computations, rather than approximations (such as polynomials). Socet Set supports the *panoramic sensor model* with compensation for the sensor movement. A panoramic camera can be imported and is modelled as a cylinder.

Thus, in the first window, the user must enter the image name, the photo data, the camera calibration parameters, and the camera location parameters. The user can also choose to apply corrections for atmospheric refraction, but whenever this option was chosen the software could not align the images.

In the photo data window, the user inputs the image size in mm. By using appropriate sign combinations, the user can rotate the image. In our case, the scanning resolution is 7.5 μm. In the photo data window, Socet Set displays the image size in pixels. From this, it is easy to define the image size in mm, just by multiplying the number of pixels by 0.0075 mm.

In the camera location window, the software asks for a number of parameters, which can be found in the ephemeris data of CORONA. However, as mentioned in chapters 2 and 4, the ephemeris data are not available or not easily accessible and so it is necessary to use some best approximation data taken from published sources and to calculate the rest.

In this model, the parameters needed are focal length (609.602 mm, [NRO, 1967a]), scan rate (35.5 degrees/sec, [Madden, 1996]), start and end scan angles (angle in decimal degrees of the first/last scan line relative to the centre aim point. A positive angle is to the left of the camera; negative to the right), pass designation (descending, [Peebles, 1997]), orbit inclination (83 deg. [Peebles, 1997]), orientation angles ({omega, phi, kappa} or {heading, roll, pitch}), mounting angle ({omega, phi, kappa}={0, ±15.23, 0}, [McDonald, 1997]), location ({X/Lon/Easting, Y/Lat/Northing, Elevation}). From all these parameters, there is need to calculate the start and end scan angles, the orientation angles, and the location. Other parameters are known from published sources.

The start and end scan angles were calculated from measures on film.

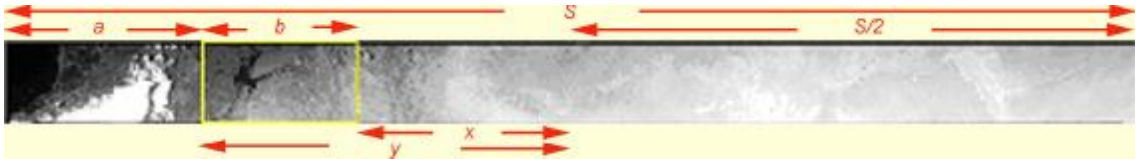

Figure 7-4 – Start and end scan angles measurements.

The film distance ***b*** was measured straight onto the scanned image by measuring the number of pixels and transforming it into cm. The film distance ***a*** was manually measured onto the film. The distance ***S*** was measured onto film, and found to be the same for all films in the application, 75.5 cm. Thus, from the above it is easy to calculate the film distance ***x***, from the equation $x = S/2 - a - b$, and film distance ***y*** is similarly defined. To transform the centimetres into degrees, one must know the scan angle of the film. McDonald (1997) defines a precise number for the camera scan angle, 71.16°. Thus, it is easy to define the start and end scan angles.

For the camera location parameters, one should separately calculate the Northing/Easting from the elevation. For the elevation parameter, some objects near the centre of the filmstrip (where the scale distortions are less) were used. The size of the objects was measured on the ground and on the image. Thus, different scales were defined. By averaging, one could easily calculate elevation from the equation: $f/H = 1/R$, where f is the focal length, H is the elevation, R is the defined scale.

For the Northing/Easting parameters, with the use of triangles (known data are start-end scan angle, tilt angle and height), one can calculate the horizontal distances $C_S C_O$ and $C_O C_A$, where C_S the centre of the scanned part of the film, C_O the centre of the film strip, and C_A the camera position. Then, with a simple system rotation (with the use of orbit inclination angle), one can calculate the Northing/Easting difference of the C_A from the C_S.

One of the key inputs to the import process is the camera orientation. This is generally expressed as three angles: omega, phi, kappa; or heading, roll, pitch. In the case that there are no orientation angles provided with the photo, one could either let Socet Set estimate them during the triangulation process, or estimate heading and roll just by looking at the photo. Pitch is very hard to visualise and is usually set to zero.

For the camera calibration parameter, the user can input the information of focal length and primary points in a file, and load it in the import process.

After the import process, the user can choose to use (or not) GCPs in the triangulation stage. The triangulation setup is used to define the triangulation job. Strip and image information can be entered here. The next step is the point measurement, which can be automatic or interactive. And the last step is the initialisation and solution of the triangulation process.

Summarising, the required data needed for the SocetSet panoramic camera model are shown in Table 7-4:

Table 7-4 - Parameters needed in SocetSet panoramic camera model

Field	Description
Focal length (mm)	Focal length in millimetres. 609.602 mm in CORONA.
Scan rate	Camera sweep rate in degrees per second. 35.5 in CORONA
Start scan angle End scan angle	Angle in decimal degrees of the first scan line relative to the center aim point. A positive angle is to the left of the camera; negative to the right.
Pass Designation	Direction of the sensor's orbit. Orbits crossing the equator north to south have a descending designation. "Descending" in CORONA mission 1110.
Orbit inclination	Inclination of the sensor's orbit in decimal degrees relative to the equator. 83 degrees in CORONA mission 1110.
Orientation angle	See discussion above.
Mounting angle	Angle of the camera relative to the platform. (0, ±15.23°,0) in CORONA.
X/Lon/Easting Y/Lat/Northing Elevation	Camera position in the project ground coordinate system. See discussion about calculation above.

*Information is taken from SocetSet user's manual. CORONA data are taken from Madden (1996), Peebles (1997), NRO (1967a), McDonald (1997).

The author would like to thank Dr Jon Mills for allowing access to the Geomatics lab facilities of University of Newcastle. Also, the author would like to thank Bob Taft of Leica-Geosystems for providing the panoramic camera module of Socet Set.

7.5.2. Empirical non-metric camera model approach

ERDAS OrthoBase is a module included in the ERDAS Imagine software. Like Socet Set, it includes sensor modelling, to establish the internal characteristics associated with a specific camera or sensor with its main purpose being the orthorectification of the imagery. However, there is no panoramic camera model, thus the only choice was the usage of the non-metric camera model for CORONA space photography. In the case of IKONOS, a new sensor model was included in the ERDAS

Enhancements of ERDAS Imagine 8.5 for the users, and it is included in ERDAS Imagine 8.6 standard installation package.

Prior to performing any tasks in ERDAS OrthoBase, a *block* must be created. *Block* is a term used by ERDAS Ltd. to describe and characterise all of the information associated with a photogrammetric project (i.e. Coordinate system, sensor model, imagery, GCPs, geometric relationships, etc.)

In the non-metric camera model, the minimum requirements are an approximate focal length and the scanning resolution used to digitise the film. The coordinate system is defined according to the GCPs. Pyramid layers[40] must be created. Thus, pan and zoom will be quick procedures and the drawing speed will increase. The next step is the point measurement; that is the GCPs and their image positions.

The most difficult task was to allocate common points between the IKONOS imagery and the CORONA imagery because of the 30 years time difference and changes to the cultural landscape. It was also difficult to find common points between the maps and the IKONOS imagery. The first step was registration of CORONA to IKONOS and maps to IKONOS with the use of the Geometric Correction tool of ERDAS Imagine; thus identifying the GCPs. The height information was derived from the maps, using simultaneous display of the three data sources (maps, CORONA, IKONOS).

Afterwards, it was straightforward to put the same points in the CORONA imagery and create a first approximation of the geometric relationship between the image and the ground. Main purpose is the usage of IKONOS as a 'reseau plate', as explained earlier in this chapter. The next step was the automatic tie point creation, which produced excellent results (See following paragraphs).

However, ERDAS OrthoBASE does not create a DEM and it is not possible to 'visualise' the stereo model. For this purpose, the Stereo Analyst module of ERDAS Imagine was used. The block file was imported into Stereo Analyst and it was possible to display the stereo model as an anaglyph image in red-blue colours, and visualise it with red-blue glasses. Stereo Analyst allows the user to extract the height information for any point of the stereo model. Thus, it was possible to assess the quality of the height information.

[40] Pyramid layers are coarser copies of an original image. The coarsest level of resolution is used to draw the entire data set. As the display zooms in, finer layers of resolution are used. Drawing speed is maintained because fewer pixels are needed to represent overviews of large areas.

7.6. Results

7.6.1. Panoramic camera approach results

At the outset, it was impossible to import the imagery. The reason was that the atmospheric refraction algorithm was *on*. Once this was switched to *off* mode, the images were successfully imported. The internal orientation was resampling the image to 1 m pixel size, this resulted in the image not being recognised by the triangulation process. Therefore, the internal orientation was not used.

The best results using the rigorous approach gave a uniform error of around 160 pixels to all points of one image and about 20 pixels to all points in the other image. In particular, the total RMSe was about 20m in each direction but the specific residuals were more than 1,000 m! The reasons for this error are unknown. The uniformity of the error made me think that perhaps the difference in the size of the scanned images was of importance. But this is unlikely to be the case, since the software itself indirectly recognises the fact that the images can have different size. Thus, it is possible the error comes from the panoramic camera parameters. The nominal values of some of the parameters, plus the lack of orientation angles can play an important role in the final errors. Unfortunately, the algorithms of the panoramic model used by Socet Set are not known, thus it was not possible to search for the source of such an error.

After personal communication with Pournelle and Hunt (2002) who tried all available models (even SocetSet), it seems that the available panoramic film models, like those for frame cameras, presume boundaries on altitude and incidence angles that cannot work for orbital satellite platforms. Thus, the models presume a trapezoidal reprojection, which is not the case of CORONA. However, orthorectification seems to be the solution, because this is what the U.S. Government was using for the CORONA imagery (Pournelle and Hunt, 2002).

The creation of the stereopair was limited to the south area (stereopair 009-015). There was no attempt to produce a stereopair in the central and northern areas.

This approach should be tried again with other CORONA imagery from an area where ground control is available and reliable. Thus, there will be more certainty as to the use of the panoramic model and the results.

7.6.2. Non-metric camera approach results

The results from ERDAS OrthoBase gave small errors and the resulting stereo images seemed of good quality. The CORONA images came from the 1110 mission, and formed three stereopairs, the 007-013, 008-014, and 009-015. Apart from the stereopairs, a strip of CORONA images was tested with poor results. In all stereopairs, the GCPs were sampled many times, until a satisfactory RMS error value was obtained. All tables with RMS errors are included in Appendix V.

7.6.2.1. Stereopair 007-013.

This stereopair covers the North part of the area of interest, which is the most 'changed' part of our area. Thus, it was difficult to allocate GCPs. Moreover, the IKONOS imagery covered only the south part of the stereopair, thus offering ground control in only a part of the stereopair. However, the RMS error is not very high. In figure 7-5, the triangles represent the ground control points and the squares the tie points. A tie point is a point whose ground coordinates are not known, but is visually recognisable in the overlap area between two or more images.

Table 7-5 – Triangulation Report Summary 007-013

Residuals – 12 control points			Residuals - 26 points	
mX	mY	mZ	ImageX	ImageY
2.7573 pixels	2.7965 pixels	1.9954 pixels	1.1988 mm	1.1719 mm

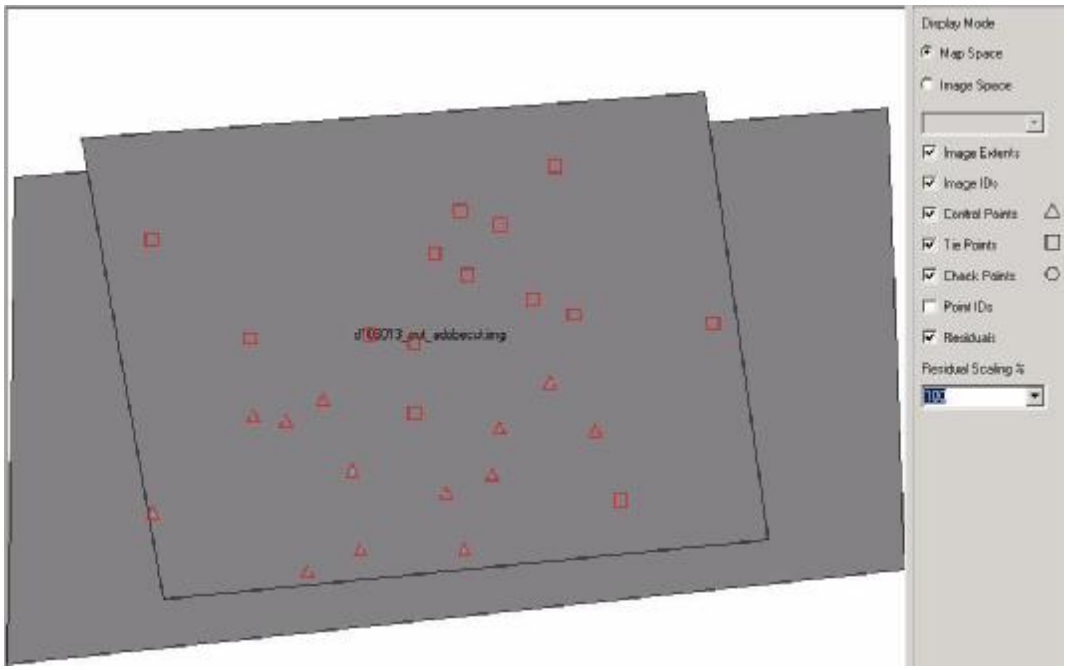

Figure 7-5 – Distribution of GCPs and tie points in 007-013 stereopair

7.6.2.2. Stereopair 008-014.

The stereopair 008-014 covers the south part of the North area of interest, and the north part of the South area of interest. Thus, there is no ground control in between the two areas. To improve the results, some ground control was sampled from the registered to IKONOS images. In figure 7-6, the GCPs on the top and bottom parts of the imagery are derived directly from IKONOS. The GCPs in the middle come from registered CORONA images. The blue lines (seen at the bottom triangles) represent the distribution of the error.

Table 7-6 – Triangulation Report Summary 008-014

Residuals – 15 control points			Residuals - 30 points	
mX	mY	mZ	ImageX	ImageY
2.2204 pixels	4.7820 pixels	5.4893 pixels	2.2562 mm	2.3988 mm

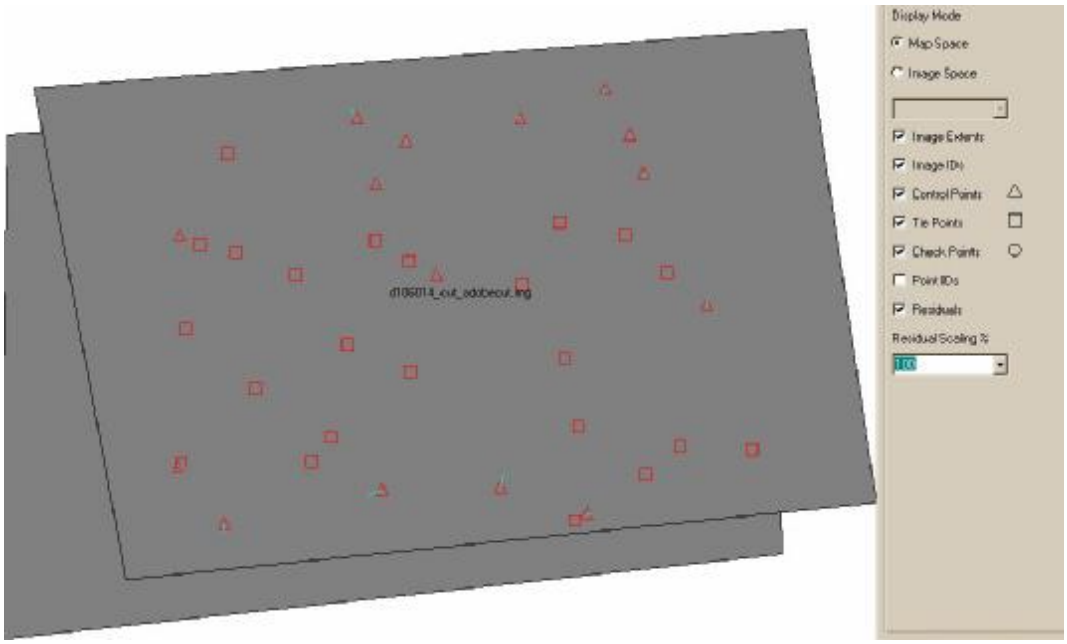

Figure 7-6 – Distribution of the GCPs and tie points in 008-014 stereopair.

7.6.2.3. Stereopair 009-015

In stereopair 009-015, the South area of interest is covered. The north-west part of the images is covered by Lake Qatina, and so there is no ground control there. In figure 7-7, the distribution of the points is shown.

Table 7-7 – Triangulation Report Summary 009-015

Residuals – 17 control points			Residuals - 34 points	
mX	mY	mZ	ImageX	ImageY
5.3475 pixels	6.5942 pixels	1.0211 pixels	0.5233 mm	0.5226 mm

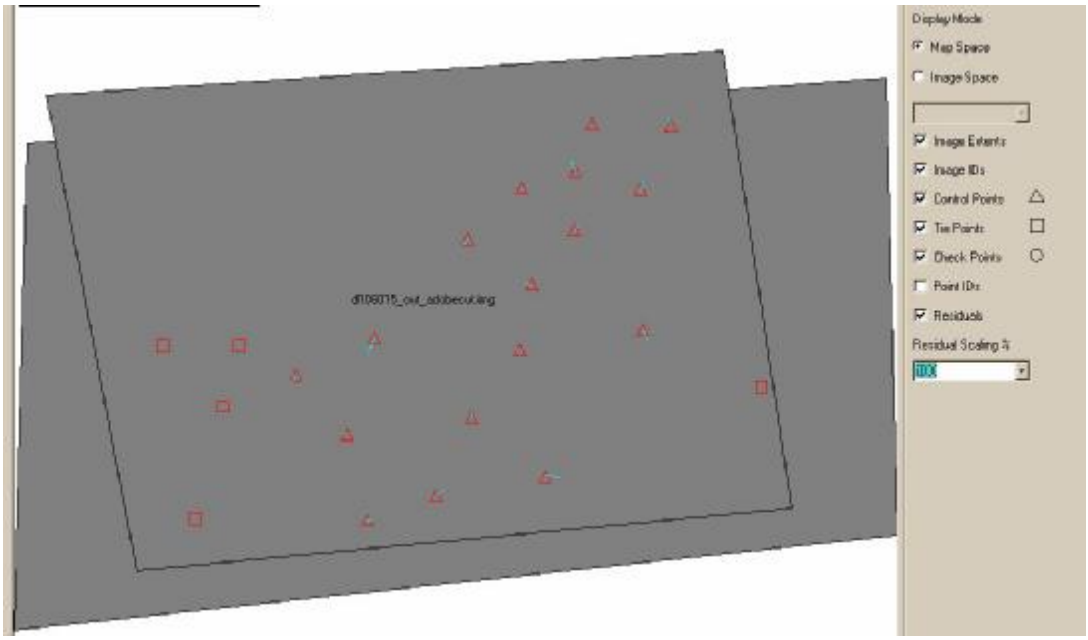

Figure 7-7 – Distribution of GCPs and tie points in 009-015 stereopair.

7.6.2.4. Strip of CORONA images

A strip of photographs consists of images captured along a flight line, usually with a minimum overlap of 60%. For the CORONA strip of images to be used, there is the assumption that all photos are captured at approximately the same flight height and with a constant distance between exposure stations. In general, CORONA successive images usually have an approximate 8-10 % overlap along-track, at the centre. There are examples of CORONA imagery with more than the 8-10 % approximate overlap. For example mission 1041, where due to the failure of the booster cut-off switch, the satellite went into a highly eccentric orbit, which resulted in significant image degradation (Peebles, 1997). Simultaneously, the different orbit resulted into more overlap between the images of the same camera. For KH-4B in particular, the overlap at the centre of successive images is 7.6 % (NRO, 1967a; Ondrejka, 2000), and the FMC (Forward Motion Compensation) system was made to maintain constant overlap. It should be noted that during the 1960s there was no interest in the creation of a strip, but mostly an interest in a good *B/H* ratio, in combination with the other advantages of panoramic camera (spatial resolution, swath width). Also, the images should contain as little redundant information as possible for film economy. To achieve this, the aft and forward tilted camera design was used, and the angle was chosen to allow a near-100 % overlap in the stereopair.

Table 7-8 – Triangulation Report Summary strip

Residuals – 43 control points			Residuals - 98 points	
mX	mY	mZ	ImageX	ImageY
9.1609 pixels	18.5102 pixels	15.0687 pixels	9.1985 mm	8.6691 mm

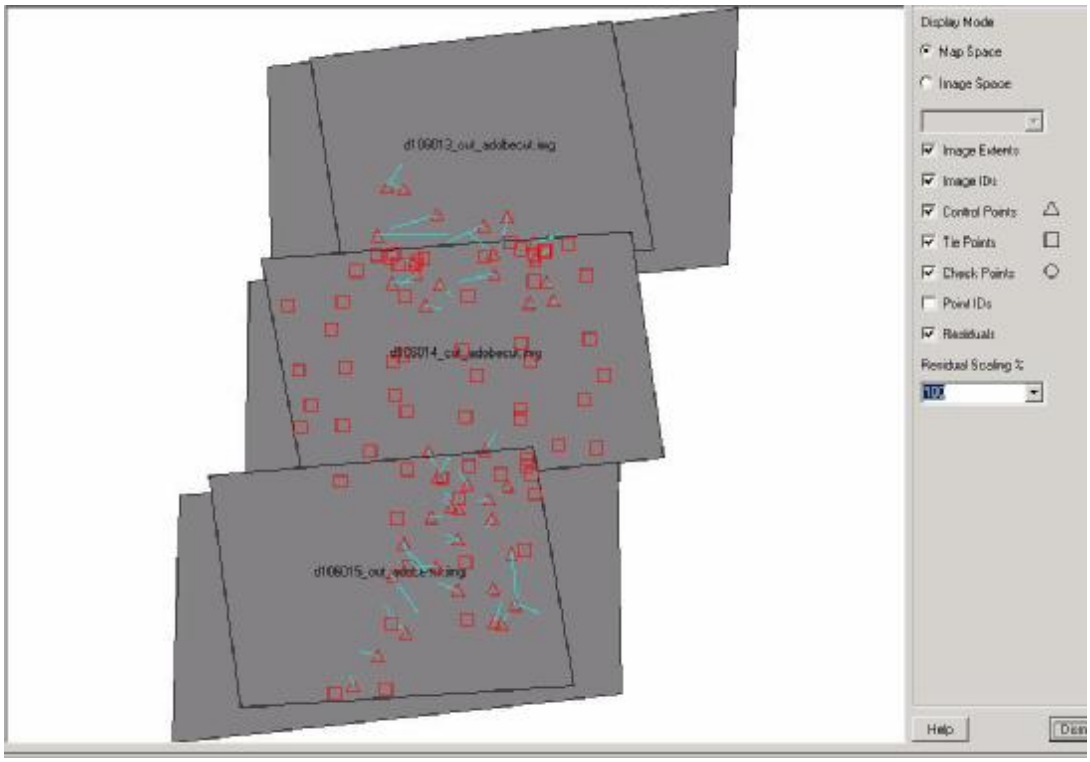

Figure 7-8 – Distribution of GCPs and tie points in the strip stereopair.

However, the overlap changes across the flight line because of the Earth's curvature (the bow-tie shape of CORONA imagery on the ground – see chapter 3). To calculate the overlap for every location on the CORONA imagery, one must use the equations of Slama *et al.* (1980), p. 943 and the parameters of the CORONA KH-4B and KH-4A panoramic camera systems coverage given in NRO (1967a) and NRO (1967b) respectively. After performing these calculations, the overlap of successive CORONA images is 9.40-9.47% at the edge (depending on the satellite's altitude, calculated for altitude 80-120 nautical miles).

The particular parts of the CORONA film used in this research showed the overlap to fall between 7.6% and 9.4%, which is not a lot, but a strip of images was tried with the results presented in table 7-8. In figure 7-8 the blue lines represent the combined errors in X and Y directions. The larger are the lines, the larger is the error of the particular point. Point shifts and outliers removal did not improve the situation.

7.6.3. Illustrations

The following illustrations were produced after loading the block file of OrthoBASE into the Stereo Analyst module of Erdas IMAGINE. The North is towards the left part of the illustrations. For viewing the anaglyphs, glasses may be found in an envelope at the end of the thesis. Initially, OrthoBASE Pro was not available, and it was not possible to automatically produce a DEM. Thus, the stereo analyst was used for a qualitative assessment of the DEM, and for photointerpretation purposes. The left image was put in red colour mask and the right image in blue-green colour mask. With a proper pair of 3D-glasses, the reader will be able to see 3D in the following illustrations.

The captions guide the reader from the easiest feature to see to the hardest to see. Illustration 1 shows Tell Nebi Mend, the largest of tells in the area. But apart from the tell (that the reader should easily see), there are other distinctive features in the area. For example, the riverbanks may be interpreted, and there are two smaller tells and another village whose houses show up.

Illustration 2 shows a factory next to the river that has tall buildings in comparison to low buildings of a nearby village. Illustrations 3 and 4 display archaeological features of smaller size. While in illustration 3 the tell depth is distinguishable, in illustration 4 is very difficult to 'see' the heights of the walls and cairns, even though they are detectable because of their contrast with the surrounding soil.

A comparison with the maps side-by-side would not prove fruitful because the human eye perceives much more than is seen in topographic maps.

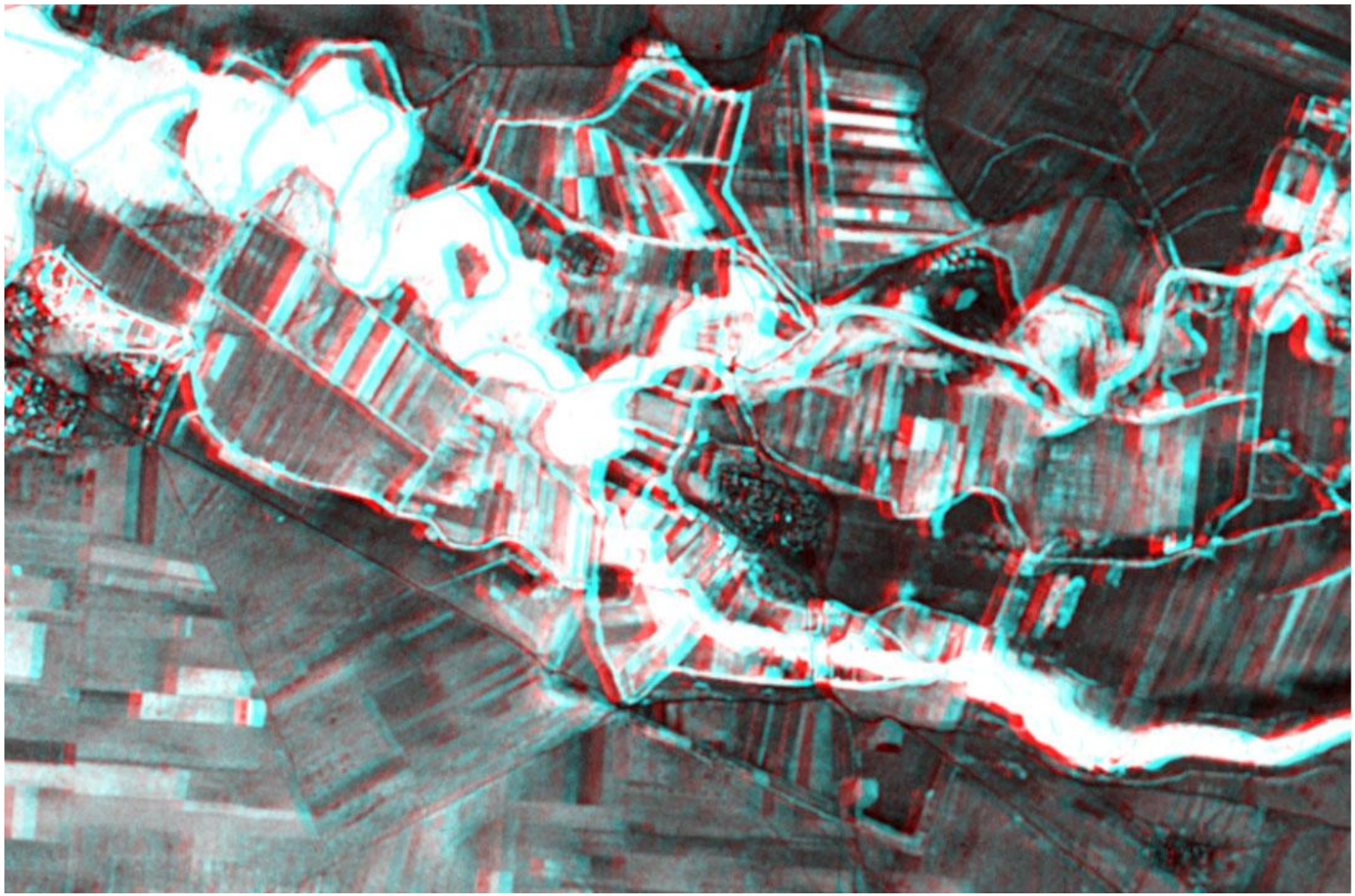

Illustration 1 – This image shows a 30m high tell, which can be very easily identified. The light toned linear feature towards top left of the tell is a deep trench left by an archaeological excavation from the 1920s. The tell is called Nebi Mend (ancient Kadesh). Also, a wall of Roman town can be seen forming a square at the west of the tell.

Illustration 2 – This image shows tall buildings from the village Qatina and the nearby factory standing out from the otherwise flat landscape. The factory produces fertilisers for the farms, and it pollutes the lake with chemicals. The square area at the southwest of the village is the construction of another factory, which is visible in modern IKONOS imagery. Also visible is a water channel at the far north of the image, the dam at the end of the channel, and a tell west of the factory, within the lake.

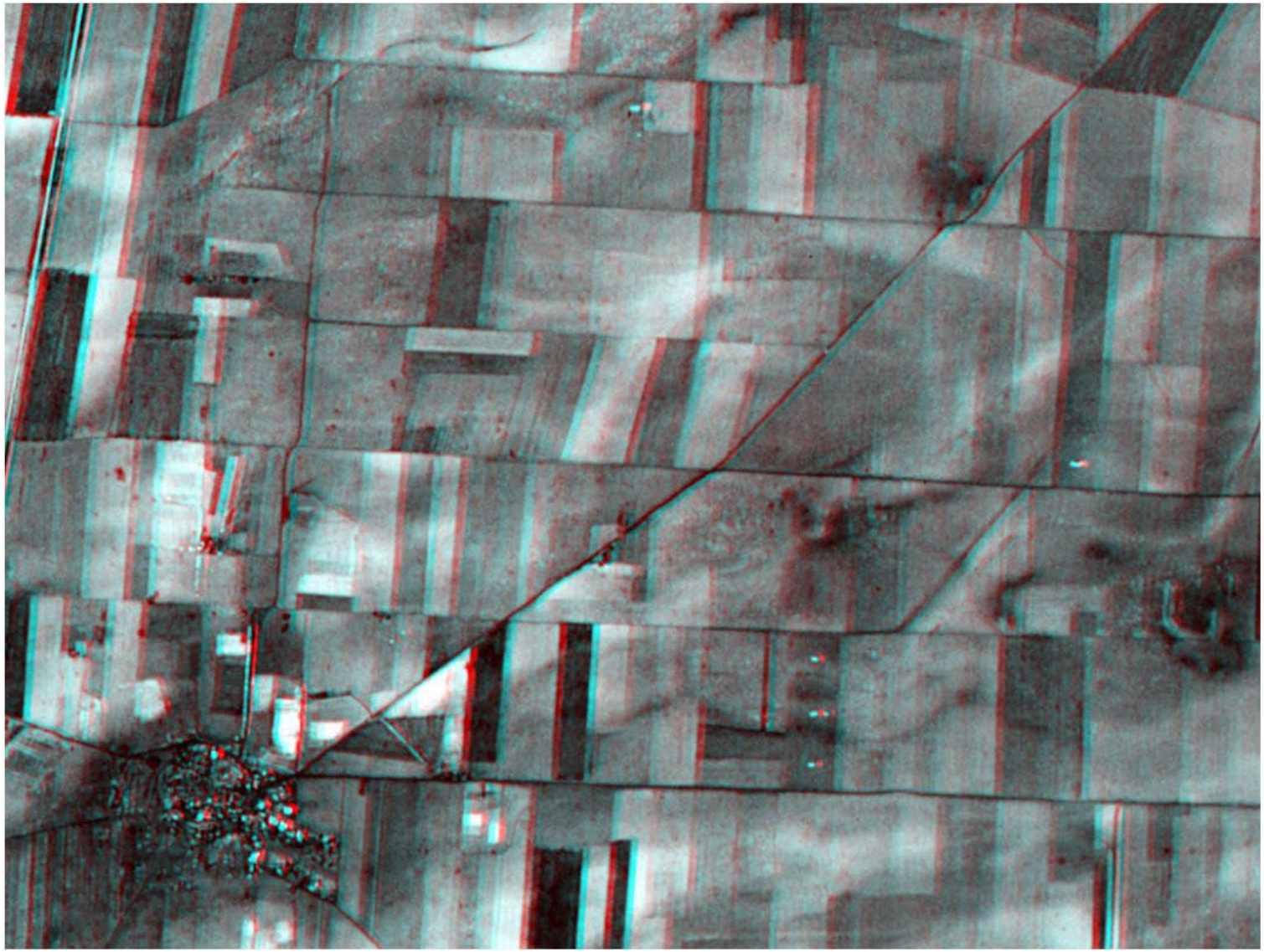

Illustration 3 – This image shows more subtle topographic characteristics: a smaller tell, and the village of Al Mubarakiyah. The lower right hand side of this image shows a horseshoe shaped tell. The bright line around its top is a military track. The landscape is mostly flat, and such imagery scale cannot depict small height differences.

Illustration 4 – This image displays the North part of the area of interest. This is a network of walls separating the fields, and cairn-like structures within the fields, made of basalt stone. Their height varies from 0.50m to 2m. Although they can be detected, it is not possible to see their 3D structure. This is because of the scale and the limits in the capability of CORONA to detect.

7.7. Discussion

This chapter presents an analysis of the stereoscopic potential of CORONA and IKONOS Geo imagery. Because of the lack of GCPs and RPCs, and the lack of ephemeris data, it was not possible to produce a DEM from the IKONOS Geo imagery. Thus, the project proceeded to create a DEM and to extract height information from CORONA data. The GCPs were taken from IKONOS (the horizontal values) and the contour lines from published Syrian maps (the height values).

To achieve this, two methods were tried. A rigorous approach with an existing software model specialised in panoramic camera and an empirical approach with a non-metric camera model.

The rigorous approach needed specific ephemeris data that are not available or very difficult to obtain. Thus, they could only be approximated and calculated with the help of existing information and metadata. However, the triangulation RMSe was not within acceptable limits, and no matter what was done, the rigorous approach was problematic. It seems that the existing panoramic models are restricted to aerial photogrammetry approaches and they do not take into consideration a space mission. This means that the underlying algorithms should be updated to include the space borne panoramic cameras.

The empirical approach had minimum requirements of focal length and scanning resolution. These requirements were both available. With the use of IKONOS as a reference system, the CORONA stereopairs were created, and thus the DEM could be automatically or manually extracted. The RMSe was smaller than the image registration RMSe discussed in chapter 4. This shows that the orthorectification process gives more accurate results than simple image registration. This is mainly due to the inclusion of height data in the ground control. The triangulation reports are presented in Appendix V.

The strip of CORONA images was not successful even though point shifts and outliers removals were tried. The reason for this is the shortage of ground control in the overlapping areas and the relatively small overlaps. Generally it would be much better if a strip could be formed instead of three stereopairs, because there would be control on the extracted heights and a control-connection between the three stereopairs.

The ability of CORONA imagery to detect archaeological features based on height information is displayed in the illustrations of paragraph 7.6.3. Features such as tells of 6 m height are distinguishable, but features like 1-2 m height walls and cairns are not perceived even though they are there.

The CORONA-CORONA automatically extracted DEM is assessed qualitatively and quantitatively in Chapter 8.

8. Digital elevation model production and assessment

8.1. Automatic DEM extraction

There are many techniques that can be used to produce DEMs and the choice of methods depends on the available data, software, and know-how. Generally, these techniques can be summarised in two parts (Polidori, 2002): first, the computation of the 3-axis coordinates for a large number of terrain points; second, the sampling of the resulting information in order to meet the user's needs. In other words, first the computation of the DEM and then the creation of a data structure to display the results.

During automatic DEM extraction, the first part may be achieved either by differential techniques (for example, radar interferometry), or by photogrammetry by digital matching of points. Three categories of digital matching may be identified: area-based matching (or signal-based matching), where the grey-levels of a window (a vector of pixels) can determine the correspondence between two images[41]; feature based matching, where the matching point belongs to image features therefore it is less sensitive to geometric deformations between the images[42]; and relation based (or structural) matching [(ERDAS, 2002), (Paparoditis & Dissard, 2002)].

Wang (1998) has demonstrated that by using structural matching, one does not need any *a-priori* information to perform fully automated matching of image features, even with images from non-metric cameras or with non-perspective geometry. Structural matching is a technique that was first used in computer vision technologies, where the spatial resolution was high enough to increase the demand for better matching. Forte & Jones (1999) review the range of structural matching methods reported in the computer vision literature.

ERDAS OrthoBase Pro automatically creates a DEM in three steps. First, it applies a digital image matching for DEM mass point collection. With the use of Förstner interest operator[43] (Förstner and Gülch, 1987), it identifies a series of feature points such as road intersections or centres of circular features on each image (left and right) of the pair. The cross-correlation coefficients are calculated for each matching feature point, and the

[41] It is very difficult to find optimal matching points between two images, because of geometric and radiometric differences that occur due to the platform's attitude and the landscape relief.
[42] It is not as 'universal' as the area-based technique, and there is need for some a-priori information like approximate orientation parameters and image overlap.
[43] Interest operator is a search window that runs particular algorithms for the detection of interest points (and features). In this case, the Förstner algorithms are run and the point with values greater than some threshold or extreme maxima in the neighbourhood is the match point.

points with the higher correlation (0.8-1.0) are chosen as a matching pair. In other words, it utilises feature-based matching technique, but it is also looking at the topological and geometrical relations among the features. The parameters of the digital image matching can be customised according to each user's needs. Among the parameters, the search window size, the correlation window size and the correlation coefficient limit have the most influence.

The second step is the ground point coordinate determination. From the first step, a set of points is chosen in the left and right images. With the use of the space forward intersection technique[44], the ground coordinates of the points are computed. Thus, the mass points are created. "A mass point is a discrete point located within the overlap portion of at least one image pair, and whose 3D ground coordinates are known." (ERDAS, 2002). The mass points are then used as a basis for the third step, the DEM construction.

Because of the high triangulation errors associated with CORONA strip of images, it was decided to extract a DEM from each of the three stereopairs, and later merge the three DEMs.

Before beginning DEM extraction, some common parameters were applied to all stereopairs. A trim frame of 2.5 % is applied to all overlaps. The trimming occurs after the mass points are extracted and before the DEM generation. Thus, the DEM is clipped to remove less accurate edges. The correlation area is reduced by a 5 % frame, thus preventing the extraction of erroneous mass points that may be present at the edges of the images. The reduction occurs before the mass points extraction.

The second part of DEM extraction includes three main approaches: regular sampling, where most information has square constant size (for example an image file where the information is included in the pixel); semi-regular sampling, where there is a very dense regular sampling and only useful points are selected; and irregular sampling, where points may be located anywhere (like Triangular Irregular Networks - TINs). The size or the density of the sampling is not of vital importance since computer performance is now adequate for this task.

In this research, four files were created, the DEM image file, the contour shapefile, the image quality file and the DEM extraction report. The DEM image file pixel size

[44] Space forward intersection is a technique commonly used to determine ground coordinates of points in the overlapping areas of a pair of images, based on known interior and exterior orientation. The latter are considered known after the triangulation.

was chosen to be 17 m thus enabling for a minimum interest operator size[45]. According to ERDAS (2002), this file may be categorised as semi-regular grid. The contour lines were chosen to be 10 m. Because of problems caused in the DEM extraction, all clouds and their shadows were excluded from the extraction, and they appear as black "islands" in the DEM. The extraction strategy was chosen to be ***flat areas***[46] strategy with ***adaptive change***[47] applied. In case anomalies are detected in the DEM, they may be edited with simple interpolation[48] through ERDAS.

In the following paragraphs, the results of the DEM extraction are presented. For the general mass points quality results, ERDAS OrthoBASE Pro uses a 3x3 interest operator to calculate an elevation value from the neighbouring DEM postings. The extracted elevation value is subtracted from the interpolated value to compute the difference, and the standard deviation is captured. If the difference is three or more times larger than the standard deviation, then the interpolated value is used and the point is considered *Suspicious*. DEM points that do not have any immediate neighbours are considered *Isolated*. All the other points are categorised according to the correlation between the mass points that the interest operator provided.

[45] The methodology of the software for the DEM extraction requires a DEM cell size equal or higher to the maximal correlation window size, whose side has size of 7 pixels. Thus, the DEM cell size could not be less than 7 pixels size.

[46] In flat areas strategy, the search size is 7 x 3 pixels, which is adequate because of the absence of errors caused by high relief.

[47] With the adaptive change set ON, the ERDAS OtrthoBASE Pro computes and analyzes the terrain features after each pyramid and sets the strategy parameters accordingly. Thus, the extracted mass points are expected to have fewer errors, unless there are some unusually high peaks and low valleys on the terrain that are not detected in the previous pyramid layer; thus, they're unlikely to be subsequently detectable.

[48] The ERDAS is using "multisurface functions" interpolation technique, by Wang, Z. (1990).

8.1.1. Stereopair 007-013

In this stereopair, there were a lot of clouds present, thus causing "islands" in the DEM. The clouds had to be excluded from the process, along with their shadows.

General Mass Point Quality (in parenthesis is the correlation value):

Excellent % (1-0.85): 64.38 %

Good % (0.85-0.70): 7.43 %

Fair % (0.70-0.5): 0.0000 %

Isolated %: 0.0000 %

Suspicious %: 28.19 %

With 11 GCPs and 14 tie points, the global accuracy was (all values in metres):

Minimum, Maximum Error: -7.243, 5.715

Mean Error: -0.864

Mean Absolute Error: 2.766

Root Mean Square Error (RMS ERROR): 3.377

Absolute Linear Error 90 (LE90): 5.476

NIMA Absolute Linear Error 90: +/- 3.189

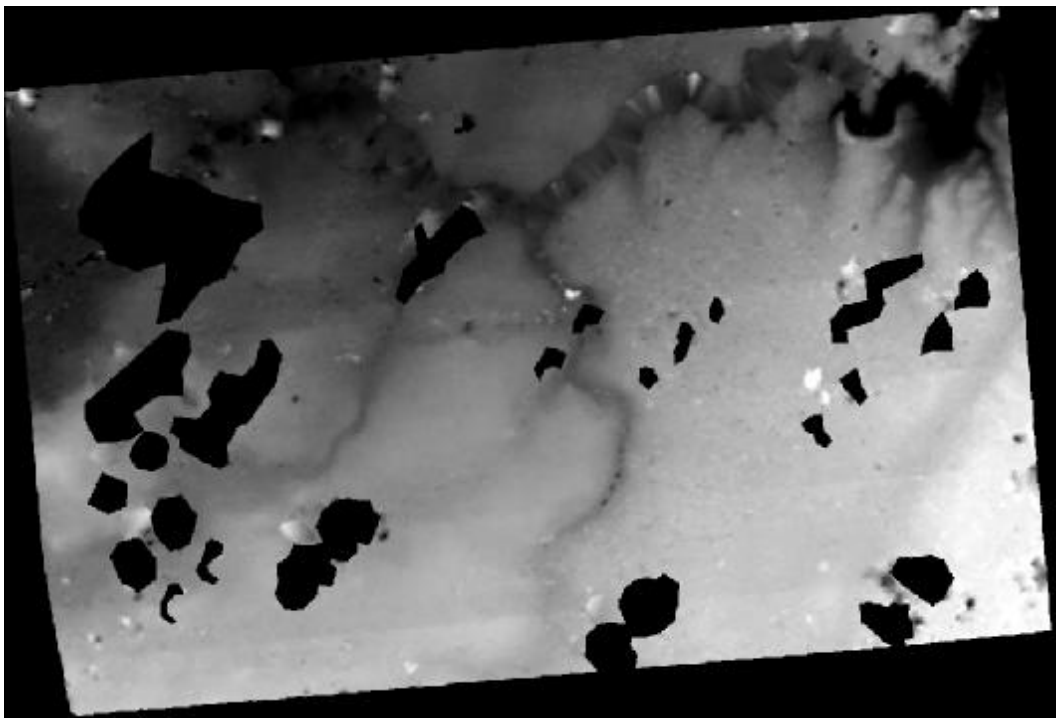

Figure 8-1 – The DEM image of the north area. The black patches are clouds and their shadows. Maximum height: 558 m, Minimum height: 282 m.

8.1.2. Stereopair 008-014

General Mass Point Quality (in parenthesis is the correlation value):

Excellent % (1-0.85): 69.73 %

Good % (0.85-0.70): 0.69 %

Fair % (0.70-0.5): 0.0000 %

Isolated %: 0.0000 %

Suspicious %: 29.58 %

With 11 GCPs and 21 tie points, the global accuracy was (all values in metres):

Minimum, Maximum Error: -10.846, 10.506

Mean Error: -0.732

Mean Absolute Error: 3.624

Root Mean Square Error (RMS ERROR): 4.461

Absolute Linear Error 90 (LE90): 6.188

NIMA Absolute Linear Error 90: +/- 4.280

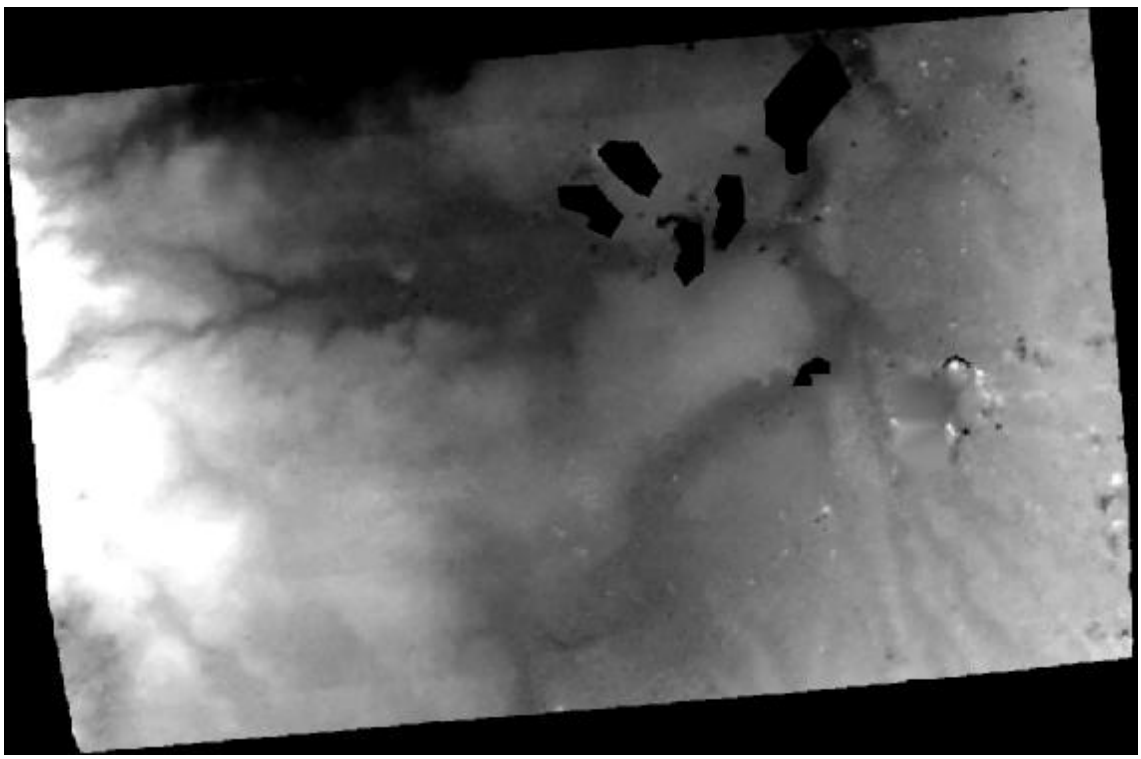

Figure 8-2 – The DEM image of the central area. The black patches are clouds and their shadows. Maximum height: 621 m, Minimum height: 425 m.

8.1.3. Stereopair 009-015

General Mass Point Quality (in parenthesis is the correlation value):

Excellent % (1-0.85): 67.03 %

Good % (0.85-0.70): 0.0000 %

Fair % (0.70-0.5): 0.0000 %

Isolated %: 0.0000 %

Suspicious %: 32.97 %

With 13 GCPs, the vertical accuracy was (all values in metres):

Minimum, Maximum Error: -7.622, 3.816

Mean Error: -1.726

Mean Absolute Error: 2.905

Root Mean Square Error: 3.830

Absolute Linear Error 90: 7.014

NIMA Absolute Linear Error 90: +/- 4.109

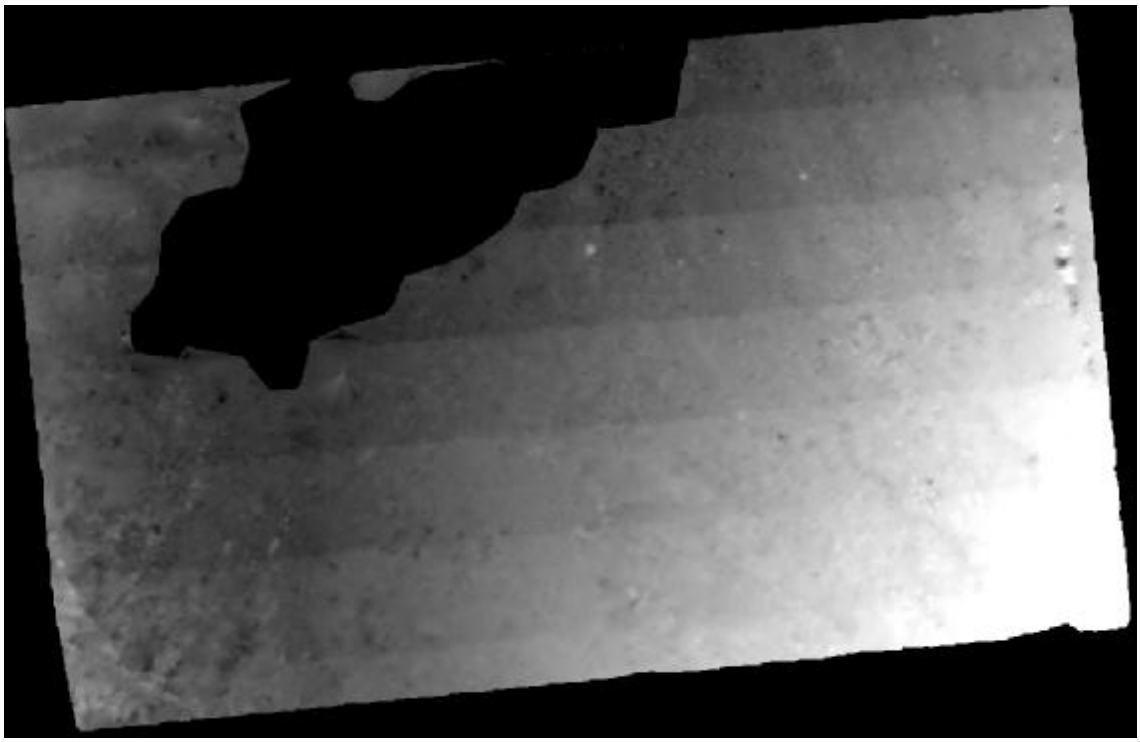

Figure 8-3 – The DEM image of the south area. The black patch is lake Qatina. Maximum height: 671 m, Minimum height: 463 m.

8.1.4. Comparisons

In this section, the automatically extracted DEMs are assessed qualitatively. To achieve this, the DEMs are compared with the maps contour lines, the DGPS soft detail points, the ASTER DEM and the SRTM-3 DEM. The last three are independent sources of height data, thus appropriate for the assessment. The purpose of the comparison is to assess the limits of application in archaeology for the automatically extracted DEM.

The contour lines come from maps of low quality (see paragraph 4.3.1). However, they still display an image of the general topography in the area, and it was the only height data source for the GCPs. Thus, the maps contour lines are overlaid with the contour lines extracted from the CORONA DEM in figure 8-8, and they are compared with the DEMs in figure 8-9. This is a qualitative comparison for the general topography accuracy of the CORONA DEM. Also, in figures 8-4, 8-5 and 8-6, the CORONA DEM is sampled along the map contour lines to give a profile of the topography to compare with the height data on the maps.

The DGPS soft detail points are used for quantitative assessment of the CORONA DEM. During the September 2002 visit to the area of interest, other researchers studying the geomorphology of the Orontes valley (Bridgland *et al.*, 2003) used differential GPS points to measure river terrace features. They established their points with the use of a base GPS of known coordinates and a "rover" GPS. Because these points were not taken from 'sensitive' areas (crossroads, bridges, etc.), the Syrian authorities allowed their use. But, for the same reason, it is impossible to identify these points precisely on the imagery. However, it was possible to detect these points from their Easting and Northing coordinates, and then compare their height with the height information taken from the CORONA data stereopair.

The ASTER DEM is an inexpensive source of height data, provided as a 'standard' ASTER data product. The 'relative' ASTER DEM (without ground control) has been shown by others to give a relative accuracy of 10 m and the 'absolute' ASTER DEM (with ground control) a vertical and horizontal accuracy of 7 m. For these reasons, it was chosen to assess the quality of the CORONA DEM.

The SRTM-3 DEM is another inexpensive source of height data. The accuracy report is still under preparation but the nominal value is about 5m vertical, depending on the relief of the ground (Farr, 2004).

For the comparison of CORONA height information with the map contour lines, the spatial profile tool of ERDAS Imagine was used. The CORONA DEM was sampled along the maps contour line (see figures 8-4, 8-5, and 8-6), and in charts 8-1, 8-2, and 8-3 the contour line (steady height, straight purple line) is displayed against the DEM sampled values (blue line).

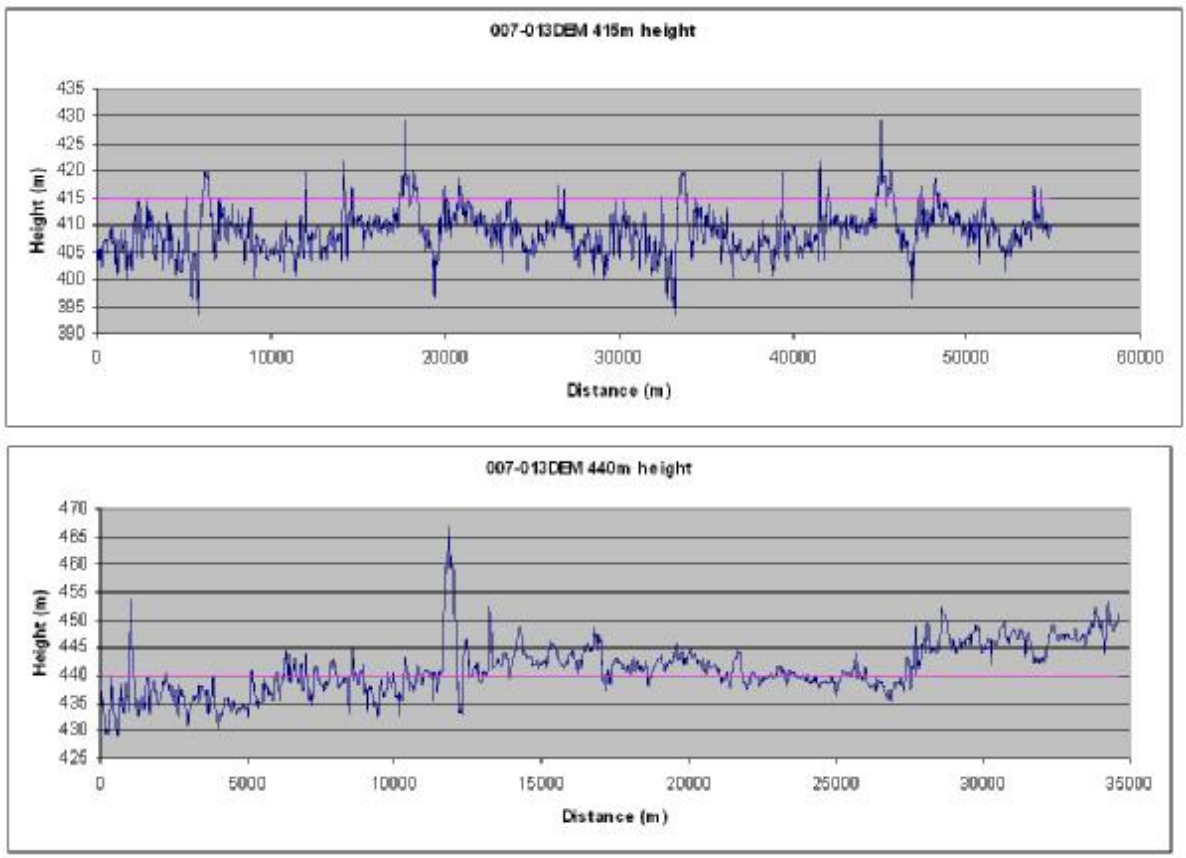

Chart 8-1 - DEM-map comparison. The purple line is the contour line (steady height) and the blue line represents the sampled spatial profile of the DEM along the contour line.

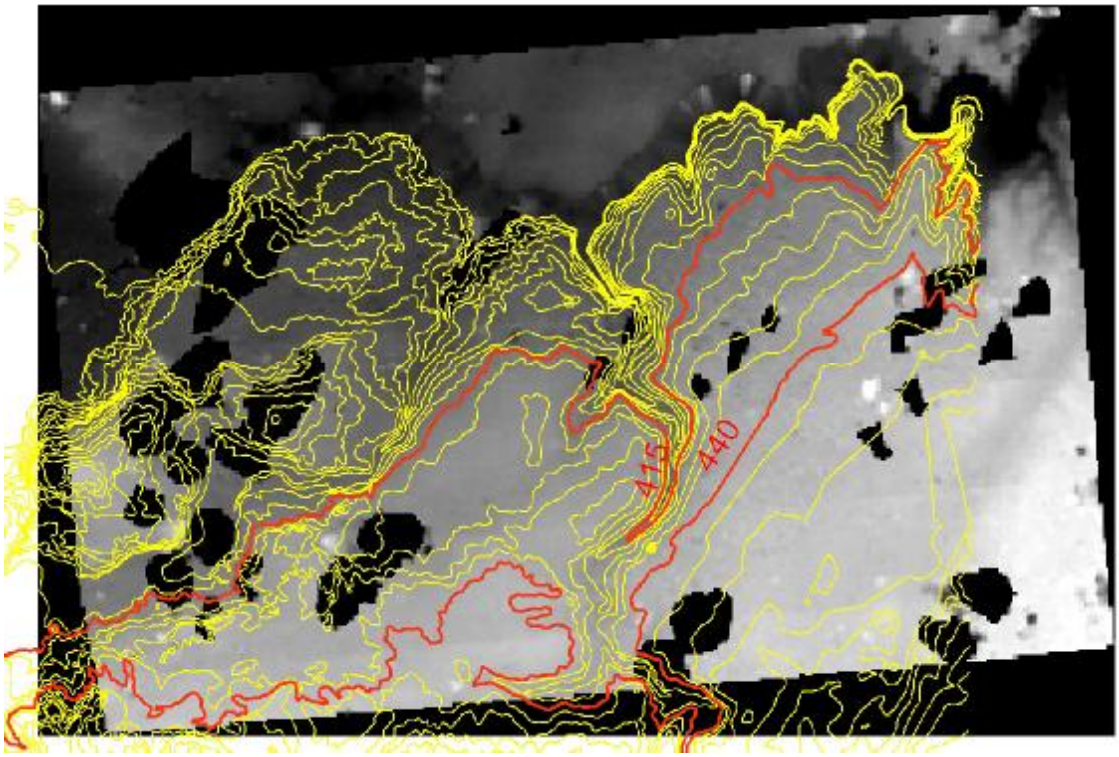

Figure 8-4 – The sampled contour line of the chart 7-1.

The 007-013 DEM was sampled along two contour lines (415m and 440m) from right to left as presented in the figure 8-4. A systematic error is visible in contour line of 415m, which was also visible in a random sampling in the contour line of 410m (not presented here). This "offset" appears in the beginning of the sampling of 440m. It is possible that the systematic error is a result of the lack of ground control at the central-upper part of the imagery (see figure 7-5).

Table 8-1 – Statistics on the sampling lines for 007-013 DEM.

	415m sampling line	440m sampling line
Maximum height	429.24 m	467.01 m
Minimum height	393.32 m	428.84 m
Average height	408.68 m	441.26 m
Standard Deviation	4.01 m	4.66 m

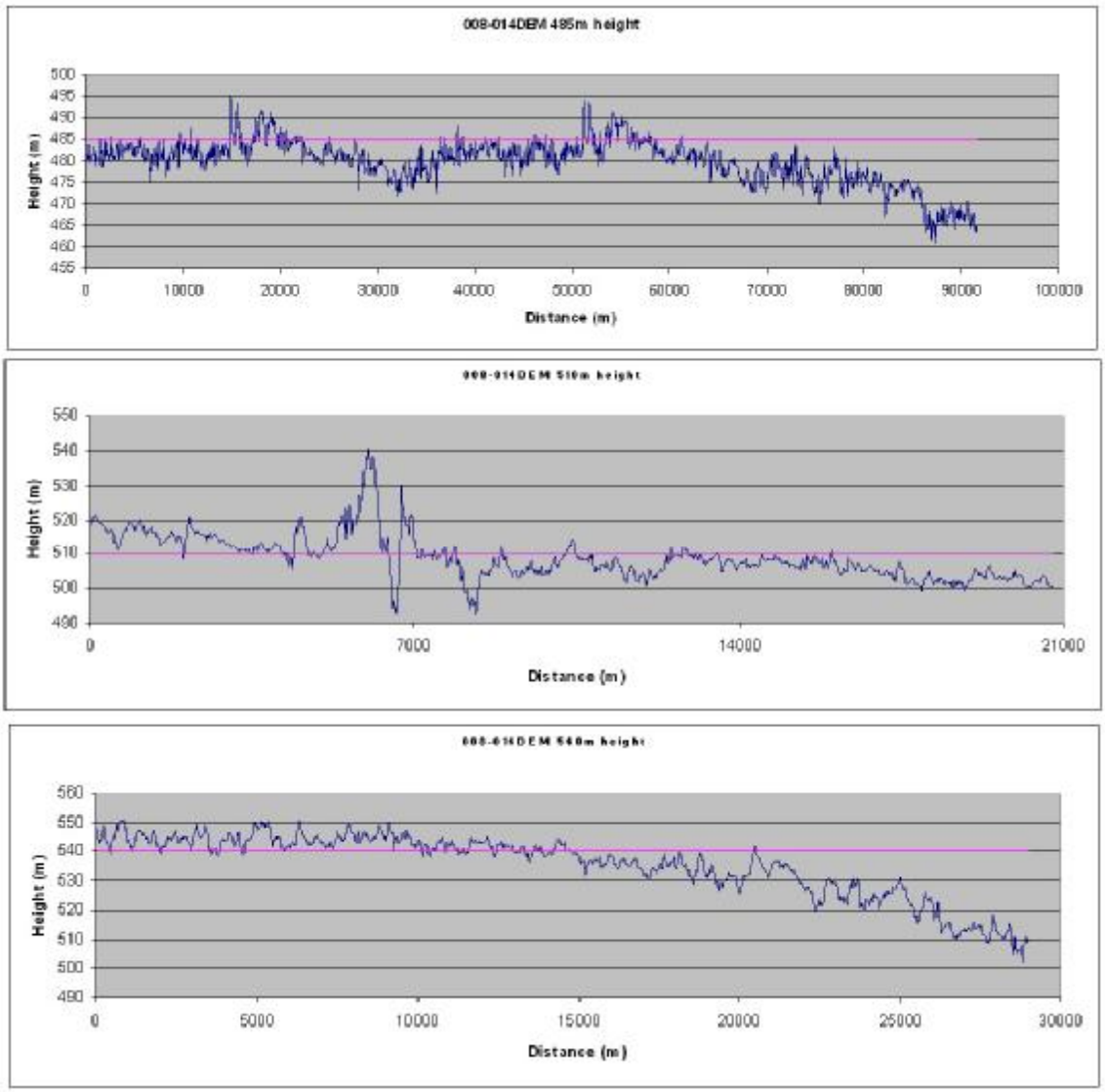

Chart 8-2 – DEM-map comparison. The purple line is the contour line (steady height) and the blue line represents the sampled spatial profile of the DEM along the contour line.

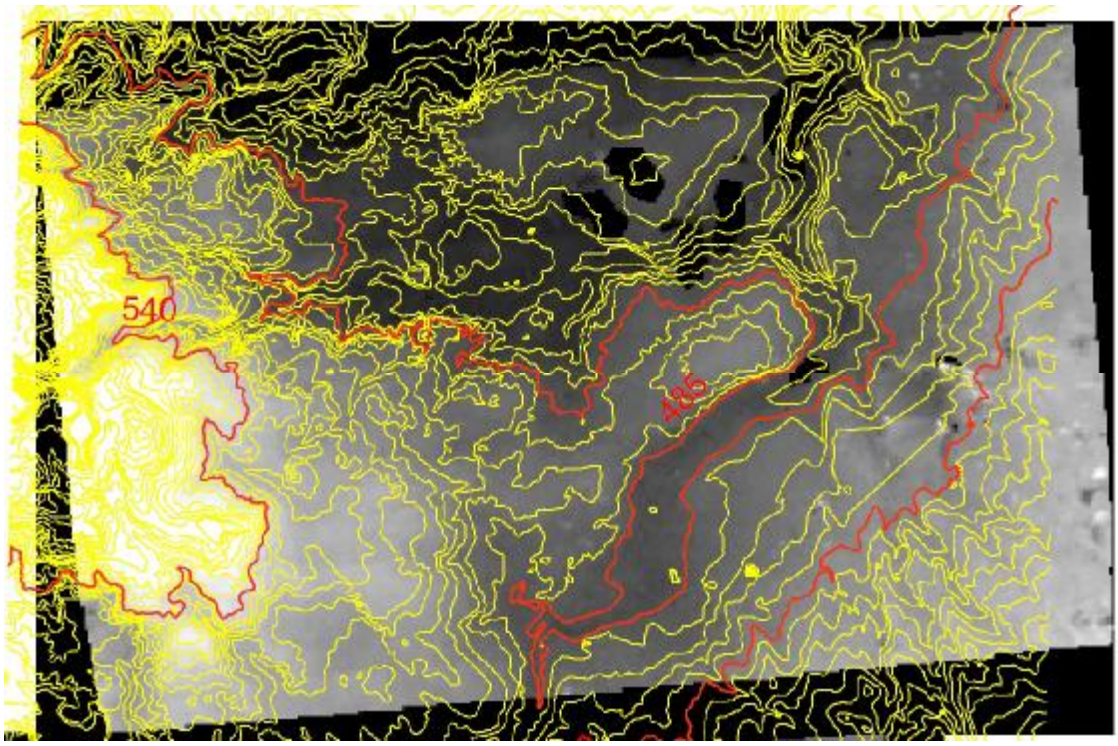

Figure 8-5 – The sampled contour line of the chart 8-2.

The 008-014 DEM was sampled along the 485m, 510m and 540m contour lines. The 485m and 510m lines were sampled from right to left. The 540m line was sampled from bottom to top. An intense drifting can be noticed in the top left of the DEM and a lighter drifting in the lower central part. This can be because of problematic ground control in the upper left part of the imagery.

Table 8-2 – Statistics on the sampling lines for 008-014 DEM.

	485m sampling line	510m sampling line	540m sampling line
Maximum height	494.97 m	540.59 m	551.04 m
Minimum height	461.02 m	492.49 m	502.13 m
Average height	479.84 m	509.06 m	535.64 m
Standard deviation	5.16 m	6.49 m	10.59 m

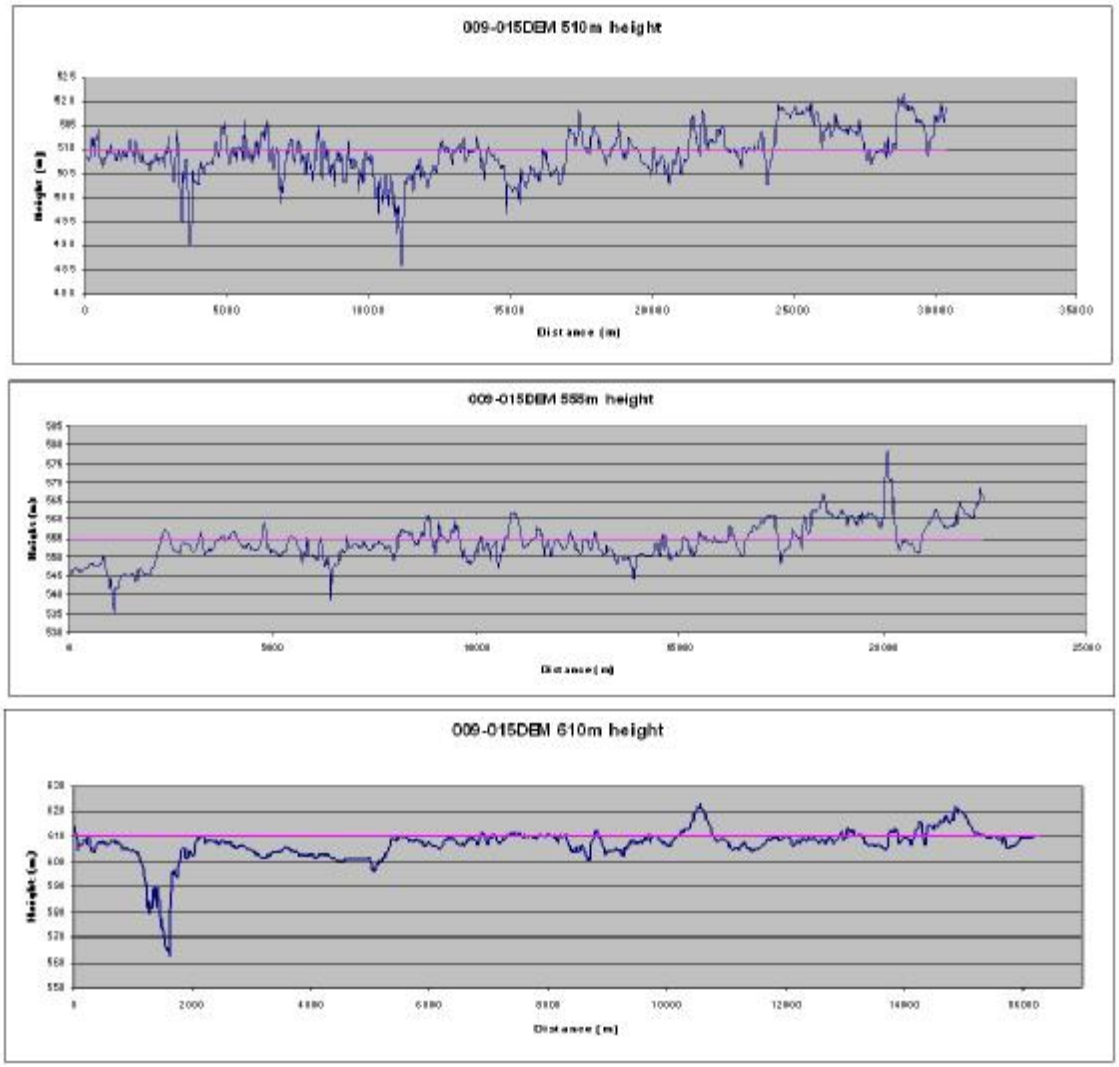

Chart 8-3 - DEM-map comparison. The purple line is the contour line (steady height) and the blue line represents the sampled spatial profile of the DEM along the contour line.

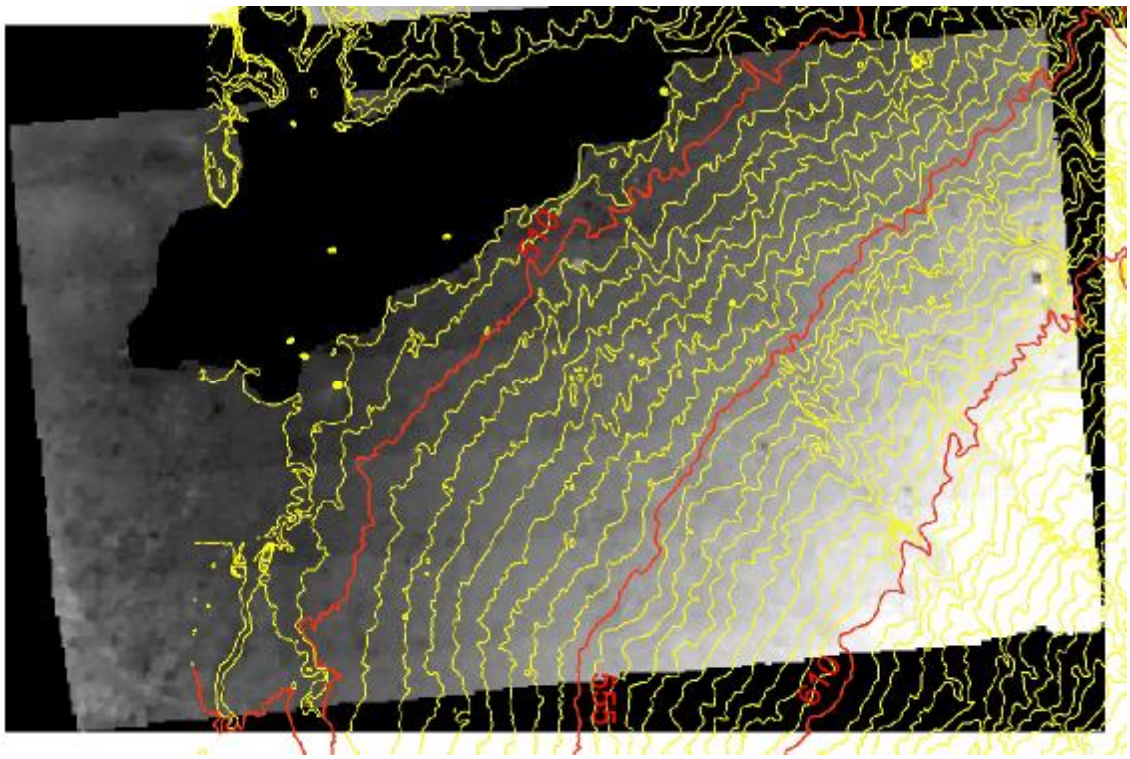

Figure 8-6 – The sampled contour line of the chart 8-3.

The 009-015 DEM was sampled along the contour lines 510m, 555m and 610m, all from top to bottom. On the contrary to the previous two DEMs, here the results present no offset or drifting. This can be explained by the fact that the ground control is much better (see figure 7-7).

Table 8-3 – Statistics on the sampling lines for 009-015 DEM.

	510m sampling line	555m sampling line	610m sampling line
Maximum height	521.94 m	578.04 m	623.08 m
Minimum height	486.14 m	534.79 m	562.33 m
Average height	509.41 m	554.00 m	606.81 m
Standard deviation	4.78 m	5.04 m	6.24 m

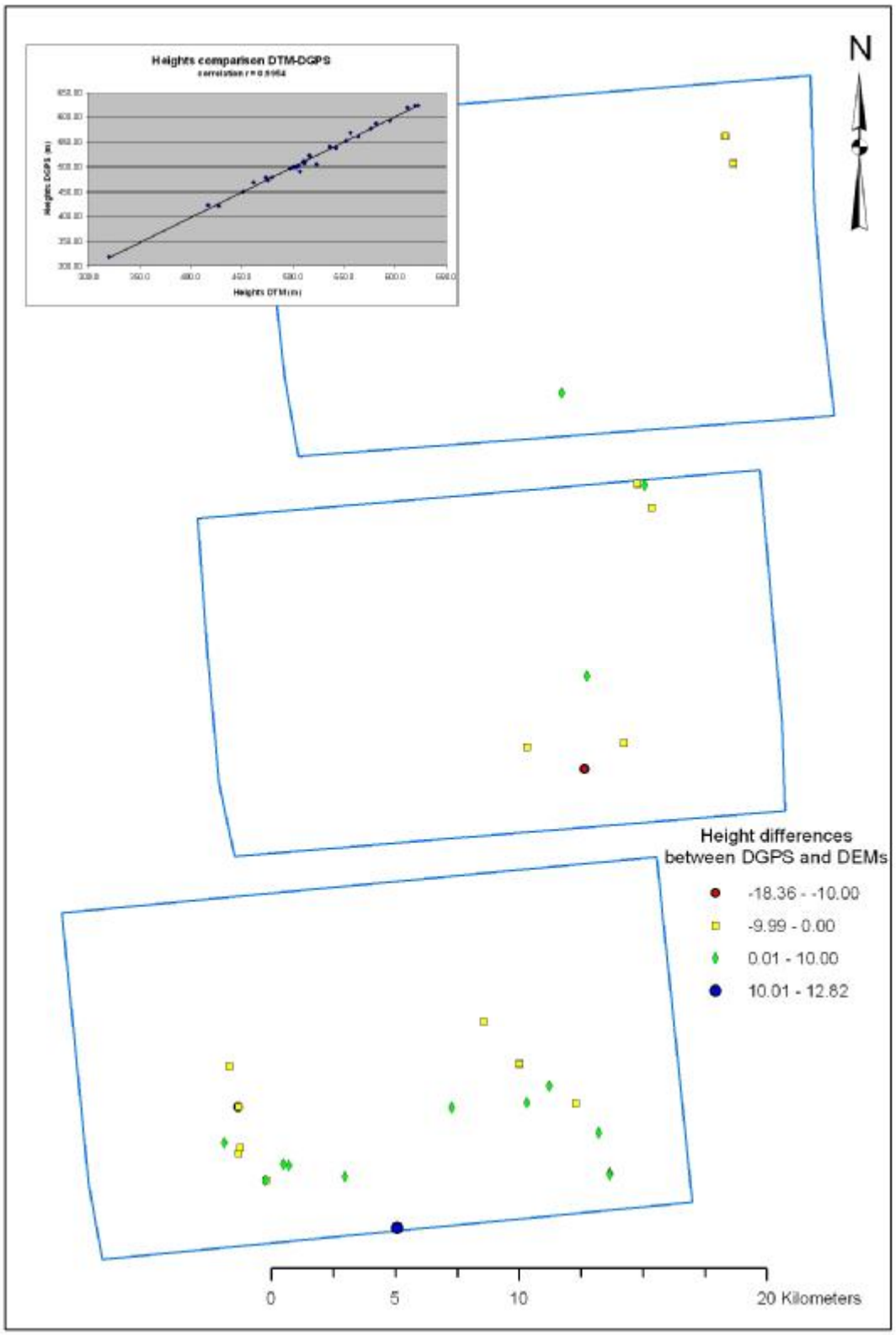

Figure 8-7 – The spatial distribution of the DGPS check points within the DEM footprint is shown here in with the DEM-DGPS chart. Correlation r = 0.9954.

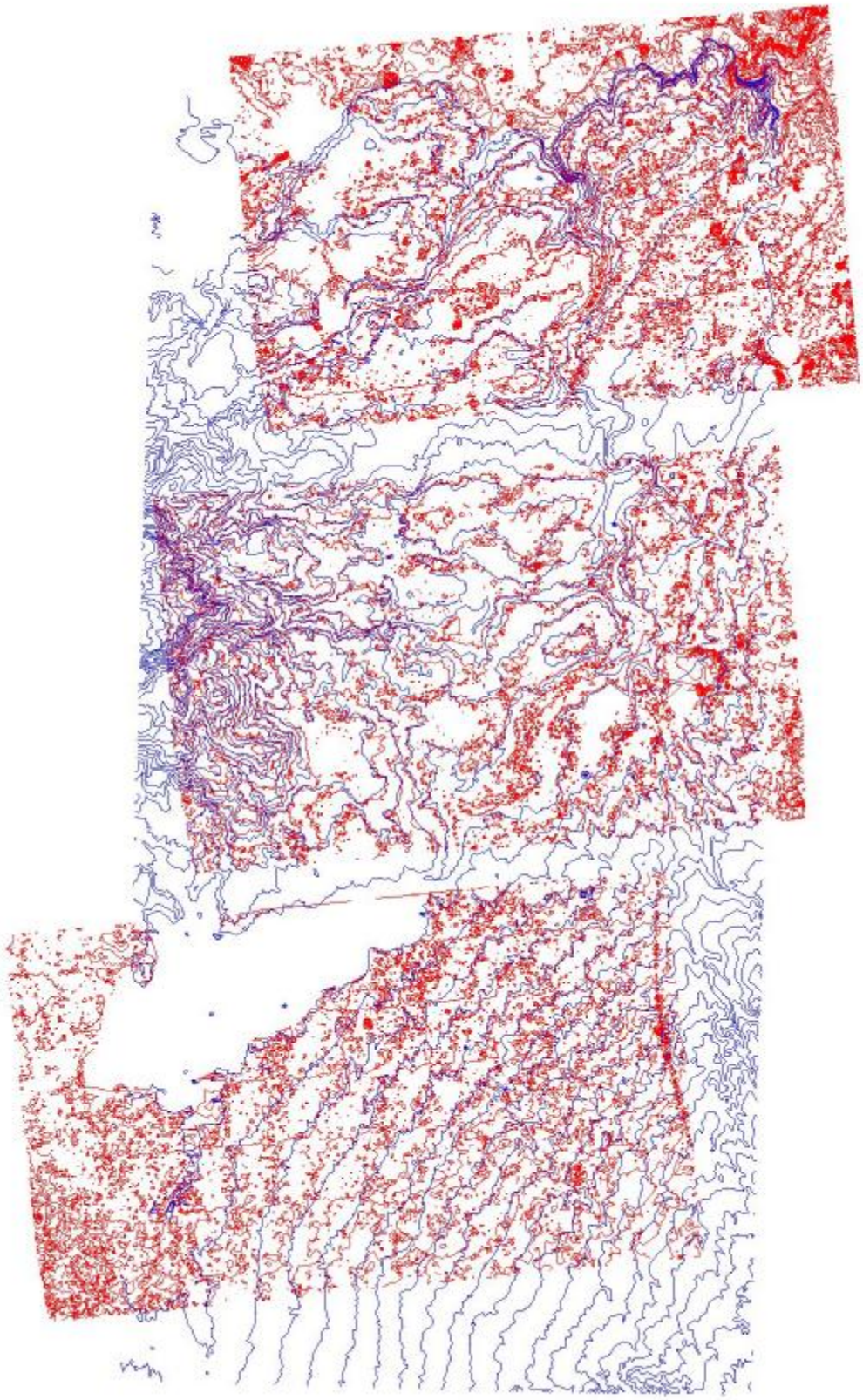

Figure 8-8 – Contour comparison. The blue line shows contours of the map at 10 m intervals, the red line shows the contours derived from the DEM. The visual inspection shows a good fit.

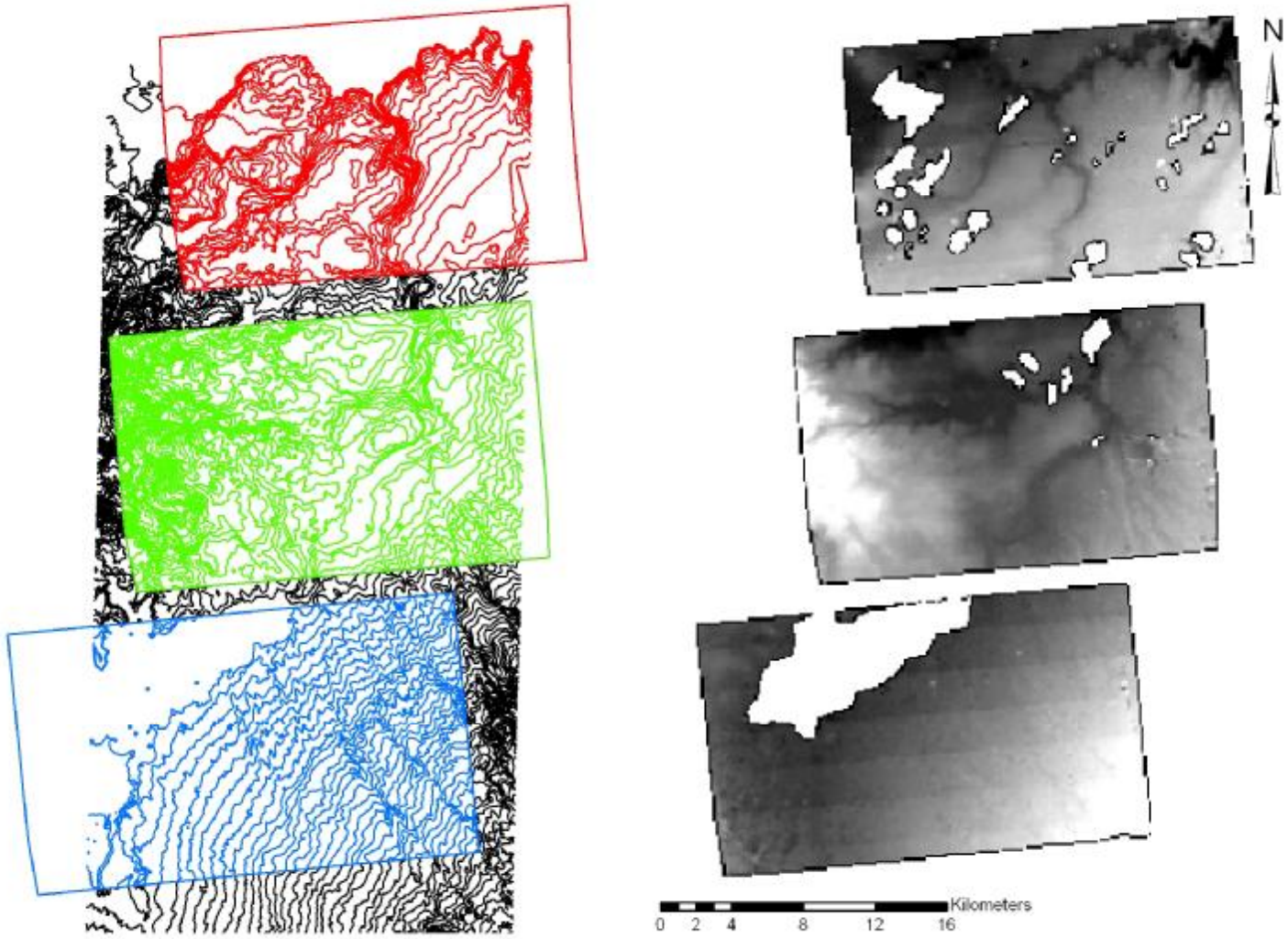

Figure 8-9 – Quality comparison between the map contour lines and the CORONA extracted DEM.

Figure 8-7 displays the comparison between DGPS points and the DEM derived height data. The correlation is very high (0.9954), and the residuals appear to be distributed randomly. Because DGPS points are an independent set of data, the comparison is more objective than the comparison with the contour lines. The accuracy is probably better than the contour lines, but they lack spatial distribution. It is apparent from figure 8-7 that the DGPS points are not equally distributed over the area of interest and so they cannot be used to fully evaluate the DEM products.

A visual comparison between the map contour lines at 10 m[49] interval and the DEM derived contour lines of 10m[50] is shown in figure 8-8. The comparison shows a good fit at this viewing scale. However, it is not perfect. The striping effect is intense in the south area, and this is visible in the contour lines presented in red in figure 8-8. Also, the DEM derived contour lines are irregular, meaning that they do not form clear contour lines. There is need for further processing through interpolation to produce contour lines as they appear on the maps.

In figure 8-9 the left part shows the contour lines of the maps, highlighting the areas that the CORONA DEMs cover. The right part shows the CORONA extracted DEMs. By visual comparison of the two parts, one may see qualitatively that the DEM gives more information when compared with map contour lines. For example, in the central area, at the west of the Orontes river, a smaller valley becomes instantly apparent in the DEM. It is formed by a tributary of the Orontes river that is not clear on the maps. In the central DEM, at the bottom right corner, the lines of relief are more apparent than on the maps (see also figure 8-16). Similar lines may be seen in the southern DEM running from southeast towards the lake (see also figure 8-17). For an enlarged view of the DEMs, please see figures 8-1, 8-2, and 8-3.

Irrespective of the imperfections in DEM derived contour lines, or the annoying striping effect of the southern area, the automatically extracted DEM gives a good representation of the landscape. It also provides information about features that are not apparent on the published Syrian topographic maps.

[49] They are 10m interval for comparison purposes. The original contour lines are 5m interval (as seen in figure 8-9).
[50] The 10m interval of the contours is an interpolated approximation. The DEM pixel size is 17m.

8.1.4.1. Comparison with ASTER DEM

After careful search and selection in the USGS databases, two ASTER DEMs were available for comparison. They were the only ones with a small overlap with the CORONA DEM. ASTER DEMs are generated from two along-track level 1A images in near infrared bands 3N (nadir-viewing) and 3B (backwards-viewing). The two cameras have a 27.7° intersection angle and a 0.6 base to height ratio (Toutin, 2001b). The ASTER DEM can be created as a no GCPs 'relative' DEM with relative accuracy up to 10m, or a with GCPs 'absolute' DEM with vertical and horizontal accuracy up to 7m[51].

Table 8-4 - ASTER DEM data

ASTER DEM metadata production:	*12/04/2002*	*21/02/2002*
Image taken on:	28/10/2000, 08:41	12/01/2002, 08:24
Cell size	30m	30m
DEM type	Relative	Relative
Quality Rating	Good	Good
Solar Azimuth Angle	158.4163	167.9550
Solar Elevation Angle	30.9475	41.3460
Processing Level	Grid 3	Grid 3
Operation Mode Class	Calibration, Normal	Calibration, Normal
Cloud cover	57 %	3 %
DEM correlation success	94 %	87 %
SWIR/TIR/VNIR1/VNIR2 observation mode	ON/ON/ON/ON	OFF/OFF/ON/OFF

For the comparison of the ASTER and CORONA DEMs, the ERDAS Imagine utility 'change detection' was used (or 'image differencing'). This utility reads the pixel values (which show height information in the DEM image) from two images which are assigned as 'before image' and 'after image', and produces a third image from their subtraction in the formula:

Before image – After image = Final image

The final image gets the smaller pixel size (in our case, the CORONA DEM, 17m) and its boundaries are defined by the use of AOI (Area Of Interest) layer. The ASTER DEM was assigned the 'after image' character, and the CORONA DEM the 'before image'. Thus, the minus differences mean higher ASTER pixel values, while the plus differences show higher CORONA pixel values.

[51] For more resources on ASTER, please see: (February 2001)
http://asterweb.jpl.nasa.gov
http://www.gds.aster.ersdac.or.jp
http://edcdaac.usgs.gov/dataproducts.html
http://terra.nasa.gov

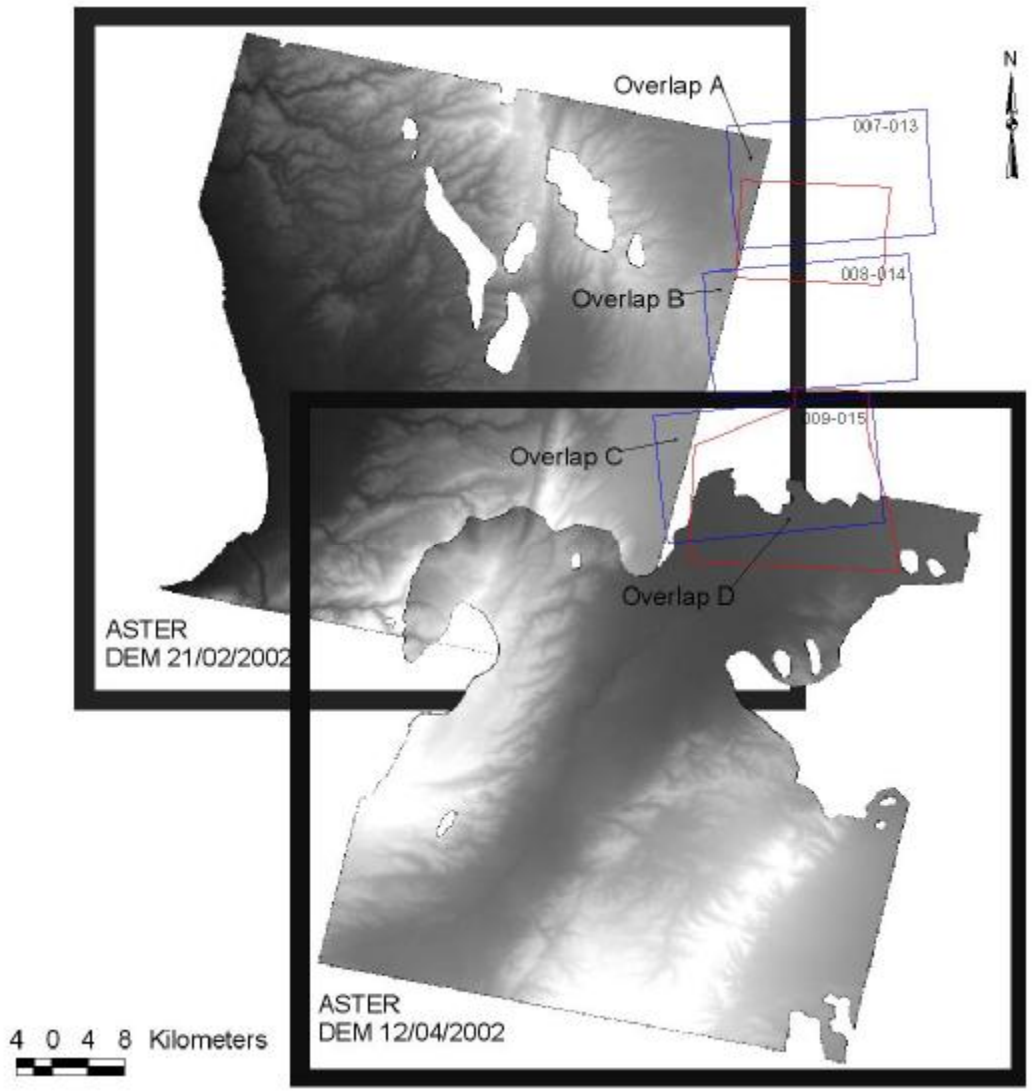

Figure 8-10 – Illustration of the ASTER DEMs and the overlaps with the automatically extracted CORONA DEMs (blue line). The Homs area of interest is displayed with red line.

Table 8-5 - Statistics of the differences of CORONA DEM – ASTER DEM

Statistics	*Overlap A*	*Overlap B*	*Overlap C*	*Overlap D*
Maximum (m)	28.42	30.71	78.52	49.27
Minimum (m)	-98.55	-40.30	-16.46	-117.91
Mean (m)	-35.64	-8.00	20.30	-28.28
Median (m)	-40.03	-12.29	17.56	-29.64
Mode (most frequently occurring)	-48.46	-22.87	17.56	-29.64
Standard Deviation	13.25	12.81	7.53	11.68
Pixels in one standard deviation	71.04 %	74.71 %	82.35 %	80.48 %
Total overlap number of pixels	71744	67724	104908	275010

The results of the comparison show a substantial difference between the two DEMs. One might expect to find large differences at the edges (maximum-minimum) of the distribution. However, the differences of overlap C and D are gathered around the mean

with more than 80% of them within one standard deviation. Concerning overlap A, figure 7-5 shows that the area of the overlap had little ground control (only one tie point). As for overlap B, the mean difference of -8 m with the 74.71% of the points within one standard deviation is the best match of all the overlaps, even though it is the smallest in size.

In the series of comparisons A, B, and C shown in table 8-5, one may notice that the difference is changing in a North-South direction. In overlap A, the ASTER DEM is obviously higher that the CORONA DEM. In overlap B, the differences indicate an intersection between the two DEMs, because of the distribution of the differences with both positive and negative values. In overlap C, the ASTER DEM is lower than the CORONA DEM. When comparing the ASTER DEM with the contours from the maps, the same results are seen. An illustration of the relationships can be seen in figure 8-11.

Is there a systematic error in the ASTER DEM (possibly from pitch of the platform), or is there an error in the contour lines of the maps? The only way to check for this question, it is the use of the DGPS points. In figure 8-7, one may see the distribution of the DGPS points across the CORONA DEM area, and the height differences between DGPS and CORONA DEM. The figure does not display any systematic error. The distribution of the height differences illustrates that the systematic error noticed in the ASTER-CORONA DEM cannot be because of the map contour lines. This would suggest that the systematic error is included in the ASTER data, thus the ASTER relative DEM cannot be used as a reliable model with which to check the accuracy of the CORONA DEM. The initial idea was to compare ASTER with CORONA DEMs to assess CORONA data, but this is not possible.

ASTER DEMs produced by USGS have been validated in the past with satisfactory results (Hirano *et al.*, 2003; Fujisada *et al.*, 2001). However, in this study the ASTER DEMs are not accurate. The ASTER relative DEM is certainly useful data for a study, but the researcher should be sceptical and careful about the way these data should be used. There is lack of ground control for the ASTER relative DEMs and this should be taken into account by whoever is using them.

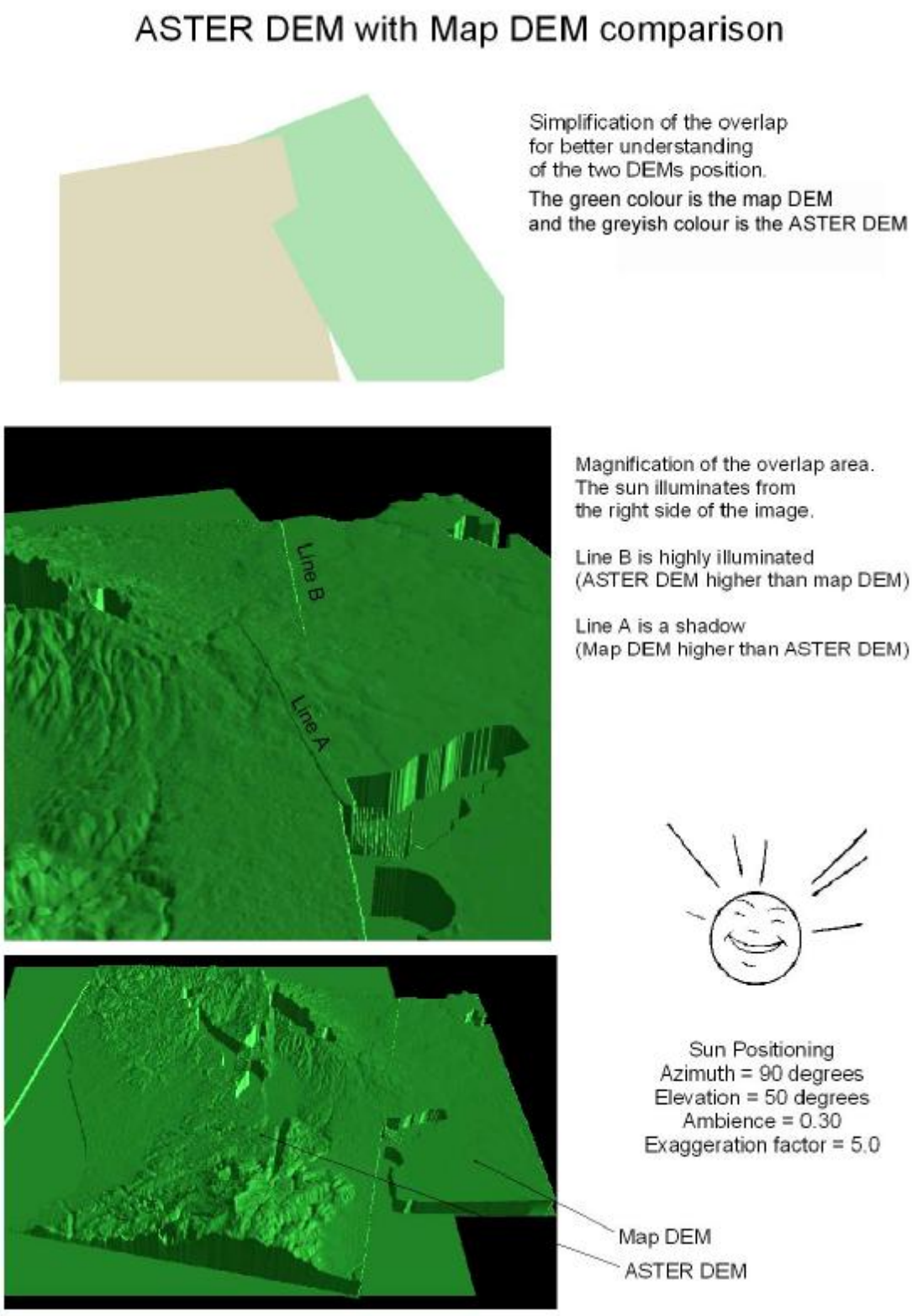

Figure 8-11 – Illustration of the ASTER DEM inclination from North to South (from higher heights to lower), when compared with the DEM created from the maps' contour lines.

8.1.4.2. Comparison with SRTM-3

On 1 April 2004, NASA published the SRTM (Shuttle Radar Topography Mission) three arc-second data of Homs area in the World-Wide-Web. SRTM was launched on 11 February 2000 and flew for 11 days. The purpose of the SRTM was to generate a near-global DEM using radar interferometry. The instrument imaged almost all landmass between 56 degrees south and 60 degrees north latitude. The data were acquired in X- and C-bands and were processed at one arc-second resolution (SRTM-1) by the German aerospace centre (DLR) and NASA-JPL respectively.

The SRTM-3 DEMs are being developed from C-band radar observations and they are generated by three-by-three averaging of the SRTM-1. The edge-rows and edge-columns overlap with the neighbour DEMs. The SRTM-3 is in 16-bit signed format and each tile contains 1201 lines and 1201 samples per line. Apart from the online description[52], a detailed description of the SRTM as well as an evaluation of the DEM product quality can be found in Rabus ***et al.*** (2003).

The SRTM-3 data are unedited and many contain regions with no data (some are visible in figure 8-12), and some anomalously high (spike) or low (well) values. Also, water surfaces generally produce very low radar backscatter. Thus, they will appear noisy or rough, in the elevation data. Similarly, the coastlines will not be well defined.

The data are free to download in .hgt format[53]. The procedure to transfer the .hgt to .img format is time consuming but straightforward. First, all .hgt files are renamed to .bil format. Then, import the .bil as a generic format and put the 16-bit unsigned and 1201x1201 pixels file size. The 'swap byte' option must be ticked in order to read the Motorola ("big endian") standard. Then, in the viewer, go to Utility→layer info→Edit→Change map model. There, in the projection field put Geographic Lat/Lon and in the units field put degrees. The .hgt filename shows the lower left corner in degrees. In our case the filename is N34E036. The data are divided into one by one degree latitude and longitude images in "geographic" projection. Thus, the upper left corner should be X=36 and Y=35, with pixel size 0.00083333… degrees (reflects the 90m pixel size). In layer info still, click on Edit→Add/change projection. There pick Geographic Lat/Lon, WGS84 and WGS84. Alternatively, freeware is available online for direct format translation[54].

[52] ftp://edcsgs9.cr.usgs.gov/pub/data/srtm/Documentation/ (Accessed: April 2004).
[53] ftp://edcsgs9.cr.usgs.gov/pub/data/srtm/ (Accessed: April 2004).
[54] http://www.visualizationsoftware.com/3dem/downloads.html (Accessed April 2004)

At this stage, the dataset has a projection Lat/Lon with all the parameters set. But in most applications the coordinate system uses meters and not degrees for units. To reproject the dataset to a more specific coordinate system, go to the main menu of Erdas and click on Interpret→Utilities→Reproject. Select output projection (in this case UTM 37N) and rigorous approach.

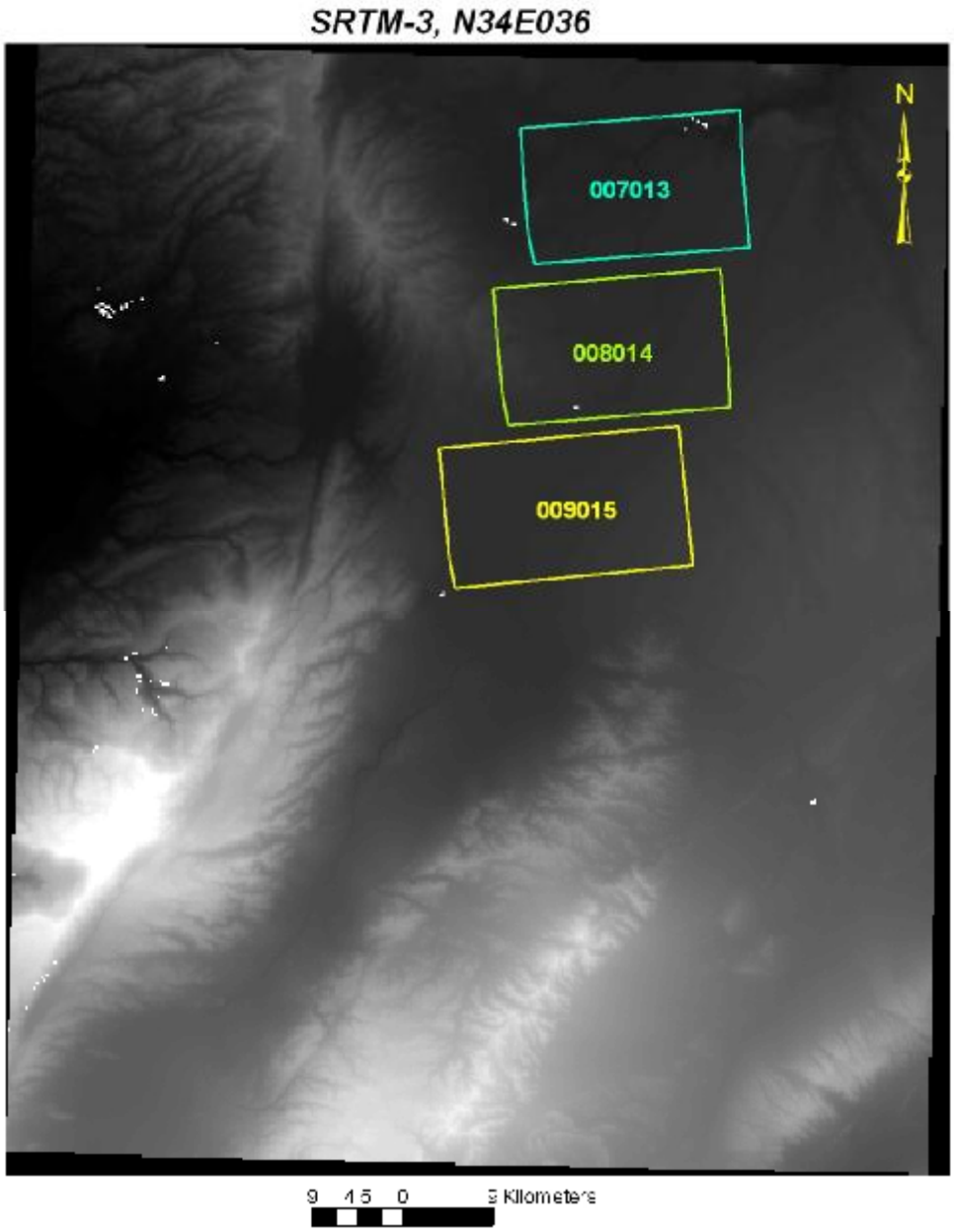

Figure 8-12 – Illustration of the SRTM-3 and the CORONA DEMs in UTM 37N projection.

For the comparison between the SRTM-3 and the CORONA DEMs, the same methodology as the ASTER DEM – CORONA DEM comparison was applied. The 'before image' is CORONA DEM and the 'after image' is SRTM-3. Thus, the positive

pixel values that appear in table 8-6 show CORONA DEM being higher than SRTM-3, and the negative pixel values show CORONA DEM being lower than SRTM-3.

Table 8-6 - Statistics of the differences of CORONA DEM – SRTM-3

Statistics	*007013-SRTM*	*008014-SRTM*	*009015-SRTM*
Maximum (m)	128.57	89.43	92.39
Minimum (m)	-125.97	-93.27	-50.74
Mean (m)	3.30	2.24	1.30
Median (m)	1.98	1.32	-0.59
Mode (most frequently occurring)	-0.70	0.34	-0.47
Standard Deviation	8.98	7.97	5.03
Pixels in one standard deviation	81.36%	71.94%	77.37%
Total overlap number of pixels	1125898	1064586	1269917

The results show big differences at the edges (maximum-minimum) of the points' distribution. However, this applies to a very small number of points and this can be seen by the percentage of pixels within one standard deviation. The mode of the distribution occurs in less than a metre difference, and the average occurs at 3.30, 2.24 and 1.30 m respectively. This shows a very good fit between the SRTM-3 and the CORONA DEM.

Some caveats were noticed in SRTM-3 DEM of the Homs area. A few areas were blank of data, and where the river has steep banks (north part of 007013 stereopair) the height values were anomalous. The lake Qatina coastline is not clear and there are no obvious anomalous values. This could be assigned to the shallow waters and the flat surrounding area.

8.1.5. Site detection assessment

In the previous sections, the qualitative assessment showed good detection of the ground relief including channels and small valleys. But the archaeological sites are small in relation to the pixel size of the DEMs. Thus, this section intends to qualitatively and quantitatively assess the CORONA extracted DEM for the possible detection of archaeological sites such as tells, or other man-made or modified sites.

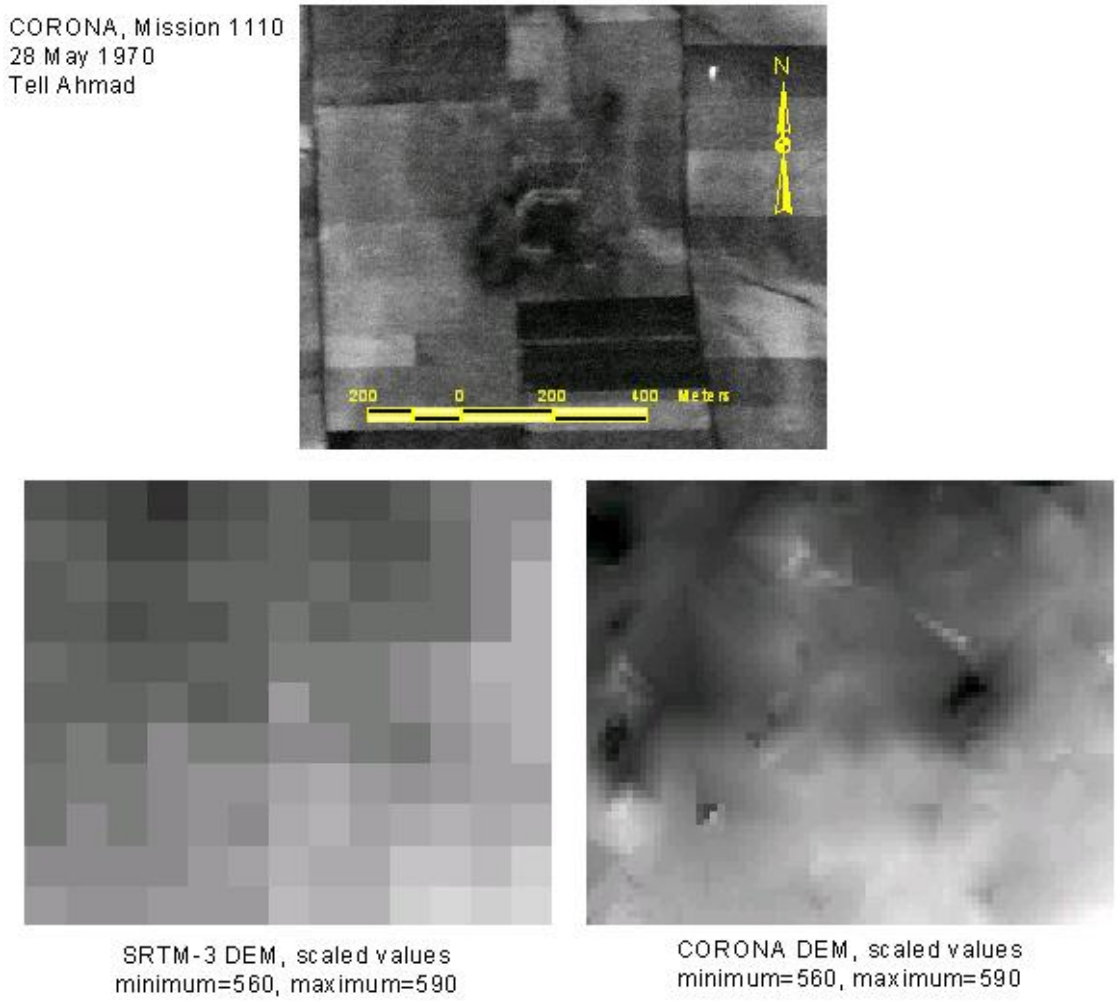

Figure 8-13 – Tell detection in the CORONA automatically extracted DEM and the SRTM-3 DEM.

Figure 8-13 shows an example of a tell and associated DEMs from CORONA and SRTM-3. It is very difficult for a photointerpreter to detect a tell just by looking in the particular displayed DEM image alone. The difference in pixel size between the SRTM-3 and CORONA DEMs is apparent.

But when the image is displayed on the side of the DEM (see figure 8-13), then assumptions about the tell position can be made with a fair degree of accuracy, and it is possible to take measurements. The heights in the CORONA DEM are smoothed. For this reason, the measurements are not going to be accurate. The profile of the pixels showed a smooth increase of heights. This does not reflect the local topography of tells, which are steep sided hills. The measurements were not able to estimate the height or area of the tell, because of this smoothing.

8.2. Manual DEM extraction

The above process of automatic DEM extraction is rapid, efficient and accurate enough for applications that look at the relief of the whole landscape. But when there is need for better accuracy and larger scale, and need to focus on particular features, then the interpreter should go for the manual approach. This can be done in the *Stereo Analyst* module of ERDAS Imagine software. In this way, the interpreter has a 3D view of the area, with the features included. The 3D is created through the anaglyphic viewing technique. Filters of complementary hues (red and green, or red and blue) are used to separate left and right images of the stereopair. The interpreter wears a pair of glasses, which cover the eyes with blue or green (in one eye) and red (in the other eye). Thus, each eye sees only one image. But when the information from the two images arrives in the brain, the result is a stereo view of the area. Although inexpensive, this method has limitations. The source data is restricted to black and white imagery.

Examples of this kind of stereo viewing are the illustrations presented in section 7.6.3. Through these illustrations, one may see particular archaeological features resolved in the CORONA DEM. Although in illustration 1, the tell Nebi-Mend is obvious, the tell in illustration 3 does not come out equally well. In illustration 4, the walls and cairns cannot be seen in depth, even though they are easily detected. This means that there is a limit to the height of features that can be reached from CORONA data.

When using a DEM created by sensor model information (like the 'block' file of OrthoBASE Pro), then the Stereo Analyst automatically places (rotation, scale and transformation) the imagery to provide a clear stereo view of the objects. Thus, the software automatically corrects the y-parallax for every part of the image the user is viewing. By manually correcting the x-parallax in every point, so that the floating cursor is resting on the object, the interpreter can get information about the three-dimensional position of the object. By applying this manual approach, it was possible to estimate the height of a tell, which was later confirmed by surveying. However, the anaglyphic stereo-viewing is tiring for the eyes and makes it very difficult to correct the x-parallax to create a contour line. Generally stereo-viewing is relatively non-demanding when compared to automated DEM extraction. But for this process, the software demands a lot of computing power that did not exist in the resources of this research. However, it is a more accurate approach than the automatic extraction.

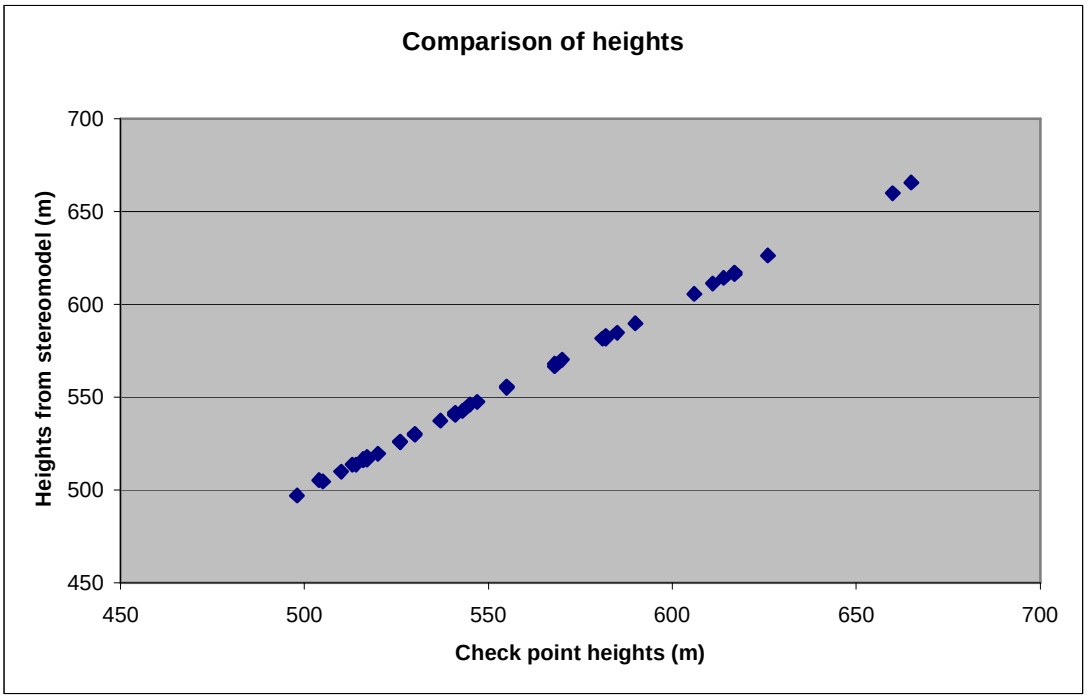

Figure 8-14 – Correlation graph betweem the points from the stereomodel and the check points.

This was confirmed with the 'position tool' of the Stereo Analyst module and the DGPS points. The position tool is used to enter 3D check point coordinates, which are then compared to the position displayed in the 3D stereo viewer. If the check point is correct, the 3D floating cursor should rest on the feature or object of interest. If a check point is incorrect, the difference in E, N, H directions between the original position and the displayed position can be visually interpreted and recorded.

Thus, the differential GPS points were used as check points in the resulting DEM of the stereopairs. The mean absolute height difference was 0.46m, with maximum 1.35m and minimum 0.01m. The correlation graph is shown in figure 8-14. The correlation coefficient is *r=0.9999*. These numbers show a much better correlation than the automatically DTM extracted – DGPS correlation (*r=0.9954*). This better correlation might be explained by the fact that through manual measurement one can have exact coincidence of points.

Without the application of the sensor model, the interpreter is still able to manually create a 3D view of the area, simply by moving the images and applying filters on them (Palmer, 2002). This can also be done in simple image processing software like Adobe Photoshop, which is less expensive than ERDAS Imagine. This limits the user to qualitative interpretation of the area with possible illusions (see paragraph 4.1.4.2).

Accurate measurements of the heights and distances are impossible without the sensor model.

There are more ways to display an area in 3D. For a review of the existing techniques see McAllister (1993). Each of these displays has advantages and disadvantages. The main disadvantage is the lack of measurements when the display is done without the use of a sensor model.

8.3. Discussion

Table 8-7 displays a summary of all the comparisons in paragraph 8.1.4 and the errors from paragraphs 8.1.1, 8.1.2, and 8.1.3. All these errors refer to the mass points. The minimum-maximum error describes the range of the errors. The other errors are computed with the comparison of the model height and a reference height. The number of tie points and GCPs determines the number of reference points. The RMS error indicates the magnitude of error. Absolute LE90 is used to describe the error associated with the 90% of the DEM based on the three-axis reference points used. NIMA LE90 is based on the assumption that a normal distribution exists with the DEM errors computed using three-axis reference points (ERDAS, 2002).

Table 8-7 - Summary of the stereopairs evaluation

	007-013	**008-014**	**009-015**
N° of tie points/GCPs	14/11	21/11	0/13
Minimum, maximum error	-7.243 m, 5.715 m	-10.846 m, 10.506 m	-7.622 m, 3.816 m
Mean error, mean absolute error	-0.864 m, 2.766 m	-0.732 m, 3.624 m	-1.726 m, 2.905 m
RMS error, LE90, NIMA LE90	3.377, 5.476, ± 3.189	4.461, 6.188, ± 4.280	3.830, 7.014, ± 4.109
General mass point quality	71.81% Vs 28.19%	70.42% Vs 29.58%	67.03% Vs 32.97%
Contour lines with profile tool:			
Maximum, minimum	15.06 m, 0.12 m	12.05 m, 0.002 m	17.30 m, 0.001 m
Mean	7.30 m	2.92 m	3.07 m
	DEM results – DGPS points comparison correlation value: r = 0.9954		

There are a few questions that need to be answered. Is the number of reference points good enough for the validation of the DEM extraction? Which are the errors that are already included in the reference points? In other words, which is the quality of the reference points? Is there a comparison criterion reflecting the application requirement, and is it good enough to validate the results? (Polidori, 2002)

The number of reference points obtained was the best possible under the circumstances. The raw Geo IKONOS imagery was used as a horizontal reference; the contour lines of the maps were used as a height reference. And because of difference in time and information content, it was very difficult to define common identifiable points.

Partially, the second question is already answered. The maps were registered to IKONOS, thus there is a horizontal error included in the height reference inclusion. It should be also noted that in the case of the 008-014 stereopair, some of the reference points were sampled from the registered-to-IKONOS CORONA imagery, because of the lack of adequate control for the triangulation process. Thus, the registration errors will be transferred to the DEM extraction. Perhaps this explains the magnitude of error in this stereopair in comparison with the other two, when at the same time there are more reference points than the other two stereopairs.

The third question seeks for a comparison criterion that reflects the application requirement and is good enough for the validation of the results. In other words, it seeks to define a statistical index and the magnitude of the comparison criterion. The statistics in table 8-7 may not be meaningful enough, mainly because of the small number of reference points and the invisible errors that are included, but it is still a valuable statistical index. Fortunately, the DGPS points can be used as independent checkpoints, and these provide a helpful validation of the results even if these data are limited in this study. An interesting approach is to map the spatial behaviour of the errors. Horizontally, this is illustrated in figures 7-5, 7-6, and 7-7. Vertically, this is illustrated in figures 8-7, 8-8, and 8-9. Unfortunately, the horizontal and vertical errors are not derived from the same points, since different points were used for each control. It may not give any quantitative evaluation, but qualitatively proves to be very useful.

In all DEM image files, one may notice the horizontal stripes running across the flight path of CORONA satellite. These lines add an extra error to the DEM results. This must be identified. The striping appears along the Y-axis of the satellite (that is, across the flight line). This excludes the GCPs as a possible source of the distortion. Also, the striping appears in an irregular order and strength. The 009-015 (South) stereopair shows the strongest striping, the 007-013 (North) stereopair is next and the 008-014 (Centre) stereopair shows the lightest striping (almost negligible).

Could this be caused by the CORONA geometry? If this is the case, then why is the striping appearing in random order and strength? In paragraph 2.1.13 of the thesis, it is mentioned that the roll drum printer of USGS introduces a slight stretch in the Y-axis. Perhaps, this is the reason of the error.

The DEM extraction comes from two series of films. The stripes could have been created because of a difference in the film pre-processing.

Before the start of the PhD, the three films 007, 008, and 009 were scanned in a drum scanner. The drum scanners spin the film around on a drum while a fixed laser or other beam light looks at the art as it spins. They are hot because the beam is picked up by a much more sensitive PMT (Photo Multiplier Tube). A drum scanner beam can be focussed as small as you want. You can move the drum really slowly and get almost unlimited resolution. Of course, the film must be soaked in oil before being mounted to the drum, and the film cleaned afterwards. Unfortunately, there are no records about the exact way these films were scanned.

Because of the above, there was a suspicion that one series of the films was distorted because of the drum scanning. The motion of the film in the drum scanner follows the stripes. The hotter is the scanner, the more is the distortion on the film. This could explain the irregular appearance of the striping effect on the imagery, if the films were scanned without an order. The equal width of the stripes can be interpreted by the equal width of the scanner's rollers.

For this reason, duplicate set of 007, 008, and 009 films was ordered by USGS, and scanned using a photogrammetric scanner. Thus, the two series of films now have identical pre-processing. The new DEM extraction showed no stripes in 008-014 and 009-015 stereopairs. But in 007-013 stereopair the stripes appeared again, with more strength than before.

After discussion with Jacobsen (personal communication, 2004), the image scanning parameters were suspected, because the different sets of images were scanned at different times. This means that the brightness, contrast and gamma are different from one image to the other, and this became obvious in the MVA study of chapter 6. However, this is not enough to describe the striping effect.

Brown and Bara (1994) mention that some scanning irregularities can only be detected with the application of filters. During the application of spatial enhancement with a 3x3 filter that returned standard deviation (see figure 5-13 in paragraph 5.3.4), a grid was noticed in the film. The standard deviation filter was applied backwards in the methodology to try to identify the source of the grid. Thus, the non-geocorrected images were filtered and the grid appeared again. Then, the raw imagery was filtered and the grid appeared there too. The film was checked on a light table with a magnifying glass and no grid was detected. From this, it seems that the source of the grid is the digital scanning.

Kasser (2002c) mentions that even if a preliminary calibration is applied on the scanner, some irregularities may continue existing, for example calibration errors or dust particles that will affect the radiometric precision of the scanning. In particular for matrix CCD scanner (like the one used in this project, see Appendix IV for details), Kasser (2002c) mentions that they will be periodic and annoying artefacts due to repetition of errors according to a regular paving, and of radiometric discontinuities between successive positions of the matrix.

According to Thom (2002), when one tries to get as much geometric precision and spatial resolution as possible by using the smallest scanning step, then there may be loss in the radiometric precision and resolution of the scanned imagery if one is not careful to obtain optimum radiometric quality. Thus, there may be more interpretability because of the more accurate representation of the ground, but simultaneously there may be problems with the radiometric precision. It would not be surprising if the small scanning step combined with the subsistence of irregularities is the actual source of the creation of the grid, which subsequently results in the striping effect in the DEM. Thom (2004) believes that the grid is a scanning artefact, most probably due to the bad correction of the black level of the CCD sensor in the scanner. Figure 8-15 shows that the grid matches the stripes of the DEM. However, the vertical lines of the grid do not seem to influence the automatic DEM extraction.

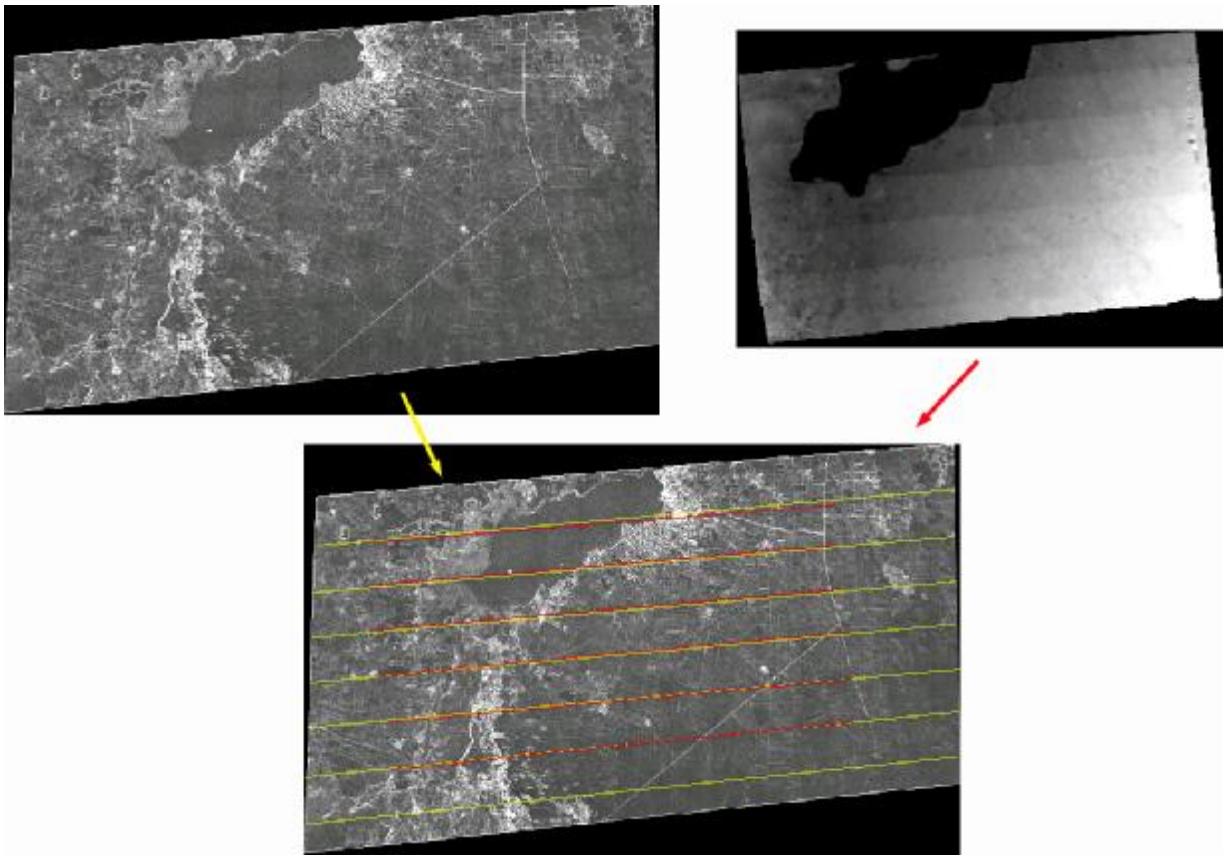

Figure 8-15 – The grid and the stripes show a good fit.

Whatever the reason is for this striping effect it is highlighted by the ERDAS method for automatic DEM extraction. The grid influences the stripes only towards one direction because height is a function of x-parallax and therefore no stripes occur in y axis of the grid. The problem is possibly insufficient radiometric/geometric calibration of the photogrammetric scanner. The creation of a DEM with another software should not present different results.

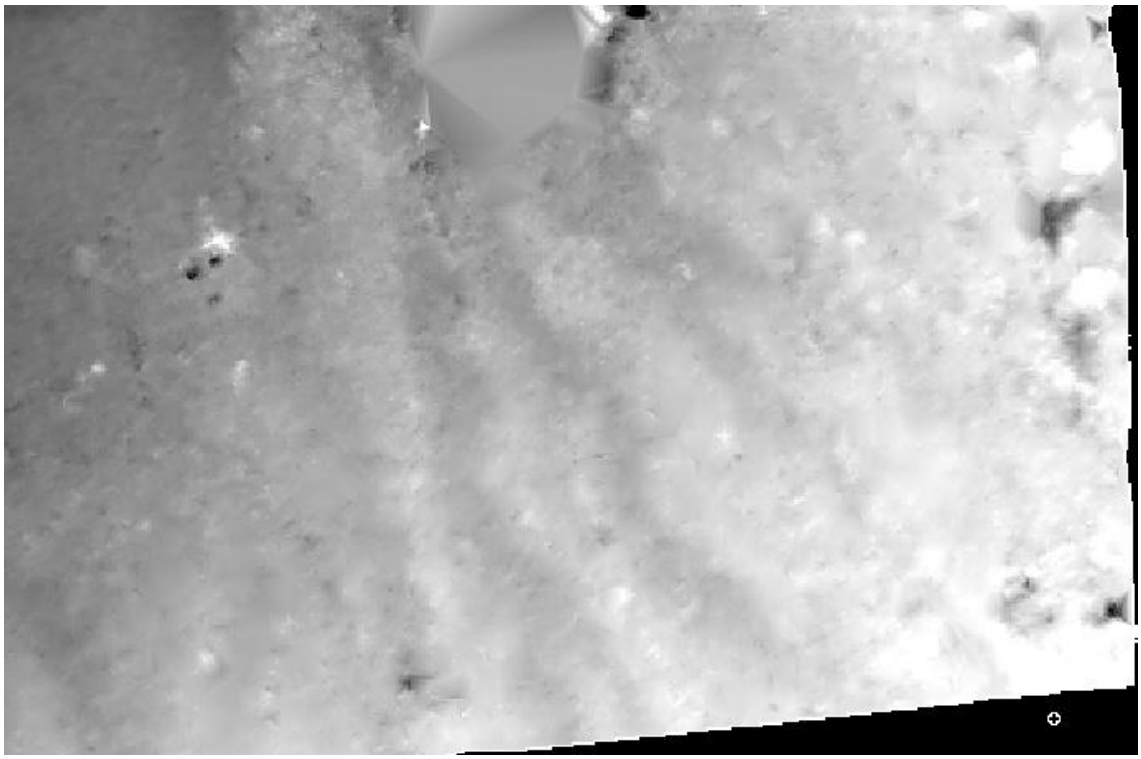

Figure 8-16 – The DEM pinpointed channels south of Homs city running from Southeast towards Northwest.

Figure 8-17 – Channels in the south area, South West of lake Qatina, running from Southeast towards Northwest.

The quality of the DEM is not what one would call ‘excellent’, since only two thirds of the mass points have a strong correlation, and one third are suspicious. Also, the random comparison of the DEM sampled points with the map contour lines shows that the DEM is not ‘excellent’ at all.

The visual inspection shows that the automatically extracted DEM is a good representation of the terrain, thus giving information that cannot be found in the maps. With close inspection and some enhancement of the DEM image, one can identify areas of interest that are not readily apparent from the contours of the map.

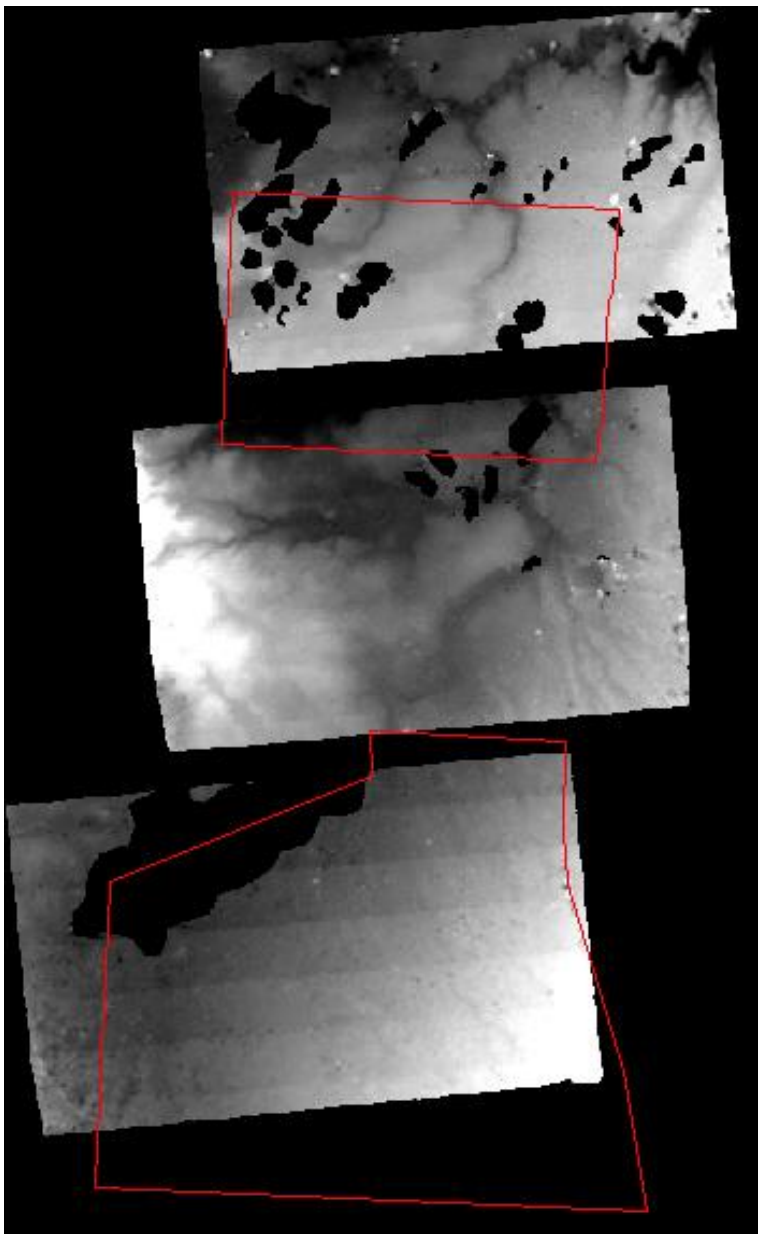

Figure 8-18 – The DEM images of the Homs area. The red line defines the boundaries of the area of interest. The black patches are clouds with their shadows, and lake Qatina.

But even if one looks into the 3D perspective of the DEM, there can be information that a cartographer cannot easily depict on a map. For example, after loading the DEM into VirtualGIS viewer, one may exaggerate the heights. And then, with the ***sun-positioning*** tool, "throw light" on the DEM from different angles. The shadows of the terrain will highlight various shapes, some of them with particular interest. An example of such an application comes from Parmegiani and Poscolieri (2003), who applied landscape archaeology by means of viewshed analysis, height profiles drawing and 3D representation of the obtained DEMs.

When moving into a larger scale, things change. One must think of the pixel size and the interpretation limits it offers. Since the pixel size of the DEM is 17 m, the interpretation of objects is restricted. The interpolation of the automatic DEM extraction method smoothes the heights and makes the distinction of obvious sites (like tells) extremely difficult.

The manual approach is suggested for the extraction of quantitative information from the stereopair. It is expected that with a proper photogrammetric work station, it will be easy and straightforward to create contour lines and make direct measurement of features with satisfactory precision.

8.4. Conclusions

The research has demonstrated that accurate three-dimensional information can be extracted from CORONA imagery using only a small number of ground control points (GCPs). Satellite ephemeris and attitude data, and specialist panoramic image processing software, all of which are difficult to obtain, are not in fact necessary.

If good quality map data are not available, the horizontal location of GCPs can be obtained from IKONOS satellite imagery. In this study, height information was derived from maps although points fixed from a Differential GPS can also be used and may even improve the accuracy of the model (Galiatsatos *et al.*, 2002).

The same software (ERDAS OrthoBASE Pro) for the triangulation and DEM extraction was used by Altmaier & Kany (2002) but in a more intense landscape, with DGPS-measured GCPs. Their accuracy is not as good as in the Homs area. Most probably this is because of the intense landscape of Southern Morocco, which contrasts with the relatively flat area of Homs. Schmidt *et al.* (2001a) created a DEM from CORONA imagery with the use of VirtuoZo software, again in the same South Morocco area. The accuracy was close to that reported by Altmaier & Kany (2002).

Since they cooperated in other papers [Goossens *et al.* (2001), Schmidt *et al.* (2001b)], it can be assumed that the GCPs were derived from the same DGPS measurements.

Shin (2003) developed a more rigorous approach with few ground control points. Schenk *et al.* (2003) compare the rigorous approach of Shin (2003) against affine transformation and rational function models. Sohn *et al.* (2004) compare three methods in the DEM extraction: the removal of distortions in panoramic photography according to Slama *et al.* (1980), the time-dependent model of Case (1967) with simplified parameters and need for ground control, and the terrain-dependent rational function model as described by Tao *et al.* (2002).

Simple 3D display of the stereopairs may be of value to rapid and inexpensive photointerpretation, but it may contain errors that are not immediately obvious and it lacks the rigour of a stereo model. A stereo model can be derived without fieldwork and this may be valuable for planning landscape surveys and carrying out desk based assessments of cultural resources.

The automatic extraction of DEM information from a stereo model is rapid with a good control on the errors, and it offers an adequate overview of the relief in the area of interest. Actually, the DEM view of the geomorphology offers a better picture to the photointerpreter than the map contour lines. The easiness and speed of automatic DEM extraction make it superior to the manual DEM extraction. But the latter offers better control, and a much better approach for larger scales and quantitative information extraction. Thus, the automatic and the manual approach are complementary, each with a different objective.

However, the scanning process of the film affects the automatic DEM extraction. This research proved the relationship of film scanning with the stripes on the DEM. It showed that the film scanning should be done with care. Further research on this problem must be done to identify the exact source of the stripes and eliminate it.

For an archaeologist, the most sensible approach would be the use of stereopairs for photointerpretation, and the automatic DEM extraction for a view of the geomorphology. The manual DEM extraction needs expertise and expensive hardware and software. These are not always available in an archaeology group. On the other hand, measurements of specific features may be taken with a good degree of precision after manual correction of the x and y parallax.

9. Discussion and conclusions

9.1. Introduction

This thesis had two principal objectives. The first was to investigate the characteristics of the CORONA series of satellite imagery, in order to assess its potential for application in landscape archaeology. The second was to use a specific case study to demonstrate how CORONA and IKONOS satellite imagery could assist with archaeological landscape research. Through these two directions, the CORONA data position was defined among satellite data. The CORONA data were being assessed qualitatively through photointerpretation and quantitatively through spectral and radiometrical analysis and by assessment of the height information contained in stereopairs.

It was difficult to find adequate information about CORONA data and so a review of the technical characteristics and applications was undertaken. After the declassification of CORONA imagery in 1995, a huge database of imagery[55] and documents[56] opened to the world. Although several books about CORONA have been published, e.g. Ruffner (1995), Peebles (1997), McDonald (1997), Day *et al.* (1998), and Madden (1996), all of them focus on the history of CORONA project, and give very little information on photogrammetry problems.

The value of CORONA is slowly becoming recognised in Earth and environmental science and in archaeology. Steady streams of papers are now appearing that use CORONA to assist with change detection. However, very few of these publications discuss the problems and pitfalls of CORONA on the one hand, and the advantages of the 3-D information on the other. A few studies have begun to address technical issues to help guide future projects, e.g. Shin (2003). Others have simply used the images in place of photography.

Also, the declassification of CORONA created questions that needed to be researched. More recently, Cloud (2000), through the research project of Clarke (2000), studied on the history of CORONA and how it influenced the developments in cartography and geodesy. Shin (2003) researched the creation of a rigorous model for panoramic photography from space. However, archaeological applications using

[55] Executive Order 12951, 22nd February 1995.
[56] Executive Order 12958, 17th April 1995. Amended by Executive Order 13292, 25th March 2003.

CORONA began to appear in parallel with this technical research, e.g. Kennedy (1998), Ur (2003), and it is not always clear from these publications whether the authors of the former were fully aware of the technical issues being explored by CORONA specialists and photogrammetrists. Thus an important aim of this thesis was to bring together the technical data and explore its implications for a real-life archaeological investigation. But none assessed CORONA to identify advantages and weaknesses and provide practical information for the potential user of this kind of imagery. These are the main reasons for the creation of chapter 2: the sparseness and generality of practical information on CORONA and the lack of an in-depth understanding of the satellites and camera systems of the CORONA program.

The CORONA is positioned through comparison among other satellite data in chapter 3. CORONA's positioning among other satellites also defines the best data synergy for processing and data extraction. The implementation of approaches such as DEM creation, change detection, or image fusion is of value for any application, and CORONA data have the potential to contribute to all of these approaches.

9.2. Progress on technical understanding of CORONA

9.2.1. Preprocessing.

Before any processing approach takes place, the CORONA data should be converted into a form compatible with the format of the other data, and it must be free of geometric distortions, which in the case of CORONA are twenty-seven in number. CORONA data is most useful if collocated with other satellite data into a GIS in order to take advantage of GIS capabilities. This was the main subject of chapter 4.

Chapter 4 discussed the best approach for translation of CORONA negatives to digital format using a photogrammetric scanner with an optical resolution as close as possible to the film resolution of the relative CORONA mission. Tappan *et al.* (2000) preferred to photointerpret CORONA straight from the film without any translation. This is a rigorous approach, but it inhibits the GIS potential of data integration. Bindschadler & Vornberger (1998) scanned the film to a satisfactory scale for their application, while Palmer (2002) preferred to create prints of larger scale and then scan the prints on a flatbed scanner. Palmer's choice was based on the lack of expertise and resources, and although simple it may be appropriate for the demands of his application.

There are several approaches for the correction of the CORONA data distortions. Sohn *et al*. (2004), Schenk *et al.* (2003), and Shin (2003) identify rigorous and other approaches for the panoramic photography of CORONA. Panoramic photography was an innovative and fashionable method developed in 1960s-70s, but is little used today. Another fashionable method was strip photography (Case, 1967). Thus, the best source of information for these data is the past publications. Slama *et al.* (1980) was a very good source for the correction for panoramic data. Note that some of the authors in Slama *et al.* (1980) were main contributors in the CORONA program. Other important publications are Case (1967) and Devereaux (1973).

From the above publications, the most important point is that if there is ground control then the ephemeris data are not required (Ondrejka, 2000; Slama *et al.*, 1980). Thus, there is no need for an orbital model approach. However, a key problem with archaeological survey in the Middle East is the lack of ground control in many cases, mainly because of local security restrictions. For this reason, it was impossible to establish a DGPS points network using hard points (simultaneously considered as 'sensitive points' by the security) for the geocorrection of the satellite imagery. The solution was that the data were registered to the IKONOS imagery that had the most information content, the best geometry and reliability, and the least offset from a real coordinate system. However, the best approach for the CORONA data proved to be orthorectification, which demands height data and the existence of frames from both aft and forward cameras for the area of interest.

Another key problem with archaeological survey in the Middle East is the lack of information concerning the local coordinate system. This made difficult the navigation in the area especially when both CORONA and the maps could not show the current landscape situation. The integration of IKONOS imagery in the data of the project helped in the establishment of a basemap, on which all other data were registered. This basemap was in UTM coordinate system, which in combination with the present picture of landscape from IKONOS helped with the navigation in the area of interest.

9.2.2. Qualitative assessment

During the processing stage, there were two main approaches: photointerpretation and image analysis. The first involves direct human interaction, and thus it is good for spatial assessment but not for quantitative accuracy. The latter has high quantitative

accuracy but low spatial assessment capability. Today, both techniques are used in a very specific and complementary way, and the approaches have their own roles.

Here it is important to mention that exact practice will depend on existing expertise and resources, and the particular application. A photogrammetrist would look for the highest possible accuracy to bring CORONA to a point where one can extract reliable quantitative information. An archaeologist would look for the best enhancement that will make the sites visible on the existing landscape. Within the Homs landscape, it was demonstrated by Beck (in prep) that accuracy was more important in the basalt area where the features (networks of walls and cairns) are more complex than the marls area where the landscape is flat and simple.

The photointerpretation approach involves many elements and levels, which are described in chapter 5 along with the existing computing help through image enhancements and transformations. Archaeologists are accustomed to using low altitude aerial photography. Satellite images, which are of lower spatial resolution, may at first appear to be of little value. However, satellite imagery can provide a variety of advantages that stem from spectral, radiometrical, temporal properties; when combined with recent advances in spatial resolution (e.g. IKONOS, Quickbird) and declassifications of fine resolution data (e.g. CORONA, GAMBIT), provide a powerful set of tools for surveying archaeological landscapes (Kouchoukos, 2001; Bewley *et al.*, 1999).

In the photointerpretation approach, CORONA proved its value for archaeology with the detection of numerous archaeological sites, which until today were unrecorded and/or unmapped. Examples within the thesis illustrate the spatial resolution and the historical value of the CORONA imagery. However, the same examples also illustrated that CORONA imagery is limited to the features it can resolve. This limitation also depends on the knowledge of the area and the experience of the photointerpreter.

Among the enhancements applied on CORONA imagery, of particular interest was the spatial enhancement through a 3x3 standard deviation filter. It amplified and made visible a scanning artefact, which seems to be related to systematic noise detected in the automatic DEM extraction.

9.2.3. Spectral assessment

Surprisingly, very little work has been done to assess the spectral characteristics of archaeological soil marks or traces. In the Homs study area many sites appear on satellite images because of higher brightness in contrast with the surrounding environment. In this thesis ground-based spectroradiometry was used to investigate these on- and off-site differences.

In an effort to understand what the image data is showing, surface soil samples were taken from transects crossing the sites, starting and ending at a decent distance outside the perceived borders of the site. These soil samples were then examined for their particles size, their organic content, and their reflected radiance.

The field and laboratory spectroradiometry measurements proved an increase in the reflected radiance from the on-site samples when compared to the off-site samples.

The integration of the laboratory measurements on soil samples showed a higher proportion of sand fraction in the on-site samples, in contrast with the off-site samples. The positive correlation of sand with the soil reflectance showed that there is a relationship between the proportion of sand and brightness within the site.

According to Wilkinson (2003) and Wilkinson *et al.* (2004), the sites of the Northern Syria present light and fine-grained anthropogenic soil, which stands out from the darker and red-hued calcareous soils of the plains. This does not happen in the Homs area. The organic content and the fine grains of the samples showed a negative correlation with brightness, and they were more abundant off-site than on-site. The source of this difference between this study and the studies of Wilkinson is still unknown. It is possible that the fine-grained proportions of the samples were eroded by the strong winds of the Homs area. There is need for further research towards this direction through more sampling and laboratory analysis.

The existence of MVA imagery offered the opportunity to assess whether the sites of archaeological interest were view-dependent. CORONA proved to have the potential for directional detection of land classes, thus substituting the spectral capability it lacks. The assessment showed that tells and khirbets are not view angle dependent. However, CORONA proved discriminating capability of land cover.

The image pair should be scanned under the same scanning parameters to improve the radiometric and geometric accuracy of the directional detection. Otherwise artefacts of processing will be included in the image.

On the other hand, IKONOS may have had a small difference in the view angle but it proved potential to discriminate land cover through an MVA study. Because of the multispectral IKONOS image, which is well co-registered to the panchromatic IKONOS image (Helder *et al.*, 2003), the spectral component may be combined with the directional component for detection of different land covers in the area of interest.

9.2.4. Quantitative assessment – DEM creation

The existence of a stereopair of CORONA frames in the area of interest offered the chance to investigate the extraction of height information and the creation of a DEM (Chapter 7), and then assess it (Chapter 8). Two main approaches were followed: a rigorous approach with readily available panoramic model, and an empirical approach with a non-metric camera model.

This research showed that the readily available panoramic models that exist in photogrammetric software presume boundaries on altitude and incidence angles that cannot work for orbital satellite platforms. Pournelle and Hunt (2002) reached the same conclusion. Shin (2003) recognised this lack of a rigorous model for panoramic imagery from space and developed it.

On the other hand, the non-metric camera approach though empirical proved to be rapid and easy, simultaneously providing acceptable errors and good results. Altmaier & Kany (2002) and Schmidt (2003) also used the non-metric camera approach for the creation of DEM under different circumstances (more intense relief, use of different software) with success. In all cases of empirical approach, the main advantage of the CORONA imagery capability for DEM generation is the cost and time per square km of covered area, which prove to be minimum. Sohn *et al.* (2004) showed that the application of a mathematical algorithm to remove panoramic deformation could improve the DEM accuracy, in the expense of cost and time.

The processing through the readily available panoramic model showed more difficulty of use than the non-metric camera model, mainly because of the demand for more parameters. However, the absence of reliable ground control proved to be the main difficulty for the application of a more elaborate approach in the DEM creation.

Although the creation of a DEM has many advantages, the cost of specialised software and the lack of expertise is forbidding for many archaeologists. Palmer (2002) used simple image processing software to overlay the images and create an anaglyph.

Thus, he got an image of the relief, and proceeded on photointerpretation. However, this method is prone to illusive conclusions.

An effort to create DEM from IKONOS imagery proved pointless because of the lack of ephemeris data, GCPs and RPCs. The lack of ground control did not allow the construction of a DEM from IKONOS imagery. Despite the low *B/H* ratio, it was shown by Jacobsen (2003) that a DEM is achievable. However, all the applications that created DEM from IKONOS data either had RPCs (Grodecki *et al.*, 2004; Dial & Grodecki, 2003b), or had GCPs in a rigorous approach (Valadan Zoej & Sadeghian, 2003; Toutin, 2003), or had GCPs in other approaches (Fraser *et al.*, 2002a; Fraser & Yamakawa, 2004).

9.2.5. Quantitative assessment – DEM extraction assessment

The creation of the DEM allowed an assessment of the ability of CORONA to resolve features from their height. The photointerpretation of anaglyphic images showed that large tells (Tell Nebi-Mend, about 20 m height) are easily distinguishable, and medium tells (Tell Ahmad, about 10 m height) are distinguishable with some effort. The height of the walls and cairns of the north area (less than 2 m height) was not perceived in the CORONA DEM, even though it was still easy to detect them. Thus, the range of height was constrained.

The extraction of the CORONA DEM followed two approaches: the automatic extraction and the manual extraction. The latter could not be accomplished because of some fault to the software that caused it to be demanding in computing power, even in the relatively non-demanding stereo-viewing. However, specific points were sampled and compared with the DGPS points. The automatically extracted CORONA DEM was assessed against contour lines on maps, the ASTER DEM, the SRTM-3 DEM and DGPS points from soft detail points. The assessment showed a good fit. The assessment also showed that the ASTER relative DEM is not accurate and the user should be careful about its use.

The assessment of the two approaches for DEM extraction in contrast to the same set of DGPS points proved that the manual extraction approach is more accurate than the automatic. However, the automatic approach is rapid and it still gives an accurate view of the geomorphology in the area of interest. The manual approach needs expertise and expensive hardware and software. For these reasons, it is suggested that the automatic

DEM extraction is appropriate to obtain a view of the landscape relief, and the manual DEM extraction for the purpose of measuring heights from archaeological sites.

The general assessment of the DEM followed the quality assessment suggested by Polidori (2002). The resulting DEM showed a systematic error that emerged in the form of stripes running across the flight axis from one edge of the image to the other. After discussion with Jacobsen (personal communication, 2004), the problem was thought to be the result from the image scanning. Filtering of the image revealed a grid that appears in the scanned imagery. The 3x3 standard deviation filter was applied to the raw imagery and the grid appeared again. According to Kasser (2002c), this grid can be a shortcoming of irregularities that subsist (dust particles, calibration errors), even after a preliminary calibration. Thom (2002) shows that the smaller the step of scan, the better will be the precision and the spatial resolution, but there may also be loss of radiometric precision if one is not careful of the radiometric quality.

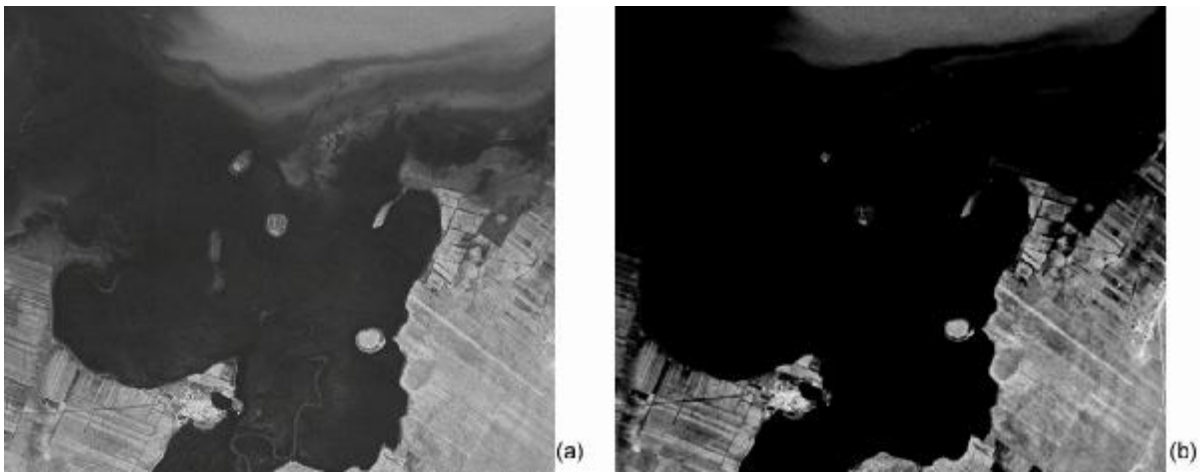

Figure 9-1 – Difference in scanning between attention in radiometry detail (a) and attention to geometric precision with high contrast (b).

In practical applications, the impact of radiometric quality on the geometric precision is not easy to evaluate. Generally, weakly contrasted details can be separated when attention has been given to the radiometric quality. Figure 9-1 shows the implications of this issue to landscape archaeology. Furthermore, when the images are scanned with insufficient care in the radiometry quality, it may cause problems in applications where radiometric quality is important, e.g. image matching, MVA studies.

9.3. The application of CORONA for landscape assessment

9.3.1. Other applications

At the beginning of this research, there were very few known applications of CORONA imagery. As this research proceeded, more and more people recognised the value of CORONA data, and they integrated CORONA in their applications.

One of the advantages of CORONA is that it extends the historic data archive of remote sensing data to 1960. This is very helpful for the detection of long-term changes. As Donoghue (1999, p.273) states: "*At a global or regional scale remote sensing offers the only practical method of change detection*".

Bindschadler & Vornberger (1998) co-registered CORONA with AVHRR and SPOT data for the detection of changes. CORONA imagery afforded a direct view of the configuration of the ice sheet in the early 1960s, greatly extending the limited surface observations made in 1958 to 1959.

Tappan *et al.* (2000) combined the geodetic and synoptic qualities of the ARGON photograph with the high-resolution CORONA photographs. They detected changes in land use and land cover by comparing CORONA and ARGON with Landsat imagery. Again, the historical value of CORONA is shown in this work. The photography depicted the area of west-central Senegal before the recent drought cycle, from when no aerial photos or other wide area surveys exist.

The above-mentioned examples of the use of CORONA data in change detection applications do not exploit the spatial resolution of CORONA. Schmidt (2003), Trelogan *et al.* (2002), and Musaoglu *et al.* (2004) apply visual change identification between CORONA and IKONOS, CORONA and IRS 1-C panchromatic, and CORONA and SPOT-5 panchromatic respectively.

The work of Trelogan *et al.* (2002) also highlights the historical value of CORONA for the archaeological record with the identification of buried archaeological remains that today are impossible to detect because of the extensive landscape modification. With the aid of CORONA, Cerasetti & Mauri (2002) detected archaeological evidence that give light to the supply system of ancient outposts. Today this evidence is covered by vegetation that makes surveying impossible. Kennedy (1998) shows the historical value of CORONA imagery through examples of archaeological sites that today are

flooded by lakes, which formed behind a succession of large dams along the river Euphrates.

The works of Altmaier & Kany (2002) and Palmer (2002) highlight the moderate cost of CORONA imagery and the capability to provide accurate enough information through simple and rapid processing approaches. The main focus was on quantitative and qualitative information respectively.

The spatial resolution of CORONA makes it comparable to aerial photography of high altitude. Ur (2002, 2003), Kennedy (1998, 2000), Comfort *et al.* (2000), Comfort & Ergec (2001), and Wilkinson (2000a, 2003) highlight the importance of the CORONA imagery for Middle East, because of the unavailability or limited availability of aerial photography. This advantage of CORONA is stretched outside the Middle East area, for example Romania (Oltean, 2000), Morocco (Altmaier & Kany, 2002), Armenia (Palmer, 2002), and other places in the world where historical data like aerial photography or maps do not exist or are limited. A more elaborate approach for the application of CORONA imagery in landscape archaeology has started by Gheyle *et al.* (2004a, 2004b) in the Altai republic of south Siberia.

Because of the advantages of CORONA, in particular low cost and historical value, it has been taken up avidly by archaeologists (Kennedy, 2000). From the above applications, it is apparent that archaeologists mostly photointerpret CORONA data. The main reason is that archaeologists lack the expertise of processing satellite data, and thus there is hesitation and ambiguity for routinely employing satellite data in archaeological approaches (Grosman, 2000). However, advances in information technology can stimulate changes in the field routine, and the combination of all available data in a multi-layer analysis is essential (Schmidt, 2004). When it comes to integration, the scale of the application defines the need for accuracy. The high-resolution sensors are more appropriate for the detailed mapping associated with archaeological sites. This demands high accuracy and as rigorous approaches as possible, always depending on the existing data.

9.3.2. Application of CORONA for Homs landscape assessment

This work helped the Homs archaeological project in the following ways:

It improved our understanding of the properties of CORONA, and thus our ability to interpret the features visible in the imagery. The research on the properties of

CORONA showed the strengths and limitations of the imagery quality, thus allowing for the optimum conversion of the film to a more compatible and accessible form for photointerpretation and image analysis.

It allowed us to compare and contrast between different sets of imagery, through their co-registration. The research on CORONA program showed the variety among the missions, and the availability of many sets of frames for the Homs area. Thus, data from different seasons, with different cloud cover, and from different years were provided and co-registered for the Homs project. The mission differences along with the seasonal and annual differences allowed for the creation of a dataset that could provide a variety of information one single image could not include. The importance of seasonal and annual differences is also illustrated in Kennedy (1998).

It identified navigation and mapping problems faced in the Middle East by researchers and provided possible solutions using the available information. An approach of simple plane geometry was developed during navigation in the area for the translation of the GPS UTM readings to the local coordinate system whose parameters were unavailable at that time. Among the different empirical approaches for mapping with CORONA, orthorectification proved to be the more accurate approach.

It identified the best approach for data integration according to the existing information. It was not possible to establish a network of accurate GCPs in the Homs area, and thus have a georeferenced set of data. The research showed that co-registration of all data was the best solution for data integration. When IKONOS arrived, it was the best available source for the creation of a basemap. However, for proper geocorrection of data, an accurate GCPs network should be established in the future.

It identified the potential limits of CORONA in DEM creation. The existence of CORONA stereopair in the area offered the chance for research on the height information that can be provided by the stereomodel. The limitations of the DEM were identified quantitatively and qualitatively. The DEM itself proved helpful in photointerpretation and terrain analysis approaches.

It identified the potential limits of CORONA in MVA studies. Often in archaeological applications oblique photography is mostly used because it offers a clearer rendering of most types of archaeological site and may record details that cannot be sufficiently well discerned on an equivalent vertical view (Wilson, 1982). Various examples of this issue are presented in Beresford & St Joseph (1979). But none before had used MVA imagery for the detection of archaeological sites. The CORONA imagery provided oblique

photography from two different view angles. The archaeological site presented view-angle independency, but CORONA MVA imagery showed potential for the distinction among different land cover.

It identified the presence of different types of archaeological remains, which could subsequently be identified in the field (tells, flat sites, walls, cairns) in a way that Landsat could not do. Landsat is not a substitution for aerial photography. On the contrary, CORONA offers information of the same scale with high altitude aerial photography. With care in scanning to acquire geometric and radiometric precision, CORONA imagery provided detailed information of the landscape and thus identified areas of archaeological interest, which were subsequently confirmed as archaeological sites.

It identified the potential of CORONA in photointerpretation. The spatial resolution, the extraction of DEM, and the MVA capability of CORONA improved greatly its potential in photointerpretation. The height information along with the high detail of the ground provided an improved picture of the landscape. The MVA capability provided directional component in the process and thus one extra tool to distinguish different land cover.

It made it clear that archaeological residues in the marl zone have a distinctive reflectance, which raised questions regarding the nature of archaeological deposits, which were subsequently investigated in the laboratory. Researchers never before used the approach of field spectroradiometry across the archaeological site. This approach identified a distinctive reflectance of the archaeological site soil in contrast to the surrounding background soil. Further work in the laboratory identified the reasons for this distinctive reflectance. Future research could confirm/expand these results.

It provided affordable high-resolution data which is largely free from the landscape 'clutter' of recent decades and which is valuable for time-change analysis when used in conjunction with more recent high-resolution imagery. In this study too, CORONA imagery proved its historical value through detection of archaeological evidence that today are destroyed due to landscape modification and degradation. In conjunction with IKONOS imagery, the landscape difference was visually obvious. Thus, the changes could be visually detected and recorded.

9.4. Conclusions

This research showed through a case study in Orontes valley of Syria that CORONA series of satellite imagery when elaborately handled is a very useful tool for landscape archaeology. The approach was as detailed as possible and the assessment ranged from the quality of the CORONA data themselves to the identification of strengths and limitations in the provision of qualitative and quantitative information. The archaeology users need greater familiarity with the characteristics of CORONA, and this research provided as detailed an assessment as possible.

However, the final decision about the best approach for CORONA imagery use in landscape archaeology is left to the reader. CORONA imagery includes a lot of information and this research showed ways to derive the maximum of this information. As a survey engineer and photogrammetrist, the author applauds precision and accuracy, which in archaeological applications are not always considered of high value. Below is a summary of the conclusions of the thesis, which will help in the final decision by identifying the values and limits of CORONA imagery for archaeological studies.

The image quality varies according to the satellite mission, and thus the prospective user should have different expectations about what can be derived from each image. This issue was never before addressed in the literature. The moderate cost allows for purchase of multiple images, and thus minimises the chances for cloud-covered features, simultaneously increasing potential of the dataset of the project. The research showed that satellite designs KH-1, KH-2 and KH-3 have mainly qualitative value, while the satellite designs KH-4, KH-4A, and KH-4B also have quantitative value.

If scanned with care, the CORONA image quality proves to provide high detail of the ground features. The scan should be better done in photogrammetric scanner for better geometric and radiometric control in the conversion from analogue to digital format. The geometric precision of the scanning should be done in balance with the radiometric precision, if the user wishes to get the most from the image interpretability. Also, the scanner should be sufficiently calibrated and the scanning parameters should be kept the same among the images. However, the detail and process of digitising of CORONA imagery depends on the application needs and directions.

Some of the users of CORONA imagery stop in the digitising phase and they do not proceed to correction of the panoramic distortion, or geocorrection of the imagery. This is mainly because of lack of expertise, lack of readily available software for correction of the panoramic distortion, or simply lack of ground control. This research showed directions in the rigorous approach of panoramic model. It also illustrated the usefulness of data integration on a common basemap, and argued on the possible approaches for the integration of the datasets of the Homs project. The problem of image geocorrection is common in Middle East, where the establishment of accurate ground control network is not allowed. The argument followed in the thesis can be a pilot study for other studies that face the same problem.

The integration of the satellite image data of the project showed the historical value of CORONA imagery for landscape archaeology. It provided information and detail of archaeological evidence that modern imagery could not detect because of landscape modifications (which are intense in the area of interest) that destroyed or masked several traces of archaeological interest. The image data integration also highlighted the low cost of CORONA imagery per square km of useful data. CORONA imagery was the cheapest among the satellite data of the project.

The photointerpretation showed the ability of CORONA imagery to provide qualitative information. This ability depends highly on the previous steps of image selection and careful digitising. The ground resolution of CORONA imagery was adequate for the detection and mapping of sites of archaeological interest, and the application of landscape studies.

Some of the archaeological sites were detected in CORONA imagery because of reflectance difference with the surrounding environment. After field survey and laboratory measurements of on-site and off-site soil samples, this research showed that the proportion of sand fraction could be the reason for the reflectance differences. In contrast with studies in the North-East of Syria that assumed the fine grains and organic content to be the positive reasons for reflectance differences, this research showed through experimental measurements that the organic content and the fine grains were less on-site than off-site and were negatively correlated with reflectance. Until the writing of this thesis, there is no known spectroradiometry study of archaeological sites

The existence of a stereopair of CORONA imagery allowed for research in extraction of height information, and assessment of the directional properties. Never before was CORONA imagery used for a MVA study. The results of the directional

properties assessment strongly suggested that vegetation is angle dependent, and thus it is possible to separate and identify vegetation from dark soils in CORONA imagery. This is very helpful for the photointerpretation of CORONA imagery when ground truth is impossible, especially when multispectral data is not available. On the contrary, archaeological sites were not view-angle dependent.

The extraction of height information helped in the quantitative assessment of CORONA imagery. Comparisons with other height data proved the capability of the CORONA stereopair to describe the real surface. The height information fine-tuned the photointerpretation approach, thus improving the capability of CORONA to resolve ground features. The quantitative assessment showed the limits of the imagery in the identification of features because of their height. Although rapid and accurate enough, the automatic DEM extraction showed artefacts whose source seems to be insufficient radiometric/geometric calibration of the scanner. Although slow and expensive in time and computing power, manual DEM extraction showed higher accuracy in height extraction information than the automatic approach.

9.5. Future research directions

The research on CORONA data understanding could well be expanded and thus be completed with a visit to NRO library where a vast amount of documents about CORONA are open to the public. The present research showed that every mission was different and unique in operational design and this is an issue of importance for detailed studies. Thus, possible fields of expansion include research on characteristics for every mission and creation of a database with particular details (film, filters, lens system) about every mission that was run in the CORONA program.

This research showed that the conversion of CORONA film to digital form should be done with care in both geometric and radiometric precisions. The result of the automatic DEM extraction included a first time seen systematic error, which should be further researched to identify its source. The focus should be on the photogrammetric scanning calibration and the USGS film duplication.

The stereopair generation could perhaps be improved with the application of the mathematical algorithm that Sohn *et al.* (2004) propose, or the application of the rigorous model of Shin (2003). This should be subject of future research. However, the absence of ground control proves the difficulty of the application of a more elaborate

approach in the DEM creation. The rigorous approach with ready panoramic models and the model of Shin should be tried with imagery where good ground control exists.

Apart from the DEM generation, the CORONA imagery also showed potential in change detection and image fusion. These two fields should be researched for further expansion of the possible ways to use CORONA in landscape archaeology. All applications until now detected changes visually. Further research should try to develop methodology for the automatic or semi-automatic change detection between declassified imagery and modern satellite imagery. As for image fusion, no known application has fused CORONA with other image data.

The laboratory measurements of the soil samples showed different results than what was expected according to other archaeological studies in Syria. These results should be confirmed with further sampling and laboratory analysis from other archaeological sites in the area. Then, the reasons for this difference could be better established.

Apart from the CORONA program, the value of ARGON and LANYARD should be researched for landscape archaeology. The research could also be expanded to the new declassification and include HEXAGON and GAMBIT programs. The latter programs may not have their documents declassified, but still there is need for integration of this historical imagery to modern applications.

The IKONOS imagery showed that there is potential for MVA studies. The directional component of a MVA study can be combined with the spectral component of IKONOS multispectral imagery for a more elaborate approach to the detection of differences among features in the area of interest. According to Helder *et al.* (2003), the IKONOS panchromatic and multispectral imagery are well co-registered, thus the integration of spectral component with the directional component of the higher resolution panchromatic image shows potential that needs to be further researched.

Last but not least, the CORONA and IKONOS imagery could be assessed in applications in other areas, where the landscape is different, i.e. semi-arid or arid environment; where the geomorphology is different, i.e. intense relief; or where the geology is different, i.e. rocky ground.

10. References

- Abraham, V, (1961), Relative geometric strength of frame, strip and panoramic cameras, *Photogrammetric engineering*, vol. 27, No.5, pp. 755-766.

- Abrams, M., (2000), The Advanced Spaceborne Thermal Emission and Reflection Radiometer (ASTER): data products for the high spatial resolution imager on NASA's Terra platform, *International journal of remote sensing*, vol.21, No.5, pp.847-859.

- Abrams, M, and Hook, S., (1999), ASTER User Handbook: version 1, Jet Propulsion Laboratory, California institute of technology, NASA.

- Abuelgasim, A.A., Gopal, S., Irons, J.R., and Strahler, A.H., (1996), Classification of ASAS multiangle and multispectral measurements using artificial neural networks, *Remote sensing of environment*, vol. 57, issue 2, pp. 79-87.

- Al-Roussan, N., Cheng, P., Petrie, G., Toutin, Th., and Valdan Zoe, M.J., (1997), Automated DEM extraction and orthoimage generation from SPOT level 1B imagery, *Photogrammetric engineering and remote sensing*, 63, pp. 965-974.

- Altmaier, A., and Kany, C. (2002), Digital surface model generation from CORONA satellite images, *ISPRS Journal of photogrammetry and remote sensing*, vol. 56, No. 4, pp. 221-235.

- Angstrom, A., (1925), The albedo of various surfaces of ground, *Geographical Annals*, 7: 323.

- Atzberger, C., (2002), Soil optical properties – A review, University of Trier, Remote sensing department, D-54286 Trier, Germany.

- Baltsavias, E., and Waegli, B. (1996), Quality Analysis and Calibration of DTP Scanners, *International archives of photogrammetry and remote sensing*, Vol.31, No B//1.

- Bannari, A., Morin, D., Bénié, G.B., and Bonn, F.J., (1995), A theoretical review of different mathematical models of geometric corrections applied to remote sensing images, *Remote sensing reviews*, vol.13, pp.27-47.

- Barnsley, M.J., (1994), Environmental monitoring using multiple-view-angle (MVA) remotely sensed data. In: Foody, G., and Curran, P. (eds.), *Environmental remote sensing from regional to local scales*, John Wiley and Sons, pp.181-201.

- Barnsley, M.J., Allison, D., and Lewis, P., (1997), On the information content of multiple view angle (MVA) images, *International journal of remote sensing*, vol.18, No.9, pp.1937-1960.

- Baumgardner, M.F., Silva, L.F., Biehl, L.L., and Stoner, E.R., (1985), Reflectance properties of soils, *Advances in Agronomy*, 38, pp.1-44.

- Beck, A.R., (in prep), The evaluation of CORONA and IKONOS satellite imagery for archaeological applications in a semi-arid environment, PhD thesis, Department of Archaeology, University of Durham, UK.

- Beck, A.R., Philip, G., Donoghue, D.N.M., and Galiatsatos, N., (in press), Geo-locating declassified CORONA satellite photography for archaeological surveys and cultural resource management applications: an interim paper, *Workshop on aerial archaeology and remote sensing*, Siena, Italy.

- Behrens, C.A. and Sever, T.L. (eds.), (1991), Proceedings of the Applications of Space Age Technology in Anthropology Conference. NASA, Mississippi.

- Beresford, M.W., and St Joseph, J.K.S., (1979), Medieval England: an aerial survey, Cambridge university press.

- Bewley, R., Donoghue, D.N.M., Gaffney, V., van Leusen M., and Wise A., (1999), Archiving aerial photography and remote sensing data: a guide to good practice, Oxbow Books.

- Bindschadler, R., and Vornberger, P., (1998), Changes in the west Antarctic ice sheet since 1963 from declassified satellite photography, *Science*, vol.279, 30th January, pp.689-692.

- Boyle, W.S., and Smith, G.E., (1970), Charged coupled semiconductor devices, *Bell systems technical journal*, 42, 587.

- Bridgland, D.R., Philip, G., Westaway, R., and White, M., (2003), A long Quaternary terrace sequence in the Orontes river valley, Syria: a record of uplift and of human occupation, *Current Science*, vol.84, No.8, pp.1080-1089.

- Brigham, E.O., (1988), The fast Fourier transform and its applications, N.J. Prentice-Hall.

- Brown, D., and Bara, T., (1994), Recognition and reduction of systematic error in elevation and derivative surfaces from 7 ½ minute DEMs, *Photogrammetric engineering and remote sensing*, vol.60, No.2, pp.189-194.

- Bruce, V., Green, P., and Georgeson, M.A., (1996), Visual Perception: physiology, psychology, and ecology. Psychology Press Ltd., a member of the Taylor and Francis group.

- Buiten, H.J., and Van Putten, B., (1997), Quality assessment of remote sensing image registration – analysis and testing of control point residuals, *ISPRS journal of photogrammetry and remote sensing*, vol.52, pp.57-73.

- Bush, G.W., (2003), Further amendment to Executive Order 12958, as amended, Classified national security information, 25 March 2003, Washington D.C.

- Calkins, H.W. and Tomlinson, R.F., (1977), Geographic Information Systems: methods and equipment for land use planning. Ottawa, International Geographical Union, Commission of Geographical Data Sensing and Processing and U.S. Geological Survey.

- Campbell, J.B., (2002), Introduction to remote sensing, 3rd edition. Taylor and Francis, London.

- Campbell, N.A., (1996), The decorrelation stretch transformation, *International journal of remote sensing*, 17, pp. 1939-1949.

- Cao, C. and Lam, N.S., (1997), Understanding the scale and resolution effects in remote sensing and GIS. In: Quattrochi, D.A., and Goodchild, M.F. (eds.), *Scale in remote sensing and GIS*, CRC Press.

- Case, J.B., (1961), The utilization of constraints in analytical photogrammetry, *Photogrammetric engineering*, vol.28, No.4, pp. 766-778.

- Case, J.B., (1967), The analytical reduction of panoramic and strip photography, *Photogrammetria*, p.127-141.

- Cerasetti, B., and Mauri, M., (2002), The Murghab delta palaeochannel reconstruction on the basis of remote sensing from space, *Proceedings of the conference: Space applications for heritage conservation*, Strasbourg, France.

- Chen, L., and Lee, L., (1992), Progressive generation of control frameworks for image registration, *Photogrammetric engineering and remote sensing*, vol.58, No.9, pp.1321-1328.

- Clark C.D., Garrod S.M., and Parker Pearson M. (1998), Landscape archaeology and Remote Sensing in southern Madagascar, *International journal of remote sensing*, vol. 19, No 8, pp. 1461-1477.

- Clarke, C.K., (2000), *Project CORONA*, University of California

http://www.geog.ucsb.edu/~kclarke/Corona/Corona.html (Accessed: January 2000)

- Clinton, W.J., (1995a), Release of imagery acquired by space-based national intelligence reconnaissance systems, Executive Order No.12951, 22 February 1995, Washington D.C.

- Clinton, W.J., (1995b), Classified national security information, Executive Order No. 12958, 17 April 1995, Washington D.C.

- Cloud, J., (2000), Hidden in plain sight: CORONA and the clandestine geography of the cold war, *PhD thesis*, Department of Geography, University of California Santa Barbara.

- Colwell, R.N. (ed.), (1960), Manual of photographic interpretation, American society of photogrammetry.

- Colwell, R.N. (ed.), (1983), Manual of Remote Sensing, Falls Church, Virginia: American Society of Photogrammetry.

- Comfort, A., Abadie-Reynal, C., and Ergec, R., (2000), Crossing the Euphrates in antiquity – Zeugma seen from space, *Anatolian studies*, vol.50.

- Comfort, A., and Ergec, R., (2001), Following the Euphrates in antiquity – north-south routes around Zeugma, *Anatolian studies*, vol.51.

- Congalton, R.G., and Green K., (1999), Assessing the Accuracy of remotely sensed data: Principles and practices, Lewis Publishers.

- Cook A.E., and Pinder III J.E. (1996), Relative accuracy of rectifications using co-ordinates determined from maps and the Global Positioning System, *Photogrammetric engineering and remote sensing*, Vol. 62, No 1, pp. 73-77.

- Cook, M., Peterson, B., Dial, G., Gerlach, F., Hutchins, K., Kudola, R., and Bowen, H., (2001), IKONOS technical performance assessment. *Proceedings of SPIE*, vol. 4381-10, Orlando.

- Cox, C., (1992), Satellite Imagery, aerial photography and wetland archaeology - An interim report on an application of remote sensing to wetland archaeology: the pilot study in Cumbria, England. *World Archaeology*, 24(2), pp. 249-267.

- Craig, N. (2004), *Yanomamö Remote Sensing and GIS research*, Yanomamö Group Projects.
(http://titicaca.ucsb.edu/~craig) (Accessed: March 2004)

- Custer, J.F., Eveleigh, T., Klemas, V., and Wells, I., (1986), Application of LANDSAT data and synoptic remote sensing to predictive models for prehistoric archaeological sites: an example from the Delaware coastal plain. *American Antiquity*, 51, pp. 572-588.

- Dartnall, H.J.A., Bowmaker, J.K., and Mollon, J.D., (1983), Human visual pigments: microspectrophotometric results from the eyes of seven persons, *Proceedings of the royal society of London*, B, 220, pp. 115-130.

- Davis, C.H., and Wang, X., (2003), Planimetric accuracy of Ikonos 1m panchromatic orthoimage products and their utility for local government GIS basemap applications, *International journal of remote sensing*, vol.24, No.22, pp.4267-4288.

- Day D.A., Longson J.M., and Latell B. (eds.) (1998), Eye in the sky – The story of CORONA spy satellites, Smithsonian Institution Press, Washington and London.

- De Leeuw, A.J., Veugen, L.M.M., and Van Stokkom, H.T.C., (1988), Geometric correction of remotely-sensed imagery using ground control points and orthogonal polynomials, *International journal of remote sensing*, vol.9, Nos.10 and 11, pp.1751-1759.

- Deveraux, Jr. A.B., (1973), Investigations into the feasibility of employing a hypothetical panoramic-frame camera system in aerial triangulation, PhD submitted in the Geodesy department of The Ohio State University.

- Dial, G., and Grodecki, J., (2002), Block adjustment with rational polynomial camera models, *Proceedings of ASPRS 2002 conference*, 22-26 April, Washington D.C., unpaginated CD-ROM.

- Dial, G. and Grodecki, J., (2003a), Applications of IKONOS imagery, *Proceedings of ASPRS 2003 conference*, Anchorage.

- Dial, G., and Grodecki, J., (2003b), IKONOS stereo accuracy without ground control, *Proceedings of ASPRS 2003 conference*, Anchorage.

- Dial, G., Gibson, L., and Poulsen, R., (2001), IKONOS satellite imagery and its use in automated road extraction, in: Baltsavias E., Gruen A., Van Gool L., (eds.), *Automated extraction of man made objects from aerial and space images (III)*, Balkema Publishers, Lisse, The Netherlands.

- Donoghue, D.N.M., (1999), Remote Sensing, *Progress in physical geography*, vol.23, No.2, pp.271-281.

- Donoghue, D.N.M., Philip, G., Galiatsatos, N., and Beck, A.R., (2002), Satellite imagery for archaeological applications: a case study from the Orontes valley, Syria. In: Bewley, R.H., and Raczkowski, W. (eds.), *Aerial Archaeology Developing Future Practice NATO Science Series – Series 1: Life and Behavioural Sciences*, Volume 337, IOS Press.

- Dowman I, Tao,V. (2002), An update on the use of rational functions for photogrammetric restitution, *ISPRS Highlights*, vol. 7, No.3, pp. 22-29.

- Dowman I., Dolloff J.T., (2000), An evaluation of rational functions for photogrammetric restitution, *International archives of photogrammetry and remote sensing*, Vol. XXXIII, part B3, Amsterdam.

- Drake, N.A., (1997), Recent aeolian origin of surficial gypsum crusts in southern Tunisia: geomorphological, archaeological and remote sensing evidence, ***Earth surface processes and landforms***, vol.22, pp.641-656.

- Drake, N.A., Mackin, S., and Settle, J.J., (1999), Mapping vegetation, soils and geology in semiarid shrublands using spectral matching and mixture modelling of SWIR AVIRIS imagery, ***Remote sensing of environment***, vol.68, pp.12-25.

- Eastman Kodak Company, (1970), Kodak panatomic-X aerial film 3400, Technical information data sheet.

- Eastman Kodak Company, (1992) (edited 7-95), Kodak plus-X aerocon II film 3404, Technical information data sheet.

- Ehlers, M., and Welch, R., (1987), Stereo-correlation of Landsat TM images, ***Photogrammetric engineering and remote sensing***, 53, pp. 1231-1237.

- Ehlers, M., (1997), Rectification and registration In: Star, J.L., Estes, J.E., and McGwire, K.C., (eds.), ***Integration of geographic information systems and remote sensing: Topics in remote sensing 5***, Cambridge University Press.

- ERDAS LLC. , (2002), IMAGINE OrthoBASE user's guide including IMAGINE OrthoBASE Pro, Leica Geosystems, GIS and mapping division, Atlanta, Georgia.

- Evans, I. S., (1972), General geomorphometry, derivatives of altitude and descriptive statistics. In: Chorley, R.J., (ed.), ***Spatial analysis of geomorphology***, (London: Methuen), pp. 17-90.

- Farr, T., (2004), Reply in the discussion forum for users of SRTM data. http://pub7.bravenet.com/forum/537683448/fetch/394357/ (Accessed: July 2004)

- Felber, P. (2002), Charge-coupled devices: a literature study as a project for ECE 575, Illinois institute of technology.

- Feranec, J., (1999), Interpretation element "association": analysis and definition, *International journal of applied Earth observation and geoinformation*, vol.1, issue 1, pp.64-67.

- Florinsky, I.V., (1998), Combined analysis of digital terrain models and remotely sensed data in landscape investigations, *Progress in physical geography*, 22, 1.

- Förstner, W., and Gülch, E., (1987), A fast operator for detection and precise location of distinct points, corners and centers of circular features, *Intercommision conference on fast processing of photogrammetric data*, Interlaken, Switzerland, pp.281-305.

- Forte, P. and Jones, G.A., (1999), Posing structural matching in remote sensing as an optimisation problem. In: Kanellopoulos, I., Wilkinson, G.G., and Moons, T., (eds.), *Machine vision and advanced image processing in remote sensing*, Springer-Verlag, Berlin.

- Fowler, M.J.F. (1996), High-resolution satellite imagery in archaeological application: a Russian satellite photograph of the Stonehenge region, *Antiquity*, 70, pp. 667-71.

- Franklin, S.E., and Giles, P.T., (1995), Radiometric processing of aerial and satellite remote-sensing imagery, *Computers and Geosciences*, vol.21, No.3, pp. 413-423.

- Fraser, C.S., and Hanley, H.B., (2003), Bias compensation in rational functions for IKONOS satellite imagery, *Photogrammetric engineering and remote sensing*, vol. 69, No. 1, January 2003, pp.53-57.

- Fraser, C.S., Hanley, H.B., and Yamakawa, T., (2002a), Three-dimensional geopositioning accuracy of IKONOS imagery, *Photogrammetric record*, vol. 17, No. 99, pp. 465-479.

- Fraser, C.S., Harry, B., Hanley, H.B., and Yamakawa, T., (2002b), High-precision geopositioning from IKONOS satellite imagery, ***Proceedings of ASPRS 2002 conference***, 22-26 April, Washington D.C., unpaginated CD-ROM.

- Fraser, C.S., and Yamakawa, T., (2004), Insights into the affine model for high-resolution satellite sensor orientation, ***ISPRS journal of photogrammetry and remote sensing***, vol.58, pp.275-288.

- Fritz, L.W. (1996), The era of commercial earth observation satellites, ***Photogrammetric engineering and remote sensing***, Vol.62, No 1, pp. 39-45.

- Fujisada, H., Iwasaki, A., and Hara, S., (2001), ASTER stereo system performance, ***Proceedings of SPIE***, vol. 4540, pp. 39-49.

- Galiatsatos, N., Donoghue, D.N.M., and Philip, G., (2000), CORONA space photography and landscape archaeology in Syria, ***26th annual conference of the remote sensing society "Adding value to remote sensing data"***, Leicester, England.

- Galiatsatos, N., Donoghue, D.N.M., Philip, G., and Beck, A.R., (2001), Technical aspects of satellite remote sensing with reference to archaeological applications, ***Workshop on aerial archaeology and remote sensing***, Siena, Italy.

- Galiatsatos, N., Donoghue, D.N.M., and Philip, G., (2002), Stereo applications for CORONA and the use of IKONOS for ground control: case study from Orontes valley, Syria, ***Space applications for heritage conservation***, Strasbourg, France.

- Gao, J., (2001), Non-differential GPS as an alternative source of planimetric control for rectifying satellite imagery, ***Photogrammetric engineering and remote sensing***, vol.67, No.1, pp.49-55.

- Gardiner, V., and Dackombe, R., (1983), Geomorphological Field Manual, George Allen and Unwin Ltd., London, UK.

- Georgopoulos, A. (1998), ***Notes in Digital Photogrammetry***, NTUA, Athens.

- Gerlach, F. (2000), Characteristics of Space Imaging's one-meter resolution satellite imagery products, *International archives of photogrammetry and remote sensing*, vol. 33, Part B1, Amsterdam 2000.

- Gheyle, W., Bourgeois, J., Goossens, R., de Wulf, A., and Willems, T., (2004a), Localisation of Scytho-Siberian burial mounds and detailed mapping of remote areas (topography, geomorphology, and DEM), by means of CORONA satellite imagery, *24th EARSeL Symposium: New strategies for European remote sensing*, Dubrovnik, Croatia.

- Gheyle, W., Trommelmans, R., Bourgeois, J., Goossens R., Bourgeois, I., de Wulf, M., Willems, T., (2004b), Evaluating CORONA: a case study in the Altai republic (south Siberia), *Antiquity*, vol.78, No.300, pp.391-403.

- Going, C., (2002), A neglected asset. German aerial photography of the Second World War period. In: Bewley, R.H., and Raczkowski, W. (eds.), *Aerial Archaeology Developing Future Practice NATO Science Series – Series 1: Life and Behavioural Sciences*, Volume 337, IOS Press.

- Gonzalez, R.C. and Woods, R.E., (2002), Digital image processing, Prentice Hall Inc., U.S.A.

- Goodchild, M.F., Egenhofer M.J., Kemp K.K., Mark D.M., and Sheppard E., (1999), Introduction to the Varenius project, *International journal of geographical information science*, vol. 13, no.8, 731-745.

- Goossens, R., De Man, J., and De Dapper, M., (2000), Research on the possibilities of CORONA-satellite-data to replace conventional aerial photographs in Geo-archaeological studies, practice on Sai (Sudan), *20th EARSeL (European Association of Remote Sensing Laboratories)*, June 2000, Dresden, Germany.

- Goossens, R., Schmidt, M., Altmaier, A., Benoit, F., and Menz, G., (2001), Extraction of Digital Elevation Models and ortho-images from CORONA KH4B

data, *Proceedings of ISPRS Workshop: High resolution mapping from space*, Hannover, Germany.

- Gracia, I., and Petrou, M., (1999), Non-linear line detection filters. In: Kanellopoulos, I., Wilkinson, G.G., and Moons, T., (eds.), *Machine vision and advanced image processing in remote sensing*, Springer-Verlag, Berlin.

- Grodecki, J., (2001), IKONOS Stereo Feature Extraction—RPC Approach, *Proceedings of ASPRS 2001 conference*, 23-27 April, St. Louis.

- Grodecki, J., and Dial, G., (2001), IKONOS geometric accuracy, *Proceedings of Joint Workshop of ISPRS working groups I/2, I/5 and IV/7 on "High resolution mapping from space 2001*, university of Hannover, Germany.

- Grodecki, J., Dial, G., and Lutes, J., (2003), Block adjustment of high resolution satellite images described by rational polynomials, *Photogrammetric engineering and remote sensing*, vol.69, No.1, pp.59-68.

- Grodecki, J., Dial, G., and Lutes, J., (2004), Mathematical model for 3D feature extraction from multiple satellite images described by RPCs, *Proceedings of ASPRS 2004 conference*, Denver, U.S.A.

- Grosman, D., (2000), personal communication.

- Gu, X.F., Guyot, G., and Verbrugghe, M., (1992), Evaluation of measurement errors in ground surface reflectance for satellite calibration, *International journal of remote sensing*, vol. 13, pp. 2531-2546.

- Hall, R.C., (1997), Post War Strategic Reconnaissance and the Genesis of the project Corona. In: McDonald, Robert A., (ed.) (1997), *Corona Between the Sun and the Earth The First NRO Reconnaissance Eye in Space*, American Society for Photogrammetry and Remote Sensing, Bethesda, MD.

- Hanley, H.B., and Fraser, C.S., (2001), Geopositioning accuracy of IKONOS imagery: indications from two dimensional transformations, *Photogrammetric record*, vol. 17, No. 98, pp. 317-329.

- Hapke, B, (1993), Theory of reflectance and emittance spectroscopy, Topics in Remote Sensing series, Cambridge University Press.

- Happel, B., (2000), personal communication.

- Helder, D., Coan, M., Patrick, K., and Gaska, P., (2003), IKONOS geometric characterisation, *Remote sensing of environment*, vol.88, pp.69-79.

- Hirano, A., Welch, R., and Lang H., (2003), Mapping from ASTER stereo image data: DEM validation and accuracy assessment, *ISPRS Journal of photogrammetry and remote sensing*, 57, pp. 356-370.

- Hoffer, R.M., (1978), Biological and physical considerations in applying computer-aided analysis techniques to remote sensor data. In: Swain, P.H., and Davis, S.M. (eds.), *Remote sensing: the quantitative approach*, McGraw-Hill.

- Hoffman, R.R., and Markman, A.B. (eds.), (2001), Interpreting remote sensing imagery: human factors, Lewis publishers.

- Horne, J.H., (2003), A tasselled cap transformation for IKONOS images, *ASPRS 2003 Annual conference proceedings*, Anchorage, Alaska.

- Hothem, D., Irvine, J. M., Mohr, E., and Buckley, K. B. (1996), Quantifying Image Interpretability for Civil Users, *Proceedings of the ASPRS/ACSM Annual Convention and Excibition*, Baltimore, ASPRS: pp. 292-298.

- Hyman, A.H., and Barnsley, M.J., (1997), On the potential for land cover mapping from multiple-view-angle (MVA) remotely-sensed images, *International journal of remote sensing*, vol.18, No.11, pp.2471-2475.

- Irons, J.R., Weismiller, R.A., and Petersen, G.W, (1989), Soil Reflectance. In: Asrar, G., (ed.), *Theory and applications of optical remote sensing*, John Wiley & Sons, Inc.

- Jacobsen, K., (2003), Mapping with IKONOS images, *Proceedings of 22nd EARSeL Symposium*, Prague, Czech Republic.

- Jacobsen, K., (2004), personal communication.

- Jakeman, A.J., Beck M.B., and McAleer M.J., (1996), Modelling change in environmental systems, John Wiley and Sons.

- Jensen, J.R. (1996), Introductory digital image processing – A Remote Sensing perspective, Prentice Hall.

- Kardoulas, N.G., Bird A.C., and Lawan A.I., (1996), Geometric correction of SPOT and Landsat imagery: A comparison of Map- and GPS-derived control points, *Photogrammetric engineering and remote sensing*, Vol. 62, No 10, pp. 1173-1177.

- Kasser, M., (2002a), Digital image acquisition with airborne CCD cameras, in: Kasser, M. and Egels, Y., (eds.), *Digital Photogrammetry*, Taylor and Francis: London and New York.

- Kasser, M., (2002b), Geometry of aerial and spatial pictures, in: Kasser, M. and Egels, Y., (eds.), *Digital Photogrammetry*, Taylor and Francis: London and New York.

- Kasser, M., (2002c), Use of scanners for the digitisation of aerial pictures, in: Kasser, M. and Egels, Y., (eds.), *Digital Photogrammetry*, Taylor and Francis: London and New York.

- Kauth, R.J., and Thomas, G.S., (1976), The tasselled cap – a graphic description of the spectral-temporal development of agricultural crops as seen by Landsat,

Proceedings LARS 1976 Symposium on machine processed remotely sensed data, Purdue university.

- Kawachi, D.A., (1966), Image geometry of vertical and oblique panoramic photography, *Photogrammetric engineering*, pp. 298-306.

- Kennedy, D. (1998), Declassified satellite photographs and archaeology in the Middle East: case studies from Turkey, *Antiquity*, 72, pp. 553-561.

- Kennedy, D., (2000), Aerial archaeology in the Middle East: the role of the military – past, present … and future? In: Bewley, R.H., and Raczkowski, W. (eds.), *Aerial Archaeology Developing Future Practice NATO Science Series – Series 1: Life and Behavioural Sciences*, Volume 337, IOS Press.

- Kennedy, H. (ed.), (2001), The ESRI Press dictionary of GIS terminology, Environmental Systems Research Institute, Inc., Redlands, California.

- Kim, K.T., Jesek, K.C., and Sohn, H.G., (2001), Ice shelf advance and retreat rates along the coast of Queen Maud Land, Antarctica, *Journal of geophysical research*, vol.106 (C4), pp.7097-7106.

- Konecny, G., (2003), Geoinformation: Remote sensing, Photogrammetry and Geographic Information Systems, Taylor and Francis, London.

- Kooistra, L., Wehrens, R., Buydens, L.M.C., Leuven, R.S.E.W., and Neinhuis, P.H., (2001), Possibilities of soil spectroscopy for the classification of contaminated areas in river floodplains, *International journal of applied earth observation and geoinformation*, vol. 3, Issue 4, pp.337-343.

- Kouchoukos, N., (2001), Satellite images and Near Eastern landscapes, *Near Eastern archaeology*, vol.64, No.1-2, pp.80-91.

- Landgrebe, D., (1997), The evolution of Landsat Data Analysis, *Photogrammetric engineering and remote sensing*, Vol. 63, No. 7, July 1997, pp. 859-867.

- Leachtenauer, J.C. (1996), National Imagery Interpretability Rating Scales Overview and Product Description, *Proceedings of the ASPRS/ACSM Annual Convention and Excibition*, Baltimore, ASPRS: pp. 262-272.

- Leachtenauer, J.C., Daniel K., and Vogl, P.T. (1997), *Digitising Corona Imagery: Quality vs. Cost*. In McDonald, Robert A., (ed.) (1997), *Corona Between the Sun and the Earth The First NRO Reconnaissance Eye in Space*, American Society for Photogrammetry and Remote Sensing, Bethesda, MD.

- Lee J., Huh, Y., Seo, B. and Kim, Y., (2002), Improvement the positional accuracy of the 3D terrain data extracted from IKONOS-2 satellite imagery, *ISPRS commission III Symposium "Photogrammetric computer vision"*, vol.34, part 3B, pp.142-145, Graz, Austria.

- Light, D.L., (1996), Film cameras or digital sensors? The challenge ahead for aerial imaging, *Photogrammetric engineering and remote sensing*, vol.62, No.3, pp.285-291.

- Lillesand, T.M., and Kiefer, R.W., (1992), Remote sensing and image interpretation, John Wiley and Sons, New York.

- Lillesand, T.M., and Kiefer, R.W., (2000), Remote sensing and image interpretation, John Wiley and Sons, New York.

- Liverman, D., Moran E. F., Rinfuss R. R., and Stern P. C. (1998), People and pixels: Linking Remote Sensing and Social Science, National Academy Press, Washington, D.C.

- Longshaw, T.G., (1974), Field spectroscopy for multispectral remote sensing: an analytical approach, *Applied optics*, vol. 13, pp.1487-1493.

- Lutes, J., (2004), Accuracy analysis of rational polynomial coefficients for IKONOS imagery, *Proceedings of ASPRS 2004 conference*, Denver, U.S.A.

- Madden, F.J., (1996), The CORONA camera system: Itek's contribution to world stability, self-published.

- Marcolongo, B., and Barisano, E., (2000), Télédetection et archéologie: concepts fondamentaux, état de l'art et examples. In: Pasquinucci M., and Trément, F., (eds.), *Non-destructive techniques applied to landscape archaeology*: 15-30. The Archaeology of Mediterranean Landscapes 4. Oxford: Oxbow.

- Markham, B. L., and Barker J. L. (eds.) (1985), Special LIDQuA (Landsat-D Image Data Quality Assessment Programme) Issue, *Photogrammetric engineering and remote sensing*, American Society for Photogrammetry and Remote Sensing.

- Marr, D., (1982), Vision: A computational investigation into the human representation and processing of visual information, Freeman, San Francisco.

- Mather, P., (1999), Computer processing of remotely sensed images: an introduction, John Wiley and Sons Ltd.

- McAllister, D.F., (ed.), (1993), Stereo computer graphics and other true 3D technologies, Princeton University Press, New Jersey.

- McDonald, R.A., (1995), CORONA: Success for Space Reconnaissance, A look into the Cold War, and a Revolution for Intelligence, *Photogrammetric engineering and remote sensing*, vol. 61, No 6, June 1995, pp. 689-720.

- McDonald, R.A., (ed.), (1997) CORONA Between the Sun and the Earth The First NRO Reconnaissance Eye in Space, American Society for Photogrammetry and Remote Sensing, Bethesda, MD.

- McGlone, C., Mikhail, E., and Bethel, J., (eds.) (2004), Manual of Photogrammetry, fifth edition, American Society of Photogrammetry and Remote Sensing (ASPRS).

- McGwire, K.C., (1996), Cross-validated assessment of geometric accuracy, *Photogrammetric engineering and remote sensing*, vol.62, No.10, pp.1179-1187.

- Milton, E.J., (1987), Principles of field spectroscopy, *International journal of remote sensing*, vol.8, pp. 1807-1827.

- Milton, E.J., Emery, D.R., and Kerr, C.H., (1997), NERC equipment pool for field spectroscopy: preparing for the 21st century, in *Proceedings of the 23rd Annual Conference of the Remote Sensing Society*, Nottingham, UK.

- Milton, E.J., and Goetz, A.F.H., (1997), Atmospheric influences on field spectrometry: Observed relationships between spectral irradiance and the variance in spectral reflectance. In: Guyot, G., and Phulpin, T., (eds.), *Physical measurements and signatures in remote sensing, volume I*. Courchevel, France.

- Mohr, E., Hothem, D., Irvine, J. M., and Erdman, C. (1996), The Multispectral Imagery Interpretability Rating Scale (MS IIRS), *Proceedings of the ASPRS/ACSM Annual Convention and Exhibition*, Baltimore, ASPRS: pp. 300-310.

- Montgomery, O.L., (1976), An investigation of the relationship between spectral reflectance and the chemical, physical and genetic characteristics of soils, Dissertation for the degree of Doctor of Philosophy, Department of Agronomy, Purdue University, West Lafayette, Ind.

- Morad, M., Chalmers, A.I., and O'regan. P.R., (1996), The role of mean-square error in the geo-transformation of images in GIS, *International journal of geographical information systems*, vol.10, No.3, pp.347-353.

- Mott, R.K., (1975), The use of satellite imagery for very small-scale mapping, *Photogrammetric record*, 8, pp. 458-475.

- Murai, S., (1986), Cartographic accuracy of stereo space photographs taken by large format camera: a case study in Japan, *Proceedings of the ISPRS Symposium*

Mapping from modern imagery, Edinburgh, Scotland, September 8-12 (Edinburgh, Scotland, Remote Sensing Society/ISPRS), Vol. 26, pp.732-737.

- Musaoglu, N., Bektas, F., Saroglu, E., Ustun, B., Kaya, S., Goksel, C., and Kandal, N., (2004), Use of CORONA, Landsat TM, SPOT 5 images to assess 40 years of land use/cover changes in Cavusbasi, *24th EARSeL Symposium: New strategies for European remote sensing*, Dubrovnik, Croatia.

- National Aerospace Laboratory NLR, (2004), Satellite information table. http://www.npoc.nl/EN-version/satelliteinfo/satellitetabel.html (Accessed: March 2004).

- National Reconnaissance Office (NRO), (1967a), The KH-4B Camera System, National Photographic Interpretation Centre, September 1967.

- National Reconnaissance Office (NRO), (1967b), The KH-4A Camera System, National Photographic Interpretation Centre, March 1967.

- National Reconnaissance Office (NRO), (1967c), J-3 photographic system: technical proposal system analysis studies, National Photographic Interpretation Centre, May 1967.

- National Reconnaissance Office (NRO), (1970a), CORONA technical information volume 1, National Photographic Interpretation Centre, December 1970.

- National Reconnaissance Office (NRO), (1970b), CORONA technical information volume 2, National Photographic Interpretation Centre, December 1970.

- National Reconnaissance Office (NRO), (1998), NRO Freedom of Information Act Handbook. Found online: http://www.nro.gov/foia/nrohb_1.pdf

- Novak, K., (1992), Rectification of digital imagery, *Photogrammetric engineering and remote sensing*, vol.58, No.3, pp.339-344.

- Oltean, I.A., (2000), The use of satellite imagery for the transcription of oblique aerial photographs. In: Bewley, R.H., and Raczkowski, W. (eds.), *Aerial Archaeology Developing Future Practice NATO Science Series – Series 1: Life and Behavioural Sciences*, Volume 337, IOS Press.

- Ondrejka, R., (2000), personal communication.

- Open GIS Consortium, 1999, The OpenGIS™ Abstract Specification, Topic 7: The Earth Imagery Case (99-107.doc), http://www.opengis.org/techno/specs.htm

- Obukhov, A.I., and Orlov, D.S., (1964), Spectral reflectivity of the major soil groups and possibility of using diffuse reflection in soil investigations, *Soviet soil science*, vol.2, pp.174-184.

- Oštir, K., Stančič, Z., & Trušnovec, M., (1999), Multispectral classification of satellite images. In: Gillings, M., Mattingly, D., & van Dalen, J. (eds.). *Geographic Information Systems and landscape archaeology*: 125-31. The Archaeology of Mediterranean Landscapes 3. Oxford: Oxbow.

- Palà, V., and Pons, X., (1995), Incorporation of relief in polynomial-based geometric corrections, *Photogrammetric engineering and remote sensing*, vol.61, No.7, pp.935-944.

- Palmer, R., (2002), A poor man's use of CORONA images for archaeological survey in Armenia, *Proceedings of the conference: Space applications for heritage conservation*, Strasbourg, France.

- Paparoditis, N., and Dissard, O., (2002), 3D data acquisition from visible images, in: Kasser, M. and Egels, Y., (eds.), *Digital Photogrammetry*, Taylor and Francis: London and New York.

- Parmegiani, N., and Poscolieri, M., (2003), DEM data processing for a landscape archaeology analysis (lake Sevan – Armenia), *The international archives of the*

Photogrammetry, Remote Sensing and Spatial Information Sciences, vol. XXXIV, Part 5/W12, pp. 255-258.

- Peebles, C., (1997) The CORONA project: America's first spy satellites, Naval Institute Press, Annapolis, Maryland.

- Peli, T., and Lim, J.S., (1982), Adaptive filtering for image enhancement, *Optical engineering*, 21, pp. 108-112.

- Petrie, G., Al-Roussan, N., El-Niweiri, A.H.A., Li, Z., and Valladan Zoej, M. J., (1997), Topographic mapping of arid and semi-arid areas in the Red Sea region from stereo space imagery, *EARSEL Advances in remote sensing*, 5, 11-29.

- Philip, G., Donoghue, D.N.M., Beck, A., and Galiatsatos, N., (2002a), CORONA satellite photography: a case study from Orontes valley, Syria. *Antiquity*, 76, pp. 109-118.

- Philip, G., Jabour, F., Beck, A., Bshesh, M., Grove, J., Kirk A., and Millard, A., (2002b), Settlement and landscape development in the Homs region, Syria: research questions, preliminary results 1999-2000 and future potential. *Levant*, 34, pp.1-23.

- Philipson, W.R. (ed.), (1997), Manual of photographic interpretation, Science and engineering series, American society of photogrammetry and remote sensing.

- Pike, J., (1998), National Interpretability Rating Scales.
  http://www.fas.org/irp/imint/niirs.htm (Accessed: January 2000)

- Planet, W.G., (1970), Some comments on reflectance measurements of wet soils, *Remote sensing of the environment*, vol.1, pp.127-129.

- Polidori, L., (2002), DSM quality: Internal and external validation, in: Kasser, M. and Egels, Y., (eds.), *Digital Photogrammetry*, Taylor and Francis: London and New York.

- Ponikarov, V., Kozlov, V., Artemov, A., and Kalis, A., (1963). Geological Map of Syria 1:200,000 (Sheets I-36-XVIII; I-37-XIII). Syrian Arab Republic Ministry of Industry. Moscow: VC.O. Technoexport.

- Pournelle, J., and Hunt, L., (2002), personal communication.

- Powell, R.M., (1997), Evolution of Standard Agena: CORONA's spacecraft, In McDonald, Robert A., (ed.) (1997), *Corona Between the Sun and the Earth The First NRO Reconnaissance Eye in Space*, American Society for Photogrammetry and Remote Sensing, Bethesda, MD.

- Proy, C., Tanré, D., and Deschamps, P.Y., (1989), Evaluation of topographic effects in remotely sensed data, *Remote sensing of environment*, vol.30, issue 1, pp.21-23.

- Pujol, A., Sole, A., Ponsa, D., Varona, J., and Villanueva, J.J., (1999), Satellite image segmentation through rotational invariant feature eigenvector projection. In: Kanellopoulos, I., Wilkinson, G.G., and Moons, T., (eds.), *Machine vision and advanced image processing in remote sensing*, Springer-Verlag, Berlin.

- Rabus, B., Eineder, M., Roth, A., and Bamler, R., (2003), The shuttle radar topography mission – a new class of digital elevation models acquired by spaceborne radar, *ISPRS Journal of photogrammetry and remote sensing*, vol. 57, pp.241-262.

- Radeva, P., Sole, A., Lopez, A.M., and Serrat, J., (1999), Detecting nets of linear structures in satellite images. In: Kanellopoulos, I., Wilkinson, G.G., and Moons, T., (eds.), *Machine vision and advanced image processing in remote sensing*, Springer-Verlag, Berlin.

- Rees, G., (1999), The remote sensing data book, Cambridge university press.

- Reeves, R.G. (ed.), (1975), Manual of remote sensing, American society of photogrammetry.

- Richards, J.A., and Jia, X., (1999), Remote Sensing digital image analysis – An introduction, Springer-Verlag Berlin Heidelberg.

- Richelson, J.T., (1999), U.S. Satellite Imagery, 1960-1999, National Security Archive Electronic Briefing Book No 13.
  http://www.gwu.edu/~nsarchiv/NSAEBB/NSAEBB13/ (Accessed: December 1999)

- Ridley, H.M., Atkinson, P.M., Aplin, P., Muller, J.P., and Dowman, I., (1997), Evaluating the potential of the forthcoming commercial U.S. high-resolution satellite sensor imagery at the Ordnance Survey®, *Photogrammetric engineering and remote sensing*, Vol. 63, No 8, pp. 997-1005.

- Rocchini, D., (2004), Misleading information from direct interpretation of geometrically incorrect aerial photographs, *The photogrammetric record*, vol.19, issue 106, pp.138-148.

- Ruffner, K. (ed.), (1995), CORONA: America's First Satellite Program, Center for the Study of Intelligence, Government Printing Office, Washington D.C.

- Salomonson, V.V. (ed.) (1984), Special Issue on Landsat-4, *IEEE Transactions on geoscience and remote sensing*, IEEE.

- Sarris, A., and Jones, R., (2000), Geophysical and related techniques applied to archaeological survey in the Mediterranean: a review, *Journal of Mediterranean Archaeology* vol. 13, No.1, pp. 3-75.

- Schaepman, M., (1998), Calibration of a field spectroradiometer – Calibration and characterisation of a non-imaging field spectroradiometer supporting imaging spectrometer validation and hyperspectral sensor modelling. PhD Thesis, Remote Sensing series, Volume 31, Remote Sensing Laboratories, University of Zurich.

- Schaepman, M., and Dangel, S., (2000), Solid laboratory calibration of a nonimaging spectroradiometer, *Applied optics*, vol.39, pp. 3754-3764.

- Schenk, T, Csathó, B., and Shin, S.W., (2003), Rigorous panoramic camera model for DISP imagery, *Proceedings of the ISPRS Workshop "High resolution mapping from space"*, Hannover, Germany.

- Schmidt, A., (2004), Remote sensing and geophysical prospection, *Internet archaeology*, issue 15.

- Schmidt, M., Goossens, R., and Menz, G. (2001a), Processing techniques for CORONA satellite images in order to generate high-resolution digital elevation models (DEM), In: Begni, G., (ed.), *Observing our environment from space: New solutions for a new millennium*, Lisse, The Netherlands, pp. 191-196.

- Schmidt, M., Goossens, R., Menz, G., Altmaier, A., and Devriendt, D., (2001b), The use of CORONA satellite images for generating a high-resolution digital elevation model, *Proceedings of the 2001 IGRASS Symposium*, Sydney.

- Schmidt, M., (2003), Development of a fuzzy expert system for detailed land cover mapping in the Dra catchment (Morocco) using high resolution satellite images, Dissertation for the degree of Doctor of Philosophy, University of Bonn, Germany.

- Scholz, D.K., (1997), Declassified Intelligence Satellite Photographs available from the US Geological Survey. In McDonald, Robert A., (ed.) (1997), *Corona Between the Sun and the Earth The First NRO Reconnaissance Eye in Space*, American Society for Photogrammetry and Remote Sensing, Bethesda, MD.

- Schott, J.R., (1997), Remote Sensing: The image chain approach, Oxford university press, Oxford.

- Schowengerdt, R.A., (1997), Remote Sensing: Models and methods for image processing, Academic Press.

- Scollar, I., Tabbagh, A., Hesse, A., and Herzog, I., (1990), Archaeological prospecting and Remote Sensing, Cambridge University Press.

- Selander, J.M., (1997), Image coverage models for declassified CORONA, ARGON and LANYARD satellite photography – a technical explanation. In: McDonald, Robert A., (ed.) (1997), *Corona Between the Sun and the Earth The First NRO Reconnaissance Eye in Space*, American Society for Photogrammetry and Remote Sensing, Bethesda, MD.

- Sever, T., (1990), Remote Sensing applications in archaeological research: Tracing prehistoric human impact upon the environment, Ph.D. dissertation, University of Colorado, Boulder. Available: University Microfilms, Ann Arbor.

- Sever, T.L., (1998), Validating prehistoric and current social phenomena upon the landscape of Peten, Guatemala. In Liverman, D., Moran E. F., Rinfuss R. R., and Stern P. C., (eds.), People and pixels: Linking Remote Sensing and Social Science, National Academy Press, Washington, D.C.

- Shafique, N.A., Fulk, F., Cormier, S.M., and Autrey, B.C., (2002), Coupling hyperspectral remote sensing with field spectrometer to monitor inland water quality parameters, AVIRIS workshop proceedings.

- Sheets, P., and Sever, T., (1988), High tech wizardry, *Archaeology*, 41 (6), Nov/Dec, pp. 28-35.

- Shin, S.W., (2003), Rigorous model of panoramic cameras. Dissertation presented in partial fulfilment of the requirements for the degree Doctor of Philosophy. Department of civil and environmental engineering and geodetic science, Ohio State University, 104 p.

- Sibiryakov, A. (2000), DTM generation from Russian TK-350 space imagery in the PC-based photogrammetric system Z-space, *International archives of photogrammetry and remote sensing*, vol. XXXIII, part B4, Amsterdam.

- Sinclair Optics Inc., (1997), OSLO User's Guide – Petzval.len – A Petzval Lens. http://www.sinopt.com/usrguide/examples/petzval.html (Accessed: December 1999)

- Slama, C.C., Theurer, C., and Henriksen, S.W., (eds.) (1980), Manual of Photogrammetry, American Society of Photogrammetry.

- Slater, P.N., (1980), Optics and optical systems, Addison-Wesley publishing company.

- Slater, P.N., Biggar, S.F., Holm, R.G., Jackson, R.D., Mao, Y, Moran, M.S., Palmer, J.M., and Yuan, B., (1987), Reflectance and radiance based methods for the in-flight absolute calibration of the multispectral sensors, *Remote sensing of environment*, vol. 22, pp. 11-37.

- Smith, F.D., (1997), *The design and engineering of Corona's Optics*. In McDonald, Robert A. (ed.) (1997), *Corona Between the Sun and the Earth The First NRO Reconnaissance Eye in Space*, American Society for Photogrammetry and Remote Sensing, Bethesda, MD.

- Smith, P.A., and Atkinson, S.F., (2001), Accuracy of rectification using topographic map versus GPS ground control points, *Photogrammetric engineering and remote sensing*, vol.67, No.5, pp.565-570.

- Sohn, H.G., Jesek, K.C., and Van Der Veen, C.J., (1998), Jacobshavn glacier, west Greenland: 30 years of spaceborne observations, *Geophysical research letters*, vol.25, No.14, pp.2699-2702.

- Sohn, H.G., and Kim, K.T., (2000), Horizontal accuracy assessment of ARGON imagery, *Journal of Korean society of civil engineers*, vol.4, No.1, pp.59-65.

- Sohn, H.G., Kim, G., Yom, J., (2004), Mathematical modelling of historical reconnaissance CORONA KH-4B imagery, *The photogrammetric record*, vol.19, issue 105, pp. 51-66.

- Spaceimaging product guide (2004)
  http://www.spaceimaging.com/whitepapers_pdfs/IKONOS_Product_Guide.pdf (Accessed: July 2004)

- Spaceimaging web page (2004)

http://www.spaceimaging.com/products/ikonos/spectral.htm (Accessed: March 2004).

- Stein, C., and Cullen, B., (1994), Satellite Imagery and Archaeology - A Case Study From Nikopolis. *American Journal Of Archaeology*, 98(2).

- Strahler, A., and Strahler, A., (1997), Physical geography: science and systems of the human environment. Wiley and Sons, Inc.

- Sussman, R, Green, G., and Sussman, I., (1994), Satellite imagery, human ecology, anthropology, and deforestation in Madagascar, *Human Ecology*, 22(3).

- Tao, C.V., and Hu, Y., (2001), A comprehensive study of the rational function model for photogrammetric processing, *Photogrammetric engineering and remote sensing*, vol 67, No.12, pp. 1347-1357.

- Tao, C.V., Hu, Y., Mercer, J.B., Schnick, S., and Zhang, Y., (2000), Image rectification using a generic sensor model – rational function model, *International archives of photogrammetry and remote sensing*, vol. XXXIII, part B3, Amsterdam.

- Tao, C.V., Hu, Y., and Schnick, S., (2002), Photogrammetric exploitation of IKONOS imagery using the rational function model, *Proceedings of ASPRS 2002 conference*, 22-26 April, Washington D.C., unpaginated CD-ROM.

- Tappan, G.G., Hadj, A., Wood, E.C., and Lietzow, R.W., (2000), Use of Argon, Corona and Landsat imagery to assess 30 years of land resource changes in west-central Senegal, *Photogrammetric engineering and remote sensing*, vol.66, No.6, pp.727-735.

- Taylor, M.M., (1973), Principal components colour display of ERTS imagery, *Third Earth resources technology satellite-1 Symposium*, NASA SP-351, pp. 1877-1897.

- Thom, C., (2002), Relations between radiometric and geometric precision in digital imagery, in: Kasser, M. and Egels, Y., (eds.), *Digital Photogrammetry*, Taylor and Francis: London and New York.

- Thom, C., (2004), personal communication.

- Torlegard, K., (1992), Sensors for photogrammetric mapping: Review and prospects, *ISPRS journal of photogrammetry and remote sensing*, vol.47, pp.241-262.

- Toutin, T., and Cheng, P., (2000), Demystification of IKONOS, *Earth Observation Magazine*, vol.9, No 7, pp.17-21.

- Toutin, T., (2001a), Review article: Elevation modelling for satellite visible and infrared (VIR) data, *International journal of remote sensing*, vol. 22, No. 6, pp. 1097-1125.

- Toutin, T., (2001b), DEM generation from new VIR sensors: IKONOS, ASTER and Landsat-7, *IEEE-IGARSS Proceedings*, Sydney, Australia, July 9-13.

- Toutin, T., (2002), DEM from stereo Landsat 7 ETM^+ data over high relief areas, *International journal of remote sensing*, vol. 23, No. 10, pp. 2133-2139.

- Toutin, T., (2003), Error tracking in IKONOS geometric processing using a 3D parametric model, *Photogrammetric engineering and remote sensing*, vol.69, No.1, pp.43-51.

- Toutin, T., (2004), Review article: Geometric processing of remote sensing images: models, algorithms and methods, *International journal of remote sensing*, vol.25, No.10, pp.1893-1924.

- Townshend J. R. G., Cushnie J., Hardy J., and Wilson A. (1987), Thematic Mapper Data – Characteristics and use, NERC.

- Trelogan, J., Crawford, M., and Carter, J., (2002), Monitoring the ancient countryside: remote sensing and GIS at the Chora of Chersonesos (Crimea, Ukraine), *Proceedings of the conference: Space applications for heritage conservation*, Strasbourg, France.

- Trombold, C.D., (1991), Ancient road networks and settlement hierarchies in the New World, Cambridge University Press.

- Turker, M., and Gacemer, A.O., (2004), Geometric correction accuracy of IRS-1D PAN imagery using topographic map versus GPS control points, *International journal of remote sensing*, vol.25, No.6, pp.1095-1104.

- Ur, J., (2002), Settlement and landscape in northern Mesopotamia: The tell Hamoukar survey 2000-2001, *Akkadica*, vol.123, No.1, pp.57-88.

- Ur, J., (2003), CORONA satellite photography and ancient road networks: A northern Mesopotamian case study, *Antiquity*, vol. 77, No. 295, pp. 102-115.

- Urwin, N., and Ireland, T., (1992), Satellite Imagery and Landscape Archaeology: An interim report on the environmental component of the Vinhais Landscape Archaeology Project, North Portugal. *Mediterranean Archaeology*, 5, pp. 121-131.

- USGS web page, (2004a)

  http://edc.usgs.gov/guides/disp1.html (Accessed: March 2004)
  http://edc.usgs.gov/products/satellite/declass1.html (Accessed: March 2004)
  http://edc.usgs.gov/products/satellite/declass2.html (Accessed: March 2004)

- U.S. Geological Survey (USGS), (2004b), Satellite image analysis of environmental change, International program at the EROS (Earth Resources Observation Systems) Data Center.

  (http://edcintl.cr.usgs.gov/sahel.html) (Accessed: March 2004)

- Valadan Zoej, M.J.V., and Sadeghian, S., (2003), Rigorous and non-rigorous photogrammetric processing of IKONOS Geo image, *Proceedings of ISPRS joint workshop "High resolution mapping from space"*, Hannover, Germany.

- Verhoeven, K., and Dales, L., (1994), Remote sensing and Geographical Information Systems (GIS) for archaeological research (applied in Mesopotamia). In: Gasche, H., Tanret, M., Janssen, C., & Degraeve, A., (eds.), *Cinquante-deux reflexions sur le Proche-Orient ancien*: 519-39. Ghent: Peeters.

- Vick, C., (1999), *Exploiting Corona Imagery*, 15 February 1999. http://www.fas.org/eye/corona.htm (Accessed: December 1999)

- Wang, Y. (1998), Principles and applications of structural image matching, *ISPRS Journal of photogrammetry and remote sensing*, vol. 53, No. 3, pp. 154-165.

- Wang, Z., (1990), Principles of Photogrammetry (with Remote Sensing), Beijing, China: Press of Wuhan Technical University of Surveying and Mapping, and Publishing House of Surveying and Mapping.

- Welch, R., Jordan, R.T., and Luvall, J.C., (1990), Geocoding and stereo display of tropical forest multi-sensor datasets, *Photogrammetric engineering and remote sensing*, 56, pp. 1389-1392.

- White, K., and El Asmar, H.M., (1999), Monitoring changing position of coastlines using Thematic Mapper imagery, an example from the Nile Delta, *Geomorphology*, vol.29, pp.93-105.

- Wilkie, D.S., and Finn, J.T., (1996), Remote Sensing Imagery for Natural Resources Monitoring: A guide for first-time users, Columbia University Press.

- Wilkinson, T.J., (2000a), personal communication.

- Wilkinson, T.J., (2000b), Regional approaches to mesopotamian archaeology: the contribution of archaeological survey, *Journal of Archaeological Research* 8, pp. 219-67.

- Wilkinson, T.J., and Tucker, D., (1995), *Settlement in the north Jazira, Iraq: a study of the archaeological landscape*. London: British School of Archaeology in Iraq.

- Wilkinson, T.J., French, C.A.I., Matthews, W., and Oates, J., (2001), Geoarchaeology, landscape and the region. In: Oates, D., Oates, J., and McDonald, H., (eds.), *Excavations at Tell Brak 2: Nagar in the third millennium BC*, Cambridge: McDonald Institute for archaeological research.

- Wilkinson, T.J., (2003), Archaeological landscapes of the Near East, The university of Arizona Press, Tucson, U.S.A.

- Wilkinson, T.J., Ur, J., and Casana, J., (2004), From nucleation to dispersal: trends in settlement pattern in the northern fertile crescent. In: Alcock, S.E., and Cherry, J.F., (eds.), *Side-by-side survey: comparative regional studies in the Mediterranean world*, Oxbow Books.

- Williams, M., (2002), personal communication.

- Wilson, D.R., (1982), Air photo interpretation for archaeologists, B.T. Batsford Ltd., London.

- Wiseman, J., (1992), Archaeology and Remote Sensing in the Region of Nikopolis, Greece. *Context*, 9, pp. 1-4.

- Woodcock, C.E., and Strahler, A.H., (1987), The factor of scale in Remote Sensing, *Remote sensing of environment*, 21:311-32.

- Yamaguchi, Y., Fujisada, H., Tsu, H., Sato, I., Watanabe, H., Kato, M., Kudoh, M., Kahle, A.B., and Pniel, M., (2001), ASTER early image evaluation, *Advances in Space Research*, vol.28, No.1, pp.69-76.

- Zitová, B., and Flusser, J., (2003), Image registration methods: a survey, *Image and vision computing*, vol.21, pp.977-1000.

- Zhou, G., and Jezek, K.C., (2002), Satellite photograph mosaics of Greenland from the 1960s era, *International journal of remote sensing*, vol. 23, No. 6, pp. 1143-1159.

- Zhou, G., and Jezek, K.C., (2004), Satellite navigation parameter-assisted orthorectification for over 60°N latitude satellite imagery, *Photogrammetric Engineering & Remote Sensing*, vol.70, No.9.

- Zomer, R., Ustin, S., and Ives, J., (2002), Using satellite remote sensing for DEM extraction in complex mountainous terrain: landscape analysis of the Makalu Barun National Park of eastern Nepal, *International journal of remote sensing*, vol.23, No.1, pp.125-143

11. Appendix 1 – Data header file

11.1. Reference data

Reference data can aid in the analysis, interpretation and validation of the remotely sensed data. They can also be used for verification of the information extracted from remotely sensed data. The reference data usually vary with the application. They may include maps, ground control points, ground truth data and more.

Four basic considerations drive all reference data collection (Congalton and Green, 1999):

- What should be the source data for the reference samples? Can existing maps or existing field data be used as reference data? Should the information be collected from aerial sources or field visits?
- What type of information should be collected from each sample? Should measurements be taken or are observations adequate?
- When should the reference data be collected? During initial field investigations when the map is being made, or only after the map is completed? What are the implications of using old data for accuracy assessment?
- How do we ensure that the reference data are collected correctly, objectively, and consistently?

11.1.1. Maps

Existing maps of the area can provide valuable information. This includes:

- names of sites and cities and villages
- digital elevation model
- ground truth data
- ground control points
- general guidance in the area

The maps that will be used in the research project are actually photocopies of original printings at 1:25.000 scale. One of the problems is that the maps are in an Arabic language and it is difficult to understand the co-ordinate system (projection, ellipsoid, datum) used in the grid of the map. There is the assumption that a TM (Transverse Mercator) projection is used, but it is not possible to understand the datum or the ellipsoid so as to define the system. The latter, combined with the fact that there

are distortions from the photocopier, leads to the usage of the maps only as reference and in support of the imagery. More details on the maps are reported in paragraph 4.2.1.1.

11.1.2. Ground remote sensing data

The reference data involve collecting measurements or observations about objects, areas, or phenomena that are being remotely sensed (Lillesand and Kiefer, 2000). Some of these measurements may include geophysics devices (i.e. magnetometer, resistivity instrument, ground penetrating radar, seismic instrument and Electromagnetic Sounding Equipment), and field spectroradiometry.

11.1.3. GPS

One problem of the research project is that there is no accurate co-ordinate basis for the integration of all data in a GIS. The high-resolution satellite data definitely need strong co-ordinate foundation with high accuracy. The maps are not adequate for geocorrection of high accuracy, because they may have distortions from the photocopier. Also, the existing aerial photographs, maps and geodetic data concerning the study area are under military control, and it will be difficult to get access to them. GPS offers a solution to this problem.

In the year 2000, the US government announced the declassification of the GPS signal by cancelling the SA (Selective Availability) decoding. This allows field measurements of accuracy up to 5-10 meters depending on the GPS device. A triangulation network could be set up in the study area, and with the use of differential GPS it could provide very high accuracy co-ordinates, and so, a strong basis for the integration of data. The main problem for the use of GPS lies in two factors. The first is the big differences in ground features from the CORONA photographs to today's situation. It will be very difficult to define ground features appearing in the 1970 photographs on today's landscape. The second is that the use of differential GPS is not allowed in Syria. Unless the 5 meters accuracy is enough, the solution will be constant comparison of the GPS measurements with imagery and maps to eliminate confusion and provide a relative co-ordinate system based mainly in registration rather than geocorrection.

However, the GPS-based geocorrection seems to be the best technique to be applied for the CORONA and IKONOS data, since it is more accurate than the map-based geocorrection (Cook and Pinder, 1996, Kardoulas ***et al.***, 1996).

11.2. Satellite data

The satellite data are extensively studied in chapter 3. For this reason, only the header file information is presented here, along with thumbnails of the images.

11.2.1. Landsat TM-5

01 October 1987 (Scene ID: LT5174036008714610) – Bands 3,2,1

24 May 1987 (Scene ID: LT5174036008727410) – Bands 3,2,1

11.2.2. Landsat ETM+ 7

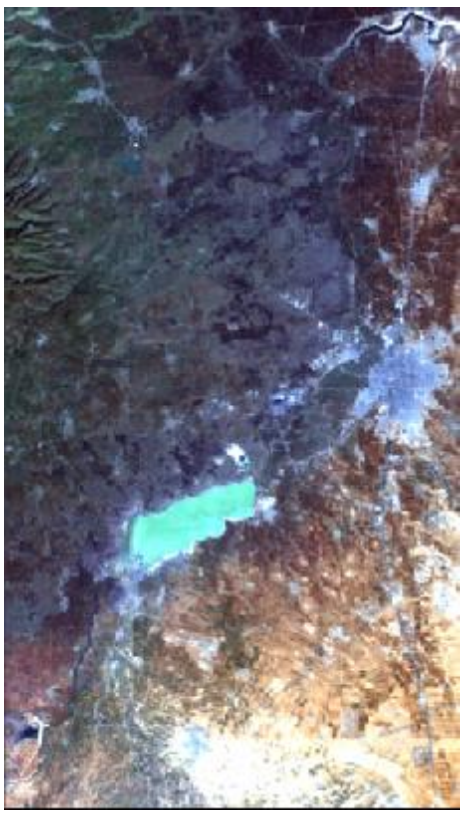

14 January 2000 (Scene ID: LE7174036000001450) – Bands 3,2,1

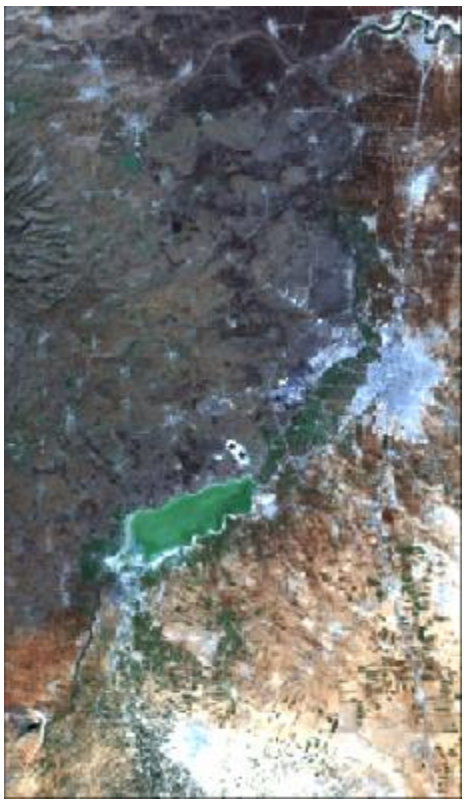

28 October 2000 (Scene ID: LE7174036000030250) – Bands 3,2,1

11.2.3. IKONOS

Processing Level: Standard Geometrically Corrected

Interpolation Method: Cubic Convolution

Multispectral Algorithm: None

Stereo: Mono

MTFC Applied: Yes

DRA Applied: No

05 September 2000

Panchromatic, partial. Interpolation method: bicubic

Image ID: 2000090508090020000010501090

Scan Direction: 0 degrees

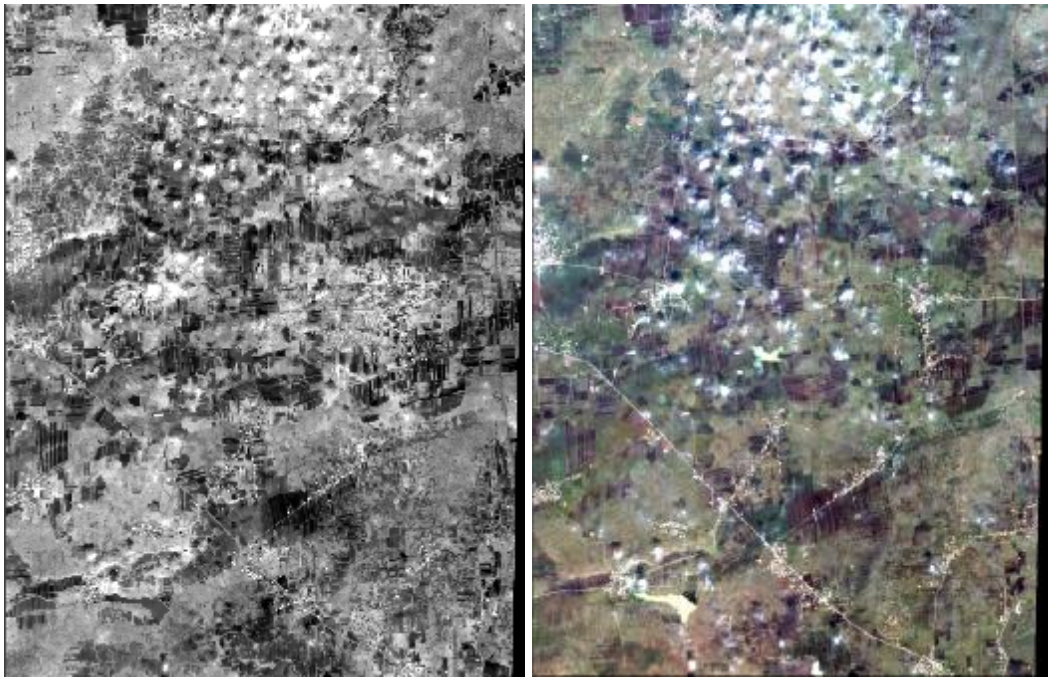

03 February 2002 (Disk 1_of_1)

Panchromatic & Multispectral, North area

Image ID Pan&MS, west area: 2002020308234080000011610757 (MS display – Bands 3,2,1)

Scan Azimuth: 359.96 degrees

Scan Direction: Forward

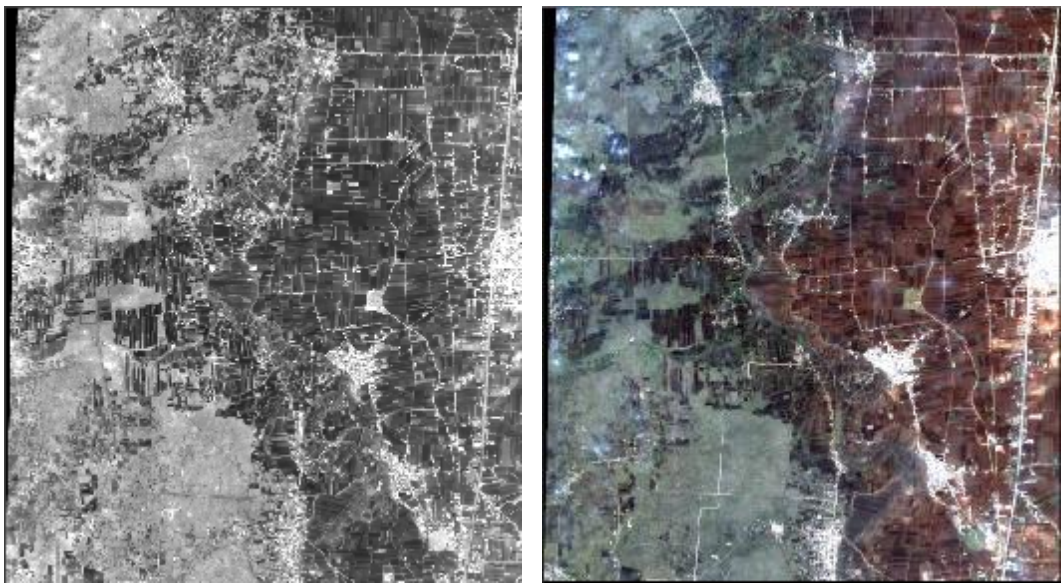

Image ID Pan&MS, east area: 2002020308234080000011610756 (MS display – Bands 3,2,1)

Scan Azimuth: 179.97 degrees

Scan Direction: Reverse

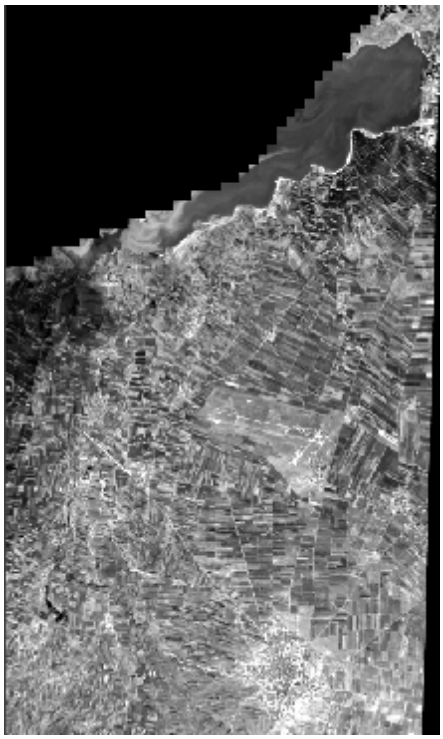

26 January 2002 (Disk 1)

Panchromatic & Multispectral, SouthWest area

Image ID Pan&MS, west area: 20020126083137700000011603150 (MS display – Bands 3,2,1)

Scan Azimuth: 180.03 degrees

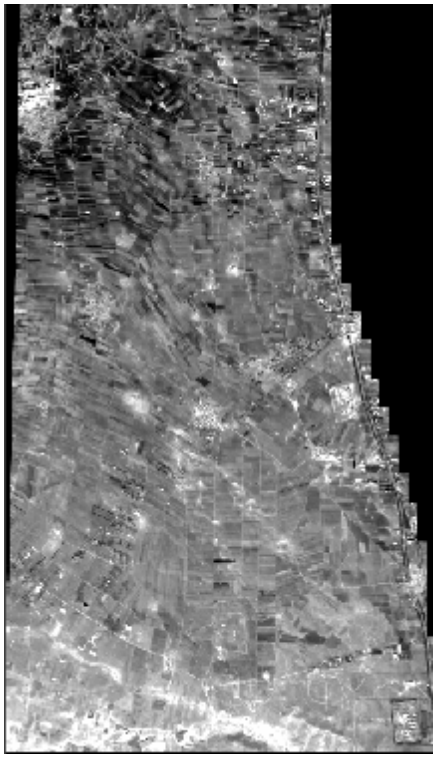

Scan Direction: Reverse

03 February 2002 (Disk 2)

Panchromatic & Multispectral, SouthEast area

Image ID Pan&MS, east area: 2002020308234080000011610756 (MS display – Bands 3,2,1)

Scan Azimuth: 179.97 degrees, Scan Direction: Reverse

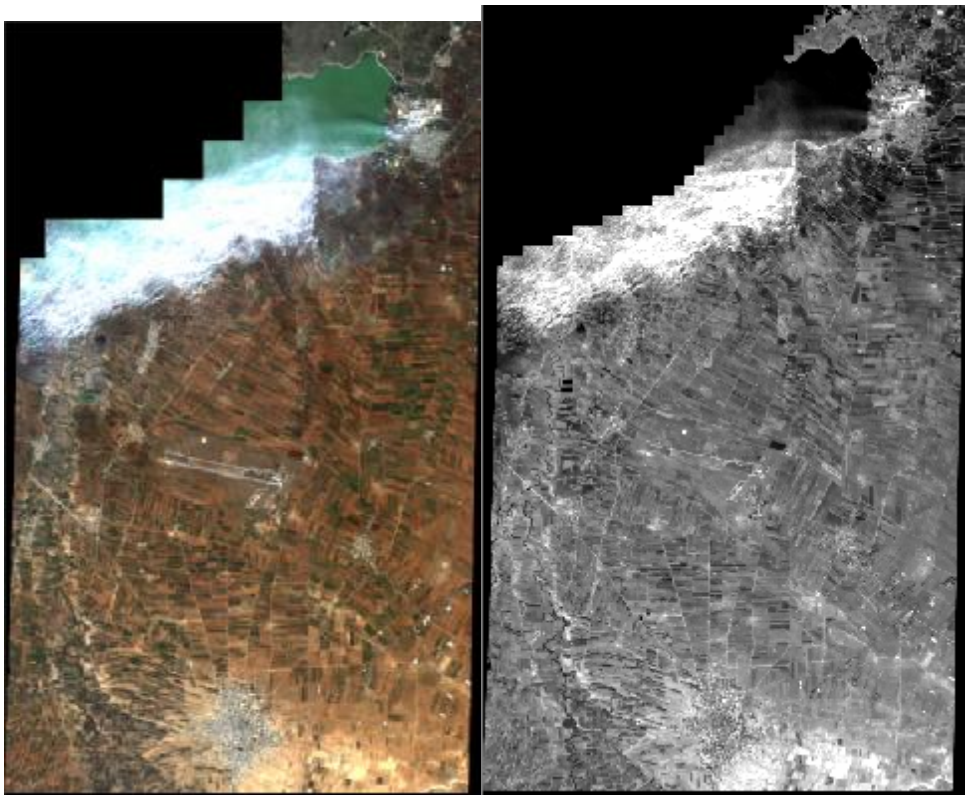

03 February 2002 (Disk 3)

Panchromatic & Multispectral, SouthWest area

Image ID Pan&MS, west area: 2002020308234080000011610757 (MS display – Bands 3,2,1)

Scan Azimuth: 359.96 degrees

Scan Direction: Forward

11.2.4. CORONA

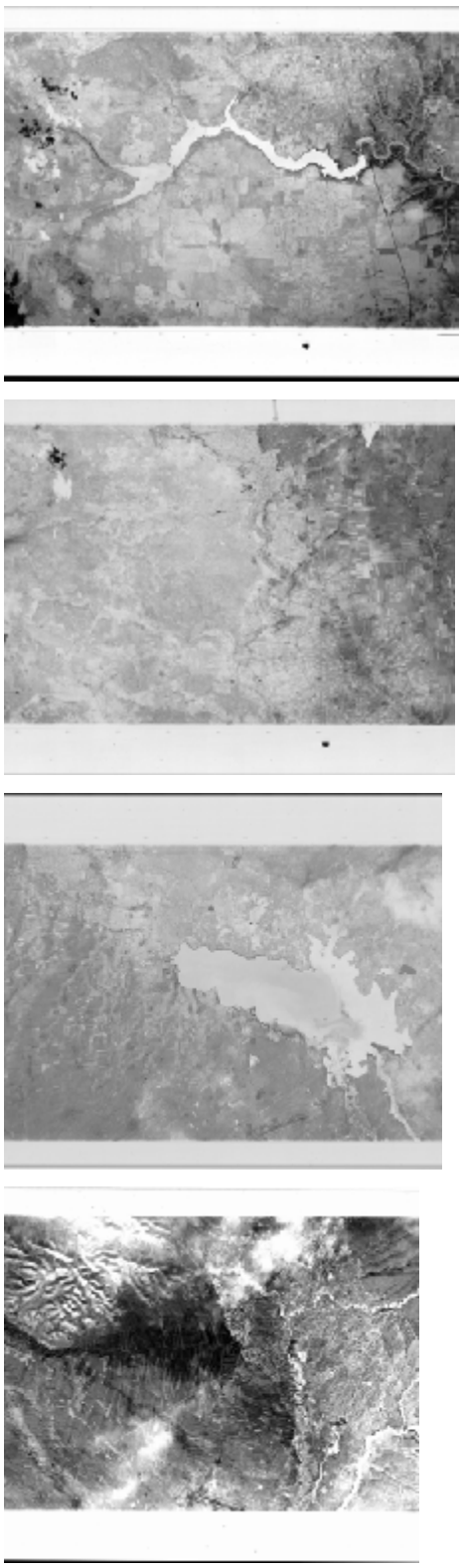

17 December 1969 – Mission 1108 – Aft camera – D203042, 43,44,45

Remarks: Cameras operated satisfactorily and the mission carried 811 ft of aerial color film (SO-242) added to the end of the film supply.

Orbit: Inclined 81.48°, period 88.61°, perigee 159km, apogee 251km

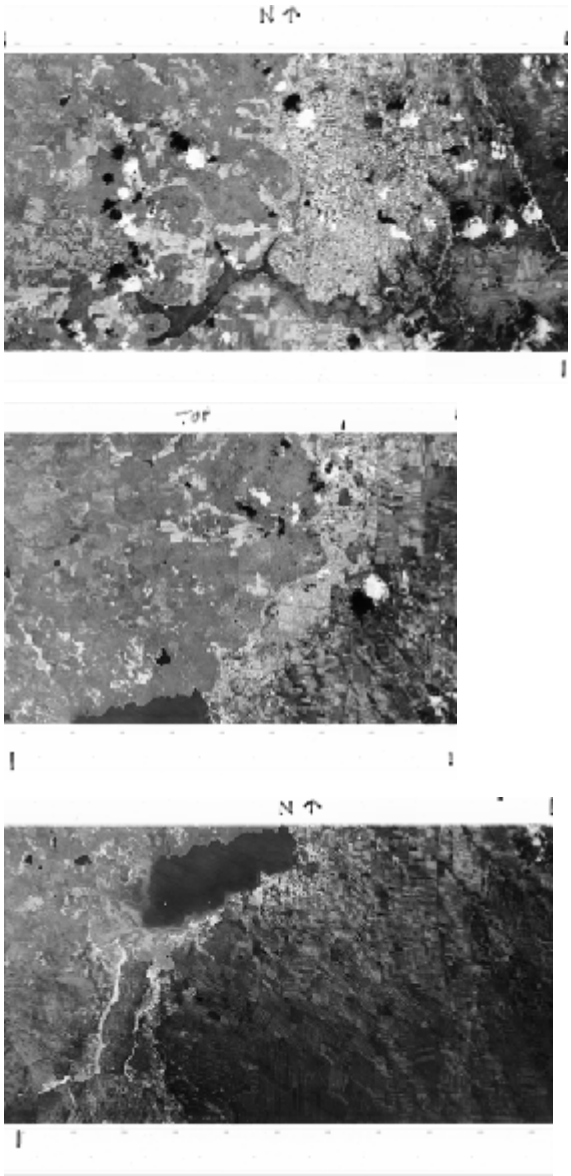

Mission 1110 – Forward camera – 007, 8,9

Remarks: The overall image quality is less than that provided by recent missions and 2,000 feet of S0-349 (new film) was spliced into the regular film. Also, the film 3414 was spliced in both cameras. First observation of electrostatic discharge spots.

Orbit: Inclined 83.00°, period 88.62°, perigee 162km, apogee 247km

28 May 1970

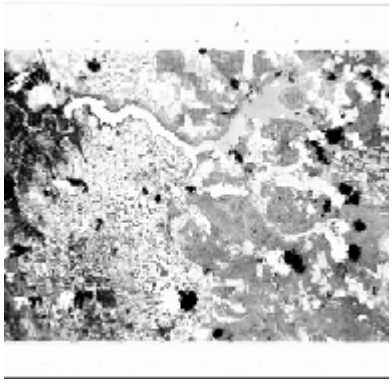

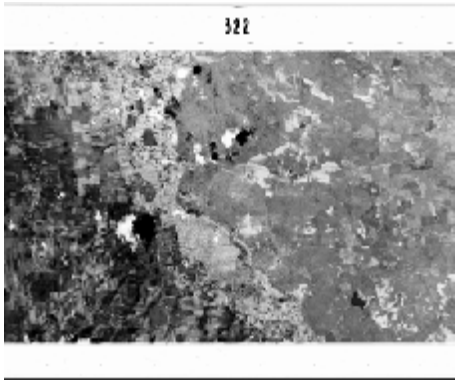

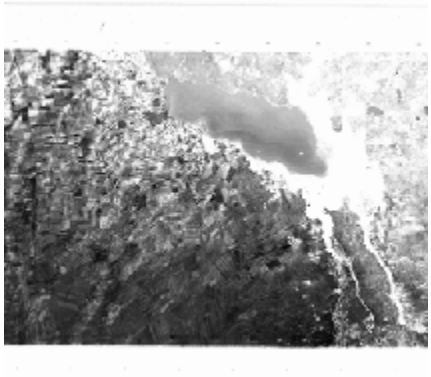

Mission 1110 – Aft camera – D106013, 14,15

Remarks: The overall image quality is less than that provided by recent missions and 2,000 feet of S0-349 (new film) was spliced into the regular film. Also, the film 3414 was spliced in both cameras. First observation of electrostatic discharge spots.

Orbit: Inclined 83.00°, period 88.62°, perigee 162km, apogee 247km

28 May 1970

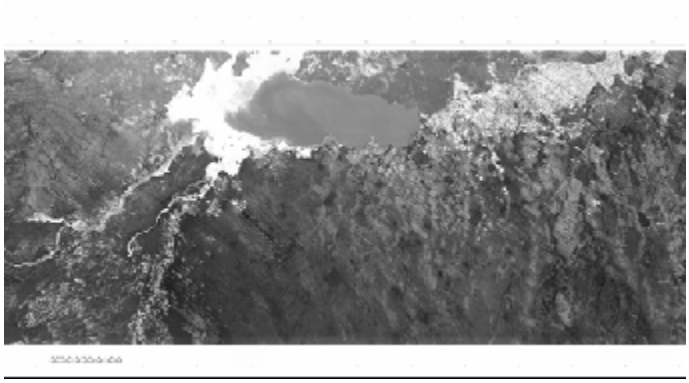

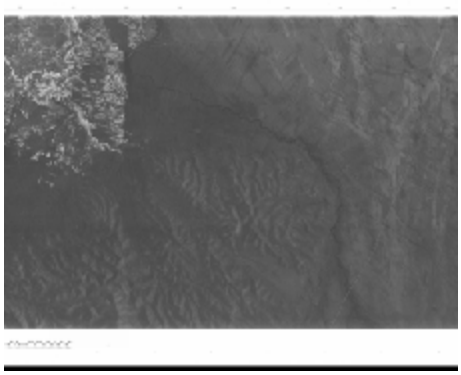

Mission 1111 – Aft camera – D135001, 2

Orbit: Inclined 60.00°, period 90.04°, perigee 158km, apogee 398km

Remarks: Unusually low inclination to cover Middle East targets. Due to the unusual launch time (18:25), the satellite passed over the Middle East at about 18:30 local time. The overall image quality is good. First full load of 3414 film; first in-flight focus-adjust test; first focus set for 60° nominal temperature; highest quality imagery to date; electrostatic spotting pattern associated with the recovery operation.

31 June 1970

11.2.5. HEXAGON

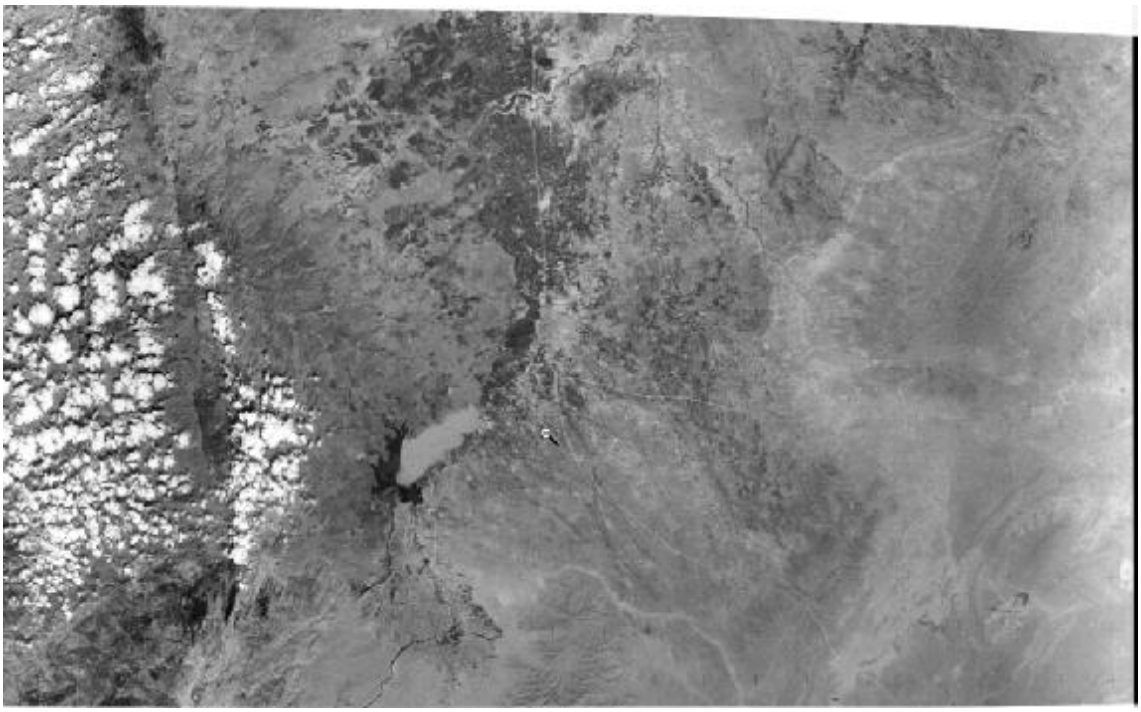

Mission 1210 – Frame 10 - DZB1210-500148L010001

15 July 1975

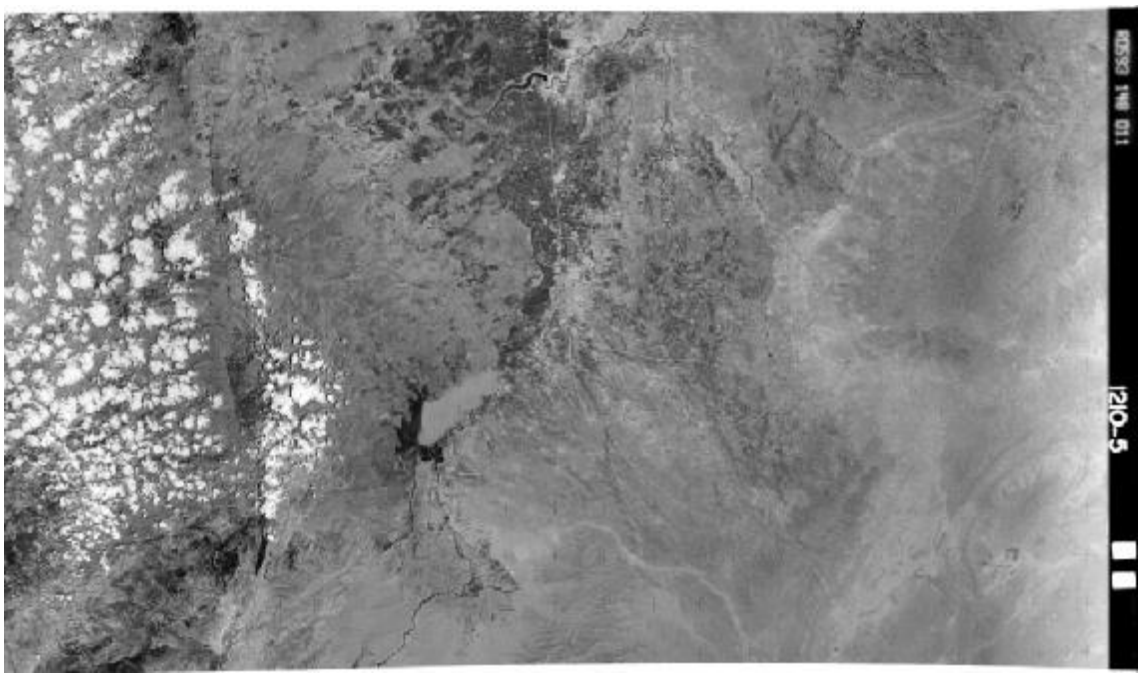

Mission 1210 – Frame 11 - DZB1210-500148L010001

15 July 1975

11.2.6. ASTER

Date: 1st of May 2001
Two DEMs, two level 1B images, two SWIR images, two VNIR images, and two TIR images.

Table 11-1 – ASTER data

Granule	Date	Centre point	Footprint	Sample image
SC:AST_L1B.003:2003043841 Cloud cover 29	01 May 2001, 08:31:32	34.81 Lat, 36.93 Lon;	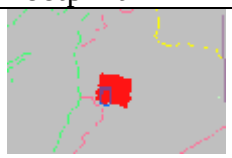	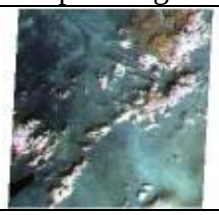
SC:AST_L1B.003:2003043844 Cloud cover 36	01 May 2001, 08:31:41	34.28 Lat, 36.79 Lon;	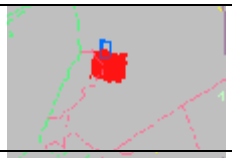	
SC:AST_06S.003:2003069969 Quality flag OK	01 May 2001, 08:31:32	34.81 Lat, 36.93 Lon;	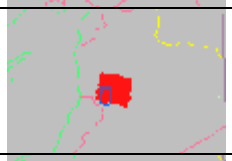	Cloud cover 29
SC:AST_06S.003:2003069934 Quality flag OK	01 May 2001, 08:31:41	34.28 Lat, 36.79 Lon;	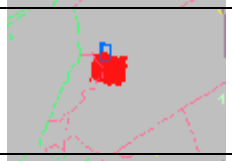	Cloud cover 36
SC:AST_06T.003:2003069976 Quality flag OK	01 May 2001, 08:31:32	34.81 Lat, 36.93 Lon;	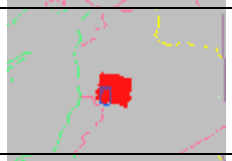	Cloud cover 29
SC:AST_06T.003:2003069937 Quality flag OK	01 May 2001, 08:31:41	34.28 Lat, 36.79 Lon;	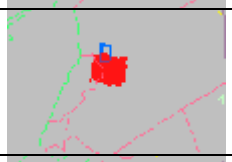	Cloud cover 36
SC:AST_06V.003:2003069961 Quality flag OK	01 May 2001, 08:31:32	34.81 Lat, 36.93 Lon;	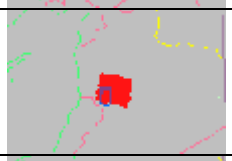	Cloud cover 29
SC:AST_06V.003:2003069923 Quality flag OK	01 May 2001, 08:31:41	34.28 Lat, 36.79 Lon;	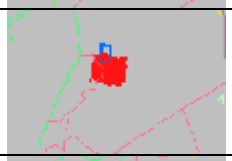	Cloud cover 36
SC:AST14DEM.003:2005910150 Quality flag OK	28 Oct 2000, 08:41:14	34.70 Lat, 36.20 Lon;	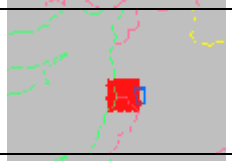	
SC:AST14DEM.003:2006359665 Quality flag OK	12 Jan 2002, 08:24:09	34.32 Lat, 36.47 Lon;	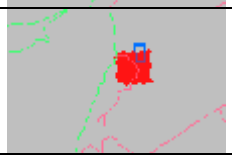	

12. Appendix II – Accessing CORONA data

Exploiting CORONA imagery (from Charles Vick, 1999).

The 1996 release of declassified CORONA imagery to the National Archives immediately raised the issue of how to actually access this product. While the government established an order fulfilments process, in practice the regularly available EROS Data Centre products were found to be inadequate for historical documentation or publication. This USGS product was been found to be noticeably out of focus, and to have automatic exposure processing features that rendered many scenes unusable [since much of the Soviet Union was snow-covered many scenes are bright with high contrast, which the USGS processing system interprets as a simple over-exposure, and which it automatically corrects by printing the entire scene a dark grey]. It was soon concluded that the USGS system as then implemented was unlikely to generate scenes that would be useful in analytical projects requiring detailed imagery. While ordering second generation negatives would avoid these processing artefacts, processing this product would require complicated and expensive equipment that would be beyond the reach of the typical historian or policy analyst afford.

In the early years of the CORONA program the intelligence community had used microscopes to obtain overview and detailed photographs, before it developed simpler means and huge multi-floored enlargers at the National Photographic Interpretation Centre, (NPIC). Today they use much more sophisticated softcopy systems to accomplish the same objective. But the earliest direct optical methods remain a useful approach to exploiting this early CORONA imagery.

The Edmond's Scientific Optical catalog provides pointers to obtaining Kodak literature on photography through a microscope. Adapters for the old reliable SLR Minolta 100/101 camera are suitable for adaptation to microscopes. Edmond's Scientific provided more up to date standardized adapters for this kind of operation.

The development of the means to accomplish this photography proved to be a very steep learning curve proceeding over one and a half years of trial and error testing. Prior to eventual success came many errors, until it became clear that the processes must be followed very meticulously to achieve results that surpass those of the standard USGS product, and rival those originally achieved by the intelligence community in the early days of CORONA.

The entire process of acquiring CORONA imagery takes about a one and a half week from start to finish. This alone is one advantage over the USGS procedure, which takes several times longer from beginning to end. The start of the process consists of assembling the best maps and ground based photography of the area of interest, along with the most accurate possible geographic coordinates of the site. This kind of complete data is frequently not available, but every effort must be made to develop a familiarity with the target of interest.

One of the most critical steps is research at the Library of Congress to examine and copy the 1:500:000 scale Tactical Pilotage Charts (TPCs), which are typically the most detailed maps available for areas of interest outside the United States. Information obtained through this process defines to the extent possible the geographic details that will help to identify the facility of interest in the CORONA imagery.

Upon arrival at the National Archives and Record Administration [NARA] facility in Suitland Maryland, you must first shed in a locker all those things that you do not need for the task at hand. The rest that you need must be approved by the Archives and stamped before you enter. Otherwise the guards will not let you in or out with the material you arrived with, much less the new material you want to leave with. This is an extremely strict security operation.

Once you get in with a new identification card required to do research there you go the Maps/Cartography room on the third floor. There you fill out forms to obtain World Aviation Charts, (WAC) charts of the area of interest. There at the Cartography room is a chart that is a map of the world divided into the boxes that define the charts and the coordinates home you on to those charts that you desire to see. Once you have ordered the charts on the NARA form the Archivist at certain times will pull those you desire for your review. In all cases you have to sign into the room you are in as well as for the documents you are reviewing both when you receive them and return them. These WAC charts allow you to define many critical data points that must be thoroughly documented for the photographs documentation and reference. Do not lose this data. First the WAC charts allow you to define the best of the photography minus cloud cover. The archives does not provide charts of data or how to do it but it does or you can provide paper that is stapled together with hand written charts to fill out the data required. You will have to develop the chart for your own use. They must include the following data point across the long length of the charts. A 11" by 17" sheet of paper can contain the following data columns for each WAC chart chosen:

Sequence number, Target name, Date photo taken, Mission number, KH-4, 4A, and 4B (here the mission numbers define the Camera type which affects scale analysis across the frame's centre), Frame Number, Revolution Number, F (forward) or A (Aft) camera, film orientation to the north/south direction seen only on the WAC, a can number area, and last but not least, a notes area

Only once you have defined this extensive data area can you ask for the Can number box of data from behind the Cartography desk. By matching this data you have written down you can define the two can number of the forward (F) and (A) Aft camera's. At this point, after spending the better part of three days researching this mass of information, you can now order the film to review it, which should take about a half a day to a full day. For beginners it is advised to not get to many cans or charts. In the beginning you may have to cross-reference the WAC photographic film charts with the film you are studying to define the actual target you are researching and trying to find its classic signature configuration.

Once you have defined the film frame you want to photograph you can then finally begin to set up the photographic equipment to do the photography through the microscope. This process is very straightforward and meticulous in its requirements and procedures. Because of the limits of the equipment available at the NARA Cartography division, specifically its microscope capability and configuration, the microscope is not of the design that allows direct adaptation of the camera to its optical tube through a direct or side T-mount arrangement. This means that a camera must be placed on a very heavy tripod beside the light table that the moveable microscope is mounted with three degrees of movement available. The answer to this problem is to firmly lock the table in place and to firmly settle the tripod with the camera mounted on it minus its lenses. In place of the lenses the microscope becomes your focusing lenses. Adapting to the microscope from the camera body is accomplished through the use of a camera type compatible T-mount and a standard microscope tube adapter connected to the T-mount.

Once the camera is properly mounted on the microscope you can begin to do the focus work and adjust the camera height accordingly. Depending on the lens used it is advisable to use black tape to seal the area of light seepage between the adapter and the microscope optical tube. This especially applies when you are using close up enlargement lenses of 15X and 20X. It is not required for the 10X lenses in the NARA microscopes. It is very easy to pull out the 10X lenses and replace it with your own 15X or 20X lens, but do not leave it there when you leave. Always return everything to as

you found it. The camera used must have a through the lens viewfinder as well as a through the lens light meter. In all cases only bracket shooting of the frame desired of up to five or more frames would succeed in getting a good picture usable for publication. The camera must allow you to control the timing manually for the exposures and as such precludes the use of all modern automatic SLR cameras of today except for very expensive Nikon. An old out of production Minolta 100/101 camera has been used with great success.

Once the film is placed in the camera you can begin taking pictures through the microscope which will require as much as 15 to 30 minutes per-frame taken to get the right focus. You must also check that the camera is very steady and that the microscope break switch is on to locked it down to prevent any motion from the microscope to be directed to the film from the camera action as the photographs are taken. Regardless some motion from the process will appear in the pictures but by being very careful you can minimize it to the max between frames as they are taken.

Once you have taken the photographs you take the B&W film to your local photo print shop to get them printed very carefully. It pay to know a good shop that will work with you to get the job done. Once you get the pictures back check the quality for a lack of debris in the frames prints and throw out those frames not usable.

Then you must label the photographs from your data table and the second records you have kept of what you have shot on each roll of film. This is most critical or it is all lost and worthless for documentation. While shooting the pictures it is advisable to use the Archives lead belts to hold down the edge of the film but be careful that they are not allowed to scratch the film. Remembering that the film is on a light table means it is critical that you bring black photographic paper to frame the area of the film you are going to photograph so as to prevent glare showing up on the photo's much as you used black tape to prevent light seepage before on the microscope.

Getting CORONA reports from NRO

In accordance with the FOIA (Freedom of Information Act), 5 U.S.C. § 552. as amended, and Section 502 of Intelligence Authorization Act of 2003, the NRO library processes requests from the Index of declassified CORONA, ARGON and LANYARD records.

The FOIA[57] governs how a request will be processed by the NRO. Additionally the NRO is in compliance with DoD (Department of Defence) Regulation 5400.7-R, "Department of Defence Freedom of Information Act Program", which can be found at Part 286 of Chapter 32 of the CFR (Code of Federal Regulations).

The FOIA is a Federal Law that establishes the public's right to request existing records from Federal government agencies. Any person can file a FOIA request. To do this, one must send a letter by mail of FAX (703) 808-5082 to *FOIA coordinator*. In the request letter, the person must state it is a FOIA request. Then the person must describe the requested specific records in enough detail that can be located with a reasonable amount of effort. Or, the request must contain enough event-related information (date and circumstances surrounding the event the record covers) to permit the conduct of an organised research. Last but not least, the person must state the willingness to pay the applicable fees. There can be a fee waiver, if the justification is good enough.

The FOIA allows fees to be charged to certain categories of requesters. However, it also provides that waivers or reductions of fees be given if disclosing the records is in the public interest, that is, records which significantly enhance the public's knowledge of NRO operations and activities. The NRO request takes 20 working days and it works on a first come first served basis.

For more details in how to request a NRO record, please read the NRO (1998). An example of a request is seen below. This example received a fee waiver.

[57] Known by its legal citation 5 U.S.C. §552, along with "The National Reconnaissance Office Freedom of Information Act Program Regulation", 32 CFR (Code of Federal Regulations) Part 296.1

Date: 3 March 2004

Barbara Freimann
Chief, Information Access and Release Centre
14675 Lee Road
Chantilly, VA 20151-1715

Dear Ms Freimann:

This is a request under the Freedom of Information Act (5 U.S.C. §552). I request that a copy of the following records (taken from the *Index of the declassified CORONA, ARGON and LANYARD records*) be provided to me:

Ref#	Title	Date	Pages	Barcode#
2/C/0016	STUDY: J3 SYSTEMS ANALYSIS STUDIES	670706	33	1400029889
2/C/0061	DOC: THE KH-4A CAMERA SYSTEM	670301	13	1400070603
5/A/0071	DOC: TECHNICAL PROPOSAL SYSTEM ANALYSIS STUDIES J-3 PHOTOGRAPHIC SYSTEM	670515	140	1400006307
5/E/0035	CORONA TECHNICAL INFORMATION	701231	94	1400029849
5/E/0036	CORONA TECHNICAL INFORMATION	701231	71	1400029848
	Total number of pages:		351	

In order to help you determine my status for the purpose of assessing fees, you should know that I am affiliated with an educational scientific institution, and this request is made for a scholarly or scientific purpose and not for a commercial use.

I am willing to pay fees if my request for a waiver is denied.

I request a waiver of fees for this request because disclosure of the requested information to me is in the public interest. It is likely to contribute significantly to public understanding of the operations or activities of the NRO and is not primarily in my commercial interest. The requested information will be used in my PhD thesis.

I include a telephone number at which I can be contacted if necessary to discuss any aspect of my request.

Sincerely,

Nikolaos Galiatsatos
University of Durham
Department of Geography
South Road
Durham DH1 3LE
United Kingdom

Email: nikolaos.galiatsatos@durham.ac.uk
Tel: 0044 7968 091474
Office: 0044 191 334 1922

13. Appendix III – Panoramic camera distortions correction and IEFP method

This appendix includes the corrections for the panoramic distortions as presented by Slama *et al.* (1980, p.201-207), and the approach of instantaneous equivalent frame photographs (IEFP) as presented by Case (1967).

13.1. Distortions

x and y : coordinates of any image point in the photograph. The +x axis is in the direction of flight.

x_p : panoramic distortion component

x_s : scan distortion component

x_{im} : IMC distortion component

X and Y : coordinates of any point in the ground datum plane

f : camera focal length

H : flight height above datum

α : camera scan angle

δ : angular velocity of the camera scan arm

t : scan time of the camera

V : velocity of the aircraft

v : velocity of the image in the focal plane

φ : primary tip angle of convergent camera

13.1.1. Panoramic distortion

It is the displacement of images of ground points from their expected perspective positions, caused by the cylindrical shape of the negative film surface and the scanning action of the lens.

$$\left.\begin{array}{l} y_p = f_a \\ a = \tan^{-1}\dfrac{Y}{H} \end{array}\right\} \Rightarrow y_p = f \cdot \tan^{-1}\frac{Y}{H}$$

$$x_p = \frac{f}{H} x \cdot \cos a$$

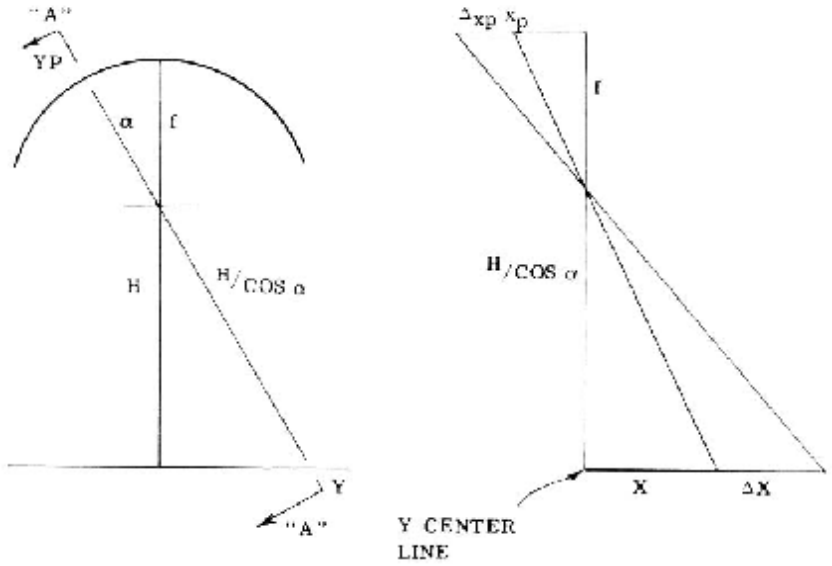

Figure 13-1 – Geometric relationship of panoramic distortion.

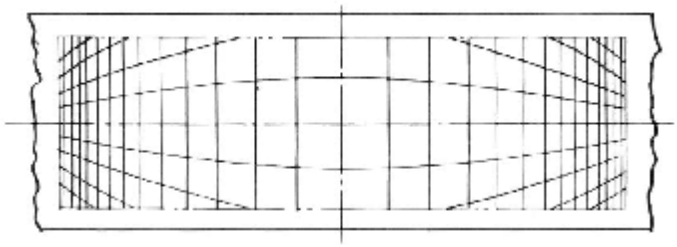

Figure 13-2 – Panoramic distortion.

13.1.2. Scan positional distortion

It is the displacement of images of ground points from their expected cylindrical positions caused by the forward motion of the vehicle as the lens scans.

$$\left.\begin{aligned} x_s &= \frac{f}{H}\cdot V\cdot t\cdot \cos a \\ t &= \frac{a}{d} \end{aligned}\right\} \Rightarrow x_s = \frac{V\cdot f\cdot \cos a}{H\cdot d}$$

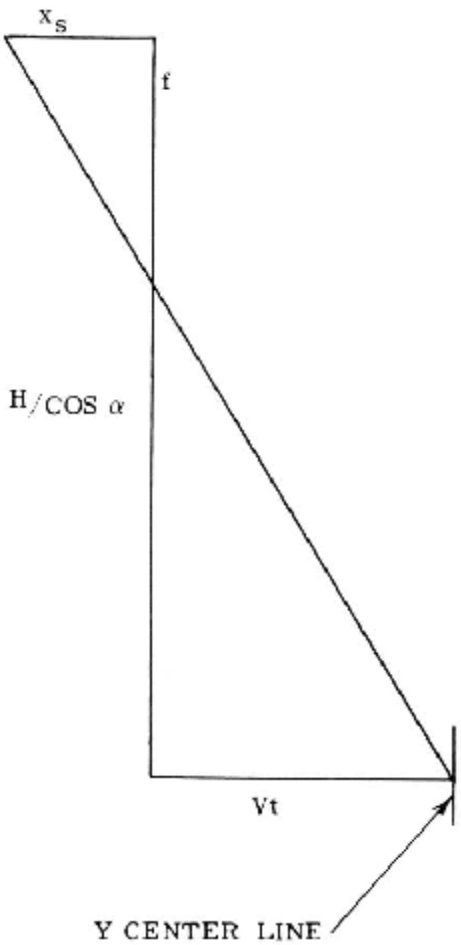

Figure 13-3 – Geometric relationship of scan positional distortion.

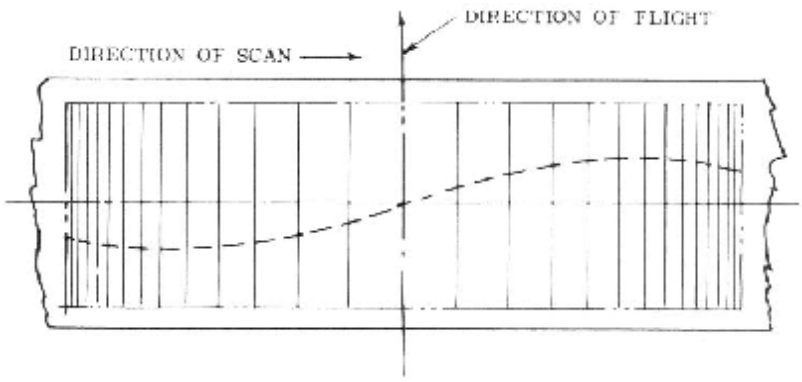

Figure 13-4 – Scan positional distortion superimposed on panoramic distortion.

13.1.3. IMC distortion

It is the displacement of images of ground points from their expected cylindrical position caused by the translation of the lens or negative surface, a motion used to compensate for image motion during exposure time.

$$v = \frac{dx_{im}}{dt} = \frac{f \cdot V \cdot \cos a}{H} \Rightarrow \left. \begin{array}{l} dx_{im} = \dfrac{f \cdot V \cdot \cos a}{H} dt \\ dt = \dfrac{da}{d} \end{array} \right\} \Rightarrow x_{im} = -\frac{V \cdot f}{H \cdot d} \cdot \sin a$$

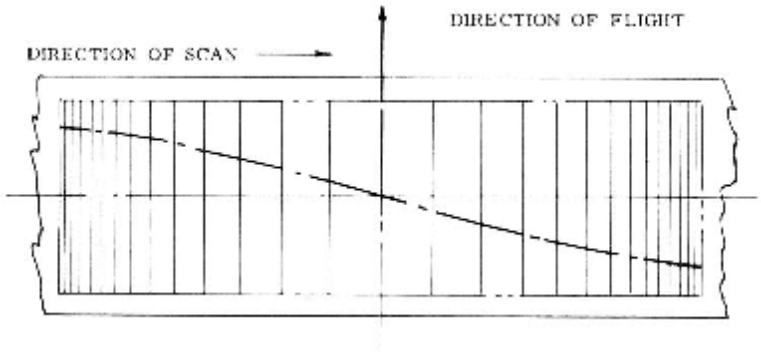

Figure 13-5 – Effect of IMC distortion of centreline scan.

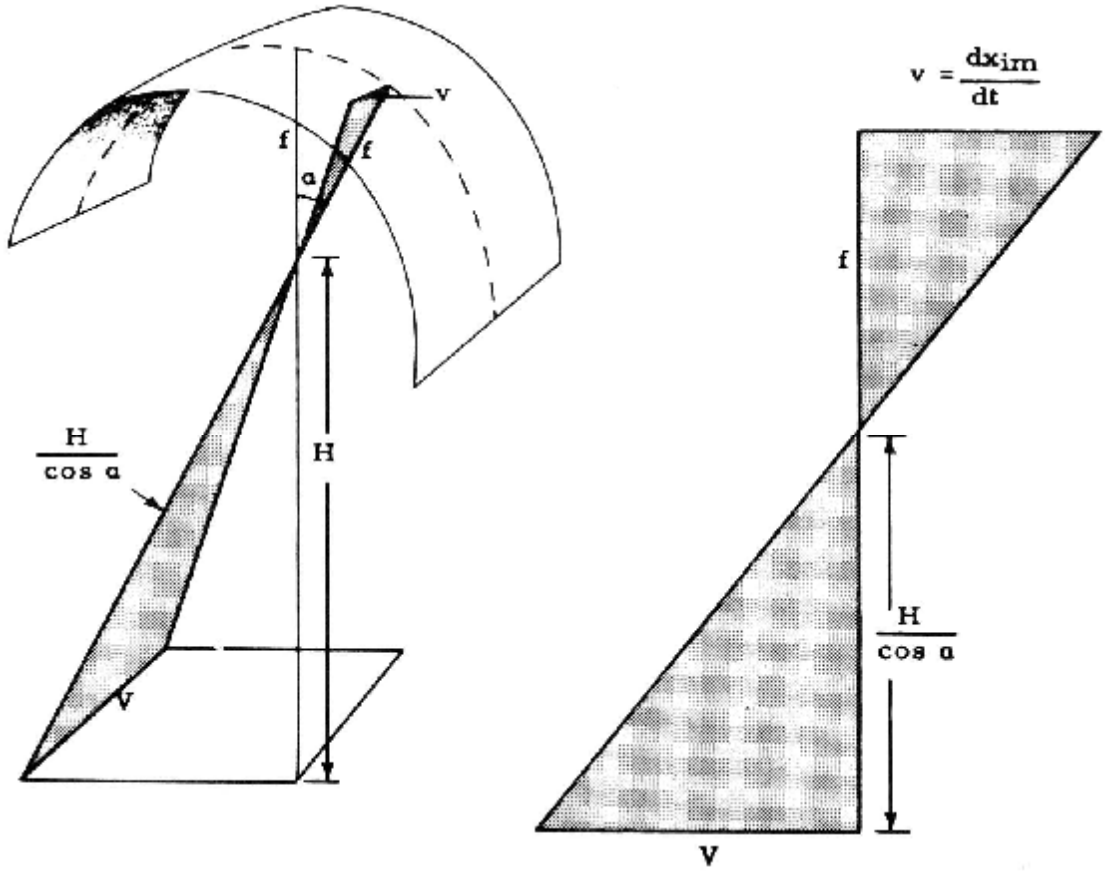

Figure 13-6 – Geometry of IMC distortion.

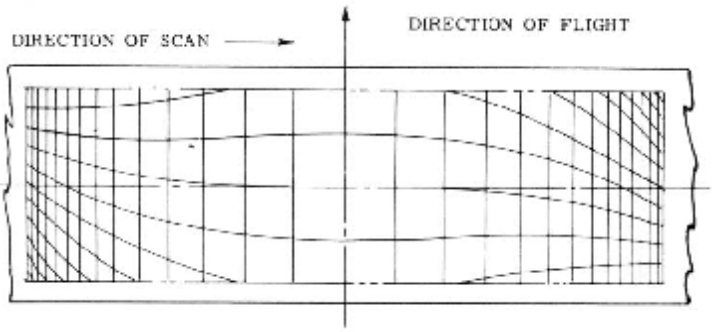

Figure 13-7 – Resultant image in the vertical panoramic camera.

13.1.4. Tipped panoramic distortion

It is the displacement of images of ground points for their expected vertical panoramic positions caused by tipping of the scan axis within the vertical plane of the flight path. It is additive distortion to the previously mentioned ones.

α = scan angle

N = nadir of 0° scan

PP = principal point for 0° scan

H = altitude

φ = primary tip angle

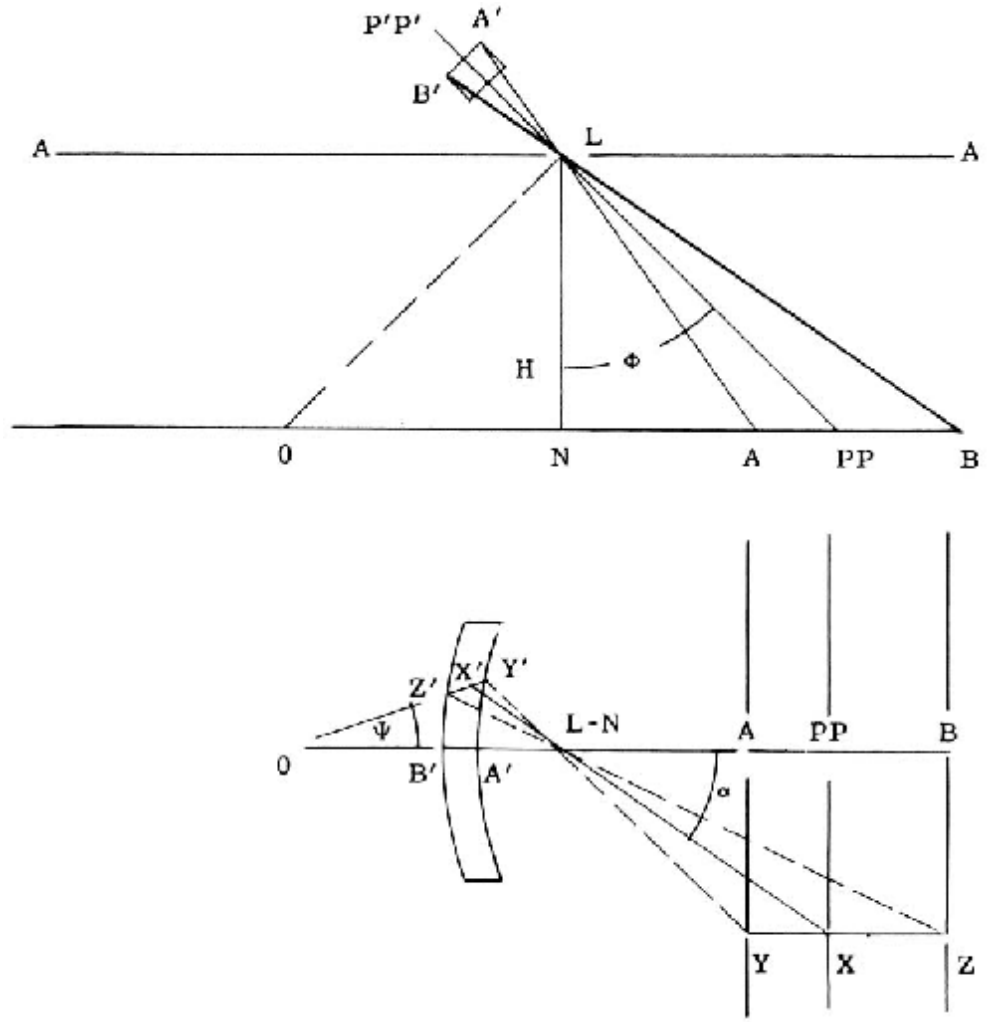

Figure 13-8 – Geometry of tipped panoramic distortion.

Distance N-PP = $H \cdot \tan j$

Distance PP-X = $H \cdot \dfrac{\tan a}{\cos j}$

$$\tan(90° - j) = \frac{\tan(90° - j)}{\sin a} \Rightarrow \cot y = \frac{\cot j}{\sin a} \Rightarrow \tan y = \sin a \cdot \tan j$$

The ground line Y-Z is parallel to the line A-B (flight line). In the image, line Y'-Z' forms an image angle y with the line A'-B'.

Line Y'-Z' on the film is a trace of the intersection of the oblique scanning plane and the oblique cylinder surface. The developed trace is geometrically a portion of an ellipse.

For stereoscopic viewing, the photographs must be adjusted so that the epipolar rays are parallel to the eye base.

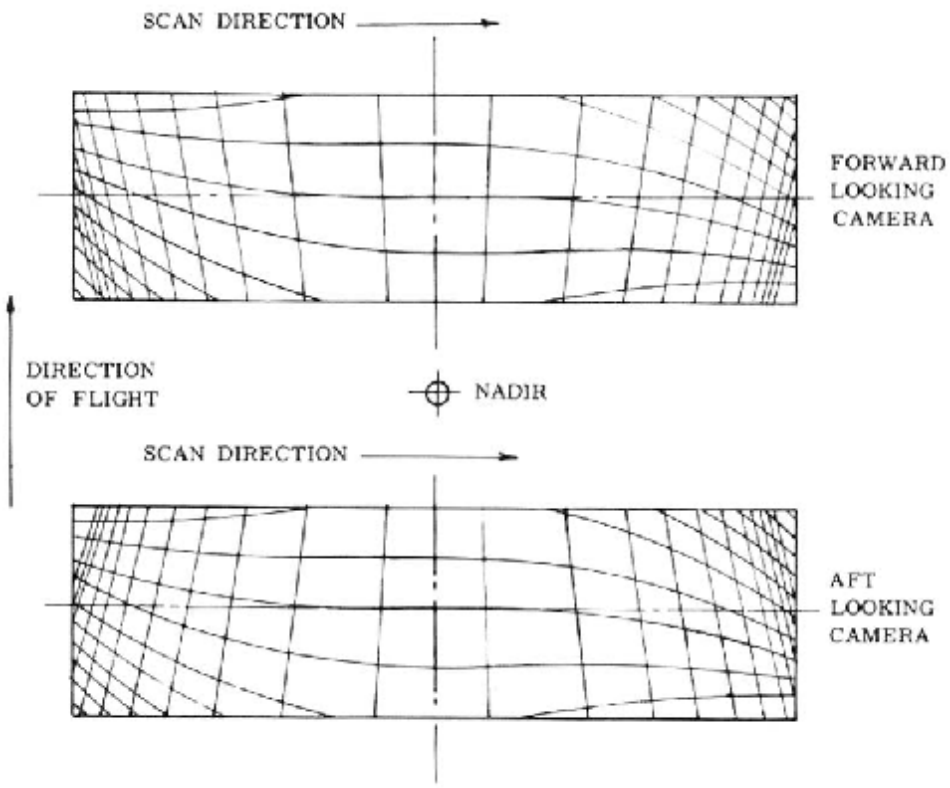

Figure 13-9 – Images of a unit grid on the ground obtained with a pair of convergent panoramic cameras in flight.

13.2. Sources of distortion in panoramic camera – internal geometry

The sources of distortions that influence the geometric fidelity of panoramic cameras are:

Optical (by lens distortions and by errors in the principal distance determined):

Lens distortions are normally of the order of only a few μm. In several panoramic cameras, the film is positioned with respect to the lens by a scanning arm. Due to the floating action of the film over four rollers, the mechanical scan radius is not the principal imaging distance. The true distance from the nodal point of the lens to the film during scanning must be known.

Optical-Mechanical:

- failure of lens to rotate about the nodal point or optical bar rotation axis
- irregular motions of the lens scan, scanning arm, scanning prism(s) or mirror(s), slit or film driver
- wobble of optical and mechanical scanning components across the width of the format

These errors are thought to have a negligible effect on the internal geometry, otherwise the effect on the image quality would be incompatible with the high resolution of the panoramic system.

Mechanical:

- film motion during scan while it is supposed to be a stationary, or film out of the focal plane
- irregularity of IMC motion, or wrong IMC.

13.3. Calibration tasks

The principal task of interior geometry calibration is to make it possible to recover, for any image point, two coordinates, which locate this point unambiguously and accurately. These two coordinates are the scan angle α and the cross angle β.

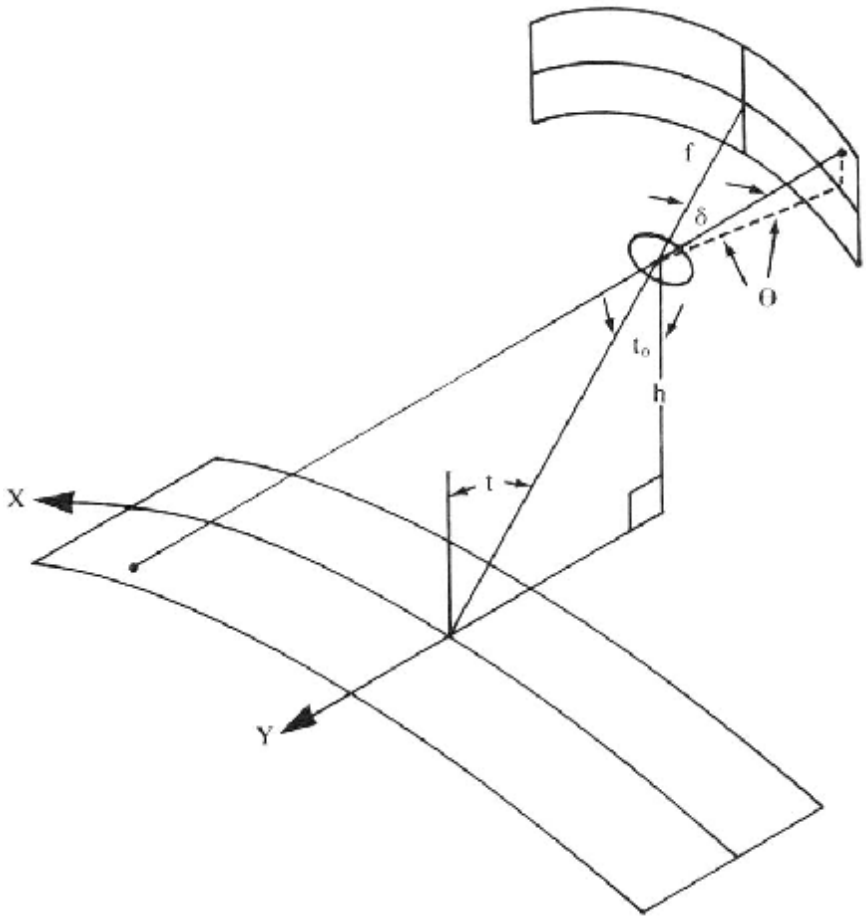

Figure 13-10 – Panoramic camera footprint (Slama *et al.*, 1980, p.942).

The central principal point is defined as the intersection of the film surface with the intersection of two planes:

- the plane through the scan axis which bisects the total scan angle and which, hence, is the medial plane of symmetry of the camera and is vertical when the camera is in its nominal attitude; and
- the plane normal to the scan axis which contains the rear nodal point of the lens.

The central principal point may be defined as the point of inflection of the IMC trace made by the principal ray on the film.

13.4. Cameras like HYAC (film stationary during scanning)

Because the film may slip during one scan, the essential feature of any calibration must be to fix the position, by means of fiducials, of any segment of the film during its exposure with respect to the geometry of the camera. It is not adequate to rely on time markers on the film, which indicate the position of the scan arm with respect to the beginning and end of one in terms of time. Time markers do not make it possible to ascertain whether the cause of nonuniform spacing of supposedly equidistant time marks is instability of the film (differential shrinkage), slippage of the film or nonuniform scan rate.

The film although positioned exactly at the time of exposure by the rollers, rests on guide rails. During the instant of exposure, the film is lifted from the rails by the rollers. However, the illumination of the fiducial holes can be arranged so that the light passes the holes in a direction normal to the slit plane. Thus, any shift of the fiducial mark (image) due to the lift of the film can be avoided. Because the fiducial holes are a rigid part of the camera, their position in the camera can be expressed in terms of angles α and β. Both of these angles are defined solely wit h reference to the camera system.

The central problem of calibration thus can be reduced to the problem of measuring the positions of the fiducial holes. This might be accomplished by a combination of mechanical and photogrammetric mensuration procedures and by using the following inherent relationships:

$$a = \frac{x - x_{pp}}{r}$$

$$b = \frac{y - y_{pp} - C \cdot \sin a}{f}$$

where

x and y are the coordinates of the fiducial mark

x_{pp} and y_{pp} are the coordinates of the principal point

r is the radius of the cylinder to which the film-guide rails are fitted and whose axis is coincident with the scan axis

f is the focal length

C sinα is the lens shift due to image motion compensation, where $C = \frac{f \cdot V}{H \cdot d}$

where

v = flight speed

H = flight height

f = focal length

δ = rate of scan.

13.5. Collinearity equations

Let's assume that for a beam of rays, we know the interior and exterior orientation data (f, x_o, y_o, Δr, X_o, Y_o, Z_o, ω, φ, κ), where

Interior orientation:

f = the focal distance (constant)

x_o, y_o = the image coordinates of the principal point

Δr = the characteristic curve of the radial transformation of the lens

Exterior orientation:

X_o, Y_o, Z_o = the geodetic coordinates of the projection center

ω, φ, κ = three sequential rotation angles; roll ω, pitch φ, yaw κ.

Let's also assume that we measured the image coordinates (x_μ, y_μ) of the image μ of a point M on the negative.

Then the vectors OM and Oμ must, according to the geometry model of the central projection, to be on the same line. If the geodetic coordinates of M are (X_M, Y_M, Z_M), then the two vectors will be:

$$Om = \begin{bmatrix} x_m - x_o \\ y_m - y_o \\ -f \end{bmatrix} \qquad OM = \begin{bmatrix} X_M - X_O \\ Y_M - Y_O \\ Z_M - Z_O \end{bmatrix}$$

To collineate these vectors, then one of them must rotate according to (ω, φ, κ). This can be done with the use of a rotation matrix **M**. And to make them equal, we'll multiply one of them of a scale factor λ. Thus:

$$\begin{bmatrix} x_m - x_o \\ y_m - y_o \\ -f \end{bmatrix} = l\,\mathbf{M} \begin{bmatrix} X_M - X_O \\ Y_M - Y_O \\ Z_M - Z_O \end{bmatrix}$$

This equation is called **Collinearity equation.** It's the most basic equation of photogrammetry, because it connects the image coordinates with the geodetic coordinates of a point, with the help of the interior and exterior orientation data.

It has to be noted that the scale factor λ is only for the particular point M. Thus, it's very difficult to apply this equation for every point of the image, since we'll have to determine the scale factor for every single point. But after the dividing of the first and second equations with the third, then we have:

$$x = -f\,\frac{m_{11}(X - X_O) + m_{12}(Y - Y_O) + m_{13}(Z - Z_O)}{m_{31}(X - X_O) + m_{32}(Y - Y_O) + m_{33}(Z - Z_O)}$$

$$y = -f\,\frac{m_{21}(X - X_O) + m_{22}(Y - Y_O) + m_{23}(Z - Z_O)}{m_{31}(X - X_O) + m_{32}(Y - Y_O) + m_{33}(Z - Z_O)}$$

,where m_{ij} the parts of **M.**

$$\mathbf{M} = \begin{bmatrix} m_{11} & m_{12} & m_{13} \\ m_{21} & m_{22} & m_{23} \\ m_{31} & m_{32} & m_{33} \end{bmatrix} = \begin{bmatrix} \cos f \cos k & \cos w \sin k + \sin w \sin f \cos k & \sin w \sin k - \cos w \sin f \cos k \\ -\cos f \sin k & \cos w \cos k - \sin w \sin f \sin k & \sin w \cos k + \cos w \sin f \sin k \\ \sin f & -\sin w \cos f & \cos w \cos f \end{bmatrix}$$

These collinearity equations apply to frame photography.

13.5.1. Panoramic photography

Since the panoramic camera scans through an angle θ while exposing imagery, the projective equations must take into account this rotation as though it were an additional, constantly changing, tilt of the camera. This is accomplished by premultiplying the rotation matrix **M**, by the rotation matrix representing the scan angle. Thus, the collinearity equation becomes:

$$\begin{bmatrix} x \\ 0 \\ -f \end{bmatrix} = l \begin{bmatrix} 1 & 0 & 0 \\ 0 & \cos q_{\mathrm{M}} & \sin q_{\mathrm{M}} \\ 0 & -\sin q_{\mathrm{M}} & \cos q_{\mathrm{M}} \end{bmatrix} \mathbf{M} \begin{bmatrix} \mathrm{X_M} - \mathrm{X_O} \\ \mathrm{Y_M} - \mathrm{Y_O} \\ \mathrm{Z_M} - \mathrm{Z_O} \end{bmatrix}$$

Because the coordinate y is in the normal direction of the slit, it is considered 0 (zero).

In order to get the collinearity equation similar to the frame photography, we first premultiply both sides with the transpose of the scan angle rotation matrix, and then we divide both sides with cosθ. Thus:

$$\begin{bmatrix} x/\cos q \\ f\tan q \\ -f \end{bmatrix} = \frac{l}{\cos q}\mathrm{M}\begin{bmatrix} \mathrm{X_M}-\mathrm{X_O} \\ \mathrm{Y_M}-\mathrm{Y_O} \\ \mathrm{Z_M}-\mathrm{Z_O} \end{bmatrix}$$

, and the collinearity equations become:

$$x' = x/\cos q = -f\frac{(m_{11})_j(X-X_O)+(m_{12})_j(Y-Y_O)+(m_{13})_j(Z-Z_O)}{(m_{31})_j(X-X_O)+(m_{32})_j(Y-Y_O)+(m_{33})_j(Z-Z_O)}$$

$$y' = f\tan q = -f\frac{(m_{21})_j(X-X_O)+(m_{22})_j(Y-Y_O)+(m_{23})_j(Z-Z_O)}{(m_{31})_j(X-X_O)+(m_{32})_j(Y-Y_O)+(m_{33})_j(Z-Z_O)}$$

Here the $\mathbf{M}_j$ symbolizes the attitude at point j, at the moment t_j.

But panoramic photography is not static like frame photography, but dynamic. Thus, it is dependent on time. To determine the time t_j of a point j, we use the y coordinate of that point, y_j. If the origin is placed at the midpoint of exposure, the scan angle of the j point will be given by:

$$q_j = \frac{y_j}{f}$$

If the scan rate θ' is given then the time t_j would be given by:

$$t_j = T + \frac{q_j}{q'}$$

Where T is the time of exposure of the y-coordinate origin, that is the time of exposure of the midpoint of the photograph. Since the scan rate can be subject to error or can vary, a more exact determination of time might be made if time marks are placed on the panoramic film (Abraham, 1961). The precise time of each mark, placed at regular intervals along the edge of the film, would be known, and the time of the jth point could then be found by interpolation between the two nearest time marks.

To model the camera motion, there are actually two ways. We can either assume that the model of the camera is continuous (assume that discontinuities are statistically insignificant), or attempt to account for these discontinuities by some special technique, such as treating the photo as a set of discrete "framelets". In the case of the space panoramic photography, we can assume that discontinuities are statistically insignificant and thus transform the panoramic image in a series of instantaneous equivalent frame photographs.

The latter provides a means for performing analytical operations with panoramic photography when the position and attitude of the camera are unknown (or not well known), just like in the case of CORONA. If on the other hand, the position and the attitude were known, then the latter collinearity equations may be used without resort to the instantaneous equivalent frame photographs (IEFP).

For example, the camera position coordinates are expressed as functions of the parameters of the orbit and of the time of exposure, i.e.:

$X_o=g_1(a, b, c, \ldots, t_j)$

$Y_o=g_2(a, b, c, \ldots, t_j)$

$Z_o=g_3(a, b, c, \ldots, t_j)$

where X_o, Y_o, Z_o are the camera position coordinates at the time t_j; a, b, c, etc., are the parameters of the orbit; and t_j the time of the exposure of the jth image point is determined from time marks on the film. The linearization of the orbit equations and their introduction into the linearized form of the collinearity equations is described in Case (1961).

Now, there are no orbital information available, thus we have to use the IEFP method. We assume that the satellite flies parallel to the earth's surface and the earth is flat. To transform the panoramic photograph to IEFP, the inverse of the collinearity equations is first employed to project the panoramic photo coordinates down to the ground. That is:

$$X = X_O + (Z - Z_O)\left[\frac{(m_{11})_j\, x' + (m_{12})_j\, y' - (m_{31})_j\, f}{(m_{13})_j\, x' + (m_{23})_j\, y' - (m_{33})_j\, f}\right]$$

$$Y = Y_O + (Z - Z_O)\left[\frac{(m_{12})_j\, x' + (m_{22})_j\, y' - (m_{32})_j\, f}{(m_{13})_j\, x' + (m_{23})_j\, y' - (m_{33})_j\, f}\right]$$

Since the camera is assumed to be flying straight and level, the camera station coordinates are simply taken as:

$X_o=V\Delta t_j$

$Y_o=0$

$Z_o=H$

,where H is the altitude of the spacecraft, V is the spacecraft velocity, and Δt_j is the difference in time from the origin (e.g. the midpoint of exposure) to the jth photo point. Δt_j could be determined from the time marks, or $\Delta t_j=\theta_j/\theta'$.

After all the measured photocoordinates have been projected to the ground, the resulting ground points are projected back up to the IEFP. For this operation the collinearity equations are used directly, that is:

$$x_F = -f_F \frac{(m_{11})_F (X - X_{OF}) + (m_{12})_F (Y - Y_{OF}) + (m_{13})_F (Z - Z_{OF})}{(m_{31})_F (X - X_{OF}) + (m_{32})_F (Y - Y_{OF}) + (m_{33})_F (Z - Z_{OF})}$$

$$y_F = -f_F \frac{(m_{21})_F (X - X_{OF}) + (m_{22})_F (Y - Y_{OF}) + (m_{23})_F (Z - Z_{OF})}{(m_{31})_F (X - X_{OF}) + (m_{32})_F (Y - Y_{OF}) + (m_{33})_F (Z - Z_{OF})}$$

, where x_F, y_F the IEFP coordinates of the jth point on the panoramic photograph; f_F is the principal distance of the IEFP; $\mathbf{M}_F$ is the rotation matrix of the IEFP; X_{oF}, Y_{oF}, Z_{oF} are the geodetic coordinates of the camera station for the IEFP; and X, Y, Z are the geodetic coordinates of the ground point corresponding to the j^{th} point imaged on the panoramic camera as determined from the inverse of the collinearity equations of the panoramic camera.

However, the employment of IEFP requires some additional handling data. The camera position and attitude and the positions of all ground points must be known if the transformation from the panoramic photography to IEFP is going to be made with certainty. And yet, the purpose of such analytical procedures as the resection, absolute orientation and block adjustment is to determine just those parameters, the premise being that, to begin with, those parameters will be unknown or not very well known. A procedure involving iteration suggests itself as a solution to this dilemma. First, the panoramic photography is transformed to IEFP using the best available or nominal values for the camera station and ground control parameters. The resection, absolute orientation or block adjustment is then performed and improved values for the camera station and ground control parameters are obtained. The transformation of the panoramic photography is repeated by employing these parameters. The iteration is continued until no further improvement is observed.

14. Appendix IV – Technical specifications of instrumentation

Specifications of the spectroradiometer
(GER1500)

Spectral range	350 nm to 1050 nm
Number of channels	512
Type of sensor	Silicon array
Resolution	3 nm FWHM (Full Width Half Maximum)
Integration speed	5-160 ms
Unit size	15 cm wide, 8 cm high, 26 cm long
Unit weight	1,8 kg maximum
Internal memory	483 scans
Sighting	Diode laser at 635 nm
Power	6 Volt rechargeable nickel metal hydride battery
Display	LCD, 8 digits, 2 rows
Options:	
Field-of-view	Standard (3º - .1º) Fiber Optic 15º FOV Cosine Receptor

Specifications of the Handheld GPS receiver
(Garmin GPS12XL Personal Navigator)

Size	14,6 x 5,1 x 3,4 cm
Weight	269 g w/ batteries
Temperature range	-15º to 70ºC
Receiver	12 parallel channel, differential ready
Acquisition time	Approximately 15 sec (warm start) Approximately 45 sec (cold start) Approximately 5 min (AutoLocate™)
Update rate	1/second, continuous
Position accuracy	1-5 m with DGPS corrections 15 m RMS (subject to SA)
Velocity accuracy	0,1 knot RMS steady state
Dynamics	6g
Input	Four 1,5 Volt AA batteries or 10-32 vDC

Specifications of the photogrammetric scanner
(Vexcel VT4000)

Physical & environmental	75 x 58.5 x 83 cm, 77 kg Desktop configuration Power configurable 960 Volt Amps Max
Spatial resolution	Variable from 7.5 μm to 120 μm
Spectral resolution	Monochrome 8-bit / Colour 24-bit
Mechanical resolution	Active scanning area 25.4 x 50.8 cm Maximum IFOV 12 x 12 cm
Software calibration	Autosizing, Autofocus, Autopositioning, Autocalibration for grey balance
Speed (scan times for 23 x 23 cm image)	25μm monochrome 3 min / colour 6 min 12.5μm monochrome 12 min / colour 25 min
Light source	Cold cathode, variable intensity (SW control)
Optical system	16 to 1 magnification range, 2-axis zoom
Camera	1024 x 1024 CCD
Radiometric uniformity	2 grey values RMS
Geometric accuracy	1/3 pixel RMS (i.e. 2.5μm RMS at 7.5μm resolution)

15. Appendix V – Error matrices

15.1. CORONA imagery registration to IKONOS

15.1.1. Mission 1108 – Aft camera – D203043,44,45

Remarks: Cameras operated satisfactorily and the mission carried 811 ft of aerial color film added to the end of the film supply.
Orbit: Inclined 81.48, period 88.61, perigee 159, apogee 251
17 December 1969
Only the frames 043, 044 and 045 covered the area of interest.
RMSe after registration to Ikonos (before the GPS correction), in pixels.
All images were resampled with nearest neighbourhood method, and rectified with 3rd polynomial.

CORONA 043

Control point error: (X)0.9569, (Y)1.8136, (Total)2.0506

Row	Point ID	X input	Y input	X Ref.	Y Ref.	Xresidual	Yresidual	RMS erro	Contrib
1	GCP #1	7571.137	-3393.669	291351.733	3853613.279	0.128	-1.022	1.03	0.502
2	GCP #2	6916.551	-3996.548	290065.419	3852050.860	0.805	-1.085	1.351	0.659
3	GCP #3	7719.073	-4005.039	291842.722	3852240.523	0.806	0.515	0.956	0.466
4	GCP #4	6268.351	-3817.359	288573.767	2852312.818	-1.182	5.405	5.533	2.698
5	GCP #5	6444.727	-2903.086	288716.785	3854468.520	0.586	1.593	1.698	0.828
6	GCP #6	7274.903	-2583.933	290469.300	3855413.788	-2.968	-2.472	3.863	1.884
7	GCP #7	7183.100	-2066.226	290130.535	3856600.189	0.232	-1.533	1.55	0.756
8	GCP #8	5903.881	-1822.422	287209.011	3856838.951	1.449	-2.433	2.832	1.381
9	GCP #9	7330.912	-1037.191	290174.290	3859044.681	-1.719	-2.773	3.263	1.591
10	GCP #10	8361.573	-495.377	292338.420	3860594.953	0.519	1.579	1.662	0.811
11	GCP #11	6840.385	-63.933	288806.599	3861224.608	0.552	2.449	2.51	1.224
12	GCP #12	7661.52	-610.892	290802.3	3860140.116	0.707	0.310	0.772	0.376
13	GCP #13	5795.178	-1387.491	286837.729	3857839.813	0.521	2.149	2.211	1.078
14	GCP #14	4631.478	-1360.291	284216.295	3857593.999	-1.535	-1.657	2.259	1.101
15	GCP #15	1707.363	-1890.403	277807.118	3855602.718	1.139	2.972	3.183	1.552
16	GCP #16	1658.298	-1293.43	277505.321	3856988.505	1.394	2.402	2.777	1.354
17	GCP #17	2283.042	-1354.76	278930.996	3857006.13	-0.536	1.931	2.004	0.977
18	GCP #18	2924.798	-1842.103	280531.573	3856029.072	0.370	0.911	0.984	0.48
19	GCP #19	3912.413	-1018.414	282498.475	3858216.029	-0.524	0.391	0.654	0.319
20	GCP #20	4320.525	-689.564	283320.589	3859094.342	0.669	-0.201	0.699	0.341
21	GCP #21	4790.414	-279.982	284254.944	3860180.072	0.043	-0.728	0.729	0.356
22	GCP #22	3541.939	-16.537	281355.817	3860480.64	-0.23	-0.983	1.009	0.492
23	GCP #23	2443.863	-153.416	278914.288	3859874.072	-0.038	-0.508	0.509	0.248
24	GCP #24	2097.102	-331.359	278183.952	3859365.072	-0.778	0.355	0.855	0.417
25	GCP #25	1114.613	-75.851	275874.188	3859707.589	-0.269	-2.519	2.533	1.235
26	GCP #26	1473.541	-714.621	276896.678	3858295.304	-0.47	-0.623	0.78	0.38
27	GCP #27	988.38	-924.503	275867.859	3857677.065	0.37	0.812	0.892	0.435
28	GCP #28	2842.334	-2856.021	280659.068	3853642.561	-0.124	0.899	0.908	0.443
29	GCP #29	1868.341	-3007.136	278525.3	3853030.195	0.875	-1.638	1.857	0.905
30	GCP #30	1232.029	-3365.692	277206.454	3852032.824	-1.113	-0.201	1.131	0.551
31	GCP #31	1840.565	-3534.87	278627.3	3851797.307	-0.16	-2.167	2.173	1.06
32	GCP #32	2906.134	-3671.223	281050.181	3851765.446	-1.156	-0.42	1.23	0.6
33	GCP #33	3906.052	-3105.613	283116.588	3853334.523	0.459	-1.59	1.655	0.807
34	GCP #34	4522.233	-3566.209	284628.3	3852430.642	1.178	-0.126	1.184	0.577
	Count	35	35	35	35	35	35	35	35
	Mean	4361.081	-1859.858	283743.82	3856368.447	0	0	1.742235	0.8495
	Min	988.38	-4005.039	275867.859	3851765.446	-2.968	-2.773	0.509	0.248
	Max	8361.573	-16.537	292338.42	3861224.608	1.449	5.405	5.533	2.698
	Stddev	2379.03	1338.217	5406.24727	3098.39833	0.971287	1.840905	1.09777	0.5353

CORONA 044

Control point error: (X) 1.3138, (Y) 1.1598, (Total) 1.7525

Row	Point ID	X input	Y input	X Ref.	Y Ref.	Xresidual	Yresidual	RMS erro	Contrib
1	GCP #1	6404.098	-2720.19	281696.325	3838217.188	-2.031	-0.56	2.106	1.202
2	GCP #2	7097.398	-3291.45	283431.438	3837073.805	1.73	0.022	1.73	0.987
3	GCP #3	7237.24	-2308.06	283440.868	3839400.648	1.305	1.343	1.872	1.068
4	GCP #4	9103.657	-2941.07	287795.154	3838403.43	-1.053	-0.308	1.097	0.626
5	GCP #5	8742.428	-3957.08	287289.139	3835958.979	1.335	0.324	1.373	0.784
6	GCP #6	9958.513	-4223.87	290060.702	3835647.523	0.14	-0.038	0.145	0.082
7	GCP #8	7520.086	-4077.25	284603.111	3835366.982	-0.936	0.213	0.96	0.548
8	GCP #9	6801.304	-3633.58	282875.497	3836200.637	1.554	-1.671	2.282	1.302
9	GCP #10	6538.26	-3992.88	282391.785	3835308.044	-1.354	1.143	1.772	1.011

10	GCP #11	5958.486	-3566.79	280967.861	3836135.524	-1.025	-0.99	1.425	0.813
11	GCP #12	5729.493	-4419.15	280727.157	3834111.503	0.798	-0.443	0.913	0.521
12	GCP #13	6325.827	-4929.61	282207.901	3833103.791	0.487	2.825	2.867	1.636
13	GCP #14	8121.19	-5427.35	286328.794	3832424.833	-0.321	0.764	0.828	0.473
14	GCP #15	9668.478	-5581.6	289787.233	3832455.481	-1.464	-1.174	1.877	1.071
15	GCP #16	8305.656	-6009.37	286906.38	3831140.001	2.137	-1.574	2.655	1.515
16	GCP #17	5449.614	-6847.42	280845.569	3828503.828	-0.1	0.492	0.502	0.287
17	GCP #18	4826.246	-5021.84	278900.222	3832487.561	-1.375	-1.583	2.096	1.196
18	GCP #19	5476.819	-5557.61	280511.477	3831438.765	-1.628	0.209	1.642	0.937
19	GCP #20	3767.157	-6030.05	276865.827	3829914.106	-0.338	1.936	1.965	1.121
20	GCP #21	2686.704	-6124.86	274498.906	3829407.245	2.971	-0.193	2.977	1.699
21	GCP #22	3530.942	-5006.25	276011.804	3832183.072	1.408	-1.146	1.815	1.036
22	GCP #23	6384.597	-6275.21	282738.207	3830041.997	-0.663	-0.983	1.186	0.677
23	GCP #24	10048.95	-6251.43	290809.207	3831026.456	0.197	1.188	1.204	0.687
24	GCP #25	1459.951	-7057.54	272066.132	3826960.237	-0.775	-1.179	1.411	0.805
25	GCP #26	1655.501	-5758.14	272059.104	3829973.644	-1.001	1.383	1.707	0.974
	Count	25	25	25	25	25	25	25	25
	Mean	6351.944	-4840.39	282232.632	3833315.411	0	0	1.61628	0.92232
	Minimum	1459.951	-7057.54	272059.104	3826960.237	-2.031	-1.671	0.145	0.082
	Maximum	10048.95	-2308.06	290809.207	3839400.648	2.971	2.825	2.977	1.699
	Stddev	2409.743	1328.782	5206.43378	3340.985011	1.34085	1.183747	0.691138	0.39437

CORONA 045

Control point error: (X) 1.5002, (Y) 1.3465, (Total) 2.0158

Row	Point ID	X input	Y input	X Ref.	Y Ref.	Xresidual	Yresidual	RMS erro	Contril
1	GCP #1	3361.65	-664.42	274065.003	3826203.044	-2.551	-2.816	3.8	1.885
2	GCP #2	5365.457	-1107.367	278767.385	3825708.877	-0.865	1.563	1.786	0.886
3	GCP #3	2619.249	-14.274	272129.952	3827550.297	1.998	1.649	2.59	1.285
4	GCP #4	3088.501	-1402.404	273725.493	3824401.979	-0.231	0.221	0.32	0.159
5	GCP #5	2745.929	-2080.411	273196.311	3822712.669	-2.06	-2.93	3.582	1.777
6	GCP #6	3189.209	-2454.474	274338.758	3821969.458	-0.314	1.457	1.49	0.739
7	GCP #7	2736.638	-2843.585	273455.662	3820940.686	-0.21	2.189	2.199	1.091
8	GCP #8	2626.185	-3352.019	273393.977	3819721.663	1.946	-0.456	1.999	0.992
9	GCP #9	3290.656	-3210.008	274839.508	3820235.313	0.708	0.719	1.009	0.5
10	GCP #10	4080.217	-2338.675	276310.942	3822476.972	0.378	-0.269	0.464	0.23
11	GCP #11	4732.343	-2538.274	277851.877	3822187.292	1.699	-0.442	1.755	0.871
12	GCP #12	4260.594	-3571.562	277139.237	3819654.04	-2.221	-1.103	2.48	1.23
13	GCP #13	8136.087	-3673.031	285820.959	3820475.916	-0.209	0.853	0.878	0.436
14	GCP #14	8493.835	-2742.495	286320.133	3822727.444	-3.096	-0.722	3.179	1.577
15	GCP #15	9672.645	-2470.763	288871.533	3823686.694	2.253	0.794	2.388	1.185
16	GCP #16	9336.401	-3319.193	288378.881	3821619.242	-0.183	-1.14	1.154	0.573
17	GCP #17	9930.693	-895.106	288945.22	3827438.424	0.148	1.661	1.667	0.827
18	GCP #18	9325.046	-479.946	287450.423	3828238.457	-1.449	-2.076	2.532	1.256
19	GCP #19	8303.277	-1100.463	285368.911	3826509.972	-0.041	-0.36	0.362	0.18
20	GCP #20	7478.845	-1602.577	283694.207	3825113.925	2.054	0.287	2.074	1.029
21	GCP #21	5610.718	-2740.556	279891.207	3821954.477	1.37	0.184	1.382	0.686
22	GCP #22	6384.719	-519.414	280860.682	3827360.527	0.931	0.157	0.944	0.468
23	GCP #23	6904.374	-1010.564	282199.506	3826346.349	-0.054	0.581	0.583	0.289
	Count	23	23	23	23	23	23	23	23
	Mean	5724.925	-2005.72	279870.2507	3823705.814	4.35E-05	4.35E-05	1.765957	0.8761
	Minimum	2619.249	-3673.03	272129.952	3819654.04	-3.096	-2.93	0.32	0.159
	Maximum	9930.693	-14.274	288945.22	3828238.457	2.253	2.189	3.8	1.885
	Stddev	2630.482	1118.059	5884.631	2769.759	1.533935	1.376841	0.993919	0.4930

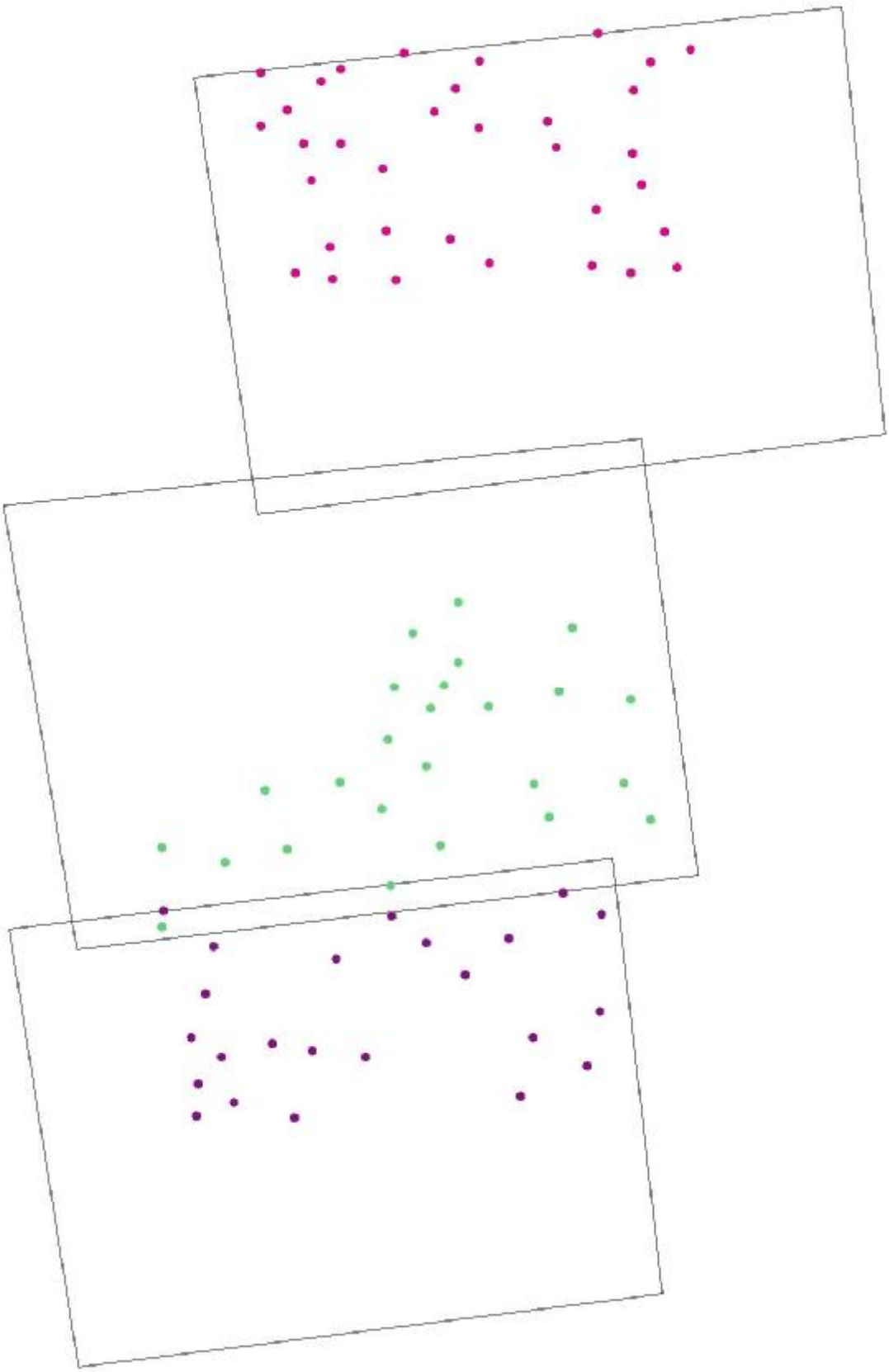

Figure 15-1 – Distribution of points in the area of interest and within the frames 043, 044 and 045 of the CORONA mission 1108. The top image footprint is 043, the bottom is 045 and the middle is 044.

15.1.2. Mission 1111 – Aft camera – D135001, 2

Orbit: Inclined 60.00, period 90.04, perigee 158, apogee 398

Remarks: Unusually low inclination to cover Middle East targets. Due to the unusual launch time (18:25), the satellite passed over the Middle East at about 18:30 local time. The overall image quality is good.

31 June 1970

RMSe after registration to Ikonos (before the GPS correction), in pixels.

All images were resampled with nearest neighbourhood method. Image 001 was rectified with 3rd polynomial, while image 002 with 2nd polynomial.

CORONA 002

Control point error: (X) 2.8527, (Y) 1.1200, (Total) 3.0647

GCP Tool

Row	Point ID	X input	Y input	X Ref.	Y Ref.	Xresidual	Yresidual	RMS erro	Contrit
1	GCP #1	5867.197	-397.164	282499	3824141.428	3.207	0.946	3.344	1.091
2	GCP #2	8693.076	-108.31	287604.494	3828364.203	-1.963	0.12	1.966	0.642
3	GCP #3	7558.173	-1071.33	286505.832	3824904.097	-4.634	-2.162	5.113	1.668
4	GCP #4	5942.937	-2057.895	284560.187	3820856.667	-0.898	1.726	1.946	0.635
5	GCP #5	3051.524	-748.754	277578.571	3819850.374	-0.606	-0.469	0.766	0.25
6	GCP #6	9215.791	-1163.158	289818.332	3826855.097	4.751	0.446	4.772	1.557
7	GCP #7	6850.493	-2831.903	287157.066	3820425.07	1.765	-0.962	2.01	0.656
8	GCP #8	9543.545	-2654.304	292073.562	3824179.286	-1.623	0.356	1.662	0.542
	Count	8	8	8	8	8	8	8	8
	Mean	7090.342	-1379.102	285974.631	3823697.028	-0.00012	0.000125	2.697375	0.88012
	Minimum	3051.524	-2831.903	277578.571	3819850.374	-4.634	-2.162	0.766	0.25
	Maximum	9543.545	-108.31	292073.562	3828364.203	4.751	1.726	5.113	1.668
	Stddev	2154.913	1022.276	4486.20526	3098.688864	3.049758	1.19724	1.555249	0.50734

CORONA 001

Control point error: (X) 1.1069, (Y) 1.4473, (Total) 1.822

GCP Tool

Row	Point ID	X input	Y input	X Ref.	Y Ref.	Xresidual	Yresidual	RMS erro	Contril
1	GCP #1	10379.518	-1857.136	281695.832	3838209.097	-2.69	-0.207	2.698	1.481
2	GCP #2	10797.938	-2673.714	283435.582	3837073.847	1.891	0.691	2.014	1.105
3	GCP #3	11684.293	-3613.728	286208.082	3836264.597	-0.098	-1.525	1.528	0.839
4	GCP #4	10748.705	-3948.507	284758.834	3834399.196	0.363	-1.166	1.221	0.67
5	GCP #5	9403.611	-3314.818	281452.082	3834001.347	0.083	1.834	1.836	1.008
6	GCP #6	8503.893	-4026.223	280523.332	3831437.097	-1.283	-0.75	1.486	0.816
7	GCP #7	9524.896	-4527.035	283037.082	3831703.097	0.644	0.78	1.011	0.555
8	GCP #8	11903.485	-4884.709	288035.832	3833935.597	-0.087	-2.501	2.503	1.374
9	GCP #9	13187.204	-2950.795	288425.332	3839562.847	-0.855	0.379	0.935	0.513
10	GCP #10	11875.699	-2361.729	285190.082	3839096.597	0.978	-0.105	0.984	0.54
11	GCP #11	13012.004	-4736.141	290043.082	3835643.347	0.444	2.13	2.176	1.194
12	GCP #12	10091.14	-5659.011	285368.147	3830126.853	-0.269	1.341	1.368	0.751
13	GCP #13	10684.484	-7036.295	288006.525	3828087.979	-0.425	0.289	0.514	0.282
14	GCP #14	11332.274	-6494.629	288676.082	3829962.847	0.319	-1.681	1.711	0.939
15	GCP #15	9463.684	-6402.238	284975.798	3827872.624	-0.846	1.259	1.517	0.833
16	GCP #16	8367.64	-7123.618	283675.405	3825121.993	-0.479	2.051	2.107	1.156
17	GCP #17	7699.322	-7203.716	282507.082	3824159.097	1.521	-1.58	2.193	1.204
18	GCP #18	8127.346	-4625.564	280475.046	3829773.972	-0.534	-0.799	0.962	0.528
19	GCP #19	6988.453	-3624.34	277192.082	3830363.847	-0.471	-2.272	2.32	1.274
20	GCP #20	7750.99	-3343.878	278325.082	3831879.347	1.861	1.509	2.396	1.315
21	GCP #21	6930.318	-2680.413	276013.082	3832186.347	1.669	0.047	1.67	0.916
22	GCP #22	4857.324	-4415.014	274066.582	3826201.097	-1.13	-0.129	1.137	0.624
23	GCP #23	4295.11	-3898.097	272426.207	3826533.996	-1.4	-0.329	1.438	0.789
24	GCP #24	6144.286	-5283.646	277455.582	3826055.347	-1.27	0.826	1.515	0.832
25	GCP #25	6344.124	-6815.744	279531.869	3823298.157	0.211	-0.711	0.741	0.407
26	GCP #26	3847.471	-4862.653	272693.806	3824114.063	2.023	-0.671	2.132	1.17
27	GCP #27	3509.078	-5688.653	272989.082	3822114.597	-0.184	3.409	3.414	1.874
28	GCP #28	3301.245	-6445.376	273460.332	3820400.847	0.015	-2.12	2.12	1.163
	Count	28	28	28	28	28	28	28	28
	Mean	8598.412	-4660.622	281451.534	3830342.131	0	0	1.701679	0.934
	Minimum	3301.245	-7203.716	272426.207	3820400.847	-2.69	-2.501	0.514	0.282
	Maximum	13187.204	-1857.136	290043.082	3839562.847	2.023	3.409	3.414	1.874
	Stddev	2905.9547	1565.4249	5360.90064	5325.519335	1.127164	1.473726	0.663204	0.3640

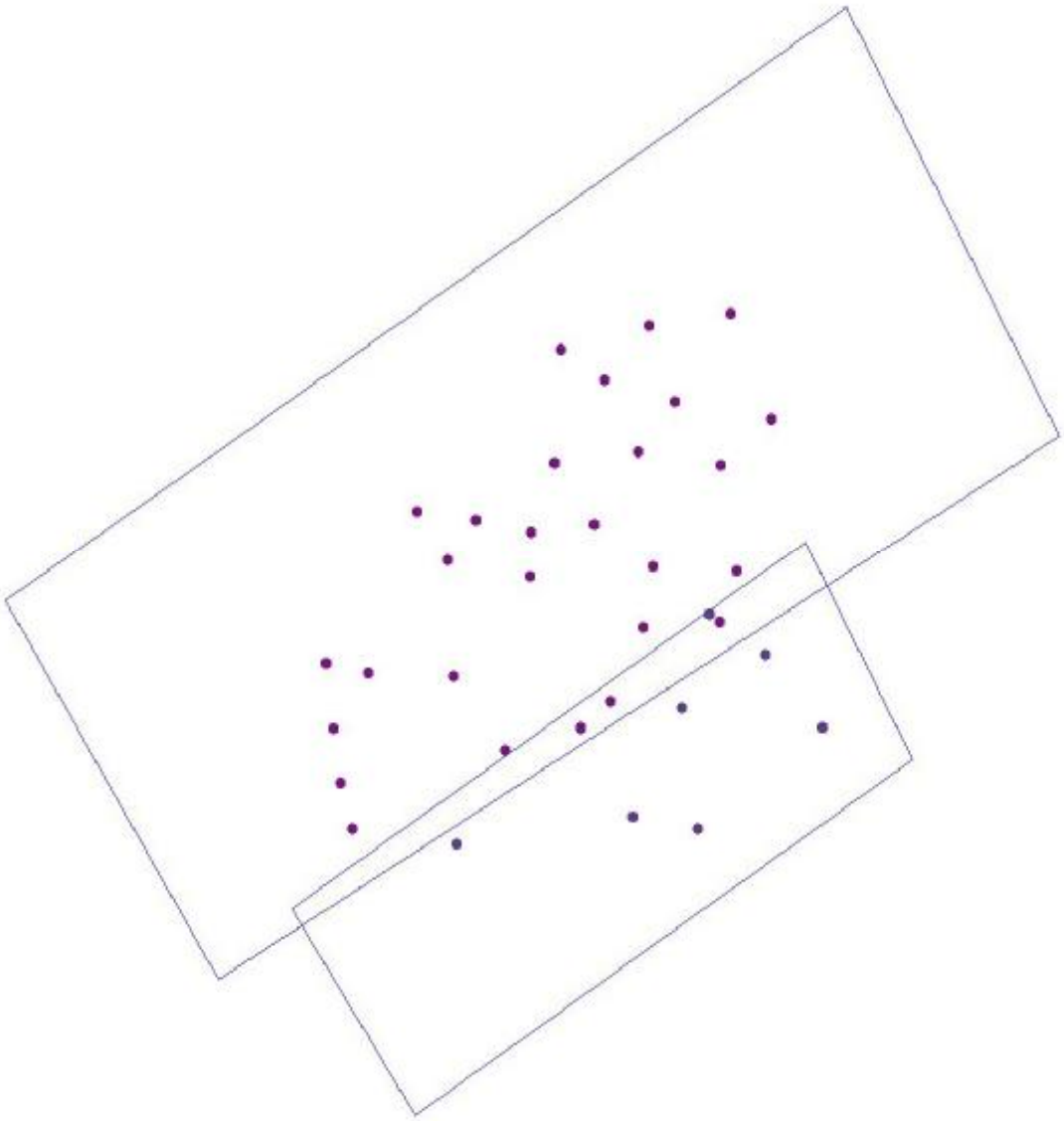

Figure 15-2 – Distribution of registration points in the frames 001 and 002 of the CORONA mission 1111. The top image footprint is from frame 001 and the bottom is from frame 002.

15.1.3. Mission 1110 – Forward camera – 007, 8,9

Remarks: The overall image quality is less than that provided by recent missions and 2,000 feet of S0-349 (new film) was spliced into the regular film.

Orbit: Inclined 83.00, period 88.62, perigee 162, apogee 247

28 May 1970

15.1.4. Mission 1110 – Aft camera – D106013, 14,15

Remarks: The overall image quality is less than that provided by recent missions and 2,000 feet of S0-349 (new film) was spliced into the regular film.

Orbit: Inclined 83.00, period 88.62, perigee 162, apogee 247

28 May 1970

From mission 1110, only the frames 007, 8 and 9 were registered and geocorrected. The frames 013, 14 and 15 were only used into the stereoscopy part of the research. However, all frames were orthorectified through the stereopairs procedure.

All images (007, 008, and 009) were resampled with nearest neighbourhood method. Images 007 and 009 were rectified with 3rd polynomial, while image 008 was rectified with 2nd polynomial method.

CORONA 007

Control point error: (X) 0.6115, (Y) 0.9516, (Total) 1.1311

GCP Tool

Row	Point ID	X input	Y input	X Ref.	Y Ref.	X residual	Y residual	RMS erro	Contri
1	GCP #1	8241.702	-3900.777	290576.76	3861913.758	-0.19	-0.454	0.492	0.435
2	GCP #2	8123.849	-6146.446	290386.784	3856457.658	-0.269	0.424	0.502	0.444
3	GCP #3	7321.676	-5231.129	288430.504	3858495.937	-0.151	1.212	1.221	1.079
4	GCP #4	8949.045	-4715.994	292297.501	3860107.019	0.201	-0.311	0.371	0.328
5	GCP #5	6872.909	-6328.69	287378.371	3855715.489	-0.001	-1.353	1.353	1.196
6	GCP #6	8365.184	-7218.172	291003.559	3853898.953	0.181	0.019	0.182	0.161
7	GCP #7	6601.359	-5440.353	286700.7	3857812.606	-0.346	-1.234	1.282	1.133
8	GCP #8	5302.41	-4310.791	283535.547	3860246.208	0.866	-1.541	1.767	1.562
9	GCP #9	5159.458	-4956.37	283197.906	3858647.517	0.712	0.14	0.726	0.641
10	GCP #10	3783.944	-6905.98	279822.894	3853519.339	0.091	0.569	0.577	0.51
11	GCP #11	4467.354	-6427.005	281512.345	3854877.833	0.191	0.148	0.242	0.214
12	GCP #12	2963.853	-5977.761	277799.857	3855596.585	0.411	-1.547	1.6	1.415
13	GCP #13	5276.494	-6181.506	283493.922	3855686.922	-0.32	0.821	0.881	0.779
14	GCP #14	2130.232	-5299.191	275733.373	3857075.173	0.151	0.348	0.38	0.336
15	GCP #15	3352.203	-5424.021	278763.676	3857067.011	-0.772	1.485	1.673	1.479
16	GCP #16	3154.996	-4904.925	278278.155	3858288.985	-0.969	-1.384	1.69	1.494
17	GCP #17	3646.075	-3968.576	279492.533	3860702.121	1.592	0.823	1.792	1.584
18	GCP #18	4148.149	-4107.837	280718.301	3860477.856	-0.412	1.238	1.304	1.153
19	GCP #19	4718.022	-3831.147	282104.81	3861276.119	-0.352	-0.816	0.889	0.786
20	GCP #20	4908.59	-3453.675	282559.301	3862234.926	-1.117	-0.35	1.17	1.035
21	GCP #21	7440.949	-4521.956	288692.115	3860238.072	-0.284	0.794	0.843	0.745
22	GCP #22	6762.966	-4100.507	287054.835	3861100.072	0.785	0.97	1.248	1.103
	Count	22	22	22	22	22	22	22	22
	Mean	5531.428	-5152.4	284069.716	3858247.098	0	0	1.008409	0.8914
	Minimum	2130.232	-7218.172	275733.373	3853519.339	-1.117	-1.547	0.182	0.161
	Maximum	8949.045	-3453.675	292297.501	3862234.926	1.592	1.485	1.792	1.584
	Stddev	2007.191	1079.163	4879.32569	2655.312952	0.62593	0.974042	0.524348	0.4635

CORONA 008

Control point error: (X) 1.5145, (Y) 1.888, (Total) 2.4208
GCP Tool

Row	Point ID	X input	Y input	X Ref.	Y Ref.	X residual	Y residual	RMS erro	Contri
1	GCP #1	5056.219	-6754.971	281696.889	3838209.221	0.925	2.034	2.235	0.923
2	GCP #2	7531.431	-6945.555	287773.332	3838391.509	3.23	-1.416	3.527	1.457
3	GCP #3	7132.356	-5822.626	286761.704	3841057.07	-1.844	4.594	4.95	2.045
4	GCP #4	5398.079	-5671.912	282531.747	3840969.824	1.346	-3.158	3.432	1.418
5	GCP #5	6366.047	-7142.97	284917.282	3837586.409	-3.481	-1.458	3.774	1.559
6	GCP #6	9321.68	-1346.126	291850.786	3852244.473	0.047	-1.165	1.166	0.482
7	GCP #7	9126.15	-742.881	291365.907	3853617.249	-0.337	0.572	0.663	0.274
8	GCP #8	8768.815	-16.456	290500.077	3855239.198	0.431	1.13	1.209	0.499
9	GCP #9	8564.48	-1363.193	290062.446	3852050.315	-0.766	-1.352	1.554	0.642
10	GCP #10	4301.194	-393.756	279818.571	3853513.75	-1.261	1.112	1.682	0.695
11	GCP #11	5056.432	-159.224	281652.961	3854205.765	0.66	-0.973	1.175	0.486
12	GCP #12	5772.939	-557.283	283382.999	3853398.414	-0.01	-1.524	1.524	0.63
13	GCP #13	5329.694	-1172.662	282321.301	3851859.072	0.632	0.837	1.049	0.433
14	GCP #14	7485.67	-359.329	287476.485	3854196.072	0.429	0.767	0.879	0.363
	Count	14	14	14	14	14	14	14	14
	Mean	6800.799	-2746.353	285865.178	3848324.167	0	0	2.0585	0.8504
	Minimum	4301.194	-7142.97	279818.571	3837586.409	-3.481	-3.158	0.663	0.274
	Maximum	9321.68	-16.456	291850.786	3855239.198	3.23	4.594	4.95	2.045
	Stddev	1700.005	2929.811	4063.30103	7138.742909	1.571758	1.959782	1.321896	0.5460

CORONA 009

Control point error: (X) 0.7488, (Y) 1.5748, (Total) 1.7438

GCP Tool

Row	Point ID	X input	Y input	X Ref.	Y Ref.	X residual	Y residual	RMS erro	Contrib
1	GCP #1	7098.601	-345.805	281690.088	3838209.889	0.217	-1.248	1.267	0.
2	GCP #2	7542.536	-1299.657	282768.6	3836038.915	-1.902	1.394	2.358	1.
3	GCP #3	8387.744	-1107.742	284815.726	3836673.195	1.079	1.686	2.002	1.
4	GCP #4	10015.168	-2651.658	288751.523	3833330.266	0.586	0.982	1.144	0.
5	GCP #5	8358.314	-2055.195	284753.874	3834410.856	-0.882	2.756	2.893	1.
6	GCP #6	4086.866	-3894.428	274198.436	3828963.945	-0.132	0.243	0.277	0.
7	GCP #7	5273.727	-3438.386	277189.661	3830363.16	0.513	-0.59	0.781	0.
8	GCP #8	6241.419	-3288.647	279591.006	3830951.956	0.031	-1.711	1.711	0.
9	GCP #9	8347.44	-3637.698	284749.188	3830589.846	0.286	-2.08	2.099	1.
10	GCP #10	6700.594	-2026.014	280726.207	3834115.972	0.491	0.555	0.741	0.
11	GCP #11	7692.272	-2836.107	283151.776	3832383.902	1.377	0.042	1.377	0
12	GCP #12	9413.147	-1496.218	287280.218	3835959.751	-0.791	1.774	1.942	1.
13	GCP #13	9906.496	-503.09	288433.232	3838396.101	-0.228	-1.71	1.725	0.
14	GCP #14	10571.008	-1725.773	290049.312	3835643.657	-0.064	0.924	0.926	0.
15	GCP #15	10863.811	-3692.349	290805.583	3831014.411	0.176	0.422	0.457	0.
16	GCP #16	9428.705	-3701.984	287366.863	3830672.999	0.658	-3.779	3.836	
17	GCP #17	8651.677	-372.984	285435.579	3838458.771	0.451	-1.534	1.599	0.
18	GCP #18	9688.909	-4798.77	288010.142	3828082.673	-1.141	-1.475	1.864	1.
19	GCP #19	6760.96	-4809.048	280861.771	3827364.362	-0.784	0.727	1.069	0.
20	GCP #20	7509.495	-3844.97	282706.2	3829897.071	-0.221	-0.689	0.724	0.
21	GCP #21	7899.674	-5835.414	283669.053	3825121.907	0.648	0.699	0.953	0.
22	GCP #22	4869.412	-4881.195	276142.728	3826718.998	-0.536	1.711	1.793	1.
23	GCP #23	5193.749	-6218.507	276929.014	3823462.701	0.895	-2.048	2.235	1.
24	GCP #24	6227.641	-5961.957	279524.727	3824381.085	-0.855	1.105	1.397	0.
25	GCP #25	9058.3	-6042.93	286502.681	3824902.385	0.128	1.842	1.847	1.
	Count	25	25	25	25	25	25	25	
	Mean	7831.5066	-3218.661	283444.128	3831444.351	0	0	1.56068	0.
	Minimum	4086.866	-6218.507	274198.436	3823462.701	-1.902	-3.779	0.277	0.
	Maximum	10863.811	-345.805	290805.583	3838458.771	1.377	2.756	3.836	
	Stddev	1847.0427	1836.867	4515.19359	4601.917882	0.764333	1.607461	0.794029	0.455

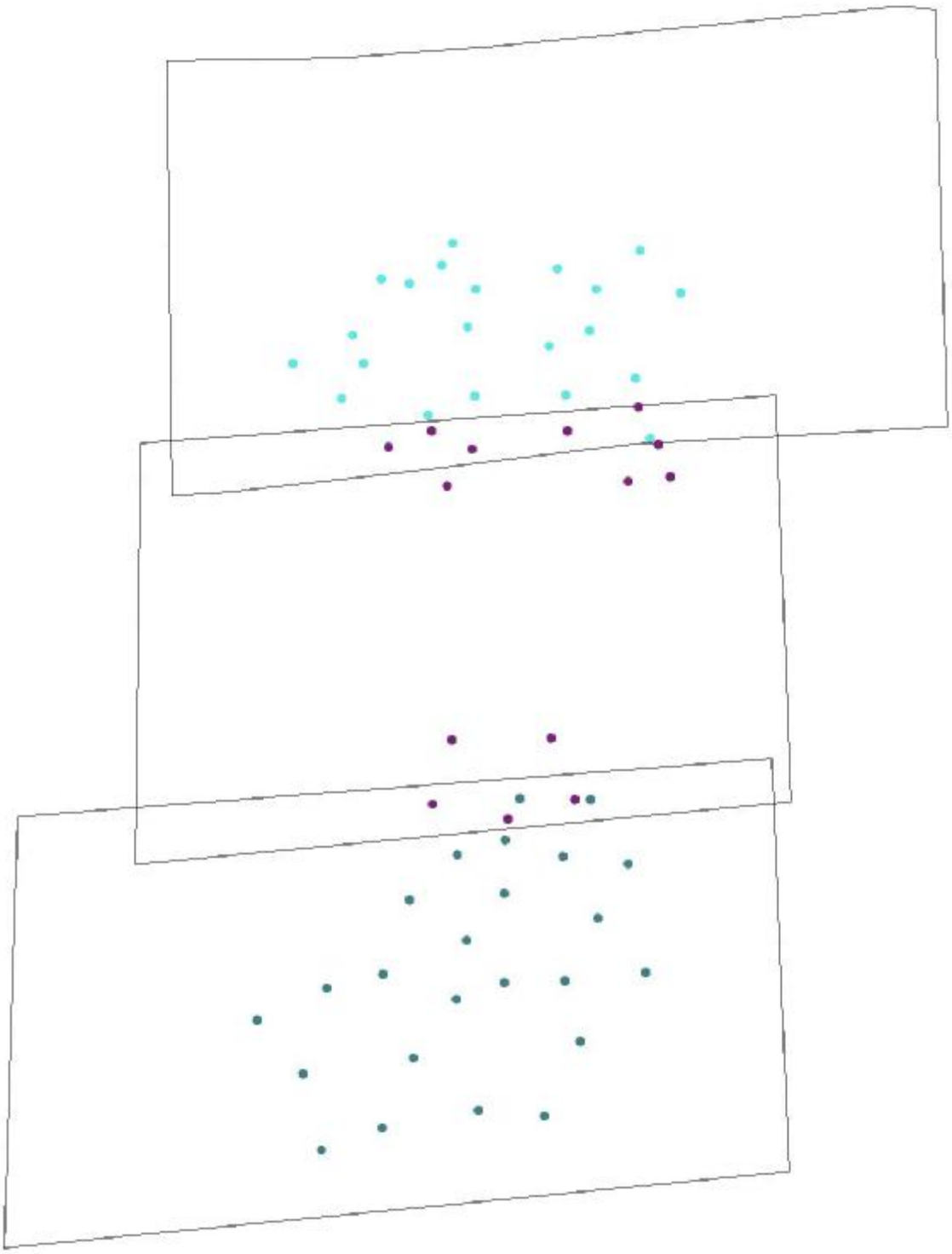

Figure 15-3 – Distribution of points in the area of interest and within the frames 007, 008 and 009 of the CORONA mission 1110. The top image footprint is 007, the bottom is 009 and the middle is 008.

15.1.5. Mission 1110. 007-013 stereopair

007-013 stereopair control point error (in pixels): (Total) 1.2860, (X) 2.7573 (12), (Y) 2.7965 (12), (Z) 1.9954 (12), (x) 1.1988 (26), (y) 1.1719 (26)

The triangulation report with OrthoBASE:[58]

The input image coordinates						
Image ID = 1				Image ID = 2		
Point ID	X	Y		Point ID	X	Y
2	8241.702	3900.777		2	6490.538	4333.221
3	7321.676	5231.129		3	5362.226	5696.577
4	8949.045	4715.994		4	7089.875	5159.618
5	6872.909	6328.69		5	4736.938	6837.864
6	6601.359	5440.353		6	4597.708	5920.643
7	5159.458	4956.37		7	3206.592	5426.86
8	4467.354	6427.005		8	2252.193	6951.899
10	5276.494	6181.506		10	3124.303	6691.958
11	2130.232	5299.191		11	65.379	5794.853
14	3646.075	3968.576		14	1839.594	4431.7
15	4148.149	4107.837		15	2322.177	4572.437
16	4718.022	3831.147		16	2941.652	4288.271
18	7440.949	4521.956		18	5590.284	4970.809
19	6461.905	1706.161		19	5021.567	2162.982
20	6129.885	3069.731		20	4485.149	3515.369
21	5440.306	2893.936		21	3819.531	3344.638
22	6128.559	4174.584		22	4312.112	4626.656
23	8001.602	2568.55		23	6436.743	3003.23
24	3591.476	2782.82		24	1985.026	3242.537
25	9322.074	5820.265		25	7319.954	6293.696
29	8378.729	493.145		29	7089.505	969.828
31	6964.493	2101.472		31	5463.914	2547.879
32	7492.637	1351.927		32	6097.129	1812.734
34	10855.59	3205.064		34	9210.83	3623.9
36	2083.916	1126.137		36	766.476	1610.134
38	8635.97	2868.221		38	7026.521	3295.917
45	6871.349	1086.148		45	5516.963	1553.466

Affine coefficients from file (pixels) to film (millimeters)

Image ID	A0	A1	A2	B0	B1	B2
1	-51.8400	0.007500	-0.000000	27.5062	0.000000	-0.007500
2	-36.0000	0.007500	-0.000000	26.8687	0.000000	-0.007500

THE OUTPUT OF SELF-CALIBRATING BUNDLE BLOCK ADJUSTMENT

the no. of iteration =1 the standard error = 1.2863
the maximal correction of the object points = 2.47839

the no. of iteration =2 the standard error = 1.2860
the maximal correction of the object points = 0.22511

the no. of iteration =3 the standard error = 1.2860
the maximal correction of the object points = 0.00077

The exterior orientation parameters

Image ID	Xs	Ys	Zs	Omega	Phi	Kappa
1	336175.2473	3916076.5099	172713.5573	-17.3739	15.1190	5.2476

[58] The output image x,y units = pixels. The output angle units = degrees. The output ground X,Y,Z units = meters.

2	3418033368	3821904.9134	174221.9556	13.4054	17.2591	4.9938

The interior orientation parameters of photos[59]

Image ID	f (mm)	Xo (mm)	Yo (mm)
1	609.6020	0.0000	0.0000
2	609.6020	0.0000	0.0000

The residuals of the control points

Point ID	rX	rY	rZ
2	5.1756	-1.7825	3.1837
3	-2.6931	2.6039	1.2767
5	-0.841	1.9732	2.6463
6	-3.8519	0.3223	-0.3233
7	-1.02	4.8871	1.0179
8	3.4582	-2.638	1.8109
10	3.7035	-4.0962	-0.3794
11	1.8707	3.6867	3.0079
14	-2.2373	-1.5099	-0.7997
16	-1.094	1.3069	-2.1675
18	0.4425	-0.7206	-1.7629
15	-2.2443	-3.764	
4			-2.6373
	aX = 0.0557	aY = 0.0224	aZ = 0.4061
	mX = 2.7573	mY = 2.7965	mZ = 1.9954

The coordinates of object points (total object points = 27):

Point ID	X	Y	Z	Overlap
2	290576.7601	3861913.758	443.55	2
3	288430.5044	3858495.937	444.5	2
5	287378.3706	3855715.489	445.1	2
6	286700.7003	3857812.606	425	2
7	283197.9064	3858647.517	428.65	2
8	281512.3454	3854877.833	445	2
10	283493.9219	3855686.922	445	2
11	275733.3732	3857075.173	419	2
14	279492.5326	3860702.121	400	2
16	282104.81	3861276.119	400	2
18	288692.1152	3860238.072	437.5	2
15	280718.3005	3860477.856	392.9852	2
4	292285.4233	3860118.086	452	2
19	286272.1414	3866742.472	384.0522	2
20	285508.6584	3863426.091	399.0833	2
21	283843.0949	3863695.603	387.7686	2
22	285527.8042	3860771.018	416.6205	2
23	289961.3432	3865024.303	417.9328	2
24	279355.0097	3863561.191	380.1799	2
25	293221.416	3857551.347	461.836	2
29	290762.4518	3869971.394	389.8315	2
31	287480.7179	3865911.551	399.0128	2
32	288707.1852	3867784.169	377.4993	2
34	296673.8624	3864122.112	435.7874	2
36	275683.1185	3867237.649	383.204	2
38	291467.5873	3864450.656	433.4887	2
45	287229.4252	3868289.439	383.9102	2

[59] This table is the same for all CORONA-CORONA stereopairs

The residuals of image points:

Point	Image	Vx	Vy		Point	Image	Vx	Vy
2	1	-0.806	-1.371		20	1	0.162	-0.008
2	2	-2.704	-0.702		20	2	-0.161	-0.017
3	1	0.65	1.047		21	1	-0.266	0.013
3	2	1.698	1.404		21	2	0.265	0.029
4	1	-0.56	0.34		22	1	-0.716	0.034
4	2	-0.014	-0.251		22	2	0.708	0.075
5	1	0.027	0.522		23	1	1.537	-0.063
5	2	1.141	1.195		23	2	-1.537	-0.153
6	1	1.674	0.324		24	1	0.295	-0.016
6	2	1.426	0.247		24	2	-0.295	-0.033
7	1	0.388	1.923		25	1	0.629	-0.023
7	2	0.361	2.217		25	2	-0.616	-0.059
8	1	-2.122	-1.395		29	1	-0.973	0.039
8	2	-0.074	-0.986		29	2	0.986	0.096
10	1	-2.06	-1.741		31	1	-0.24	0.011
10	2	-0.802	-1.873		31	2	0.241	0.025
11	1	0.769	0.975		32	1	0.244	-0.01
11	2	-1.667	1.636		32	2	-0.246	-0.025
14	1	1.62	-0.484		34	1	0.891	-0.028
14	2	0.1	-0.722		34	2	-0.889	-0.08
15	1	1.226	-1.475		36	1	0.038	-0.002
15	2	0.869	-1.521		36	2	-0.038	-0.004
16	1	-0.636	0.881		38	1	-0.479	0.019
16	2	0.884	0.441		38	2	0.479	0.047
18	1	0.003	-0.115		45	1	-0.91	0.041
18	2	-0.722	-0.547		45	2	0.919	0.094
19	1	-0.032	0.001					
19	2	0.032	0.003					

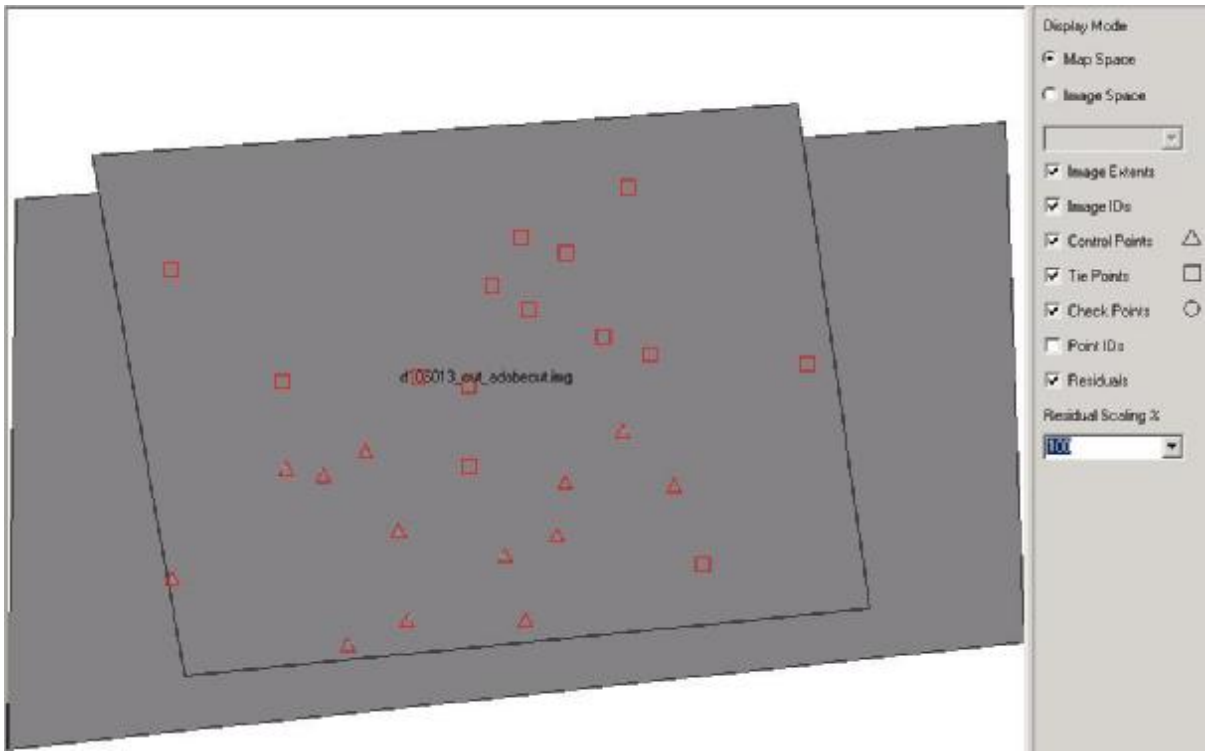

Figure 15-4 – Distribution of GCPs and tie points within the stereopair 007-013.

15.1.6. Mission 1110. 008-014 stereopair.

008-014 stereopair control point error (in pixels): (Total) 2.2204 (X) 4.7820 (15), (Y) 5.4893 (15), (Z) 6.1165 (15), (x) 2.2562 (30), (y) 2.3988 (30)
The triangulation report with OrthoBASE:[60]

The input image coordinates						
Image ID = 1				Image ID = 2		
Point ID	x	y		Point ID	x	y
1	7132.356	5822.626		1	5639.875	6462.625
2	5398.079	5671.912		2	3891.597	6315.155
3	9321.68	1346.126		3	8514.531	1946.859
4	9126.15	742.881		4	8402.69	1361.191
5	8768.815	16.456		5	8149.05	660.686
8	5056.432	159.224		8	4469.937	808.22
9	5772.939	557.283		9	5113.467	1187.9
10	5329.694	1172.662		10	4575.982	1784.404
11	7485.67	359.329		11	6835.44	998.533
12	4381.039	5167.637		12	2945.536	5787.612
13	5815.38	3996.205		13	4600.284	4593.656
14	3562.827	4040.983		14	2316.208	4637.842
15	4913.58	3526.225		15	3771.331	4120.875
16	4157.672	2431.382		16	3200.356	3032.174
17	5816.745	2363.537		17	4868.995	2961.527
18	7474.561	2862.326		18	6452.226	3448.147
19	8093.965	4018.84		19	6898.805	4609.958
20	8284.937	5045.945		20	6938.975	5655.631
21	9646.872	2888.711		21	8625.693	3467.208
22	9792.614	5492.594		22	8407.269	6106.287
23	2759.93	1848.414		23	1906.022	2448.315
24	3161.977	527.312		24	2538.697	1167.063
25	5327.378	2006.092		25	4439.764	2608.919
27	8052.126	1972.713		27	7163.676	2568.406
28	9025.616	2259.533		28	8093.442	2846.667
30	10873.24	5653.811		30	9486.417	6266.548
29	2563.932	3071.516		29	1488.422	3655.504
31	2509.907	5006.368		31	1069.567	5623.411
32	8218.348	6421.7		32	6658.204	7078.315
26	2474.45	5048.12		26	1027.375	5666.625
33	4679.07	4847.2		33	3305.625	5462.625
35	3282.98	2000.97		35	2401.125	2601.125
36	9289.03	5857.8		36	7839.625	6486.875
37	6216.05	2595.6		37	5229.875	3188.875
38	10240.71	3420.82		38	9148.125	3995.625
39	3140.29	5934.44		39	1537.875	6587.125
40	8401.25	6332.16		40	6858.375	6980.375
41	2472.02	1676.81		41	1649.375	2277.375

Affine coefficients from file (pixels) to film (millimeters)

Image ID	A0	A1	A2	B0	B1	B2
1	-42.4088	0.007500	0.000000	27.1313	0.000000	-0.007500
2	-42.2550	0.007500	0.000000	27.2587	0.000000	-0.007500

[60] The output image x,y units = pixels. The output angle units = degrees. The output ground X,Y,Z units = meters.

THE OUTPUT OF SELF-CALIBRATING BUNDLE BLOCK ADJUSTMENT

the no. of iteration =1 the standard error = 2.2204
the maximal correction of the object points = 0.37289

the no. of iteration =2 the standard error = 2.2204
the maximal correction of the object points = 0.00132

the no. of iteration =3 the standard error = 2.2204
the maximal correction of the object points = 0.00000

The exterior orientation parameters

Image ID	Xs	Ys	Zs	Omega	Phi	Kappa
1	338001.4370	3899871.1905	172856.9394	-17.3393	16.9004	5.3946
2	343780.5569	3806676.2484	174219.3816	13.2754	18.0431	5.1947

The residuals of the control points

Point ID	rX	rY	rZ
1	3.0785	-11.823	-0.6392
2	-11.9497	5.1267	-4.2987
3	2.2467	5.7237	9.8572
4	0.6516	3.4485	2.2755
5	-2.4507	5.7399	6.5893
8	-5.8109	-7.7863	-7.1953
9	2.3305	2.291	-10.8097
10	3.7852	-4.0106	-1.9287
11	-4.4816	-1.6479	-3.1846
26	7.7938	1.5632	10.2042
37	1.3669	-3.6906	-4.3533
38	-0.2854	-5.2356	1.3136
39	-2.4612	8.7265	7.5924
40	6.0747	2.0053	-5.6208
41	0	0	0
	aX = -0.0074	aY = 0.0287	aZ = -0.0132
	mX = 4.782	mY = 5.4893	mZ = 6.1165

The coordinates of object points (total objects points = 38)

Point ID	X	Y	Z	Overlap
1	286761.7038	3841057.07	498	2
2	282531.7466	3840969.824	486.7	2
3	291850.7863	3852244.473	480	2
4	291365.9067	3853617.249	477	2
5	290500.0768	3855239.198	465.2	2
8	281652.9608	3854205.765	452	2
9	283382.9988	3853398.414	477.5	2
10	282321.3005	3851859.072	485	2
11	287476.4845	3854196.072	450	2
26	275272.657	3841801.682	530.214	2
37	284479.93	3848641.74	480.23	2
38	294108.051	3847566.236	520.27	2
39	276929.099	3839752.427	510.274	2
40	289848.281	3840130.367	540.22	2
41	275328.312	3850057.592	512.6314	2
12	280025.8414	3841977.137	524.4056	2
13	283532.1163	3845174.608	492.0156	2
14	278003.9582	3844546.448	522.7864	2
15	281327.8836	3846107.353	490.9433	2
16	279466.8712	3848582.463	464.0678	2
17	283510.4994	3849105.161	464.2251	2
18	287523.1293	3848279.018	494.9115	2
19	289036.208	3845646.58	496.4539	2
20	289529.633	3843218.294	504.3916	2
21	292685.1976	3848688.596	507.415	2
22	293147.3019	3842508.72	525.2657	2

23	276036.7997	3849701.098	503.0091	2
24	277027.8674	3852948.912	444.0889	2
25	282321.0279	3849857.09	461.3401	2
27	288872.8305	3850511.845	474.241	2
28	291192.5421	3850040.423	490.4081	2
30	295711.8756	3842385.444	538.2132	2
29	275546.1866	3846696.506	550.816	2
31	275368.1681	3841915.475	540.8504	2
32	289414.1283	3839862.167	518.6609	2
33	280755.9066	3842830.622	501.1601	2
35	277324.4485	3849440.709	489.8004	2
36	291962.4136	3841502.244	520.7952	2

The residuals of image points

Point	Image	Vx	Vy		Point	Image	Vx	Vy
1	1	-2.61	-4.817		22	1	0.677	-0.027
1	2	0.749	-5.071		22	2	-0.666	-0.066
2	1	2.679	3.205		23	1	0.53	-0.033
2	2	5.528	2.415		23	2	-0.531	-0.064
3	1	1.276	1.246		24	1	0.194	-0.012
3	2	-1.396	3.375		24	2	-0.196	-0.023
4	1	0.43	1.193		25	1	-0.016	0.001
4	2	-0.724	1.641		25	2	0.016	0.002
5	1	1.265	1.898		26	1	-0.093	-1.018
5	2	1.885	3.33		26	2	-3.275	1.17
8	1	0.139	-2.296		27	1	1.045	-0.047
8	2	3.29	-3.725		27	2	-1.05	-0.109
9	1	-3.966	2.081		28	1	1.41	-0.059
9	2	-0.836	-0.277		28	2	-1.415	-0.142
10	1	-3.35	-1.531		29	1	1.168	-0.073
10	2	0.053	-1.83		29	2	-1.16	-0.141
11	1	0.606	-0.179		30	1	1.35	-0.049
11	2	2.488	-0.829		30	2	-1.326	-0.126
12	1	-0.229	0.013		31	1	0.583	-0.037
12	2	0.224	0.026		31	2	-0.572	-0.07
13	1	-0.9	0.047		32	1	-0.923	0.042
13	2	0.891	0.099		32	2	0.901	0.093
14	1	-0.204	0.012		33	1	0.12	-0.007
14	2	0.202	0.024		33	2	-0.118	-0.014
15	1	0.252	-0.014		35	1	0.664	-0.04
15	2	-0.25	-0.029		35	2	-0.664	-0.079
16	1	0.833	-0.048		36	1	-0.175	0.007
16	2	-0.832	-0.097		36	2	0.171	0.017
17	1	-0.659	0.034		37	1	-2.543	-1.028
17	2	0.659	0.073		37	2	0.587	-1.916
18	1	0.118	-0.006		38	1	1.311	-2.387
18	2	-0.117	-0.012		38	2	-0.393	-2.156
19	1	-0.41	0.018		39	1	2.519	2.628
19	2	0.407	0.042		39	2	0.975	4.427
20	1	0.441	-0.02		40	1	-4.822	1.362
20	2	-0.435	-0.045		40	2	-1.75	0.218
21	1	1.069	-0.043		41	1	0.208	-0.013
21	2	-1.069	-0.105		41	2	-0.209	-0.025

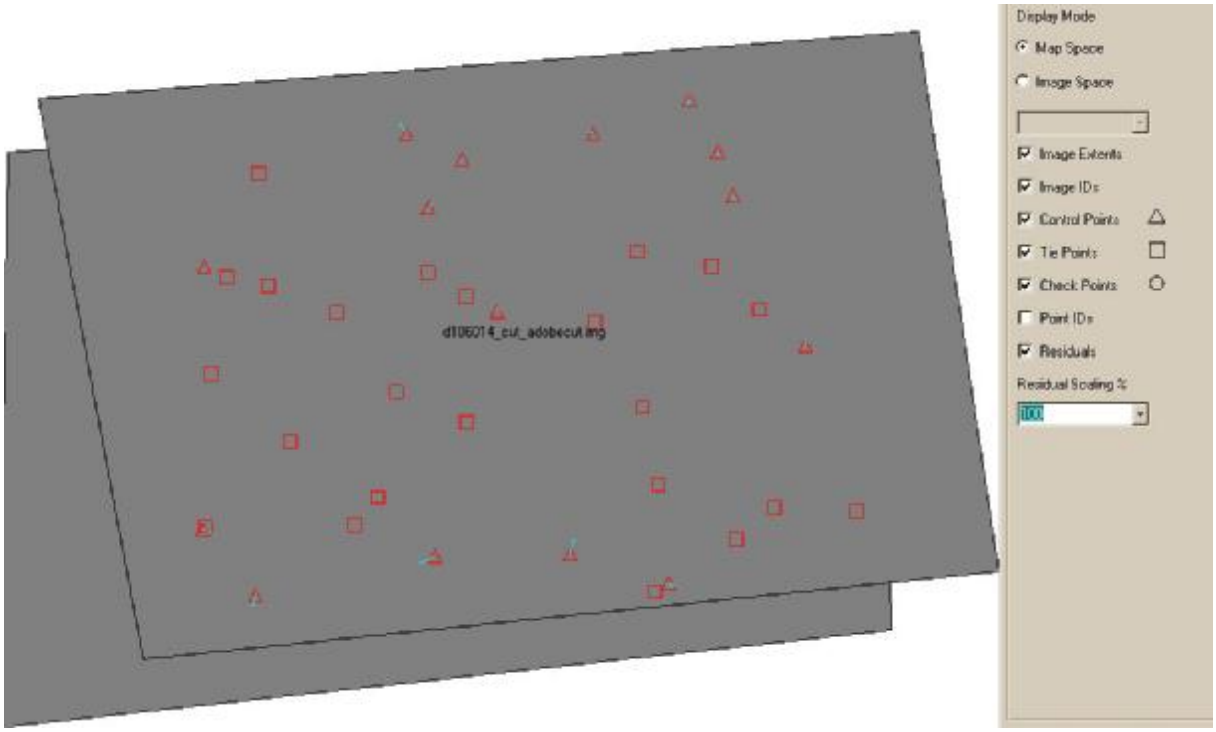

Figure 15-5 – Distribution of GCPs and tie points within the stereopair 008-014.

15.1.7. Mission 1110. 009-015 stereopair.

009-015 stereopair control point error (in pixels): (Total) 0.8045, (X) 5.3475 (17), (Y) 6.5942 (17), (Z) 1.0211 (17), (x) 0.5233 (34), (y) 0.5226 (34).

The triangulation report with OrthoBASE:[61]

The input image coordinates						
Image ID = 1				Image ID = 2		
Point ID	x	y		Point ID	x	y
2	7542.812	1299.786		2	6810.286	1916.452
3	8388.198	1108.796		3	7677.09	1721.195
5	8358.555	2054.743		5	7503.278	2646.313
6	5274.565	3437.454		6	4183.537	4059.761
7	4087.347	3894.48		7	2904.022	4537.557
8	6700.802	2026.226		8	5854.694	2639.541
9	7691.777	2836.34		9	6713.598	3431.479
10	9412.567	1495.655		10	8639.454	2086.502
11	9905.615	503.18		11	9269.618	1116.614
14	9429.077	3701.989		14	8324.56	4275.334
15	8651.982	372.601		15	8050.298	1004.501
16	6761.033	4809.161		16	5446.122	5434.459
17	7508.754	3845.001		17	6363.93	4445.473
18	7900.466	5835.441		18	6434.687	6473.281
19	4868.688	4881.214		19	3510.097	5530.937
20	5194.355	6219.181		20	3596.398	6911.219
21	6228.291	5962.406		21	4700.624	6631.41
24	3230.224	3378.889		24	2138.608	4021.691
26	2618.983	5925.631		26	1018.97	6631.141
27	2998.65	4282.885		27	1729.533	4938.311
29	2095.798	3274.252		29	1018.97	3925.652
33	11291.86	4786.058		33	10051.45	5348.602

Affine coefficients from file (pixels) to film (millimeters)

Image ID	A0	A1	A2	B0	B1	B2
1	-50.3287	0.007500	-0.000000	27.3937	0.000000	-0.007500
2	-38.4637	0.007500	0.000000	27.6188	0.000000	-0.007500

THE OUTPUT OF SELF-CALIBRATING BUNDLE BLOCK ADJUSTMENT

the no. of iteration =1 the standard error = 0.8046
the maximal correction of the object points = 16.49830

the no. of iteration =2 the standard error = 0.8045
the maximal correction of the object points = 3.86896

the no. of iteration =3 the standard error = 0.8045
the maximal correction of the object points = 0.02593

the no. of iteration =4 the standard error = 0.8045
the maximal correction of the object points = 0.00045

The exterior orientation parameters

Image ID	Xs	Ys	Zs	Omega	Phi	Kappa
1	337493.2557	3885041.3592	173431.6899	-17.6040	17.3734	5.2799
2	344303.4038	3789304.7666	174085.4260	13.6560	19.9809	4.7391

[61] The output image x,y units = pixels. The output angle units = degrees. The output ground X,Y,Z units = meters.

The residuals of the control points

Point ID	rX	rY	rZ
2	2.1839	1.3914	0.9366
3	-4.4935	-9.1258	0.7502
5	2.2155	-4.9415	0.9414
6	-6.5682	15.1793	0.5303
7	-3.8391	7.4848	-1.8347
8	-6.3851	6.468	-0.0758
9	-6.1725	-1.8496	-0.7085
10	2.2503	-7.4147	-0.0842
11	-2.4672	-6.3253	-0.7448
14	5.6471	11.4065	-1.3826
15	-0.1846	-0.1389	0.4626
16	0.941	-3.6476	0.2922
17	-2.8879	-0.68	-1.225
18	13.0426	0.6687	1.6482
19	-4.8221	-1.3103	0.6497
20	3.8635	0.3656	1.304
21	7.6763	-7.5305	-1.4595
	aX = 0	aY = 0	aZ = 0
	mX = 5.3475	mY = 6.5942	mZ = 1.0211

The coordinates of object points (total object points = 22).

Point ID	X	Y	Z	Overlap
2	282770.7841	3836040.306	513.9366	2
3	284811.2327	3836664.069	520.7502	2
5	284756.0898	3834405.915	541.9414	2
6	277183.0924	3830378.339	517.5303	2
7	274194.5965	3828971.43	503.1653	2
8	280719.8222	3834122.44	515.9242	2
9	283145.6034	3832382.052	540.2915	2
10	287282.4681	3835952.336	544.9158	2
11	288430.7648	3838389.776	536.2552	2
14	287372.5102	3830684.406	588.6174	2
15	285435.394	3838458.632	514.4626	2
16	280862.7119	3827360.714	547.2922	2
17	282703.3118	3829896.391	552.425	2
18	283682.0954	3825122.576	586.6482	2
19	276137.9058	3826717.688	521.7147	2
20	276932.8775	3823463.067	531.304	2
21	279532.4031	3824373.555	553.5405	2
24	272048.1275	3830053.63	505.3301	2
26	270391.6323	3823531.337	523.9602	2
27	271425.605	3827752.421	510.6125	2
29	269167.9288	3830053.564	508.0329	2
33	291872.3104	3828507.945	641.6607	2

The residuals of image points

Point	Image	Vx	Vy		Point	Image	Vx	Vy
2	1	-0.187	-0.447		16	1	-0.268	-0.183
2	2	0.125	0.518		16	2	0.248	0.114
3	1	-0.667	-0.356		17	1	-0.654	0.674
3	2	0.829	0.226		17	2	0.73	-0.567
5	1	-0.218	-0.535		18	1	-0.146	-1.023
5	2	0.169	0.422		18	2	-0.23	0.966
6	1	-0.204	0.088		19	1	-0.777	-0.169
6	2	0.362	0.423		19	2	0.916	0.29
7	1	0.183	1.05		20	1	-0.123	-0.707
7	2	-0.094	-0.833		20	2	0.01	0.69
8	1	-0.188	0.26		21	1	-0.843	0.534
8	2	0.362	-0.011		21	2	0.615	-0.625
9	1	0.171	0.414		24	1	0.151	-0.012
9	2	0.012	-0.466		24	2	-0.15	-0.016
10	1	1.235	-0.177		26	1	1.203	-0.101

10	2	-1.293	-0.231		26	2	-1.177	-0.132
11	1	0.572	0.259		27	1	-0.048	0.004
11	2	-0.498	-0.525		27	2	0.047	0.005
14	1	-0.018	0.7		29	1	0.37	-0.032
14	2	-0.179	-0.391		29	2	-0.369	-0.042
15	1	-0.24	-0.198		33	1	0.689	-0.038
15	2	0.251	0.24		33	2	-0.68	-0.057

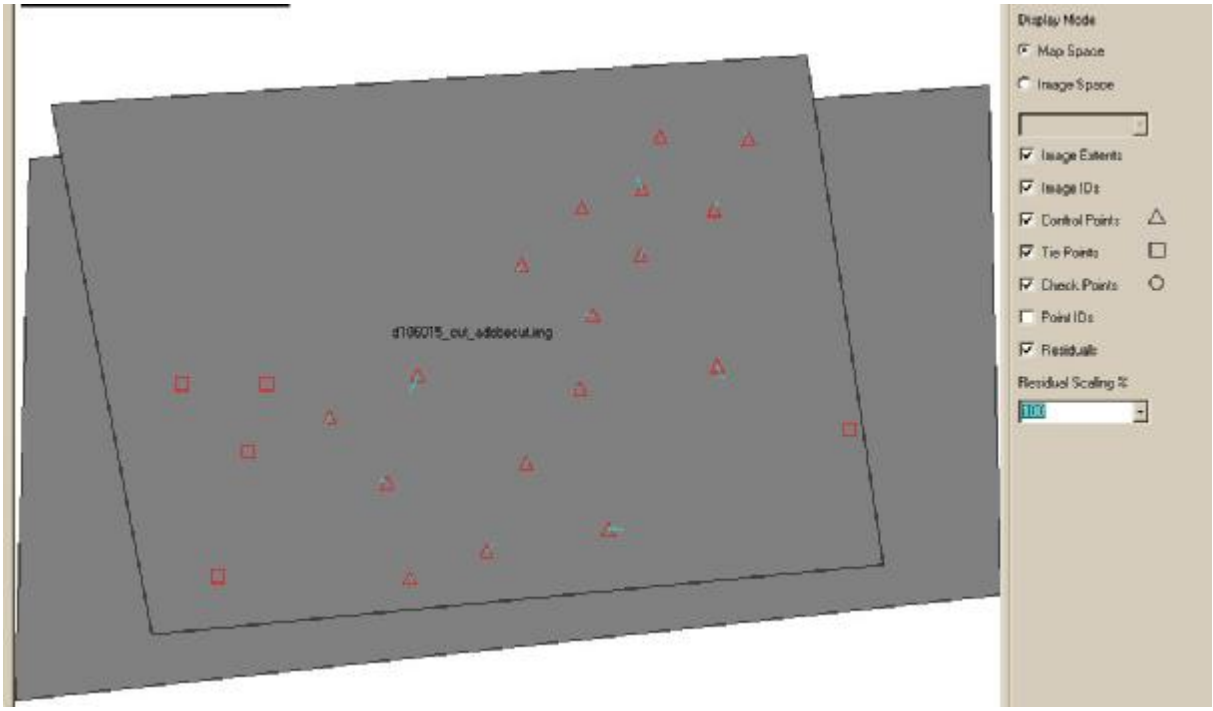

Figure 15-6 – Distribution of GCPs and tie points within the stereopair 008-014.

15.1.8. Mission 1110. Strip of stereopairs

Strip control point error (in pixels): (Total) 9.1609, (X) 18.5102 (43), (Y) 15.0687 (43), (Z) 25.4593 (36), (x) 9.1985 (98), (y) 8.6691 (98).
The triangulation report with OrthoBASE:[62]

The input image coordinates								
Image ID = 1			Image ID = 4			Image ID = 3		
Point ID	x	y	Point ID	x	y	Point ID	x	y
2	8123.849	6146.446	2	6049.125	6639.625	28	7542.536	1299.657
3	7321.676	5231.129	3	5362.375	5699.375	29	8387.744	1107.742
5	6872.909	6328.69	5	4736.375	6838.125	30	10015.17	2651.658
6	6601.359	5440.353	6	4598.375	5918.625	31	8358.314	2055.195
7	5159.458	4956.37	7	3206.375	5426.875	34	8347.44	3637.698
8	4467.354	6427.005	8	2252.625	6951.875	35	6700.771	2025.843
11	3352.203	5424.021	11	1287.125	5915.125	36	7692.272	2836.107
12	3646.075	3968.576	12	1839.875	4431.875	37	9413.147	1496.218
13	4148.149	4107.837	13	2322.375	4572.125	38	9906.496	503.09
24	4520.819	6699.837	21	6013.345	7160.455	41	9428.705	3701.984
23	3783.692	6905.693	90	1129.754	6523.039	42	8651.677	372.984
27	6902.94	6946.411	91	5303.531	6543.051	43	9688.909	4798.77
21	8162.256	6648.04	93	2586.25	6789.379	44	6760.96	4809.048
90	3299.395	6011.271	94	2277.988	6936.362	46	5193.749	6218.507
91	7384.268	6048.199	95	6313.084	6956.674	108	10657.87	208.451
93	4767.557	6272.414	96	6019.933	7007.489	110	9705.875	133.625
94	4489.015	6413.098	98	1693.902	6529.95	111	7882.415	97.225
95	8426.828	6451.365	101	1569.65	6625.462	139	8378.821	796.95
96	8147.898	6498.414	103	2362.778	6840.63	140	10773.6	863.847
107	2693.875	6434.125	104	1777.039	6868.821	142	6473.152	1255.174
106	6614.375	6389.375	106	4461.073	6903.301	144	10427.5	2612.152
104	3990.375	6346.625	107	433.156	6964.09	145	8595.29	2801.376
103	4558.125	6321.375	112	7110.753	6762.236	146	6857.587	2806.06
101	3747.625	6113.125	113	5616.042	6772.921	150	6334.421	4469.903
98	3852.625	6020.375	114	6371.443	6878.395	151	8617.898	4541.354
112	9180.518	6268.595				159	4652.335	6397.01
113	7722.64	6272.599				160	6197.674	6425.575
114	8475.011	6377.998				163	8157.435	1022.113
						164	6689.595	2039.95
						165	8359.625	2048.625
						166	9330.375	898.375
						167	7745.125	21.375
						169	6352.875	3010.875
						171	9459.375	4710.875
						174	5917	5394
						177	10104.16	4242.645

The input image coordinates								
Image ID = 5			Image ID = 6			Image ID = 2		
Point ID	x	y	Point ID	x	y	Point ID	x	y
17	5639.014	6464.354	28	6808.181	1916.071	17	7132.356	5822.626
18	3893.087	6313.985	29	7675.195	1721.072	18	5398.079	5671.912
19	8515.518	1947.293	30	9071.643	3213.272	19	9321.68	1346.126
20	8403.023	1359.318	31	7502.159	2647.87	20	9126.15	742.881
21	8148.408	661.472	34	7245.035	4223.527	21	8768.815	16.456
22	7759.175	1965.668	35	5855.39	2639.175	22	8564.48	1363.193
23	3686.095	1037.956	36	6712.778	3432.283	23	4301.194	393.756
24	4468.99	808.014	37	8639.649	2086.422	24	5056.432	159.224
25	5112.342	1187.503	38	9270.657	1116.931	25	5772.939	557.283

[62] The output image x,y units = pixels. The output angle units = degrees. The output ground X,Y,Z units = meters.

26	4576.215	1785.889	41	8323.214	4275.696	26	5329.694	1172.662
27	6835.357	999.241	42	8049.943	1005.449	27	7485.67	359.329
59	3287.027	3448.409	43	8422.275	5384.618	59	4317.733	2854.093
60	3189.761	4479.075	44	5447.036	5433.372	60	4399.459	3880.87
61	2124.638	6161.377	46	3598.235	6912.861	61	3640.645	5524.803
62	5760.538	4100.044	108	10051.13	823.625	62	6887.4	3511.864
63	7517.86	3806.067	109	9954.625	573.375	63	8589.779	3219.136
64	6888.905	5572.985	110	9124.625	763.625	64	8225.726	4966.093
65	7970.052	6529.958	111	7332.375	747.125	65	9423.385	5898.761
66	9756.149	4435.428	139	7715.635	1418.739	66	10903.37	3861.058
67	1630.946	2285.382	140	10076.46	1457.014	67	2452.892	1683.181
68	602.468	4532.444	142	5754.815	1883.816	68	1846.138	3944.765
2	8183.106	161.132	144	9487.753	3171.181	42	6568.676	6818.711
5	6896.907	376.042	145	7624.638	3385.015	38	7799.661	6973.081
8	4458.665	537.549	146	5881.896	3410.905	108	8535.504	6708.075
93	4787.432	374.421	150	5072.244	5093.124	109	8403.625	6455.375
94	4484.172	522.295	151	7374.625	5135.554	110	7603.125	6615.125
95	8443.987	460.029	159	3006.38	7105.285	111	5814.875	6537.125
96	8155.722	514.768	160	4587.72	7114.108	116	10386.06	642.732
98	3911.398	145.433	163	7463.609	1640.08	117	8704.482	701.306
101	3789.498	240.036	164	5841.795	2652.997	118	1156.765	839.513
103	4568.014	428.286	165	7504.966	2641.899	119	4721.698	848.491
104	3992.285	468.643	166	8642.555	1506.272	120	2801.428	864.072
106	6627.287	444.543	167	7207.729	677.342	121	6635.64	987.677
107	2673.073	589.4	169	5341.177	3619.672	122	8297.624	2644.318
91	7455.125	82.375	171	8201.369	5297.997	123	6442.885	2667.855
90	3358.375	151.875	174	4485.206	6045.751	124	4641.79	2674.313
109	6841.625	7111.125	177	8925.051	4812.603	125	10458.45	2691.668
111	4169.756	7211.129				126	1495.945	2856.607
112	9225.831	261.334				127	2880.159	2882.328
113	7760.181	298.282				128	4724.893	4410.264
114	8500.668	384.381				129	10225.44	4576.424
116	9658.81	1255.217				130	1562.66	4589.557
117	7989.781	1321.217				131	2800.436	4651.142
118	500.601	1453.236				132	8242.87	4694.703
119	4026.123	1472.757				133	6549.871	4743.919
120	2122.522	1492.906				134	10573.93	6105.683
121	5899.349	1604.039				135	4772.745	6167.615
122	7307.771	3231.808				136	8417.648	6243.858
123	5446.477	3258.655				137	6645.654	6249.65
124	3641.841	3273.177				138	2768.055	6329.917
125	9465.433	3266.11				167	5678.875	6463.125
126	456.999	3444.585						
127	1839.283	3470.543						
128	3426.792	5015.495						
129	8976.512	5163.981						
130	189.538	5194.571						
131	1432.935	5253.689						
132	6948.815	5295.632						
133	5221.258	5355.785						
134	9119.317	6735.737						
135	3165.853	6826.372						
136	6890.83	6891.219						
137	5071.83	6908.306						
138	1080.543	6999.628						
167	4042.375	7134.375						

Image ID	A0	A1	A2	B0	B1	B2
1	-51.8400	0.007500	-0.000000	27.5062	0.000000	-0.007500
2	-42.4088	0.007500	0.000000	27.1313	0.000000	-0.007500
3	-50.3287	0.007500	-0.000000	27.3937	0.000000	-0.007500
4	-36.0000	0.007500	-0.000000	26.8687	0.000000	-0.007500
5	-42.2550	0.007500	0.000000	27.2587	0.000000	-0.007500
6	-38.4637	0.007500	0.000000	27.6188	0.000000	-0.007500

THE OUTPUT OF SELF-CALIBRATING BUNDLE BLOCK ADJUSTMENT

the no. of iteration =1 the standard error = 9.1582
the maximal correction of the object points = 85.16162

the no. of iteration =2 the standard error = 9.1547
the maximal correction of the object points = 68.69908

the no. of iteration =3 the standard error = 9.1609
the maximal correction of the object points = 1.08402

the no. of iteration =4 the standard error = 9.1609
the maximal correction of the object points = 0.04321

the no. of iteration =5 the standard error = 9.1609
the maximal correction of the object points = 0.00110

the no. of iteration =6 the standard error = 9.1609
the maximal correction of the object points = 0.00012

The exterior orientation parameters

Image ID	Xs	Ys	Zs	Omega	Phi	Kappa
1	230581.8068	3794401.9222	170571.2817	21.7719	-17.2585	6.2692
2	337770.5962	3899901.1497	173044.3803	-17.3318	16.8164	5.3820
3	337544.8091	3885619.9611	173118.5632	-17.8110	17.4001	5.3542
4	232498.7468	3899196.3826	175809.5578	-11.5482	-16.7000	6.1160
5	344256.9551	3805946.3066	173740.4261	13.5419	18.2083	5.0547
6	226196.0434	3877761.7246	174787.6025	-14.8662	-16.4471	4.3974

The residuals of the control points

Point ID	rX	rY	rZ
2	25.6325	-8.2695	29.3984
3	-5.0321	29.671	17.4168
5	-21.2589	-17.0875	-10.4934
6	-32.2645	14.262	22.8331
7	-39.7685	12.6595	11.2982
8	-18.7572	-10.0885	2.8273
11	62.7367	-0.7515	-28.6255
17	9.8968	-13.9225	3.9962
18	6.1745	14.2254	33.8102
19	4.8584	2.0392	0.2636
20	5.2637	3.7924	4.1146
21	13.3518	-10.3982	32.5015
22	8.8282	6.2454	10.3795
24	-13.6511	9.7248	-7.129
25	12.2028	11.0628	19.2959
26	14.3112	3.5236	24.657
27	-30.3001	6.5038	-63.763
28	9.6363	-0.9312	39.1384
29	-11.9842	-14.7038	-8.3802
30	3.9389	37.8119	34.0548
31	-9.9201	-4.1239	-22.4408
34	-17.5981	-6.6861	-51.7413
36	-15.3706	0.3374	-18.8413
37	-5.7001	9.8486	-1.1293
38	-7.1878	7.5392	-3.6661
41	-5.5096	6.0202	-17.5016
42	-9.1845	-14.3543	0.1056
43	14.3687	-24.0828	14.707
44	-18.4575	-24.3609	-49.0578
46	-1.1113	-8.7715	-0.3973
163	-6.1801	-6.6012	14.7664
165	-8.7126	2.8202	-20.4479

166	-8.9463	0.9388	-11.1246
171	6.375	-17.1742	-14.079
174	-14.3105	-3.5104	-28.9012
177	22.9637	7.5796	45.9137
13	-15.7566	-7.7633	
23	20.8639	-0.4416	
167	9.9308	-16.4739	
169	23.6921	34.6265	
35	22.2183	29.4425	
12	12.1748	-19.3015	
164	13.8105	26.0966	
	aX = 0.1458	aY = 1.0924	aZ = 0.1044
	mX = 18.5102	mY = 15.0687	mZ = 25.4593

The coordinates of object points (total object points = 105)

Point ID	X	Y	Z	Overlap
2	290386.7839	3856457.658	461.7	3
3	288430.5044	3858495.937	444.5	2
5	287378.3706	3855715.489	445.1	3
6	286700.7003	3857812.606	425	2
7	283197.9064	3858647.517	428.65	2
8	281512.3454	3854877.833	445	3
11	278763.6762	3857067.011	435	2
17	286761.7038	3841057.07	510	2
18	282531.7466	3840969.824	493.7	2
19	291850.7863	3852244.473	480	2
20	291365.9067	3853617.249	477	2
21	290500.0768	3855239.198	465	4
22	290062.4461	3852050.315	475	2
24	281652.9608	3854205.765	452.5	3
25	283382.9988	3853398.414	477.5	2
26	282321.3005	3851859.072	485	2
27	287476.4845	3854196.072	450	3
28	282768.6002	3836038.915	513	2
29	284815.7262	3836673.195	520	2
30	288751.5226	3833330.266	582	2
31	284753.8743	3834410.856	541	2
34	284749.1875	3830589.846	568	2
36	283151.7759	3832383.902	541	2
37	287280.2178	3835959.751	545	2
38	288433.232	3838396.101	537	3
41	287366.8631	3830672.999	590	2
42	285435.5786	3838458.771	514	3
43	288010.1418	3828082.673	611	2
44	280861.7709	3827364.362	547	2
46	276929.014	3823462.701	530	2
163	284261.3911	3836824.067	517	2
165	284756.373	3834419.861	541	2
166	287067.9471	3837353.094	530	2
171	287453.3191	3828231.31	606	2
174	278762.8289	3825698.627	543	2
177	288996.883	3829525.586	617	2
13	280718.3005	3860477.856	519.1975	2
23	279818.5713	3853513.75	517.7412	3
167	283244.425	3839112.969	572.2864	4
169	279861.7208	3831662.557	604.4676	2
35	280726.2073	3834115.972	612.8165	2
12	279492.5326	3860702.121	520.4317	2
164	280707.2616	3834083.461	612.9504	2
90	278665.5719	3855603.804	493.028	3
91	288602.9114	3856515.554	442.7541	3
93	282224.168	3855324.665	429.8045	3
94	281548.0613	3854909.397	443.2376	3
95	291158.4992	3855763.354	523.4624	3

96	290477.0862	3855580.798	504.9258	3
107	277194.0877	3854410.19	559.6627	3
106	286726.2437	3855484.713	429.0377	3
104	280334.8405	3854949.636	464.7429	3
103	281713.8881	3855152.776	438.6649	3
101	279748.5855	3855467.844	467.2302	3
98	280004.6395	3855721.176	459.6339	3
112	292992.9479	3856387.227	587.5998	3
113	289431.7101	3856041.856	467.0494	3
114	291270.9074	3855957.648	525.8709	3
59	279880.3943	3847612.819	530.8204	2
60	280081.0936	3845137.728	542.5678	2
61	278199.794	3840918.599	568.4356	2
62	286134.8394	3846594.932	518.9711	2
63	290194.7529	3847663.782	484.1578	2
64	289389.8727	3843394.872	518.905	2
65	292286.6159	3841426.682	519.6299	2
66	295684.531	3846655.087	513.5565	2
67	275302.593	3850054.543	568.0939	2
68	273767.0459	3844412.277	647.048	2
108	290200.7573	3839255.378	562.7522	3
109	289867.9825	3839832.976	532.9764	3
110	287935.2326	3839219.316	511.1517	3
111	283585.0534	3838948.556	564.0641	4
116	294308.2046	3854097.885	491.2253	2
117	290374.9912	3853635.667	477.4934	2
118	272113.3716	3851838.533	613.62	2
119	280857.3288	3852511.251	504.6986	2
120	276159.2039	3852088.563	514.455	2
121	285472.4626	3852559.807	492.8644	2
122	289480.7575	3848970.605	487.6183	2
123	285042.9906	3848521.026	507.0928	2
124	280666.1909	3848111.841	505.3488	2
125	294583.6159	3849321.378	504.0556	2
126	272904.3079	3846997.838	614.3557	2
127	276347.4975	3847238.987	585.8613	2
128	280882.5132	3843921.431	544.3169	2
129	294132.3362	3844800.627	519.8709	2
130	273029.1816	3842742.018	631.8752	2
131	276132.7828	3842889.665	621.6526	2
132	289423.2051	3844053.818	515.1747	2
133	285336.5954	3843531.254	508.8993	2
134	295032.6299	3841213.959	533.7926	2
135	281004.9869	3839610.746	557.5022	2
136	289897.0671	3840343.511	535.1873	2
137	285600.759	3839878.588	529.3763	2
138	276011.0048	3838695.762	590.5855	2
139	284781.3887	3837390.819	518.2186	2
140	290502.4194	3837763.449	614.1366	2
142	280212.6375	3835945.005	659.2238	2
144	289745.4178	3833559.438	652.256	2
145	285325.3751	3832667.119	524.359	2
146	281114.019	3832290.681	568.9822	2
150	279803.9093	3828097.488	536.6226	2
151	285398.4901	3828424.286	519.7013	2
159	275571.108	3822890.911	566.2276	2
160	279407.4016	3823124.411	431.2236	2

The residuals of image points

Point	Image	Vx	Vy		Point	Image	Vx	Vy
2	4	-14.045	-2.376		31	6	7.003	6.272
2	1	-18.826	-2.563		31	3	1.321	-3.886
2	5	-1.964	-3.006		34	6	13.743	7.364
3	4	15.39	14.192		34	3	0.771	0.842
3	1	-18.188	14.05		36	6	8.457	7.398

5	4	15.54	-13.821		36	3	3.94	-1.646
5	1	14.348	-4.321		37	6	1.735	11.974
5	5	-0.007	-2.64		37	3	2.286	-2.996
6	4	18.689	6.518		38	6	3.048	10.024
6	1	0.928	9.964		38	3	3.569	-0.382
7	4	18.065	6.428		38	2	1.296	1.905
7	1	11.232	8.267		41	6	3.985	3.944
8	4	13.805	-8.972		41	3	0.122	5.604
8	1	7.467	0.675		42	6	4.423	-13.973
8	5	2.794	-1.641		42	3	2.53	-0.567
11	4	-27.796	-0.475		42	2	5.449	-2.339
11	1	-18.542	-6.767		43	6	-6.049	-29.765
17	2	-5.146	-6.516		43	3	-4.508	5.154
17	5	-1.057	-5.764		44	6	14.526	-0.571
18	2	0.962	1.339		44	3	1.002	-5.697
18	5	1.808	9.205		46	6	1.072	0.441
19	2	0.838	0.522		46	3	0.472	-7.409
19	5	-5.046	0.456		163	6	1.218	-7.668
20	2	0.19	0.904		163	3	4.446	-0.66
20	5	-3.993	1.732		165	6	5.811	8.599
21	4	-17.752	-16.628		165	3	1.06	-0.982
21	2	1.309	2.121		166	6	4.946	5.354
21	1	-4.16	-7.408		166	3	2.399	-1.487
21	5	-0.684	1.997		171	6	0.251	-20.103
22	2	-1.295	1.15		171	3	-4.622	8.972
22	5	-4.167	3.441		174	6	9.195	7.514
24	2	0.677	-1.678		174	3	1.927	-2.034
24	1	12.666	8.968		177	6	-15.528	-13.469
24	5	1.65	4.916		177	3	-4.365	6.588
25	2	-3.522	2.323		167	6	-2.237	-33.06
25	5	-2.335	6.622		167	3	-10.686	7.742
26	2	-3.006	-1.603		167	2	-3.124	2.275
26	5	-2.542	3.985		167	5	1.964	-4.825
27	2	0.812	-0.015		169	6	-12.003	20.756
27	1	30.193	0.129		169	3	-9.466	6.112
27	5	-0.388	0.909		164	6	-7.388	10.547
28	6	-8.485	-8.58		164	3	-5.622	10.175
28	3	1.122	-1.482		90	4	-4.14	9.051
29	6	6.915	-6.205		90	1	-4.716	-5.971
29	3	3.928	-3.441		90	5	9.25	-2.444
30	6	-8.52	21.351		91	4	5.673	-1.944
30	3	2.404	1.974		91	1	-2.948	2.144
23	2	-8.89	-0.272		91	5	-2.8	0.395
23	1	-9.144	6.112		93	4	5.825	-6.578
23	5	-7.725	-8.637		93	1	1.085	3.141
13	4	-1.217	-4.223		93	5	-7.078	3.356
13	1	15.184	-2.109		94	4	5.311	-5.427
12	4	-19.825	-11.773		94	1	0.463	3.313
12	1	11.585	-7.677		94	5	-5.965	2.09
35	6	-11.076	11.449		95	4	-6.227	3.616
35	3	-9.062	11.474		95	1	1.827	-4.139
59	2	0.608	-0.04		95	5	4.382	0.047
59	5	-0.606	-0.064		96	4	-4.939	-0.499
60	2	-0.26	0.017		96	1	4.557	-2.277
60	5	0.257	0.027		96	5	0.533	1.909
61	2	-0.51	0.035		98	4	-0.364	2.616
61	5	0.499	0.054		98	1	-2.088	-3.044
62	2	0.029	-0.002		98	5	2.561	0.746
62	5	-0.029	-0.003		101	4	0.098	3.858
63	2	1.259	-0.066		101	1	-3.601	-3.42
63	5	-1.254	-0.116		101	5	3.625	0.097
64	2	-0.383	0.021		103	4	5.742	-5.213
64	5	0.377	0.036		103	1	-0.097	2.535
65	2	-0.679	0.034		103	5	-5.82	2.759
65	5	0.665	0.06		104	4	3.63	0.18

66	2	1.626	-0.072		104	1	-3.218	0.661
66	5	-1.616	-0.138		104	5	-0.505	-0.356
67	2	1.295	-0.093		106	4	5.211	-10.762
67	5	-1.299	-0.146		106	1	5.508	4.496
68	2	2.122	-0.158		106	5	-10.585	5.52
68	5	-2.097	-0.24		107	4	-2.165	18.314
120	2	0.697	-0.049		107	1	-14.607	-6.119
120	5	-0.703	-0.078		107	5	17.457	-10.211
121	2	-0.624	0.036		108	6	0.192	11.973
121	5	0.63	0.062		108	3	1.701	-9.091
122	2	0.679	-0.036		108	2	-1.95	-2.654
122	5	-0.679	-0.063		109	6	-1.622	6.869
123	2	-0.234	0.014		109	2	-1.286	-4.184
123	5	0.234	0.023		109	5	2.929	-2.499
124	2	0.363	-0.024		110	6	-0.029	0.052
124	5	-0.363	-0.038		110	3	0.438	-0.257
125	2	2.502	-0.115		110	2	-0.426	0.21
125	5	-2.505	-0.217		111	6	1.508	-22.257
126	2	2.381	-0.179		111	3	-5.422	11.737
126	5	-2.369	-0.273		111	2	0.067	8.202
127	2	0.546	-0.039		111	5	3.736	3.367
127	5	-0.544	-0.06		112	4	-9.157	19.91
128	2	-0.462	0.03		112	1	-10.845	-7.561
128	5	0.456	0.048		112	5	18.947	-10.843
129	2	1.78	-0.083		113	4	1.277	-0.857
129	5	-1.76	-0.154		113	1	-0.284	-0.188
130	2	2.019	-0.152		113	5	-0.969	1.111
130	5	-1.986	-0.23		114	4	-4.932	6.574
131	2	0.379	-0.027		114	1	-1.99	-5.054
131	5	-0.373	-0.042		114	5	6.734	-1.361
132	2	0.455	-0.024		116	2	1.458	-0.067
132	5	-0.449	-0.042		116	5	-1.479	-0.128
133	2	-0.646	0.038		117	2	0.714	-0.037
133	5	0.637	0.063		117	5	-0.723	-0.066
134	2	0.727	-0.033		118	2	2.22	-0.168
134	5	-0.712	-0.062		118	5	-2.238	-0.26
135	2	-1.49	0.097		119	2	-0.507	0.033
135	5	1.453	0.153		119	5	0.512	0.053
136	2	-0.548	0.029		146	6	-0.014	5.234
136	5	0.535	0.05		146	3	0.077	-5.26
137	2	-1.598	0.095		150	6	0.025	7.134
137	5	1.559	0.155		150	3	0.152	-7.206
138	2	-0.135	0.01		151	6	-0.021	-6.654
138	5	0.132	0.015		151	3	-0.144	6.606
139	6	0.044	-4.269		159	6	0.105	9.749
139	3	-0.03	4.236		159	3	0.288	-9.987
140	6	-0.126	13.381		160	6	-0.108	-10.921
140	3	0.085	-13.043		160	3	-0.328	11.056
142	6	0.08	-9.257		145	6	-0.015	5.545
142	3	-0.085	9.32		145	3	0.08	-5.5
144	6	-0.032	9.555					
144	3	0.126	-9.347					

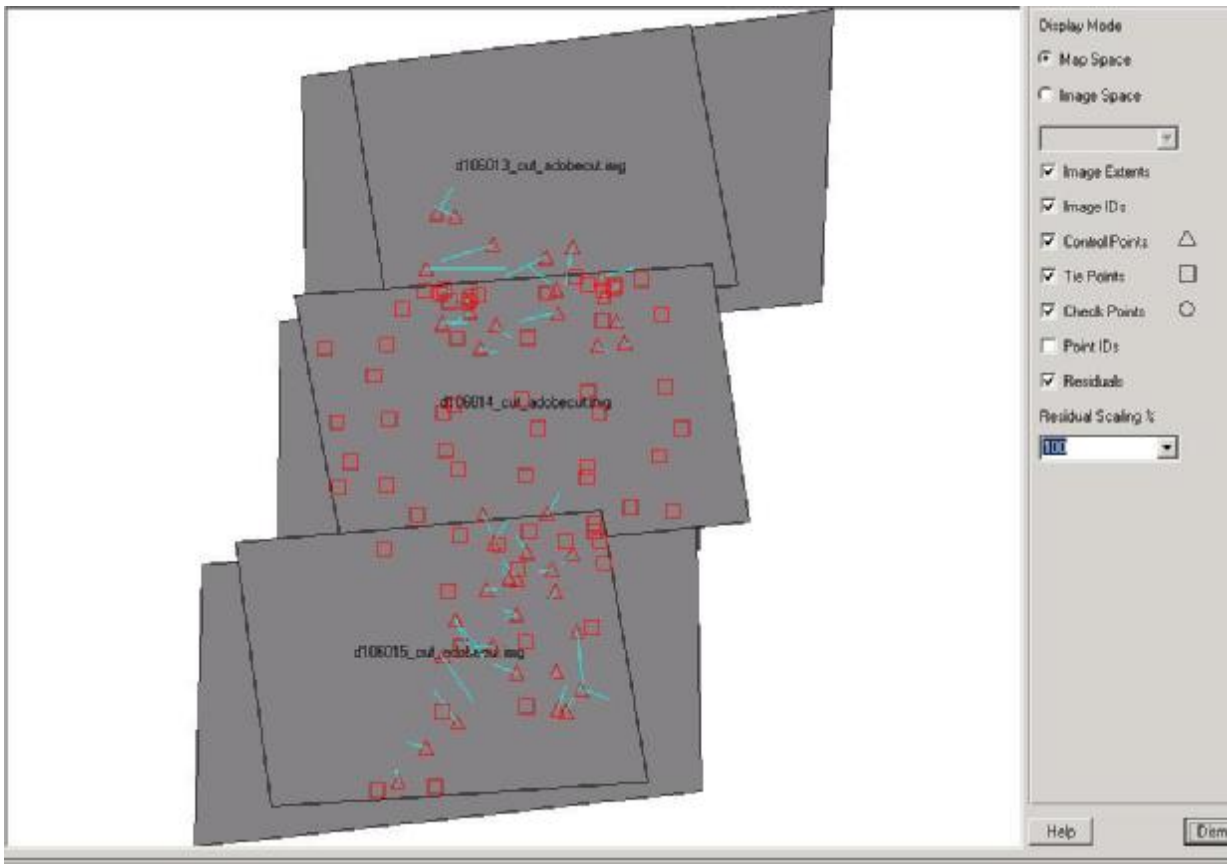

Figure 15-7 – Distribution of GCPs and tie points within the strip of stereopairs 007-013, 008-014, 009-015.

.